

# **HANDBOOK OF PLASMA PROCESSING TECHNOLOGY**

**Fundamentals, Etching, Deposition,  
and Surface Interactions**

Edited by

**Stephen M. Rossnagel**

IBM Thomas J. Watson Research Center  
Yorktown Heights, New York

**Jerome J. Cuomo**

IBM Thomas J. Watson Research Center  
Yorktown Heights, New York

**William D. Westwood**

Bell-Northern Research  
Ottawa, Canada



**NOYES PUBLICATIONS**

**Park Ridge, New Jersey, U.S.A.**

**Copyright © 1990 by Noyes Publications**

**No part of this book may be reproduced or utilized in any form or by any means, electronic or mechanical, including photocopying, recording or by any information storage and retrieval system, without permission in writing from the Publisher.**

**Library of Congress Catalog Card Number: 89-22834**

**ISBN: 0-8155-1220-1**

**Printed in the United States**

**Published in the United States of America by**

**Noyes Publications**

**Mill Road, Park Ridge, New Jersey 07656**

**10 9 8 7 6**

**Library of Congress Cataloging-in-Publication Data**

**Handbook of plasma processing technology : fundamentals, etching, deposition, and surface interactions / edited by Stephen M. Rossnagel, Jerome J. Cuomo, William D. Westwood.**

**p. cm.**

**Includes bibliographical references.**

**ISBN 0-8155-1220-1 :**

**1. Plasma engineering. 2. Semiconductors--Etching. 3. Plasma etching. I. Rossnagel, Stephen M. II. Cuomo, J.J. III. Westwood, William D. (William Dickson), 1937-  
TA2020.H37 1989  
621.044--dc19**

**89-22834**

**CIP**

## **MATERIALS SCIENCE AND PROCESS TECHNOLOGY SERIES**

### *Editors*

Rointan F. Bunshah, University of California, Los Angeles (*Materials Science and Technology*)

Gary E. McGuire, Microelectronics Center of North Carolina (*Electronic Materials and Processing*)

**DEPOSITION TECHNOLOGIES FOR FILMS AND COATINGS:** by *Rointan F. Bunshah et al*

**CHEMICAL VAPOR DEPOSITION IN MICROELECTRONICS:** by *Arthur Sherman*

**SEMICONDUCTOR MATERIALS AND PROCESS TECHNOLOGY HANDBOOK:** edited by *Gary E. McGuire*

**SOL-GEL TECHNOLOGY FOR THIN FILMS, FIBERS, PREFORMS, ELECTRONICS AND SPECIALTY SHAPES:** edited by *Lisa A. Klein*

**HYBRID MICROCIRCUIT TECHNOLOGY HANDBOOK:** by *James J. Licari* and *Leonard R. Enlow*

**HANDBOOK OF THIN FILM DEPOSITION PROCESSES AND TECHNIQUES:** edited by *Klaus K. Schuegraf*

**IONIZED-CLUSTER BEAM DEPOSITION AND EPITAXY:** by *Toshinori Takagi*

**DIFFUSION PHENOMENA IN THIN FILMS AND MICROELECTRONIC MATERIALS:** edited by *Devendra Gupta* and *Paul S. Ho*

**SHOCK WAVES FOR INDUSTRIAL APPLICATIONS:** edited by *Lawrence E. Murr*

**HANDBOOK OF CONTAMINATION CONTROL IN MICROELECTRONICS:** edited by *Donald L. Tolliver*

**HANDBOOK OF ION BEAM PROCESSING TECHNOLOGY:** edited by *Jerome J. Cuomo, Stephen M. Rossnagel, and Harold R. Kaufman*

**FRICTION AND WEAR TRANSITIONS OF MATERIALS:** by *Peter J. Blau*

**CHARACTERIZATION OF SEMICONDUCTOR MATERIALS—Volume 1:** edited by *Gary E. McGuire*

**SPECIAL MELTING AND PROCESSING TECHNOLOGIES:** edited by *G.K. Bhat*

**HANDBOOK OF PLASMA PROCESSING TECHNOLOGY:** edited by *Stephen M. Rossnagel, Jerome J. Cuomo, and William D. Westwood*

### **Related Titles**

**ADHESIVES TECHNOLOGY HANDBOOK:** by *Arthur H. Landrock*

**HANDBOOK OF THERMOSET PLASTICS:** edited by *Sidney H. Goodman*

**SURFACE PREPARATION TECHNIQUES FOR ADHESIVE BONDING:** by *Raymond F. Wegman*

This book is dedicated to the memory of Professor John Thornton of the University of Illinois, and formerly of Telic Corporation. John was a pioneer, an innovator, and a tireless teacher in the fields of sputtering and thin film technology. He was a colleague and friend of each of the editors and the majority of contributing authors to this book. His intelligence, integrity, and dedication have touched many of us.



---

## Preface

---

The field of plasma-based thin film processing has grown rapidly over the past two decades. The technologies discussed in this book are the basis for the revolutionary increase in computer capabilities, as well as for such applications as tool coatings, food packaging and architectural coatings on skyscraper windows.

Plasma processing technology has a number of manifestations, from simple dc discharges up to the complicated electron cyclotron resonance (ECR) plasmas intended for single wafer processing. Films are deposited and etched by a range of devices, including rf diodes, magnetrons, broad beam ion sources, hollow cathode sources and more. Each of these techniques can operate in primarily non-chemical modes with inert gases, or can easily be switched to reactive modes, where a surface can be chemically eroded or a specific chemical compound deposited. A number of hybrid technologies have emerged, such as ion plating, ion cluster beam and activated, reactive evaporation deposition techniques.

In addition to simply the plasma process, a wealth of knowledge has been generated on ion-surface interactions. The impact of ions at many times the thermal energy of the surface can strongly change the structure as well as the chemistry of the surface. Techniques such as these allow one to explore materials not available in bulk form, and to produce new compounds, phases or structures.

Much remains to be accomplished in terms of plasma-based processing technologies. The fundamental understanding of the plasma itself is still at a crude level; the most sophisticated models are making progress in understanding the operation of simple rf diode plasmas. Classical plasma physics, as it applies to, perhaps, high temperature fusion plasmas, is beginning to make some sense of processing plasmas. However, the application of magnetic fields and the practical situation of using reactive, molecular species in the plasmas dramatically complicates the level of understanding.

This book is intended to provide a perspective look at a range of thin film plasma processing technologies. The authors were selected to represent the state-of-the-art understanding. The chapters are not just the classical review-type chapter found in many texts, but provide a more concise view of the level of understanding of the field today, without wading through the entire history of each field.

Yorktown Heights, NY  
October, 1989

Stephen M. Rossnagel

---

## About the Editors

---

**Stephen M. Rossnagel** is presently a research staff member at the IBM T.J. Watson Research Center, Yorktown Heights, New York. His current research is in plasma-based processing, particularly in ion beam and magnetron areas. He received his doctorate in physics from Colorado State University, and has held positions at Princeton University and at the Max Planck Institute in Garching, West Germany. Dr. Rossnagel has published extensively in areas of magnetron sputtering and also film modification by ion bombardment. He has published over 58 research papers and book chapters, and co-edited two books. He is the author of 6 patents, and is chairman of the Plasma Science Technology Division of the American Vacuum Society.

**Jerome J. Cuomo** is presently Manager of the Materials Processing Laboratory at the IBM T.J. Watson Research Center, Yorktown Heights, New York. Dr. Cuomo received his Ph.D. at Odense University and is particularly involved in the study of materials and the processing of materials by sputtering, ion beam and plasma processes. He has made important contributions to the development of  $\text{LaB}_6$  electron emitters and  $\text{Si}_3\text{N}_4$  as dielectric layers, and also pioneered work in chemical vapor deposition, dendritic solar thermal absorbers, sputtered amorphous silicon, amorphous magnetic bubble domain materials, ion beam modification and synthesis of materials, enhanced plasma processes, and high  $T_c$  superconductors. Dr. Cuomo has been active in various capacities in the American Vacuum Society and the Materials Research Society. He is a member of the Advisory Committee to the Materials Science Department of North Carolina State University and Pennsylvania State University and is an Adjunct Professor at Cornell University. He is the author or co-author of 56 patents, 197 patent publications and 85 research papers, chapters in several books and is co-editor of two books. He is distinguished by having the highest patent level in the IBM Corporation.

**William D. Westwood** is presently Manager of Advanced Materials and Devices at Bell-Northern Research's Advanced Technology Laboratory, Ottawa, Canada. He received his Ph.D. from the University of Aberdeen, Scotland in solid state physics. He then joined Northern Electric R&D Laboratory to work on magnetic oxide ceramics, and developed sputtering methods for fabricating thin films of these oxides. His research interests have centered on this technique since then. From 1966 to 1968, he was a faculty member at Flinders University in Australia. In 1969, he headed a group at Bell-Northern Research studying thin films for hybrid circuits, and from the sputtering aspects of this work evolved research on integrated optics. He has also been involved in technology research for electronic office applications, such as facsimile and displays. Since 1982, he has been involved in III-V semiconductor device technology for high speed electronics and optoelectronics. He has co-authored over 100 technical papers, co-edited a book, and has more than 20 patents. He has served the American Vacuum Society as a director, and is presently the Clerk of the society.

---

## Contributors

---

**Jes Asmussen**  
Michigan State University  
East Lansing, MI

**Soren Berg**  
University of Uppsala  
Uppsala, Sweden

**Rointan F. Bunshah**  
University of California, Los Angeles  
Los Angeles, CA

**Joseph L. Cecchi**  
Princeton University  
Princeton, NJ

**Chandra V. Deshpandey**  
University of California, Los Angeles  
Los Angeles, CA

**David B. Fraser**  
Intel Corporation  
Santa Clara, CA

**David W. Hoffman**  
Ford Research Center  
Dearborn, MI

**Chris M. Horwitz**  
University of New South Wales  
Kennsington, Australia

**Harold R. Kaufman**  
Front Range Research  
Fort Collins, CO

**Roger Kelly**  
IBM, Thomas J. Watson Research  
Center  
Yorktown Heights, NY

**Joseph S. Logan**  
IBM, Thomas J. Watson Research  
Center  
Yorktown Heights, NY

**Gerald Lucovsky**  
North Carolina State University  
Raleigh, NC

**Robert J. Markunas**  
Research Triangle Institute  
Research Triangle Park, NC

**Donald M. Mattox**  
Sandia National Laboratories  
Albuquerque, NM

**Robert C. McCune**  
Ford Research Center  
Dearborn, MI

**James J. McNally**  
U.S. Air Force Academy  
U.S. Air Force Academy, CO

**Russell Messier**  
Pennsylvania State University  
University Park, PA

**Claes Nender**  
University of Uppsala  
Uppsala, Sweden

**Gottlieb S. Oehrlein**  
IBM, Thomas J. Watson Research  
Center  
Yorktown Heights, NY

**Lawrence J. Pilione**  
Pennsylvania State University  
University Park, PA

**Rafael Reif**  
Massachusetts Institute of Technology  
Cambridge, MA

**Raymond S. Robinson**  
Colorado State University  
Fort Collins, CO

**Stephen M. Rossnagel**  
IBM, Thomas J. Watson Research  
Center  
Yorktown Heights, NY

**David N. Ruzic**  
University of Illinois  
Urbana, IL

**David Sanders**  
Lawrence Livermore National  
Laboratory  
Livermore, CA

**David V. Tsu**  
North Carolina State University  
Raleigh, NC

**William D. Westwood**  
Bell-Northern Research  
Ottawa, Canada

**Isao Yamada**  
Kyoto University  
Sakyo, Kyoto, Japan

**Joseph E. Yehoda**  
Pennsylvania State University  
University Park, PA

## NOTICE

To the best of the Publisher's knowledge the information contained in this book is accurate; however, the Publisher assumes no responsibility nor liability for errors or any consequences arising from the use of the information contained herein. Final determination of the suitability of any information, procedure, or product for use contemplated by any user, and the manner of that use, is the sole responsibility of the user. The book is intended for informational purposes only. Expert advice should be obtained at all times before implementation of any procedure described or implied in the book, and caution should be exercised in the use of any materials or procedures for plasma processing which could be potentially hazardous.

---

# Contents

---

## PART I GENERAL INFORMATION

<b>1. TECHNIQUES FOR IC PROCESSING . . . . .</b>	<b>2</b>
<i>David B. Fraser and William D. Westwood</i>	
<b>1.1 Introduction. . . . .</b>	<b>2</b>
<b>1.2 Plasma Processing in Microelectronics . . . . .</b>	<b>4</b>
1.2.1 Cleaning . . . . .	7
1.2.2 Deposition . . . . .	7
1.2.2.1 Sputtering . . . . .	7
1.2.2.2 Reactive Sputtering . . . . .	9
1.2.2.3 Step Coverage. . . . .	9
1.2.2.4 PECVD . . . . .	10
1.2.2.5 Etching . . . . .	11
<b>1.3 Summary. . . . .</b>	<b>12</b>

## PART II PLASMA FUNDAMENTALS

<b>2. INTRODUCTION TO PLASMA CONCEPTS AND DISCHARGE CONFIGURATIONS . . . . .</b>	<b>14</b>
<i>Joseph L. Cecchi</i>	
<b>2.1 Introduction. . . . .</b>	<b>14</b>
2.1.1 The Plasma State. . . . .	14
2.1.2 Brief Survey of Plasmas . . . . .	15
2.1.3 Plasmas for Thin Film Deposition and Etching . . . . .	16
2.1.4 An Elementary View of Plasma Reactors . . . . .	17
2.1.4.1 Planar Reactors. . . . .	18
2.1.4.2 Barrel Reactors. . . . .	19

2.1.4.3 Downstream Plasma Reactors . . . . .	20
<b>2.2 Fundamental Plasma Discharge Concepts . . . . .</b>	<b>20</b>
2.2.1 Debye Shielding . . . . .	20
2.2.2 Plasma Oscillations . . . . .	23
2.2.3 Particle Orbits. . . . .	24
2.2.3.1 Effects of Electric and Magnetic Fields . . . . .	24
2.2.3.2 Adiabatic Invariants. . . . .	27
2.2.4 Collisional Processes. . . . .	30
2.2.4.1 Electron-Neutral Elastic Collisions . . . . .	31
2.2.4.2 Electron-Electron Collisions . . . . .	32
2.2.4.3 Electron Impact Inelastic Collisions . . . . .	33
2.2.4.4 Ion Collision Processes . . . . .	35
2.2.5 Diffusion and Particle Losses . . . . .	36
2.2.6 Sheaths . . . . .	36
2.2.6.1 Non-Conducting or Isolated Surfaces. . . . .	36
2.2.6.2 Sheath Near a Conducting Electrode . . . . .	37
<b>2.3 Electron Heating and Energy Distribution . . . . .</b>	<b>38</b>
2.3.1 Interaction of Electrons with a Static Electric Field . . . . .	38
2.3.2 Interaction of Electrons with a Time Dependent Electric Field and Magnetic Field . . . . .	43
2.3.3 Interaction of Electrons with a Time Dependent Electric Field in the Presence of a Static Magnetic Field . . . . .	45
2.3.4 The Electron Energy Distribution Function . . . . .	46
<b>2.4 Breakdown. . . . .</b>	<b>47</b>
2.4.1 DC Breakdown . . . . .	47
2.4.2 RF Breakdown . . . . .	50
<b>2.5 Glow Discharges . . . . .</b>	<b>51</b>
2.5.1 DC Glow Discharge . . . . .	51
2.5.1.1 The Cathode Region . . . . .	52
2.5.1.2 Secondary Electron Generation . . . . .	53
2.5.1.3 Ionization in the Cathode Sheath . . . . .	53
2.5.1.4 Ion Charge Exchange in the Cathode Sheath. . . . .	54
2.5.1.5 The Anode Sheath. . . . .	54
2.5.1.6 The Negative Glow Region . . . . .	54
2.5.1.7 Beyond the Negative Glow . . . . .	55
2.5.1.8 The Positive Column . . . . .	57
2.5.1.9 Summary of the dc Glow Discharge . . . . .	58
2.5.2 RF Glow . . . . .	58
2.5.2.1 Self Bias and Plasma Potential . . . . .	59
2.5.2.2 Discharge Characteristics. . . . .	65
2.5.2.3 RF Discharge Modeling. . . . .	65
2.5.2.4 Summary of the rf Glow Discharge . . . . .	66
<b>2.6 References . . . . .</b>	<b>66</b>
<b>3. FUNDAMENTALS OF SPUTTERING AND REFLECTION . . . . .</b>	<b>70</b>
<i>David N. Ruzic</i>	
<b>3.1 Introduction. . . . .</b>	<b>70</b>
3.1.1 Sputtering Regimes . . . . .	70



<b>3.2 Modeling</b>	72
3.2.1 TRIM	72
3.2.2 Fractals	73
3.2.3 Fractal TRIM	74
3.2.4 Reflection	76
3.2.5 Molecular Dynamics	77
<b>3.3 Experimental Yields</b>	81
<b>3.4 Exceptions</b>	85
<b>3.5 References</b>	87

#### **4. BOMBARDMENT-INDUCED COMPOSITIONAL CHANGE WITH ALLOYS, OXIDES, OXYSALTS, AND HALIDES . . . . . 91**

*Roger Kelly*

<b>4.1 Introduction</b>	4
4.1.1 The Early Situation	91
4.1.2 Bombardment-Induced (Gibbsian) Segregation, BIS	93
4.1.3 Bombardment-Induced Mixing	95
4.1.4 Bombardment-Induced Decomposition	96
4.1.5 Redistribution	97
4.1.6 Surface Binding Energies of Oxides and Halides	98
4.1.7 General Comments	100
<b>4.2 The Role of the Surface Binding Energy</b>	100
4.2.1 The Surface Binding Energy in Cascade Sputtering	100
4.2.2 The Bulk Binding Energy, $W$	102
4.2.3 The Surface Binding Energy for Alloys	103
4.2.4 Application to Compositional Change with Alloys	104
4.2.5 The Surface Binding Energy for Oxides and Halides	107
4.2.5.1 Cation Atom Binding	108
4.2.5.2 Anion Atom Binding	108
4.2.6 Application to Compositional Change with Oxides	109
4.2.6.1 Metal Atom Yields from Oxides	109
4.2.6.2 Preferential Effects	109
<b>4.3 The Role of Segregation</b>	111
4.3.1 Equilibrium Segregation	111
4.3.2 Bombardment-Induced Segregation, BIS	112
4.3.3 Evaluation of $K_b$	115
4.3.4 Application to Compositional Change with Alloys	120
<b>4.4 The Role of Bombardment-Induced Decomposition</b>	121
4.4.1 General Comments	121
4.4.2 Surface Binding Energy	127
4.4.3 Stochastic Rearrangement	127
4.4.4 Energy-Limited Rearrangement	127
4.4.4.1 Mass Differences	127
4.4.4.2 Bombardment-Induced Amorphization	128
4.4.4.3 Point-Defect Accumulation	128
4.4.4.4 Volatility, Diffusional Transport, BIS	128
4.4.5 Equilibrium Rearrangement	128
<b>4.5 Overview</b>	130

<b>4.6 References . . . . .</b>	<b>131</b>
---------------------------------	------------

### PART III NON-REACTIVE PLASMA PROCESSES

<b>5. RF DIODE SPUTTER ETCHING AND DEPOSITION . . . . .</b>	<b>140</b>
---	------------

*Joseph S. Logan*

<b>5.1 Introduction. . . . .</b>	<b>140</b>
5.1.1 History . . . . .	140
<b>5.2 RF Discharges. . . . .</b>	<b>141</b>
5.2.1 Breakdown. . . . .	141
5.2.2 RF Self-Bias . . . . .	141
5.2.3 Frequency Effect . . . . .	143
5.2.4 Electrical Models. . . . .	143
<b>5.3 Equipment. . . . .</b>	<b>146</b>
5.3.1 System Designs . . . . .	146
5.3.2 Cathode Design. . . . .	148
5.3.3 RF Power Supply . . . . .	149
5.3.4 Matching Networks . . . . .	150
<b>5.4 RF Sputter-Deposition . . . . .</b>	<b>151</b>
5.4.1 Direct rf Sputter-Deposition . . . . .	151
5.4.2 Film Composition . . . . .	152
5.4.3 Substrate Bias Effects. . . . .	152
5.4.4 Material Transport and Uniformity . . . . .	153
<b>5.5 Sputter Etching Applications. . . . .</b>	<b>154</b>
5.5.1 Comparison to dc Sputter-Etching . . . . .	154
5.5.2 Surface Cleaning . . . . .	154
5.5.3 Patterning . . . . .	154
5.5.4 Uniformity. . . . .	155
<b>5.6 Practical Matters . . . . .</b>	<b>155</b>
5.6.1 Power Measurements and Power Loss . . . . .	155
5.6.2 Current Measurement. . . . .	156
5.6.3 Voltage Measurement. . . . .	157
5.6.4 Rate Measurement. . . . .	157
5.6.5 RF Leakage . . . . .	157
<b>5.7 References . . . . .</b>	<b>157</b>

<b>6. MAGNETRON PLASMA DEPOSITION PROCESSES . . . . .</b>	<b>160</b>
---	------------

*Stephen M. Rossnagel*

<b>6.1 Introduction. . . . .</b>	<b>160</b>
<b>6.2 Experiments. . . . .</b>	<b>163</b>
6.2.1 Sputtering at the Cathode Surface . . . . .	163
6.2.2 Gas Rarefaction Effects . . . . .	164
6.2.3 Plasma Measurements. . . . .	166
6.2.4 Interactions: Effects on Plasma . . . . .	169
6.2.5 Interactions: Effects on Sputtered Material . . . . .	171
6.2.6 Interactions at the Sample Surface . . . . .	176
<b>6.3 Summary. . . . .</b>	<b>180</b>

6.4 References . . . . .	181
<b>7. BROAD-BEAM ION SOURCES . . . . .</b>	<b>183</b>
<i>Harold R. Kaufman and Raymond S. Robinson</i>	
7.1 Introduction . . . . .	183
7.2 Gridded Ion Sources . . . . .	184
7.2.1 General Description . . . . .	184
7.2.2 Present Technology . . . . .	185
7.3 Gridless Ion Sources . . . . .	187
7.3.1 General Description . . . . .	187
7.3.2 Present Technology . . . . .	192
7.4 Concluding Remarks . . . . .	192
7.5 References . . . . .	192

## PART IV REACTIVE PLASMA PROCESSES

<b>8. REACTIVE ION ETCHING . . . . .</b>	<b>196</b>
<i>Gottlieb S. Oehrlein</i>	
8.1 Introduction . . . . .	196
8.1.1 Basic RIE Apparatus and Reaction Steps . . . . .	196
8.1.2 RIE Processes in Semiconductor Technology . . . . .	198
8.2 Etch Directionality . . . . .	200
8.2.1 General Considerations . . . . .	200
8.2.2 Fluorine-vs. Chlorine-vs. Bromine-Based Plasmas . . . . .	200
8.2.3 Doping Effect . . . . .	202
8.2.4 Etch Directionality Through Sidewall Passivation . . . . .	203
8.2.5 Aspect Ratio Dependence of Etch Rate . . . . .	205
8.3 Plasma Chemical Considerations . . . . .	206
8.3.1 Effect of Oxygen Addition . . . . .	206
8.3.2 Effect of Hydrogen Addition . . . . .	209
8.3.3 Other Gas Additives . . . . .	209
8.3.4 Loading Effect . . . . .	209
8.4 Etch Selectivity . . . . .	211
8.4.1 General Considerations . . . . .	211
8.4.2 Silicon Dioxide to Silicon Etch Selectivity . . . . .	212
8.4.3 Silicon to Silicon Dioxide Etch Selectivity . . . . .	215
8.5 Contamination and Damage Issues . . . . .	215
8.5.1 Survey of RIE Damage Effects . . . . .	215
8.5.2 Silicon Surface Modifications Due to Selective SiO <sub>2</sub> ; Si RIE . . . . .	217
8.5.3 Etch Rate Dependence of Lattice Damage . . . . .	219
8.5.4 Post-RIE Surface Recovery Treatments . . . . .	220
8.6 Reactor, Equipment Considerations . . . . .	221
8.6.1 Reactor Types . . . . .	221
8.6.2 Reactor Materials . . . . .	221
8.6.3 Chamber Cleanliness, Process Reproducibility Issues . . . . .	222
8.6.4 Single Wafer vs. Batch Reactors . . . . .	223

8.7	<b>End Point Detection and Plasma Diagnostics</b> . . . . .	225
8.7.1	General Considerations . . . . .	225
8.7.2	Laser Interferometry, Reflectance . . . . .	225
8.7.3	Optical Emission Spectroscopy . . . . .	225
8.8	<b>Current Trends</b> . . . . .	226
8.9	<b>References</b> . . . . .	228
9.	<b>REACTIVE SPUTTER DEPOSITION</b> . . . . .	233
	<i>William D. Westwood</i>	
9.1	<b>Introduction</b> . . . . .	233
9.2	<b>Plasma-Based Sputtering Techniques: Hysteresis Effects</b> . . . . .	233
9.3	<b>Reaction Kinetics: Models</b> . . . . .	237
9.4	<b>Sputtered Species</b> . . . . .	237
9.4.1	Cluster Emission . . . . .	237
9.4.2	Negative Ion Emission . . . . .	238
9.5	<b>Plasma-Based Sputtering Systems</b> . . . . .	240
9.5.1	Diode Systems . . . . .	240
9.5.2	Magnetron Systems . . . . .	243
9.5.3	Modified Magnetron Systems . . . . .	249
9.5.4	Monitoring Systems . . . . .	252
9.6	<b>Reactive Sputter Deposition with Ion Beams</b> . . . . .	255
9.7	<b>Conclusions</b> . . . . .	256
9.8	<b>References</b> . . . . .	257
10.	<b>PLASMA ENHANCED CHEMICAL VAPOR DEPOSITION OF THIN FILMS FOR MICROELECTRONICS</b> . . . . .	260
	<i>Rafael Reif</i>	
10.1	<b>Introduction</b> . . . . .	260
10.2	<b>Nonequilibrium Glow Discharges</b> . . . . .	261
10.3	<b>Potentials in RF Glow Discharges</b> . . . . .	263
10.4	<b>Qualitative Model for PECVD</b> . . . . .	266
10.5	<b>Commercial PECVD Systems</b> . . . . .	269
10.6	<b>PECVD of Dielectric Films</b> . . . . .	271
10.7	<b>PECVD of Polycrystalline Silicon Films</b> . . . . .	273
10.8	<b>PECVD of Epitaxial Films</b> . . . . .	274
10.8.1	Silicon . . . . .	274
10.8.2	Gallium Arsenide . . . . .	277
10.9	<b>PECVD of Refractory Metals and Their Silicides</b> . . . . .	277
10.9.1	Refractory Metals . . . . .	277
10.9.2	Refractory Metal Silicides . . . . .	278
10.10	<b>PECVD of Diamond Films</b> . . . . .	279
10.11	<b>Other Plasma Deposition Configurations</b> . . . . .	279
10.12	<b>Summary</b> . . . . .	280
10.13	<b>References</b> . . . . .	280
11.	<b>ELECTRON CYCLOTRON RESONANCE MICROWAVE DISCHARGES FOR ETCHING AND THIN FILM DEPOSITION</b> . . . . .	285
	<i>Jes Asmussen</i>	

11.1	Introduction. . . . .	285
11.2	Energy Coupling and Power Balance in Steady State Microwave Discharges. . . . .	286
11.3	Microwave Energy Coupling vs Pressure in a Uniform Magnetic Field Gradient . . . . .	290
11.4	Microwave Energy Coupling in a Nonuniform Static Magnetic Field . . . . .	292
11.5	Microwave System Considerations . . . . .	293
11.6	Fundamental ECR Applicator Configurations . . . . .	296
11.6.1	Waveguide Applicators . . . . .	297
11.6.2	Cavity Applicators. . . . .	299
11.7	Microwave Plasma Processing Reactors . . . . .	301
11.8	Discharge Characteristics. . . . .	304
11.9	Discussion . . . . .	305
11.10	References . . . . .	306
12.	HOLLOW CATHODE ETCHING AND DEPOSITION . . . . .	308
	<i>Chris M. Horwitz</i>	
12.1	Introduction. . . . .	308
12.2	Discharge Confinement Effects . . . . .	309
12.2.1	Diode . . . . .	309
12.2.2	Hollow Cathode . . . . .	311
12.3	Etched Sidewall Angle Control. . . . .	315
12.3.1	Mechanism. . . . .	315
12.3.2	Special Machine Designs . . . . .	317
12.4	Etching Performance . . . . .	318
12.4.1	SiO <sub>2</sub> Selectivity and Etching . . . . .	318
12.4.2	Device Processing; SiO <sub>2</sub> Etch . . . . .	323
12.4.3	Si Etching . . . . .	326
12.5	Si Deposition Performance . . . . .	329
12.5.1	Substrate Processes . . . . .	329
12.5.2	Experimental Results. . . . .	330
12.6	Conclusions . . . . .	333
12.7	References . . . . .	334

## PART V RELATED PLASMA PROCESSES

13.	ION PLATING . . . . .	338
	<i>Donald M. Mattox</i>	
13.1	Introduction. . . . .	338
13.2	Processing Plasma Environment . . . . .	339
13.3	Bombardment Effects on Surfaces and Film Growth . . . . .	341
13.4	Vaporization Sources for Ion Plating. . . . .	343
13.5	Bombardment Effects on Film Properties. . . . .	344
13.5.1	Film Adhesion . . . . .	344
13.5.2	Film Morphology, Density . . . . .	345
13.5.3	Residual Film Stress. . . . .	346

13.5.4	Crystallographic Orientation . . . . .	347
13.5.5	Gas Incorporation . . . . .	347
13.5.6	Surface Coverage . . . . .	347
13.5.7	Other Properties . . . . .	347
13.6	<b>Problem Areas . . . . .</b>	348
13.7	<b>Applications . . . . .</b>	350
13.8	<b>Summary . . . . .</b>	350
13.9	<b>References . . . . .</b>	351
<b>14.</b>	<b>IONIZED CLUSTER BEAM (ICB) DEPOSITION TECHNIQUES . . . . .</b>	<b>356</b>
	<i>Isao Yamada</i>	
14.1	<b>Introduction . . . . .</b>	356
14.2	<b>Experimental Techniques . . . . .</b>	357
14.3	<b>Film Deposition with ICB . . . . .</b>	361
14.3.1	Kinetic Energy Range of ICB and Effects of the Kinetic Energy . . . . .	362
14.3.2	Film Deposition by Reactive ICB Techniques . . . . .	365
14.3.3	Film Deposition by Simultaneous Use of ICB and Microwave Ion Sources . . . . .	366
14.4	<b>Summary . . . . .</b>	368
14.5	<b>References . . . . .</b>	368
<b>15.</b>	<b>THE ACTIVATED REACTIVE EVAPORATION (ARE) PROCESS . . . . .</b>	<b>370</b>
	<i>Chandra V. Deshpandey and Rointan F. Bunshah</i>	
15.1	<b>Introduction . . . . .</b>	370
15.1.1	Historical Developments . . . . .	371
15.2	<b>Evaporation Processes for the Deposition of Compound Films . . . . .</b>	373
15.2.1	Direct Evaporation . . . . .	373
15.2.2	Reactive Evaporation Processes . . . . .	373
15.2.2.1	Using a Compound Evaporant . . . . .	373
15.2.2.2	Using a Metal Evaporant . . . . .	374
15.3	<b>Thermodynamic and Kinetic Factors in Reactive Evaporation Process . . . . .</b>	374
15.3.1	Thermodynamic Factors . . . . .	374
15.3.2	Kinetic Factors . . . . .	374
15.4	<b>Role of Plasma in Evaporation Based Processes . . . . .</b>	375
15.4.1	Influence of Plasma on Growth Kinetics of the Deposits . . . . .	375
15.4.1.1	Plasma-Source Reactions in ARE Processes . . . . .	375
15.4.1.2	Plasma Volume Reactions . . . . .	375
15.4.1.3	Plasma Substrate Reactions . . . . .	376
15.5	<b>Implementation of the Activated Reactive Evaporation Process . . . . .</b>	376
15.5.1	Basic ARE Processes . . . . .	376
15.5.2	Modification of the Basic ARE Process . . . . .	377
15.5.3	Low Pressure Plasma Deposition (LPPD) Process . . . . .	377

15.5.4	Processing Using Plasma Electron Beam Guns . . . . .	379
15.5.5	Activated Reactive Evaporation Process Using an Arc Evaporation Source . . . . .	380
<b>15.6</b>	<b>Recent Developments in the ARE Process . . . . .</b>	<b>380</b>
15.6.1	New Approaches to Produce the Various Species . . .	380
15.6.2	New Plasma Excitation Modes and Geometries . . .	381
<b>15.7</b>	<b>Structure and Properties of the Films . . . . .</b>	<b>381</b>
<b>15.8</b>	<b>Materials Synthesized Using the Activated Reactive Evaporation Process. . . . .</b>	<b>382</b>
<b>15.9</b>	<b>Future Outlook and Perspective . . . . .</b>	<b>382</b>
<b>15.10</b>	<b>Conclusions . . . . .</b>	<b>382</b>
<b>15.11</b>	<b>References . . . . .</b>	<b>383</b>
<b>16.</b>	<b>FORMATION OF THIN FILMS BY REMOTE PLASMA ENHANCED CHEMICAL VAPOR DEPOSITION (REMOTE PECVD). . . . .</b>	<b>387</b>
	<i>Gerold Lucovsky, David V. Tsu and Robert J. Markunas</i>	
<b>16.1</b>	<b>Introduction. . . . .</b>	<b>387</b>
<b>16.2</b>	<b>Background – CVD Processes . . . . .</b>	<b>388</b>
<b>16.3</b>	<b>The Remote CVD Deposition Process . . . . .</b>	<b>390</b>
16.3.1	Overall Deposition Reactions. . . . .	390
16.3.2	Deposition Chamber Design and Process Variables . .	393
<b>16.4</b>	<b>Chemical Reaction Pathways in the Remote PECVD Process . . . . .</b>	<b>394</b>
16.4.1	The Deposition Analysis System. . . . .	394
16.4.2	Deposition of Hydrogenated Amorphous Silicon . .	395
16.4.3	Deposition of Silicon Based Dielectrics . . . . .	398
16.4.3.1	Silicon Dioxide ( $\text{SiO}_2$ ) . . . . .	398
16.4.3.2	Silicon Nitride: $\text{Si}_3\text{N}_4$ . . . . .	400
16.4.3.3	Silicon Oxynitrides [ $(\text{SiO}_2)_x(\text{Si}_3\text{N}_4)_{1-x}$ ] . . . . .	401
<b>16.5</b>	<b>Selected Bulk Properties of Deposited Thin Films . . . . .</b>	<b>401</b>
16.5.1	Hydrogenated Amorphous Silicon . . . . .	401
16.5.2	Silicon Dielectrics . . . . .	402
<b>16.6</b>	<b>Remote PECVD Dielectric Films in Device Structures . . . . .</b>	<b>402</b>
16.6.1	Silicon Dielectrics in MOS Capacitors and FETs . .	402
16.6.2	Amorphous Silicon Devices . . . . .	403
<b>16.7</b>	<b>Recent Developments in Remote PECVD. . . . .</b>	<b>403</b>
16.7.1	Integrated Processing with In Situ Process Diagnostics and In Situ Surface Analysis . . . . .	403
16.7.2	Other Material Systems. . . . .	403
16.7.3	Subcutaneous Oxidation Processes During Remote PECVD . . . . .	403
<b>16.8</b>	<b>Summary. . . . .</b>	<b>404</b>
<b>16.9</b>	<b>References. . . . .</b>	<b>405</b>
<b>17.</b>	<b>SELECTIVE BIAS SPUTTER DEPOSITION . . . . .</b>	<b>409</b>
	<i>Soren Berg and Claes Nender</i>	
<b>17.1</b>	<b>Introduction. . . . .</b>	<b>409</b>

17.2	Substrate Dependent Bias Sputter Deposition . . . . .	410
17.3	Deposition-Etching Balance in Bias Sputtering . . . . .	411
17.4	Sputtering Yield Values at the Film-Substrate Interface . . . .	413
17.5	Selective Bias Sputter Deposition . . . . .	414
17.6	Selective Bias Sputter Etching . . . . .	416
17.7	The Self Limiting Etch Depth Technique . . . . .	417
17.8	Conclusions . . . . .	418
17.9	References . . . . .	418
<b>18.</b>	<b>VACUUM ARC-BASED PROCESSING . . . . .</b>	<b>419</b>
	<i>David Sanders</i>	
18.1	Introduction. . . . .	419
18.2	Categories of Vacuum Arcs . . . . .	420
18.2.1	The Discrete Cathodic Arc . . . . .	421
18.2.2	The Diffuse Arcs . . . . .	425
18.2.3	Summary of Arc Types. . . . .	425
18.3	Source Design Considerations . . . . .	425
18.3.1	General Considerations. . . . .	426
18.3.1.1	Arc Initiation . . . . .	426
18.3.1.2	Arc Control . . . . .	427
18.3.1.3	Plasma Control . . . . .	428
18.3.2	Specific Examples . . . . .	430
18.4	Coatings from Arcs (Structures and Properties) . . . . .	436
18.5	Applications and Opportunities . . . . .	439
18.5.1	Non-Coating Applications . . . . .	440
18.6	Gaps in Understanding . . . . .	441
18.7	Conclusion. . . . .	441
18.8	References . . . . .	442
<b>PART VI</b>		
<b>PLASMA SURFACE INTERACTIONS</b>		
<b>19.</b>	<b>ION-SURFACE INTERACTIONS: GENERAL UNDERSTANDINGS . .</b>	<b>448</b>
	<i>Russell Messier, Joseph E. Yehoda and Lawrence J. Pilione</i>	
19.1	Introduction. . . . .	448
19.2	Preparation-Ion Bombardment Relations . . . . .	448
19.3	Ion Bombardment-Property Relations . . . . .	451
19.4	Ion Bombardment-Structure Relations . . . . .	455
19.5	The Interaction of Ions with the Growing Film . . . . .	457
19.6	Conclusions . . . . .	462
19.7	References . . . . .	462
<b>20.</b>	<b>ION ASSISTED DEPOSITION. . . . .</b>	<b>466</b>
	<i>James J. McNally</i>	
20.1	Introduction. . . . .	466
20.2	Background . . . . .	466
20.3	Experimental Apparatus . . . . .	467
20.3.1	Ion Source . . . . .	467



20.3.2	Operational Considerations . . . . .	468
20.3.3	Ion Preclean of Substrates . . . . .	469
20.3.4	Ion Assisted Deposition . . . . .	471
20.3.4.1	Procedures . . . . .	473
20.3.5	Dual Ion Beam Sputtering (DIBS). . . . .	473
20.4	Properties of IAD Films . . . . .	476
20.5	Properties of Dual IBS Films . . . . .	479
20.6	Advantages and Limitations. . . . .	480
20.7	Conclusion. . . . .	481
20.8	References . . . . .	481
<b>21.</b>	<b>MICROSTRUCTURAL CONTROL OF PLASMA-SPUTTERED REFRACTORY COATINGS. . . . .</b>	<b>483</b>
	<i>David W. Hoffman and Robert C. McCune</i>	
21.1	Introduction. . . . .	483
21.1.1	Primitive Microstructures . . . . .	483
21.1.2	Comparative Modification Strategies . . . . .	487
21.2	Bias Sputtering . . . . .	489
21.2.1	Fundamental Aspects of Bias Sputtering . . . . .	490
21.2.2	Applications. . . . .	492
21.2.2.1	Impurity Atom Resputtering and Ion Implantation Effects. . . . .	492
21.2.2.2	Control of Film Stress and Microstructure . . . . .	492
21.2.2.3	Control of Film Topography . . . . .	495
21.3	Coincidental Control of Coatings Deposited by Plasma Sputtering . . . . .	496
21.3.1	Internal Stresses and Physical Properties . . . . .	497
21.3.2	Special Investigations and Applications . . . . .	502
21.4	Modelling of Matter-Energy Co-Deposition in Refractory Coatings . . . . .	506
21.5	References . . . . .	509
	<b>INDEX . . . . .</b>	<b>518</b>

---

# Techniques for IC Processing

---

**David B. Fraser and William D. Westwood**

## 1.1 INTRODUCTION

The driving force for the rapid development of plasma based processing over the past 15 years has been the microelectronics industry and in particular, the fabrication of silicon integrated circuits. There has been a consistent annual doubling of the complexity of these circuits: today, memory chips containing over 1 million transistors have been in production for a few years, chips with 4 million transistors are beginning production, chips comprising over 16 million transistors are being developed, and plans are being developed for circuits with 4 times that number of active devices. This increased complexity is driven by the need to provide more functionality and to reduce the cost of providing it. If the automobile industry had been able to do the same over this time period, a racing car would cost less than \$10. The large increase in the number of transistors has been accomplished primarily by reducing their size; whereas feature sizes (e.g. transistor gate length) were  $20\mu\text{m}$  in the early 1970's, they are now  $0.7\mu\text{m}$  or less.

These very high transistor count chips utilize CMOS (Complementary Metal Oxide Semiconductor) technology, because of its low power dissipation. However, other technologies for circuit fabrication have also developed rapidly. Bipolar silicon technology provides higher clock speeds than CMOS (400 MHz VS 40 MHz) and has also evolved from larger to smaller feature sizes to provide higher performance. Gallium arsenide MESFET (Metal Semiconductor Field Effect Transistor) circuits have developed in the past few years;  $1\mu\text{m}$  features are standard but  $0.5\mu\text{m}$  and even  $0.25\mu\text{m}$  transistor gate lengths are in production for microwave integrated circuits.

In all these technologies, circuit fabrication involves a number of process steps carried out sequentially. The precise nature of the steps and the sequence in which they are performed may vary, but they are generically similar. They may involve:

- (i) Epitaxial growth of doped Si or GaAs layers on a Si or GaAs substrate respectively.

- (ii) Ion implantation of dopants (B and P into Si, Si into GaAs) selectively in depth and location. The implant damage must then be annealed out.
- (iii) Ion implantation of non-dopants (e.g. protons) to deliberately cause damage and thus lower conductivity to provide electrical isolation of devices.
- (iv) Deposition of dielectric layers to isolate conducting layers. In MOS technology, the gate oxide is thermally grown on the silicon, thus consuming some of the silicon: the thermal oxide provides a lower density of interface states (i.e. states within the electron energy band gap of the semiconductor) which affect transistor performance. However, dielectric films are required in other stages of the process to provide electrical isolation between conducting interconnects as well as for other functions, such as passivation, scratch protection, etc. Silicon nitride is usually deposited, as well as various form of silicon dioxide, sometimes doped with B,P, etc.
- (v) Patterning a mask to define specific features. This usually involves covering the wafer with photosensitive material (resist), exposing it to energy (ultra-violet or X-ray photons, electron or ion beams) to change its structure locally so that the pattern can be developed. Once the pattern is established in the photosensitive material, it provides the mask for the next step in patterning.
- (vi) Etching the pattern in the semiconductor (e.g. GaAs) in one of the dielectric layers (e.g.  $\text{Si}_3\text{N}_4$ ), or in a metal film (e.g. Al).
- (vii) Planarization of the surface to allow for the next process stage. For example, it is very difficult to carry out the patterning step on non-planar surfaces. For optical lithography, the depth of focus may be only  $1\mu\text{m}$  whereas the wafer surface may have larger height variations after several processing steps. Planarization may involve the deposition of an organic layer, such as polyimide, which fills the depressions coupled with some etching process to remove material from the high points.
- (viii) Deposition of a polycrystalline semiconductor, particularly Si, for transistor gates.
- (ix) Cleaning between process steps. Many process steps depend on starting with a clean surface: for example, epitaxial growth of Si on Si, ohmic contact formation between GaAs and Ni-Ge-Au. In fabrication of a typical circuit, there may be 10-12 mask levels, each requiring a different process step and a clean surface for the process. Since each mask level involves photolithography, removal of residual resist at each stage is vital.

Twenty years ago, all of these steps, except metallization, involved a chemical process carried out in either liquid or gas phase. Chemical vapor deposition was used to deposit semiconductor and dielectric films. These are relatively high temperature processes; poly-silicon is obtained by cracking silane at  $625^\circ\text{C}$ . Etching was carried out using acid or alkaline solutions and sometimes required slightly elevated temperatures. Etching  $\text{SiO}_2$  required hydrogen fluoride acid baths, for example. Similar solutions, such as Garo's

acid or organic solvents or several combinations of chemicals were used to provide clean surfaces between process steps.

Today, many of these deposition and etching process steps are instead based on the chemistry and physics of plasmas. This book deals with these processes over a broad range of deposition and etching technologies. In general, plasma processes are often quite complex, difficult to understand and usually require significantly more equipment than the wet chemical processes which they replace. A plasma can be thought of as a special state of matter in which the number densities of positive and negative (usually electron) charges are equal, on average, but these individual densities may be quite high ( $10^9$  to  $10^{14}\text{cm}^{-3}$ , see Chap. 2). Typically only a small percentage ( $< 1\%$ ) of the gas is ionized. However, the properties of transistors are very sensitive functions of the electronic charge carrier density in the transistor channel. Many years of research were required to control the charges in MOS transistors and reduce them to an acceptable level of  $10^{10}\text{cm}^{-2}$ . It therefore seems contradictory to expose these structures, during processing, to the energetic environment of a plasma of any kind. Yet, plasmas now provide the most practical way to carry out many of the process steps involved. Some of these steps, and the advantages provided by the plasma, are discussed briefly below while the rest of the book will examine in more detail a broad range of plasma processes which are relevant to the deposition and etching of films, both for microelectronics, and for other fields.

## 1.2 PLASMA PROCESSING IN MICROELECTRONICS

A cross section of one cell of a CMOS circuit is shown schematically in Fig. 1. This is just one of the many complex microelectronic structures now being fabricated. It provides a good example of the different process steps discussed above. We will concentrate here on these steps which directly involve the use of plasmas. Although ion implantation is a very important step, it utilizes plasmas only indirectly. The ions for implantation are generated by a plasma in the source. However, they are extracted from this plasma, analyzed and accelerated through a high vacuum region to the substrate to be implanted. While the efficient extraction of high ion current densities is an important topic in the design of implanters, since it affects wafer capacity, there is no direct affect of the plasma on wafer processes. Therefore, ion implantation will not be discussed here.

There are two aspects of plasmas which are important in processes: physical and chemical. Any plasma contains positive and negative charges in equal number densities. Because electrons have a much higher mobility, any surface in contact with the plasma will develop a negative potential with respect to the plasma. The resulting electric field reduces the electron current density to the surface until it equals the ion current density and the electrical neutrality of the plasma is thus maintained. The ions are accelerated to the surface by the electrical field; they arrive with an energy up to a maximum value of  $eV_f$ , where  $-V_f$  is the floating potential of the surface relative to the plasma. In dc discharge plasmas,  $V_f$  is normally a few volts, and the effect of these low energy  $\text{Ar}^+$  ions, for example, may be insignificant. However, the ion energy can easily be increased by applying a potential  $-V_b$  (relative to ground) to the surface; the ion energy is then  $e(V_b + V_f)$  and this may have a significant effect on the surface. For example, sputtering will take place when this energy exceeds about 20eV. In rf discharges, floating surfaces may develop even higher negative potentials, so that sputtering may occur even without supplying a bias to the sample deliberately. The actual potential depends on the geometry



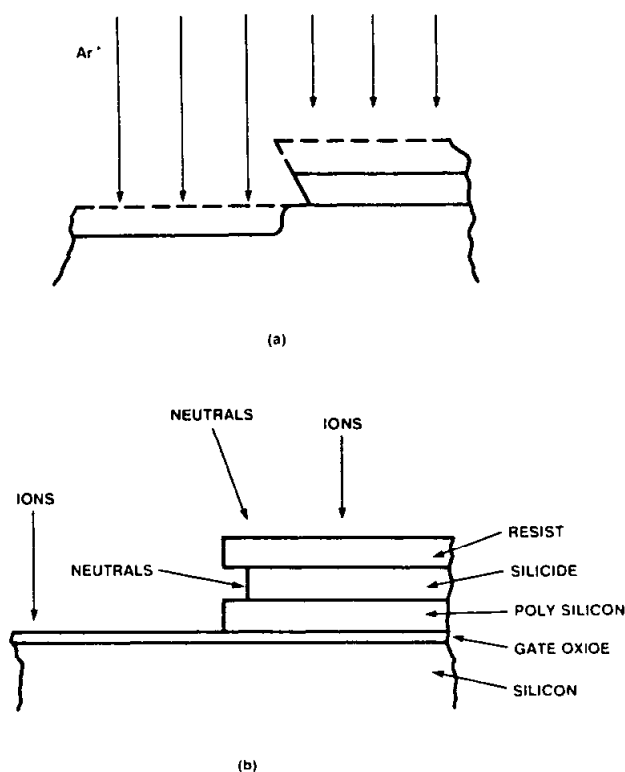


**Figure 2:** (a) Physical effects caused by the plasma. The substrate is sputtered by energetic ( $>20\text{eV}$ ) ions, except in the region protected by the mask overhang because the ions are at normal incidence on the substrate. (b) Removal of material from under the mask due to chemical reaction with a neutral radical generated in the plasma. Since they are uncharged, they can reach all surfaces.

Care must be taken to ensure that no unexpected reactions take place. For example, water vapor is the most common constituent of the background gas in most vacuum systems after pumpdown. It is absorbed on the chamber walls, when a system is open, or on the surfaces introduced into the system (e.g. substrates and holders): the water vapor then desorbs from the surface in the vacuum system; the desorption rate may be increased by substrate heating or by ion bombardment from the plasma. Water vapor is then dissociated within the plasma into O, OH and H fragments. Both O and OH are very reactive with many metals to form oxides: the remaining hydrogen is not efficiently pumped in many vacuum systems, and is easily incorporated in many film materials.

In most plasma situations, both the physical and chemical effects may be important and should be considered carefully. Thus, combined effects of the situations shown in Fig. 2 can occur. The relative importance of the physical and chemical effects will, of course, depend on the circumstances of each case: the reactivities, the substrate potential, and the ion species in the plasma are the important parameters. However, these depend in turn on the plasma volume, gas flows, excitation volume, etc. These are considered in following chapters.

With these two effects of plasmas in mind, we may consider their application in microelectronics processing. Here we briefly review the various process steps required in fabricating the device in Fig. 1 and the plasma requirements.

### 1.2.1 Cleaning

Successful fabrication of complex ICs requires many lithography steps in which each mask is accurately aligned with the previous patterns on the wafer. A sequence of 9-13 individual masks may be required to complete the process. For each stage, the wafer is covered with a layer of photoresist which is exposed using the mask and the resulting pattern developed, producing areas which are free from photoresist. This pattern is used in the next process step. For example, the remaining resist may prevent etching of a  $\text{SiO}_2$  layer from the Si wafer in these areas. After etching, the photoresist is removed, leaving the  $\text{SiO}_2$  layer in selected areas, as required for the next process step. Alternatively, the mask may be used to selectively deposit films in unmasked areas: when the photoresist is removed, the excess metal is removed.

It is clearly required that following the etching or deposition step the photoresist is thoroughly removed, both before etching the  $\text{SiO}_2$  and before proceeding to the next process step. If it is not thoroughly removed in the first case, regions of  $\text{SiO}_2$  will remain, after etching, in additional uncontrolled areas.

Photoresists are hydrocarbon-based polymers, with the cross-linking being determined by the exposure and development. All traces of polymer should be removed by the developer or the photoresist stripper. However, this is often not the case, particularly when the photoresist has been subjected to extreme conditions. The last traces of hydrocarbon can be removed in a suitable oxidizing atmosphere, by conversion to  $\text{CO}_2$  and  $\text{H}_2\text{O}$ . The process for this should ideally not require high temperatures nor produce damage to either the Si or  $\text{SiO}_2$ .

An oxygen plasma supplies atomic oxygen which reacts rapidly with the hydrocarbon to form volatile  $\text{CO}_2$  and  $\text{H}_2\text{O}$ . Although any  $\text{O}_2$  plasma would provide the necessary reactive oxygen substrate damage is minimized by ensuring that  $\text{O}_2^+$  ions do not reach the surface being etched.

### 1.2.2 Deposition

The fabrication of a CMOS circuit involves the deposition of a variety of films, including polycrystalline silicon,  $\text{Si}_3\text{N}_4$ , and  $\text{SiO}_2$  which may be doped with B and P, Al-Si alloys and possibly diffusion barriers such as TiN. Other microelectronic devices require different materials to be deposited: for example, epitaxial GaAs, Au/Ge/Ni and  $\text{WSi}_x$  for GaAs integrated circuits. Some of these films (e.g. Al-Si,  $\text{WSi}_x$ ) can be deposited by a purely physical method, such as sputtering or evaporation, while others require a chemical method, such as plasma enhanced chemical vapor deposition (PECVD); reactive sputtering, which is widely used to deposit TiN, combines both chemical and physical aspects. Evaporation is preferred for lift-off processes because of the line-of-sight deposition. However, it is difficult to control alloy composition, and the adhesion of the film is often low, requiring the use of additional adhesion layers.

**1.2.2.1 Sputtering.** Evaporation was the first method used to deposit metals for microelectronics, such as Al, for interconnect conductors. With the increased complexity of integrated circuits came the need for different materials. Alloys of Al-Si or Al-Si-Cu have been widely used to obtain smaller line widths and to decrease electromigration in the conductors. However, the elemental constituents of alloys evaporate independently

and the individual evaporation rates are proportional to the respective vapor pressures at the source temperature.

It is difficult to obtain from an alloy source an evaporated flux ratio which represents the original alloy composition and the source composition changes with time. Initially, the more volatile component evaporates from the charge and the flux is enriched in this component but the flux will eventually become rich in the other component as the source nears exhaustion. The scarcity of alloys which evaporate congruently (i.e. without change in composition) makes evaporation unattractive for alloy deposition.

The situation for sputtering is quite different because of the momentum transfer processes responsible for ejecting atoms from the alloy target. The sputtering yields  $S_A$  and  $S_B$  for the two elements in the binary alloy target AB represent the probabilities of these atoms being ejected. The numbers which are ejected are, therefore, proportional to the product of these probabilities and the numbers of A and B atoms which are present within the sputtering depth. In equilibrium, the surface composition of the target changes such that the composition of the elements in the sputtered flux is the same as the original alloy composition.

The sputtering mechanism is therefore, clearly advantageous for the deposition of alloys. Two points must be emphasized, however. First, the sputter mechanism alone is responsible for producing the correct flux ratio and other target effects will change this ratio. If the target temperature is too high, diffusion will occur and will modify the surface composition, so that the sputtered flux has a different composition from the alloy target.

Second, the sputtering process responsible for the correct equilibrium flux requires that the target be a homogeneous alloy and not simply a mixture of the two components. Sintered powder composite targets do not satisfy this requirement although they are sometimes used for deposition of silicides. If the target used to deposit  $TaSi_2$  contains grains of Ta and Si, even if they are extremely small ( $<5\text{nm}$ ), the alloy sputtering mechanism does not apply because sputtering occurs within individual Ta and Si grains rather than from an alloy in which atoms are homogeneously mixed. Then, the relative fluxes of Ta and Si will depend on the area ratio of Ta and Si grains and the elemental sputter yields for Ta and Si. Although the resulting film is a Ta-Si alloy, the sputtering process does not make use of the inherent advantage of the alloy sputtering process and there is no reason to expect the film to have the desired  $TaSi_2$  composition. However, a constant composition (i.e. Ta/Si ratio) may be obtained if the relative areas of Ta and Si in the target are constant.

Since the vapor pressure of metals is very low except at elevated temperatures, the sticking coefficient for the different species in the sputtered fluxes is effectively unity and the film composition will be the same as the composition of the flux. However, the film composition may differ from the incident flux if energetic ions and neutrals reach the substrate and cause sputtering there.

The sputtering process is basically simple, although practical systems are actually quite complex because substrates must be transported, and gases and pressures controlled. A plasma is generated by applying either dc or rf power in a suitable geometry and the target is biased to accelerate ions of the sputtering gas to it. At present, most systems use



a magnetron target arrangement; a magnetic field constrains the electrons to generate ions within a few millimeters of the target surface (Chap. 6).

**1.2.2.2 Reactive Sputtering.** By adding a gas which reacts with a sputtered metal in the presence of the plasma, compound films can be deposited using basically the same sputtering system as that used for metals. This topic is treated in detail in Chap. 9. As an example, TiN is often used as a diffusion barrier because it is refractory and has high conductivity. It is deposited quite easily by adding  $N_2$  while sputtering a Ti target provided a sufficient  $N_2$  supply is maintained.  $N_2^+$  ions are formed in the plasma and bombard both the target and substrate: the N atoms resulting from the impact dissociation react with the Ti. The energy and flux of the  $N_2^+$  ions are determined by the sputtering parameters such as bias potentials and power.

**1.2.2.3 Step Coverage.** In microelectronics, the films are often deposited onto a patterned wafer on which there are many steps which must be covered. For conductors, for example, the alloy must be continuous over each step and it is desirable that the film thickness be the same on the vertical wall of the step as on the flat surface since this will minimize high resistance regions at each step. However, this is obviously difficult because it would require that the sputtered flux normal to the side wall be the same as the flux to the wafer surface. In the usual system geometry, the substrate is parallel to the target and the sputtered atom flux is predominantly normal to the substrate surface so that the flux to the side wall is quite small (Fig. 3).

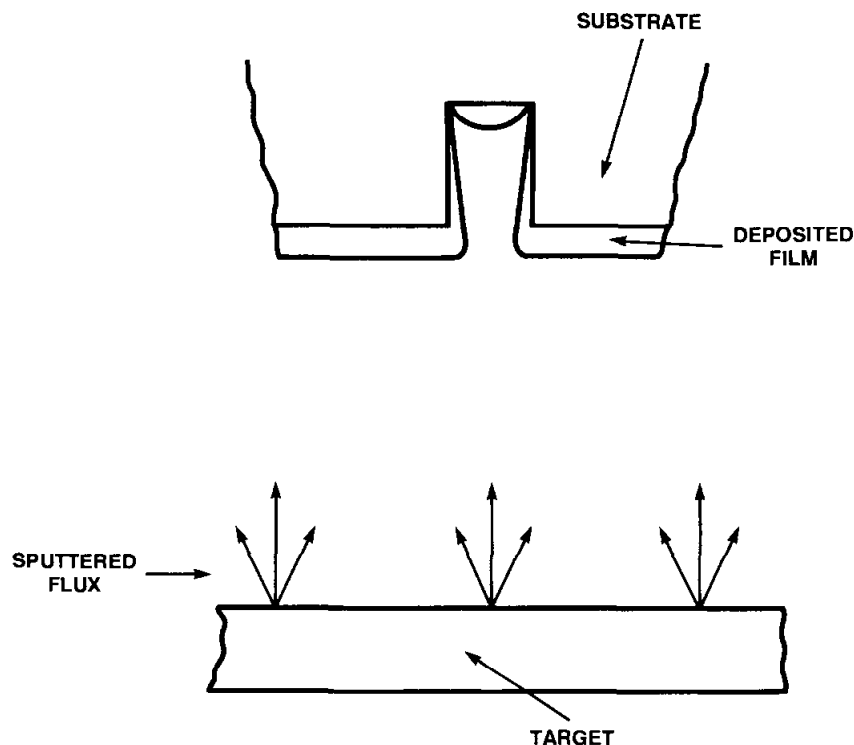


**Figure 3:** Schematic of the problem of step coverage during sputtering.

By applying bias to the substrate, ions are accelerated to the substrate and cause sputtering (usually termed resputtering) of the film. If the resputtering ratio is high (i.e. the thickness removed from the flat surface is comparable to the thickness deposited), the film thickness on the side walls will be increased by collecting the resputtered atoms, while the thickness on the top wafer surface is reduced. However, the alloy composition can be changed significantly by the resputtering. In fact, the step coverage by Al-Si alloys is greatly improved by applying substrate bias even when the resputtering ratio is negligible. This is most likely due to ion bombardment enhanced diffusion, which may be the most important mechanism for Al alloys but is probably insignificant for refractory metals.

The ability to improve step coverage is a significant advantage and is easily implemented because of the plasma environment in which the sputter deposition is carried out. It should be noted, however, that the enhancement of step coverage by bias sputter deposition may be incompatible with some masking techniques.

**1.2.2.4 PECVD.** Chemical vapor deposition has been used in IC fabrication almost since it began, and is still used in many cases. In its simplest form, it requires increasing the temperature of the substrate to a value at which the required chemical reaction takes place at a useful rate in a controlled manner. Perhaps the simplest case is the deposition of silicon from  $\text{SiH}_4$  and  $\text{N}_2$  and silicon nitride from  $\text{SiH}_4$  and  $\text{NH}_3$  at  $625^\circ\text{C}$ .

While these are well understood reactions, they do require quite high temperatures. In PECVD, the chemical effects of the plasma allow the reactions to proceed at much lower temperatures (See Chap. 10). Lower temperatures are desirable to prevent diffusion of dopants during these subsequent processes.

Films deposited by PECVD have increased in importance for IC processing as device dimensions have decreased and imposed the requirement for much tighter tolerances on the dopant location. In depositing these films, it is the chemical aspects of the plasma which are usually of prime importance. However, physical effects of the plasma may be important in determining the film properties. For example,  $\text{Si}_3\text{N}_4$  films may have high compressive stress when deposited in plasma conditions where substantial ion bombardment of the substrate occurs.

There are two basic plasma arrangements in which the physical effects may be quite different. These are shown schematically in Fig. 4. In the downstream arrangement (Fig. 4(a)), the plasma generation is remote from the substrate, so that physical effects are minimized. The gas reactants may be introduced either into the plasma region or near the substrate. In the parallel plate reactor (Fig. 4(b)), the substrate is immersed in the plasma and is therefore subject to physical effects such as ion bombardment.

Films can be deposited at temperatures determined by the plasma environment and the heat generated by the reactions. While no elevated temperatures are required for the chemical reaction, the film properties may be improved by heating. For example, silicon films deposited from  $\text{SiH}_4$  will be amorphous and will contain a significant fraction of hydrogen, in the form  $\text{SiH}_x$ , unless the substrate temperature is above  $600^\circ\text{C}$ .  $\text{SiO}_2$  films are deposited from  $\text{SiH}_4$  and  $\text{N}_2\text{O}$ , just as in the CVD case. However, silicon nitride can be deposited using either  $\text{NH}_3$  or  $\text{N}_2$ . Whereas  $\text{N}_2$  cannot be used in CVD because of its low reactivity, (due to the stability of the molecule), its reactivity in the plasma is high due

to dissociation processes. There are advantages to using  $N_2$  in reducing NH bonding in the  $Si_3N_4$  films as well as being more convenient.

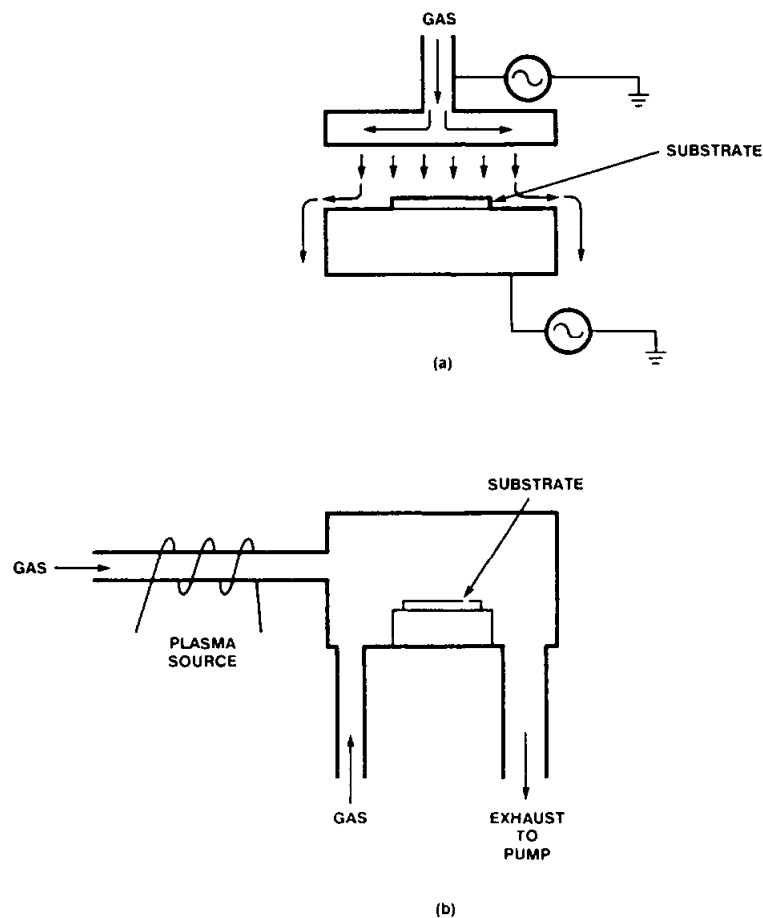


**Figure 4:** Schematic of (a) downstream and (b) parallel plate plasma deposition systems.

**1.2.2.5 Etching.** The selective removal of one material from another is an important part of IC processing (Chap. 8). In the example already discussed in (a), the  $SiO_2$  has to be removed from the underlying silicon but it is important that no significant amount of silicon be removed. Typically the dopants necessary for device operation are within 100 nm of the wafer surface and must remain there throughout processing. Thus, while it is possible to remove the  $SiO_2$  by a physical method, such as sputtering, this is not acceptable for a process step since sputtering will etch the silicon at a faster rate than it removes the  $SiO_2$  and may also introduce damage or impurities into the exposed Si.

For selectivity, a chemical reaction is required which etches one layer (e.g.  $SiO_2$ ) but not the other (e.g. Si). For wet chemical etching, this often involves mixtures of several chemicals with competing interactions with the exposed surfaces. Just as chemical reactions for depositing films are made possible by injecting suitable gases into a plasma, so are chemical reactions for etching. The arrangements to do this are similar to these in Fig. 4. The chemical reaction must, in this case, convert the material to be removed into a volatile gas which will thus desorb from the surface within the plasma environment and be pumped out of the system.

A wide variety of gases are used in reactive plasma etching to etch different materials. For example,  $\text{BCl}_3$ ,  $\text{SiCl}_4$ ,  $\text{Cl}_2$  and  $\text{CCl}_4$  are all used to etch Al alloys and  $\text{CF}_4$ ,  $\text{C}_2\text{F}_6$ ,  $\text{CHF}_3$ ,  $\text{NF}_3$ ,  $\text{SF}_6$ ,  $\text{SiF}_4$ ,  $\text{CFCl}_3$ ,  $\text{CF}_2\text{Cl}_2$  and  $\text{CF}_3\text{Cl}$  are used to etch  $\text{SiO}_2$ . Mixtures of gases, such as  $\text{CF}_4 + \text{O}_2$  are also used. Due to the variety of reactions that may occur, a large number of species may exist in the plasma.

As discussed with reference to Fig. 2, the type of etching which takes place will depend on the balance between the physical and chemical effects in the plasma. One effect not considered was the deposition onto a side wall of a non-volatile product, such as a polymer or C. If this polymer or carbon compound does not react chemically with the etch gas species, it will remain on the wall, preventing any further reaction because it cannot be sputtered away since the ions do not reach the side wall. This can be used to the advantage of the operation in that it inhibits undercutting of masks and results in a more anisotropic etch. The technique is known as "sidewall blocking" (Chap 8).

### 1.3 SUMMARY

Despite the apparent anomaly of subjecting an IC, during processing, to an environment containing charged species, plasmas obviously play an important role in IC fabrication. The two aspects, physical and chemical, are important although their relative importance will change with the application, the plasma equipment and the gases being used. A plasma is, however, a very complex environment in which to carry out these processes. Only an improved understanding of the plasma environment will make it possible to fully utilize the various process methods and to develop new methods.

## 2

---

# Introduction to Plasma Concepts and Discharge Configurations

---

Joseph L. Cecchi

## 2.1 INTRODUCTION

### 2.1.1 The Plasma State

A plasma is a gas containing charged and neutral species, including some or all of the following: electrons, positive ions, negative ions, atoms, and molecules. On average a plasma is electrically neutral, because any charge imbalance would result in electric fields that would tend to move the charges in such a way as to eliminate the imbalance. As a result, the density of electrons plus the density of negative ions will be equal to the density of positively charged ions (1). An important parameter of a plasma is the *degree of ionization*, which is the fraction of the original neutral species (atoms and/or molecules) which have become ionized. Plasmas with a degree of ionization much less than unity are referred to as *weakly ionized*. The presence of a relatively large population of neutral species will dominate the behavior of this type of plasma. In *fully ionized* plasmas, the degree of ionization approaches unity, and neutral particles play little or no role.

To form and sustain a plasma requires some energy source to produce the required ionization. In steady state, the rate of ionization must balance the losses of ions and electrons from the plasma volume by recombination and diffusion or convection to the boundary. Plasma is often referred to as the *fourth state of matter*, since it occurs by adding energy (heat) to a gas. There is not, however, a distinct phase change in going from a neutral gas to a plasma; the process is more continuous.

The plasmas we will consider here are initiated and sustained by electric fields which are produced by either direct current (dc) or alternating current (ac) power supplies. Typical ac frequencies of excitation are 100 kHz, at the low end of the spectrum, 13.56 MHz in the radio frequency (rf) portion of the spectrum, and 2.45 GHz in the microwave region. These plasmas are also referred to as *electric discharges*, *gaseous discharges*, or *glow discharges* (the latter because they emit light). In fact, there is a slight distinction between the terms *plasma* and *discharge*. Strictly speaking, there are regions of a dis-

charge (such as cathode sheaths) which do not actually fulfill the definition of a plasma (which will be presented below). As a practical matter, however, this distinction is not usually significant. Since the plasmas of interest here are always part of an electric discharge, we will tend to use the various terms interchangeably.

### 2.1.2 Brief Survey of Plasmas

Although plasmas are not common terrestrially, they do represent the most ubiquitous form of matter in the universe. Because electrons play such an important role in plasmas, it is useful to categorize plasmas by electron densities and electron energies. As we shall see, the electrons in a plasma have a distribution of energies, so we will typically use an average electron energy. In a number of cases, the electrons will have a Maxwellian distribution (2), which can be described in terms of the electron energy  $\epsilon$  as,

$$f(\epsilon) = 2(\epsilon)^{1/2} / ((\pi)^{1/2} (kT)^{3/2}) \exp(-\epsilon/kT) \quad (1)$$

where  $f(\epsilon)$ , the electron energy distribution function, is proportional to the number of electrons having an energy between  $\epsilon$  and  $\epsilon + d\epsilon$ ,  $k$  is Boltzmann's constant, and  $T$  is the electron temperature. The electron energy is given by

$$\epsilon = (1/2)mv^2 \quad (2)$$

where  $m$  is the electron mass and  $v$  is the magnitude of the electron velocity. The constants in Eq. (1) are such that if we integrate over all energies, we get:

$$\int f(\epsilon) d\epsilon = 1 \quad (3)$$

The average energy can be obtained by the integral:

$$\int \epsilon f(\epsilon) d\epsilon = (3/2)kT \quad (4)$$

Thus, the electron temperature  $T$  for a Maxwellian electron energy distribution is a measure of the average energy of the electrons.

The Maxwellian distribution is also called the *equilibrium* distribution, because it represents a case where the electrons are in thermodynamic equilibrium. In a number of cases, especially weakly ionized plasmas,  $f(\epsilon)$  will not be Maxwellian; however, it is quite common to still speak of an electron temperature  $T$  when referring to the average electron energy.

A convenient unit for the electron temperature is the electron volt (eV) which is equivalent to a temperature of approximately 11600 K. In Fig. 1, typical values of electron densities and temperatures are shown for a variety of plasmas. They range from the very rarified and cold interstellar plasmas up to the dense and hot plasmas used for controlled fusion. The plasmas of interest here are the process plasmas, which have electron densities in the range of  $1 \times 10^9$  to  $1 \times 10^{12} \text{ cm}^{-3}$ , and average electron energies

between 1 and 10 eV. The degree of ionization for these plasmas varies from about  $10^{-6}$  to as high as 0.3. At the lower end of the density, energy, and ionization scale are the discharges that are formed between planar electrodes, while the upper end of this scale applies to discharges sustained at a frequency that corresponds to some natural frequency for the plasma (such as electron cyclotron resonance (ECR) plasmas).

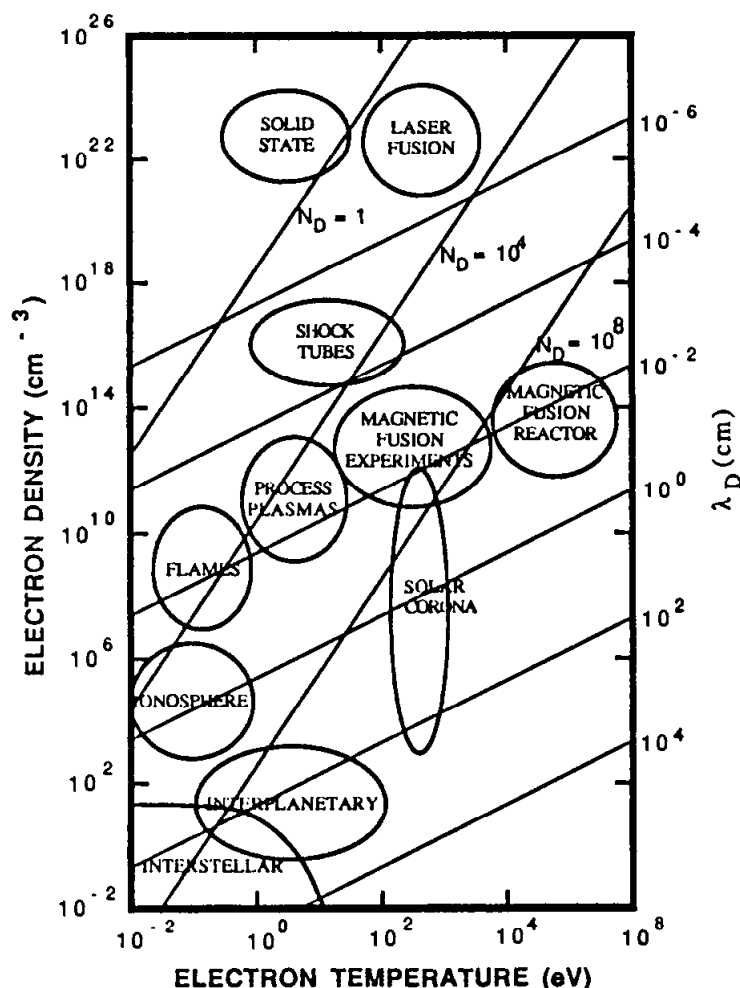


**Figure 1:** Electron density and temperature ranges for a variety of natural and man-made plasmas. Lines of constant Debye length ( $\lambda_D$ ) are shown, along with lines of constant number of electrons in a Debye sphere ( $N_D$ ). The region labelled **PROCESS PLASMAS** delineates the parameter ranges for the plasmas used for thin film deposition and etching.

### 2.1.3 Plasmas for Thin Film Deposition and Etching

The extensive use of plasmas for the deposition and etching of thin films derives from two salient features. Firstly, plasmas are capable of efficiently generating chemically active species. Examples of this include atomic chlorine for the etching of silicon and  $\text{CH}_x$  ( $x = 0-3$ ) for the deposition of amorphous hydrogenated carbon. The generation of chemically active species in a plasma is initiated by the bombardment of molecules and atoms by the plasma electron, which have sufficient energy to break chemical bonds. The products of the electron bombardment processes, which include radicals and ions, can

undergo further reactions, often at high rates, to form additional chemically reactive species.

As a generator of reactive species, a plasma reactor is similar to more conventional chemical reactors (3) which utilize thermal activation of chemical reactions that typically proceed with Arrhenius rates  $\kappa$  of the form.

$$\kappa = A \exp(-B/RT), \quad (5)$$

where  $A$  is the pre-exponential factor,  $B$  the activation energy for the reaction,  $R$  the universal gas constant, and  $T$  the absolute temperature. For a given reaction, which fixes  $A$  and  $B$ , the rate depends only on temperature. In actual practice, other factors, such as fluid flow, heat transfer, and mass transfer will play important roles. Nevertheless, the conventional reactor, with its Arrhenius rates, will be comparatively simpler than a plasma reactor, in which the chemistry is governed by many elementary processes that depend in very complicated ways on the plasma parameters. The additional complications of a plasma reactor are generally offset by greater process efficacy (e.g., higher rates or unique capability). It is clear that the design and operation of plasma reactors requires an understanding of the plasma and the processes that occur within it, and this is one of the major objectives of this chapter.

The second feature that makes plasma discharges so useful is their ability to generate ions and to accelerate the ions to energies of 50 - 1000 eV in the vicinity of the deposition or etching substrate. Energetic ions are useful for sputtering, as in the sputter deposition of metals. Energetic ions can also play a synergistic role in the deposition or etching of thin films. A prominent example of this is the anisotropic etching of semiconductor devices (4,5), where the etch rate perpendicular to the substrate (the direction of the energetic ion impingement), can be enhanced over that lateral to the substrate surface by a variety of ion bombardment-activated processes.

Ions are formed in a plasma principally by electron bombardment ionization. The ions can then be accelerated in relatively strong electric fields which, in certain discharge configurations, exist outside the main plasma volume near the substrate. The formation of such strong electric fields in the so-called sheath region of the discharge follow quite naturally, as we shall see.

In this section, we have taken a *process* point of view of a plasma, which is certainly appropriate in the context of this book. It is clear, however, that for any process, we need a stable equilibrium plasma discharge in the "background" of the process of interest. This will involve a number of elementary collisional interactions (including ones responsible for the process of interest), as well as the interaction of plasma electrons and ions with electric and possibly magnetic fields. In this chapter we will examine these topics, also.

#### **2.1.4 An Elementary View of Plasma Reactors**

Although we will consider a number of aspects of plasmas and discharges in this chapter, we are primarily interested in these topics as they relate to the plasma reactors that are used for thin film processes. Therefore to provide some general framework for



what is to follow, we will consider here some general characteristics of the most common types of reactors.

**2.1.4.1 Planar Reactors** Perhaps the most ubiquitous class of plasma reactor is one in which the plasma is formed between planar parallel electrodes (6,7), which are attached to the power source. This includes configurations with a single electrode in a metallic containment vessel, the latter comprising the second electrode.

The importance of the plasma electrons in generating chemically active species in the plasma volume, and the edge electric fields accelerating ions into the substrate suggests a schematic picture in which a reactor is decomposed into two regions. The embodiment of this for a planar geometry is shown in Fig. 2. Here, we see the plasma volume where chemically reactive species (and/or ions) are generated, in which there is only a small electric field. Adjacent to this is a "plasma free" sheath region of strong electric field. Although this picture is only approximate, it represents a useful framework for examining relevant plasma and sheath phenomena. It also underlies the approach to many of the advanced plasma deposition and etch tools which are constructed to afford independent or nearly independent control of the two regions.

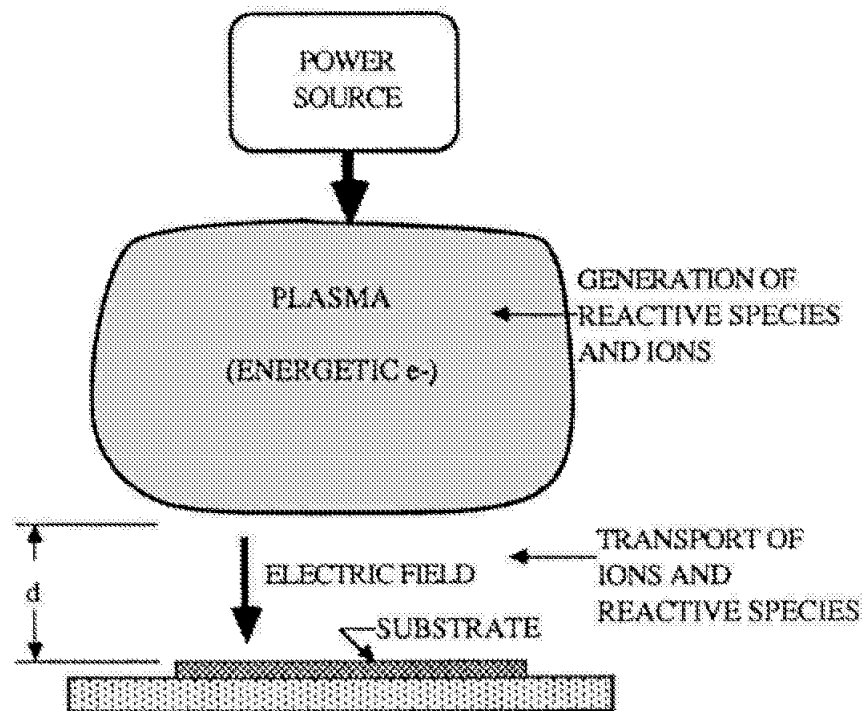


**Figure 2:** Generic plasma reactor for thin film deposition and etching. A power source supplies energy to the main plasma discharge where reactive species and ions are generated. These species are transported to the substrate or wafer for deposition or etching. In many configurations, there is an electric field in the vicinity of the substrate which accelerates the ions.

In many types of plasma reactors, the electrodes between which the plasma is sustained are not simply planar, an example being the hollow cathode discharge (see Chap. 11). Even in such cases, the discharge will still exhibit the bulk plasma/sheath dichotomy, though the geometry of the regions will be more complicated.

The operation of planar reactors can be enhanced by the addition of magnetic fields. This is usually accomplished by introducing a magnetic field that is nominally parallel to an electrode, as in a magnetron sputter source (see Chap. 6) or a magnetically enhanced reactive ion etcher (8). As we shall see, the magnetic field will increase the ionization efficiency of the electrons. This results in higher density plasmas with decreased sheath voltage.

**2.1.4.2 Barrel Reactors.** A barrel reactor (9) is a tubular-shaped structure, in which a plasma is sustained either by inductively coupling an ac power supply through a coil which surrounds the reactor (Fig. 3(a)), or by capacitatively coupling via external rings (Fig. 3(b)). For this configuration, the electric field is established inside the non-conducting vacuum vessel without internal electrodes. Consequently, this reactor does not develop the larger sheath electric fields that a planar reactor does, so that ion bombardment usually plays little or no role. The main application of barrel reactors is for isotropic etching, including the removal of organic materials as in resist stripping.

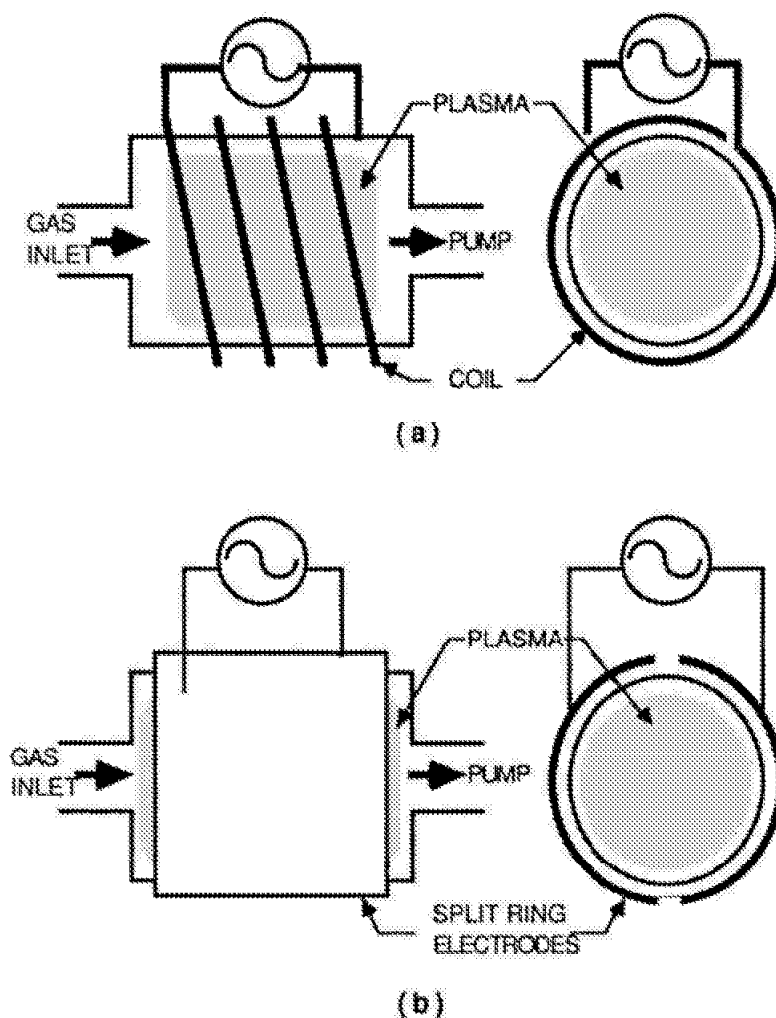


**Figure 3:** (a) Inductively coupled plasma reactor. An alternating current power source creates a time varying current, the magnetic field from which generates a voltage that sustains the discharge. (b) Capacitively coupled plasma reactor. Similar to (a), except the two plates are used to create an electric field to sustain the discharge.

**2.1.4.3 Downstream Plasma Reactors** Another class of plasma reactor is the *downstream* reactor (10-12), in which the region of the bulk plasma is separated by a large distance (i.e., much more than a cathode sheath thickness) from the substrate. Such plasmas are usually electrodeless, being sustained by microwaves introduced by some radiation launching structure. An important example of the downstream plasma reactor is the electron cyclotron resonance (ECR) plasma reactor (11,12). This apparatus includes a magnetic field. Electrons are heated by a microwave source which is applied at a frequency that corresponds to that of the electrons circulating in the magnetic field. The processes that are involved in ECR apparatus will be considered in detail below.

Oftentimes in the downstream geometry, ion bombardment of the substrate is not wanted. Owing to the separation of the plasma from the substrate, this is easily accomplished. In situations where ion bombardment of the substrate is essential to a process, it is possible to provide this by substrate bias and/or by taking advantage of the behavior of particles in magnetic field gradients.

The downstream configuration represents an even further emphasis on separating the bulk plasma from the environment of the substrate. For this reason, the downstream configuration is an important approach to advanced deposition and etch tools.

## 2.2 FUNDAMENTAL PLASMA DISCHARGE CONCEPTS

In this section, we will consider the fundamental plasma discharge concepts which underlie the operation of plasma reactors for deposition and etching. The concepts discussed here are covered extensively in a number of excellent plasma physics texts (13-17) and therefore, in some cases, we will present results with only limited derivations.

In presenting formulae, there is always the question of appropriate units. In general, we will use the International System (SI) nomenclature (previously referred to as rationalized MKS units). However, in some cases, we will deviate from this standard either for convenience, or to follow convention.

### 2.2.1 Debye Shielding

In general, the characteristics of plasmas will differ greatly depending on things like the constituent atoms and molecules, densities, energies, and degree of ionization. There is, however, one universal plasma characteristic which was noted earlier: the free charges in the plasma will move in response to any electric field in such a way to decrease the effect of the field. In particular, it is usually the lighter and more mobile electrons that respond to electric fields, and in what follows we will adopt a simplified, but reasonably accurate, picture of a discharge in which the ions are assumed stationary, and the electrons are free to move in response to any electric fields.

We have already noted one implication of this tendency of plasma electrons to decrease electric fields. There will not be regions of a plasma with excess positive or negative charge, because if there were, an electric field would arise that would move electrons to effectively eliminate any charge imbalance. This feature is called *quasineutrality*.

In addition, if a "test" charge is inserted in a plasma or an electric field is imposed on a plasma, the plasma electrons will move in such a way as to diminish the effects. This is the phenomena of Debye shielding, which we will examine more quantitatively by assuming that we place a positive test charge  $Q$  in a plasma. We further assume that before inserting the test charge, the plasma was quasineutral, with equal electron and ion densities given by  $n$ . In free space the charge would give rise to an electric potential  $V_0$  given by (18)

$$V_0 = Q/(4\pi\epsilon_0 r) \quad (6)$$

where  $r$  is the distance from the charge, and  $\epsilon_0$  is the permittivity of free space and is equal to  $8.85 \times 10^{-12}$  farad/m. The total potential  $V$  will include the effects of the plasma electrons and ions, along with the test charge, and is given by Poisson's equation,

$$\nabla^2 V = -\rho/\epsilon_0 \quad (7)$$

where  $\rho$  is the total charge density in the plasma. The charge density is

$$\rho = e(n_i - n_e) + Q\delta(r) \quad (8)$$

where  $\delta(r)$  is the Dirac delta function (18), which specifies that  $Q$  is a point charge, and  $n_i$  is the ion density, which, since the ions are assumed to be immobile, may be taken as equal to  $n$ . For simplicity, we have assumed that there are only positive ions in the plasma.

The existence of the potential  $V$  will cause the electron density to be altered. If we assume that the electrons are in thermodynamic equilibrium at temperature  $T$ , then we can write

$$n_e = n \exp(eV/kT). \quad (9)$$

If we now assume that

$$eV/kT \ll 1 \quad (10)$$

we can expand the exponential term and rewrite Poisson's equation as

$$\nabla^2 V = - (en/\epsilon_0)(1 - 1 - (eV/kT)) + Q\delta(r) \quad (11)$$

or

$$\nabla^2 V = V/\lambda_D + Q\delta(r), \quad (12)$$

where the quantity  $\lambda_D$  is called the Debye length and is given by

$$\lambda_D = ((\epsilon_0 kT)/(ne^2))^{1/2} \quad (13)$$

$$= 743(T_e(\text{eV})/n(\text{cm}^{-3}))^{1/2}.$$

The solution to Eq. (12) is

$$V(r) = (Q/4\pi\epsilon_0) \exp(-r/\lambda_D). \quad (14)$$

The plasma thus modifies  $V_0$  from its free space value (Eq. (6)) by attenuating it exponentially with a characteristic decay length of  $\lambda_D$ . This effect is called Debye shielding, and quite generally describes how a plasma will respond to an electric field. Plasma electrons will collect in the vicinity of the test charge to screen its effect. Fig. 4 shows this effect schematically.

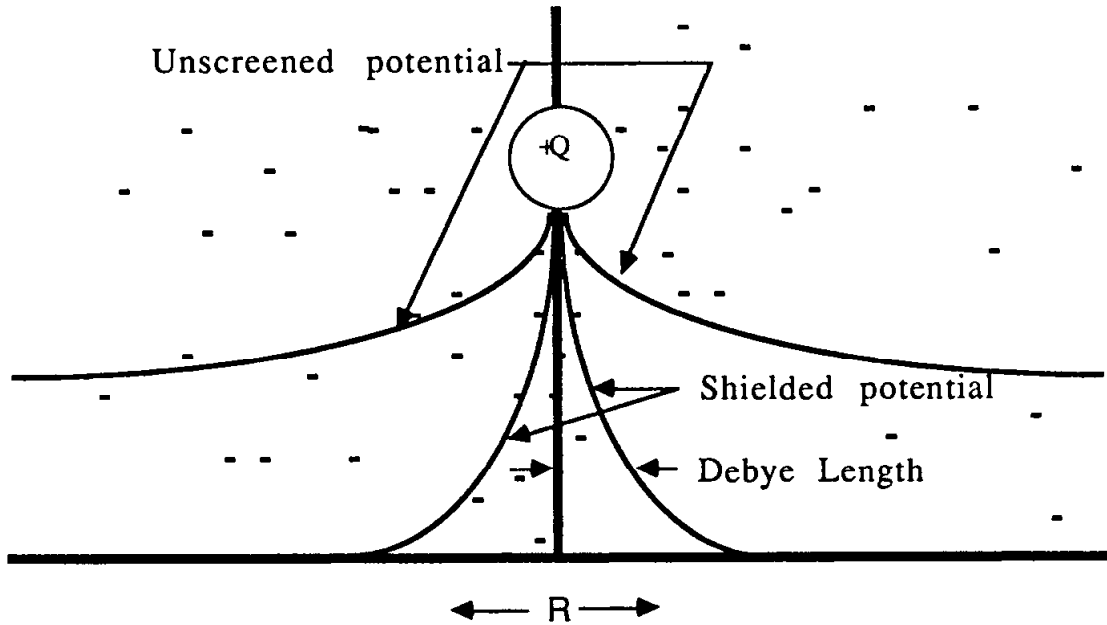


**Figure 4:** Schematic of the unshielded electrostatic potential from a point charge  $Q$  compared to the Debye shielded potential that occurs when the charge is immersed in a plasma. The electron density increases in the vicinity of the charge, creating the exponential fall-off in the potential.

The solution (Eq. 14) makes sense only if many electrons are involved in the shielding process. Since the shielding falls off exponentially, we can quantify this by calculating the number of electrons  $N_D$  in a sphere of radius  $\lambda_D$ , called a Debye sphere,

$$N_D = (4\pi/3)\lambda_D^3 n. \quad (15)$$

In fact, the criterion that  $N_D \gg 1$  is generally taken as the definition of a plasma. Lines of constant  $N_D$  are plotted in Fig. 1. Clearly, the dependence of  $N_D$  on  $n$  and  $T_e$  is such that for  $T_e$  above 1 eV, any plasma with a density less than  $1 \times 10^{18} \text{ cm}^{-3}$ , will easily satisfy

the large  $N_D$  criterion. Implicit in our definition of a plasma is the criterion that the *size* of the plasma is large compared to  $\lambda_D$ , since, otherwise, the shielding would not be complete.

If we were to use (Eq. 14) to calculate the potential energy associated with the *shielding* (i.e., subtract out the contribution from the test charge with  $Q = e$ ), we would find that  $N_D$  was proportional to the ratio of the particle kinetic energy,  $kT$ , to the Debye shielding potential energy. It may seem somewhat paradoxical that the Debye shielding potential energy *decreases* relative to the kinetic energy for an increasing number of particles in a Debye sphere; however, we can understand this in terms of a reduced "shielding" requirement on a individual electron as  $N_D$  increases.

For the plasmas of interest here, the relevant range of  $\lambda_D$  is from 0.01 to 1 mm, with 0.1 mm being a good average for weakly ionized planar discharges. The value of  $N_D$  varies from about  $1 \times 10^4$  to  $1 \times 10^7$ , which easily satisfies the definition of a plasma.

### 2.2.2 Plasma Oscillations

If a charge imbalance does occur in a plasma, we have seen how the electrons will move to shield out its effects. This does not happen instantaneously, however. A reasonable estimate of the time it takes for the shielding to "get in place," would be the time required for an electron to move a Debye length. This time  $t_p$  is

$$t_p = \lambda_D / v = ((\epsilon_0 m e) / (n e^2))^{1/2}. \quad (16)$$

Furthermore, we might imagine that the electrons, moving under the force of the electric field from the charge imbalance, may "overshoot" and execute an oscillatory motion. A more rigorous treatment of this problem (19) reveals that this is the case. The electrons will oscillate at a frequency which is just the inverse of  $t_p$  called the *plasma frequency*  $\omega_p$ ,

$$\omega_p = t_p^{-1} = 5.64 \times 10^4 \cdot (n(\text{cm}^{-3}))^{1/2} \quad (17)$$

Collisions will damp out this oscillatory motion, so that the shielding electrons will eventually assume the static distribution in Eq. (14).

In the absence of magnetic fields, this is the only "normal mode" of a plasma. In the presence of magnetic fields, however, plasmas display a number of additional oscillatory modes. Detailed discussion of these, which is beyond the scope of this chapter, can be found in a number of excellent references (20,21). We will, however, consider the important case of electron cyclotron oscillations in Sect. 2.2.5.3.

The oscillatory modes of a plasma establish its response to externally applied electromagnetic radiation. A discussion of the dielectric properties of plasmas is given in Sect. 2.2.5.2. We note here the general observation that the plasma will screen out an oscillating field with a frequency below  $\omega_p$ , but above this frequency, the electrons cannot respond fast enough to accomplish the shielding.

### 2.2.3 Particle Orbits

The charged particles in a plasma will move in response to electric and magnetic fields. These fields may arise from external sources (such as a power supply or an electromagnet) or from collisional interactions among the particles. In the next section, (2.2.4) we will consider the effects of collisions. In this section, we will look at how charged particles move in electric and magnetic fields of various kinds and in various combinations. We will confine our discussion to fields that do not change in time and will generalize to time varying fields in Sect. 2.2.5. We know from Sect. 2.2.1 that the plasma will modify external fields we attempt to put on. We will deal with this complication in Sect. 2.2.7, where we will consider plasma sheaths, and again in our discussion of glow discharges (Sect. 2.4).

**2.2.3.1 Effects of Electric and Magnetic Fields.** In the presence of an electric field  $\mathbf{E}$  and magnetic field  $\mathbf{B}$ , a particle of charge  $q$  and velocity  $\mathbf{v}$  will experience a force  $\mathbf{F}$  given by:

$$\mathbf{F} = q\mathbf{E} + q\mathbf{v} \times \mathbf{B}. \quad (18)$$

The quantities  $\mathbf{F}$ ,  $\mathbf{E}$ ,  $\mathbf{v}$ , and  $\mathbf{B}$  are all vectors, and  $\times$  denotes the vector cross product. Particle orbits are calculated by using Newton's second law to relate the particle acceleration  $\mathbf{a}$  to the force:

$$\mathbf{F} = m\mathbf{a}, \quad (19)$$

where  $m$  is the particle mass. We will now consider a number of cases to illustrate typical particle motions.

$\mathbf{E} = \text{constant}, \mathbf{B} = 0$

In this case, a particle will experience a constant acceleration in the direction of  $\mathbf{F}$  given by

$$\mathbf{a} = q\mathbf{E}/m. \quad (20)$$

$\mathbf{E} = 0, \mathbf{B} = \text{constant}$

The magnetic force acts in a direction perpendicular to the velocity of the charged particle. If a particle is at rest ( $\mathbf{v} = 0$ ), then there is no force and the particle remains at rest. For a nonzero velocity, let us define the component of velocity of the particle parallel to  $\mathbf{B}$  to be  $v_{\parallel}$  and the velocity component perpendicular to  $\mathbf{B}$  to be  $v_{\perp}$ . For the case of  $v_{\parallel} = 0$ , the particle will move in a circular orbit perpendicular to the direction of  $\mathbf{B}$ . The radius of the orbit is called the gyro radius  $\rho$  and is given by

$$\rho = mv_{\perp}/qB, \quad (21)$$

where  $B$  is the magnitude of  $\mathbf{B}$ . Noting that the kinetic energy  $W$  of the particle is given by

$$W = mv_{\perp}^2/2. \quad (22)$$

we can write the gyro radius as

$$\rho = (2mW)^{1/2}/qB \quad (23)$$

Thus, for particles of the same energy, the heavier species will have larger circular orbits.

As a particular example, let us consider an electron in a 100 G (0.01 T) magnetic field. If the electron energy is 100 eV, then the gyro radius would be 2.4 mm. At 1000 eV, the gyro radius would increase to 7.5 mm. If we now consider a  $\text{Cl}^-$  ion at 100 eV and 1000 eV, we find that its gyro radii are 62 cm and 197 cm respectively.

These parameters are typical of the cathode region of a magnetron discharge. Thus, the electrons will tend to execute circular orbits near the cathode (though, as we will see, this will be modified by field gradients and collisions). This will have the effect of "confining" the electrons in a region there they can efficiently ionize, with attendant improvement in plasma performance. The ions, with gyro radii much larger than the reactor, will be largely unaffected. Processes such as anisotropic etching, which rely on ion orbits being perpendicular to the wafer, will not be disturbed by the magnetic field.

The frequency of rotation of a particle in a magnetic field is called the gyro frequency or cyclotron frequency  $\omega$  and is given by

$$\omega = qB/m. \quad (24)$$

Here,  $\omega$  is given in units of radians/s, and is related to  $f$  the frequency in Hz by

$$\omega = 2\pi f. \quad (25)$$

We note that, although the gyro radius will increase with particle energy,  $\omega$  is independent of the particle energy. As we will see below, this fact underlies our ability to couple energy efficiently to plasma electrons by using an ac power source with a frequency that matches the natural rotational frequency of the electron in a magnetic field. In particular, if  $B = 875$  G, then  $f = 2.45$  GHz. This is a typical combination for electron cyclotron resonance plasma reactors.

The component of the particle velocity parallel to the magnetic field,  $v_{\parallel}$ , is not affected by  $\mathbf{B}$ . Thus, the general orbit of a charged particle in a magnetic field is a helix, as shown in Fig. 5. The sign of the charge will determine the sense of the helix; electrons and ions will have opposite directions of rotation.



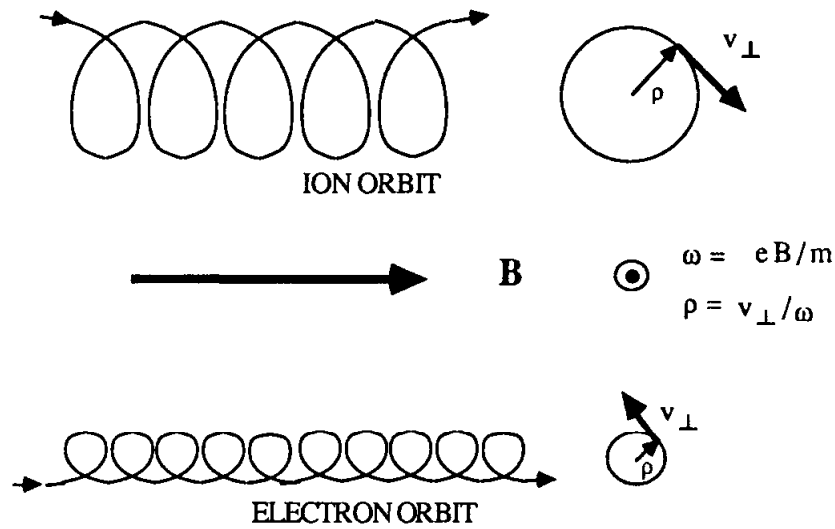


**Figure 5:** Orbits of ions and electrons in a homogeneous static magnetic field  $\mathbf{B}$ . A particle follows a helical orbit, with a gyro frequency  $\omega$  that is independent of the particle energy. The gyro radius depends on  $\omega$  and the perpendicular velocity as noted.

$\mathbf{E} = \text{constant}, \mathbf{B} = \text{constant}$

If  $\mathbf{E}$  is parallel to  $\mathbf{B}$ , then it acts on the particle just as in Eq. (20), i.e.,  $\mathbf{B}$  has no effect on the component of velocity parallel to itself. If  $\mathbf{E}$  is perpendicular to  $\mathbf{B}$ , then the particles will undergo a drift motion which is perpendicular to both  $\mathbf{E}$  and  $\mathbf{B}$  and has a magnitude given by  $v_{\mathbf{E} \times \mathbf{B}}$ :

$$v_{\mathbf{E} \times \mathbf{B}} = E/B. \quad (26)$$

This drift velocity is independent of the particle charge and mass, although implicit in the derivation of Eq. (26) is the assumption that the particles are free to undergo gyro motion. Collisions may interrupt the gyro motion, in which case Eq. (26) will not be valid. This drift will operate on electrons in the cathode region of a magnetron, where the cathode electric field has a component perpendicular to the magnetic field, and the electron gyro radius is small. It will not affect the ions, because their gyro radii are larger than the reactor.

### Nonuniform Fields

A nonuniform electric field will result in an acceleration which changes in space. It is difficult to generalize about the results of this. The main implication is that Eq. (20) will be more difficult to solve.

A nonuniform magnetic field will result in additional drift motion. In particular, a field gradient will produce a drift velocity  $v_g$ , which is perpendicular to both the field and the gradient, given by

$$v_g = (v_\perp^2/\omega)(\mathbf{B} \times \nabla B/2B^2). \quad (27)$$

Unlike the  $\mathbf{E} \times \mathbf{B}$  drift, a gradient drift will depend upon the particle mass, charge, and velocity. If the magnetic field is curved, the particle will experience a drift velocity  $v_c$ , which is perpendicular to both the field and its direction of curvature, given by

$$v_c = (v_\parallel^2/\omega)(\mathbf{R}_c \times \mathbf{B})/(BR_c^2). \quad (28)$$

Here  $\mathbf{R}_c$  is the radius of curvature of the field. As in the gradient drift,  $v_c$  depends upon the particle mass, charge, and velocity. As in the case of the  $\mathbf{E} \times \mathbf{B}$  drifts, it is implicit in the above two formulae that the particles undergo full gyro radii. If we again consider a magnetron discharge, the magnetic field will usually have both curvature and a gradient, so that the drifts in Eqs (27) and (28) will affect the electrons in the discharge (22), providing the rate of collisions is low enough to permit the electrons to execute their gyro motion.

**2.2.3.2 Adiabatic Invariants** In general, the effects of a nonuniform magnetic field are complicated to predict. Under certain circumstances, however, we can take advantage of quantities which are invariant with changes in  $B$ . One example of this is the magnetic moment  $\mu$  which is defined as (23)

$$\mu = W_\perp/B, \quad (29)$$

where  $W_\perp$  is the perpendicular energy of the particle given by

$$W_\perp = mv_\perp^2/2. \quad (30)$$

If a particle passes through a changing field slowly, then  $\mu$  is constant., and is referred to as an adiabatic invariant. "Slowly" in this case means that from the particle's point of view, the field is changing at a rate less than the gyro frequency. This is a bit difficult to calculate exactly, but for most cases of interest this condition is met.

One application of the constancy of  $\mu$  is in a magnetic mirror, which is a configuration, shown schematically in Fig. 6(a), where the magnetic field gets stronger at the ends. Let us assume that the strength of the field is  $B_0$  and  $B_M$  at its minimum and maximum respectively. Let us also assume that the particle has velocity components at the point where  $B = B_0$  of  $v_\parallel$  and  $v_\perp$ . Then, if the particle does not undergo collisions in the time it takes to traverse the mirror, total energy  $W$  is also conserved and given by

$$W = mv_\parallel^2/2 + mv_\perp^2/2. \quad (31)$$

Using Eqs. (30) and (31), we can write an expression for  $v_{\parallel}$

$$\begin{aligned} v_{\parallel} &= (2(W - (mv_{\perp}^2)/2))^{1/2}. \\ &= (2(W - \mu B)/2)^{1/2}. \end{aligned} \quad (32)$$

Now, if the particle moves into a region of stronger magnetic field, it will gain perpendicular energy at the expense of parallel energy. If  $B$  increases to the point that  $W = \mu B$ , then  $v_{\parallel}$  will go to zero and the particle will reverse its direction and thus be "reflected" by the magnetic mirror. For this to happen, the particle must start out with sufficient perpendicular velocity. We can quantify this in terms of the pitch angle  $\Theta$ , shown in Fig. 6(b), which is the angle the velocity vector  $\vec{v}$  makes with  $v_{\parallel}$ . At  $B_0$  the magnetic moment is given by

$$\mu = W_{\perp}/B_0 \quad (33)$$

and at the maximum field, if mirroring is to occur,  $W_{\perp} = W$ , so we can write

$$\mu = W/B_M. \quad (34)$$

Thus from Eqs. (33) and (34), we have that

$$B_0/B_M = W_{\perp}/W, \quad (35)$$

or

$$B_0/B_M = v_{\perp}^2/(v_{\perp}^2 + v_{\parallel}^2). \quad (36)$$

Now  $\sin \Theta = v_{\perp}/v$ , so we can write

$$\sin^2 \Theta = R_M^{-1}, \quad (37)$$

where  $R_M$  is the mirror ratio defined by

$$R_M = B_M/B_0. \quad (38)$$

Particles with pitch angles greater than  $\Theta$  given in Eq.(37) will be reflected in the mirror, while particles with smaller pitch angle have too much parallel velocity to undergo reflection.

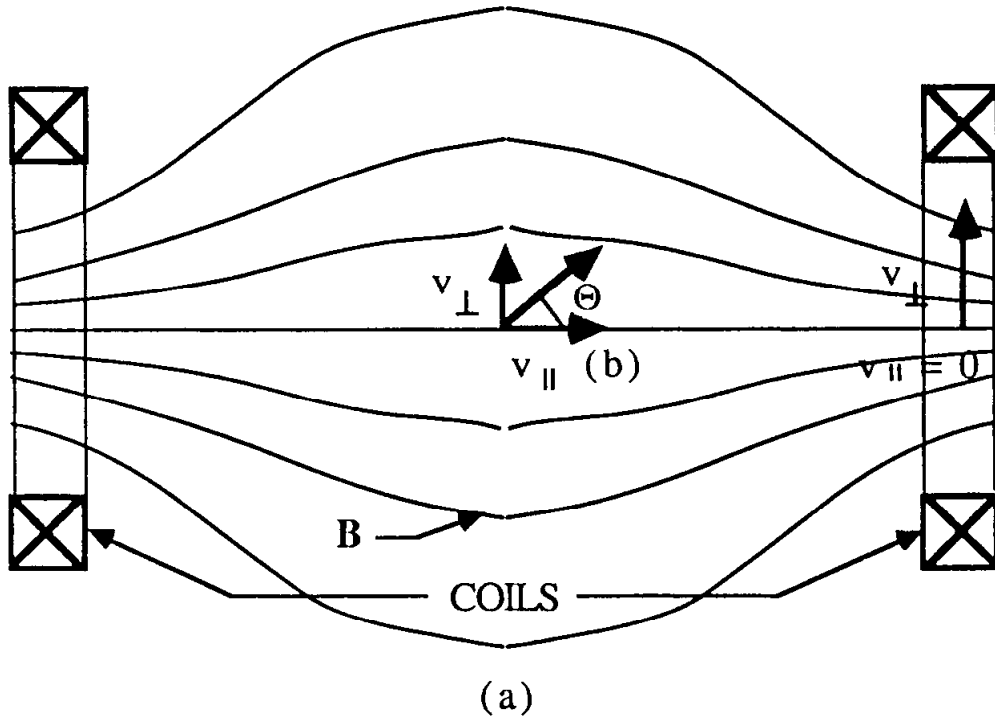


**Figure 6:** (a) Magnetic mirror field configuration produced by a pair of Helmholtz coils. Mirroring takes place as a result of conservation of the particle magnetic moment when the parallel velocity goes to zero. (b) Parallel and perpendicular components of the velocity, showing the pitch angle  $\Theta$ .

In many magnetron configurations, the field gradients will be such as to provide some mirroring of electrons (22). Clearly, at some point, the electrons will undergo collisions, thus disrupting the conservation of  $\mu$ , but at low pressures, their confinement is increased by this effect. Also, it is possible to utilize mirror confinement in an electron cyclotron resonance (ECR) reactor to increase the confinement of the electrons.

Some ECR reactors make use of a sort of "reverse" mirror in which electrons can *gain* parallel energy by moving into a magnetic field which is *decreasing* (24). In a downstream configuration, if the magnetic field at the substrate is  $B_0$  and the maximum field in the ECR region is  $B_M$ , then the electrons which leave the discharge and stream towards the substrate will increase their parallel energy at the expense of perpendicular energy. Let us assume that in the resonance region, since the electrons are being accelerated by the resonant electric field, the energy of the electron is totally perpendicular,  $W = W_{\perp}$ . Then the parallel energy at the substrate is

$$W_{\parallel s} = W - W_{\perp s} = \mu B_M - \mu B_0. \quad (39)$$

This can be rewritten as

$$W_{\parallel s}/W = (1 - B_0/B_M). \quad (40)$$

If the magnetic field at the substrate is  $1/4$  times the field in the resonance region, then 75% of the electron energy will be converted to parallel energy. The electrons streaming rapidly from the discharge will set up an electric field which will accelerate the ions into the substrate.

#### 2.2.4 Collisional Processes

Collisions are generally characterized by a cross section  $\sigma$  which has the dimensions of area. If an electron collided with a "hard sphere" of radius  $a$ , then  $\sigma = \pi a^2$  (see Fig. 7).

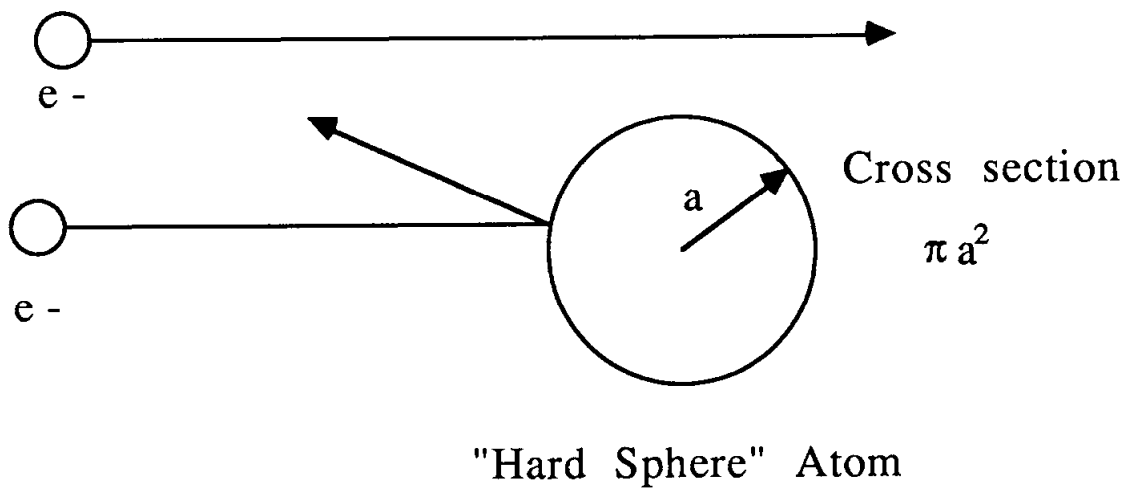


**Figure 7:** Hard sphere atom cross section. Electrons that approach within a distance  $a$  of the center will undergo a collision, while those that have a larger impact parameter will not collide.

The cross section is a measure of the probability that a given process will occur. For some complicated processes there may not be a corresponding physical picture as above, although  $\sigma$  still will have units of area. If we are considering electron - neutral collisions where  $N$  is the neutral density, then the quantity,

$$\lambda = (N\sigma)^{-1}, \quad (41)$$

is the collision *mean free path*. This is the average distance travelled by the electron between collisions or processes.

Another important quantity which is related to the cross section is the *collision frequency*. If  $v$  is the electron velocity, then the collision frequency  $\nu$  is defined by

$$\nu = N\sigma v \quad (42)$$

and has units of  $\text{sec}^{-1}$ . The time between collisions is just  $\nu^{-1}$ .

Collisions fall into two general categories: *elastic collisions*, which are those for which the internal energy of the colliding partners is unchanged by the collision, and *inelastic collisions*, in which internal energy changes. Internal energy refers to electronic excitations in atoms or electronic, vibrational, and rotational excitations in molecules. Ions will, in general, have different states of internal energy, however, an electron does not.

In weakly ionized plasmas ( $n_e/N < 10^{-4}$ ), collisions between electrons and neutrals will be very important in establishing the electron energy distribution function. In fact, the dominance of electron-neutral collisions is responsible for the general character of these glow discharges, which behave very differently from plasmas with higher degrees of ionization, where electron-electron collisions dominate.

In what follows we will consider example of some important collisions processes. Additional information can be found in the references (25,26).

**2.2.4.1 Electron-Neutral Elastic Collisions** The elastic cross section for electron-neutral collisions  $\sigma_N$  will depend on the electron velocity. Examples of  $\sigma_N$  for the rare gases is shown in Fig. 8. For rare gases heavier than He, the cross section has a **minimum** at low electron velocities, rises to a peak which increases with mass, and then falls off at higher velocities. The minimum is called the Ramsauer effect and arises from the quantum mechanical wave nature of the electron. The increase in the maximum cross section with mass is related to the increased size of the atom. At higher electron velocities, the interaction time is shortened, so that the collision has less effect on the electron.

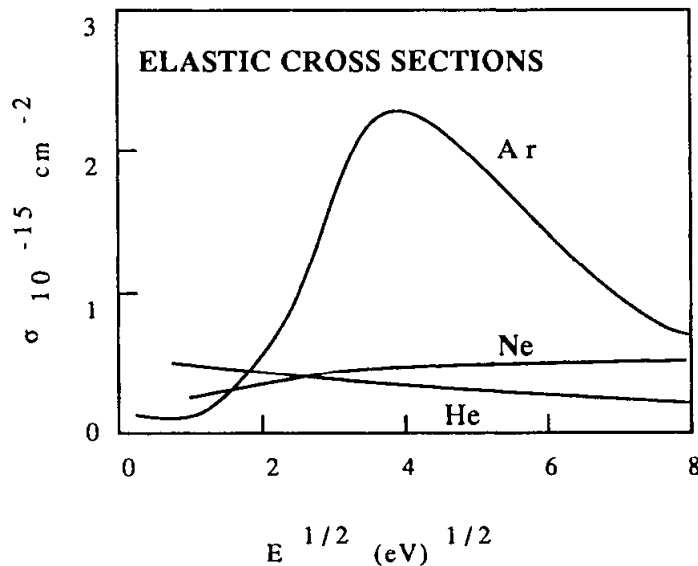


**Figure 8:** Elastic scattering cross sections for electrons of energy  $E$  incident on He, Ne, and Ar.

The average amount of energy transferred from the electron to the neutral is  $E_t$ , given by (27)

$$E_t = \delta E. \quad (43)$$

$E$  is the electron energy and  $\delta$  is given by

$$\delta = (2m/M)E, \quad (44)$$

and  $m$  and  $M$  are the electron and neutral mass respectively. Since the neutral mass is much larger than the electron mass (e.g., for Ar,  $(2m/M) = 1/40,000$ ), very little energy is transferred to the neutral in an elastic collision. However, the electron will experience a large change in the direction of its velocity, and hence its momentum is changed. We will see why this is important when we consider how an electron moves in an electric field.

From Eq. (42), we can write the collision frequency for electron-neutral elastic collisions  $\nu_N$ , as

$$\nu_N = N\sigma_N v \quad (45)$$

where  $v$  is the electron velocity. From Eq. (45) we can see that  $\nu_N$  will depend on the neutral gas pressure. As noted previously, collisions will affect the behavior of electrons in a magnetic field. At higher pressures, where  $\nu_N \gg \omega_c$ , electrons will be unable to execute a full cyclotron orbit, and their drift motion will be interrupted.

**2.2.4.2 Electron-Electron Collisions** Electron-electron collisions are characterized by a cross section  $\sigma_{e-e}$  which is given by

$$\sigma_{e-e} = e^4 \ln \Lambda / (4\pi\epsilon_0^2 (mv^2)^2) \quad (46)$$

where

$$\Lambda = 12\pi(\epsilon kT/e^2)^{3/2}/n^{1/2}. \quad (47)$$

and  $m$ ,  $e$ ,  $v$ ,  $n$ ,  $T$  are the mass, charge, velocity, density and temperature of the electrons, respectively. The term  $\ln \Lambda$  is called the Coloumb logarithm. The collision frequency for electron-electron elastic collision will be given, from Eq. (42) as

$$\nu_{e-e} = n\sigma_{e-e} v. \quad (48)$$

In electron-electron collisions, since the masses are equal, the electrons can exchange energy very effectively, unlike an electron-neutral collision, where there is a large mass difference. Hence, electron-electron collisions will become important even at low degrees of ionization. We quantify this in terms of the parameter  $P$ , defined by Eq. (28)

$$P = \nu_{e-e}(v_0)/\delta\nu_m(v_0) \quad (49)$$

where we evaluate the electron-electron and electron-neutral collision frequencies at a velocity  $v_0$  given by

$$v_0 = (2kT/m)^{1/2}, \quad (50)$$

with  $T$  the electron temperature.  $P$  is the ratio of the rate of electron energy loss by electron-electron collisions to that for electron-neutral collisions. When  $P > 1$ , electron-electron collisions will become important. Due to the factor  $\delta$ , this condition will occur for degrees of ionization around  $10^{-4}$  or  $10^{-3}$ . In ECR discharges, where the degree of ionization is above this, electron-electron collisions will dominate, while in planar reactors, with lower degrees of ionization, electron-neutral collisions will be most important. This will have important implications for the electron energy distribution function, as we shall see in the next section.

**2.2.4.3 Electron Impact Inelastic Collisions** Though the inelastic cross sections are often much smaller than the elastic ones, the electron can lose a much larger fraction of its energy given by (29)

$$(M/(m + M))E. \quad (51)$$

Since  $M \gg m$ , virtually all of the electron energy is available for inelastic processes.

As a first example, we will consider the inelastic processes that result when an electron impacts an atom like He. In the He atom, the electrons occupy certain discrete states, as in Fig. 9.

There are a number of important processes shown here. The first is ionization,



where ions and additional electrons are created. Another process is electronic excitation,



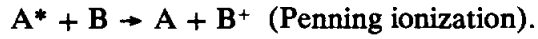
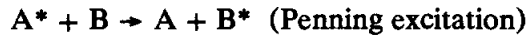
where the electrons in the He atom are promoted to excited states. The lifetime of many of the He excited states is very short (typically 100 ns or less), so that excitation is frequently followed by radiative decay,



where a photon of frequency  $\nu$  is emitted. Certain states in He have much longer lifetimes. These *metastable* states, which are shown in Fig. 9, can have lifetimes of 1 ms or longer. The metastable states also have considerable energy (e.g., 20 eV for He) and if they collide with ground state neutrals, they may cause excitation or ionization. These



are the *Penning* processes, which, for metastable species  $A^*$  colliding with species  $B$  look like



These processes will increase the ionization rates and excitation rates in plasmas, and this is one reason why rare gases like He and Ar are added to process plasma discharges.

### He Atomic Energy Levels

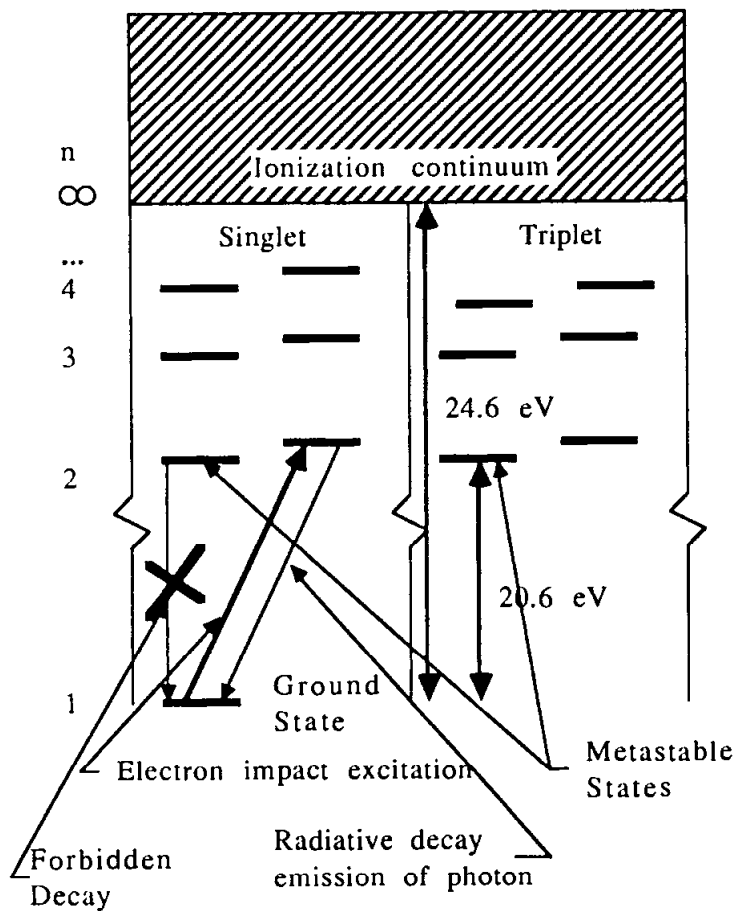
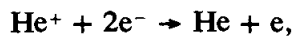
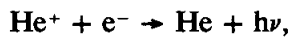


**Figure 9:** Atomic energy levels for He, showing the singlet and triplet series. The energy necessary to ionize is 24.6 eV, while the energy for the first electronic excitation is 20.6 eV. States which are forbidden to decay to the ground state have long lifetimes and are called metastable states.

The inverse processes, where electrons are lost by recombination can also be important. One example is three body recombination,

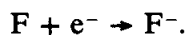


where two electrons are necessary to conserve momentum. Another recombination process is *radiative recombination*,



where energy and momentum are balanced by emission of a photon after recombination.

An important process for electron loss that can occur in a plasma where the neutral species has a high electron affinity (such as halogen discharges) is electron capture, shown here for fluorine



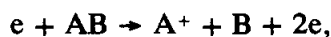
Each process will have a cross section associated with it. In all of these processes, the incident electron will lose an amount of energy equal to that required for the inelastic process. For the electron loss processes, the entire energy of the electron is lost.

In rare gas atoms, electron excitation requires an amount of energy which is very close to that for ionization, and therefore, the cross sections are quite similar. Owing to this, for rare gas plasmas, we can reasonably assume that where light is emitted (radiative decay following electron excitation), ionization is probably also occurring. Note that the excitation process represents an important energy loss mechanism for the electrons.

Atoms other than the rare gases will generally have lower lying levels for excitation, as will molecules, which have rotational and vibrational states which require much less energy than excited electronic states. Electron energy losses will therefore be greater than in non-rare gas plasmas. When an electron collides with a molecule (which we will represent as AB), a number of processes may occur. *Dissociation*, such as



can result in the formation of chemically reactive radicals. Another important process is *dissociative ionization*,

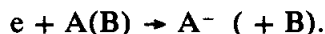


where ions and radicals may be formed. The dissociation products of molecules may react to form additional species. The chemically active species may also undergo surface reactions, as in etching or deposition.

Some electron loss processes associated with molecules are *associative recombination*



and *dissociative attachment*



**2.2.4.4 Ion Collision Processes** There are a few ion impact processes which are crucial to the discharge. The first is secondary electron emission from a surface bombarded by an energetic ion. This process is usually characterized by a coefficient  $\gamma$  which is the ratio of the number of electrons emitted for each incident ion. Typically  $1/10 > \gamma > 1/20$ .

Another important ion process is that of charge transfer:



where A and B can be the same species. This process is an important loss mechanism for energetic ions in the sheath region of discharges.

### 2.2.5 Diffusion and Particle Losses

At the pressures typical of deposition and etching ( $10^{-4} - 10^{-1}$  Torr), the loss of charged particles by the volume processes discussed in Sect. 2.2.4 are relatively small. The dominant charged particle loss mechanism is diffusion and convection to the reactor boundaries (walls or electrodes), where recombination will occur rapidly on the solid surfaces. In Sect. 2.3.1, we will introduce the concept of mobility, and will consider how electrons move convectively due to an electric field. In this section, we will consider diffusion, which can be described by the equation of conservation of particles,

$$\delta n / \delta t + \nabla \cdot \Gamma = S, \quad (52)$$

where  $n$  is the particle density,  $S$  is the net volume production rate, and  $\Gamma$  is the particle flux given by Fick's Law

$$\Gamma = -D \nabla n, \quad (53)$$

with  $D$  the diffusion coefficient. The choice for the diffusion coefficient depends on a number of things. At low enough densities, the diffusion coefficient is given by (30)

$$D = (v^2 / 3\nu), \quad (54)$$

where  $v$  is the particle velocity and  $\nu$  is the collision frequency for momentum transfer. This means that electrons would tend to diffuse much faster than ions. However, as the electron and ion densities become greater, electric fields will arise because of this disparity in diffusion rates, and this will tend to equalize the rates. This latter type of diffusion is called *ambipolar*, and in the extreme limit, which occurs for electron densities above  $10^9 \text{ cm}^{-3}$ , both electrons and ions diffuse at two times the slower ion rate (31-33).

### 2.2.6 Sheaths

**2.2.6.1 Non-conducting or Isolated Surfaces** We have already examined the effects of Debye shielding which occurs inside the plasma volume. We will now explore the manifestation of this effect at the plasma edge. At the boundary, electrons and ions will diffuse out of the plasma, as noted previously, owing to their thermal energies. From simple kinetic theory, the flux  $j$  is

$$j = (nv/4), \quad (55)$$

where,  $n$  is the particle density and  $v$  the thermal velocity which is given by

$$v = (3kT/m)^{1/2} \quad (56)$$

with  $T$  the (ion or electron) temperature and  $m$  the mass. In the absence of any sheath effects, and for electron temperatures equal to or greater than the ion temperature, the electron velocity will be much greater than the ion velocity.

Let's consider what happens near a non-conducting wall (or an isolated conducting wall). The electron flux to the wall will be higher initially, owing to their greater thermal velocities. However, this will cause the plasma to become more positive, since there is an excess of positive ions left behind. An electric field will develop which will retard the electrons and accelerate the ions, in such a way to make the net current zero. The magnitude of the potential which the plasma acquires is about  $(3kT_e/e)$ , where  $T_e$  is the electron temperature. As we might guess, this potential falls off from the wall into the plasma over a distance of the Debye length  $\lambda_D$  (Eq. (13)), as shown in Fig. 10.

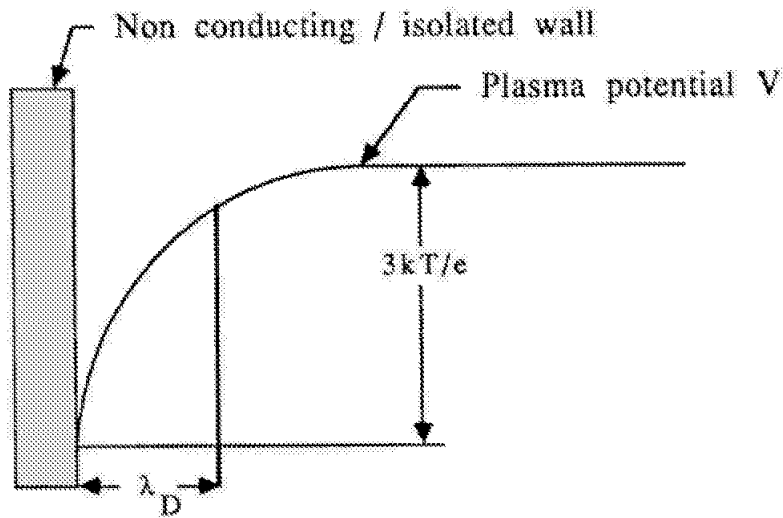


**Figure 10:** Behavior of the plasma potential in the vicinity of a non-conducting or isolated wall. The characteristic fall-off for the sheath potential is the Debye length (Eq. (13)).

**2.2.6.2 Sheath Near a Conducting Electrode.** Let us now consider the case of a surface across which current flows (e.g., the cathode in a dc glow). The form of the potential in this region can be found from Poisson's equation. We will assume that the potential on the electrode is negative and large, which will have the effect of attracting ions and repelling electrons. We will take the electron density in the sheath region to be zero. The current density  $J$  is then given by

$$J = nev, \quad (57)$$

where  $n$  is the ion density,  $e$  is the electronic charge, and  $v$  is the ion velocity. The potential  $V(x)$  obeys

$$(d^2V/dx^2) = -ne/\epsilon_0. \quad (58)$$

The ion velocity is related to the potential  $V$  by conservation of energy

$$mv^2/2 = eV. \quad (59)$$

From these two equations, we have

$$(d^2V/dx^2) = (1/\epsilon_0)(m/2e)^{1/2}(1/V)^{1/2}. \quad (60)$$

Multiplying this equation by  $(dV/dx)$  and integrating,

$$(dV/dx)^2 = (4/\epsilon_0)(m/2e)^{1/2}(1/V)^{1/2}. \quad (61)$$

Taking the square root of both sides and integrating,

$$J(x) = (4\epsilon_0/9)(2e/m)^{1/2}(V^{3/2}/x^2), \quad (62)$$

which is the Child-Langmuir Law for space charge-limited current flow. The resulting sheath thickness will be many times the Debye length.

In addition to this "free fall" sort of sheath, in which we assumed that the ions did not make any collisions, it is also possible to have a mobility-limited sheath, where the ion velocity is determined by its mobility (34).

## 2.3 ELECTRON HEATING AND ENERGY DISTRIBUTION

The discharges of interest here are sustained by some dc or ac power source which establishes an electric field in the plasma. As we shall see, plasma electrons will gain energy from being accelerated in the electric field. In steady state, a balance is established between the energy which the electrons gain from the electric field and the energy which they lose through collisional and other loss processes described above. The energetic electrons are responsible for most of the ionization, which produces additional electrons and ions to sustain the discharge against the various loss processes. There is clearly a very complicated interplay among the many processes which work to establish the energy balance and particle balance which is necessary for maintaining a discharge. In this section, we will examine how the electrons are "heated" by the external power source and how the electron energy distribution function is established.

### 2.3.1 Interaction of Electrons with a Static Electric Field

An electric field will accelerate all charged particles, however, the electrons with their smaller mass will be accelerated more (35), and we will now consider the result. From Eqs. (10) and (18), when an electron is subjected to an electric field  $E$ , it experiences a force given by

$$F = -eE, \quad (63)$$

and an acceleration

$$\mathbf{a} = -e\mathbf{E}/m. \quad (64)$$

We will assume that electron-neutral collisions dominate, as is the case for planar or barrel reactors. Let us consider the effect of elastic collisions, assuming, as an example, that electrons are moving in Ar at a pressure of 30 mTorr ( $N = 1 \times 10^{15} \text{cm}^{-3}$ ). Then, since the average elastic collision cross section is about  $1 \times 10^{-15} \text{cm}^2$ , we note that from Eq. (41) the mean free path  $\lambda$  is about 1 cm. If the angle between the electron velocity and the electric field is  $\theta$ , then the electron will gain an average amount of energy

$$eE\lambda \cos \theta, \quad (65)$$

between collisions.

The electron will lose only a relatively small amount of energy during each elastic collision. If  $W$  is the electron energy, then the amount lost,  $\Delta W$ , is from Eqs. (43) and (44)

$$\Delta W = (2m/M)W, \quad (66)$$

which for Ar ( $M=40$  AMU) is

$$\Delta W = 2 \times 10^{-4} W. \quad (67)$$

Although little *energy* is exchanged in this elastic collision, it does have a profound effect on the electron *velocity*, i.e., there is a large *momentum* change. The electron velocity will be redirected after the elastic collision, as shown schematically in Fig. 11. Thus, the elastic collisions effectively transform the *directed* energy which the electrons acquire from the electric field into *random* energy. This begins to establish the electron energy distribution function, and the electrons "heat up."

Eventually a steady state is reached where the energy gained by the electrons between collisions is equal to the energy lost during the collision. Since the energy lost is a small fraction of the total energy, the electrons will heat up to a sufficiently high energy to establish this balance. This means that the random velocity will be much greater than the directed velocity which the electron gains from acceleration in the electric field.

We can examine this more quantitatively by writing Newton's second law including the effect of collisions. The electrons will attain an average directed velocity, or drift velocity,  $u$ , due to the electric field. Collisions will cause the electrons to lose their directed momentum,  $\mu$ , at the rate given by  $\nu_m$ , where  $\nu_m$  is the collision frequency for momentum loss. Though all types of electron collisions will contribute to the momentum loss, it is usually the elastic collisions that dominate, so we will take  $\nu_m = \nu_N$ . Newton's second law is then

$$(d/dt)(mu) = -eE - mu\nu_N. \quad (68)$$

In Eq. (68) we are ignoring the random thermal motion. However, writing the equation is justified because the average random velocity is zero. Equation (68) is called the Langevin equation (36).

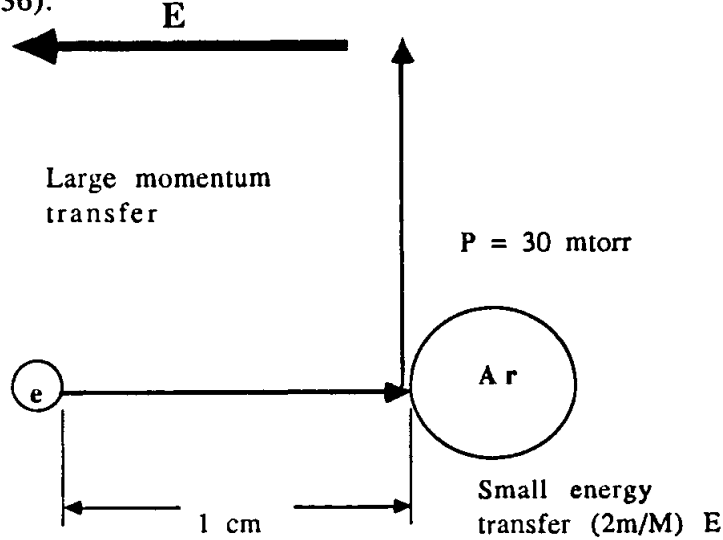


**Figure 11:** Elastic collisions between electrons and Ar transform the directed energy which the electrons gain from acceleration in the electric field to random thermal energy, thus causing heating of the electrons. There is very little energy transfer in an electron-neutral elastic collision, owing to the large mass difference between the electron and neutral; however, the electron will have its momentum randomized by the collision.

In steady state, the solution to Eq. (68) is

$$u = \mu E \quad (69)$$

where  $\mu$  is the electron mobility defined as

$$\mu = e/(m\nu_N). \quad (70)$$

From Eqs. (69) and (70), we can see that the drift velocity is proportional to the quantity  $(E/N)$ . This ratio of the electric field to the neutral density (or pressure) will arise in many of the formula we will derive here.

The current density  $J$  due to the directed motion of the electrons is given by

$$J = -enu, \quad (71)$$

where  $e$  is the electron charge and  $n$  is the electron density. From Eq. (69) we can write

$$J = \sigma E, \quad (72)$$

where  $\sigma$  is the electrical conductivity given by

$$\sigma = ne^2/(m\nu_N). \quad (73)$$

We will now consider the energy balance. The rate at which the external power source puts energy into the electrons is

$$P_{in} = JE = \sigma E^2. \quad (74)$$

The rate at which energy is lost due to collisions is

$$P_{out} = n \delta W \nu_N + n \sum_i W_i \nu_i, \quad (75)$$

where the first term is the energy loss rate due to elastic collisions and the second term is the sum over all inelastic processes, with energy loss  $W_i$  and collision frequency  $\nu_i$ . To simplify the present discussion, we will assume that the elastic loss term dominates. In steady state,  $P_{in} = P_{out}$ , so that from Eqs. (74) and (75), we get

$$n \delta W \nu_N = \sigma E^2 = ne^2 E^2 / (m \nu_N). \quad (76)$$

Solving Eq. (76) for  $W$  we get

$$W = e^2 E^2 / (\delta m \nu_N^2). \quad (77)$$

As an example, let us consider He at 0.5 torr pressure in a typical electric field of 1 V/cm (100 V/m). Then Eq. (77) would predict an electron energy of approximately 5 eV. The energy lost per collision ( $\delta W$ ) is 0.00125 eV, which, in steady state, is just equal to the energy which an electron gains from the electric field between collisions. Since such a small fraction of the electron's energy is lost in a collision, the electrons must heat up to 5 eV to provide the energy balance. The small energy transfer results in negligible heating of the neutrals, which therefore usually remain at room temperature (37).

From Eqs. (77) and (42) we can write  $\nu_N$  as

$$\nu_N = N \sigma_n v. \quad (78)$$

Then, if we take  $v$  to be the average thermal velocity, we have

$$W = mv^2/2, \quad (79)$$

and from Eqs. (42), (78) and (79) we can write



$$W = (e/\sigma_N(2\delta)^{1/2})(E/N). \quad (80)$$

This shows that electron energy depends linearly on the quantity  $(E/N)$ . From Eqs. (69-70) and (77-79) we can derive the ratio of the drift velocity  $u$  to the average thermal velocity  $v$ ,

$$u/v = (\delta/2)^{1/2}. \quad (81)$$

For Ar, this ratio is  $3.5 \times 10^{-3}$ . Thus, the drift velocity is a small fraction of the average thermal velocity which the electrons attain by virtue of the collisions, which transform the directed energy the electron gains from the electric field to thermal energy.

The inclusion of inelastic processes will modify the energy balance because, in those processes, an electron can lose a large fraction of its energy. This will result in a lower electron energy than that predicted by Eq. (77). It will also result in a larger ratio of  $u/v$ . However, the cross sections for inelastic processes are usually smaller than for elastic processes, so that the electrons will still be hotter than the neutrals.

Thus far we have considered only the steady state. If we were to solve the time dependent equation, we would find that, to achieve steady state, an electron would have to undergo approximately  $\delta^{-1}$  collisions (38). In a dc electric field, the electron would have to move a distance  $d$  in the field given by

$$d = u/(\delta\nu) = eE/(m\delta\nu^2). \quad (82)$$

Using the previous example of He at 0.5 torr, we find that the drift distance is 5 cm.

In what we have derived above, we have not invoked the existence of a plasma. The derivations would be entirely appropriate for a beam of electrons going through a neutral gas. One important aspect of a plasma is Debye shielding. Which raises the question of how do we actually get an electric field into a plasma? In fact, we cannot introduce just any arbitrary value of the electric field into a plasma. The limiting criterion is that the potential across a Debye sphere must be less than the thermal energy:

$$eE\lambda_D < W. \quad (83)$$

Now from Eq. (80), we can write  $W$  as

$$W = eE\lambda/(2\delta)^{1/2} \quad (84)$$

Where  $\lambda$  is the collision mean free path,

$$\lambda = (N\sigma)^{-1} \quad (85)$$

Therefore, our criterion Eq. (83) is just

$$\lambda_D < \lambda / (2\delta)^{1/2}. \quad (86)$$

Taking Ar at 30 mTorr as an example, we find that the right hand side is 200cm. This is clearly much larger than the Debye length, so we are well within the limits of our criterion.

### 2.3.2 Interaction of Electrons with a Time Dependent Electric Field and Magnetic Field

We will now consider the particle motion that results from using an ac power source at frequency  $\omega$ , with no magnetic field present. It is convenient to write the electric field as a complex quantity (18)

$$\vec{E} = \vec{E}_0 \exp(j\omega t), \quad (87)$$

where  $j = \sqrt{-1}$ , and  $E_0$  is the amplitude of the field which is independent of time. Since the electric field changes direction, the resulting motion of the particles will be oscillatory, as will be the particle drift velocity. We can solve the Langevin equation Eq. (68) to derive a mobility and conductivity given by

$$\mu = e/m(\nu + j\omega), \quad (88)$$

and

$$\sigma = ne^2/m(\nu + j\omega). \quad (89)$$

Let us now examine the power input to the electrons in this case. It will be given by

$$P_{in} = \text{Re}(JE), \quad (90)$$

where Re denotes the real part of the complex quantity. From Eqs. (72), (87) and (89) we get

$$P_{in} = ne^2 E_0^2 / (m\nu_{eff}), \quad (91)$$

where  $\nu_{eff}$  is an "effective" collision frequency given by

$$\nu_{eff} = \nu(1 + (\omega/\nu)^2). \quad (92)$$

Let us examine some special cases. If  $\omega = 0$ , we recover the dc case. If there were no collisions (i.e.,  $\nu = 0$ ), we find from Eqs. (89) and (90) that  $P_{in}$  averages to zero. The reason for this is that the drift velocity and electric field would be  $90^\circ$  out of phase, and

thus no power could be transferred. As in the dc field case, the collisions transform the directed energy that the electrons gain from the oscillating electric field to the random energy that represents electron heating.

If  $\omega \gg \nu$ , then the mobility and conductivity are similar to the dc case with  $n$  replaced by  $\omega^2/\nu$ . The power input would therefore decrease with increasing frequency.

Although it is not obvious from our derivations here, a more detailed calculation would reveal the fact that the maximum power input occurs when  $\omega = \nu$  (33). This can be seen qualitatively by the following argument. If the ac power frequency is much lower than the collision frequency, then the particles make numerous collisions during each ac cycle which prevents the particles from reaching the maximum energy during the ac oscillations. On the other hand, if  $\omega \gg \nu$ , then the particles undergo many oscillations between collisions, but this does not increase their energy. When  $\omega = \nu$ , the electrons make approximately one collision for every cycle of the ac power, and that represents the optimum for transforming energy from the electric field to the electron energy distribution.

We noted in Sect. 2.2.2 that if the frequency of an ac electric field were above the plasma frequency, it would not be shielded, because the plasma electrons are incapable of responding on such a fast time scale. If  $\omega$  is below  $\omega_p$ , we would like to know how far the field would penetrate into the plasma. We will consider a number of cases.

For a typical planar reactor with an electron density of  $10^{10} \text{ cm}^{-3}$ , the plasma frequency is around 1 GHz. Most commercial planar equipment utilize 13.56 MHz power, which seems to contradict the discussion above. This is easily resolved by noting that in a planar reactor, we are not really launching rf radiation, because the wavelength of the 13.56 MHz source is over 20 m, which is much larger than the reactor. We are in what is called the *near zone* (18). In this sense, the plasma will respond much as it would to a dc field, and the criterion noted in the last section apply.

If we wanted to use an oscillating electric field with a wavelength short compared to the plasma size, then the associated field would be attenuated if its frequency were below the plasma frequency. In particular, if this radiation were such that the electric field it produced in the plasma pointed in the direction of propagation, then it would be attenuated in a Debye length.

If, on the other hand, we introduced radiation where the electric field was perpendicular to the direction of propagation, the wave would penetrate a distance  $\delta_s$ , called a skin depth, given by

$$\delta_s = c/\omega_p. \quad (93)$$

Notice this is like the Debye length, except that the speed of light replaces the average thermal velocity of the electrons. Thus, the "fast" electromagnetic wave can penetrate deeper by a factor of typically 1000 times the Debye length. For a process plasma with a typical  $\lambda_D$  of 0.01 cm, the radiation may penetrate to a distance of about 10 cm.

Radiation at frequencies higher than the plasma frequency will be phase shifted by the plasma, with the amount of phase shift depending on  $\omega_p$ . Since  $\omega_p$  depends on density, the phase shift can be used to deduce the plasma electron density (39).

### 2.3.3 Interaction of Electrons with a Time Dependent Electric Field in the Presence of a Static Magnetic Field

A quantitative discussion of this case, which is beyond the scope of this chapter, can be found in the references (40). We will consider this problem heuristically, utilizing a number of our previous derivations. We know from Sect. 2.2.3 that in a magnetic field, the particles undergo a natural circular motion in a plane perpendicular to the magnetic field (we can neglect motion along the field for this discussion). The angular frequency of this electron cyclotron motion is from Eq. (24)

$$\omega_c = eB/m, \quad (94)$$

and is independent of the particle energy. If we introduce an electric field of frequency  $\omega$  which is resonant with  $\omega_c$ , then we will be able to accelerate electrons synchronously. As the electron's perpendicular energy increases, the gyro radius will increase, but the cyclotron frequency will remain constant, and therefore the particles will remain in phase with the applied field. As in all the previous cases, if we want to heat the electrons, we will need collisions to transform this directed energy to random thermal energy. However, one big difference here is that the electron energy is increasing with each ac cycle, so that there is no need to have the collision frequency equal to the applied frequency. This facilitates operation at lower pressures.

Let us look more closely at the resonance condition, and assume that there is some difference  $\Delta\omega$  given by

$$\Delta\omega = \omega - \omega_c. \quad (95)$$

Then, after a time given by approximately  $(\Delta\omega)^{-1}$ , the applied electric field will start to get out of phase with the electron's natural cyclotron motion and begin to slow it down. If, however, the electron were to undergo a collision within this time, then the directed energy gained from the oscillating electric field will be transferred to the electron's thermal distribution. Thus, the criterion for optimum power coupling is

$$\nu = \Delta\omega. \quad (96)$$

In practice, there will be a number of effects that can cause a deviation between the electron cyclotron and the applied frequencies, including things like magnetic inhomogeneities.

If the collision frequency becomes of the order of  $\omega_c$  or larger, then the electrons will not be able to undergo the complete cyclotron orbit. In this case, from arguments analogous to those given above, the collisions will broaden the cyclotron resonance by an amount given in Eqs.(95) and (96). If the resonance is sufficiently broad, then there is little advantage to having a magnetic field at all.

As noted previously, the presence of a magnetic field will give rise to additional oscillatory modes in addition to that discussed in Sect. 2.2.2. One consequence of this is that radiation which is below the electron cyclotron frequency can propagate in a plasma, regardless of its relationship to the plasma frequency. This means that in an electron cyclotron reactor, the incident radiation can propagate through regions of higher magnetic field to reach an interior resonance region.

### 2.3.4 The Electron Energy Distribution Function

In Sec. 2.1.1, we defined the electron energy distribution function,  $f(\epsilon)$ , which is proportional to the number of electrons having an energy between  $\epsilon$  and  $\epsilon + \delta\epsilon$ . In particular, we looked at the Maxwellian, or equilibrium form for  $f$ . The electron energy distribution function is a very important quantity, because the rates  $k_i$  of all electron-induced processes, such as ionization and dissociation, will depend on it through the expression

$$k_i = \int \sigma_i v f(\epsilon) d\epsilon \quad (97)$$

where  $\sigma_i$  is the cross section for the particular process and  $v$  is the electron velocity.

The electron energy distribution function  $f$  will be determined by the energy input to the electrons via the electric field and the energy lost through elastic and inelastic processes, through the Boltzmann Equation (41). The solution of the Boltzmann equation is beyond the scope of this chapter; however, we will consider a few special cases.

For a dc electric field where the electron kinetics are dominated by elastic collisions between electrons and neutrals and the collision frequency is independent of electron velocity (i.e.,  $\sigma \approx v^{-1}$ ), the solution to the Boltzmann equation is a Maxwellian. If, however, the collision frequency is linear in  $v$  (i.e.,  $\sigma \approx \text{constant}$ ), then the result is the Druyvesteyn distribution, which has a form like

$$f(\epsilon) = A\epsilon^{1/2} \exp(-B\epsilon^2), \quad (98)$$

where  $A$  and  $B$  are constants. This distribution falls off faster with energy than does a Maxwellian, and arises because the collision frequency is greater for higher energy electrons.

The inclusion of inelastic processes will drastically alter the form of  $f$ . In particular, above the thresholds for the various inelastic processes,  $f$  will usually decrease rapidly. Many examples can be found in the literature (42).

In cases where electron-electron collisions are important,  $f(\epsilon)$  will tend towards a Maxwellian (43). As noted before, due to the fact that electrons can exchange energy much more efficiently than will electrons and neutrals, electron-electron collisions can become dominant at even relatively low ionization fractions. The quantity  $P$ , defined in Eq. (49), gives a more quantitative measure. The distribution will become Maxwellian for  $P > 5$ . Such conditions are commonly met in an electron cyclotron resonance reactor.

## 2.4 BREAKDOWN

In this section we will consider the breakdown processes that precede the formation of dc and rf glow discharges.

### 2.4.1 DC Breakdown

We will examine dc breakdown by considering, as an example, Ar at 30 mTorr in a system, shown in Fig. 12, comprising two electrodes connected to a dc power supply with voltage  $V_{ps}$  through a ballast resistor  $R$ .

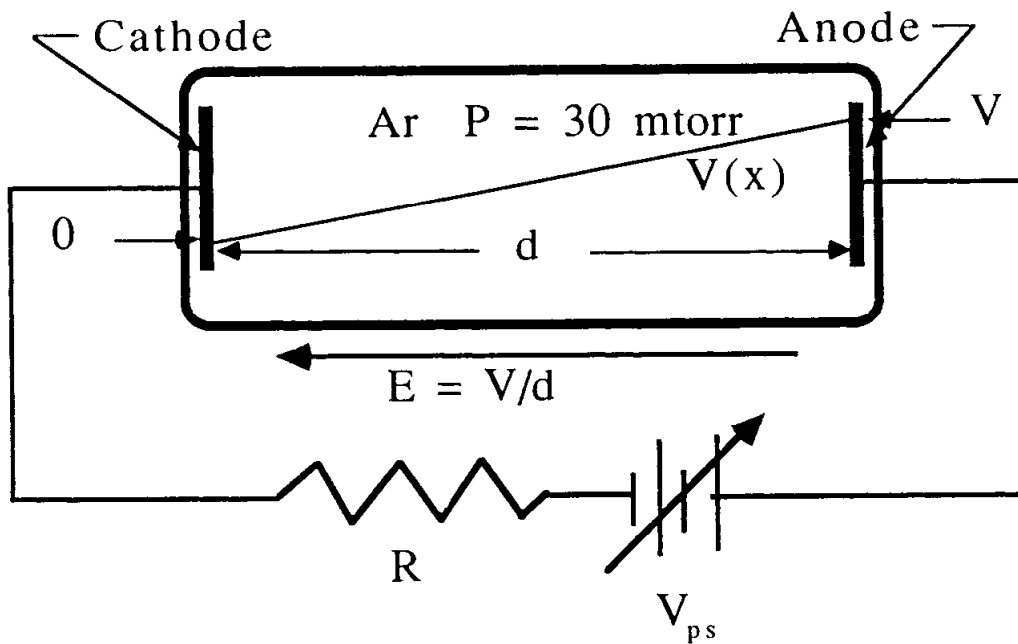


**Figure 12:** Schematic of an Ar discharge prior to breakdown. The resistance of the Ar is much greater than that of the ballast resistor  $R$ , so the entire voltage is dropped across the discharge tube.

Initially, the resistance of the neutral gas will be much greater than that of  $R$ , so the voltage across the discharge  $V = V_{ps}$ . Let us assume that there is one free electron, formed perhaps by a cosmic ray or some UV photon, near the cathode. The electric field will accelerate the electron towards the anode. Let  $\alpha$  be the probability per unit length that ionization will occur. The quantity  $\alpha$  is called Townsend's first ionization coefficient, and represents the net ionization probability, including losses. As a result of the acceleration by the electric field, the electron will gain energy (see Sect. 2.3.1) and produce ionization. This will lead to a multiplication of the number of electrons as shown in Fig. 13.

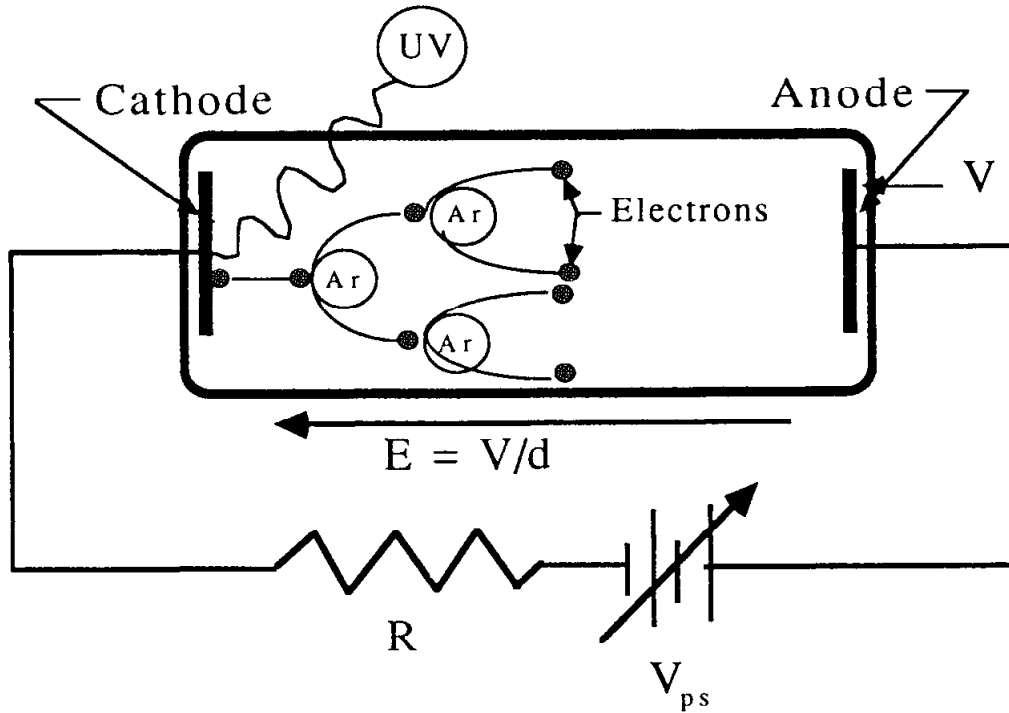


**Figure 13:** Behavior of the discharge at breakdown. An electron is created by photodesorption at the cathode. The electron is accelerated by the electric field and causes ionization, creating ions and additional electrons.

The current at the anode arising from an electron current  $I_0$  emitted from the cathode is given by

$$I_{(d)} = I_0 \exp(\alpha d). \quad (99)$$

The electric field will also accelerate ions, and when ions strike the cathode, electrons will be emitted by ion impact secondary electron emission with a probability  $\gamma$ . The total number of ions created by the first electron multiplication is  $I_0(\exp(\alpha d) - 1)$ . This will give rise to  $\gamma I_0(\exp(\alpha d) - 1)$  secondary electrons, which will also be accelerated by the electric field and cause more ionization and consequently more ions. If we add up this sequence of successive generation of secondary electrons giving rise to more ions giving rise to more secondaries, etc., we find that the total current arriving at the anode is

$$I(d) = I_0 \exp(\alpha d) / [1 - \gamma(\exp(\alpha d) - 1)] \quad (100)$$

If  $\exp(\alpha d) \gg 1$ , we can write Eq. (100) as

$$I(d) = I_0 \exp(\alpha d) / [1 - \gamma \exp(\alpha d)]. \quad (101)$$

When

$$1 - \gamma \exp(\alpha d) = 0 \quad (102)$$

the current  $I(d)$  tends to increase rapidly, a condition referred to as breakdown. Let us look a little more closely at the form of the breakdown condition. The ionization probability per unit length  $\alpha$  will be proportional to the number of collisions per unit length, multiplied by the probability that the collision will cause ionization. Thus we can write  $\alpha$  as (43)

$$\alpha = (1/\lambda) \exp(-V_i/eE\lambda), \quad (103)$$

where  $\lambda$  is the collision mean free path, and  $eE\lambda$  is just the energy gained by the electron between collisions.  $V_i$  is an *effective* ionization potential, i.e., it takes into account the effect of losses. The exponential term thus expresses the probability that the electron will cause ionization. Now, from Eq. (41), the mean free path will be inversely proportional to the neutral density or pressure  $P$  as

$$\lambda = \lambda_1/P, \quad (104)$$

where  $\lambda_1$  is a constant. Then from Eqs. (102-104) we find that the breakdown electric field  $E_B$  is given by

$$E_B = AP/(C + \ln(Pd)) \quad (105)$$

where  $A$  and  $C$  are constants which depend on the gas. We can therefore write an expression for the breakdown voltage  $V_B = E_B/d$  as

$$V_B = A(Pd)/(C + \ln(Pd)). \quad (106)$$

For large  $Pd$ , the breakdown voltage will be proportional to  $Pd$ . This is equivalent to the breakdown condition being a constant value of  $E_B/P$  for a given gas, and is consistent with  $E/P$  being a measure of the average energy gain of an electron between collisions (see Eq. 80). For this case electrons make many collisions, and therefore the breakdown condition is equivalent to a constant value of the energy gained by an electron between collisions. This means that the electric field must scale linearly with the pressure, or  $V_B$  is linear in  $Pd$ . At very small values of  $Pd$ , there are very few collisions, and therefore,  $V_B$ , the breakdown voltage rises to increase the probability of breakdown per collision. A graph of the breakdown condition for Ar is shown in Fig. 14. The minimum breakdown voltage is called the Paschen minimum.

One important application of the breakdown formalism is the design of ground shields (also called dark space shields) for the discharge electrodes. These shields are intended to prevent the formation of a plasma at the edges and behind the electrodes. For a dc discharge, they must be placed within a distance  $d_s$  such that the maximum discharge voltage  $V_M$  satisfies the condition (44)



$$V_M < V_B(Pd_s) \quad (107)$$

where  $V_B$  is the breakdown voltage for the particular gas used in the discharge evaluated at the product of pressure and distance using the shield-electrode spacing. Similar results apply to ground shields for rf discharges, although the complexity of the particle oscillation in the rf field must be considered.

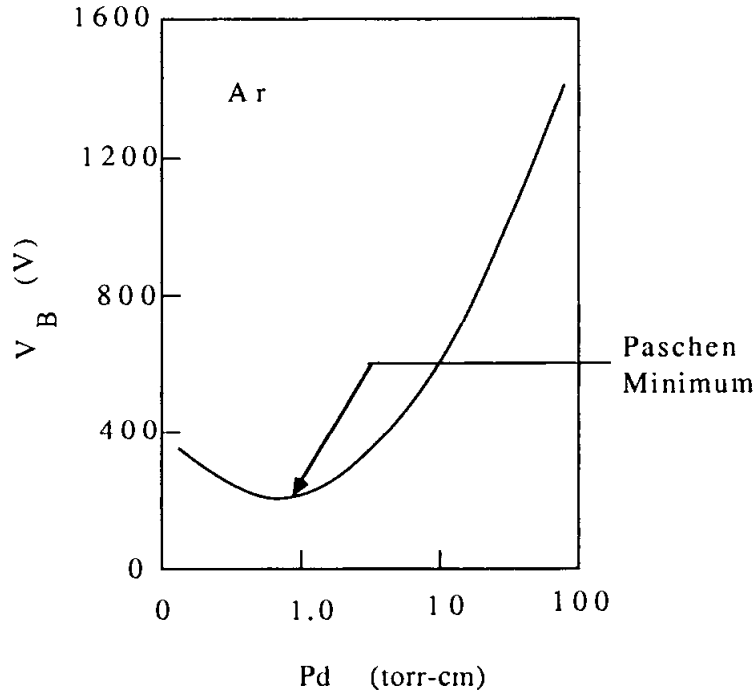


**Figure 14:** Plot of the minimum breakdown voltage for Ar as a function of the product of the Ar pressure and spacing of the electrodes.

#### 2.4.2 RF Breakdown

Breakdown in an rf field is actually somewhat simpler than that for dc, if most of the electrons are able to undergo their oscillatory motion without colliding with a wall. In this case, the alternating electric field can heat the electrons sufficiently to produce the required amount of ionization, and it is not necessary to invoke secondary electron emission processes. What is required is that the rate of ionization balance the losses due to diffusion to the walls, volume recombination, electron attachment, etc. We will consider the case which is typical of the process plasmas of interest, where diffusion losses dominate.

As we saw in Sect. 2.2.5.2, the oscillating electric field will put directed energy into the electrons, which will then heat up by undergoing collisions with neutrals. The electrons will cause ionization which must balance the diffusive losses. We assume for simplicity that the diffusion coefficient and ionization rate are independent of position. From Eq. (52) we can write the steady state diffusion equation as

$$\nabla^2 n = (\nu_i/D)/n, \quad (108)$$

where  $\nu_i$  is the ionization rate. Taking  $n = 0$  at the boundary of the plasma region, the solutions require that (53)

$$\nu_i/D = 1/\Lambda^2, \quad (109)$$

where the constant  $\Lambda$  depends on the geometry of the plasma. If the discharge is cylindrical with the radius of the cylinder  $R_D$  much larger than the length  $h_D$  (a typical planar configuration), then

$$\Lambda = h_D/\pi \quad (110)$$

If the cylinder is long and has a small radius then

$$\Lambda = R_D/2.405. \quad (111)$$

The ionization rate and  $D$  will depend on the parameter  $(E/N)$ . Then Eq. (109) in conjunction with Eq. (110) or (111) will determine the breakdown condition on  $(E/N)$  as a function of the product of  $N\Lambda$ .

## 2.5 GLOW DISCHARGES

Prior to breakdown, we started with a homogenous neutral gas with a constant electric field and a linear voltage drop. Following breakdown, a discharge forms, and rearranges itself into characteristic regions to provide optimally for particle generation and energy input to balance losses. For a dc discharge, just at breakdown, the current will increase with little increase in the voltage. This is called the Townsend discharge (46) and precedes the avalanche that signifies "full" breakdown. The first "state" after breakdown is a glow discharge. Initially, the glow will not completely cover the cathode surface. It operates at near constant voltage in this regime (called the *normal discharge*), with the current increasing as the cathode coverage increases. Eventually, the glow expands to fill the cathode surface, and subsequently, further increases in power result in increases in both voltage and current. This is called the *abnormal glow*. The salient characteristics of a glow discharge is that electrons are created by ionization and secondary electron generation from ion impact of surfaces. If the power is increased further, the cathode will begin to heat. Eventually, thermionic emission will occur, and become the dominant electron creation process. At this point the discharge voltage will decrease and the glow has evolved into an arc.

In the following sections, we will consider the main characteristics of dc and rf glow discharges. In particular, we will look at those features which pertain to our application of glow discharges to the deposition and etching of thin films.

### 2.5.1 DC Glow Discharge

It is convenient (and traditional) (47) to picture the glow discharge as comprising a number of distinct regions. Of course, this is an artificial construct; in reality the discharge

is a continuous entity. We can, however, associate particular processes and functionality with the various regions, and in this sense, the picture of the glow discharge presented here is useful. We will also consider some recent numerical modeling of the dc glow in this section, the results of which largely substantiate the simplified view presented here. Fig. 15 shows the dc glow schematically. We will now consider each region.

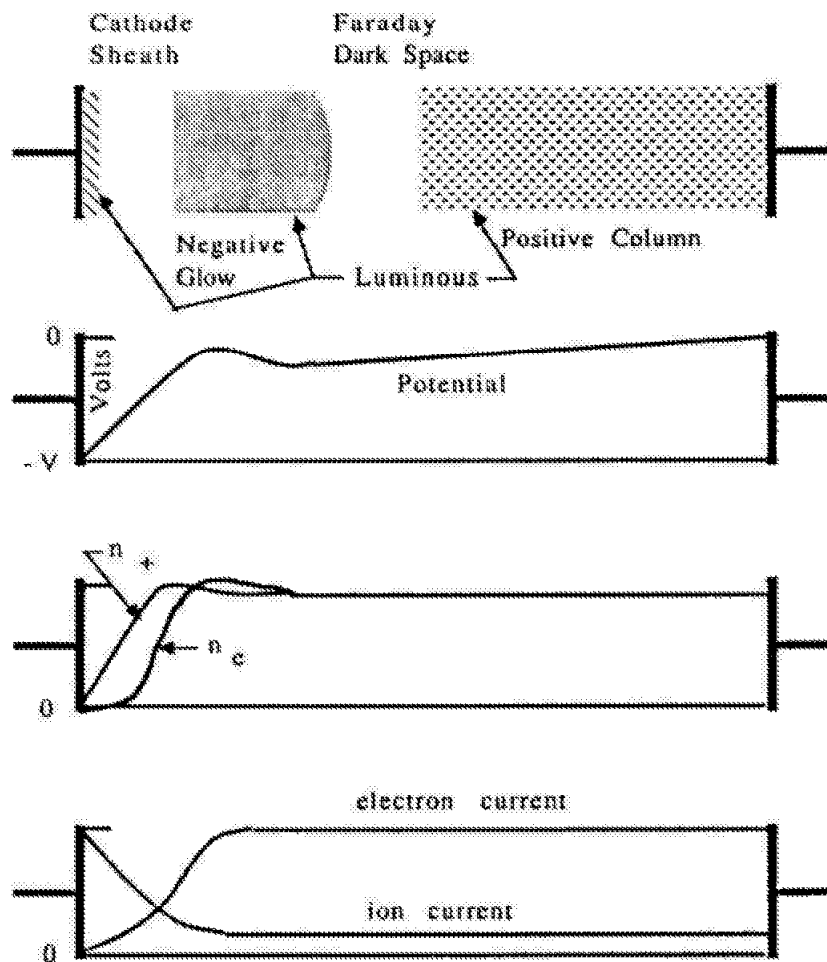


**Figure 15:** Classical picture of the architecture of a dc glow discharge. After breakdown, the discharge arranges itself into characteristic regions to provide for particle and energy input. Most of the potential is dropped across the cathode sheath region, which contains ions but very few electrons. There are approximately equal ions and electrons in the negative glow, Faraday dark space and positive column.

**2.5.1.1 The Cathode Region.** A narrow luminous layer is often observed adjacent to the cathode. The light emitted from this region is thought to be due to excitation of the neutral gas and surface bombardment by ions. Beyond this luminous region is the cathode (or Crookes) dark space, which extends to the next luminous region, the negative glow.

Whereas originally the voltage was dropped uniformly across the entire discharge tube, in the glow phase, almost the entire voltage appears across the cathode dark space. This voltage will accelerate ions from the negative glow region to the cathode where they will cause secondary electron emission with a probability of approximately 0.1 to 0.05.

The secondary electrons will be accelerated back through the cathode region by the potential and enter the negative glow.

Owing to the large electric field that exists in the cathode dark space region, the electron density is small, and the ion current is determined by space charge-limited flow or mobility-limited flow as described in Sect. 2.2.6. Assuming that we have a free fall condition (i.e., the ions do not suffer collisions in the sheath), we can use Eq. (62) to write the Child-Langmuir expression for the ion current density at the cathode,  $j_c$

$$j_c = (4\epsilon_0/9)(2e/M)^{1/2}(V_c^{3/2}/x_c^2), \quad (112)$$

where  $V_c$  and  $x_c$  are the potential drop across the cathode sheath and the sheath width respectively.

**2.5.1.2 Secondary Electron Generation.** Ion bombardment of the cathode will cause secondary electron generation. The secondary electron yield, which is the ratio of secondary electrons emitted per incident ion will depend upon the material and the ion energy. It will also depends critically on the condition of the surface, including both the crystal orientation and the degree of surface contamination. Some materials can have secondary electron coefficients which exceed unity. The energy of the secondary electrons is generally quite low, typically peaking around 2 - 5 eV (56).

**2.5.1.3 Ionization in the Cathode Sheath.** One of the greatest debates in the area of low-temperature plasma behavior is whether there is significant ionization in the cathode sheath. Much of the older literature has assumed that virtually all of the ionization needed to supply the ions which are accelerated to the cathode (and therefore lost at the cathode) occurs in the sheath (49). One observation that supports this position is that the product of the dark space thickness and the neutral pressure are constant for a given supply voltage. This behavior of  $Pd = \text{constant}$  is reminiscent of the condition for breakdown that we discussed earlier. On the other hand, for species like Ar, excitation will accompany ionization, since the energy threshold for the first excited state is similar to that for ionization (11.5eV and 15.6 eV respectively). Thus, if there is no emission, there will be little or no ionization. This point of view is consistent with that of Chapman, who uses simple calculation of ionization rates to conclude that ionization in the sheath cannot account for the observed electron density (50).

This apparent conflict may be resolved by the numerical modeling of the dc glow performed by Graves and Jensen (51). They developed a continuum model which they applied to a dc Ar discharge at 500 mTorr. While the identification of their results does not exactly follow the schematic description of the dc glow given above, they do show a sheath region of high electric field and a bulk region which seems to be identified with the negative glow region (see next section). The ionization does occur in the sheath region; however, upon close inspection, the high electric field extends beyond the sheath region into the negative glow, as does the ionization source. From their results, it would appear that ionization does occur in the sheath and in the region of the sheath-glow interface. In general, in a dc discharge sufficient ionization must occur due to the secondary electrons to sustain the plasma.

**2.5.1.4 Ion Charge Exchange in the Cathode Sheath.** Ions which are being accelerated through the sheath will, in general, undergo charge exchange collisions with the neutral species. This will alter their energy distribution at the cathode, since an ion produced by charge exchange somewhere in the sheath will not receive the full acceleration of the sheath drop. This problem has been studied both theoretically and experimentally by Davis and Vanderslice (52). They put an energy analyzer behind a small hole in the cathode to determine the energy distribution of ions arriving at the cathode. They assumed that all ions originated near the start of the sheath and that no ionization occurred in the sheath. The dominant process considered was symmetric charge exchange, given by



They assumed that the electric field was linear in the sheath. For a mean free path much shorter than the sheath thickness, Eq. (113) can be written as

$$(V_c/N_0)(dN/dV) = (1/2\lambda_{cx}) \exp(-LV/(2\lambda_{cx}V_c)), \quad (114)$$

where  $V_c$  is the cathode voltage,  $dN$  is the number of ions arriving with an energy between  $V$  and  $V+dV$ ,  $L$  is the dark space thickness, and  $\lambda_{cx}$  is the charge exchange mean free path, given by

$$\lambda_{cx} = (N\sigma_{cx})^{-1}, \quad (115)$$

with  $\sigma_{cx}$  the charge exchange cross section. Their experimental measurements were in reasonable agreement with the above expressions.

**2.5.1.5 The Anode Sheath.** Before considering the negative glow and positive column regions of the discharge, let us consider the anode sheath region (see Fig. 16). The anode sheath is, more or less, a Debye sheath. That means that there will be a voltage drop of typically  $3kT_e/e$  (see Sect. 2.2.6). For a typical discharge with  $T_e = 3-4$  eV, the plasma will be at a potential of about 9-12 V above the anode. Since there is a current flowing through the plasma, which for the dc case must be constant everywhere, then there must be a net electron current at the anode equal to the ion current at the cathode. We note, however, that there will also be an ion current at the anode, given the fact that the discharge is at +10V with respect to the anode. From the numerical calculations (51), the ion current is about 10% of the electron current at the anode. In any case, the energy of the ions bombarding the anode is sufficiently low as to not cause secondary emission. Some of the secondary electrons created at the cathode and accelerated by the cathode sheath may pass through the discharge and strike the anode with enough energy to emit additional secondary electrons. This can be an important process at low pressures.

**2.5.1.6 The Negative Glow Region.** The luminous negative glow is a plasma region characterized by nearly equal electron and ion densities, typically in the range of  $10^9 - 10^{11}\text{cm}^{-3}$ . Electron temperature measurements within the glow show typical values of 2 - 10 eV, although there is considerable question whether there is any semblance of a Maxwellian distribution in this region. Also, there is considerable non-uniformity of the

temperatures and densities in the axial direction. Since this region is a plasma, the electric field is small. The sources of energy input to the glow include the energetic secondary electrons emitted from the cathode and accelerated across the sheath, and direct acceleration of the electrons in the glow by the electric field.

The strong electric field in the cathode region is responsible for energy input to the negative glow, both through acceleration of secondary electrons, and by acceleration of glow electrons near the glow edge. Thus, the magnitude of this field will be determined self-consistently by the plasma's requirements for ionization to sustain itself.

As we saw in Sect. 2.2.3, a magnetic field nominally parallel to the cathode, as found in a magnetron configuration, will cause the electrons to undergo gyro orbits, providing the collision frequency is below the cyclotron frequency. As a consequence, the electrons will spend more time in the vicinity of the cathode and their ionization efficiency will be increased. This will result in a decrease in the sheath field and potential, and will also produce a higher density discharge.

The continuum model for the dc glow (51) displays a negative glow region adjacent to the sheath and extending to the anode. The calculated temperature for this region is about 0.7 eV, which is considerably less than is typically measured.

The negative glow region, along with the cathode and associated dark space comprise a self-sustaining discharge configuration as shown in Fig. 16. The sheath field will accelerate ions formed in the negative glow. These ions will cause secondary electrons to be emitted at the cathode. The secondary electrons will be accelerated across the sheath and represent the main energy input to the plasma. A discharge will operate with the anode at the negative glow, in which case it is called an obstructed glow.

**2.5.1.7 Beyond the Negative Glow.** Although a dc glow discharge may end with the negative glow, in general it does not. Beyond the negative glow is another dark space, called the Faraday dark space, followed by the positive column and the anode sheath, which we have already discussed. Although the positive column is not typically found in processing plasma discharges, we will now consider briefly the so-called Faraday dark space and the positive column.

Regardless of whether the energetic secondary electrons formed at the cathode and accelerated through the (Crooke-Hittorf) dark space directly cause ionization or whether they transfer their energy to the electrons in the negative glow which then cause ionization (or whether it is a combination of both types of processes), it is clear that the energetic electrons represent the main source of energy input to the glow. The extent of the negative glow is determined by the range over which the energetic electrons lose their energy. This determines the location of the cathode end of the Faraday dark space. There is, however, a small electric field in the plasma regions of the discharge, and this electric field will increase the temperature of the electrons by acceleration and subsequent scattering, as in the Langevin model discussed in Sect. 2.5.1. We noted there that it will take a certain distance before the electrons reach their equilibrium energy as a result of the electric field acceleration. Where the electrons have not yet equilibrated, we would expect no light. As the electron distribution gains energy, the inelastic processes will come into play. In order to determine the distance over which the electrons will equilibrate, let us return

to the Langevin model for a moment to recall that the distance for electrons to equilibrate with an electric field  $d$  is given by Eq. (82)

$$d = u/(\delta\nu). \quad (116)$$

where  $\delta$  is the energy transfer fraction ( $2m/M$ ) and  $\nu$  is the collision frequency. We can rewrite (116) as

$$d = \lambda/(2\delta)^{1/2}, \quad (117)$$

where  $\lambda$  is the collision mean free path. This says that the distance for the electrons to come into equilibrium with an electric field is equal to the collisional mean free path multiplied by  $(M/4m)^{1/2}$ . Let us consider as an example, Ar at a pressure of 50 mTorr ( $N = 1.8 \times 10^{15} \text{ cm}^{-3}$ ). The collision cross section is about  $4 \times 10^{-15} \text{ cm}^2$ , so that  $\lambda = 0.1 \text{ cm}$  and  $d = 14 \text{ cm}$ .

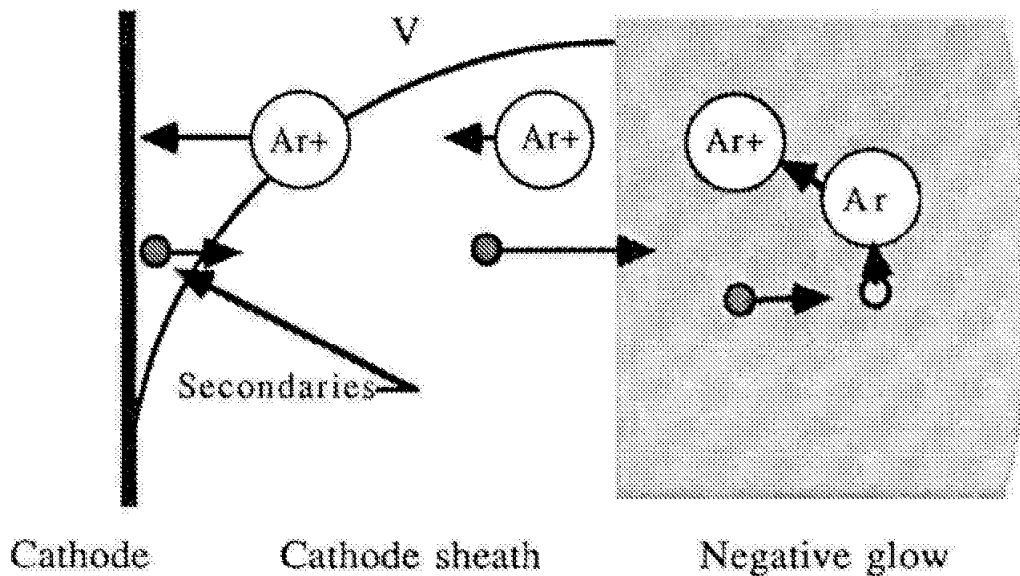


**Figure 16:** Schematic of the discharge behavior in the cathode sheath - negative glow regions. Ions from the negative glow fall through the cathode sheath causing secondary electron emission. The secondaries are accelerated back through the sheath and comprise the main energy input to the negative glow which supports the ionization process, both through direct ionization and through ionization by the high energy tail of the electron distribution. These regions comprise a self-sustaining combination.

Thus the electrons would have to drift 14 cm in the electric field to come into equilibrium. Until they have drifted that far, the electron energy will be below that necessary to excite inelastic processes, such as excitation. Since this distance is longer than the negative glow, there is another dark space, namely the Faraday dark space. As noted previously, this distance is not necessarily equal to the thickness of the Faraday dark

space, because we might expect that Ar emission would occur even before the electrons have fully equilibrated.

**2.5.1.8 The Positive Column.** In the positive column, the electrons have equilibrated with the electric field. The local electric field accelerates the electrons and represents the main energy input source. The main losses are diffusion to the walls and radiation from line emission. In electro-negative discharges, electron attachment may be an additional important loss mechanism. Since many plasma processes involve halide-containing gases, this is an important consideration. We will not consider this in the present case, however.

We will examine the positive column using the diffusion equations developed in Sect. 2.2.5. We will assume that a steady state is reached in which ionization in the positive column is balanced by diffusion of particles to the wall. If we write the source term for ionization in Eq. (52) as

$$S = n\nu_i \quad (118)$$

where  $n$  is the electron density and  $\nu_i$  is the ionization rate, then the steady state form of Eq. (52) can be written as

$$\nabla^2 n = -(\nu_i/D)n \quad (119)$$

where we have used Eq. (53) and assumed that  $D$  is independent of position. We will assume that the length of the positive column is much greater than its radius  $R_D$ . The solution (53) of Eq. (119) can be written in terms of a diffusion length  $\Lambda$  where

$$\Lambda^2 = D/\nu_i. \quad (120)$$

To satisfy the boundary conditions that  $n=0$  at  $R_D$  (recombination at the surface), we require that

$$\Lambda = R_D/2.405 \quad (121)$$

From Eq. (120), we get that

$$\nu_i = D(2.405/R_D)^2. \quad (122)$$

Then, from Sect. 2.2.4, we can write

$$\nu_i = N\sigma v = N A(T_e), \quad (123)$$

where  $A(T_e)$  is a function of the electron temperature, and from Sect. 2.2.5,

$$D = CT_e/N, \quad (124)$$



where  $C$  is a constant, and we have used the form of the ambipolar diffusion coefficient. Then, from the last three equations we get that

$$T_e/A(T_e) = (NR_D)^2/(2.405)^2 C, \quad (125)$$

From Eq. (125) we see that the electron temperature is determined by the square of the product of the neutral density and the radius of the discharge.

The positive column and other features beyond the negative glow do not usually play an important role in plasma processing (although they are very important for discharges used as light sources). One reason for studying the positive column here is that the general behavior is similar to what occurs in an rf powered discharge, as we shall see in the next section.

**2.5.1.9 Summary of the dc Glow Discharge** To recapitulate, the dc discharge comprises, firstly, a self consistent combination of a cathode surface, cathode dark space region, with associated large electric field, and the negative glow region. Ions, formed in the dark space and negative glow regions are accelerated by the cathode electric field into the cathode surface, where they cause secondary electron emission and sputtering. The secondary electrons are accelerated back across the dark space and cause ionization, either directly or by transferring their energy to electrons in the plasma. Other types of discharges, such as the hollow cathode discharge, (see Chap. 12) rely on the formation of secondary electrons, which are accelerated by sheath voltages and are the primary source of ionization which sustains the discharge.

Additionally, a dc glow discharge may have another dark space beyond the negative glow and a positive column. In these regions, electrons are heated by the local electric field, which results in a balance between ionization and losses of charged particles. The plasma in the positive column follows the Langevin model. The positive column may be arbitrarily long (54), or absent entirely, and serves to connect the anode electrically to the remainder of the discharge.

## 2.5.2 RF Glow

In a dc glow discharge, most of the input power is used to accelerate the ions through the sheath, and appears as heat when the ions strike the cathode. If the secondary electron coefficient were 0.1, then, to a good approximation, only 10% of the power will end up in the negative glow from the secondary electrons which are accelerated in the sheath. In this sense, the dc glow is a rather inefficient plasma generator, though for processes which depend on ion bombardment, such as sputtering, this is not a problem.

An even more serious limitation of a dc glow discharge is the necessity of conducting net current to sustain the discharge. This requirement generally precludes the use of insulating materials in sputtering targets, substrates, or deposited films, because the insulators would prevent dc current conduction. If the insulators did not cover the entire electrode surface, it may be possible to sustain a dc discharge, but the insulators will build up a charge, making processes difficult to control.

The use of an ac power source can alleviate both these shortcomings of the dc glow discharge. Let us start by considering a very low frequency ac power source, with a period which is long compared to the time it takes for the plasma particles to come to equilibrium with the electric field. We will further assume that there are no insulators present. In this case, the ac discharge will be very similar to the dc discharge, except that the current will reverse every half cycle. A sheath will form at the electrode which is negative during the particular half cycle of the ac power, and ions will be accelerated across this sheath. The ions, which are able to cross the sheath in a short time compared to the ac period, will gain an amount of energy roughly equal to the instantaneous ac voltage. Thus, the ions striking the electrodes will have a distribution of energies, which will extend to approximately the peak ac voltage.

If we now consider what happens if we have an insulating electrode, we would find that current would flow until the insulator charged up and terminates the discharge. On the next half cycle, however, the insulator would discharge, and current would flow in the opposite direction until the insulator charged up again. The insulator behaves like a capacitor that is charged in alternate directions by the plasma. If the ac frequency is increased to the point where the charging time is much longer than the ac period, current will flow in the plasma for the entire ac cycle. A frequency of about 50 - 100 kHz is usually sufficient to achieve this condition. In this case, also, we would find that sheaths would form and ions would be accelerated by the instantaneous field, and arrive at the electrodes with a distribution of energies up to approximately the peak ac voltage.

As the frequency of the ac source is increased, new phenomena begin to appear. The details of the various frequency-dependant effects have been reviewed by Flamm (55), and have been reported for a few specific processes (56-58). However, due to the fact that most commercial rf plasma equipment is designed to work at the FCC assigned frequency of 13.56 MHz, the use of different frequencies has not been exploited and remains an untapped opportunity for optimizing processes. We will not consider this topic further here, but will instead explore the salient features of plasma operation at 13.56 MHz. At this frequency, the massive ions have too much inertia to respond to the instantaneous electric field in the sheath regions, while the lighter electrons will. Owing to the differences in mobilities of the ions and the electrons, however, a time-average bias will arise for certain configurations.

**2.5.2.1 Self Bias and Plasma Potential.** To see how this comes about, let us consider a discharge system with one small electrode connected to an rf power source through a coupling capacitor shown in Fig. 17. The characteristic response of the plasma to a voltage  $V$  is given by the curve in Fig. 18. Owing to the much greater mobility of the electrons compared to the ions, a given positive voltage will result in a much larger electron current than the ion current which flows for the same negative voltage. In effect, the plasma behaves like a leaky diode, showing a much larger effective resistance for ion current than for electron current.

Let us now apply a square wave with peak amplitude  $V_1$  (See Fig. 19). Initially, when the applied voltage goes to  $V_1$ , the potential across the plasma is  $V_1$ . The capacitor will be charged through the effective resistance of the plasma for electron current flow, and will drop as shown in Fig. 20. When the power supply changes sign, the voltage across the plasma drops instantaneously by  $-2V_1$ , after which the voltage decays with the longer time constant associated with the higher effective resistance ion current flow. As shown

in Fig. 20, this continues until the time average electron and ion currents are equal, a condition which results in a time-average negative bias on the electrode (59). Although the derivation was presented with a square wave power source, a similar effect holds for a sine wave, as in Fig. 21.

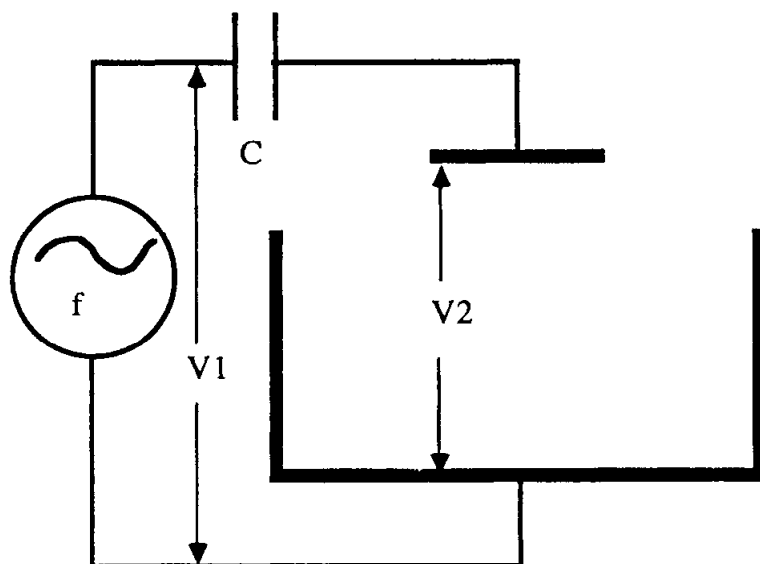


**Figure 17:** Schematic of electrode configuration for an rf glow discharge. An rf power supply is capacitively coupled to the electrodes.

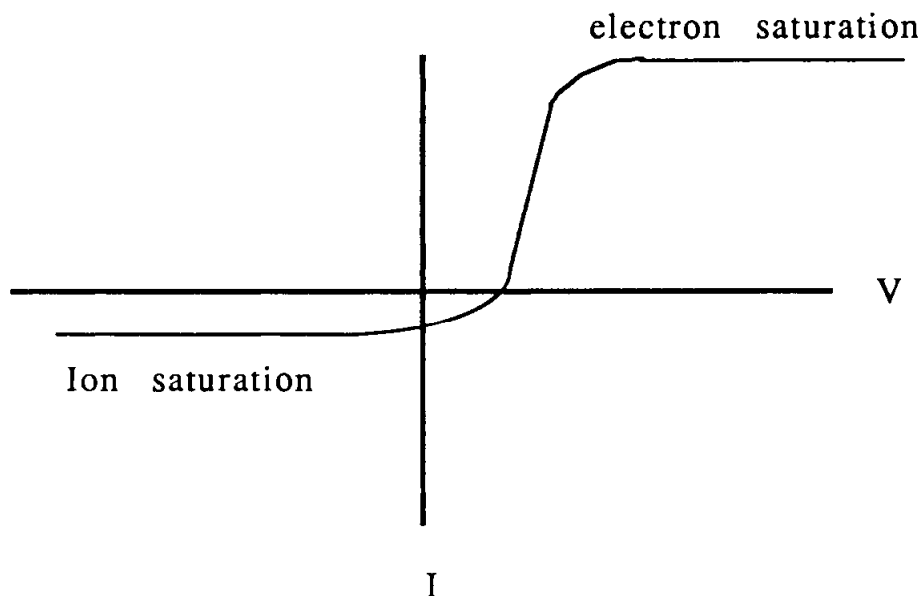


**Figure 18:** Electron and ion current as functions of the applied potential. The greater mobility of the electrons compared to the ions results in a larger electron current for a given positive voltage than the ion current which flows for an equal negative voltage.

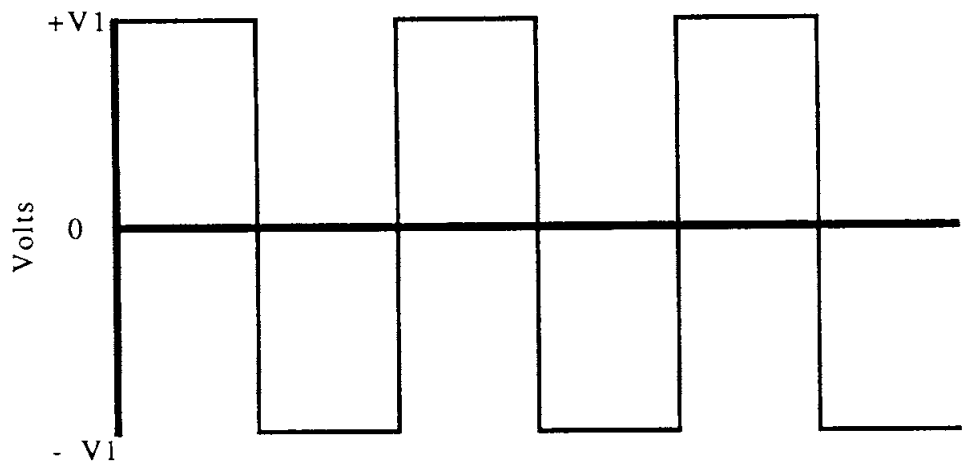


**Figure 19:** Output square wave of peak voltage  $V_1$  which is used for the circuit shown in Fig. 17.

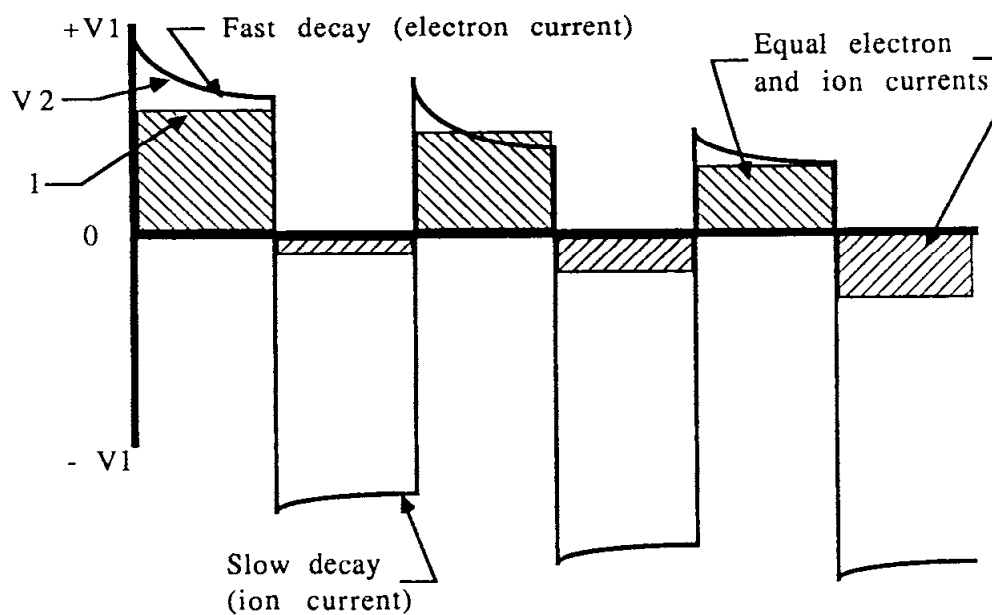


**Figure 20:** Behavior of the discharge voltage  $V_2$ , as the self bias develops to produce equal electron and ion currents. On each half cycle, the current decays as the capacitor charges from the plasma. On the half cycle where electron current flows, the decay is faster, because the plasma has an effectively lower impedance owing to the greater mobility of the electrons.

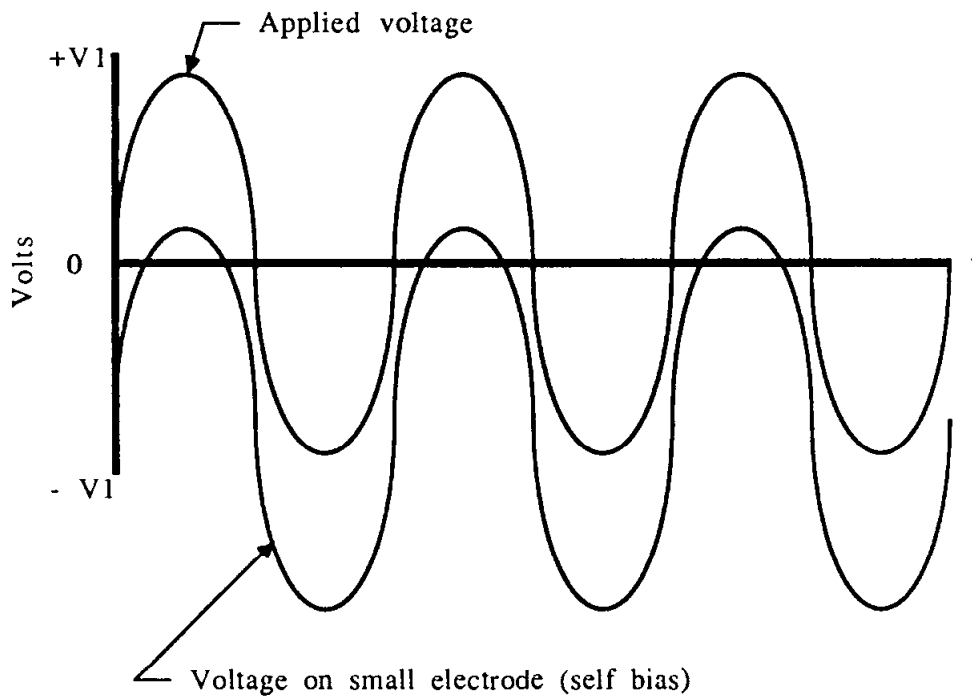


**Figure 21:** Self bias for a sine wave driven system.

Implicit in this derivation is the fact that the area of the large electrode was sufficient to permit all of the necessary currents to flow during each cycle. In other words, the limiting impedance for current flow on both half cycles occurs at the small area electrode. It is important to note that the features of the rf discharge which resulted in the self bias were the presence of the coupling capacitor (which ensures a time-average zero current), and the fact that one of the electrodes was much smaller than the other. The driven electrode is not necessarily the one where the bias occurs. The location of the capacitor is similarly irrelevant in determining the bias. In fact, if the apparatus were symmetric and totally decoupled from ground, there would be no self bias. The grounded electrode can have a bias if there is a coupling capacitor somewhere in the circuit and the grounded electrode is smaller than the driven electrode.

We noted in Sect. 2.2.6 that the plasma prefers to be more positive than the most positive surface. Then, for the case of a large bias, we would expect the plasma potential to behave as shown in Fig. 22. Even with the self bias, the small electrode is positive for some fraction of a cycle, so the time average plasma potential is usually higher than for the dc case. Ions, which cannot respond on the fast rf time scale will bombard the small electrode with an energy given by the difference between the time-average plasma potential and the time-average self bias.

Although not obvious from our simplified derivation, the magnitude of the bias will depend on the neutral pressure (4). As the pressure is increased with constant power into the discharge, the bias will decrease. This is due in part to decreases in the rf voltage, because the plasma impedance decreases as the neutral density increases. Another way of looking at this phenomenon is that at high densities, the discharge does not require as high

a sheath field to sustain itself, because it is able to put energy directly into the glow electrons as we will discuss below.

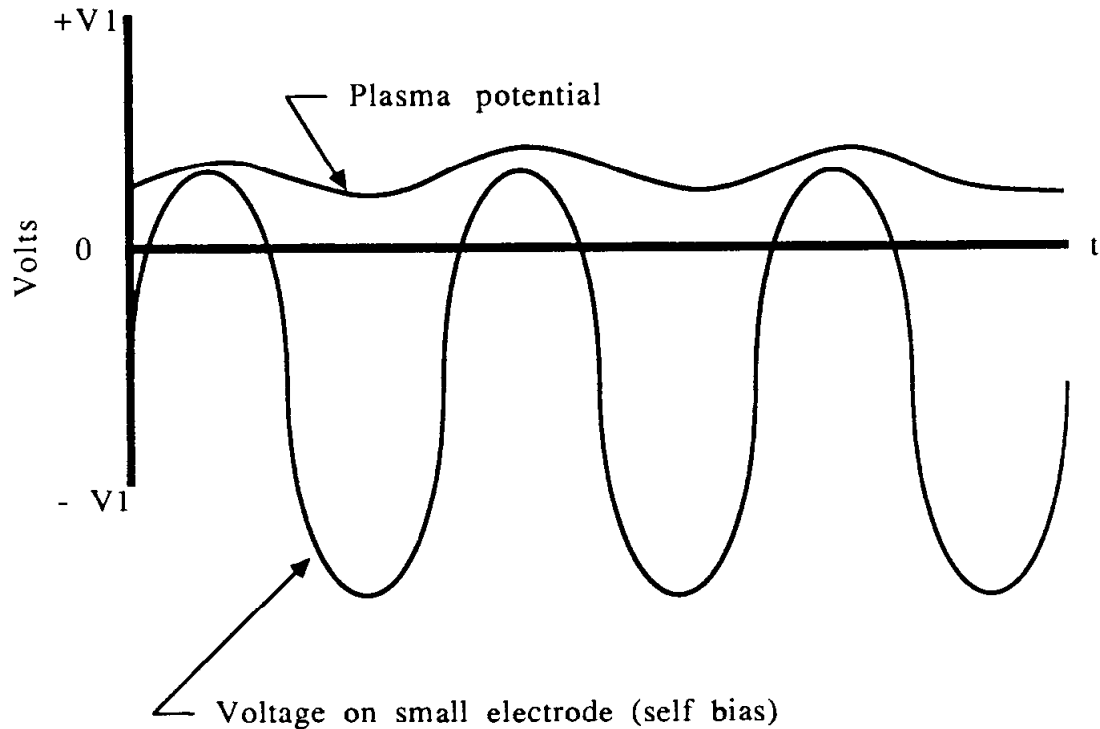


**Figure 22:** Time variation of the plasma potential shown with the self bias voltage on the small electrode. In the absence of collisions in the sheath, the ion energy at the small electrode will be the difference between the average potential and average self bias.

The asymmetric rf discharge configuration, which results in high bias, is the chosen configuration for reactive ion etching (60), where ion bombardment produces anisotropic etching. The highest bombardment energies are obtained as the pressure is lowered. Since excessive ion energy can result in damage to a wafer, however, some reactive ion etch processes are operated at higher pressures (200-300 mTorr), to reduce the ion energy both through a lower bias and collisions in the sheath. The latter effect, however, tends to destroy the directionality of the bombarding ions, which reduces their utility for anisotropic etching.

For the case of a symmetric discharge (equal area electrodes), where there is no self bias, the plasma potential appears as in Fig. 23. Here we see that the time average bias will be much greater than for the dc case, and, even though there is no bias, there will be energetic ion bombardment which will occur at both electrodes. An example of the near-symmetric etch reactor is the Reinberg etch reactor (5). In this apparatus, energetic ion bombardment occurs primarily due to the large plasma potential. An excellent summary of the self bias and plasma potential behavior has been given by Kohler, et al (61).

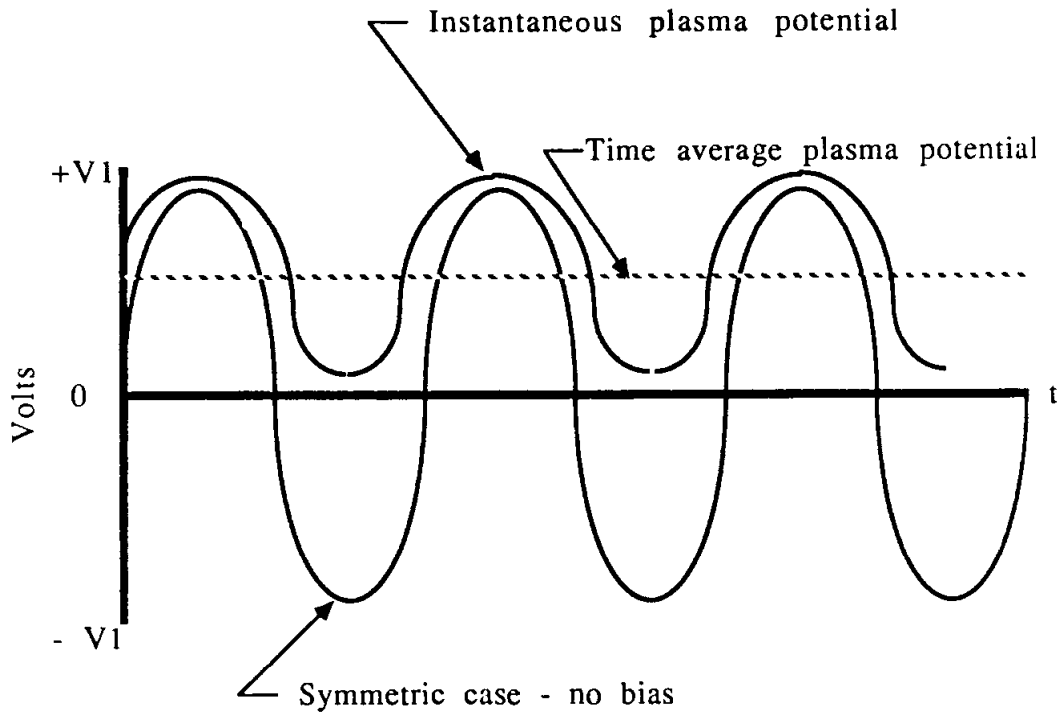


**Figure 23:** Plasma potential and self bias voltage for a symmetric discharge configuration. There is no self bias in this case, but the plasma potential is higher than for the asymmetric case. Energetic ion bombardment will occur at both electrodes. In the absence of collisions in the sheath, the ion energy at the small electrode will be the difference between the average potential and average self bias.

The sheaths in an rf discharge have large rf displacement currents flowing through them, but rather small conduction currents. The sheaths will behave like capacitors with some leakage current. The main part of the rf glow will be resistive, much as the negative glow and positive column in a dc discharge. Based on this picture, Koenig and Maissel (59) evolved an equivalent circuit of an rf discharge which provides a simple and quite useful model of the discharge.

One application of this model is the calculation of the self bias voltage division. The self bias voltage will divide between the two electrodes inversely proportional to the capacitance of the sheath regions

$$(V_a/V_b) = (C_b/C_a), \quad (126)$$

where a and b denote the two electrodes. The capacitance of the sheath regions is *roughly* given by:

$$C = \epsilon_0 A/D_s, \quad (127)$$

where A is the area of the sheath and  $D_s$  is the sheath thickness. There are two effects which make this expression difficult to use in practice: (1) the effective area of the sheath will depend on (unavoidable) stray coupling from the electrode to other surfaces, and (2)

$D_s$  will depend in a complicated way on the discharge parameters. Koenig and Maissel attempt to relate  $D_s$  to the voltage by requiring that the Child-Langmuir space charge-limited currents at each electrode be equal:

$$V_a^{3/2}/D_a^2 = V_b^{3/2}/D_b^2. \quad (128)$$

Using this expression in conjunction with the capacitive voltage division leads to the conclusion that the bias divides between the electrodes inversely proportional to the fourth power of the ratio of the electrode areas. The caveats noted above, however, conspire to render this simplistic derivation much less than adequate. More sophisticated models have been presented by Horwitz (62) and Kohler et al (61).

**2.5.2.2 Discharge Characteristics** Owing to the self bias, there will be energetic ion bombardment of the smaller electrode, with attendant secondary electron emission. (In addition, there will also be some bombardment of the larger electrode.) In this respect, an rf discharge can be similar to the dc discharge: there will be a cathode sheath and a quasi-negative glow which is energized by the accelerated secondaries. There are differences, however. Although the ions are typically going slowly enough that they will respond only to the time average potential, the electrons will generally cross the sheath region in a fraction of the rf period. This can give rise to time dependent phenomena. In particular the edge of the sheath will generally oscillate. Some researchers believe that this mechanism can put energy directly into the electrons by a "surf riding" effect (63).

One characteristic which distinguishes the rf discharge from the dc discharge is that, because the rf field is changing direction in time, it can put energy into the electron energy distribution function more readily than the dc field. In the dc case, as we saw, an electron had to drift a considerable distance in the field to come into equilibrium with it. This is the reason that the positive column is separated from the negative glow. In the rf case, however, the electrons will not experience a net drift, since the field is changing direction. They will equilibrate after a characteristic time. Owing to this, the rf discharge is more efficient than the dc discharge. In a sense, the negative glow and positive column regions overlap.

**2.5.2.3 RF Discharge Modeling** Recently, the rf discharge has been studied numerically by a number of groups using the continuum model (57,64-66). The results of the models are consistent with the qualitative description given above on the three energy input mechanisms for an rf discharge. For electro-negative discharges, where electrons may not be the dominant negative charge, the discharge characteristics are very different from that predicted by the self bias picture above. The case of  $\text{SF}_6$  discharge has been modeled and compared to experimental results by Gogolides, Nicolai and Sawin (67).

While the continuum models are very powerful, the underlying assumption is that the electron mean free path is short compared to the sheath size. It is questionable whether this assumption is valid below 50-100 mTorr, where many of the current etch processes operates. Low pressure discharges have been modelled using a Monte Carlo approach (63). In this calculation, an rf electric field profile was assumed, including an oscillating sheath boundary. While the results are not self-consistent, they do show clearly the in-



creasing importance of the "surf-riding" acceleration mechanism as the pressure is lowered.

**2.5.2.4 Summary of the rf Glow Discharge** The rf glow discharge embodies many of the same qualitative features of the dc glow discharge, with the formation of sheaths in which strong electric fields will accelerate ions and electrons. At low frequencies, where ions can follow the changing electric fields, the discharge will behave similarly to the dc case. As the frequency increases, the ions will no longer be able to follow the instantaneous electric field, but will instead respond to the time averaged fields. Here, for discharge configurations with unequal electrode areas and where the electrons are the dominant negative charge carriers, a self-bias will arise which will produce a time-average negative voltage on the smaller electrode. Ions will be accelerated by the difference between the time-average plasma potential and the time-average bias. In general, the energy of the bombarding ions in an rf discharge will increase as the driving frequency is decreased and/or the neutral pressure is decreased.

Energy input to the rf discharge occurs through three mechanisms. Energetic ions striking the electrode will cause the formation of secondary electrons. These electrons can be accelerated through the sheath and cause ionization as in the sheath and negative glow regions of the dc discharge. The oscillating electric fields in the glow can input energy directly into the electrons, much in the same way as the positive column of the dc discharge. Finally, the oscillating sheath electric field will accelerate electrons in the glow. This "surf-riding" mechanism has no direct analog in the dc discharge.

Several enhancement schemes for the rf discharge are possible. The addition of a magnetic field nominally parallel to the electrode surface will result in confinement of the electrons as described in Sects. 2.1.4 and 2.2.3. Such schemes are used for magnetically enhanced reactive ion etching (8). Their principle advantage is that the presence of the magnetic field increases the electron ionization efficiency. This results in a lowering of the sheath potential and concomitant lowering of the bombarding ion energy, with no degradation of plasma performance.

It is also possible to use microwave power, typically at 2.45 GHz, to operate a discharge. In these schemes, the power can be coupled in radiatively, obviating the need for electrodes as described in Sect 2.1.4. One very important such configuration is the electron cyclotron resonance reactor (12), which includes a magnetic field and microwave at a frequency which is matched to the cyclotron frequency of the electrons as described in Sect 2.3.3.

## 2.6 REFERENCES

1. In cases where the positively charged ions have a charge greater than unity, this equality holds with the density of positive charges multiplied by their respective charge. In the plasmas used for thin film deposition and etching, it is rare to have multiply charged ions.
2. N.A. Krall and A.W. Trivelpiece, Principles of Plasma Physics (McGraw-Hill, New York, 1973) p5.
3. J.M. Coulson and J.F. Richardson, Chemical Engineering, Vol. 3 (Pergamon Press, Oxford, 1979).

4. D.L. Flamm and V.M. Donnelly, Plasma Chemistry and Plasma Processing 1: 317 (1981).
5. L.M. Ephrath, in ULSI Science and Technology 1989 ed. by M. Osburn (The Electrochemical Society, Pennington NJ, 1989).
6. A.R. Reinberg, US Patent 3,757,733.
7. R.A. Heinecke, Sol. State Electron. 18: 1146 (1975).
8. I.Lin, D.C. Hinson, W.H. Class, and R.L. Sandstrom, Appl. Phys. Lett. 44: 185 (1984).
9. J.M. Moran and D. Maydan, Bell System Tech. J. 58: 1027 (1979).
10. D.E. Rosner and H.D. Allendorf, J. Chem. Phys. 75: 308 (1971).
11. K. Suzuki, S. Okudairi, N. Sakudo and I. Kanomata, Jpn. J. Appl. Phys. 16: 1979 (1977).
12. S. Matatsuo and Y. Adachi, Jpn. J. Appl. Phys. 21: L4 (1982).
13. Sanborn C. Brown Introduction to Electrical Discharges in Gases (John Wiley and Sons, New York, 1966).
14. Frances F. Chen, Introduction to Plasma Physics and Controlled Fusion (Plenum Press, New York, 1983).
15. V.E. Golant, A.P. Zhilinsky, I.E. Sakharov and S.C. Brown, Fundamentals of Plasma Physics (John Wiley and Sons, New York, 1977).
16. E.W. Holt and R.E. Haskell, Foundations of Plasma Dynamics (Macmillan, New York, 1965).
17. N.A. Krall and A.W. Trivelpiece, *op cit.*
18. J.D. Jackson, Classical Electrodynamics (John Wiley and Sons, New York, 1975).
19. Sanborn C. Brown, *op cit.*
20. T.H. Stix, The Theory of Plasma Waves, (McGraw-Hill, New York, 1962).
21. Frances F. Chen *op cit.*
22. J.A. Thornton and A.S. Penfold, in Thin Film Processes, ed. by J.L. Vossen and W. Kern (Academic, Orlando, 1978), p75.
23. N.A. Krall and A.W. Trivelpiece, *op cit.* p. 627.
24. T. Ono, M. Oda, C. Takahashi and S. Matsuo, J. Vac. Sci. Technol. B4: 696 (1986).
25. Sanborn C. Brown, Basic Data of Plasma Physics (John Wiley and Sons, New York, 1959).
26. B.E. Cherrington, Gaseous Electronics and Gas Lasers (Pergammon, Oxford, 1979).
27. B. Chapman, Glow Discharge Processes (John Wiley and Sons, New York, 1980) p. 12.
28. B.E. Cherrington, *op cit.* , p. 68.
29. B. Chapman, *op cit.* , p. 24.
30. Sanborn C. Brown, *op cit.* , p. 28.
31. Sanborn C. Brown, *op cit.* , p. 60.

32. Frances F. Chen, *op cit.* , p. 159.
33. C.M. Ferreira and J. Loureiro, J. Phys D: Appl. Phys. 17: 1175 (1984).
34. Sanborn C. Brown, *op cit.*, p. 204.
35. One exception to this is the sheath region of a glow discharge, where there are very few electrons and we must consider the effect of the electric field on the electrons.
36. B.E. Cherrington, *op cit.* , p. 11.
37. An exception to this is the case of a reactor with hot walls or electrodes, in which the neutral species can heat up. Also neutrals can heat by collisions with sputtered species (Chap. 6).
38. B.E. Cherrington *op cit.* , p. 18.
39. H. Meuth and E. Sevilano, in Plasma Diagnostics, Vol 1, Discharge Parameters and Chemistry ed. by O. Auciello and D.L. Flamm (Academic Press, Boston, 1989), p. 239.
40. Sanborn C. Brown, *op cit.* p. 166.
41. B.E. Cherrington, *op cit.* p. 49.
42. B.E. Cherrington, *op cit.* p. 64.
43. A. von Engel, Ionized Gases (Oxford University Press, London, 1965) p. 180.
44. Sanborn C. Brown, *op cit.* , p. 183.
45. Sanborn c. Brown, *op cit.* , p. 169.
46. J.L. Vossen and J.J. Cuomo, in Thin Film Processes, ed. by J.L Vossen and W. Kern (Academic, Orlando, 1978), p. 24.
47. Sanborn C. Brown, *op cit.* , p. 211.
48. E.N. Sickafus, Phys. Rev. B 16: 1436 (1977).
49. A. von Engel, *op cit.* , p. 234.
50. B. Chapman, *op cit.* , p. 96.
51. David B. Graves and Klavs F. Jensen, IEEE Trans on Plasma Sci. PS-14: 78 (1986)
52. W.D. Davis and T.A. Vanderslice Phys. Rev. 131: 219 (1963).
53. Sanborn C. Brown, *op cit.* , p. 29.
54. Sanborn C. Brown, *op cit.* , p 213.
55. D.L. Flamm, J. Vac. Sci. Technol. A4: 729 (1986).
56. V.M. Donnelly, D.L. Flamm and G. Collins, J. Vac. Sci. Technol. 21: 817 (1982).
57. M.R. Werrtheimer, J. Vac. Sci. Technol. A3: 2643 (1985).
58. H. Curtins, N. Wyrsh and A.V. Shah, Electron. Lett. 23: 228 (1987).
59. H.R. Koenig and L.I. Maissel, IBM J. Res. Dev. 14: 168 (1970).
60. J.D. Chin, I. Adeside, E.D. Wolf and R.C. Tiberio, J. Vac. Sci. Technol. 19: 1418 (1981)
61. K. Kohler, J.W. Coburn, D.E. Horne, E. Kay and J.H. Keller, J. Appl Phys. 57: 59 (1985).
62. C.M. Horwitz, J. Vac. Sci. Technol. A1: 60 (1983).

63. Mark J. Kushner, IEEE Trans. Plas. Sci. PS-14: 188 (1986)
64. M.S. Barnes, T.J. Colter and M.E. Elta, J. Appl Phys. 61: 81 (1987)
65. A.D. Richards, B.E. Thompson and H.H. Sawin, Appl. Phys. Lett. 50: 492 (1987).
66. J-P. Boeuf, Phys. Rev. A 36: 2782 (1987).
67. E. Gogolides, J-P. Nicolai and H.H. Sawin, J. Vac. Sci. Technol. A7: (in press).

---

## Fundamentals of Sputtering and Reflection

---

**David N. Ruzic**

### 3.1 INTRODUCTION

Sputtering and reflection of ions and neutral atoms from solid surfaces are closely related complex phenomenon. The behavior of the surface and the incident projectile depend greatly on the relative masses and energies of the atoms involved, the structure of the solid, and other factors. A model or semi-empirical expression that fits one behavioral regime such as linear-cascade response may be quite inappropriate for another response region. This chapter looks closest not at the linear-cascade, where theoretical and empirical models are well developed, but at the non-isotropic-cascade in-need-of-surface-corrections response, where both data and modeling effects are sparse. It is this low-energy surface regime that is of most interest to the plasma-processing community.

#### 3.1.1 Sputtering Regimes

When an atom or ion strikes a solid surface the collective response of the atoms in the target can be grouped into five distinct categories. Which phenomena dominates depends on the mass and atomic number,  $Z_i$ , of the incident projectile; the mass and atomic number,  $Z_t$ , of the target; and the incident energy,  $E$ . Figure 1 (1) shows these regions mapped onto two cuts through the  $Z_i, Z_t, E$  space. Though the boundaries are drawn as sharp lines, the types of collective surface behavior gradually meld into one another in reality. There is not a 50% chance of either phenomenon at one of the boundaries---instead the surface behavior incorporates features of both types of interactions.

The response that is typically described is not shaded in Fig. 1. It primarily occurs at intermediate energies (5 to 100 keV). A cascade of recoil atoms is produced along the path of the incident ion. The number of recoil atoms produced at any point depends linearly on the amount of energy lost by the incident ion at that point. At these intermediate energies, energy loss is due to electron drag from the free electrons in the solid, and screened Coulomb interactions from the nuclei. Analytic expressions for the energy loss exist, so the density and energy of the recoil cascade can be calculated. Assuming that the energy lost to the recoil atoms is isotropic, transport theory can be used to determine the number of recoil atoms that will reach the surface, overcome the potential barrier of the

work function and become sputtered atoms. The energy distribution and angular distributions of these sputtered atoms can also be determined. The sputtering yields and distributions that result fit the known data well. This transport theory approach forms the basis for most of the analytic sputtering yield, angular distribution and energy distribution expressions in the literature (1-5).

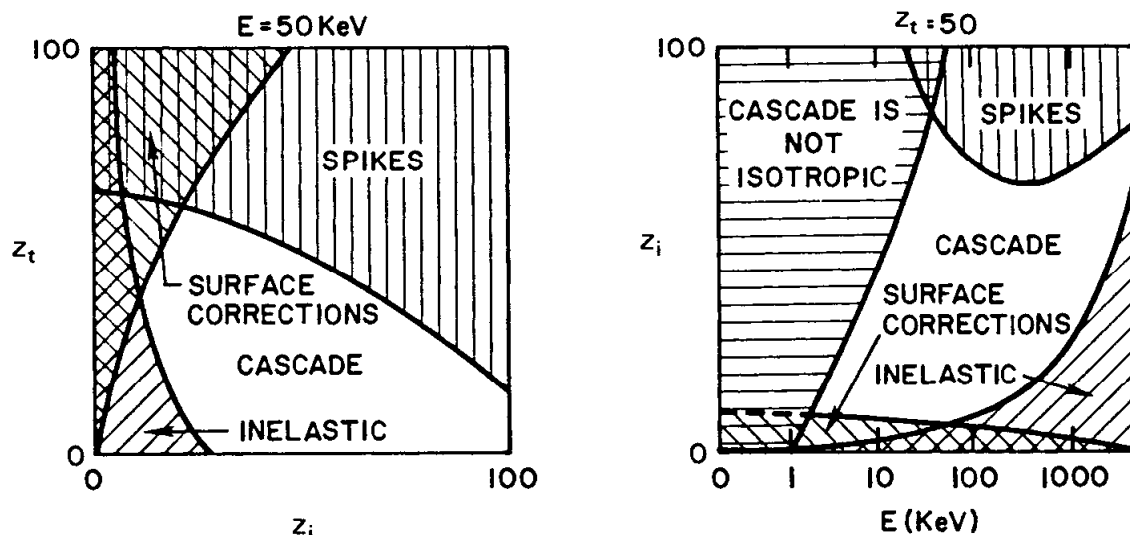


**Figure 1:** The five collective responses of a target with atomic number  $Z_t$  being struck by an atom or ion of atomic number  $Z_i$  and energy  $E$ . Two cuts through  $(Z_t, Z_i, E)$  space are shown.

If the ion energy is high (greater than about 50 keV) and the incident ion is heavier than the target atoms an entire block of atoms located along the initial path of the projectile can be set into a violent motion. This is known as the spike regime and transport theory breaks down because of non-linear effects: the next target atom for the incident projectile may well be an atom that is in motion due to the collision.

At very large energies (greater than 1000 keV) for any projectile-target pair, and at somewhat lower energies when the projectile is lighter than the target, inelastic energy loss channels must be considered. For example, energy could be lost by the ionization of inner core electrons in the solid. Transport theory can still be used, but a more complicated energy loss expression is needed.

Going to lower energies than the most-understood cascade region (ion energy is less than 5 keV, certainly less than 1 keV) the energy lost to the recoil atoms in the cascade is not isotropic. The first target atom struck by the projectile will absorb most of the lost energy and respond in an individual manner. It becomes the primary knock-on and may in turn generate additional knock-on atoms. In this regime transport theory and the analytic sputtering expressions based upon that theory cannot be used. However, empirical fits (5) to the known experimental data have been made for H and He ions.

At even lower energies (hundreds of eVs), or when the projectile mass is much less than the target, the cascade is not only anisotropic, but corrections due to the surface topology must be included. The atomic-scale roughness on the surface must be considered since the range of the particle may only be a few Å.

The sputtering interactions that are of importance to the plasma-processing community primarily fall in this last low-energy non-isotropic-cascade in-need-of-surface-correction regime. Bombardment energies are kept fairly low in plasma processing to minimize damage and contamination of the wafers: if the difference between the plasma potential and the bias potential of the sputtering target is too high, ions will be accelerated to such great energies that cluster emission and high energy reflections (which can then cause damage to the substrate) are likely to result. Therefore most sputtering systems are run such that the incident ions are less than one thousand eV. In an etching system the sheath drop, and thus the energy of the incident ions, is also kept low to avoid the damage and indiscriminate physical sputtering that could result. However, even at these lower energies some damage to the surface is inevitable and the surface of both sputtering targets and etched substrates is not atomically smooth.

Due to the relative inefficiency of the sputtering process in terms of energy, most sputtering targets or cathodes must be actively cooled. In some cases, such as magnetron sputtering, the limiting factor to high power, high rate operation is the ability to cool the cathode. The most energy-efficient range for sputtering is in the 300-800 eV ion energy range. This can be found by differentiating the sputter yield-as-a-function of energy (see Figs. 9, 10 below). There are other practical reasons for keeping the energy low as well, related to operator safety, vacuum feedthroughs, shielding, high-power supply stability and cost.

Since most of the phenomena of interest occur on atomically rough surfaces at low energies (less than 1000 eV), this regime will be examined in detail. In this regime Monte-Carlo computer simulations form the basis for analytic treatment and physical understanding. They are discussed in the next section along with new techniques to model surface roughness (6). Section 3.3 contains a review of the experimental sputtering data for  $H^+$  and  $Ar^+$  on Si, Al, Cu, Ni and C. Section 3.4 points out the numerous effects that can further influence sputtering yields such as substrate temperature, single crystal channeling, chemical reactions, preferential sputtering of alloys, cluster formation, fluence dependence and topology evolution. A brief discussion of review articles is also included.

## **3.2 MODELING**

### **3.2.1 TRIM**

The entire non-isotropic-cascade or primary-knock-on regimes of sputtering is well suited to a Monte-Carlo binary collision approach. In the **TR**ansport of **I**ons in **M**atter (TRIM) program (7,8) the target is considered to be amorphous or polycrystalline. Incident projectiles are followed until a collision occurs. The location of a collision is determined by a random variation of the particles mean-free-path for a nuclear stopping result. Electron energy loss is subtracted for the particles entire path length inside the surface. A random impact parameter and azimuthal scattering angle are chosen and the energy and momentum transfer are calculated classically. This allows the new velocity (speed and direction) and location of both the incident projectile and primary knock-on atom to be determined. They are then treated in the same manner as the incident projectile and create a new generation of knock-on atoms.

Both the original projectile and all of the atoms it collides with are followed by the program. Often the primary knock-on will create an entire cascade of its own. Atoms are followed until their energy falls below the energy needed to escape from the lattice.

When either the initial projectile or a recoil atom reaches the surface, the perpendicular-energy of the particle is compared to the surface binding energy of the target. If the particle can escape, its energy is reduced by the surface binding energy and its emission angle is refracted. If the energy is not great enough to escape, the particle is specularly reflected into the bulk and the process continues.

On the way into the target TRIM does not consider the surface to be atomically flat. Effectively, the initial starting position of the projectile is randomly distributed over a measure of its perpendicular mean free path. This surface model is quite important at low energies and has allowed TRIM to predict experimental results at normal incidence with a high degree of accuracy. At higher angles of incidence a more accurate surface model is needed.

### 3.2.2 Fractals

Real surfaces of amorphous and polycrystalline material are not flat or smoothly varying; they are approximate fractals (9,10). Figure 2 (10) shows a log-log plot of the radius of adsorbed gas atoms vs the number of those atoms it takes to completely cover an  $\text{Al}_2\text{O}_3$  surface. If the alumina were perfectly flat the slope of the line would be -2.00, since area is proportional to radius squared.  $\text{Al}_2\text{O}_3$  is not perfectly flat, however. In fact its surface is quite convoluted. It takes many more small gas atoms to cover all the surface sites than large gas atoms because the small atoms can fit into all the nooks and crannies that the large adsorbate simply plasters over. Surprisingly the points on the curve fall on a straight line. That means that the roughness is self-similar; the surface looks the same independent of the magnification with which it is viewed. The slope of the line and the fractal dimension of the surface is  $2.79 \pm 0.03$ .

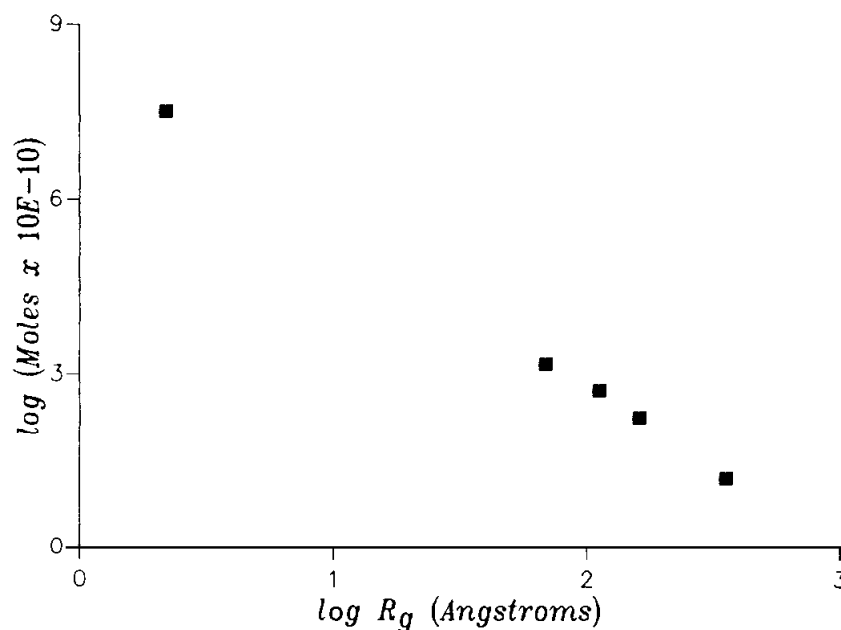


**Figure 2:** Gas adsorption as a function of adsorbate size for  $\text{Al}_2\text{O}_3$ . The slope of the line,  $2.79 \pm 0.03$  is the fractal dimension of the surface (10).



Of course, any real object can only be fractal to some finite magnification. Ultimately the atomic diameter is reached. At the other extreme, the macroscopic character of the material is realized. Fractal geometry becomes a useful construct for sputtering and reflection calculation because the mean free path for collisions within the target and the ultimate range of the projectiles fall within the range over which the targets surface is fractal. The alumina described in Fig. 2 is fractal at least over the range of 4 Å to 210 Å. Many materials have been shown to have fractal surfaces over the range of interest (11). For instance carbon black has a fractal dimension of  $2.25 \pm 0.09$  and Vulcan 3G graphite has a fractal dimension of  $2.07 \pm 0.01$ .

### 3.2.3 Fractal TRIM

The self-similar properties of fractal geometry have been utilized to add a more realistic surface model to the TRIM computer code (6,12). Basically the Fractal TRIM code calculates the distance to the first surface and the distance through the fractal in the scattering plane. If the random selection of the next path step would predict the next collision to occur beyond the first surface but still within the surface feature, the simulation is restarted using the particle's energy and incident angle on entering that surface feature. Since fractal self-similarity implies an equivalence of angular orientation as well as magnification, a three dimensional surface structure does not have to be carried through the simulation. Since a cut through an object with fractal dimension  $D$  produces a new object with dimension  $D - 1.00$ , only the individual scattering plane is modeled and the simulation becomes tractable.

Figure 3 shows the pronounced effect of surface roughness on sputtering yields. The sputtering yield of target material for 100 eV C on C is shown as a function of fractal dimension for a variety of incident angles. Also shown on this figure is the effect of the surface model in the planar TRIM code. Planar TRIM with no surface model gives exactly the same results as Fractal TRIM with  $D = 2.00$ . An effective approximate fractal dimension can be calculated for Planar TRIM which varies with incident angle of the projectile (12). These surface-corrected planar TRIM results are also shown in Fig. 3. Note that Fig. 3 does not give the self sputtering yield for C on C; reflection must be included. It does show the general dependance for the sputtering of many materials at low energy.

A striking result from Fig. 3 is that a small amount of surface roughness can lead to a large change in the sputtering yield. Yet, as surface roughness is increased the sputtering yield drops off for high angles of incidence. This effect can be explained by the schematic drawing in Fig. 4. In Fig. 4(a) a projectile is incident on a perfectly flat surface. The primary knock-on atom will be struck in a downward direction. Since at low energies the first collision is likely to have the highest chance of producing a sputtering event, sputtering is unlikely for a planar surface. This is especially true for normally incident projectiles.

A small amount of roughness (Fig. 4 (b)), allows some primary knock-ons to have a directed energy out of the plane. Thus the sputtering yield increases. Higher angles of incidence promote this effect even more. However, if the surface becomes too rough the sputtered atoms may collide with other surface features (Fig. 4 (c)) and the sputtering yield decreases.

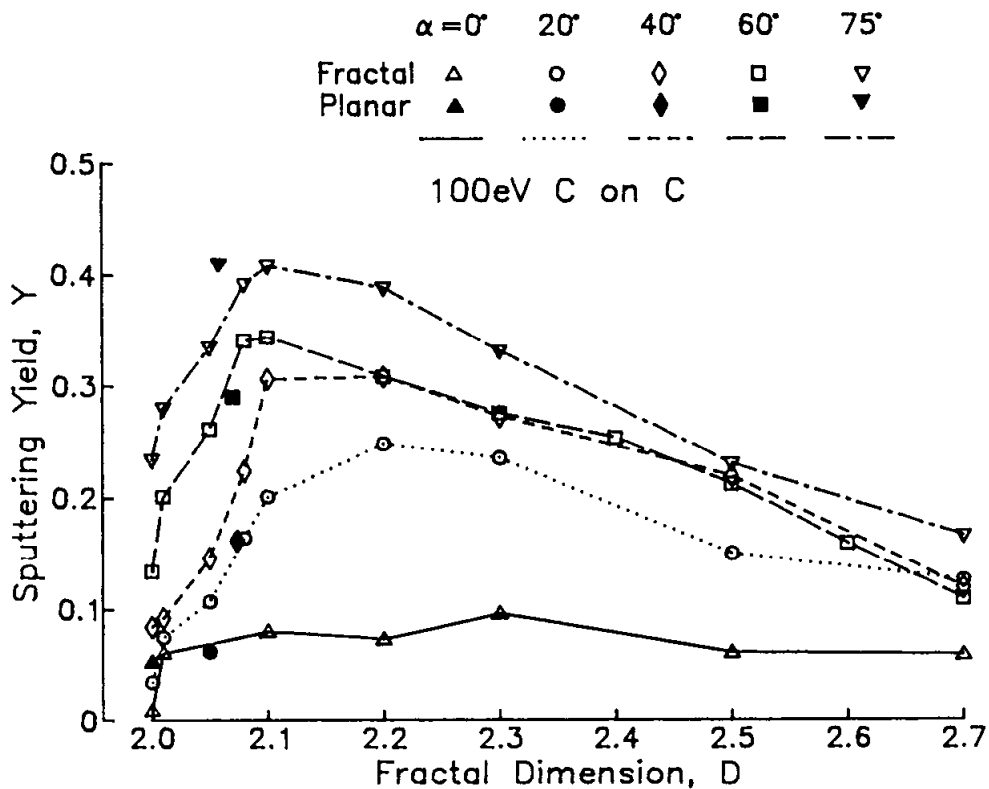


**Figure 3:** Sputtering yield of target material as a function of fractal dimension and angle of incidence for 100 eV C incident on a C target. Normal incidence is 0 degrees. Statistical errors in the yield are generally less than 5%.

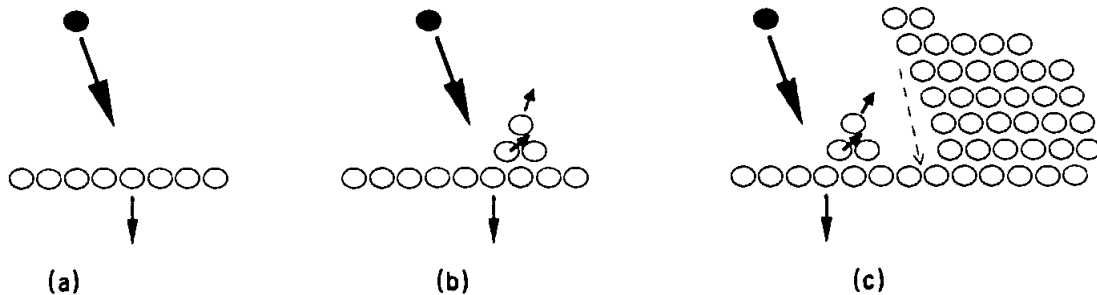


**Figure 4:** (a) On a flat surface the primary knock-on is always directed downward. (b) With some roughness, a primary knock-on could be directed out of the surface, this effect increases as angle of incidence increases. (c) For a very rough surface, sputtered atoms may be recaptured by other surface features.

At higher energies, these detailed surface effects become less important, but a realistic model of the surface remains essential to accurately portray grazing incidence events. Figure 5 shows the sputtering yield for 300 eV H on C as a function of fractal dimension for normal and 60 degree incident angles. Planar TRIM (13) overestimates the sputtering yield at 60 degrees by a factor of two compared to experiments (14). The slight variation

with fractal dimension can also explain why different types of graphite targets gave different experimental results.

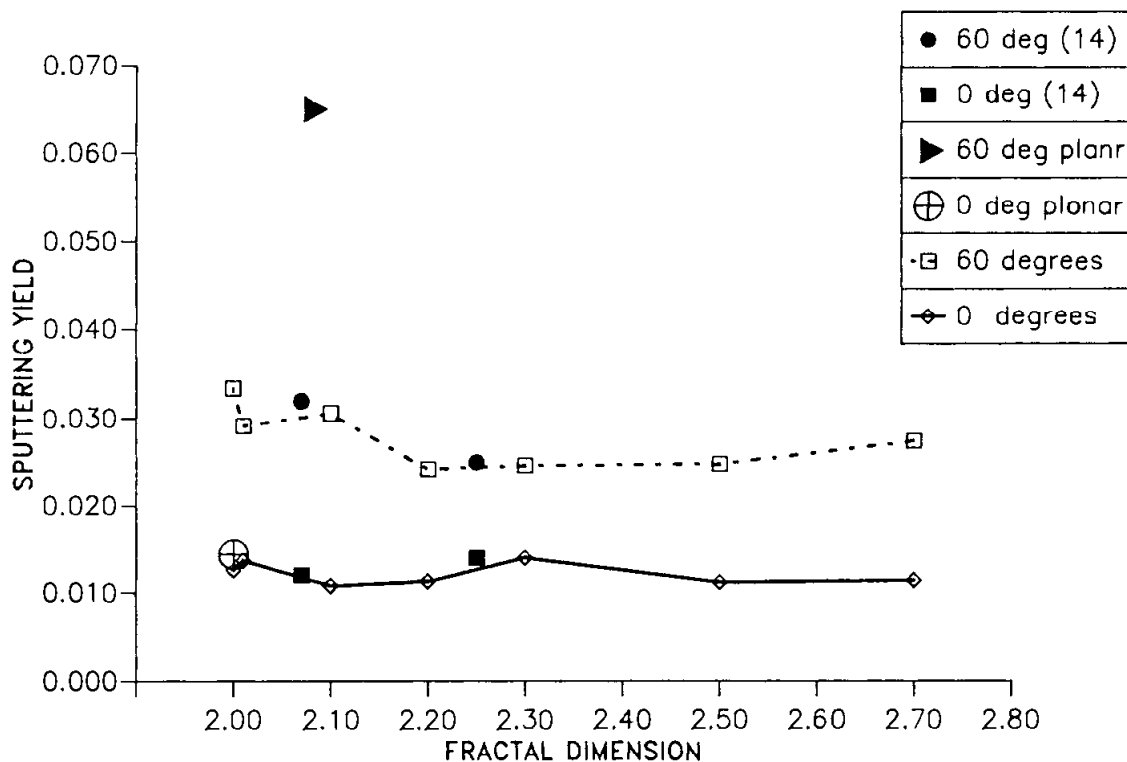


**Figure 5:** Sputtering yield as a function of fractal dimension for 300 eV H on C at normal and 60 degree incidence. Experimental points (14) are shown for a smooth and rough graphite. The fractal dimensions assigned are based on Avnir (11) and are only approximate. Planar TRIM overestimates the sputtering yield by a factor of 2-3 for the 60 degree case. Statistical errors in the yield for the simulation are less than 5%.

### 3.2.4 Reflection

Sputtering is only one of the phenomena that can occur when an ion strikes a surface. At these low energies simple reflection is often more likely. When ions reflect they almost invariably reflect as neutral atoms in their ground states (15,16). An excellent review of reflection data and computer simulations through 1984 can be found in (3). Surface roughness has a profound effect on the reflection of low-energy particles, especially at high angles of incidence (6).

Reflection from fractal surfaces shows a complimentary effect to that of sputtering. Figure 6 shows the number  $R_n$  and energy reflection  $R_e$  coefficients for 50 eV H incident on Ni as a function of fractal dimension for normal and 75 degree incident angles (6). Note how the reflection coefficients drop precipitously for the grazing incident case as soon as some surface roughness is added. This effect is not unusual to anyone who has tried to skip a rock on a choppy lake.

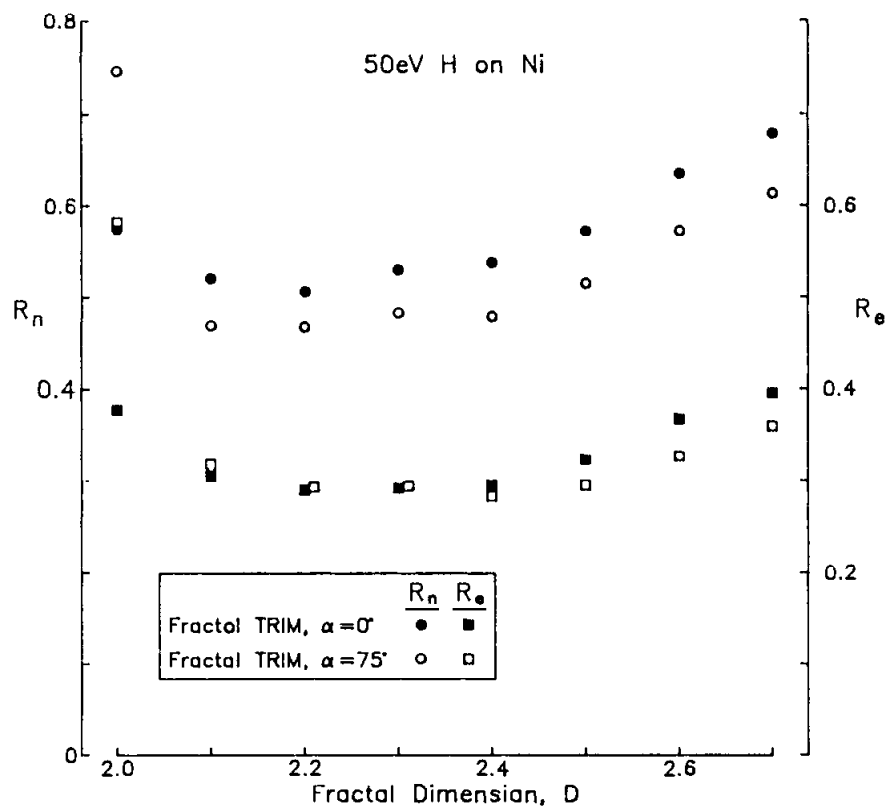


**Figure 6:** Number  $R_n$  and Energy  $R_e$  reflection coefficients for 50 eV H on Ni for normal ( $\alpha = 0^\circ$ ) and grazing ( $\alpha = 75^\circ$ ) incidence as a function of the fractal dimension of the Ni surface. Statistical error in the coefficients are generally less than 5 %. Note the dramatic drop in reflection at grazing incidence when a small amount of surface roughness is added.

At higher energies, above 100 eV, the reflection curves for normal incidence mimic the shape of the sputtering yield (Y) curves. Figure 7 shows  $R_n$  and Y as a function of fractal dimension for 200 eV Ar on Cu. The number reflected and sputter yield jump with a small amount of roughness, reach a maximum and then decrease. When a projectile is incident normally and has a moderate amount of energy it is very unlikely to reflect in one collision. Therefore if the projectile is to escape at all, its geometrical interactions with the surface are very similar to the interactions produced in the collision cascade. Therefore reflection and sputtering have a similar behavior as a function of roughness.

### 3.2.5 Molecular Dynamics

At the lowest energies, the binary collision model should break down. While the physics is quite different, Fig. 8 shows that, for at least one case, a full blown molecular dynamics treatment (17) utilizing a rough fractal-like surface (18) gives nearly the same result as Fractal TRIM. Molecular dynamics codes treat all the interactions of the atoms in the target on an equal basis. At each time step, the forces on all of the atoms in the simulation are simultaneously computed. The extreme computer resources demanded by such routines make them unsuitable for most sputtering and reflection calculations, but they make tremendous learning tools for obtaining a physical feel for low-energy interactions.

This physical feel is best comprehended visually. We have created a movie (19) of a molecular-dynamics simulation of a 10 eV hydrogen atom interacting with a rough Ni surface. To produce the same sense of the interaction through the written word requires some degree of imagination:

Imagine yourself as a hydrogen ion speeding toward a nickel surface. You are moving at 450 angstroms per picosecond (10 eV) and the gentle tug of the protruding electron cloud whose effect is known as the work function is accelerating your progress. A mountain range is coming into view---the surface is not a single crystal, there are hills and valleys below. If you could stop and look closely you'd see a surface alive with random motion. The surface is at room temperature. The mountain peaks almost seem to be swaying in the breeze. Their restoring forces are less and those atoms make larger displacements before being pulled back. The peaks may travel a whole tenth of an Angstrom.

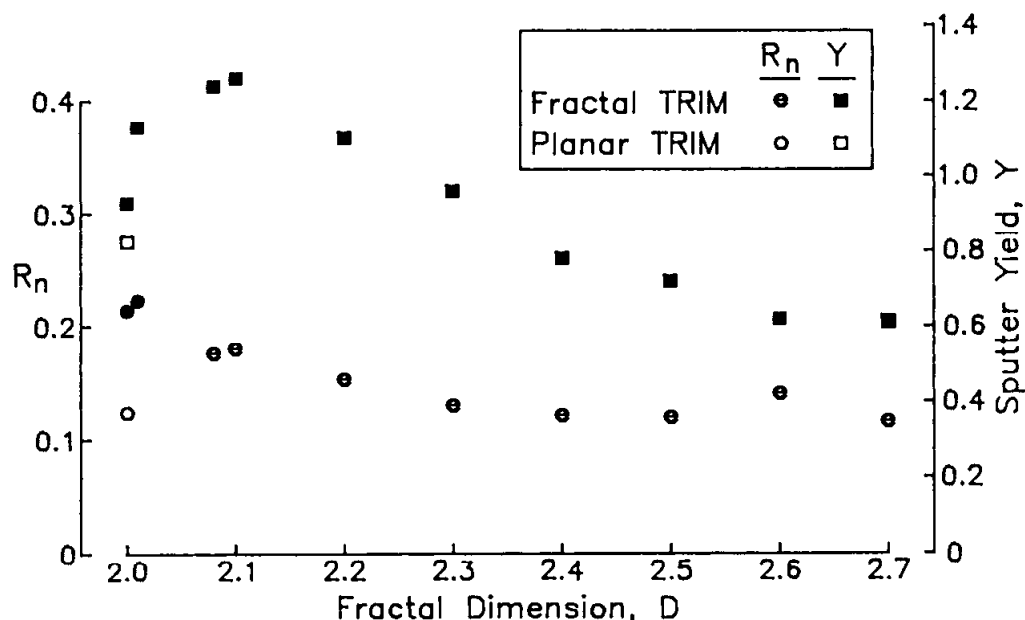


**Figure 7:** Sputtering yield and reflection as a function of fractal dimension for 200 eV Ar normally incident on Cu. Statistical errors for the sputtering yield and reflection coefficients are generally less than 5% and 10% respectively.

A look at the overall topology reminds you of a fractal. If you were twice as close everything would look the same. Of course there is a limit to this self-similar geography--the diameter of a nickel atom is 2.1 Å! The material is basically in a FCC structure with a lattice constant of 3.52 Å. So each plane of atoms is about 1.76 Å apart. The surface roughness is only fractal-like in the range of about 2 to 15 Å. In this range the surface area is proportional to the length of a side of the unit cell to the 2.3 power, i.e. the fractal dimension is 2.3.

Of course, you can't really stop. Compared to your motion the thermal motion is 400 times smaller. You whiz by apparently motionless objects. In this flight you are normally

incident to the surface heading almost directly into a valley. The electron cloud reaches up and envelopes you when you are a few Angstroms above the highest peak. Now you've become an atom. When you are still 7 Å above the floor of the valley and just 1 Å or so below the mountain tops your presence begins to be felt by the atoms in the lattice. The atom directly beneath you and the one closest to your side have their potential energy greatly increased and they are accelerated away from you. The reaction force gradually gives you a component of velocity away from the mountain side. By the time you are even with the floor of the valley you have an angle of 20 degrees with respect to the normal.

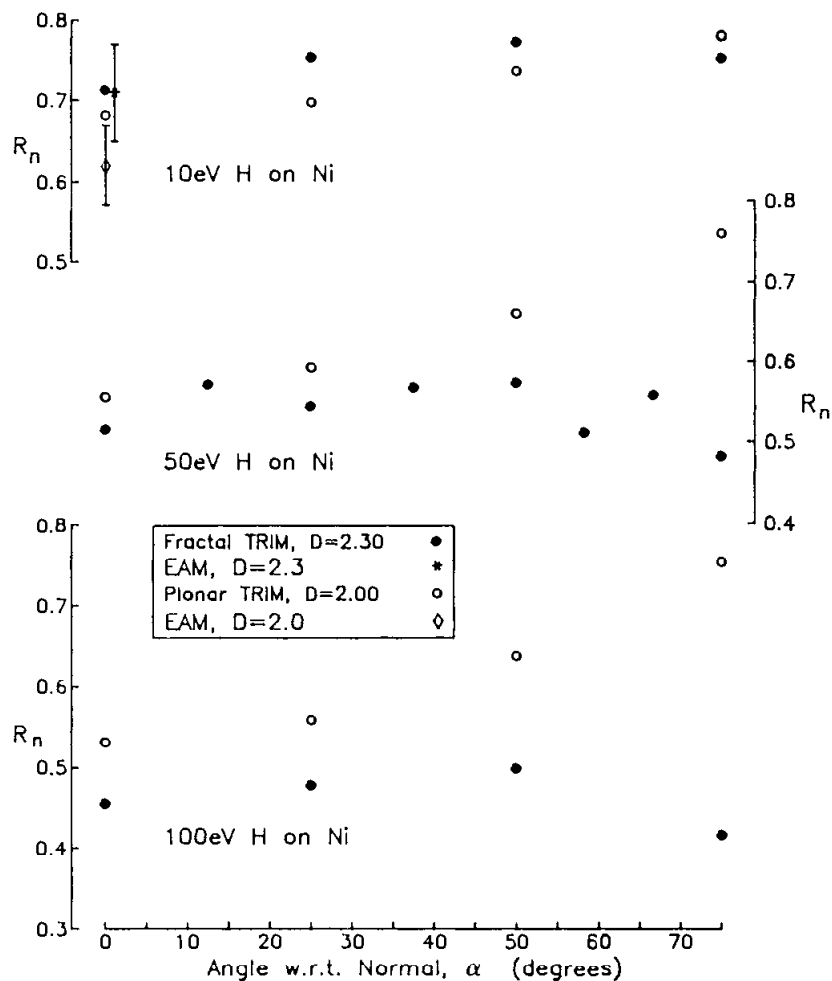


**Figure 8:** Reflection coefficients for 10, 50 and 100 eV H on Ni as a function of incident angle for a fractal Ni surface with dimension 2.30. Planar TRIM results and a molecular dynamics calculation using the Embedded Atom Method (EAM) are also shown. Note that planar TRIM predicts reflection at grazing incidence to be 2-3 times more likely than the fractal TRIM results. Statistical errors in the fractal and planar TRIM reflection coefficients are generally less than 5%.

The news of your arrival travels faster than you do. The neighbors of the atoms initially perturbed have their potentials increased, and a disturbance in the potential of the atoms travels out in waves. This potential shock wave extends about 3 or 4 atoms deep

in a rough hemisphere pointing in the direction of the initial push. If the surface were at absolute zero the disturbance would undoubtedly travel much much further, but the collective effect quickly becomes indistinguishable from the thermal noise.

By the time the first potential wave has damped itself out you have moved less than an Angstrom. New waves are made as you move closer, but a given atom can generally only initiate a wave once. It is not that these initial progenitors disappear. They have effectively not moved at all---it is that their acceleration is now constant so their potential remains the same:

$$ma = dV/dx \quad (1)$$

The velocity vectors of the initial surface were pointing in all directions. The atoms in the potential wave experience a force that slowly bends those velocity vectors around so that they point away from the incident hydrogen atom. However, due to the inertia and restoring forces of the lattice, only the nearest atoms completely turn their velocity vectors in this grazing type of collision. Even this first layer won't have turned completely until the H atom is long gone from the scene.

As you pass into the surface the potential wave effect which slowly produces displacement from your path continues until something dramatic occurs. At about 3 layers in you hit an atom head on and go careening off 135 degrees away now traversing parallel to the surface about 5 Å below the valley floor. In this type of almost binary collision the struck atom changes potential dramatically and its velocity vector immediately swings to the direction it was pushed. However, the speed only builds up to three or four times thermal velocity before its acceleration is slowed by its neighbors. Again the propagation extends only 3 or 4 layers, but the effect is more localized.

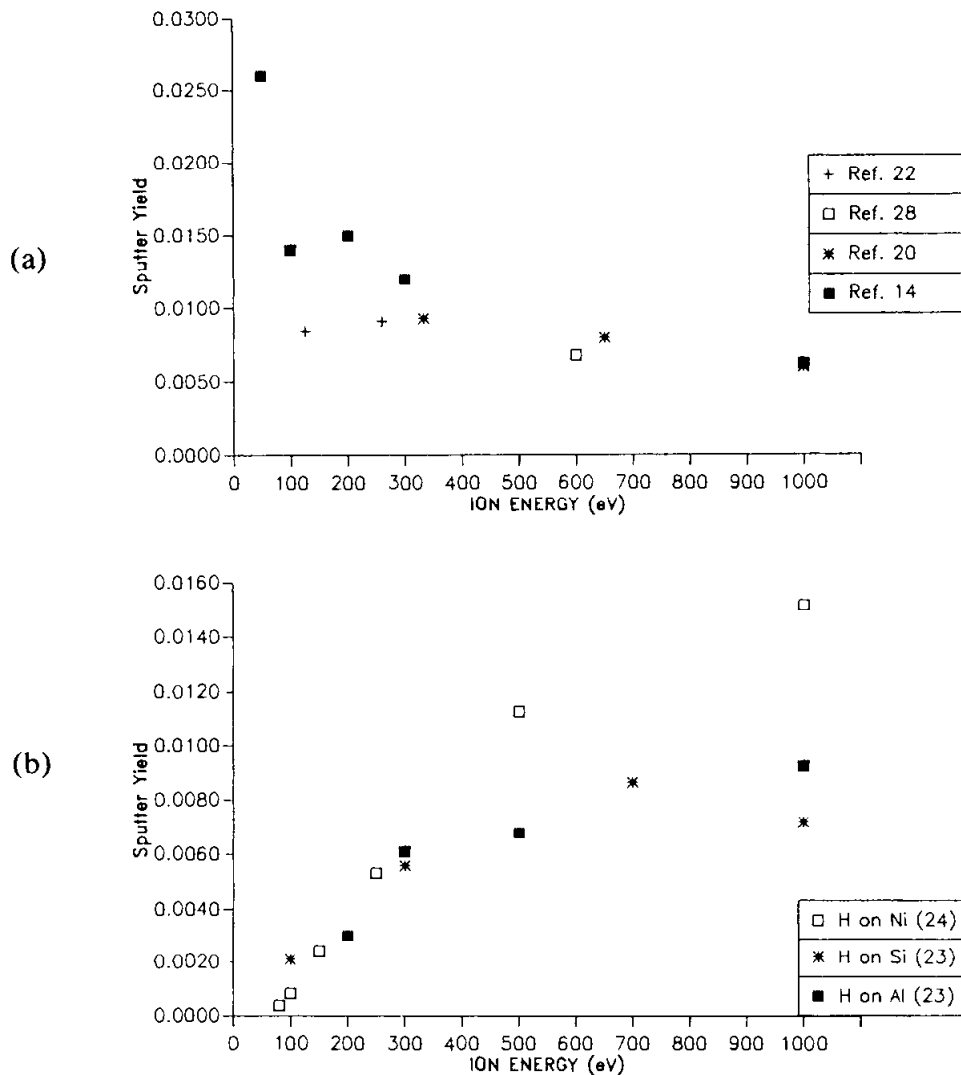
On average you make another collision every 4 Å or so. Each of these violently change your direction but effect your speed very little. Sometimes the collisions are not binary. Two or more atoms can seemingly be struck simultaneously, effecting them all fairly evenly. In each collision the energy transferred away from you is small. It will take 30 collisions or so to come to rest. About half the time you will pop back out of the surface instead. To get out you have to have enough energy to escape that electron cloud, i.e. you have to overcome the work function. If you have almost enough energy you will be drawn to just an Å or so above the surface and travel over the surface like a hover craft until you run into some relief.

So how does sputtering work? Each violent collision or gentle brush leaves a ripple of disturbed atoms with somewhat directed velocities and at least at some point in time a raised potential energy. These ripples of velocity could overlap since the hydrogen is moving much faster than the atoms in the lattice. If the interference happens just right, and one wave of disturbance pushed an atom outward toward the surface at the same time that another wave pushes the same atom outward, an atom on the surface could have a potential great enough the work function. Long ( $10^{-13}$  seconds) after the hydrogen atom hits, a sputtered nickel atom is released. It happens once for every 50,000 hydrogen atoms that strike at 10 eV at normal incidence or so.

### 3.3 EXPERIMENTAL YIELDS

The determination of the sputtering yield of a material can be done in many ways (1). As with most experiments, a large amount of effort is required for each reproducible data point. Without these experiments, however, modelling would be futile. A model should not be whole-heartedly subscribed to unless it fits at least some of the experimental data. In this section most of the experimental data from the era of clean vacuum conditions is assembled for some of the cases of interest to the plasma processing community. The total sputtering yield (sputtered atoms per incident ion) for  $H^+$  and  $Ar^+$  ions incident normal to the surface as a function of energy, up to energies of 1000 eV, are shown next.

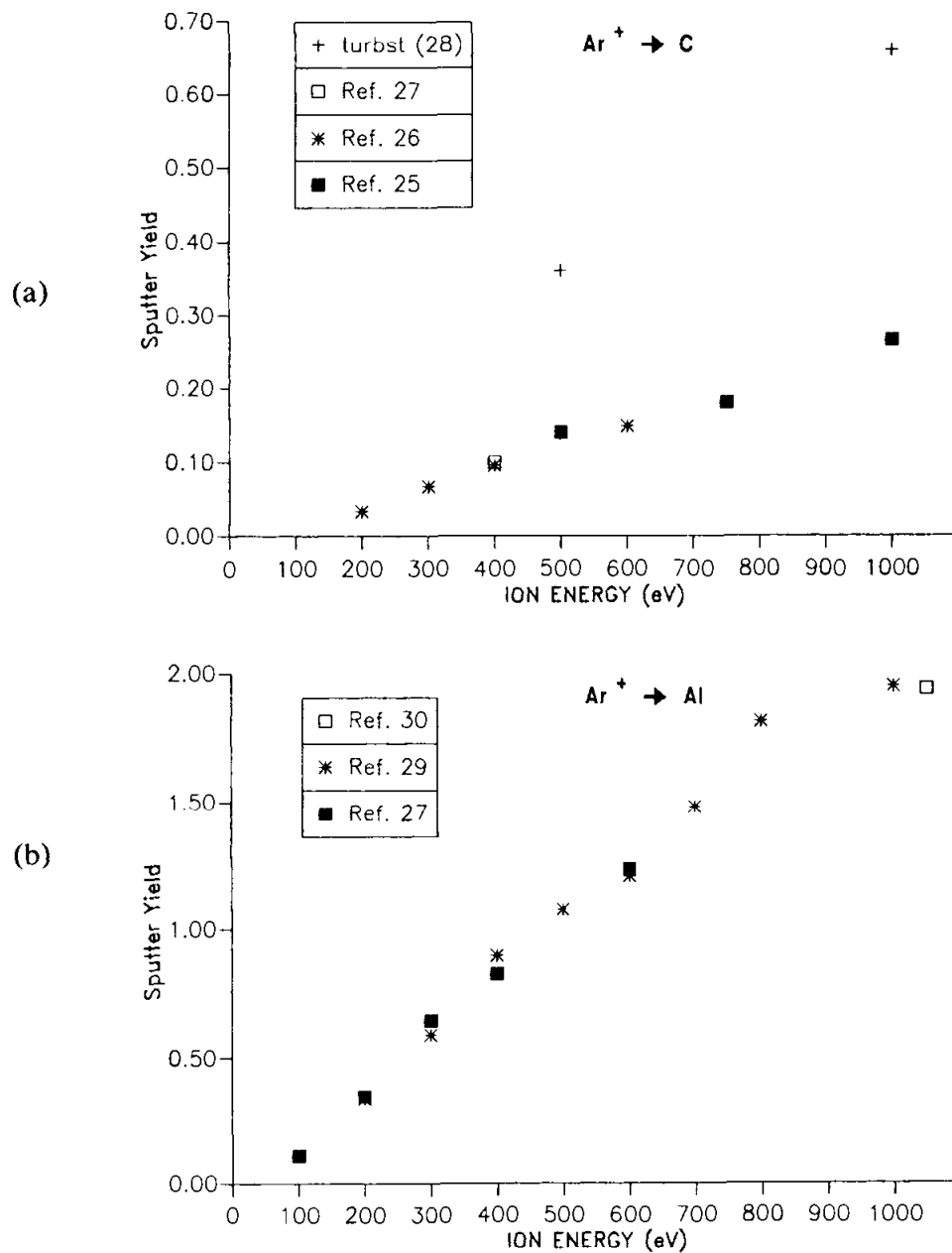
Figure 9(a) shows that the yield for H on C decreases with energy, while Fig. 9(b) shows the yield for H on Al, Si, and Ni increasing with energy. H on C is a peculiar case because of the rampant chemical effects (see Sect. 3.4), though the data in Fig. 9(a) were performed on non-heated samples and are believed to represent physical sputtering.



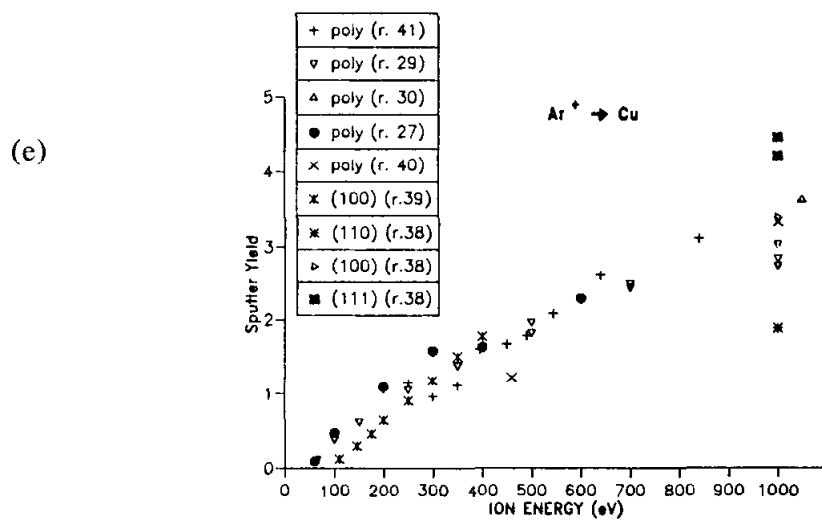
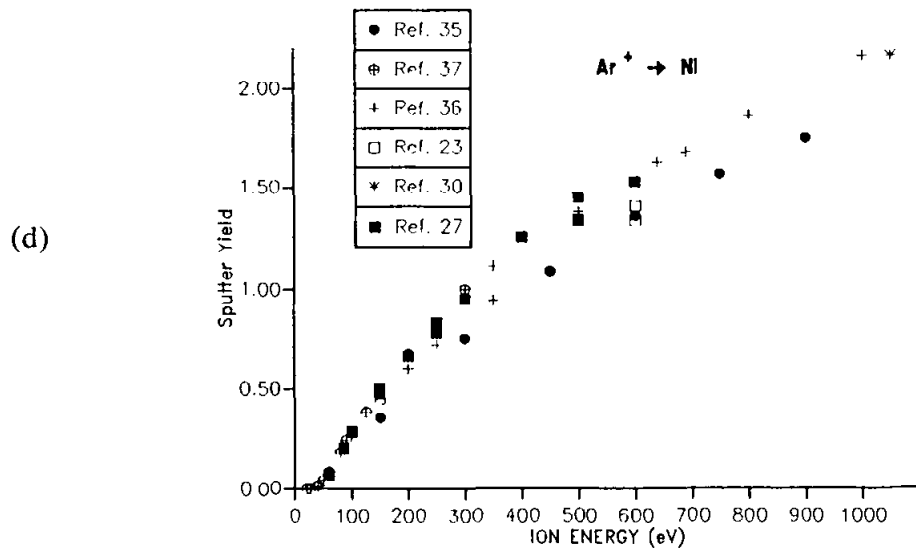
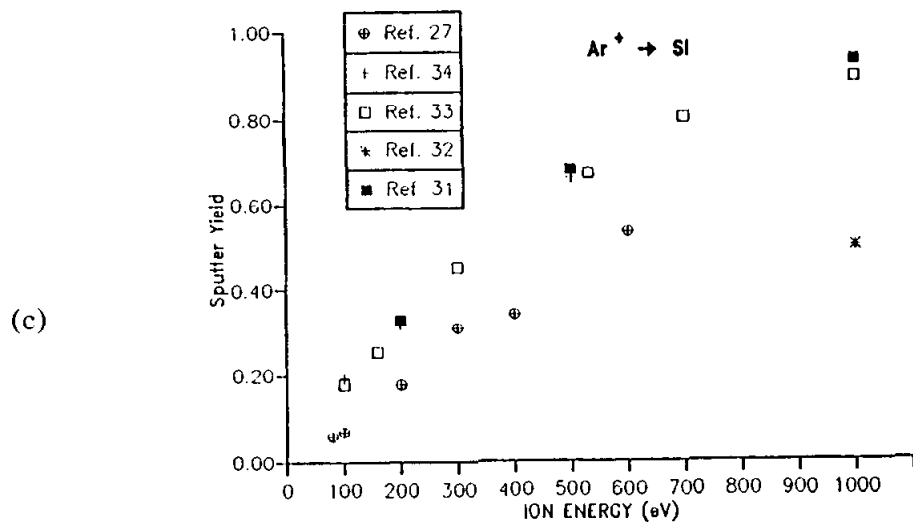
**Figure 9:** Experimental sputtering yield of  $H^+$  on (a) C, and on (b) Al, Si, and Ni.



Figure 10(a) through (e) show the yield for Ar bombarding C, Al, Si, Ni, and Cu at normal incidence. The yield increases with energy. Figure 10(a) shows experimental data for two types of carbon (diamond vs turbostratic) to differ markedly in their sputtering yield. The difference can easily be explained in terms of surface roughness. The diamond surface is likely to have a fractal dimension near 2.00 while the layered turbostratic will have some degree of roughness. As seen in Fig. 3, these difference between very flat and somewhat rough surfaces can give appreciable differences in sputtering yields.



**Figure 10:** Experimental sputtering yields of Ar<sup>+</sup> on (a) C, and (b) Al. In (a) the rougher turbostratic carbon has a higher yield than diamond as expected from the model results in Fig. 3.



**Figure 10:** continued, (c) Si, (d) Ni and (e) Cu. In (e) the effects of crystal orientation are seen at higher energies.

In Fig. 10(e) the effect of crystalline structure is apparent (see Sect. 3.4). These effects are most pronounced at higher energies (1000eV). At lower energies the long-range order of the crystallite does not matter as seen by comparing the (39) data to the spread of the other data in Fig 10(e).

Though normal incident sputtering is often the typical situation for plasma processing, substrate masks, non-normal ion beams and some magnetic configurations may introduce more glancing incident events. In the cascade region the total sputtering yield as a function of incident angle with respect to the normal,  $\theta$ , is predicted to follow a  $1/\cos \theta$  dependence. For Ar ions incident on Al, Ni and Cu at 1050 eV (Fig. 11) and H ions incident on Ni and C at 1000 eV (Fig. 12) this prediction is close to the observed values. Note however, that as the mass of the target increases, the shift is below the cosine prediction. As the incident energy is lowered the shift to a "under-cosine" distribution is quite pronounced as seen in Fig. 12. Here the total sputtering yield as a function of angle for H on C is seen as a function of energy.

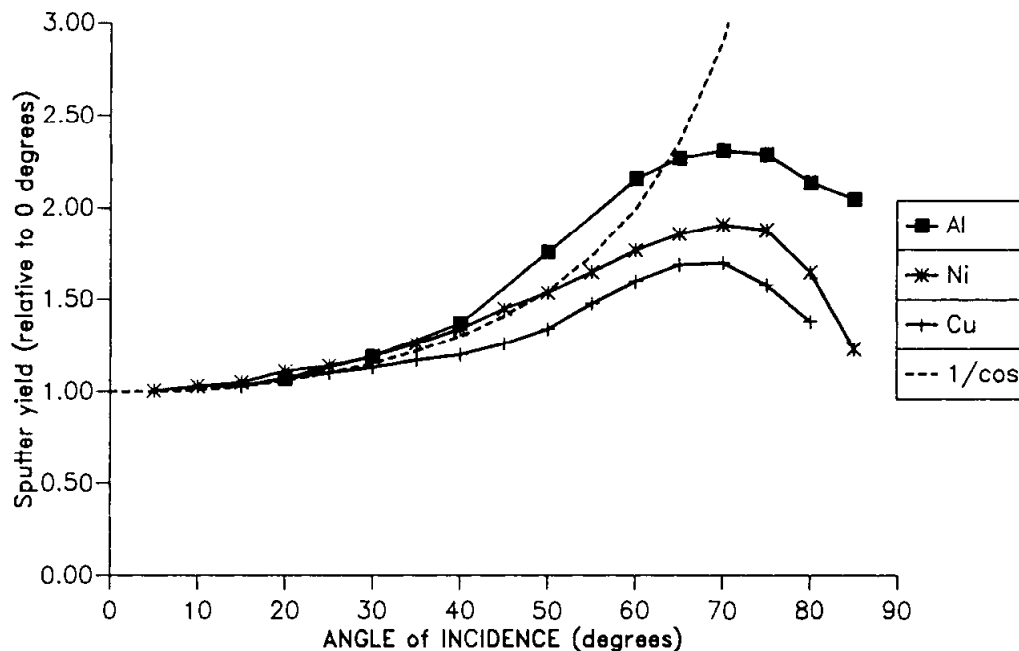


**Figure 11:** Experimental sputtering yield normalized to the yield at normal incidence as a function of angle for Ar<sup>+</sup> on Al, Ni and Cu from Ref. (30) compared to a 1/cosine function.

Both Figs. 11 and 12 show another remarkable feature. At the highest angles of incidence the sputtering yield drops. This is due to an increased number of reflections of the projectile at the grazing incident angles. In the collision with the the first atom struck---the primary knock-on---very little energy is transferred since the path of the projectile is only deflected by a small amount. At higher energies the rounding-over effect is less pronounced since the first collision is less likely to deplete a large fraction of the projectile's energy, and further interactions can take place with higher energy transfer. In these cases, many atoms along the projectile's path are set into motion and cascade theory fits well. If the surface is rough, Fractal TRIM tells us to expect an even lower sputtering yield at high angle of incidence. This is seen in Fig. 12 when comparing V800 and EK98 (rough industrial graphites) to highly oriented graphite. The sputtering yield is a factor of 2 to 3 times lower as was the prediction in Fig. 5.

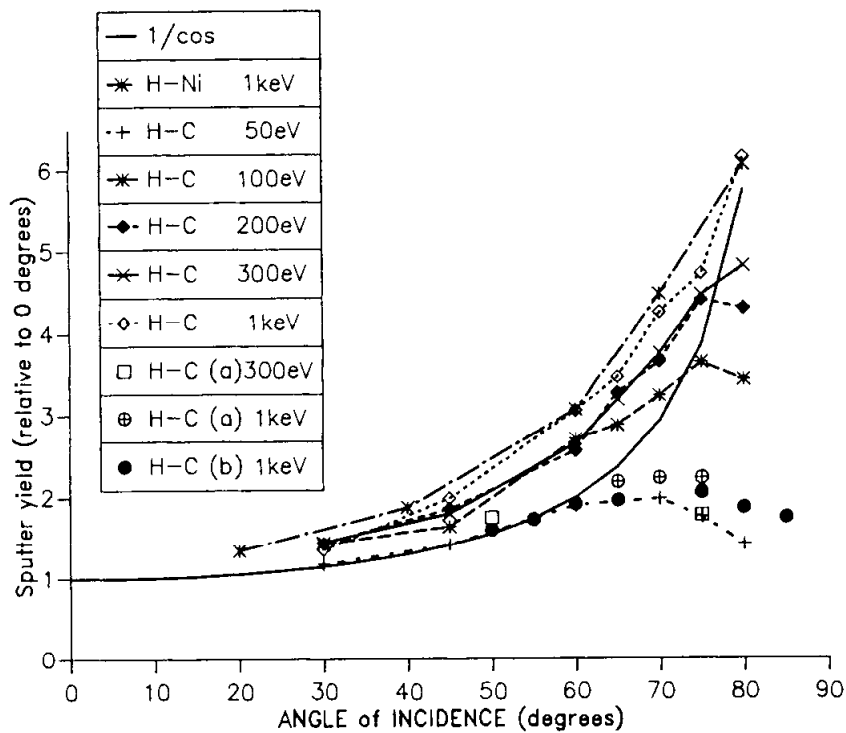


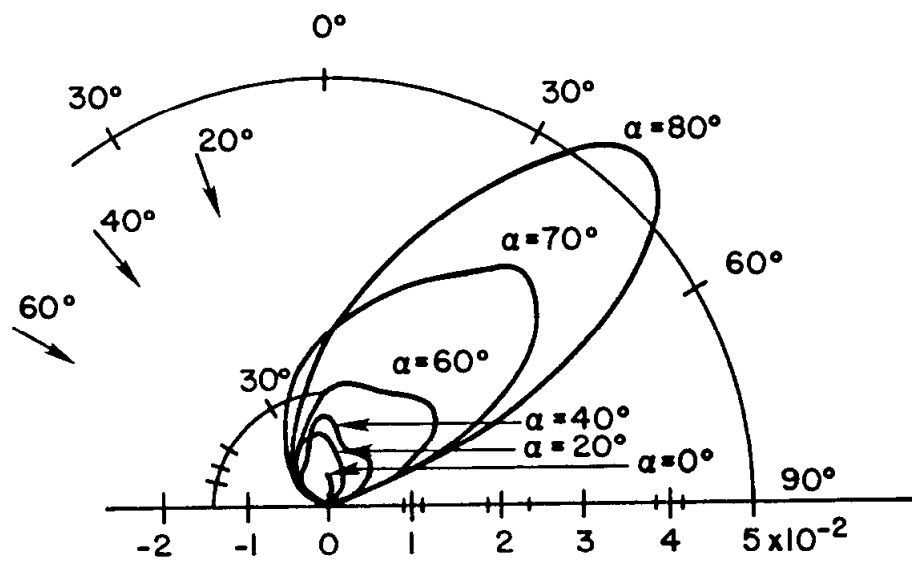
**Figure 12:** Normalized to normal incidence, experimental sputtering yields as a function of angle and energy for H on Ni and H on C. Results for a variety of graphites are also shown. The rougher technical grades of graphite, V800 and ek98, give lower sputtering yields as predicted by the fractal model. Data for H-Ni from Ref. 42, all other data from Ref. 14. NOTE: (a) V800 grade graphite, (b) ek98 grade graphite.

Linear cascade theory also predicts energy and angular distributions of the sputtered flux. For light ions at most energies, and all ions at very low energies, a cascade will not develop. Figure 13 shows a measurement (42) of the emission angle of sputtered Ni as a function of incident angle for a 1000 ev H ion beam. For lower energies and rougher surfaces, simulations (12) show that the angular distribution of sputtered atoms does not show the forward peaking seen in Fig. 13. Instead the emission is almost isotropic.

The energy of the sputtered atoms can also be predicted, but again at low energies some correction is needed (44). Figure 14 shows the energy of the sputtered atoms for Ar bombardment of Cu at a variety of energies.

### 3.4 EXCEPTIONS

Of the events that lead to sputtering only physical sputtering has been examined in this chapter. For particular pairs of atoms, chemical sputtering (the formation of volatile compounds on the target surface) can be very important. For these chemical systems the temperature of the substrate is often the yield determining factor (3,45,46). The chemical environment can be even more complicated by the presence of other reactive gases such as oxygen (47) even in very small quantities.



DIFFERENTIAL SPUTTERING YIELDS  
(ATOM/ION x STERAD)

**Figure 13:** Measured angular distribution of sputtered atoms for 1 keV H on Ni at a variety of incident angles (42).

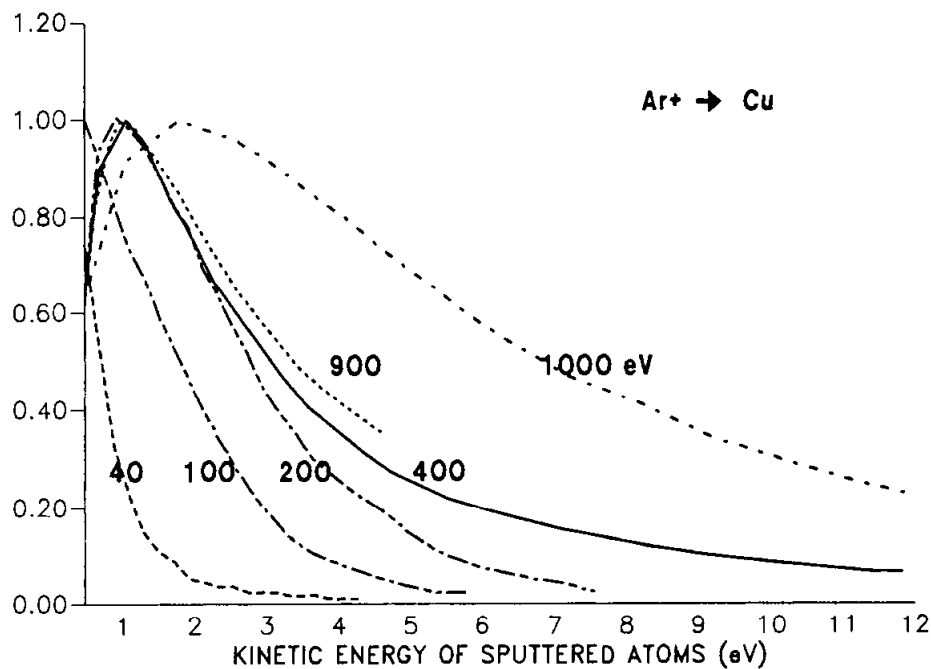


**Figure 14:** Measured energy distributions of sputtered Cu atoms from Ar bombardment at normal incidence. The curves have been scaled to all have a maximum at 1.0. 900 eV is from ref. 61. The other energies are from ref. 43.

The addition of the projectiles which become embedded in the lattice can also alter the sputtering yields (48,49). This fluence effect is due to two factors. The composition of the target is being changed and the surface topology has been altered. In fact, at high

fluence the original surface completely erodes away. Some studies have been carried out on the topography evolution (50-52) due to ion fluence, and more work utilizing fractal geometry is planned by the author.

It is because of this erosion and deposition in the first few atomic layers that channeling by single crystal targets is not a significant effect in this low-energy, surface-dominated regime (53). An excellent Monte-Carlo code, MARLOWE (54), exists to calculate the effects of a single crystal environment, but its greatest utility is simulation of much higher energy sputtering and reflection phenomena.

The changing surface morphology does not just occur due to the addition of some of the incident beam ions. When alloys are sputtered, one of the components is likely to have a higher sputtering yield than the others (55,56). Not only will the yields differ but the angular emission of species can also change (57-59). Sometimes entire clusters of atoms can be knocked loose (60). All considered, sputtering remains one of the most complicated and intriguing branches of particle-surface interactions.

In this chapter I have tried to focus on the types of sputtering phenomena that are of most interest to the plasma processing community. In this low-energy regime surface corrections play a major role, yet with their inclusion modelling can be fairly accurate in determining yields, energy and angular information. Several excellent reviews (1,3,4,61,62) of the larger picture of sputtering exist which contain many analytic and empirical formulas along with a wide variety of experimental data and modelling results.

### 3.5 REFERENCES

1. Sputtering by Particle Bombardment ed by R. Behrisch, Springer-Verlag, Berlin, 1981.
2. P. Sigmund, Theory of sputtering. I. Sputtering yield of amorphous and polycrystalline targets, Phys. Rev. 184: 383 (1969).
3. R. A. Langley, J. Bohdansky, W. Eckstein, P. Mioduszewski, J. Roth, E. Taglauer, E. W. Thomas, H. Verbeek, K. L. Wilson, Data compendium for plasma-surface interactions, Nucl. Fusion special issue: (1984).
4. P. C. Zalm, Handbook of Ion Beam Processing Technology Chap. 6, ed. by J. J. Cuomo, S.M. Rossnagel, H.R. Kaufman, Noyes, Park Ridge, NJ, 1989.
5. H. L. Bay, An analytical formula and important parameters for low-energy ion sputtering, J. Appl. Phys. 51: 2861 (1980).
6. D. N. Ruzic, and H. K. Chiu, Modeling of particle-surface reflections including surface roughness characterized by fractal geometry, J. Nucl. Mater. 162-164: 904 (1989).
7. J. P. Biersack, L. G. Hagmark, A Monte-Carlo computer program for the transport of energetic ions in amorphous targets Nucl. Instrum. Meth. 174: 257 (1980).
8. J. P. Biersack and W. Eckstein, Sputtering studies with the Monte Carlo program TRIM.SP, App. Phys. A34: 73 (1984).
9. B. B. Mandelbrot, The Fractal Geometry of Nature, Freeman, San Fransisco, 1982.

10. D. Avnir, D. Farin, and P. Pfeifer, Molecular fractal surfaces, Nature 308: 261-263 (1984).
11. D. Avnir, D. Farin, and P. Pfeifer, Chemistry in non-integer dimensions between two and three, II. Fractal surfaces of adsorbents J. Chem. Phys. 79: 3566 (1983).
12. D. N. Ruzic, The effects of surface roughness characterized by fractal geometry on sputtering, accepted in Nucl. Instr. and Meth. in Phys. Res. B (1989).
13. W. Eckstein and J. P. Biersack, Self-sputtering and reflection, Z. Phys. B63: 109 (1986).
14. A. A. Haasz, J. W. Davis, C. H. Wu, Angle of incidence dependence of light ion physical sputtering of carbon, J. Nucl. Mater. 162-164: 915 (1989).
15. W. Eckstein, F. E. P. Matschke and H. Verbeek, Reflection of hydrogen from stainless steel and Nb, J. Nucl. Mater. 63: 199 (1976).
16. J. Weng and E. Veje, Absence of excited molecules in sputtering processes, Phys. Rev. 31: 1600 (1985).
17. M. S. Daw, M. I. Baskes, Dynamical calculation of low energy Hydrogen Reflection, J. Nucl. Mater. 128-129: 676 (1984).
18. H. K. Chiu, The reflection of hydrogen off nickel surfaces as a function of fractal dimension, MS Dissertation, Univ. of Illinois, 1988.
19. D. N. Ruzic, H. K. Chiu, C. A. Hoyer, Molecular dynamics on a rough surface, a scientific video, published and available from the National Center for Supercomputing Applications, Scientific Media Services, University of Illinois, 605 E. Springfield Ave, Champaign, IL 61820 (1990).
20. J. Bohdanský, J. Roth, and M. K. Sinha, Erosion of different first wall and limiter materials by low energy hydrogen ions, Proc. 9th Symp. on Fusion Technology (Pergamon, London 1976) 541.
21. J. N. Smith, Jr., C. H. Meyer, Jr. and J. K. Layton, Hydrogen sputtering of carbon thin films deposited on platinum, J. of Nucl. Mater. 67: 234 (1977).
22. J. Bohdanský, H. L. Bay and W. Ottenberger, Sputtering yields of graphite and carbides and their potential use as first wall materials, J. of Nucl. Mater. 76 & 77: 163 (1978).
23. J. Roth, J. Bohdanský and W. Ottenberger, Data on low energy light ion sputtering, Max-Planck-Institut für Plasmaphysik Report, IPP 9/26, May 1979.
24. J. Bohdanský, H. L. Bay and J. Roth, Erosion of iron and nickel based alloys by mono- and multi-energetic light ion bombardment in the energy range from 0.1 - 8 keV, Proc. 7th Int. Vac. Congr. & 3rd. Int. Conf. Solid Surfaces p.1509 (Vienna 1977).
25. T. J. Whetten, A. A. Armstead, T. A. Grzybowski and Arthur L. Ruoff, Etching of diamond with argon and oxygen ion beams, J. Vac. Sci. Technol. A2: 477 (1984).
26. G. K. Wehner, General Mills Report No. 2309 (1962), in reference 1, Chapter 4.
27. N. Laegreid and G. K. Wehner, Sputtering yields of metals for Ar<sup>+</sup> and Ne<sup>+</sup> ions with energies from 50 to 600 eV, J. Appl. Phys. 32: 365 (1961).
28. J. N. Smith, Jr., C. H. Meyer, Jr. and J. K. Layton, Sputtering measurements on controlled thermonuclear reactor materials using auger electron spectroscopy, Nucl. Technol. 29: 318 (1976).

29. C. H. Weijzenfeld, Yield, energy and angular distributions of sputtered atoms, Thesis, University of Utrecht, (1966).
30. H. Oechsner, Sputtering of polycrystalline metal surfaces at oblique ion bombardment in the 1 keV range, Z. Physik 261: 37 (1973).
31. P. C. Zalm, Energy dependence of the sputtering yield of silicon bombarded with neon, argon, krypton, and xenon ions, J. Appl. Phys. 54: 2660 (1983).
32. A. L. Southern, W. R. Willis and Mark T. Robinson, Sputtering experiments with 1- to 5-keV Ar<sup>+</sup> ions, J. Appl. Phys. 34: 153 (1963).
33. S. Tachi, K. Miyake, T. Tokuyama, Proc. of Symp. on Dry Process, Oct. 26-27, 1981, Tokyo, p. 17 (Institute of Elec. Engr. Tokyo, 1981).
34. J. M. E. Harper, J. J. Cuomo, P. A. Leary, G. M. Summa, H. R. Kaufman, and F. J. Bresnock, Low energy ion beam etching, J. Electrochem. Soc. 28: 1077 (1981).
35. H. Fetz and H. Oechsner, Proc. 6th Int. Conf. Phenomenes d'Ionization les Gaz Vol. II p. 39 (Paris, 1963).
36. C. H. Weijzenfeld, Sputtering of polycrystalline metals by inert gas ions of low energy (100-1000 eV), J. Physica 27: 763 (1961).
37. R. V. Stuart and G. K. Wehner, Sputtering yields at very low bombarding ion energies, J. of Appl. Phys. 33: 2345 (1962).
38. G. D. Magnuson and C. E. Carlsson, Sputtering yields of single crystals bombarded by 1- to 10-keV Ar<sup>+</sup> ions, J. Appl. Phys. 34: 3267 (1963).
39. A. Van Veen and J. M. Fluit, Low yield sputtering of monocrystalline metals, Nucl. Inst. and Meth. 170: 341 (1980).
40. F. Keywell, Measurements and collision-radiation damage theory of high-vacuum sputtering, Phys. Rev. 97: 1611 (1955).
41. K. Akaishi, A. Miyahara, Z. Kabeya, M. Komizo and T. Gotch, Sputtering yields of graphite, copper, using torsion microbalance technique with keV region H<sup>+</sup>, He<sup>+</sup> and Ar<sup>+</sup> Proc. 7th Int. Vac. Congr. & 3rd Int. Conf. Solid Surfaces (Vienna 1977).
42. H. L. Bay, J. Bohdansky, W. O. Hofer, and J. Roth, Angular distribution and differential sputtering yields for low-energy light-ion irradiation of polycrystalline nickel and tungsten, J. of Appl. Phys. 21: 327 (1980).
43. R. A. Brizzolara, C. B. Cooper, and T. K. Olson, Energy distributions of neutral atoms sputtered by very low energy heavy ions, Nucl. Instr. and Meth. in Phys. Res. B35: 36 (1988).
44. W. Eckstein, Energy distributions of sputtered particles, Nucl. Instr. and Meth. in Phys. Res. B18: 344 (1987).
45. C. E. Carlston, G. D. Magnuson, A. Comeaux, and P. Mahadevan, Effect of elevated temperatures on sputtering yields, Phys. Rev. 138: 759 (1965).
46. G. S. Anderson, Low-energy sputtering yields of Ge single crystals as a Function of Temperature, J. of Appl. Phys. 38: 1607 (1967).
47. K. S. Kim, W. E. Baitinger, J. W. Amy and W. Winograd, ESCA studies of metal-oxygen surfaces using argon and oxygen ion-bombardment, J. of Electron Spect. and Rel. Phen. 5: 351 (1974).



48. P. Blank and K. Wittmaack, Energy and fluence dependence of the sputtering yield of silicon bombarded with argon and xenon, J. Appl. Phys. 50: 1519 (1979)
49. J. Kirschnner and H. W. Etzkorn, On the fluence dependence of the sputtering yield for low-energy noble gas ions, J. Appl. Phys. A29: 133 (1982).
50. G. Carter, M. J. Nobles, I. V. Katardjiev, J. L. Whitton, and G. Kiriakidis, The effect of ion species on topography evolution, Nucl. Instr. and Meth. in Phys. Res. B18: 529 (1987).
51. I. V. Katardjiev, Simulation of surface evolution during ion bombardment, J. Vac. Sci. Technol. A6: 2434 (1988). 2434-2442.
52. S. Valkealahti and R. M. Nieminen, Molecular dynamics simulation of the damage production in Al (110) surface with slow argon ions, Nucl. Instr. and Meth. in Phys. Res. B18: 365 (1987).
53. M. Hou and M. T. Robinson, Computer simulation of low-energy sputtering in the binary collision approximation, Appl. Phys. 18: 381 (1979).
54. M. T. Robinson, I. M. Torrens, Computer simulations of atomic-displacement cascades in solids in the binary-collision approximation, Phys. Rev. B9: 5008 (1974).
55. R. Shimizu, Preferential sputtering, Nucl. Instr. and Meth. in Phys. Res. B18: 486 (1987).
56. P. Sigmund, Preferential sputtering from isotopic mixtures and alloys of near-neighbor elements, Nucl. Instr. and Meth. in Phys. Res. B18: 375 (1987).
57. R. R. Olson and G. K. Wehner, Composition variations as a function of ejection angle in sputtering of alloys, J. Vac. Sci. Technol. 14: 319 (1977).
58. R. R. Olson, M. E. King, and G. K. Wehner, Mass effects on angular distribution of sputtered atoms, J. Appl. Phys. 50: 3677 (1979).
59. E. Dullni, Velocity distributions of the metal atoms sputtered from oxygen and nitrogen covered Ti- and Al- surfaces, Nuclear Instr. and Meth. in Phys. Res. B2: 610 (1984).
60. G. P. Konnen, A. Tip and A. E. de Vries, On the energy distribution of sputtered clusters, Rad. Eff. 26: 23 (1975).
61. H. Oechsner, Sputtering-a review of some recent experimental and theoretical aspects, Appl. Phys. 8: 185 (1975).
62. H. H. Andersen, Computer simulations of atomic collisions in solids with special emphasis on sputtering, Nucl. Instr. and Meth. in Phys. Res. B18: 321 (1987).

## 4

---

# Bombardment-Induced Compositional Change With Alloys, Oxides, Oxysalts, and Halides

---

Roger Kelly

## 4.1 INTRODUCTION

### 4.1.1 The Early Situation

Bombardment-induced compositional change with alloys, oxides, oxysalts, and halides has been the subject of both experimental and theoretical study for the past two decades. Concerning theoretical work, it is worth pointing out that the emphasis has changed to a remarkable extent as the experimental base has grown. Work written before 1980 tended to emphasize preferential sputtering as triggered by differences of mass, chemical binding, or volatility. Mass and chemical binding were envisaged as governing collisional sputtering, volatility as governing thermal sputtering.

Mass is now regarded to be an important factor in preferential sputtering, thence in compositional change, only under near-threshold conditions, as when  $\text{Ta}_2\text{O}_5$  is bombarded with 1 keV  $\text{H}^+$  or  $\text{He}^+$  and loses O (whereas it is largely unchanged with 1 keV Ar and Xe) (Fig. 1)(1), and in isotope sputtering, as when lighter isotopes are lost preferentially with Li, Ti, Ga, and Mo (2). With alloys the role claimed for mass other than near the threshold or with isotopes (3) was subsequently shown (4) to be largely irrelevant: this was not because the theory (3) was wrong but because bombardment-induced Gibbsian segregation (4) had been neglected and the latter can cause either a light or heavy species to be lost. (A simplified restatement of the argument of (3) about the role of mass is given in (5).) Whether or not mass plays a role with oxides and halides is less easily settled. For example,  $\text{MoO}_3$  is reduced mainly to  $\text{Mo}^{\text{IV}}$ , as expected thermodynamically, but the reduction products of  $\text{WO}_3$  include  $\text{W}^0$  (Table 8, to follow): is this an effect of mass? Also, Malherbe et al. (6) advocate a more general role for mass with oxides, equivalent to that of Ref. 3. We will in general not discuss mass except for a brief reference in Sect. 4.4.4.1. A review in the context of near-threshold effects is given elsewhere (7).

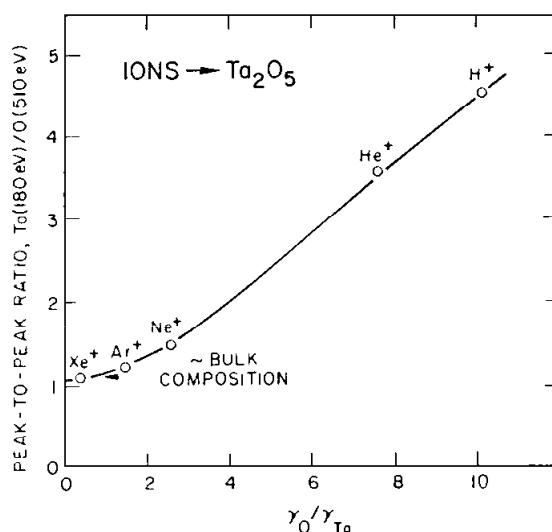


**Figure 1:** Steady-state composition ratio, Ta/O in arbitrary units, for  $\text{Ta}_2\text{O}_5$  as a function of the ratio of the energy transfer factors,  $\gamma_{\text{O}}/\gamma_{\text{Ta}}$ , for bombardment with various 1 keV ions at  $\theta_1 = 30^\circ$ . As usual,  $\gamma$  is given by  $4M_1M_2/(M_1+M_2)^2$ , "1" refers to the incident particle, and "2" refers to the target. Compositions were obtained with AES. Due to Taglauer (1).

Chemical binding, reflected explicitly in the surface binding energy and ideally proportional to  $\Delta H^a$ , the heat of atomization (8), was at one time the most popular framework for explaining preferential sputtering, thence compositional change, with alloys. It had the advantage, one lacked by the mass argument, that it gave a nearly perfect correlation: e.g. Au is known to be lost from near the surface of Au-Pd (Figs. 2 (9) and 3) and, at the same time, although it is heavier, it has a slightly lower  $\Delta H^a$ :  $\Delta H_{\text{Au}}^a = 3.82$  eV,  $\Delta H_{\text{Pd}}^a = 3.90$  eV. It is easily shown, however, that chemical binding as manifested in the surface binding energy should, at least with alloys, normally lead to significantly smaller composition changes than are observed, for example the evolution of  $\text{Au}_{0.50}\text{Pd}_{0.50}$  to  $\text{Au}_{0.498}\text{Pd}_{0.502}$  (Sects. 4.2.3 and 4.2.4). But as manifested in segregation, chemical binding can lead to very large effects indeed, for example the evolution of  $\text{Au}_{0.50}\text{Pd}_{0.50}$  to  $\text{Au}_{0.76}\text{Pd}_{0.24}$  (Fig. 3, curve labeled "annealed"; see also Refs. (5,10)). On the other hand, there is a hint that with oxides and halides the surface binding energy may play an unsuspected role. This is because energies calculated for atom removal from undisturbed surfaces can differ markedly depending on whether one considers an anion or cation, e.g. 12 eV for O in  $\text{Al}_2\text{O}_3$  and 30 eV for Al in  $\text{Al}_2\text{O}_3$  (11). The topic is pursued further below in Sect. 4.1.6 and then in Sects. 4.2.5 and 4.2.6.

The role of volatility, i.e. of thermal sputtering, is more problematical than that of mass or chemical binding. After being alternately accepted and rejected for 130 years (12), it was in a phase of acceptance in the decade 1970-1980. This was because the experiments of Nelson (13) had not yet been re-interpreted (14,15), since physically correct theories had just appeared (16,17), and since thermal effects were being widely advocated to justify the presence of ions and excited states amongst sputtered particles and to explain O loss (18,19). For example, differences in volatility (relevant if thermal sputtering occurs) were found to explain many examples of O loss from oxides, with both the correlation ("yes" or "no") and the required magnitude of the volatility ( $10^{2\pm 1}$  atm at

$\sim 4000$  K) being reasonably correct for the systems then known (19). Since then, many additional oxides have been shown to lose oxygen, including some like  $\text{HfO}_2$ ,  $\text{Nb}_2\text{O}_5$ ,  $\text{SnO}_2$ ,  $\text{Ta}_2\text{O}_5$ ,  $\text{WO}_3$ , and  $\text{ZrO}_2$  which (unlike the systems known when Ref. (19) was prepared) have very low volatility, at least for the observed extent of O loss. With alloys the best evidence for thermal sputtering relates to energy distributions, as for  $\text{Xe}^+ \rightarrow \text{Ag}$  (20,21), which showed departures from the form expected for cascade sputtering as if a thermal distribution were superimposed. Temperatures of 20,000 to 30,000 K were implied, however, and this contradicts the idea that a condensed phase cannot exceed its critical temperature, 5100 K for Ag (22), because of a "phase explosion" (23,24). There is an important qualification, namely that a phase explosion may have a natural delay time, possibly as much as  $10^{-7}$  to  $10^{-9}$  s although possibly much less (23).

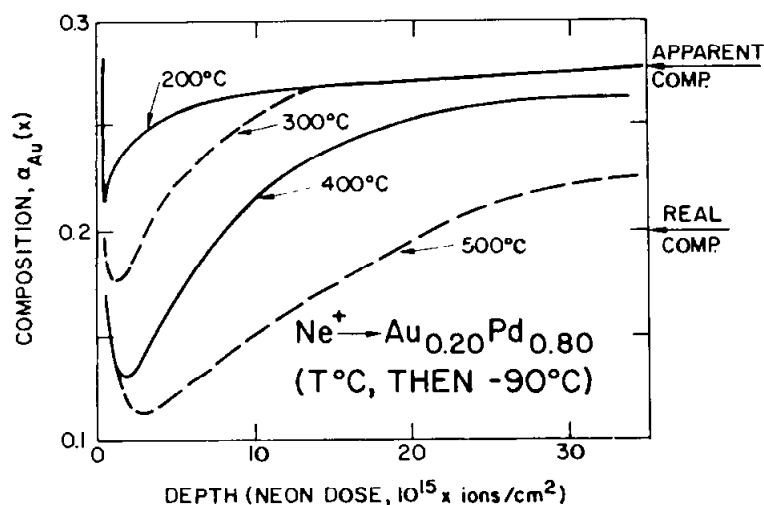


**Figure 2:** Composition-depth profiles for bombarded  $\text{Au}_{0.20}\text{Pd}_{0.80}$  as obtained by first bombarding to steady state with normally incident 2 keV  $\text{Ne}^+$  at the indicated temperatures, then quenching to  $-90^\circ\text{C}$ , and finally profiling with 2 keV  $\text{Ne}^+$ . Compositions were obtained with ISS, using the same 2 keV  $\text{Ne}^+$  as the probe ion. The reason that the bulk composition implied by the Figure,  $\text{Au}_{0.28}\text{Pd}_{0.72}$ , disagrees with the stated composition,  $\text{Au}_{0.20}\text{Pd}_{0.80}$ , is that the system is subject to on-going Pd loss as a mass effect (cf. Fig. 1). For notation, see Sect. 4.1.7. Due to Swartzfager, Ziemecki, and Kelley (9).

#### 4.1.2 Bombardment-Induced (Gibbsian) Segregation, BIS

We have been emphasizing the inadequacies of the older theoretical works, those before 1980, on the subject of what causes bombardment-induced compositional change, with their emphasis on a more or less universal role for preferential sputtering as triggered by differences of mass, chemical binding, or volatility. The first new feature was the realization of a pervading role for BIS in causing changes with alloys (4,5). Such segregation occurs in nearly all cases in the same sense as equilibrium segregation (Figs. 2 and 3), though always has a smaller numerical extent for ambient temperature (5,10). It is demonstrated in characteristic composition-depth profiles (Fig. 2), formally equivalent to those found with equilibrium segregation when there is a moving surface; in conflicts between ISS and AES or XPS analysis of bombarded surfaces (Fig. 3), which follow naturally from the profiles; conflicts between the sense of equilibrium segregation and the sense of composition change (also shown in Fig. 3); in characteristic results for yield-vs.-angle (25,26), such that the non-segregating species is emitted more nearly normal to

the surface; in delayed segregation; and in suppressed sputtering. Delayed segregation relates to such systems as a bilayer of Ni on Ag (27) or homogeneous Au-Cu (Fig. 4 (28)), where segregation was found to continue evolving for a few minutes after bombardment ceased. Such experiments show in an explicit way that chemical effects can occur during the prolonged relaxation that occurs subsequent to particle impact, a subject that was anticipated also in computer simulation (29), in work with alkali halides (30), and, particularly relevant here, in work on the decomposition of oxysalts (31-34) such as the delayed relaxation of randomized  $\text{BaSO}_4$  (containing BaO) to true  $\text{BaSO}_4$  (33). Suppressed sputtering (e.g. 35) is to be expected if segregation is sufficiently strong to exclude one component from the outer surface.

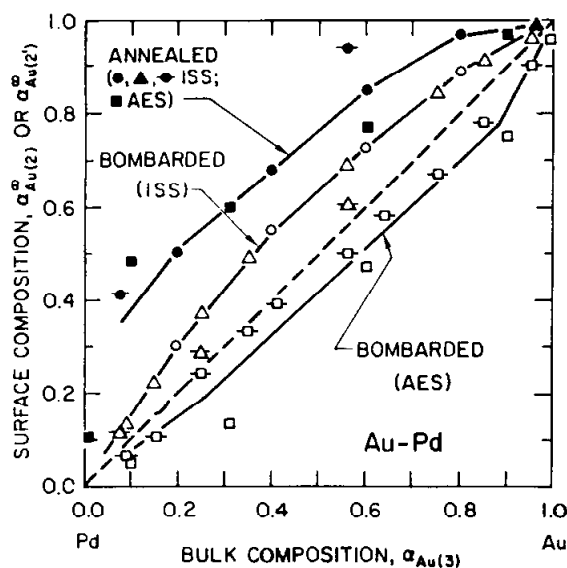


**Figure 3:** Comparison of surface or subsurface compositions with bulk compositions for Au-Pd specimens which have been either annealed or bombarded. The segregating element is seen to be Au and, in addition, the outermost atom layer of a bombarded surface is also Au rich ("ISS"); in agreement with Fig. 2, however, the subsurface region of a bombarded specimen is deficient in Au ("AES"). This example is generic of many others in which the species which segregates on annealing shows a composition spike followed by severe depletion when the specimen is bombarded. Details are as follows: ● (600°C, Ne ISS (9)); ▲ (500°C, Ne ISS (58)); ◆ (400°C, He ISS (59)); ■ (600°C, AES (60)); ○ (bombarded, Ne ISS (9)); △ (bombarded, He ISS (61)); ◀ (bombarded, He ISS (59)); □ (bombarded, AES (60)); ◻ (bombarded, AES (62)). A further point "◆" which lies in the upper left under the "E" of "bombarded" is not shown.

Segregation is, we would emphasize, not a type of sputtering, so invoking it to explain composition change constitutes a major change. We treat BIS with alloys in Sect. 4.3.

Oxides also show segregation but the evidence for it playing a role in composition change was slow to come. In such a case as  $\text{Na}^+$  on  $\text{SiO}_2$ , the movement of the  $\text{Na}^+$  was a response to the charge of the incident particle (36), an effect that can occur only under conditions of ultra-high diffusivity and that is here classified as a form of redistribution (Sect. 4.1.5). In the case of CaO in MgO, the loss of Ca during bombardment at 1250°C probably involved equilibrium segregation, the onset temperature for which is ~900°C (37). The first straightforward example, with behavior like that of an alloy, re-

lates to Na loss from  $\text{Na}_2\text{O-SiO}_2$  (38). We will not further treat BIS with oxides in what follows.

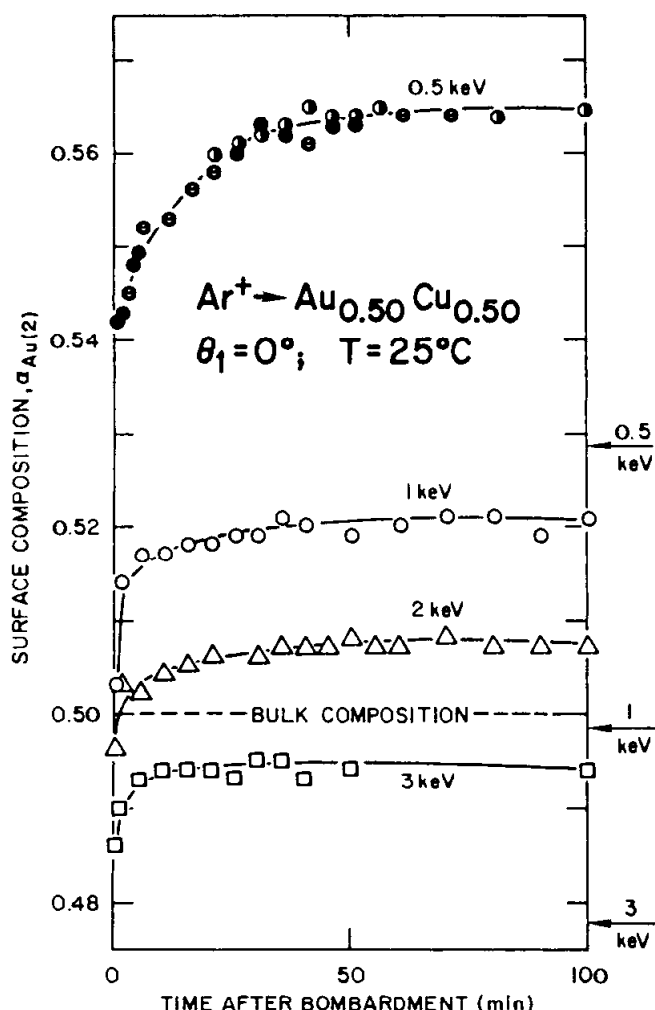


**Figure 4:** Changes in surface composition with time after stopping bombardment of  $\text{Au}_{0.50}\text{Cu}_{0.50}$  at  $25^\circ\text{C}$  with normally incident  $\text{Ar}^+$  having energies of 0.5-3 keV. Compositions were obtained with low-energy (60-69 eV) AES. The arrows mark the average steady-state compositions achieved during bombardment and differ from what is shown in the figure for  $t = 0$  only because of being averages (63). The composition changes are seen to involve an increase in the amount of Au at the surface and are in accordance with what is found with heated specimens (64). The relevant mass transport is not regarded as thermally activated diffusion but rather the post-bombardment analog of bombardment-enhanced diffusion (65). Due to Li, Tu, and Sun (28).

#### 4.1.3 Bombardment-Induced Mixing

Mixing and BIS are not the same but have such close similarities that it is worth comparing them. Furthermore, the existence of the one supports the existence of the other.

An important aspect of BIS is that, assuming it to resemble equilibrium segregation, then the driving force is only 0.06 to 0.52 eV, values which are very much less than the energies characterizing particle bombardment,  $\gtrsim 1$  keV, or recoil motion,  $\gtrsim 10$  eV (columns 2 and 3 of Table 1). Historically, mixing was described as a purely collisional (ballistic) effect, though with recognition of random and directed parts (e.g. 39). It was recently shown (40,41), however, that binary metallic systems show mixing rates which correlate with the heats of mixing (Fig. 5 (41)). Apparently a significant part of the driving force for the mixing is based on chemical energy differences and we note that the magnitude,  $\leq 1.3$  eV, is again small compared with incident particle or recoil energies (column 4 of Table 1). It is clear that there is an extreme disparity between the chemical energy differences relevant to BIS or mixing and typical bombardment or recoil energies.

When we consider BIS in Sect. 4.3 one objective will therefore be to show a way out of the paradox.

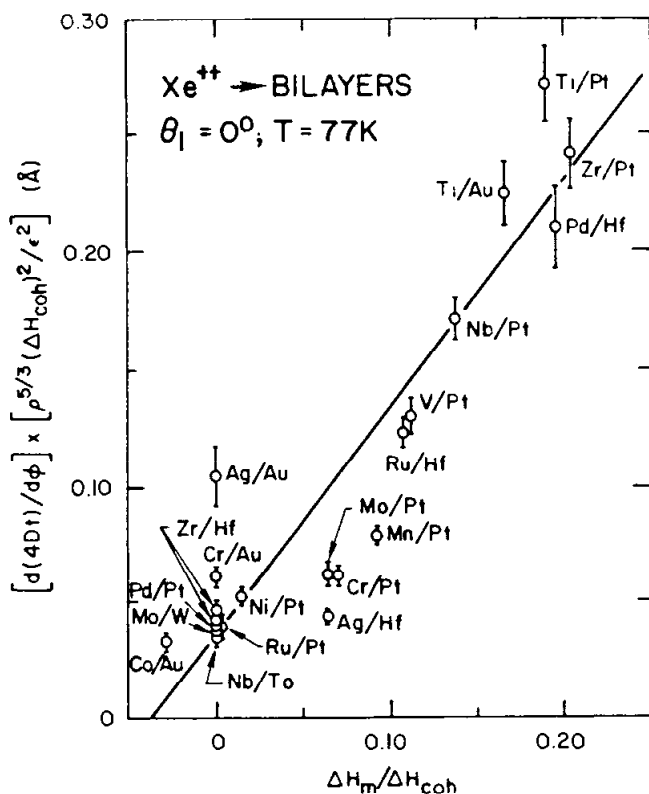


**Figure 5:** Correlation suggesting that ion-beam mixing of metallic bilayers using 600 keV  $\text{Xe}^{++}$  at 77 K scales as the heat of mixing,  $\Delta H_m$ .  $d(4Dt)/d\phi$  is the experimentally observed mixing rate,  $\phi$  is the fluence (dose),  $\rho$  is the target number density ( $\text{cm}^{-3}$ ),  $\Delta H_{\text{coh}}$  is the cohesive energy for  $A_{0.50}B_{0.50}$ , and  $\epsilon$  is the density per unit length of deposited energy. Due to Cheng et al. (41).

A further similarity is that both mixing and BIS persist to very low temperatures, at least to 20 K in the former case (42) and at least to  $-120^\circ\text{C}$  in the latter (43).

#### 4.1.4 Bombardment-Induced Decomposition

The third new feature in the post-1980 period originated with four separate groups of authors, Christie et al. (e.g. 31), Hofmann et al. (e.g. 32), Rabalais et al. (e.g. 33), and Marletta et al. (e.g. 34). They suggested what is effectively an alternative to thermal sputtering. Basically, the traditional (thermal) point of view emphasizes transient vaporization subject to the laws of equilibrium thermodynamics. When several components are present, compositional changes arise due to the loss of the more volatile species. Although this is a strictly surface process, it could influence greater depths if the surface composition change served as a diffusion boundary condition, as when a surface of  $\text{Ti}_2\text{O}_3$  triggers bombardment-enhanced out-diffusion of O from  $\text{TiO}_2$  (44). The point of view of the authors indicated above is that the cascade itself should be regarded as a source of new stoichiometries as the initially disrupted lattice relaxes (cf. Fig. 4) and various alternative stoichiometries compete. In effect, a species of chemical driving occurs similar to what is postulated to govern BIS and mixing. The laws of equilibrium thermodynamics, especially the relevance of the free energy, probably do not apply. For example, bombarded  $\text{Ca}(\text{NO}_3)_2$  (31) could return to  $\text{Ca}(\text{NO}_3)_2$  itself, but as an alternative could evolve to  $\text{CaO}$  or  $\text{Ca}_3\text{N}_2$ . The argument goes that  $\text{Ca}(\text{NO}_3)_2$  is unfavored because of a combination of point-defect accumulation, amorphization, volatility, diffusional transport, and BIS; whereas between  $\text{CaO}$  and  $\text{Ca}_3\text{N}_2$  the former is favored energetically (Fig. 6 (31)). We treat bombardment-induced decomposition in Sect. 4.4.

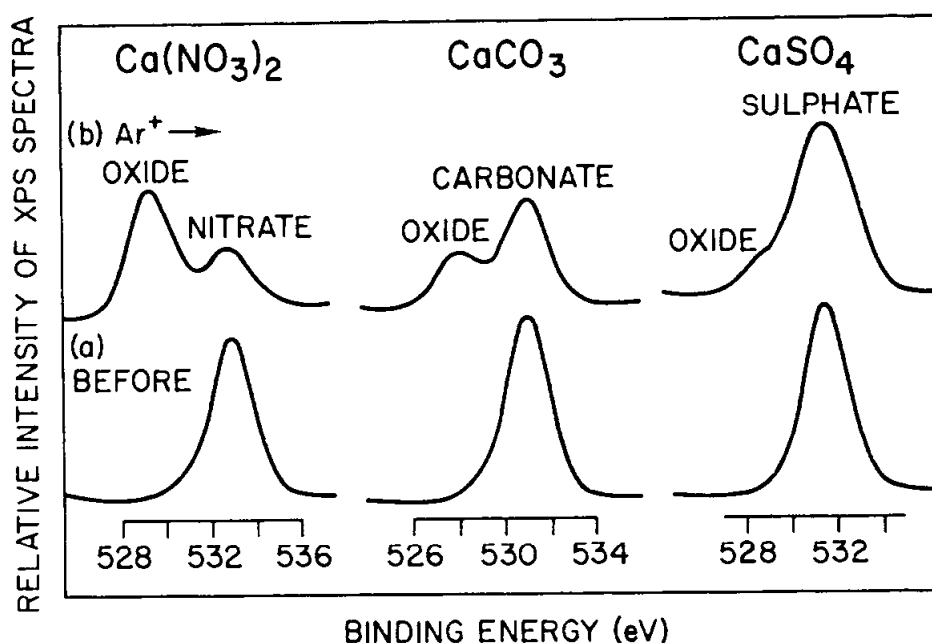


**Figure 6:** XPS spectra of the oxygen 1s photoelectron peaks from  $\text{Ca}(\text{NO}_3)_2$ ,  $\text{CaCO}_3$ , and  $\text{CaSO}_4$ : (a) before  $\text{Ar}^+$  bombardment; (b) after 3 keV  $\text{Ar}^+$  bombardment to a fluence of  $7.5 \times 10^{16}$  ions/cm<sup>2</sup> at an angle of incidence of 50°. The targets were in the form of anhydrous powders. Similar results were obtained for compounds of Ca, Sr, and Ba, with the fractional conversion to oxide being 0.92-0.94 for nitrates, 0.53-0.57 for carbonates, and 0.40-0.45 for sulfates. We agree with the authors that what is being observed is more nearly a chemical re-arrangement of atoms displaced within each cascade than, for example, a process related to the thermal spike. Whether the re-arrangement occurs on a short time scale (as envisaged by Johnson (66)) or on the rather long time scale evident in Fig. 4 is unclear. Due to Christie et al. (31).

#### 4.1.5 Redistribution

The fourth new feature in the post-1980 period was the general acceptance that composition change can be caused by point-defect fluxes or electric fields, whether or not sputtering occurs (45). We have termed this "redistribution" (46). The effect has no inherent thickness limitation, i.e. it is not confined to the outermost atom layer like BIS. A component which is transported preferentially by vacancies is depleted at the surface, while one transported as an interstitial is enriched at the surface (47). Similarly, transport due to electric fields can be in either sense (48). Transport by point defects or electric fields will be additive to BIS and, although it is really the combination which controls composition change, it is usually obvious in individual cases which effect dominates. The subject is reviewed elsewhere by Lam and Wiedersich (45).

We would note in passing that, to some extent, the terminology has been a problem, as the word "segregation" is frequently used to mean "redistribution", just as "adsorption" is used to mean "segregation". We also note, in order to forestall misunderstanding, that redistribution is normally regarded as a kinetic effect. By contrast, BIS and decomposition as developed here are essentially thermodynamic effects. The only purely collisional effect of any significance to compositional change is the role played by



mass near the threshold and with isotopes (1,2,7), as well as possible roles played by the surface binding energy.

#### 4.1.6 Surface Binding Energies of Oxides and Halides

It is clear from Sect. 4.1.2-4.1.5 that the role of preferential sputtering (in the formal sense of the term) in causing compositional change is much less important than had once been thought. Exceptions occur in the near-threshold regime (1) and with isotopes (2), while another exception relates to the surface binding energy of oxides and halides. Thus, there is recent evidence that the anions and cations in some oxides may have significantly different binding energies. That oxides have somewhat lower overall yields has long been known (Fig. 7, "total Cr" (49)) but that cation atoms are particularly reluctant to be emitted was realized only when laser-induced fluorescence was applied to the sputter products of systems such as  $\text{Cr} + \text{O}_2$ . The yield of  $\text{Cr}^0$  fell by over a factor of 100 as the ratio  $\text{flux}(\text{O}_2)/\text{flux}(\text{ions})$  increased (Fig. 7). Behavior as in Fig. 7 was subsequently rationalized by calculations in which energies were deduced using parameters appropriate to point defects in perfect oxide (11) or halide (50) surfaces. The cation binding energy was found to be unusually high for oxides of group III and beyond (11), while a similar effect was shown for halides of group II and beyond (50).

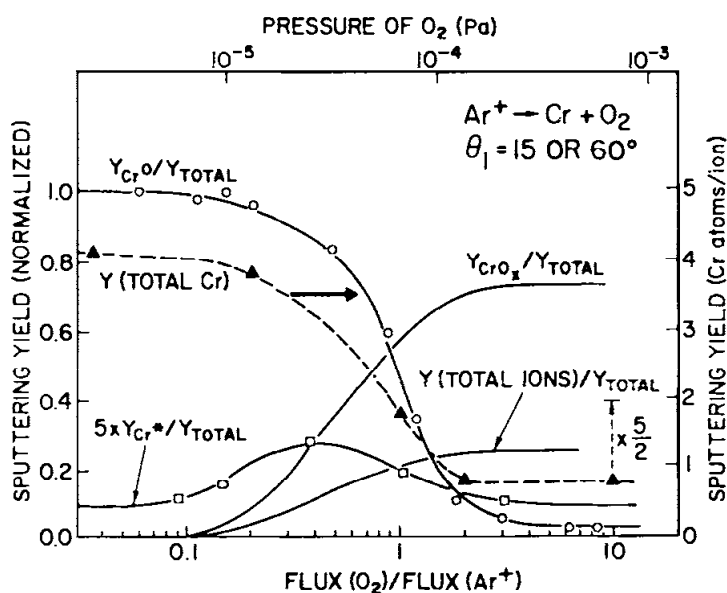


**Figure 7:** Composition of the sputtered flux as a function of the ratio of the  $\text{O}_2$  to  $\text{Ar}^+$  fluxes or of the  $\text{O}_2$  partial pressure for 15 keV  $\text{Ar}^+$  bombardment of polycrystalline Cr. All curves except that for  $Y(\text{TOTAL Cr})$  refer to the left-hand scale and give the fractional composition of the sputtered flux.  $\text{Cr}^0$  is the Cr ground state, a  $^7\text{S}_3$ ,  $\text{Cr}^*$  is the 425.4 nm transition of the state  $z^7\text{P}_4^0$ , while  $\text{CrO}_x$  denotes neutral molecules in general, of which CrO can be expected to be the dominant component. The relative yields other than that for  $\text{Cr}^*$  were obtained by LIF, "laser-induced fluorescence", at  $\theta_1 = 60^\circ$ , the  $\text{Cr}^*$  yield was obtained by light emission at  $\theta_1 = 15^\circ$ , while the total Cr yield was obtained by use of a quartz-crystal microbalance and  $\theta_1 = 15^\circ$ . The unexpected feature is the factor of 130 fall in the  $\text{Cr}^0$ , a result that has been explained (11) in terms of the surface binding energy for  $\text{Cr}^0$  being significantly higher than that for  $\text{O}^0$ . Due to Betz and Husinsky (49).

**Table 1:** Examples of chemical energy differences which can act as driving forces for changes in bombarded solids. The heat of segregation,  $\Delta H^{\text{seg}}$ , leads to BIS, while the heat of mixing,  $\Delta H_m$ , contributes to bombardment-induced mixing.  $\Delta H^{\text{seg}}$  is taken from Ref. 67;  $\Delta H_m$  is taken mainly from Ref. 68, and applies to systems with 1:1 proportions. The entries AES, FIM, ISS, and XPS are the usual acronyms referring to the methods of surface analysis.

System	$\Delta H^{\text{seg}}$ (eV) (experimental from Arrhenius plots)	$\Delta H^{\text{seg}}$ (eV) (experimental from individual data points using Eq. (10) with $\Delta S^{\text{seg}} = 0$ )	$\Delta H_m$ (eV)
Ag-Au	...	0.04-0.07 ISS	-0.048
Ag-Pd	0.09-0.13 AES	0.02-0.04; 0.098 AES	-0.052
Au-Cu	0.13 AES; 0.13 ISS	0.03-0.06 AES; 0.04-0.10 ISS	-0.053
Au-Ni	0.52 AES; 0.45 ISS	$\sim 0.4$ AES <sup>(a)</sup>	+0.078
Au-Pd	...	0.05-0.13 AES; 0.09-0.11 ISS	-0.081
Cr-Mo	...	$\sim 0.02$ AES <sup>(b)</sup>	+0.075
Cu-Ni	0.42 ISS	0.21 FIM; 0.2-0.3 ISS	+0.018
Cu-Pd	0.059 AES	0.02-0.07 AES	-0.111
Cu-Pt	...	0.1-0.2 AES, XPS; 0.09-0.2 ISS	-0.115
Mg-Al	...	0.1 AES	-0.034
Mo-W	...	$\sim 0.4$ AES	+0.021
Ni-Co	0.069; 0.18 AES	0.04-0.09 AES	0.000
Ni-Mo	...	...	-0.011
Ni-Pt	0.15; 0.25 AES; 0.11-0.24 ISS	...	-0.096
Pd-Ni	0.31 AES	0.06 AES	-0.006

(a) This information is all for dilute Au. For concentrated Au,  $\Delta H^{\text{seg}}$  is much lower,  $\sim 0.07$  (58).

(b) The information on the surface composition is not fully self-consistent (69).

Mallierbe et al. (6) advocate a similar but less extreme effect in a treatment which is somewhat empirical. The binding energy is also believed to play a role in such cases as the sputtering of Si by a combined flux of gaseous  $\text{Cl}_2$  or  $\text{XeF}_2$  and inert-gas ions (51,52). Mo shows a similar response with respect to  $\text{O}_2$ , especially at elevated temperatures (53), while in still other cases effects involving binding occur due to the incident beam, as in the sputtering of Mo (54) or W (55) by  $\text{O}^+$ . We treat surface binding energies of oxides and halides in Sects. 4.2.5 and 4.2.6.

#### 4.1.7 General Comments

It is worth commenting further on what should already be clear: the concepts of preferential sputtering and compositional change may or may not coincide. The former relates to changes in the outermost atom layers and is correctly attributed to differences of mass, chemical binding, or volatility. Refs. (1,2,3,6,11), for example, relate to preferential sputtering. Preferential sputtering is, by its nature, an essentially universal effect but it will contribute significantly towards compositional change only (a) if the change is defined by a method of analysis which is, like ISS, a true surface probe, or (b) when the system, for whatever reason, fails to show segregation, decomposition, or redistribution. Reasons include near-threshold behavior (1) and the sputtering of isotopes (2). Table 2 is an attempt to clarify the difference between preferential sputtering and compositional change.

We will use in what follows the notation of (5,56). Subscript "o" will designate a property of a cascade particle, "1" a property of the incident particle, "2" a property of a surface atom (atom layer one), "2'" a property of a subsurface atom (atom layer two), and "3" a property of a bulk atom. In Sect. 4.3.2 we will also use "2'" to represent an atom in atom layer three, which is justified if the profile is extended like those in Fig. 2. " $\alpha$ " denotes atom fraction, subscript A, B, or (in general) i a component, and superscript " $\infty$ " steady state, whence the use of such forms as  $\alpha_{A(2)}^\infty$ . M designates a metal, O oxygen, X a halogen, U the surface binding energy, Y the sputtering yield, Z the coordination number, and  $\lambda$  the mean atomic spacing. The acronyms AES, FIM, ISS, and XPS refer to the well-known methods of surface analysis.

Atoms and point defects will be designated (as is usual (57)) with the entity as the main symbol, the location as subscript, and the charge as superscript. Thus,  $\text{Mg}_{\text{Mg}}^{2+}$  is a normal Mg ion in such a compound as MgO,  $\text{V}_{\text{Mg}}$  is an Mg vacancy without associated electrons,  $\text{Mg}_i^+$  is an  $\text{Mg}^+$  interstitial,  $e^-$  is an electron, and  $h^+$  is a hole. (The charge convention of Ref. 57 is actually slightly different, being the so-called relative charge.)

It will sometimes be necessary to distinguish "s", i.e., solid or crystalline, " $\ell$ ", i.e., liquid or amorphous, and "g", i.e., gaseous or sputtered. For example, when  $\text{TiO}_2(\text{s})$  is bombarded, it evolves first to  $\text{TiO}_{2-x}(\ell)$  and then to  $\text{Ti}_2\text{O}_3(\text{s})$  by loss of  $\text{O}(\text{g})$  or  $\text{O}_2(\text{g})$ .

### 4.2. THE ROLE OF THE SURFACE BINDING ENERGY

#### 4.2.1 The Surface Binding Energy in Cascade Sputtering

Let us consider briefly the recoil-density derivation (70) of the standard relation for slow collisional (i.e. cascade) sputtering. This approach has the advantage of being

**Table 2:** Mechanisms for compositional change.

Effect	Systems where the effect is important	Role in compositional change
Preferential sputtering due to mass differences	(a) The outermost atom layer of nearly all alloys. (b) Near-threshold conditions. (c) Isotope sputtering.	Normally overwhelmed by segregation or redistribution. Loss of lighter species. Loss of lighter species.
Preferential sputtering due to differences in chemical binding	(a) The outermost atom layer of nearly all alloys. (b) Oxides of group III and beyond. (c) Systems like Si exposed to $\text{Cl}_2$ plus inert-gas ions.	Normally overwhelmed by segregation or redistribution. Loss of O; reduction of the cation (tentative). Loss of the species with the most altered binding.
Preferential sputtering due to differences in volatility	(a) Alloys with a very volatile component. (b) Alloys in general. (c) Oxides with high decomposition pressures.	(Untested) Normally overwhelmed by other effects. Loss of O; reduction of the cation (tentative).
Bombardment-induced segregation	(a) Almost all alloys. (b) The system $\text{Na}_2\text{O-SiO}_2$ .	Massive subsurface loss of the segregating species. Subsurface loss of Na.
Bombardment-induced decomposition	(a) Oxides and oxysalts in general.	Loss of O,C,N,S; reduction of the cation.
Redistribution	(a) Alloys containing Si. (b) Alloys in general.	Massive subsurface loss of Si. Subsurface loss of whichever species is redistributed.

somewhat more transparent than that based on transport theory (71) but is otherwise equivalent. An ion is regarded as starting from the reference plane  $x = 0$ , which is equivalent to the surface. During the penetration of the ion into the target, assumed to be random, a "linear" collision cascade is generated. Let  $E_1$  be the incident energy and  $C_n(x)dx$  be the differential depth-distribution function for energy deposited in elastic (nuclear, "n") events. The deposited energy creates recoiling target atoms with energy  $E_o$  and an assumed isotropic motion. If we accept the result that the recoil density has the form appropriate to the value  $m = 0$  for the power-law parameter,

$$F(E_1, E_o)dE_o \sim (\Gamma E_1/E_o^2)dE_o; \quad \Gamma = 6/\pi^2 = 0.608, \quad (1)$$

then it follows that the total number of recoils at the surface which would be able to overcome an energy barrier  $U$  is just

$$\begin{aligned} & \int_0^{\pi/2} (1/2)d\theta_o \sin \theta_o \times \int_{U/\cos^2 \theta_o} dE_o \times \Gamma E_1 E_o^{-2} \times C_n(0)L_o \\ &= (1/6)\Gamma E_1 C_n(0)L_o/U, \end{aligned}$$

where  $\theta_o$  is the polar angle of a sputtered atom,  $C_n(0)dx$  has been replaced with  $C_n(0)L_o$ , and  $L_o$  is the characteristic depth of origin of sputtered particles.  $L_o$  has been evaluated both theoretically (71) and experimentally (10,72), though unfortunately with somewhat different results (10). It is conventional to reduce  $L_o$  to  $3L_o/4$ , which is a sort of angle averaging, and this gives for the cascade sputtering yield,  $Y_{\text{cascade}}$ , the usual (70,71) form:

$$Y_{\text{cascade}} = (1/8)\Gamma E_1 C_n(0)L_o/U. \quad (2a)$$

For a binary target,  $C_n(0)$  will not partition quite stoichiometrically (3,5) but will depend on the masses. This leads to the further general result:

$$Y_{\text{cascade}} \propto 1/M^{2m}U. \quad (2b)$$

The important quantity in Eq. (2), in the context of this Section, is  $U$ . If it differs for different components of a target, then sputtering will cause a compositional change, though the change will be significant only if the difference in  $U$  is sufficient.

#### 4.2.2 The Bulk Binding Energy, $W$

Eq. (1) for the recoil density assumes, amongst other things, that the bulk binding energy,  $W$ , is zero. The possibility of a non-zero  $W$  was discussed first by Sigmund (73), where the result obtained was stated to be valid only for  $E_1 \gg E_d \gg W$ . We have obtained a very similar result and were able to show that it is more generally valid, namely for  $E_1 \gg E_d$  or  $W$  (74). The form appropriate to  $m = 0$  is

$$F(E_1, E_o, W) dE_o \sim \frac{\Gamma(E_1 + W)}{(E_o + W) E_o} dE_o, \quad (3)$$

where  $\Gamma$  is as before. We are still studying the significance of Eq. (3) to compositional change, the main reason for introducing it here being to show that the problem of  $W$  being non-zero is tractable and that  $W$  should not be perfunctorily overlooked. We also note

that, for a binary target, important compositional changes can arise if the components have different values of  $W$  (75).

#### 4.2.3 The Surface Binding Energy for Alloys

Attempts to define  $U$  for metals and alloys showing miscibility have been made repeatedly. With metals, it has been usual to identify  $U$  with the cohesive energy, i.e. the heat of atomization  $\Delta H^a$ . We would point out that, if  $U_{AA}$  is the A-A "bond strength" and if  $Z_3$  is the bulk ("3") coordination number, then we have the well-known result (76):

$$\Delta H^a = - (1/2)Z_3 U_{AA}, \quad (4)$$

which means, effectively, that the use of  $\Delta H^a$  is equivalent to regarding the sputtered atom as occupying a half-space site (A in Fig. 8). Since half-space atoms are atypical of an undisturbed surface as compared with in-surface atoms (B in Fig. 8), it follows that  $\Delta H^a$  underestimates  $U$ .

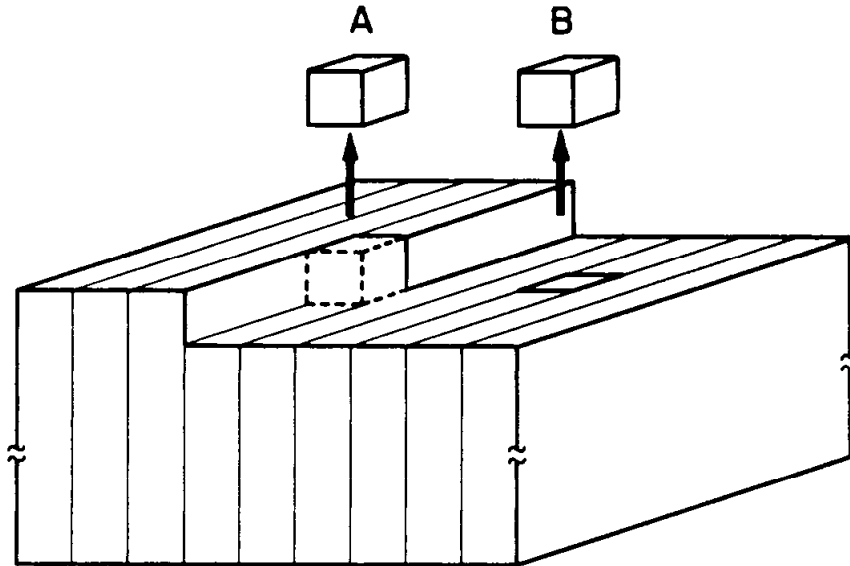


**Figure 8:** (A) Sketch of a half-space atom with coordination number  $Z_3/2$  which has been emitted by vaporization. Such an atom, which is bound by the cohesive energy or heat of atomization,  $\Delta H^a$ , is not characteristic of the sputtering process because it is atypical of an undisturbed surface. When a half-space atom is removed, there is no resulting surface vacancy but rather the jog is displaced. (B) Sketch of an in-surface atom with coordination number  $Z_2$  which, being more nearly typical of an undisturbed surface, is here assumed to be relevant to sputtering. If the expulsion is sufficiently rapid, such an atom is bound by  $(2Z_2/Z_3)\Delta H^a$ , thence by a quantity somewhat greater than  $\Delta H^a$ . A surface vacancy is always formed, i.e. whether the expulsion is rapid or slow.

Similar in spirit to the use of  $\Delta H^a$  with metals, is to describe binding in miscible alloys in terms of the cohesive energies of the pure substances (e.g. 62). However, not only is the wrong type of atom being dealt with, but such an approach neglects the fact that

binding in an alloy is governed in all cases by the statistics of site occupancy (e.g. random, ordered, segregated) and in some cases (as when species such as B or Si are involved) by changes in the character of the binding.

An approach which avoids the twin problems of  $\Delta H^a$  underestimating  $U$  and of  $\Delta H^a$  not being correct in any sense for an alloy, is based on the "quasichemical" variant of thermodynamics (5,56). It is easily applied to both metals and binary alloys as it requires knowledge only of nearest-neighbor "bond strengths",  $U_{AA}$ ,  $U_{BB}$ , and  $U_{AB}$ .<sup>\*</sup> Self-consistency is achieved if  $U_{AA}$  and  $U_{BB}$  are defined as in Eq. (4). Similarly,  $U_{AB}$  is defined in terms of the heat of mixing,  $\Delta H_m$  (76):

$$\Delta H_m \equiv \alpha_{A(3)}\alpha_{B(3)}h_m = \alpha_{A(3)}\alpha_{B(3)}Z_3[U_{AB} - (1/2)(U_{AA} + U_{BB})],$$

where  $\alpha_{i(3)}$  is the atom fraction of component  $i$  in the bulk. The surface binding energy  $U$  now follows as the sum of nearest neighbor energies under the assumption that the typical atom expelled is an in-surface atom (reasonable if  $L_0$  in Eq. (2a) is about  $0.80\lambda$  (10,72)) with atom fraction  $\alpha_{i(2)}$  and coordination number  $Z_2$ :

$$U_A = (Z_2/Z_3) [(1 + \alpha_{A(2)}) \Delta H_A^a + \alpha_{B(2)} (\Delta H_B^a - h_m)] \quad (5a)$$

for a binary alloy and

$$U = (2Z_2/Z_3)\Delta H^a = (1.42 \pm 0.08)\Delta H^a \quad (5b)$$

for a unitary system, i.e.  $\alpha_{A(2)} = 1$ . The numerical factor  $1.42 \pm 0.08$  applies to the more densely packed surfaces of fcc, hcp, and bcc. In practice, the term  $h_m$  is normally unimportant (5,56), with Si-containing systems being a marked exception (e.g. Fe-Si (68)). Nevertheless, we take it into account (Table 4, to follow).

Equation (5) should be acceptable whenever two conditions are met:  $U$  describes atom removal from an undisturbed surface and the act of removal is sufficiently rapid that the relaxation of the lattice around the surface vacancy can be neglected. If the act of removal is slow, the relaxation around the vacancy cannot be neglected. As discussed in Ref. 8,  $U$  is then somewhat smaller than in Eq. (5).

Examples of  $U$  as given by Eq. (5b), as well as experimental values where known, are given in Table 3. The agreement between theory and experiment is moderately good, though with experiment typically more similar to  $\Delta H^a$  than to Eq. (5b). The obvious problem is that atom ejection from real systems does not involve undisturbed surfaces as in Fig. 8 and as assumed in Eq. (5b). Nevertheless, we conclude that it is realistic to assume a proportionality,  $U \propto \Delta H^a$ , and this will be done in what follows.

#### 4.2.4 Application to Compositional Change with Alloys

It follows from the requirement that matter be conserved that the steady-state sputtered flux ratio for a binary alloy is, to lowest approximation,

---

<sup>\*</sup>We would note that the  $U_{ij}$  are not "bond strengths" in the formal sense but rather parameters derived from observable thermodynamic quantities.

**Table 3:** Examples of calculated and observed surface binding energies for metals.

Metal	$\Delta H^a$ (eV)	$U \approx 1.42\Delta H^a$ (Eq. (5b)) (eV)	U from experiment (eV)	Ref.
Al	3.41	4.8	3.6	(83)
Au	3.82	5.4	...	
Ba	1.89	2.7	2.1 <sup>(b)</sup>	(84)
Ca	1.85	2.6	1.3	(85)
Ce	4.38	6.2	...	
Cr	4.12	5.9	4.2 $\pm$ 0.2	(86)
			4.4 $\pm$ 0.2	(87)
Cr <sup>(a)</sup>	>4.12	>5.9	5.1 $\pm$ 0.2	(87)
Cu	3.49	5.0	...	
Fe	4.31	6.1	4.3; 5.0 <sup>(b)</sup>	(88,89)
Ge	3.88	5.5	...	
In	2.52	3.6	4.0	(90)
Mg	1.52	2.2	...	
Mo	6.82	9.7	...	
Ni	4.46	6.3	...	
Pt	5.85	8.3	...	
Rh	5.73	8.1	8.0; 11 $\pm$ 1	(90,91)
Si	4.72	6.7	...	
Sn	3.12	4.4	...	
Th	5.96	8.5	...	
Ti	4.87	6.9	4.6	(83)
U	5.42	7.7	5.4	(92)
W	8.80	12.5	...	
Zn	1.35	1.9	...	
Zr	6.31	9.0	6 $\pm$ 2	(93,94)
			6.3	(95)

<sup>(a)</sup> Stainless steel with 17% Cr and the remainder dominantly Fe.

<sup>(b)</sup> Corrected by Garrison et al. (96) for geometrical effects (97).



**Table 4:** Examples of calculated and observed surface compositions for alloys with 1:1 proportions.

System, A-B	$\Delta H_A^a$ (eV)	$\Delta H_B^a$ (eV)	$h_m^{(a)}$ (eV)	$\Delta H_B^a/\Delta H_A^a$	$U_B/U_A = \alpha_{B(2)}/\alpha_{A(2)}$ from Eqs. (5a,7)	$\alpha_{B(2)}^\infty/\alpha_{A(2)}^\infty$ from exper- iment using AES or XPS (b)
Ag <sub>0.50</sub> Au <sub>0.50</sub>	2.94	3.82	-0.193	1.30	1.14	2.0
Ag <sub>0.50</sub> Pd <sub>0.50</sub>	2.94	3.90	-0.216	1.33	1.15	2.2
Au <sub>0.50</sub> Cu <sub>0.50</sub>	3.82	3.49	-0.197	0.91	0.96	1.0
Au <sub>0.50</sub> Ni <sub>0.50</sub>	3.82	4.46	+0.295	1.17	1.08	~2.7
Au <sub>0.50</sub> Pd <sub>0.50</sub>	3.82	3.90	-0.320	1.021	1.010	1.4
Cr <sub>0.50</sub> Mo <sub>0.50</sub>	4.12	6.82	+0.229	1.66	1.29	1.7
Cu <sub>0.50</sub> Ni <sub>0.50</sub>	3.49	4.46	+0.074	1.28	1.13	1.8
Cu <sub>0.50</sub> Pd <sub>0.50</sub>	3.49	3.90	-0.461	1.12	1.054	1.6
Cu <sub>0.50</sub> Pt <sub>0.50</sub>	3.49	5.85	-0.461	1.68	1.27	2.1
Mg <sub>0.50</sub> Al <sub>0.50</sub>	1.52	3.41	-0.135	2.24	1.44	3.6
Mo <sub>0.50</sub> W <sub>0.50</sub>	6.82	8.80	+0.084	1.29	1.14	1.4
Ni <sub>0.50</sub> Co <sub>0.50</sub>	4.46	4.44	~0	0.9955	0.998	1.2
Ni <sub>0.50</sub> Pt <sub>0.50</sub>	4.46	5.85	-0.362	1.31	1.14	1.6
Pd <sub>0.50</sub> Ni <sub>0.50</sub>	3.90	4.46	~0	1.14	1.069	1.3

(a) Most entries for  $h_m$  were obtained by averaging values deduced from integral  $\Delta H_m$  for solid alloys (68) using  $h_m = \Delta H_m / \alpha_{A(3)} \alpha_{B(3)}$ . The value for Mo-W is from (77).

(b) See Table 7 for the references.

$$\frac{\text{surface flux}_A}{\text{surface flux}_B} = \frac{\alpha_{A(2)}^\infty Y_A}{\alpha_{B(2)}^\infty Y_B} = \frac{\alpha_{A(3)}}{\alpha_{B(3)}}, \quad (6a)$$

but to higher approximation,

$$\frac{\text{surface flux}_A}{\text{surface flux}_B} = \frac{\alpha_{A(2)}^\infty(1 - \beta) + \alpha_{A(2')}^\infty\beta}{\alpha_{B(2)}^\infty(1 - \beta) + \alpha_{B(2')}^\infty\beta} \times \frac{Y_A}{Y_B} = \frac{\alpha_{A(3)}}{\alpha_{B(3)}}, \quad (6b)$$

where "2'" refers to atom layer two and  $\beta$  is the fraction of sputtering from beyond atom layer one. Values of  $\beta$  (the notation  $f(\lambda)$  is also used) range from 0.11 to 0.30 with an average of 0.19 (10). In both cases  $Y_A/Y_B$ , the yield ratio, can also be written  $Y_A/Y_B = M_B^{2m}U_B/M_A^{2m}U_A$  (Eq. 2b). Eq. (6b) is most useful when BIS occurs and  $\alpha_{A(2)}^\infty$  and  $\alpha_{A(2')}^\infty$  therefore differ strongly. The overall result is that the value of  $\alpha_{A(2)}^\infty$  is controlled by 3 parameters: the power-law scattering parameter  $m$  (a rather weak dependence since  $m \approx 0$ , cf. p. 390 of Ref. 72), the subsurface sputtering fraction  $\beta$  (10), and the BIS ratio  $K^b$  (Table 7, to follow).

Using the lower approximation of Eq. (6a) it follows that the compositions will change until they obey the relation

$$\frac{\text{surface flux}_A}{\text{surface flux}_B} = \frac{\alpha_{A(2)}^\infty M_B^{2m} U_B}{\alpha_{B(2)}^\infty M_A^{2m} U_A} = \frac{\alpha_{A(3)}}{\alpha_{B(3)}} \quad (7)$$

If  $U_B/U_A$  is taken as defined by Eq. (5a), then the latter expression and Eq. (7) can be solved iteratively for  $\alpha_{B(2)}^\infty/\alpha_{A(2)}^\infty$  (column 6 of Table 4).

Table 4 (final column) also contains observed values for  $\alpha_{B(2)}^\infty/\alpha_{A(2)}^\infty$ , in all cases taken from work using AES or XPS. The outstanding feature is that the predicted compositional changes due to bond-strength effects are without exception very much less than what is observed with AES or XPS. There are two reasons for such a trend:

(i) One relates to the mathematical form of the expression for  $U_B/U_A$ . As seen in Table 4, the ratio  $U_B/U_A$  is significantly closer to unity than  $\Delta H_B^a/\Delta H_A^a$ , and it is the former which governs  $\alpha_{B(2)}^\infty/\alpha_{A(2)}^\infty$ .

(ii) The other reason is a practical problem. Systems such as Ag-Mo or Au-W, which might be expected to show a large compositional change in view of the highly dissimilar values of  $\Delta H^a$ , are not miscible.

Nevertheless, the conclusion is inescapable: compositional changes with alloys as measured by AES or XPS are not governed by bond-strength effects.

We note in passing that, even if the numerical value  $U \approx 1.4\Delta H^a$  was not fully in agreement with experiment (Table 3), at least the proportionality  $U \propto \Delta H^a$  was acceptable. This is a sufficient condition for the arguments made here to be valid.

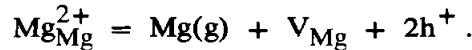
#### 4.2.5 The Surface Binding Energy for Oxides and Halides

Oxides and halides do not permit quite as straightforward a definition of  $U$  as do metals and alloys: ionized species and diatomics are emitted to an important extent and,

due mainly to the major role of polarization, oxides and halides cannot be described in simplistic terms such as pair-wise interactions (78) or quasichemical thermodynamics (5,56).

We have proposed (11) that a possible description of binding at undisturbed surfaces with oxides and halides is in terms of processes in which individual surface atoms are removed slowly to infinity, using as the basis defect theory of the type pioneered by Norgett and Lidiard and recently further refined by, amongst others, Mackrodt (57). Slow removal was suggested on the grounds that the characteristic time for electronic relaxation is of order  $10^{-15}$  s and thus distinctly shorter than the sputtering time (e.g.  $9 \times 10^{-14}$  s for a 5 eV Al atom or  $22 \times 10^{-14}$  s for a 5 eV W atom (8)). In evaluating the energies, it is convenient to take advantage of the result that, for an oxide or halide, most bulk defects have similar energies to surface defects, the divacancy binding energy apparently being the only exception (11).

**4.2.5.1 Cation Atom Binding.** Using MgO as the example, we consider the process in which a neutral Mg atom is removed slowly to infinity:

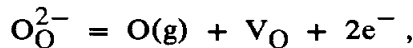


The energy change is

$$U_{\text{Mg}} = E(V_{\text{Mg}}) - I_1(\text{Mg}) - I_2(\text{Mg}) + 2E(h^+), \quad (8)$$

where  $E(V_i)$  is the lattice energy for vacancies of type i, i.e. the energy to slowly remove a lattice ion to infinity,  $I_n(M)$  is the  $n^{\text{th}}$  ionization potential of the cation M, and  $E(h^+)$  is the formation energy of a hole inclusive of electronic and ionic relaxation.

**4.2.5.2 Anion Atom Binding.** We next consider the process in which a neutral O atom is removed slowly to infinity:



where  $e^-$  is a lattice electron and the energy change is

$$U_{\text{O}} = E(V_{\text{O}}) + I_1(\text{O}^{2-}) + I_2(\text{O}^{2-}) + 2E(e^-). \quad (9)$$

Here  $I_n(\text{O}^{2-})$  is the  $n^{\text{th}}$  ionization potential of  $\text{O}^{2-}$  and  $E(e^-)$  is the formation energy of a lattice electron. In those instances where  $E(e^-)$  is the energy of an electron at the bottom of the conduction band, we have  $E(e^-) = -|E_c|$ ,  $|E_c|$  being the conduction band width.

Input parameters for calculating U for oxides, as collected from a variety of sources, are given in (11), while evaluations of Eqs. (8) and (9) as well as corresponding equations for MO diatomics and  $M^+$  ions (11) are given in Table 5. The results show that, if U for an ionic oxide is taken as the lower of that for the metal atom or O atom, then ionic oxides are more tightly bound than the corresponding metals (Table 3) by factors of 1 to 5. This result, which should be manifested in low total yields, is not surprising in view of what has long been known experimentally. What is somewhat unexpected is that, for ionic oxides of group III and beyond, O atoms as well as MO diatomics are predicted to be far more easily removed than metal atoms, so that one can expect abnormally low metal-atom

yields in appropriate circumstances as well as essentially universal preferential loss of O for group III and beyond.

**Table 5:** Examples of calculated surface binding energies in eV for oxides as in Eqs. (8) and (9). The input parameters are given in Ref. (11).

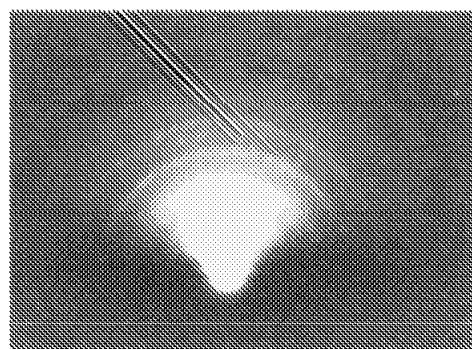
Type of binding energy, $U_i$	CaO	MgO	NiO	ZnO	Al <sub>2</sub> O <sub>3</sub>	ThO <sub>2</sub>	ZrO <sub>2</sub>
Metal atom, $U_M$	12.3	13.5	7.7	8.0	29.8	~29.7	32.2
Oxygen atom, $U_O$	~12.2	~13.1	10.9	4.8	~11.8	8.5	<7.1
MO diatomic, $U_{MO}$	~8.4	~8.2	~6.8	...	~18.2	~18.1	~19.0
Metal ion, $U_M$	14.1	15.8	10.8	10.8	28.5	~33.5	35.6

#### 4.2.6 Application to Compositional Change with Oxides

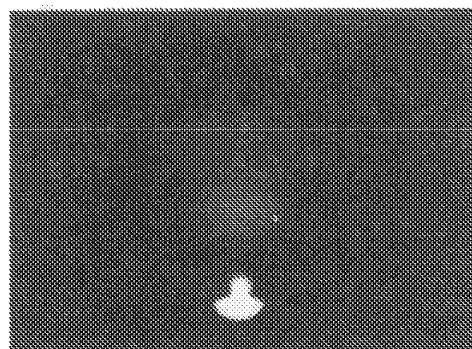
**4.2.6.1 Metal Atom Yields from Oxides.** Before considering compositional changes with oxides, we will digress in order to discuss metal-atom yields because of the light which is shed on binding energies. While it has been known for some time that total yields were generally somewhat lower for ionic oxides than for metals, whereas partial yields for ions, excited states, and MO diatomics were greatly enhanced, almost nothing was known about neutral, ground state atoms because of the difficulty in detecting them explicitly. This problem was recently overcome by using either laser-induced fluorescence (49) or secondary neutral mass-spectroscopy (79). The example of Cr, Fig. 7, reveals that metal-atom yields can fall drastically as the oxygenation of the surface increases. This in turn tentatively supports the newly proposed oxide binding energies as in Table 5.

**4.2.6.2 Preferential Effects.** Oxygen loss from oxides is well documented, leading either to well-defined changes in composition (Fig. 9 (80)) or else to an ill-defined state of understoichiometry (Fig. 10 (32)). We first note that considerations of mass are not useful for understanding such O loss, since it would follow that all oxides (except, e.g., BeO) would behave similarly and reduce to pure metal, at least at the outer surface. (Near-threshold processes as in Fig. 1 are a well-defined exception: see Sect. 4.4.4.1.) This leaves considerations of binding, with which this section is concerned, together with arguments based on bombardment-induced decomposition (Sect. 4.4).

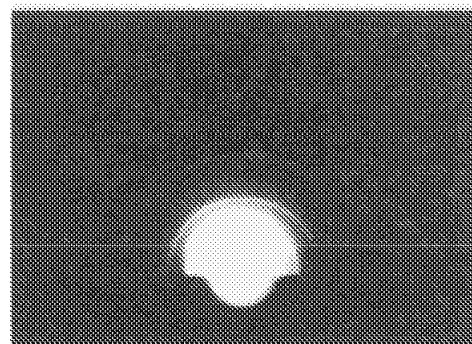
**Figure 9:** Reflection electron diffraction patterns taken at 80 kV for  $\text{TiO}_2$ : (a) before bombardment; (b) after exposure to  $5 \times 10^{15}$  ions/ $\text{cm}^2$  of 30 keV  $\text{Kr}^+$  at normal incidence; and (c) after exposure to  $6 \times 10^{16}$  ions/ $\text{cm}^2$  of 30 keV  $\text{Kr}^+$ . The patterns, respectively those of rutile  $\text{TiO}_2(\text{s})$ , amorphous  $\text{TiO}_{2-x}$ , and  $\text{Ti}_2\text{O}_3(\text{s})$ , are an explicit indication of preferential O loss which leads to a well-defined change of composition. Due to Parker and Kelly (80).



(a)



(b)



(c)

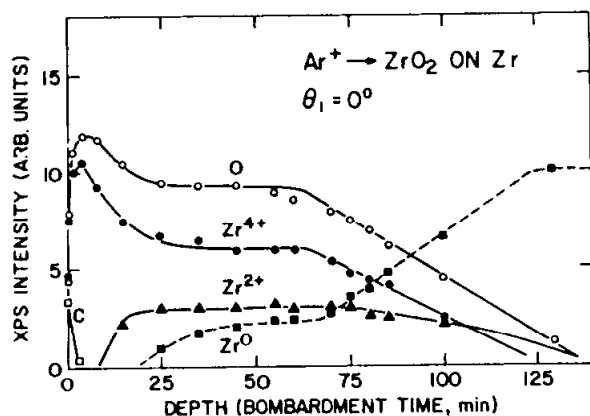


**Figure 10:** Bombardment-induced O loss from a 36 nm anodic film of  $\text{ZrO}_2$  on Zr as sensed with XPS while bombarding with 3 keV  $\text{Ar}^+$  at normal incidence. The initial rise of the O and  $\text{Zr}^{4+}$  signals is due to contaminant removal, the changes in all signals at 5-25 min are due to preferential O loss to yield an ill-defined composition  $\text{ZrO}_{0.6}$ , while the more gradual changes beyond 65 min are due to the termination of the anodic film. Due to Hofmann and Sanz (32).

What has not been generally appreciated is that a properly defined  $U$  leads naturally to preferential effects with oxides and halides: as borne out in Table 5 for ionic oxides of group III and beyond, the O atom binding at an undisturbed surface is distinctly (up to a factor of 4) smaller than the metal-atom binding. This is the result of the cations, with their greater charge, sitting in a deeper potential well. There should therefore be a universal tendency for O to be lost from appropriate oxides, as when  $\text{ZrO}_2$  evolves to  $\text{ZrO}_{0.6}$  (Fig. 10). (The latter probably consists mainly of a saturated solid solution of O in  $\alpha\text{-Zr}$ , namely  $\text{ZrO}_{0.41}$ .) Similar comments apply to  $\text{TiO}_2$  but with an important difference: O deficiency is accommodated when sufficiently slight as  $V_{\text{O}}$  plus  $\text{Ti}_{\text{Ti}}^{3+}$ , then for greater loss as shear planes, and finally as a lower stoichiometry. Experimentally, bombarded  $\text{TiO}_2(\text{s})$  shows a well-defined surface layer of  $\text{Ti}_2\text{O}_3(\text{s})$ , seen both by electron diffraction (Fig. 9) and electron spectroscopy (81), or, alternatively,  $\text{Ti}^{\text{II}}$  plus  $\text{Ti}^{\text{III}}$ , seen by XPS (82).

The same argument also explains why  $\text{TiO}_2$  evolved to  $\text{Ti}_2\text{O}_3$  rather than Ti:  $\text{Ti}_2\text{O}_3$  is metallic (44) and there is therefore no longer the large difference between  $U_{\text{Ti}}$  and  $U_{\text{O}}$  as for the more nearly ionic  $\text{TiO}_2$ . This leads to the rule that, if an ionic system has a metallic lower stoichiometry, then this stoichiometry forms under bombardment. Otherwise, there is an ill-defined state of understoichiometry as with  $\text{ZrO}_2$ .

Nevertheless, we still maintain firm reservation about whether the binding energy is the sole reason for composition change with oxides. The problem is the same as with mass: the lack of universality. Specifically, binding energy would account nicely for O loss from the highly stable  $\text{HfO}_2$ ,  $\text{SnO}_2$ , and  $\text{ZrO}_2$ , and for the greater than expected loss from  $\text{Nb}_2\text{O}_5$ ,  $\text{Ta}_2\text{O}_5$ , and  $\text{WO}_3$  (Sect. 4.4). It fails, however, to account for the stability of  $\text{Al}_2\text{O}_3$ ,  $\text{Cr}_2\text{O}_3$ , and  $\text{SiO}_2$ . Moreover, a final decision cannot yet be made owing to the lack of appropriate experiments. For example, although the highly powerful XPS approach was indeed used with  $\text{Al}_2\text{O}_3$ ,  $\text{Cr}_2\text{O}_3$ , and  $\text{SiO}_2$ , the apparent lack of O loss could have been due to the lack of diffusional deepening, with the O loss confined to the outer surface and therefore undetected.

### 4.3. THE ROLE OF SEGREGATION

#### 4.3.1 Equilibrium Segregation

One of the most difficult effects to study in thermodynamics is equilibrium segregation. With Cu-Ni, for example, it is manifested in the tendency, with specimens heated to above 400-500°C, for the outermost atom layer to be enriched by up to a factor of 40-100 in Cu since Cu has the lower bond strength (98). With Au-Cu the outermost atom layer is enriched by up to a factor of about 4 in Au since the Au atom is oversized (99). The driving force for equilibrium segregation lies in the interval 0.06 to 0.52 eV (Table 1).

It is now known that segregation occurs also when alloys are bombarded, even at very low temperatures (43). BIS is almost always in the same sense as equilibrium segregation and can be therefore assumed to have the same low driving force, 0.06 to 0.52 eV. Since sputtered atoms come mainly (70-90%) from atom layer one (10), it follows that BIS must lead to important perturbations of the sputtering process. In the case of Cu-Ni or Au-Cu this involves major Cu or Au loss variously from near the surface (as in Fig. 2)

or from orders of magnitude greater depths (100). The reason for the loss is that BIS serves to "pump" Cu or Au into the outer atom layer, where it is preferentially sputtered away so as to leave the subsurface depleted. Corresponding work with bombarded oxides is very limited even though equilibrium segregation is well known (101) and well understood (102). Examples include Ca loss from MgO during bombardment at 1250°C (37), a tentative example as it probably involved equilibrium segregation; segregation-related perturbations to composition-depth profiles in Si (103); and Na loss from Na<sub>2</sub>O-SiO<sub>2</sub> during bombardment at ambient temperature (38). The latter work is particularly important since alloy-like profiles as in Fig. 2 were inferred.

Returning to equilibrium segregation, a standard argument (4) based on minimizing the free energy of the system (surface plus bulk) suggests that the magnitude of the composition spike at equilibrium,  $\alpha_{A(2)}^\infty$ , is related to the bulk composition,  $\alpha_{A(3)}$ , by the relation:

$$\begin{aligned} \frac{\alpha_{A(2)}^\infty}{\alpha_{B(2)}^\infty} &= \frac{\alpha_{A(3)}}{\alpha_{B(3)}} \exp \left\{ \frac{\Delta H^{\text{seg}}}{kT} \right\} \times \exp \left\{ \frac{-\Delta S^{\text{seg}}}{k} \right\} \\ &= \frac{\alpha_{A(3)}}{\alpha_{B(3)}} \exp \left\{ \frac{\Delta G^{\text{seg}}}{kT} \right\} \equiv \frac{\alpha_{A(3)}}{\alpha_{B(3)}} K^{\text{eq}}, \end{aligned} \quad (10)$$

where  $\Delta H^{\text{seg}}$  and  $\Delta S^{\text{seg}}$ , the heat and entropy of segregation, are given in very general form by relations discussed by Wynblatt and Ku (104),  $K^{\text{eq}}$  will be here termed the equilibrium segregation ratio, and the sign convention used for  $\Delta G^{\text{seg}}$  is appropriate for  $\Delta G^{\text{seg}} > 0$ . (The opposite convention is also used (98).) To lowest approximation,  $\Delta H^{\text{seg}}$  is the total energy difference when an A atom in the bulk is exchanged with a B atom at the surface and  $\Delta S^{\text{seg}}$  is zero (4,105). Neglecting the heat of mixing this energy difference is

$$\Delta H^{\text{seg}} \approx (Z_v/Z_3)(\Delta H_B^a - \Delta H_A^a) \approx (1/4)(\Delta H_B^a - \Delta H_A^a),$$

where  $Z_v$  is the "vertical" coordination number, e.g.  $Z_v = 3$  for (111) of f.c.c. To higher approximation, both "bond strength" and size must be taken into account, the trends being that the segregating species has either the weaker bonds (e.g. Cu in Cu-Ni) or is oversize (e.g. Au in Au-Cu).

#### 4.3.2 Bombardment-Induced Segregation, BIS

Values of  $\Delta H^{\text{seg}}$  were given in Table 1 and we note that they are numerically small, 0.06-0.52 eV. Estimates of the onset temperatures for atomic-scale thermally activated diffusion are given in Table 6 and we note that, for systems other than Mg-Al, they are all well above ambient temperature,  $\geq 250^\circ\text{C}$ .

The information in Tables 1 and 6 might suggest that a bombardment-induced analog to equilibrium segregation, i.e. BIS, would not occur, as the driving force is too small and the required temperature too high. It is therefore important to accept that, as already discussed in Sect. 4.1.2, there is overwhelming empirical evidence that it does occur.

A further objection to BIS is that a composition spike in the first atom layer would not be stable with respect to ion-beam mixing. We cannot answer this problem explicitly

but would note that segregation could well develop subsequent to the maximum activity in each cascade, e.g. after  $\sim 0.5$  ps, when a persisting tail in the Frenkel-pair population can be expected (106). Alternatively, it could involve what we will term "chemically guided final steps" (see after Eq. (11)). In any event, we are not surprised that it has a small magnitude.

Because sputtered atoms originate mainly from the outermost atom layer (10,72), this layer must have a steady-state composition,  $\alpha_{A(2)}^\infty$ , governed by the conservation relations of Eq. (6a) or (6b).

The second atom layer, with steady-state composition  $\alpha_{A(2')}^\infty$ , bears a relation to the first governed by the kinetics of atom movement as treated first in Refs. 9,56,107,108. We here restate the argument of (56,108) in a form which differs mainly by avoiding the simplification that only atom layer one contributes to sputtering ( $\beta = 0$ ). (This is, however, not an important change.) Sites are conserved in a bombardment-induced relocation process if the lattice relaxes appropriately following each elementary jump (109,110). For example, let A tend to segregate. Then a transfer of A from (2') to (2), with a rate per second  $k_+ \alpha_{A(2')}$ , triggers a relaxation in which a converse transfer occurs. For homogeneous (i.e. stoichiometric) relaxation, the converse transfer could involve either A or B so that a net change in the system occurs only at a reduced rate  $k_+ \alpha_{A(2')} \alpha_{B(2)}$ . Concurrent with the radiation-enhanced jumps, A is added to (2) at a rate the first term of which is  $(1 - \beta)(v_B/\lambda) \alpha_{B(2)} \alpha_{A(2')}$ , where  $v_B = IY_B/N$  is the velocity of surface recession at a B site,  $I$  is the ion flux, and the factor  $\alpha_{A(2')}$  recognizes that a net change occurs in (2) only if an A is exposed in (2').\* A second term also exists,  $\sim \gamma\beta(v_B/\lambda) \alpha_{B(2)} \alpha_{A(2')}$ , where  $\gamma\beta$  with  $\gamma < 1$  is the fraction of atoms emitted simultaneously from (2) and (2'), and  $\alpha_{A(2')}$  is intended to describe atom layer three. Considering also the inverse terms by which A is lost from (2), the following rate equation is obtained:

$$\begin{aligned} d\alpha_{A(2)}/dt = & [k_+ + (1 - \beta + \gamma\beta)v_B/\lambda] \alpha_{A(2')} \alpha_{B(2)} - \\ & - [k_- + (1 - \beta + \gamma\beta)v_A/\lambda] \alpha_{A(2)} \alpha_{B(2')}, \end{aligned}$$

so that at steady state one has (Eq. 11):

$$\frac{\alpha_{A(2)}^\infty}{\alpha_{B(2)}^\infty} = \frac{\alpha_{A(2')}^\infty}{\alpha_{B(2')}^\infty} \times \frac{k_+ + (1 - \beta + \gamma\beta)v_B/\lambda}{k_- + (1 - \beta + \gamma\beta)v_A/\lambda} \equiv \frac{\alpha_{A(2')}^\infty}{\alpha_{B(2')}^\infty} \times K^b,$$

where  $k_-$  is the rate constant for a jump unfavorable to segregation and  $K^b$  is the BIS ratio (the analog of  $K^{eq}$  in Eq. (10)).

We have suggested (111) that the rate constant  $k_\pm$  be attributed to a low-energy, chemically guided final step appended to a fraction  $f$  (probably near unity) of the ballistic trajectories ending in either of the outer two atom layers. Thus if the ballistic trajectories have a rate constant  $k^b$  then BIS is governed by

$$k_\pm \approx fk^b.$$

---

\*The use of a factor such as  $\alpha_{A(2')}$  agrees with Ref. 56 and Eq. (33) of Ref. 108 but not with Ref. 9.



This identification is necessary to avoid the paradox (Sect. 4.1.3) of requiring a driving force of only 0.06 to 0.52 eV to have meaning amongst the violent motions of a cascade.

The expression for BIS, Eq. (11), is thus of similar form to that for equilibrium segregation, Eq. (10). This result differs from both Ref. 9 (their Eq. (14)) and Ref. 108 (their Eq. (34) but not (33)), where the proposed expressions can be written, in the present notation,

$$\alpha_{A(2)}^{\infty} \approx \alpha_{A(2')}^{\infty} \times K^b. \quad (12)$$

The difference between Eqs. (11) and (12) is brought out in Fig. 11, with Eq. (12) seen to be unsatisfactory. A further point of comparison is that, owing to the presence of  $v_i$  in  $K^b$ , one can expect the inequality  $K^b < K^{eq}$ .

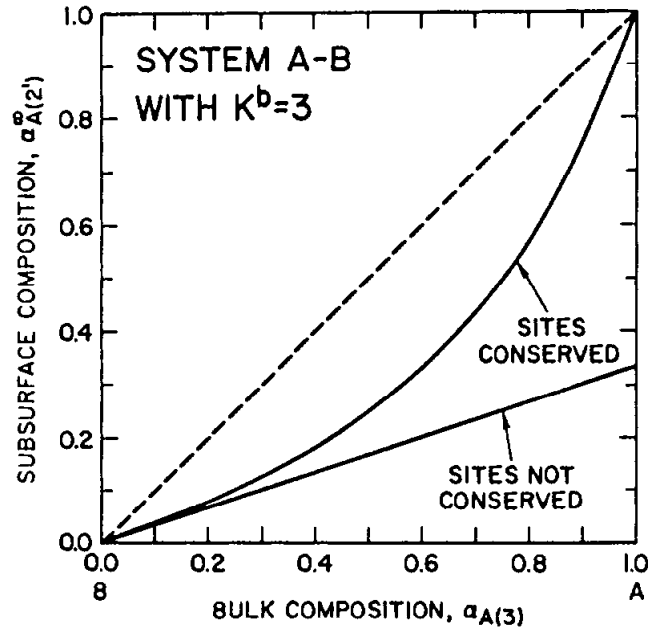


**Figure 11:** The role of site conservation in BIS shown by comparing the subsurface composition with the bulk composition, here approximated by  $\alpha_{A(2)}^{\infty}$ , for a system with  $K^b = 3$ . The two curves show the result when sites are either conserved (Eq. (11)) or not conserved (Eq. (12)). Agreement with experiment as in Fig. 3 is obtained only when sites are conserved.

The altered second atom layer acts as a boundary condition for the diffusion-like motion which accompanies all particle bombardments, and induces a composition profile such as that seen in Fig. 2 to develop extending to roughly  $\langle x \rangle + \Delta x$ , i.e. the sum of the projected range and the projected straggling. The transport in question can be assumed to be the ballistic step of the same process as that which leads to BIS and to ion-beam mixing. It follows that the effective diffusion coefficient,  $D^b$ , is just

$$D^b = (1/6)k^b m^2 \lambda^2 \simeq (1/6)(k_{\pm}/f)m^2 \lambda^2, \quad (13)$$

where  $m\lambda$  is the average length of a ballistic trajectory. At sufficient depths the bulk composition is normally resumed unless (trivially) the system is at a sufficiently high

temperature that self-diffusion can contribute (100). An approach to the high-temperature situation is seen in Fig. 2.

The simplest treatment of the region depleted by the diffusion-like motion is to assume a species-independent diffusion coefficient as in Eq. (13), to assume surface recession at average velocity,  $v$ , and either to terminate the motion abruptly at depth,  $L^b$ , or to introduce an appropriate spatially decreasing factor. The diffusion equation appropriate to the first case (diffusional freezing at depth  $L^b$ ) is

$$\partial \alpha_i(x, \phi) / \partial \phi = D^b (\partial^2 \alpha_i(x, \phi) / \partial x^2) + v (\partial \alpha_i(x, \phi) / \partial x),$$

where  $\phi$  is fluence (dose) and  $x$  is depth beneath the surface. The steady-state boundary conditions are  $\alpha_A(x) = \alpha_{A(2')}^\infty$  for  $x = 0$  and

$$D^b (\partial \alpha_A^\infty(x) / \partial x)_{L^b} + v \alpha_A^\infty(L^b) = v \alpha_{A(3)}$$

for  $x = L^b$  (112), leading to the well-known solution

$$\begin{aligned} \alpha_i^\infty(x) &= \alpha_{i(3)} - (\alpha_{i(3)} - \alpha_{i(2')}^\infty) \exp(-vx/D^b) \quad \text{for } 0 < x < L^b; \\ \alpha_i^\infty(x) &= \alpha_{i(3)} \quad \text{for } x > L^b. \end{aligned} \quad (14)$$

Eq. (14) is easily fitted to profiles as in Fig. 2 and one thereby obtains explicit values of  $v/D^b$  (56).

#### 4.3.3 Evaluation of $K^b$

$K^b$  can be evaluated in 3 ways: from profiles as in Fig. 2, from AES or XPS (but not ISS) analysis of bombarded surfaces as in Fig. 3, and by analyzing information on angular distributions (10,25,26).

The use of profiles is straightforward, as they enable Eq. (11) to be evaluated explicitly. Owing to the profiling process being imperfect, however,  $\alpha_{A(2')}^\infty$  will normally be overestimated so that  $K^b$  will be too small. AES and XPS tend to have significant subsurface sensitivity so that, to a greater or lesser extent, they sense  $\alpha_{i(2')}^\infty$  rather than  $\alpha_{i(2)}^\infty$ . This suggests that  $\alpha_{i(2)}^\infty$  be eliminated between Eqs. (6a) and (11), yielding

$$\frac{\alpha_{A(2')}^\infty}{\alpha_{B(2')}^\infty} = \frac{\alpha_{A(3)}}{\alpha_{B(3)}} \times \frac{Y_B/Y_A}{K^b} \approx \frac{\alpha_{A(3)}}{\alpha_{B(3)}} \times \frac{1}{K^b}. \quad (15)$$

The approximation is justified whenever  $U_B/U_A$  (Table 4) and  $M_B^{2m}/M_A^{2m}$  are of order unity. Since the presence of the composition spike at the surface will always cause  $\alpha_{A(2')}^\infty$  to be overestimated,  $K^b$  will again tend to be too small. Finally, one can analyze angular distributions. This method avoids the problem of estimating  $\alpha_{A(2')}^\infty$  precisely but introduces a new problem in that it depends totally on the underlying theory (109), conceived for an infinite continuous medium, being valid immediately next to the surface of a semi-infinite crystalline medium.\*

---

\*For example, the theory assumes straight-line motion for the sputtered particles (109).

**Table 6:** Onset temperatures for atomic-scale thermally activated diffusion with the alloys considered in Tables 1 and 4. The second column gives temperatures deduced from the knees in Arrhenius plots which separate the regions of radiation-enhanced and thermally activated diffusion. The third column is based on information either as in Fig. 16, where surface composition is measured during bombardment at an elevated temperature and the approximate temperature interval for the transition from BIS to equilibrium segregation can be inferred, or as in Fig. 2, where profiles deepen at a sufficiently high bombardment temperature. The final column gives experimental values for the onset temperature of equilibrium segregation, a quantity which is definable only if the time scale is restricted to "reasonable values". Systems noticeably absent are Cu-Pd and Cu-Pt, where the information was not consistent.

System	Onset temperatures from the knees in Arrhenius plots (°C)	Onset temperatures from information as in Figs. 16 or 2 (°C)	Approximate onset temperatures for equilibrium segregation (°C)
Ag-Au	350 (9)	350 (120) 250-335 (9)	300 (120)
Ag-Pd	...	...	400 (126)
Au-Cu	250-350 (43)	400 (113) 300-350 (113)	300 (117)
Au-Ni	650-750 (127)	>600 (127)	700 (128)
Au-Pd	...	400-500 (9)	400-500 (129)
Cr-Mo	...	...	~650 (69)
Cu-Ni	500-600 (9,98)	400-500 (120-122)	500 (98)
Mg-Al	...	...	125 (131)
Mo-W	...	...	~1550 (132)
Ni-Co	...	...	~525 (133)
Ni-Pt	...	...	~450 (134)
Pd-Ni	...	...	~550 (135)

Table 7 gives values of  $K^b$  as deduced in the first two ways discussed, i.e. from information as in Figs. 2 and 3. In connection with Fig. 3, Eq. (15) was used in its truncated form with  $Y_B/Y_A \approx 1$ . Figs. 12 and 13 compare values of  $K^b$  and  $K^{eq}$  for Au-Cu and Cu-Ni, which are amongst the most well studied of all alloy systems; similar information for Ag-Au is given elsewhere (111). What is striking is that  $K^b$  and  $K^{eq}$  are always in the same sense except for Ni-Pt, that  $K^b$  lies in the interval  $1.25 \leq K^b \leq 5.4$  for 14 out of 16 different systems, and that for ambient temperature the inequality  $K^b < K^{eq}$  holds. The fact that  $K^b$  and  $K^{eq}$  are almost always in the same sense suggests that bombardment leads to true chemically driven segregation rather than the closely similar phenomenon redistribution (Sect. 4.1.5). The inequality found for ambient temperature,  $K^b < K^{eq}$ , shows, however, that the role of the bombardment is not simply one of bringing the system to equilibrium at a normally inaccessible temperature (here ambient). We have suggested (67) that what is happening is that BIS is not an equilibrium process but depends on the interplay between chemically guided steps (rate  $k_{\pm}$ ) and the somewhat more numerous surface-recession steps (rate  $v_i/\lambda$ ). This is clear from the presence of  $v_i$  in  $K^b$  (Eq. (11)).

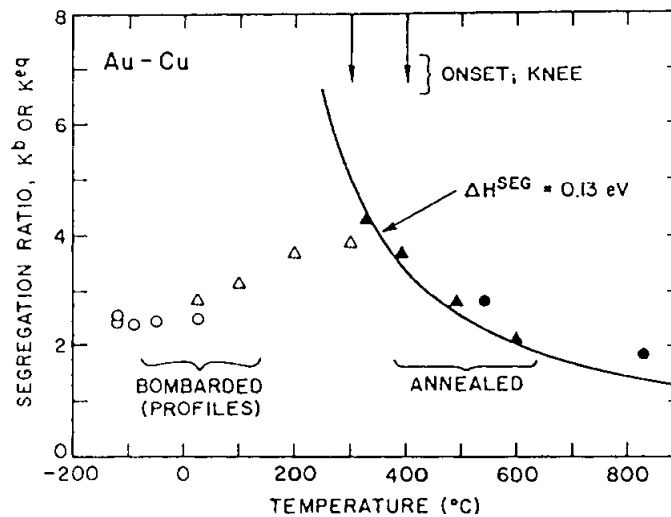


**Figure 12:** The equilibrium segregation ratio,  $K^{eq}$ , and the BIS ratio,  $K^b$ , for Au-Cu as a function of temperature. It is clear that, for ambient temperature, the inequality  $K^b < K^{eq}$  holds, suggesting that the role of the bombardment is not simply one of bringing the system to equilibrium at a normally inaccessible temperature (here ambient). Details are as follows:  $\circ$ ,  $\Delta$  (BIS evaluated from profiles by combined AES (43,113) and ISS (115,116));  $\bullet$ ,  $\blacktriangle$  (equilibrium segregation studied by ISS (117,118)).

Also shown in Figs. 12 and 13 are the onset temperatures for atomic-scale thermally activated diffusion as surveyed in Table 6 and based on information such as that in Fig. 14 (113). These temperatures serve to demarcate the domains in which the two types of segregation can be studied separately. The temperature dependence of BIS, like that of mixing (42), is seen to be relatively slight.

Values of  $K^b$  deduced from angular distributions are given in (10). They tend to be erratic but, in general, rather larger than the values in Table 7.

It is important to realize that the interpretation given here to AES or XPS analysis of bombarded surfaces conflicts strongly with most other work, whether from 10 years ago

**Table 7:** Experimental values of the segregation ratios,  $K^b$  and  $K^{eq}$ , for the alloys considered in Tables 1, 4, and 6. The second column gives  $K^b$  as deduced from profiles as in Fig. 2 using Eq. (11). The third column gives the temperature range for the profiles. The fourth column gives  $K^b$  as deduced from AES or XPS analysis of bombarded surfaces as in Fig. 3 using the truncated form of Eq. (15) (but see notes (a) and (b)). The final column gives  $K^{eq}$  for the temperature range of onset as summarized in Table 6.

System	$K^b$ from profiles as in Fig. 2	Temperature range for the profiles ( $^{\circ}\text{C}$ )	$K^b$ from AES or XPS information as in Fig. 3	$K^{eq}$ for the temperature range of onset as in Table 6
Ag-Au	1.3-2.7 (9)	200-335	2.2 (120, 136 - 138)	3.0-3.2 (139,140)
Ag-Pd	...	...	2.5 (62, 123,141-143)	1.9 126)
Au-Cu <sup>(a)</sup>	2.4-3.9 (43, 113,115,116)	-120-300	...	3.4-5.1 (117,144)
Au-Ni	1.2-4.1 (127)	100-400	2.4 (145)	55-96 (127)
Au-Pd <sup>(b)</sup>	1.4-3.1 (9)	200-500	4.3,2.4 (129,146)	~10 (147)
Cr-Mo	...	...	1.7 (69)	(Cr segregates (69))
Cu-Ni	2.5 (119); 1.7 (9)	ambient; 200	1.9 (100, 120-123)	41-104 (98)
Cu-Pd	...	...	1.5 (62)	~2 (148,149)
Cu-Pt	...	...	2.2 (62)	~6 (140,150, 151)
Mg-Al	...	...	5.4 (152)	13-19 (131)
Mo-W	...	...	1.5 (153)	(Mo segregates (132))
Ni-Co	...	...	1.25 (114)	2.8 (133)
Ni-Mo	4.5-15 (154)	ambient	...	(would expect segreg. of Ni)
Ni-Pt <sup>(c)</sup>	...	...	1.8 (62)	(Pt segregates (134,155))
Ni-W	1.0-14 (119)	ambient	...	(would expect segreg. of Ni)
Pd-Ni <sup>(d)</sup>	...	...	1.25 (123,142)	~50 (135)

(a)  $K^b$  was deduced by combining ISS measurements of  $\alpha_{\text{Au}(2)}$  (115,116) with  $\alpha_{\text{Au}(2')}$  inferred from profiles based on AES (43,113). An example is shown as Fig. 2 of Ref. 67.  $K^b$

cannot be deduced from AES or XPS analysis alone since such analysis implies that there is no compositional change, i.e.  $\alpha_{\text{Au}(2')} \approx \alpha_{\text{Au}(3)}$ .

(b)  $K^b$  was deduced by combining ISS measurements of  $\alpha_{\text{Au}(2)}$  (9,156) with  $\alpha_{\text{Au}(2')}$  inferred from AES information (129,146). The various data points are included in Fig. 3. Effectively we have used Eq. (11) instead of (15).

(c) We note that in all cases but Ni-Pt it is the first designated species which shows equilibrium segregation and which is, at the same time, lost preferentially from the subsurface. Quite surprisingly Ni-Pt shows equilibrium segregation of Pt (134,155) and bombardment-induced loss of Ni (62).

(d) A significantly lower value of  $K^{\text{eq}}$  is also reported (130).

---

(62) or contemporary (114). In this work the conservation relation of Eq. (6a) is used to deduce what is supposedly  $Y_A/Y_B$ . Our contention is that what is in every case deduced is an approximation to the product  $(Y_A/Y_B)K^b$  and that in many cases the product is close to  $K^b$  itself as in the truncated form of Eq. (15).

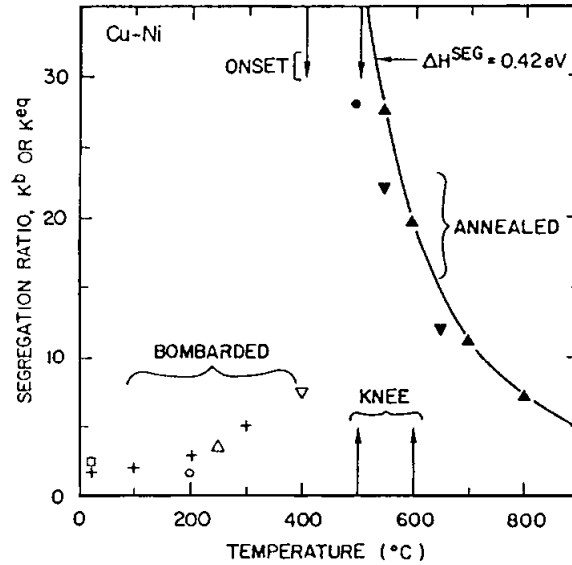


**Figure 13:** The equilibrium segregation ratio,  $K^{eq}$ , and the BIS ratio,  $K^b$ , for Cu-Ni as a function of temperature. Details are as follows:  $\circ$ ,  $\square$  (BIS evaluated from profiles by ISS (9) or multiple energy AES (119));  $\Delta$ ,  $\nabla$ ,  $+$  (BIS evaluated using AES (120,121) and the truncated form of Eq. (15). Each point "+" is the average of at least 3 (100, 120-123));  $\bullet$ ,  $\Delta$ ,  $\nabla$  (equilibrium segregation studied by ISS (98, 124) or FIM (125)).

#### 4.3.4 Application to Compositional Change with Alloys

It was emphasized in Sect. 4.1.1 that compositional changes with alloys, for example Au-Pd, cannot be explained in terms of differences in the surface binding energy. The lack of effect is inherent in the scaling  $Y_{\text{cascade}} \propto 1/M^{2m}U$  seen in Eq. (2b), together with the recognition that  $U$  must be evaluated for a mixture and not for a pure substance (Sect. 4.2.3).

If thermal sputtering were to occur then the above scaling would be replaced with  $Y_{\text{thermal}} \propto (\Delta H^a)^{-2} \exp(-\Delta H^a/k\hat{T})$ , where  $\hat{T}$  is the "thermal-spike", i.e. maximum, temperature (16,17). It is true that, because of its exponential form, this relation leads to a much stronger effect. However, the evidence for thermal sputtering, at least with metals, is still troubled (Sect. 4.1.1).

This was the situation in 1980 when the proposal was first made that the origin of compositional change with alloys was predominantly BIS. There was at the time no explicit evidence for such an effect as in Figs. 2 to 4. This information is now available and, as already noted in Sect. 4.1.2, the wide-spread occurrence of BIS, at least with alloys, must now be regarded as fully established.

In practice the following guides can be used to predict compositional changes with alloys:

- (a) The compositional change consists in subsurface loss of the component showing BIS. As discussed in Sect. 4.1.7, such loss should not be termed "preferential sputtering".
- (b) The sense of BIS is normally the same as that of equilibrium segregation. However, the magnitude tends to lie within a narrow interval for most systems,  $1.25 < K^b < 5.4$ , and in addition, for ambient temperature, the inequality  $K^b < K^{eq}$  holds.
- (c) The composition profile is as in Fig. 2, with the atom layer one composition given by Eq. (6a) or (6b) and the atom layer two composition given by Eq. (15). Because of the nature of the profile, there tends nearly always to be a conflict between ISS and AES or XPS, as well as between the sense of equilibrium segregation and the sense of compositional change. These conflicts are both apparent in Fig. 3.
- (d) Beyond atom layer two a deeply penetrating diffusion-limited profile forms which is governed to lowest approximation by Eq. (14). This profile causes the compositional change to be far more extensive than what would occur for true preferential sputtering.

#### 4.4 THE ROLE OF BOMBARDMENT-INDUCED DECOMPOSITION

##### 4.4.1 General Comments

Four separate groups of authors (31-34) have examined a long series of oxides and oxysalts by alternately bombarding them and studying the surfaces with XPS. The latter serves to detect different valence states, especially of cations and even when the states do not give stable bulk compounds. Typical results are reproduced in Figs. 6 (31) and 15 (33), Table 8 summarizes most of the results of Rabalais et al. (33,157-159) together with information on  $TiO_2$  and  $V_2O_5$ , while Table 9 summarizes various group II compounds. We note that in earlier work it was more usual to use either electron diffraction (160) or AES (1), but neither conveys as much information as XPS as far as valence states are concerned.

Table 9 includes values for the enthalpy increase (eV/atom) corresponding to the evolution of the initial substance to oxide. For example, for  $PbSO_4$  we have  $PbSO_4(s) = PbO(s) + SO_3(s)$ , whence  $2.55/6 = 0.42$ .

The trends in Tables 8 and 9 are clear. Fixed valence systems lose a volatile component (O, C, N, S) and at the same time evolve mainly to oxides rather than to carbides, nitrides, or sulfides. Variable valence systems lose oxygen and alkali metal or Ba or Ag (as is the case) and at the same time evolve towards lower valence states. Table 9 shows in addition that the ordering of the extents of decomposition, especially for a given author, are similar to the ordering of the enthalpy increases. We also see that increases up to about 0.8 eV/atom are tolerated.



**Table 8:** Summary of compositional changes as observed by Rabalais et al. (33,157-159) when oxides and oxysalts are bombarded with 4 keV Ar<sup>+</sup>. The surfaces were analysed by XPS. Because of its importance, information on TiO<sub>2</sub> and V<sub>2</sub>O<sub>5</sub> as studied mainly with XPS by other authors is included.

Substance	Loss deduced by assuming that one cation is fixed <sup>(a)</sup>	Fractional loss	Ref.
Li <sub>2</sub> CO <sub>3</sub>	0.62CO <sub>2</sub> + 0.38CO	0.82 (C)	(33)
BaCO <sub>3</sub>	0.78CO + 0.22CO <sub>2</sub>	0.84 (C)	(33)
TiO <sub>2</sub> <sup>(b)</sup>	Ti <sup>IV</sup> → Ti <sup>II</sup> , Ti <sup>III</sup>	...	(32,82)
LiNO <sub>3</sub>	0.72O <sub>2</sub> + 0.28N <sub>2</sub>	0.95 (N)	(157)
NaNO <sub>3</sub>	0.64O <sub>2</sub> + 0.36N <sub>2</sub>	0.82 (N)	(157)
NaVO <sub>3</sub> <sup>(c)</sup>	V <sup>V</sup> → V <sup>IV</sup> , V <sup>III</sup>	0.79 (Na), 0.46 (O)	(158)
V <sub>2</sub> O <sub>5</sub> <sup>(d)</sup>	V <sup>V</sup> → V <sup>III</sup>	...	...
NaNbO <sub>3</sub>	Nb <sup>V</sup> → Nb <sup>II</sup> , Nb <sup>IV</sup>	0.84 (Na), 0.53 (O)	(158)
Nb <sub>2</sub> O <sub>5</sub> <sup>(e)</sup>	Nb <sup>V</sup> → Nb <sup>II</sup> , Nb <sup>IV</sup>	0.43 (O)	(158)
NaTaO <sub>3</sub>	Ta <sup>V</sup> → Ta <sup>0</sup> etc.	0.54 (Na), 0.48 (O)	(158)
Ta <sub>2</sub> O <sub>5</sub> <sup>(f)</sup>	Ta <sup>V</sup> → Ta <sup>II</sup> , Ta <sup>I</sup> , Ta <sup>IV</sup>	0.43 (O)	(158)
Li <sub>2</sub> SO <sub>4</sub>	0.74SO <sub>3</sub> + 0.26O <sub>2</sub>	0.67 (S)	(33)
BaSO <sub>4</sub>	0.66SO <sub>2</sub> + 0.34SO <sub>3</sub>	0.62 (S)	(33)
Li <sub>2</sub> CrO <sub>4</sub>	Cr <sup>VI</sup> → Cr <sup>III</sup>	0.22 (Li), 0.51 (O)	(159)
Na <sub>2</sub> CrO <sub>4</sub>	Cr <sup>VI</sup> → Cr <sup>III</sup>	0.61 (Na), 0.48 (O)	(159)
K <sub>2</sub> CrO <sub>4</sub>	Cr <sup>VI</sup> , Cr <sup>III</sup> → Cr <sup>III</sup>	0.69 (K), 0.45 (O)	(159)
BaCrO <sub>4</sub>	Cr <sup>VI</sup> → Cr <sup>III</sup>	0.13 (Ba), 0.32 (O)	(159)
Cr <sub>2</sub> O <sub>3</sub> <sup>(g)</sup>	unestablished → Cr <sup>III</sup>	none	(159)
Na <sub>2</sub> MoO <sub>4</sub>	Mo <sup>VI</sup> → Mo <sup>IV</sup> , Mo <sup>0</sup>	0.35 (Na), 0.38 (O)	(158)
MoO <sub>3</sub> <sup>(h)</sup>	Mo <sup>VI</sup> → Mo <sup>IV</sup>	0.56 (O)	(158)
Li <sub>2</sub> WO <sub>4</sub>	W <sup>VI</sup> → W <sup>0</sup> etc.	0.69 (Li), 0.49 (O)	(158)
Na <sub>2</sub> WO <sub>4</sub>	W <sup>VI</sup> → W <sup>0</sup> etc.	0.68 (Na), 0.53 (O)	(158)
Ag <sub>2</sub> WO <sub>4</sub>	W <sup>VI</sup> → W <sup>0</sup> etc.	0.75 (Ag), 0.54 (O)	(158)
WO <sub>3</sub>	W <sup>VI</sup> → W <sup>0</sup> etc.	0.55 (O)	(158)

(a) For example, with Li<sub>2</sub>CO<sub>3</sub> Li was taken as fixed, but with Li<sub>2</sub>CrO<sub>4</sub> Cr was taken as fixed.

(b) Only Ti<sup>III</sup> is seen by electron diffraction (44).

(c) As in Fig. 8 and not Table 3 of Ref. (158).

(d) Electron diffraction (176).

- (e) Supported by other XPS studies (32,82). Only  $\text{Nb}^{\text{II}}$  is seen by electron diffraction, as if any  $\text{NbO}_2$  present were amorphous (160).
  - (f) Or else  $\text{Ta}^0$  instead of  $\text{Ta}^{\text{I}}$  (32).
  - (g) Described as " $(\text{NH}_4)_2\text{CrO}_4$ " but in fact evolved to  $\text{Cr}_2\text{O}_3$  in the target chamber vacuum.
  - (h) Described as " $\text{MoO}_2$ " but " $\text{MoO}_3$ " is more accurate. Supported by electron diffraction (176).
-

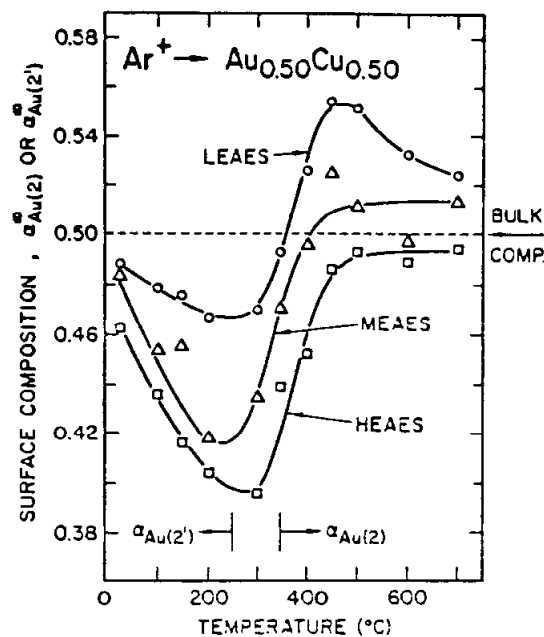


**Figure 14:** Surface ( $\alpha_{\text{Au}(2)}$ ) or subsurface ( $\alpha_{\text{Au}(2')}$ ) composition vs. bombardment temperature for  $\text{Au}_{0.50}\text{Cu}_{0.50}$  bombarded with 2 keV  $\text{Ar}^+$  and then studied with low, medium, and high-energy AES. The use of LEAES reveals that up to about 250°C there is a net subsurface loss of Au due to BIS, whereas over about 350°C there is an overall gain of Au due to equilibrium segregation. Since MEAES and HEAES are less sensitive to  $\alpha_{\text{Au}(2)}$ , they show a greater extent of loss at the lower temperatures but nearly fail to demonstrate the gain at higher temperatures. Due to Li (113).

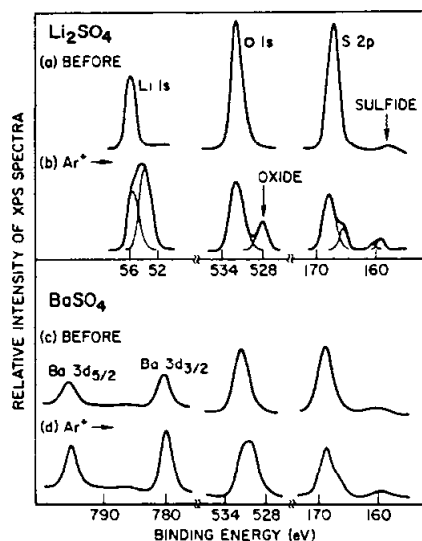


**Figure 15:** XPS spectra of metal, O, and S photoelectron peaks from  $\text{Li}_2\text{SO}_4$  and  $\text{BaSO}_4$ : (a) and (c) are before  $\text{Ar}^+$  bombardment; (b) and (d) are after 4 keV  $\text{Ar}^+$  bombardment to a fluence of  $2 - 8 \times 10^{17}$  ions/cm<sup>2</sup>. The targets were in the form of compressed powders. We agree with the authors that what is being observed is more nearly a chemical rearrangement of atoms displaced within each cascade than, for example, a process related to the thermal spike. Due to Contarini and Rabalais (33).

**Table 9:** Comparison of the extent of chemical alteration with the enthalpy increase per atom for divalent nitrates, carbonates, and sulfates bombarded with 3-8 keV Ar<sup>+</sup>. The surfaces were analyzed by XPS.

Substance	Fractional evolution to oxide due to Christie et al. (31)	Fractional evolution to oxide from other work	Enthalpy increase per atom <sup>(a)</sup> (eV/atom)
Ca(NO <sub>3</sub> ) <sub>2</sub>	0.92-0.94	...	0.30
CaCO <sub>3</sub>	0.53-0.57	0.49 (177)	0.37
	...	0.59 (34)	
CaSO <sub>4</sub>	0.40-0.45	...	0.60
Sr(NO <sub>3</sub> ) <sub>2</sub>	as above	...	0.40
SrCO <sub>3</sub>		0.41 (177)	0.49
SrSO <sub>4</sub>		...	0.69
Ba(NO <sub>3</sub> ) <sub>2</sub>	as above	...	0.46
BaCO <sub>3</sub>		0.35 (177)	0.56
		0.76 (33)	
BaSO <sub>4</sub>		0.38 (33)	0.80
Pb(NO <sub>3</sub> ) <sub>2</sub>	0.99	...	0.22
PbCO <sub>3</sub>	0.93	...	0.18
PbSO <sub>4</sub>	0.83	...	0.42
CoCO <sub>3</sub> , MnCO <sub>3</sub> , NiCO <sub>3</sub> , ZnCO <sub>3</sub>		0.80-0.83 (34)	0.09-0.24

<sup>(a)</sup> Obtained by dividing the enthalpy change for oxide formation, e.g. for PbSO<sub>4</sub>(s) = PbO(s) + SO<sub>3</sub>(s), by the number of atoms in the formula of the starting substance.

The results for various oxides, this time of a wider group of authors, are summarized in a different way in Fig. 16, which shows the enthalpy increases (eV/atom) for the observed changes vs. the number of atoms in the formula of the starting substance, i.e. the "complexity" of the substance. The trend here is that a system will tolerate enthalpy increases up to about 0.7 eV/atom (marked with arrow), this result being independent of the "complexity"; the systems  $\text{HfO}_2$ ,  $\text{Nb}_2\text{O}_5$ ,  $\text{SnO}_2$ ,  $\text{Ta}_2\text{O}_5$ ,  $\text{WO}_3$ , and  $\text{ZrO}_2$ , however, constitute exceptions. We will overlook the stability found for  $\text{Cu}_2\text{O}$  (161), as this substance lies near the limit of 0.7–0.8 eV/atom. We will also overlook the instances in which  $\text{Al}_2\text{O}_3$  (1) and  $\text{PbO}$  (162) were claimed to lose O, as well as certain instances with  $\text{Ta}_2\text{O}_5$  (1), as the work in question was carried out under near-threshold conditions as in Fig. 1.

There are at least four ways to rationalize results as in Table 8, Table 9, and Fig. 16. The first concerns the surface binding energy, while the remaining three are different aspects of bombardment-induced decomposition.

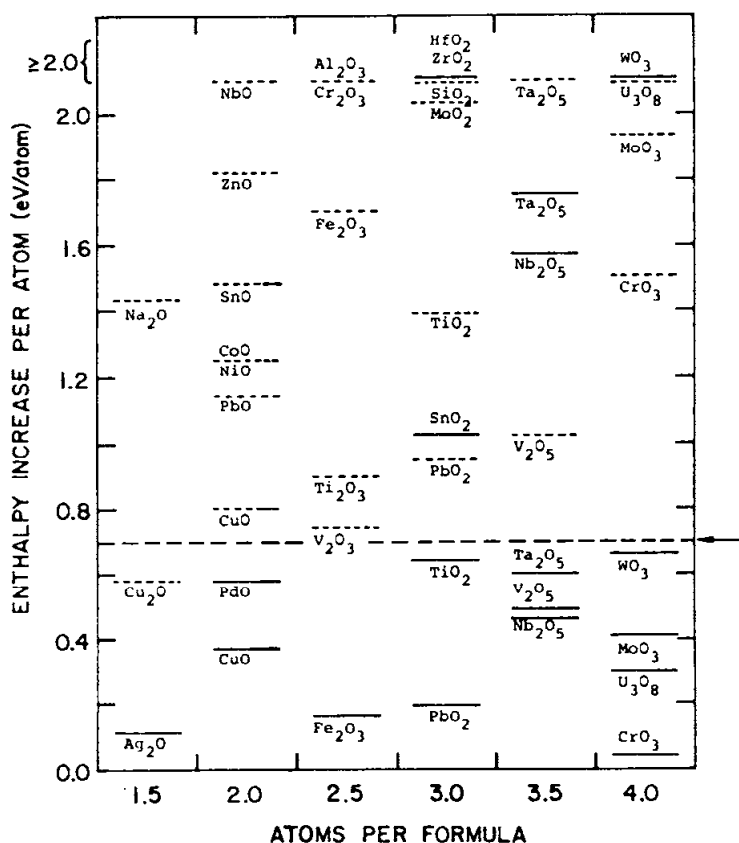


**Figure 16:** Diagram of enthalpy increase per atom (eV/atom) vs. atoms in the formula, i.e. the "complexity", for various bombarded oxides. A solid line indicates that the oxide reduced, a dashed line that it did not, with the two categories separated at about 0.7 eV/atom (arrow). This figure constitutes a trend analysis appropriate to energy-limited rearrangement as discussed in Sect. 4.4.4. Details are as follows: column 1.5 (reduction to metal), column 2.0 (reduction to Cu, Pd, Cu<sub>2</sub>O, Pb, Ni, Co, Sn, Zn, Nb), column 2.5 (reduction to Fe<sub>3</sub>O<sub>4</sub>, VO, TiO, Fe, Cr, Al), column 3.0 (reduction to PbO, Ti<sub>2</sub>O<sub>3</sub>, Pb, SnO, TiO, Mo, Si, Zr, Hf), column 3.5 (reduction to NbO<sub>2</sub>, V<sub>2</sub>O<sub>3</sub>, interpolated TaO<sub>2</sub>, VO, NbO, interpolated TaO, Ta), column 4.0 (reduction to Cr<sub>2</sub>O<sub>3</sub>, UO<sub>2</sub>, MoO<sub>2</sub>, WO<sub>2</sub>, Cr, Mo, U, W).

#### 4.4.2 Surface Binding Energy

We have already discussed in detail in Sect. 4.2.6 the possible role of the surface binding energy in governing compositional changes with oxides and oxysalts. In brief, for oxides of group III and beyond and which are reasonably ionic, the anion binding energy at an undisturbed surface should be distinctly lower than the cation binding energy, an effect which is tentatively supported by experiment (Fig. 7). The binding energy argument would be particularly relevant to the exceptions noted above:  $\text{HfO}_2$ ,  $\text{Nb}_2\text{O}_5$ , etc. The problem, as with the role of mass (Sect. 4.2.6.2), is the lack of universality: e.g. why do  $\text{Al}_2\text{O}_3$ ,  $\text{Cr}_2\text{O}_3$ , and  $\text{SiO}_2$  not show extensive O loss?

#### 4.4.3 Stochastic Rearrangement

Suppose that during the active phase of a cascade the atoms of, for example,  $\text{PbSO}_4$  become interchanged or otherwise uncoordinated. Then in the cooling phase of the cascade the system would tend to re-establish local order and one possibility is that the new order, thence stoichiometry, would form randomly. To some extent this would be guided by partial loss of a volatile species, by diffusional transport, or by BIS (Sect. 4.4.4.4, to follow). One would then expect a wide range of products, with  $\text{PbSO}_4$ , for example, evolving to a mixture of  $\text{PbO}$ ,  $\text{Pb}$ , and  $\text{PbS}$ . Since this is contrary to what is observed as the dominant process ((31); Table 9), stochastic rearrangement is evidently not the most important process. Nevertheless, an element of such rearrangement is probably relevant with most systems, as follows from these examples.  $\text{CoO}$  is largely stable but evolves to a small extent to  $\text{Co}^0$  either at ambient temperature (82) or at  $\geq 550$  K (163).  $\text{NiO}$  yields  $\text{Ni}^0$  at  $\geq 400$  K (163).  $\text{Fe}_2\text{O}_3$  evolves mainly to  $\text{Fe}^{\text{II}}$  but with some  $\text{Fe}^0$  also present (82).

#### 4.4.4 Energy-Limited Rearrangement

We again suppose that a bombarded system tends to first become uncoordinated but finally to re-establish local order. Then another possibility is that this change is energy (enthalpy) limited, i.e. constitutes what is effectively a bombardment-induced phase change. For example,  $\text{PbSO}_4$ , known to evolve mainly to  $\text{PbO}$  rather than  $\text{Pb}$  or  $\text{PbS}$  (31), will be assumed to do so because the energy increase is 0.42 eV/atom in the first case, 0.80 in the second, and 1.42 in the third. One is thus again dealing with energy differences which, in units of eV/atom, are similar to those involved in BIS and mixing (Table 1).

The argument at this stage is imperfect, as it does not explain why the system did not return to  $\text{PbSO}_4$ , given that  $\text{PbSO}_4$  constitutes the lowest energy state. By contrast, in BIS and mixing the final state that is observed is that of lowest energy. One can propose a number of reasons why the system might tend to avoid the state  $\text{PbSO}_4$  (or whatever was the ground state), although, as will be clear, no one explanation appears to cover all systems.

**4.4.4.1. Mass Differences.** Mass is most clearly relevant under near-threshold conditions, including with  $\text{Al}_2\text{O}_3$  (1),  $\text{PbO}$  (162), and  $\text{Ta}_2\text{O}_5$  (1). Nevertheless, even at higher energies near-threshold behavior might be expected for large enough mass differences, and this would explain why  $\text{WO}_3$  reduced to products including  $\text{W}^0$  but  $\text{MoO}_3$  mainly to  $\text{Mo}^{\text{IV}}$ , or why  $\text{Ta}_2\text{O}_5$  yielded products including  $\text{Ta}^0$  or  $\text{Ta}^{\text{I}}$  but  $\text{Nb}_2\text{O}_5$  stopped at  $\text{Nb}^{\text{II}}$  (Table 8). A still more general role for mass is suggested by the relation  $Y_{\text{cascade}} \propto 1/M^{2m}\text{U}$  (Eq. (2b)) and was in fact advocated by Malherbe et al. (6). As

noted previously (Sect. 4.2.6.2), however, this general role would suggest that all oxides (except, e.g., BeO) would behave similarly and reduce to pure metal, at least at the outer surface. We therefore tend to discount it.

**4.4.4.2 Bombardment-Induced Amorphization.** If the amorphization process is taken as being equivalent to fusion, then with  $\text{PbSO}_4$  one can expect a ground-state energy increase of 0.07 eV/atom, whence a decrease in the energy needed for formation of PbO from 0.42 to 0.35 eV/atom. This is an unimportant change, though with some systems the change is larger, e.g. about 0.26 eV/atom (average from (164)) for oxides of the type  $\text{MO}_2$ . Indeed, as seen in Fig. 18, the latter change is sufficient to justify the recent claim that bombarded  $\text{SnO}_2$  evolves to SnO (165).

**4.4.4.3 Point-Defect Accumulation.** Fecht and Johnson (166) have argued that point-defect accumulation can cause a phase to become unstable. For example, they show that Al would amorphize if it acquired 5% vacancies, a number that is obtained by comparing the vacancy formation energy (0.7 eV (8)) with the heat of fusion ( $<0.11$  eV for temperatures below the glass transition temperature (166)). Considering now  $\text{PbSO}_4$ , then a possible (though simplistic) description of a high oxygen vacancy concentration is the formation of  $\text{PbSO}_3$ , leading to a ground-state energy increase of  $\leq 0.43$  eV/atom. With such an increase, together with amorphization, it is possible that  $\text{PbSO}_4$  would become unstable.

**4.4.4.4 Volatility, Diffusional Transport, BIS.** To some extent the evolution of  $\text{PbSO}_4$  to PbO will be conditioned by the volatility of  $\text{O}_2$ ,  $\text{SO}_2$ , and  $\text{SO}_3$ . This effect is clearly not as important as it might seem, however, as it would be expected to lead to a universal decomposition of all oxides and oxysalts, for example  $\text{Al}_2\text{O}_3$ ,  $\text{Cr}_2\text{O}_3$ , and  $\text{SiO}_2$ . Ease of diffusional transport is somewhat different and, in principle, plays a role with selected systems. From a thermodynamic point of view these should either not lose O at all ( $\text{HfO}_2$ ,  $\text{SnO}_2$ ,  $\text{ZrO}_2$ ) or should lose less O than is observed ( $\text{Nb}_2\text{O}_5$ ,  $\text{Ta}_2\text{O}_5$ ,  $\text{WO}_3$ ). The key may lie in the fact that in most cases the diffusion coefficient for O transport in understoichiometric material is unusually large. For example,  $(4Dt)^{1/2}$  is about 1 nm for O transport in 10 min at 450 K with  $\text{ZrO}_{2-x}$  (167,168), while the corresponding distance for  $\text{Nb}_2\text{O}_{5-x}$  is about 10 nm (167,169) and for  $\text{MoO}_3$  ( $\text{MoO}_{3-x}$ ?) about 2 nm (170). (We give results for  $\text{MoO}_3$  since there is a lack of information on  $\text{WO}_3$ .)

An intriguing example is that of CoO and NiO, which in one AES study showed bombardment-induced decomposition only at elevated temperatures (163). MnO was stable up to 900 K. Are these to be considered examples involving diffusional transport or stochastic rearrangement (Sect. 4.4.3)?

Finally there is BIS. Very little is known about this effect with oxides or oxysalts except for the unique example of  $\text{Na}_2\text{O-SiO}_2$  (38). Here bombardment led to a profile like that of an alloy as in Fig. 2, thence to Na loss.

#### 4.4.5 Equilibrium Rearrangement

If the system underwent equilibrium decomposition at the transient high temperature ("thermal spike") which is conventionally assumed to exist during the cooling phase of a cascade, then changes essentially as observed could be expected. This was the point of

view taken to explain O loss from oxides (19) and the loss of both alkali metals and other volatile species from oxysalts (Fig. 15 (158)). We note, first of all, that this mechanism does not avoid the problematical cases such as  $\text{HfO}_2$ ,  $\text{Nb}_2\text{O}_5$ , etc.: i.e. just as they lie at the top of Fig. 16, they also lack volatility.

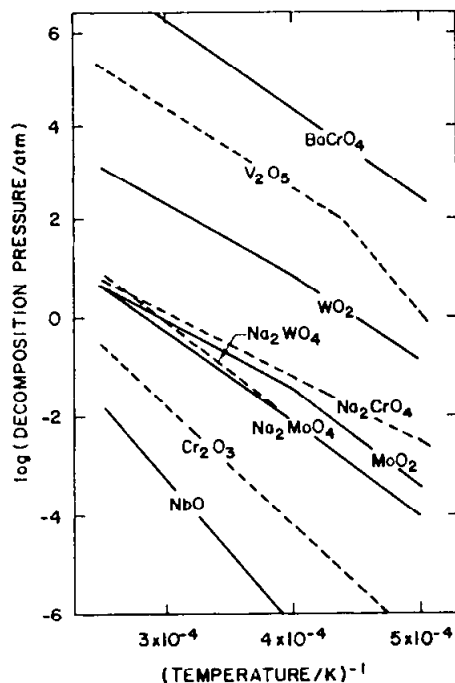


**Figure 17:** Decomposition pressure vs.  $1/T$  for oxides and oxysalts at very high temperatures. Those lying above  $\text{MoO}_2$  (including, for high enough temperatures,  $\text{Na}_2\text{WO}_4$  and  $\text{Na}_2\text{MoO}_4$ ) show a bombardment-induced loss of O, whereas the others do not. The separation between the two groups occurs at about  $10^1$  atm for a temperature of  $\sim 4000$  K. This is a similar kind of trend analysis as that shown in Fig. 16 except that it presupposes the validity of equilibrium rearrangement as discussed in Sect. 4.4.5. Due to Ho et al. (158).

The mechanism has never been properly tested, the current situation being that most tests are either a trend analysis as in Fig. 17 or Ref. 19, or are based on experiments (20,21) which are inconclusive. Our position is the same as that taken elsewhere (111) with BIS and mixing. Although we cannot disprove a thermal-spike interpretation we can propose an alternative in which chemical energy differences are important (a) without regard to the inequality (111 171),

$$(\text{driving force}) \gtrsim kT, \quad (17)$$

and (b) without violating the problem of a phase explosion (Sect. 4.1.1). The alternative was given in Sect. 4.4.4.

A further general objection also exists in that the mechanism requires chemical changes to occur in an assumed equilibrium during a time interval similar to  $10^{-12}$  to  $10^{-9}$  s. By contrast the process discussed in Sect. 4.4.4 is essentially open ended in time. For example, with  $\text{BaSO}_4$  a change in the O XPS peak was reported to take place over  $\sim 3$  hours (33), while bombarded alloys have been shown to undergo BIS for up to 10 minutes after the end of the bombardment (Fig. 4).



$\text{SnO}_2$  presents a novel sort of objection. It is known to evolve to  $\text{SnO}$  (165), but since the latter is not stable above  $\sim 270^\circ\text{C}$  (172) equilibrium rearrangement can be excluded.

#### 4.5. OVERVIEW

The main theme of this Chapter is that compositional changes with bombarded alloys, oxides, oxysalts, and halides are normally not due to preferential sputtering but rather to surprisingly weak chemical driving forces (Table 1). Preferential sputtering enters in two ways: (a) It occurs as a mass-related preferential loss under near-threshold conditions (Fig. 1), possibly under not-quite-threshold conditions if the mass difference is large enough ( $\text{WO}_3$  vs  $\text{MoO}_3$ ), and with isotopes. (b) It occurs tentatively due to the surface binding energy in the case of reasonably ionic oxides of group III and beyond (Sects. 4.2.5 and 4.2.6). In a formal sense, preferential loss based on differences of volatility (thermal sputtering) would also constitute preferential sputtering but the evidence for it is problematical (Sects. 4.1.1 and 4.4.5).

Rather, we have emphasized that weak chemical driving forces play a major role in bombarded targets even when, for reasons of the extreme energy disparity, it might be difficult to understand why this should be so. With BIS the basic result is that bombarded alloys show segregation in the same sense, although to a factor of 10-100 lesser extent, than equilibrated alloys (Fig. 12, Fig. 13, Table 7). The driving force is 0.06 to 0.52 eV/atom (Table 1) and we have suggested (see after Eq. (11)) that the result becomes understandable if a fraction  $f$  of ballistic trajectories ending in either of the outer two atom layers is followed by a low-energy, chemically guided step, while BIS thus resembles mixing. We have further suggested that BIS is the single most important reason for compositional change with alloys (Sect. 4.3.4).

Finally we have considered what has been termed bombardment-induced decomposition. This is a multifaceted phenomenon in which bombarded oxides lose O, sulfates lose S and O, and other systems lose, as is appropriate, alkali metal, Ba, Ag, C, N, etc., the result being an energy increase of  $\lesssim 0.8$  eV/atom (Fig. 16). The idea of a chemical driving force is here at first sight unfavorable in that the "ground state" (e.g.  $\text{PbSO}_4$ ) has a lower energy than the observed product (e.g.  $\text{PbO}$ ). The point of view of Fecht and Johnson (166) is relevant, however, which is that if there are sufficient bombardment-induced vacancies (simplistically, conversion of  $\text{PbSO}_4$  to  $\text{PbSO}_3$ ) then the ground state will be unstable. This is how Fecht and Johnson described bombardment-induced amorphization and other phase changes, processes which we see now to be related to those that are discussed here. Besides point-defect accumulation, the changes will also be aided by amorphization, volatility, diffusional transport, and BIS.

We have shown that the alternative of a stochastic loss of components is not as viable:  $\text{PbSO}_4$  does not evolve significantly to Pb or  $\text{PbS}$ . Nor, however, can it be excluded as playing at least a minor role in view of such systems as  $\text{CoO}$ ,  $\text{NiO}$ , and  $\text{Fe}_2\text{O}_3$ , which yield small amounts of  $\text{Co}^0$ ,  $\text{Ni}^0$ , and  $\text{Fe}^0$  in spite of the large energy increases (Fig. 16). Likewise, equilibrium loss at a transient high temperature runs into the various problems associated with thermal-spike descriptions. These are (a) Eq. (17), (b) phase explosion, (c) the severely proscribed time-scale, and (d) the evolution of  $\text{SnO}_2$  to  $\text{SnO}$ , which is stable only at low temperatures (Sect. 4.4.5).

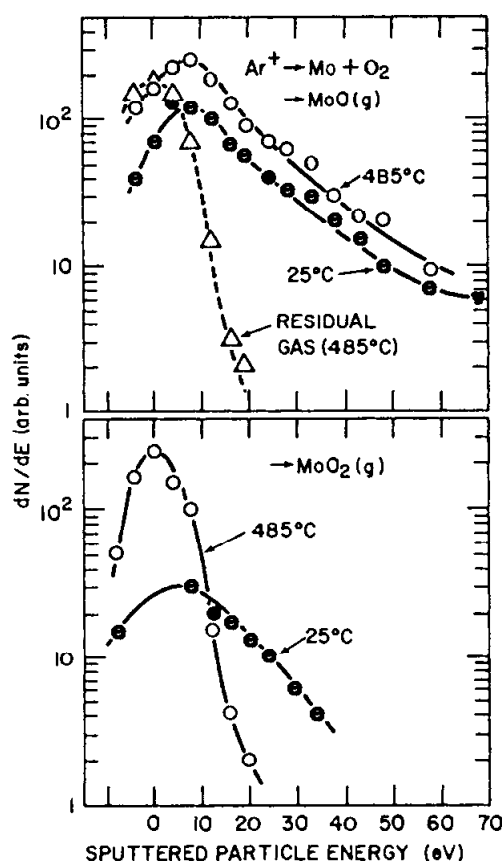


**Figure 18:** Energy distributions of neutral  $\text{MoO(g)}$  and  $\text{MoO}_2\text{(g)}$  sputtered from polycrystalline Mo exposed to  $1 \times 10^{-3}$  Pa  $\text{O}_2$ . The bombardments were carried out with 8 keV  $\text{Ar}^+$  at an angle of incidence of  $70^\circ$ . The energy scale was set to zero at the maximum of the residual gas distribution and negative energies were attributed to poor resolution. Of particular interest here is the thermal form of the  $\text{MoO}_2\text{(g)}$  distribution at  $485^\circ\text{C}$ , as if the  $\text{MoO}_2$  was released by either a stochastic or energy-limited rearrangement (a distinction is not possible) at the particular ambient temperature. Due to Saidoh et al. (173).

An important source of information has not yet been considered, namely sputtered particle energy distributions as in Fig. 18 (173). They have apparently never been obtained for the various oxysalts dealt with here and only rarely for oxides, but if the results of Fig. 18 are accepted at face value they imply that at  $485^\circ\text{C}$  the  $\text{MoO}_2\text{(g)}$  was released by either a stochastic or energy-limited rearrangement (a distinction is not possible) at the particular ambient temperature but in no case by an equilibrium rearrangement at a very high temperature. Related examples are known from work on laser-pulse sputtering, as when the species P and  $\text{P}_2$  are released from GaP and give time-of-flight spectra appropriate to the ambient temperature (174,175).

#### 4.6 REFERENCES

1. E. Taglauer, *Appl. Surf. Sci.* 13: 80 (1982).
2. H. Gnaser and I. D. Hutcheon, *Surf. Sci.* 195: 499 (1988).
3. N. Andersen and P. Sigmund, *Mat. Fys. Medd. Dan. Vid. Selsk.* 39: No. 3 (1974).
4. R. Kelly, in *Proc. Symp. on Sputtering*, eds. P. Varga et al. (Inst. für Allgem. Physik, T. U. Wien, Austria, 1980) p. 390.
5. R. Kelly and D. E. Harrison, *Mat. Sci. Engin.* 69: 449 (1985).

6. J.B. Malherbe, S. Hofmann, and J.M. Sanz, Appl. Surf. Sci. 27: 355 (1986).
7. R. Kelly, in Ion Beam Modification of Insulators, eds. P. Mazzoldi and G. W. Arnold (Elsevier, Amsterdam, 1987) ch. 2.
8. A. Oliva, R. Kelly, and G. Falcone, Nucl. Instr. Meth. B19/20: 101 (1987).
9. D. G. Swartzfager, S. B. Ziemecki, and M. J. Kelley, J. Vac. Sci. Technol. 19: 185 (1981).
10. R. Kelly and A. Oliva, Nucl. Instr. Meth. B13: 283 (1986).
11. R. Kelly, Nucl. Instr. Meth. B18: 388 (1987).
12. W. O. Hofer, in Erosion and Growth of Solids Stimulated by Atom and Ion Beams, eds. G. Kiriakidis et al. (Nijhoff, Dordrecht, Netherlands, 1986) p. 1.
13. R. S. Nelson, Phil. Mag. 11: 291 (1965).
14. R. Kelly, Surf. Sci. 90: 280 (1979).
15. K. Besocke, S. Berger, W. O. Hofer, and U. Littmark, Rad. Eff. 66: 35 (1982).
16. R. Kelly, Rad. Eff. 32: 91 (1977).
17. P. Sigmund, Appl. Phys. Lett. 25: 169 (1974).
18. A. E. Morgan and H. W. Werner, Anal. Chem. 49: 927 (1977).
19. C. J. Good-Zamin, M. T. Shehata, D. B. Squires, and R. Kelly, Rad. Eff. 35: 139 (1978).
20. M. Szymonski, R.S. Bhattacharya, H. Overeijnder, and A.E. de Vries, J. Phys. D 751 (1978).
21. D.J. Oostra, R.P. van Ingen, A. Haring, A.E. de Vries, and F.W. Saris, Phys. Rev. Lett. 61: 1392 (1988).
22. M.M. Martynyuk, Russ. J. Phys. Chem. 57: 494 (1983).
23. M.M. Martynyuk, Phys. of Combustion and Explosions 13: 178 (1977).
24. H.M. Urbassek, Nucl. Instr. Meth. B31: 541 (1988).
25. H. H. Andersen, B. Stenum, T. Sorensen, and H. J. Whitlow, Nucl. Instr. Meth. 209/210: 487 (1983).
26. S. Ichimura, H. Shimizu, H. Murakami, and Y. Ishida, J. Nucl. Mat. 128/129: 601 (1984).
27. J. Fine, T. D. Andreadis, and F. Davarya, Nucl. Instr. Meth. 209/210: 521 (1983).
28. R. S. Li, L. X. Tu, and Y. Z. Sun, Appl. Surf. Sci. 26: 77 (1986).
29. D. E. Harrison and R. P. Webb, Nucl. Instr. Meth. 218: 727 (1983).
30. H. Overeijnder, R. R. Tol, and A. E de Vries, Surf. Sci. 90: 265 (1979).
31. A. B. Christie, J. Lee, I. Sutherland, and J. M. Walls, Appl. Surf. Sci. 15: 224 (1983).
32. S. Hofmann and J. M. Sanz, J. Trace and Microprobe Tech. 1: 213 (1982-1983).
33. S. Contarini and J. W. Rabalais, J. Electron Spect. and Related Phenom. 35: 191 (1985).
34. G. Marletta, Nucl. Instr. Meth. B32: 204 (1988).
35. P. J. Rudeck, J.M.E. Harper, and P. M. Fryer, Appl. Phys. Lett. 53: 845 (1988).

36. R. A. Kushner, D. V. McCaughan, V. T. Murphy, and J. A. Heilig, Phys. Rev. B10: 2632 (1974).
37. R. C. McCune and P. Wynblatt, J. Am. Cer. Soc. 66: 111 (1983).
38. A. Torrissi, G. Marletta, A. Licciardello, and O. Puglisi, Nucl. Instr. Meth. B32: 283 (1988).
39. U. Littmark, Nucl. Instr. Meth. B7/8: 684 (1985), and preceding articles.
40. Y-T. Cheng, M. van Rossum, M-A. Nicolet, and W. L. Johnson, Appl. Phys. Lett. 45: 185 (1984).
41. Y-T. Cheng, T. W. Workman, M-A. Nicolet, and W. L. Johnson, Mat. Res. Soc. Symp. Proc. 74: 419 (1987).
42. J. Bottiger, S. K. Nielsen, and P. T. Thorsen, Proc. Mat. Res. Soc. (Europe) (Strasbourg, France, 1984) p. 111.
43. R. S. Li and T. Koshikawa, Surf. Sci. 151: 459 (1985).
44. T. E. Parker and R. Kelly, J. Phys. Chem. Sol. 36: 377 (1975).
45. N. Q. Lam and H. Wiedersich, Nucl. Instr. Meth. B18: 471 (1987).
46. R. Kelly, Nucl. Instr. Meth. 182/183: 351 (1981).
47. R. C. Piller and A. D. Marwick, J. Nucl. Mat. 71: 309 (1978).
48. H. L. Hughes, R. D. Baxter, and B. Phillips, IEEE Trans. Nucl. Sci. NS-19: 256 (1972).
49. G. Betz and W. Husinsky, Nucl. Instr. Meth. B13: 343 (1986).
50. N. Itoh and A.M. Stoneham; also R. Kelly: work in progress.
51. J. van Zwol, A. W. Kolfschoten, J. van Laar, and J. Dieleman, in Materials Modification by High-fluence Ion Beams, eds. R. Kelly and M.F. da Silva (Kluwer, Dordrecht, Netherlands, 1988) p. 117.
52. R. A. Haring, A. Haring, F. W. Saris, and A. E. de Vries, Appl. Phys. Lett. 41: 174 (1982).
53. M. Saidoh, J. Nucl. Mat. 128/129: 540 (1984).
54. J. Bohdanský and J. Roth, Rad. Eff. 89: 49 (1985).
55. E. Hechtel, J. Bohdanský, and J. Roth, J. Nucl. Mat. 103/104: 333 (1981).
56. R. Kelly and A. Oliva, see Ref. 12, p. 41.
57. W. C. Mackrodt, Sol. State Ionics 12: 175 (1984).
58. P. Biloen, R. Bouwman, R. A. van Santen, and H. H. Brongersma, Appl. Surf. Sci. 2: 523 (1979).
59. G. Hetzendorf and P. Varga, Nucl. Instr. Meth. B18: 501 (1987).
60. A. Jablonski, S. H. Overbury, and G. A. Somorjai, Surf. Sci. 65: 578 (1977).
61. P. Varga and G. Hetzendorf, Surf. Sci. 162: 544 (1985).
62. G. Betz, Surf. Sci. 92: 283 (1980).
63. R. S. Li (Institute of Metal Research, Shenyang), private communication (1988).
64. G. C. Nelson, J. Vac. Sci. Technol. A1: 1037 (1983).

65. R. S. Li, in Diffusion and Defect Data, ed. F. H. Wohlbier (Trans Tech S. A., Aedermannsdorf, Switzerland) (in press).
66. W. L. Johnson, see Ref. 51, p. 405.
67. R. Kelly, Nucl. Instr. Meth. B39: 43 (1989).
68. R. Hultgren, P. D. Desai, D. T. Hawkins, M. Gleiser, and K. K. Kelley, Selected Values of the Thermodynamic Properties of Binary Alloys (Am. Soc. for Metals, Metals Park, OH, U.S.A., 1973).
69. P. T. Dawson and S. A. Petrone, Surf. Sci. 152/153: 925 (1985).
70. G. Falcone, R. Kelly, and A. Oliva, Nucl. Instr. Meth. B18: 399 (1987).
71. P. Sigmund, Phys. Rev. 184: 383 (1969).
72. B. Jorgensen, M. J. Pellin, C. E. Young, W. F. Calaway, E. L. Schweitzer, D. M. Gruen, J. W. Burnett, and J. T. Yates, see Ref. 51, p. 83.
73. P. Sigmund, Rev. Roum. Phys. 17: 969 (1972). See in particular p. 974.
74. R. Kelly and A. Oliva, in preparation.
75. D.M. Parkin, in Structure-property Relationships in Surface-modified Ceramics (Kluwer, Dordrecht, Netherlands, 1989).
76. R. A. Swalin, Thermodynamics of Solids, 2nd. ed. (Wiley, New York, 1972), p. 144.
77. S. V. Nagender Naidu, A. M. Sriramamurthy, and P. Rama Rao, Bull. Alloy Phase Diagrams 5: 177 (1984).
78. D. P. Jackson, Rad. Eff. 18: 185 (1973).
79. H. Oechsner, H. Schoof, and E. Stumpe, Surf. Sci. 76: 343 (1978).
80. T. E. Parker and R. Kelly, in Ion Implantation in Semiconductors and Other Materials, ed. by B. L. Crowder (Plenum, New York, NY, 1973) p. 551.
81. V. E. Henrich, G. Dresselhaus, and H. J. Zeiger, Phys. Rev. Lett. 36: 1335 (1976).
82. T. Choudhury, S.O. Saied, J.L. Sullivan, and A. Abbot, J. Phys. D (in press).
83. E. Dullni, Nucl. Instr. Meth. B2: 610 (1984).
84. D. Grischkowsky, M. L. Yu, and A. C. Balant, Surf. Sci. 127: 315 (1983).
85. W. Husinsky, G. Betz, and I. Girgis, J. Vac. Sci. Technol. A2: 698 (1984).
86. W. Husinsky and G. Betz, Nucl. Instr. Meth. B15: 165 (1986).
87. W. Husinsky, P. Wurz, B. Strehl, and G. Betz, Nucl. Instr. Meth. B18: 452 (1987).
88. C. E. Young, W. F. Calaway, M. J. Pellin, and D. M. Gruen, J. Vac. Sci. Technol. A2: 693 (1984).
89. B. Schweer and H. L. Bay, Appl. Phys. A29: 53 (1982).
90. J. P. Baxter, J. Singh, G. A. Schick, P. H. Kobrin, and N. Winograd, Nucl. Instr. Meth. B17: 300 (1986).
91. J. P. Baxter, G. A. Schick, J. Singh, P. H. Kobrin, and N. Winograd, J. Vac. Sci. Tech. A4: 1218 (1986).
92. R. B. Wright, M. J. Pellin, and D. M. Gruen, Nucl. Instr. Meth. 182/183: 167 (1981).
93. W. Berres and H. L. Bay, Appl. Phys. A33: 235 (1984).

94. W. Husinsky, J. Vac. Sci. Technol. B3: 1546 (1985).
95. M. J. Pellin, R. B. Wright, and D. M. Gruen, J. Chem. Phys. 74: 6448 (1981).
96. B. J. Garrison, N. Winograd, D. Lo, T. A. Tombrello, M. H. Shapiro, and D. E. Harrison, Surf. Sci. Lett. 180: L129 (1987).
97. H. L. Bay, W. Berres, and E. Hintz, Nucl. Instr. Meth. 194: 555 (1982).
98. N. Q. Lam, H. A. Hoff, H. Wiedersich, and L. E. Rehn, Surf. Sci. 149: 517 (1985).
99. M. J. Sparnaay and G. E. Thomas, Surf. Sci. 135: 184 (1983).
100. M. Shikata and R. Shimizu, Surf. Sci. 97: L363 (1980).
101. Y. M. Chiang, A. P. Henriksen, W. D. Kingery, and D. Finello, J. Am. Cer. Soc. 64: 385 (1981).
102. E. A. Colbourn, W. C. Mackrodt, and P. W. Tasker, J. Mat. Sci. 18: 1917 (1983).
103. V. R. Deline, W. Reuter, and R. Kelly, in Sec. Ion Mass Spectrometry, SIMS V, eds. A. Benninghoven et al. (Springer-Verlag, Berlin, 1986) p. 299.
104. P. Wynblatt and R. C. Ku, Surf. Sci. 65: 511 (1977).
105. R. A. van Santen and M.A.M. Boersma, J. Catal. 34: 13 (1974).
106. L. E. Rehn and P. R. Okamoto, Nucl. Instr. Meth. B39: 104 (1989).
107. N. Q. Lam and H. Wiedersich, J. Nucl. Mat. 103/104: 433 (1981).
108. N. Itoh and K. Morita, Rad. Eff. 80: 163 (1984).
109. P. Sigmund, A. Oliva, and G. Falcone, Nucl. Instr. Meth. 194: 541 (1982).
110. A. Oliva, R. Kelly, and G. Falcone, Surf. Sci. 166: 403 (1986).
111. R. Kelly, Mat. Sci. Eng. A114: (1989).
112. R. Kelly, Surf. and Interface Anal. 7: 1 (1985).
113. R-S. Li, Surf. Sci. 193: 373 (1988).
114. E. E. Hajcsar, P. T. Dawson, and W. W. Smeltzer, Surf. and Interface Anal. 10: 343 (1987).
115. H. J. Kang, R. Shimizu, and T. Okutani, Surf. Sci. 116: L173 (1982).
116. H. J. Kang, E. Kawatoh, and R. Shimizu, Surf. Sci. 144: 541 (1984).
117. G. C. Nelson, J. Vac. Sci. Technol. A1: 1037 (1983).
118. T. M. Buck, G. H. Wheatley, and L. Marchut, Phys. Rev. Lett. 51: 43 (1983).
119. J. Bartella and H. Oechsner, unpublished.
120. M. Yabumoto, H. Kakibayashi, M. Mohri, K. Watanabe, and T. Yamashina, Thin Sol. Films 63: 263 (1979).
121. H. Shimizu, M. Ono, and K. Nakayama, J. Appl. Phys. 46: 460 (1975).
122. L. E. Rehn and H. Wiedersich, Thin Sol. Films 73: 139 (1980).
123. M. L. Yu and W. Reuter, Appl. Phys. Lett. 38: 525 (1981).
124. H. H. Brongersma, M. J. Sparnaay, and T. M. Buck, Surf. Sci. 71: 657 (1978).
125. Y. S. Ng, S. B. McLane, and T. T. Tsong, J. Vac. Sci. Technol. 17: 154 (1980).
126. G. P. Schwartz, Surf. Sci. 76: 113 (1978).
127. N. Q. Lam, H. A. Hoff, and P. G. Regnier, J. Vac. Sci. Technol. A3 : 2152 (1985).

128. J. J. Burton, C. R. Helms, and R. S. Polizzotti, J. Vac. Sci. Technol. 13: 204 (1976).
129. A. Jablonski, S. H. Overbury, and G. A. Somorjai, Surf. Sci. 65: 578 (1977).
130. K. Wandelt and G. Ertl, Z. Naturforsch. 31a: 205 (1976).
131. C. Lea and C. Molinari, J. Mat. Sci. 19: 2336 (1984).
132. P. T. Dawson and N. A. Burke, J. Electron Spect. and Related Phenom. 31: 355 (1983).
133. E. E. Hajcsar, P. R. Underhill, W. W. Smeltzer, and P. T. Dawson, Surf. Sci. 191: 249 (1987).
134. L. de Temmerman, C. Creemers, H. van Hove, and A. Neyens, Surf. Sci. 183: 565 (1987).
135. D. A. Mervyn, R. J. Baird, and P. Wynblatt, Surf. Sci. 82: 79 (1979).
136. W. Färber, G. Betz, and P. Braun, Nucl. Instr. Meth. 132: 351 (1976).
137. M. Yabumoto, K. Watanabe, and T. Yamashina, Surf. Sci. 77: 615 (1978).
138. P. H. Holloway and S. K. Hofmeister, Surf. and Interface Anal. 4: 181 (1982).
139. G. C. Nelson, Surf. Sci. 59: 310 (1976).
140. M. J. Kelley, D. G. Swartzfager, and V. S. Sundaram, J. Vac. Sci. Technol. 16: 664 (1979).
141. S. Dong, Y. Pang, J. Deng, and X. Zhu, Acta Metall. Sinica 20: B110 (1984).
142. H. J. Mathieu and D. Landolt, Surf. Sci. 53: 228 (1975).
143. F. Garbassi and G. Parravano, Surf. Sci. 71: 42 (1978).
144. W. Losch and J. Kirschner, J. Vac. Sci. Technol. 15: 1541 (1978).
145. H. G. Tompkins, J. Vac. Sci. Technol. 16: 778 (1979).
146. G. Betz, J. Marton, and P. Braun, Nucl. Instr. Meth. 168: 541 (1980).
147. G. Hetzendorf and P. Varga, Nucl. Instr. Meth. B18: 501 (1987).
148. A. D. van Langeveld, H.A.C.M. Hendrickx, and B. E. Nieuwenhuys, Thin Sol. Films 109: 179 (1983).
149. T. S. Sampath Kumar and M. S. Hegde, Appl. Surf. Sci. 20: 290 (1985).
150. A. D. van Langeveld and V. Poncet, Appl. Surf. Sci. 16: 405 (1983).
151. C. R. Barreto, R. C. Gragnani, R. A. Douglas, and V. S. Sundaram, Rev. Brasileira de Fisica 9: 217 (1979).
152. P. Braun, M. Arias, H. Stori, and F.P. Viehbock, Surf. Sci. 126: 714 (1983).
153. P. T. Dawson and S. A. Petrone, J. Vac. Sci. Technol. 18: 259 (1981).
154. J. Bartella and H. Oechsner, Surf. Sci. 126: 581 (1983).
155. D. C. Peacock, Appl. Surf. Sci. 26: 306 (1986).
156. P. Varga and G. Hetzendorf, Surf. Sci. 162: 544 (1985).
157. S. Aduru, S. Contarini, and J.W. Rabalais, J. Phys. Chem. 90: 1683 (1986).
158. S.F. Ho, S. Contarini, and J.W. Rabalais, J. Phys. Chem. 91: 4779 (1987).
159. S. Contarini, S. Aduru, and J.W. Rabalais, J. Phys. Chem. 90: 3202 (1986).
160. D.K. Murti and R. Kelly, Thin Sol. Films 33: 149 (1976).

161. J. Herion, G. Scharl, and M. Tapiero, Appl. Surf. Sci. 14: 233 (1982-83).
162. K.S. Kim, W.E. Baitinger, and N. Winograd, Surf. Sci. 55: 285 (1976).
163. M.A. Langell, Surf. Sci. 186: 323 (1987).
164. M.W. Chase, C.A. Davies, J.R. Downey, D.J. Frurip, R.A. McDonald, and A.N. Syverud, "JANAF Thermochemical Tables, 3rd ed.", J. Phys. Chem. Ref. Data 14: (1985) Suppl. 1.
165. G. Marletta (Univ. di Catania, Catania, Italy), work in progress.
166. H.J. Fecht and W.L. Johnson, Nature 334: 50 (1988).
167. D.L. Douglass, in Corrosion of Reactor Materials (Intern. Atomic Energy Agency, Vienna, 1962) p. 223.
168. T. Smith, J. Electrochem. Soc. 112: 560 (1965).
169. W.K. Chen and R.A. Swalin, J. Phys. Chem. Sol. 27: 57 (1966).
170. V.P. Elyutin, T.G. Lenskaya, Yu. A. Pavlov, and V.P. Polyakov, Sov. Phys.-Doklady 16: 581 (1972).
171. T.W. Workman, Y.T. Cheng, W.L. Johnson, and M-A. Nicolet, Appl. Phys. Lett. 50: 1485 (1987).
172. G.H. Noh, Chem. Erde 33: 243 (1974). See also Phase diagrams for ceramists, vol. IV, no. 5017 (The Am. Cer. Soc., Columbus, OH, 1981).
173. M. Saidoh, H. Gnaser, and W.O. Hofer, Appl. Phys. A40: 197 (1986).
174. T. Nakayama and N. Itoh, in Desorption Induced by Electronic Transitions, DIET II, eds. W. Brenig and D. Menzel (Springer Verlag, Berlin, 1985) p.237.
175. A. Namiki, S. Cho, and K. Ichige, Jap. J. Appl. Phys. 26: 39 (1987).
176. H.M. Naguib and R. Kelly, J. Phys. Chem. Sol. 33: 1751 (1972).
177. A.B. Christie, I. Sutherland, and J.M. Walls, Vacuum 31: 513 (1981).



## 5

---

# RF Diode Sputter Etching and Deposition

---

**Joseph S. Logan**

### 5.1 INTRODUCTION

#### 5.1.1 History

The process of sputtering and sputter-etching has been studied and used for over 100 years. Sputtering of insulating materials was difficult, using dc, due to the problem of neutralization of the charge carried to the surface of the insulator by the gas ions, with the consequent difficulty of maintaining an accelerating voltage between the surface of the insulator and the plasma. Methods of dealing with this problem include the use of neutralized ion beams and the use of independently supported discharges, both of which involve a degree of complexity greater than conventional dc discharges, and sometimes cannot be applied over large areas. In 1962, Anderson, Mayer, and Wehner (1) following an earlier proposal by Wehner (2) reported the successful use of capacitively coupled high frequency potential to sputter-etch insulating materials.

In 1965, Davidse and Maissel (3) reported the use of a simple parallel-plate diode apparatus using rf power at 13.56 MHz, to sputter-deposit insulating films. Since then, many other variations of electrode geometries, frequencies, and power control methods have been demonstrated in the sputter-deposition or sputter-etching of insulating materials and substrates. All of these applications make use of the large mobility difference between electrons and ions to provide a negative bias between insulator surface and plasma, as explained in section 5-2.

RF sputter-etching has proved to be extremely useful in the semiconductor industry for cleaning of integrated circuit metallization via contact holes, because of the insulating nature of the substrates, and because of the relatively low pressure discharge which minimizes backscattered material. It has also been very useful as a pretreatment to insulating surfaces prior to film deposition, to improve adhesion of the deposited film. Many evaporation and sputter-deposition systems (dc or rf) are provided with the ability to rf sputter-etch prior to deposition. Sputter etching is often used for pattern transfer, but because sputter-etching (dc or rf) is a high-energy process, it is rarely used for patterning

thick films, except when the energy requirements can be lowered by using chemical reaction (RIE) (see later chapter).

The major usefulness of rf sputtering is for the deposition and etching of insulators which cannot easily be done with dc because of substrate and target charging. RF sputter deposition is widely used for insulators such as silicon oxide, aluminum oxide, and other oxides where the substrate temperature limits preclude other techniques, or where compositional control is easier to achieve than for alternate methods and the films or targets are insulating. Large deposition areas can be coated uniformly without the need for substrate motion, and films can be simultaneously ion-bombarded during deposition to improve properties (bias sputtering) as has been done with conductive films/substrates and dc sputtering. Deposition by reactive rf sputtering has the advantage over dc sputtering that the oxides formed on the cathode surface do not charge up and break down in destructive arcs.

Rf sputtering has been reviewed before by several authors; in 1970 by Maissel and Glang (4), in 1971 by Vossen (5), and in 1980 by Chapman (6). This article again reviews the subject in brief, adding more detail on the practical aspects and developments since 1980.

## **5.2 RF DISCHARGES**

### **5.2.1 Breakdown**

Breakdown of a gas by rf electric fields has been studied in the past by many researchers. An extensive discussion of rf discharges is given by Jackson (7) in his review article. In general, rf capacitively coupled discharges can be started and maintained at lower pressures than dc discharges. The minimum pressure at which discharges can be maintained decreases with increasing frequency. The reason for this is that additional ionizing collisions can be induced by the rf field acting on electrons within the plasma to increase their energy.

#### **5.2.2 RF Self-bias**

At each boundary of a capacitively coupled rf discharge, a depletion, or space-charge layer is induced by the rf field, similar to the sheath observed around a probe or at the cathode of a dc discharge. Electrons are repelled from this layer over most of the rf cycle, resulting in a positive time-averaged space charge. To preserve charge neutrality overall, a time-averaged negative charge accumulates on the surface of the insulating boundary. The buildup of this negative charge on the surface of an insulated electrode connected to a high frequency voltage, and in contact with a plasma was first explained simply in a paper by Butler and Kino (8). The key principle is that with no dc path through the insulated electrode, the average flow of ions and electrons to the electrode surface during each cycle must be equal to preserve charge neutrality. The electrons, being highly mobile, can easily provide enough charge over a small fraction of the cycle to neutralize the positive ion charge which flows during the majority of the cycle. Thus, within the first rf cycle, a large electron flow establishes a negative charge at the insulator surface in response to the first positive voltage swing. Subsequently, a nearly steady saturated ion current flows during most of the rf cycle, except during a brief period near the positive

maximum, when a pulse of electron current restores the negative charge lost during the rest of the cycle. The insulator potential relative to the plasma must be positive only a few volts to draw saturation electron current. This means that the average (dc) sheath voltage is normally negative and within a few volts of the peak rf voltage after transients have decayed. This is illustrated in Fig. 1, for a typical plasma density. The two particle currents, ionic and electronic, are plotted vs time, in Fig. 2. Not shown is a large displacement current which corresponds to the oscillation of the sheath-plasma boundary as the sheath field fluctuates. This displacement current is not sinusoidal, due to the non-linear charge-voltage characteristic of the sheath, but is approximately 90 degrees ahead of the sheath voltage.

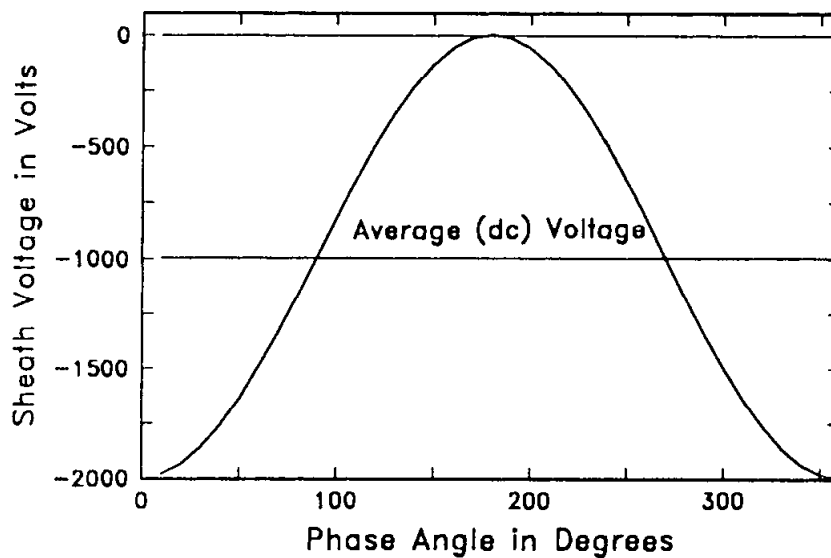


Fig.2.2.1 Voltage at an rf Plasma Boundary

**Figure 1:** Voltage at an rf plasma boundary

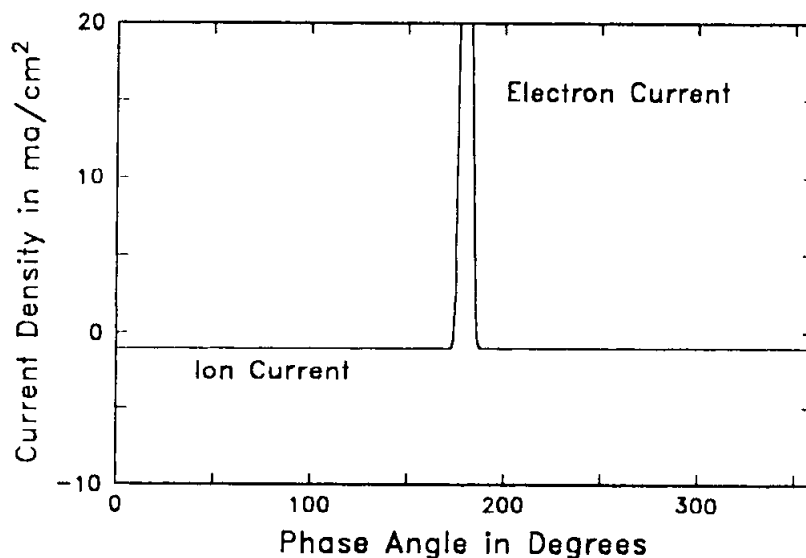


Fig.2.2.2 Current Flow at a rf Plasma Boundary

**Figure 2:** Current flow at an rf plasma boundary

### 5.2.3 Frequency Effect

At low frequencies, most of the applied voltage at the cathode appears across the dielectric target plate, and the remainder of the voltage is easily screened from the plasma by the resultant flow of either electrons or ions during the relatively long cycle time, so that the average potential between insulator surface and plasma is nearly zero. At higher frequency, less of the applied rf voltage appears across the insulator and there is insufficient time for the ion flow to completely neutralize induced charge at the insulator surface during the negative excursions. The large electron flow during positive excursions easily prevents large positive potentials from forming with respect to the plasma. The "crossover" frequency for the self-bias effect is usually estimated to be about 1 MHz, but in fact is somewhat dependent on the target capacitance and external circuit capacitance as well as on the gas composition.

### 5.2.4 Electrical Models

The simplest electrical model of a diode-type system shown in Fig. 3 was first proposed by Koenig and Maissel (9), based on the representation of each sheath boundary as a simple capacitor in parallel with a diode and a resistor. The diode carries the large electron current flow during positive excursions, the resistor represents the energy consumed by the ions falling through the boundary potential, and the capacitor represents the storage of charge (unscreened positive ions) at the boundary in response to the rf voltage difference.

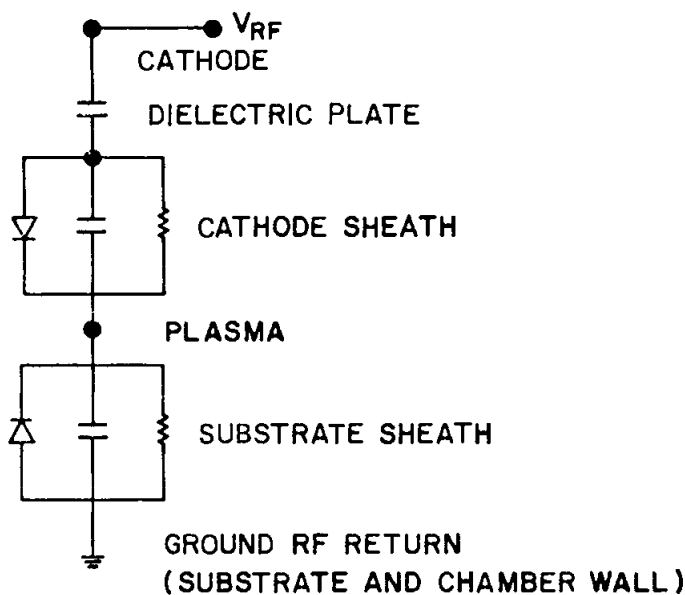


**Figure 3:** Simple model of an rf diode discharge

For most gases at frequencies above 1 MHz, this is a reasonable representation. The largest rf current is the capacitive component. The resistive component is usually less than 20% of the capacitive component, except for electronegative gases, where the discharge can become nearly resistive, with little sheath charge storage.

Koenig estimated the value of the capacitance by using the familiar Child Langmuir equation for a dc sheath to calculate the sheath thickness, and assumed that the

capacitance value is that of a vacuum capacitor with the sheath thickness and area. This simple model was used to show that the dc (and rf) voltage ratio between cathode and substrate sheaths was inversely proportional to the 4th power of the cathode to substrate area ratio in a simple diode system. Coburn (10) tried to verify the area-ratio/voltage-ratio relationship, and found that it was not valid for area-ratios far from unity. Horwitz (11) made detailed measurements in a stainless steel electrode system which showed the complex relationship in Fig. 4. Godyak (12,13) has analyzed a diode system for a restricted range of conditions (frequency, pressure), and developed integral equations for the voltage ratio which must be evaluated numerically. Others (14-16) have recently attempted to model the voltage ratio relationship, with qualitative experimental agreement, but no comprehensive model has evolved as yet which can accurately predict the voltages or voltage ratios for a wide range of system geometries. Nevertheless, the simple model of Fig. 3 is still useful for qualitative understanding of multi-electrode rf discharge systems if one recognizes that 1) the capacitances determine the rf voltage division, and 2) the capacitances are proportional to electrode area and inversely proportional to the square root of peak rf sheath voltage (approximately). Figure 5 is a model of a 3-electrode system (cathode, substrate, and wall) which is applicable to most parallel-plate systems in use today. RF power is normally applied between cathode and wall electrodes, and the resulting discharge carries rf current from the cathode and divides it between the wall and substrate in some ratio, depending on the relative areas of each, and on the return path impedance from the substrate to the wall (which is usually ground). If the substrate is powered from a second generator as in Fig. 6, then the resulting current through the substrate and into the wall can be adjusted to any value depending on the relative phase and power applied, assuming that a common exciter frequency is used. If the applied substrate voltage is in phase with the cathode voltage, then the resulting rf currents will add in the plasma and flow to the wall, giving a larger wall-to-plasma voltage. If the voltage is out of phase with the cathode, then the rf current will subtract in the plasma giving a small wall-to-plasma voltage.

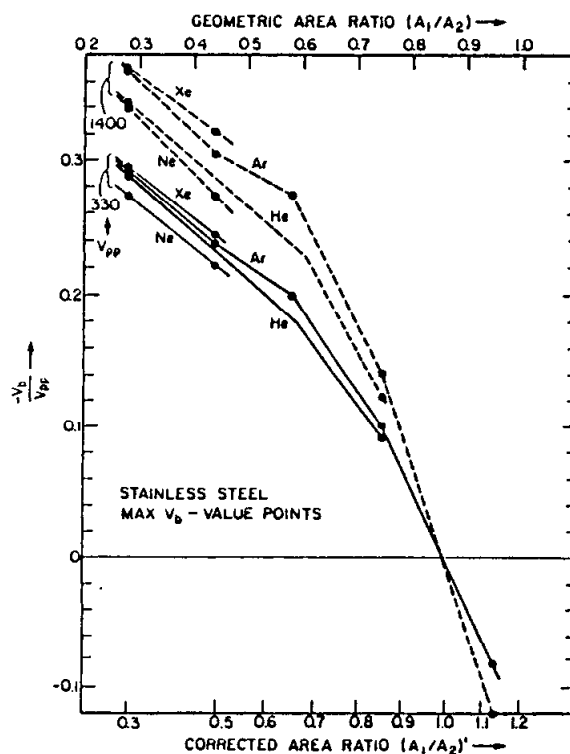


**Figure 4:** Electrode Voltage Ratio vs Electrode Area Ratio (Horwitz, ref. 11)

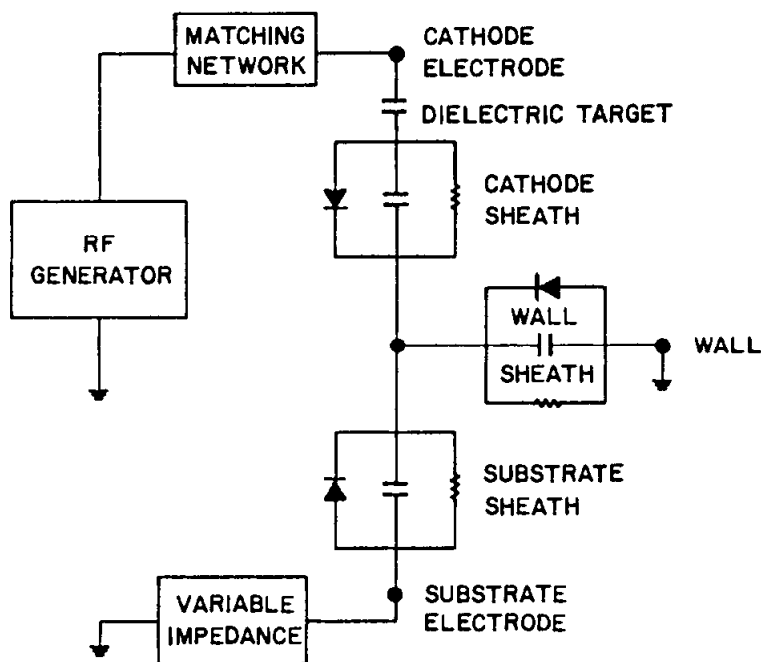


**Figure 5:** Model of a 3-electrode rf discharge (single generator)

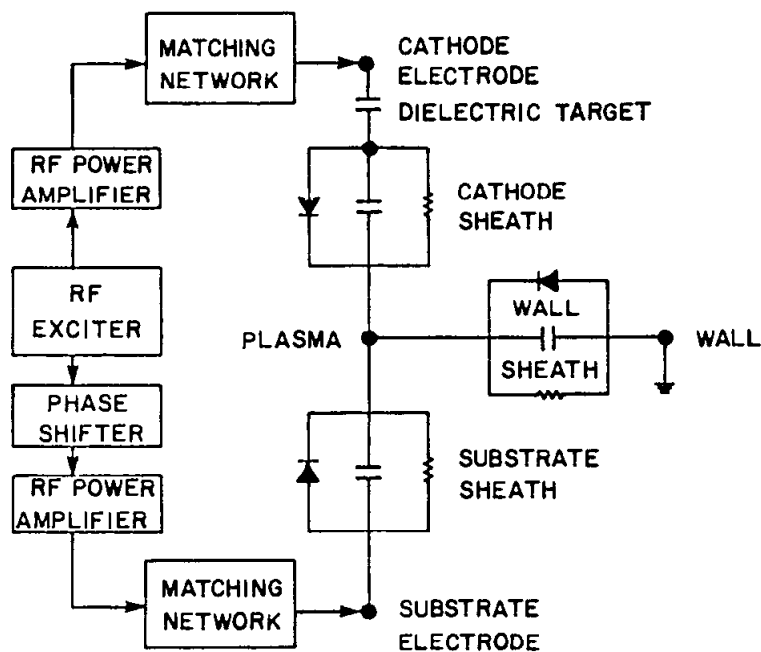


**Figure 6:** Model of a 3-electrode rf system (2 generators)

The important thing to understand about rf sputtering systems operating at frequencies above 1 MHz is that the voltage developed at any boundary with the plasma depends on the rf current density flowing through the boundary and on the plasma density. This rf current flows through the boundary capacitance creating a boundary rf voltage drop to

the plasma. This rf voltage is rectified by the highly mobile electrons so that the average (dc) value developed is approximately equal to the peak rf voltage. Thus, the sputtering (dc) voltage is intimately related to the rf voltage at each electrode or boundary. The sputtering ions respond primarily to the dc field at the boundary, and only very weakly to the rf field. Ions gain sputtering energy up to the average dc voltage at each sheath. At higher pressures ( $> 50$  mTorr), charge exchange collisions in the sheath cause the energy distribution to spread to lower energies, which can lower the total yield of sputtered material.

### 5.3 EQUIPMENT

#### 5.3.1 System Designs

The earliest rf deposition systems in practical use were simple diode parallel-plate systems, as shown schematically in Fig. 7. Use is sometimes made of axial magnetic field to enhance the plasma density, and a frequency of 13.56 MHz is widely used for excitation because of the ease of compliance with FCC rules and ready availability of equipment. The rf power is typically connected to the cathode electrode through a cable and a matching network which serves to maximize power transfer from the rf generator.

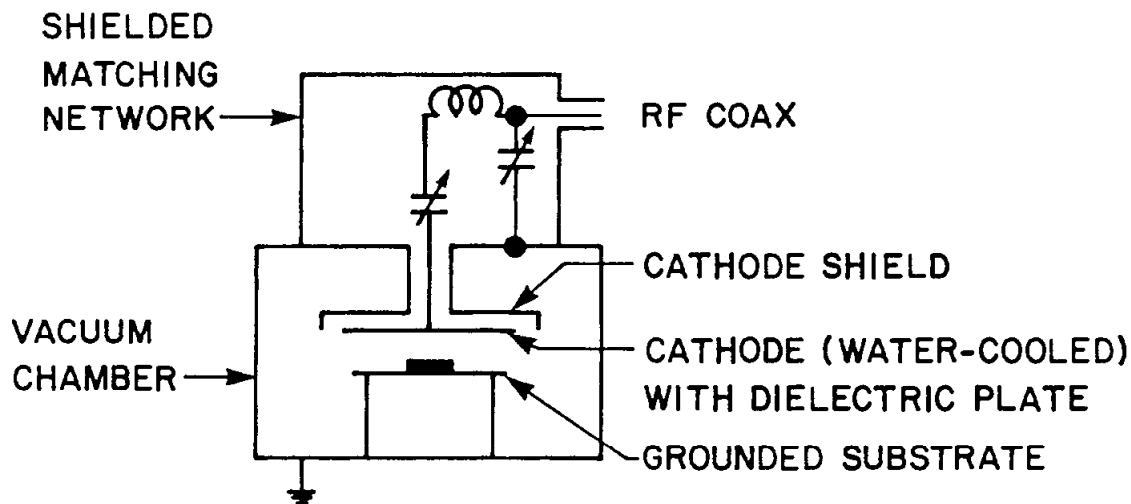


**Figure 7:** Early diode rf sputtering system

In a deposition system, the substrate may be placed on a grounded surface, typically at a spacing of 2 to 5 cm from the dielectric source. For some applications, it is desirable to bias (sputter-etch) the substrate during deposition, so the substrate support is constructed like a second cathode, as in Fig. 8. Cooling is often required, because of the ion and electron bombardment at the substrate, and heat transfer between the substrate and its support can be a problem.

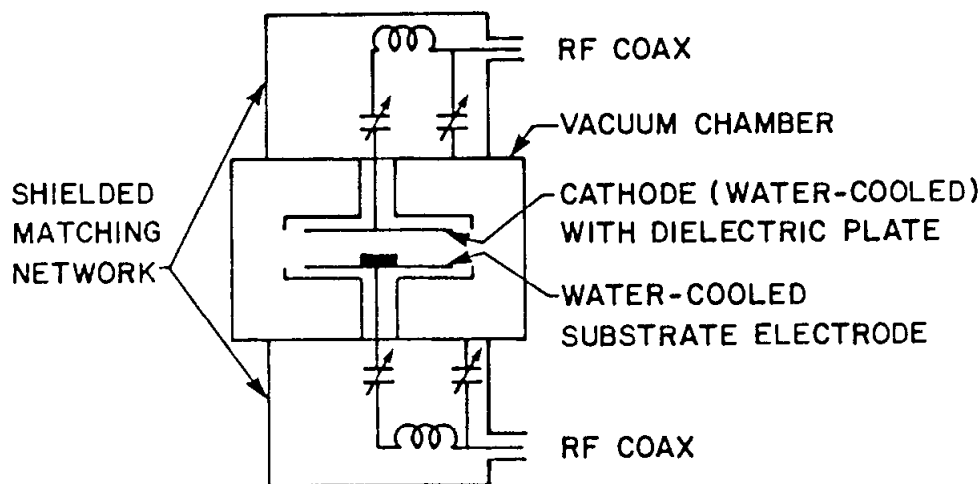


**Figure 8:** Substrate bias added to diode system

For rf etching purposes, rf power is applied to the substrate electrode, usually a water-cooled cathode on the bottom as in Fig. 9. Additionally, a counter-electrode, sometimes called a "catcher" (17) is often used in close proximity opposite the substrate to be etched, in order to minimize backscattered material. The "catcher" may contain a pattern of deep holes or annular rings in which to trap sputtered material.

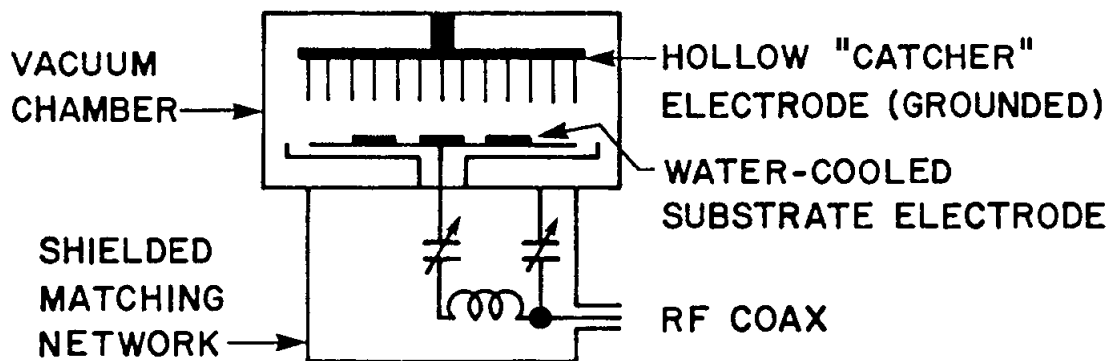


**Figure 9:** Sputter-etch system

As with dc sputtering systems, other geometries can be used, such as cylindrical or rectangular cathodes, but as system size increases, there is the possibility that non-uniformities in sputtering will be experienced due to either inductive voltage drops, or due to standing waves in the plasma itself. The author has had experience with a small parallel plate system at a frequency of 40 MHz, in which a non-symmetrical rf connection to the cathode resulted in a deposition profile which was non-symmetric (higher rate closer to the point of rf attachment). Also, a large cylindrical rf sputtering system with a cathode diameter of 20 cm and length 1 m was found to have a significant sputtering rate variation along the axis when used with an axial magnetic field at 13 MHz. In the case of the small parallel-plate system, the non-uniformity could be attributed to an inductive voltage drop, and in the coaxial case at lower frequency, standing waves in the plasma is the more likely reason.



An unusual rf system design was reported by Holland (18) in which the target is attached to a split cathode. The cathode is then driven by a balanced rf drive (i.e. ungrounded but equal amplitude, opposite phase) as shown schematically in Fig. 10. This arrangement allows a grounded substrate to be biased with respect to the plasma by unbalancing the drive.

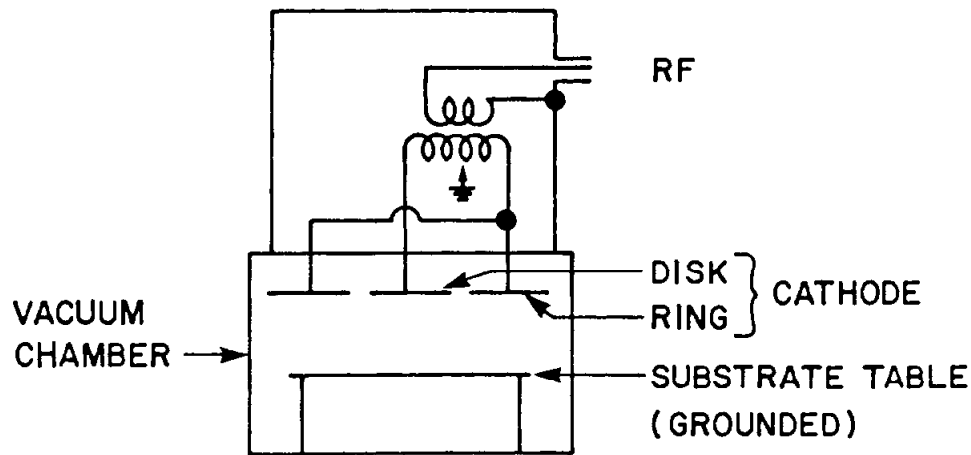


**Figure 10:** Balanced rf drive system

### 5.3.2 Cathode Design

In most systems, the target material is a plate which is thermally bonded to a water-cooled metal electrode. The bonding agent may be indium or indium-tin solder, or it may be a conductive epoxy. In some applications, a thermal grease may be used. A grounded metal shield surrounds the metal electrode at a close spacing, typically 3 mm, to prevent sputtering of the metal electrode. Often, the target plate is allowed to extend beyond the edge of the metal electrode to better shield the metal from sputtering. Alternatively, shielding can be accomplished by burying the metal electrode in a dielectric cavity as in Fig. 11 which minimizes stray capacitance. Another alternative is to incorporate the metal electrode as part of the chamber wall, as in Fig. 12. This last alternative substantially reduces stray capacitance-induced losses, especially for large diameters.

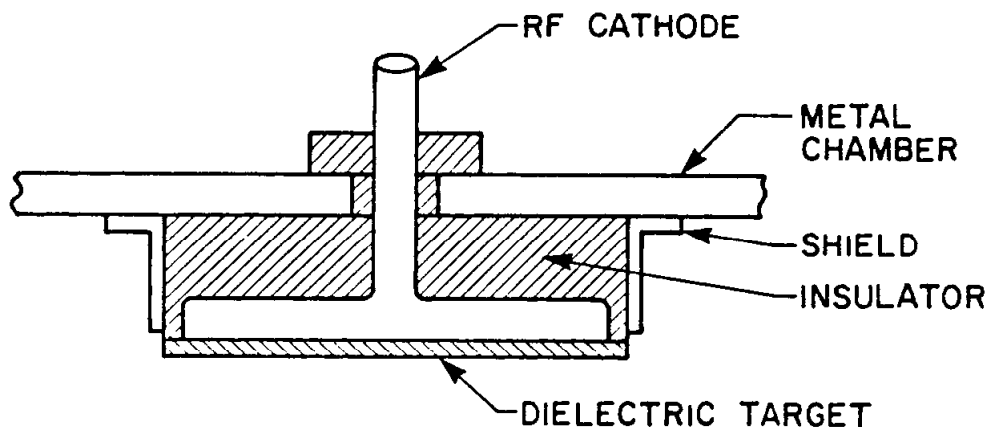


**Figure 11:** Dielectrically shielded cathode

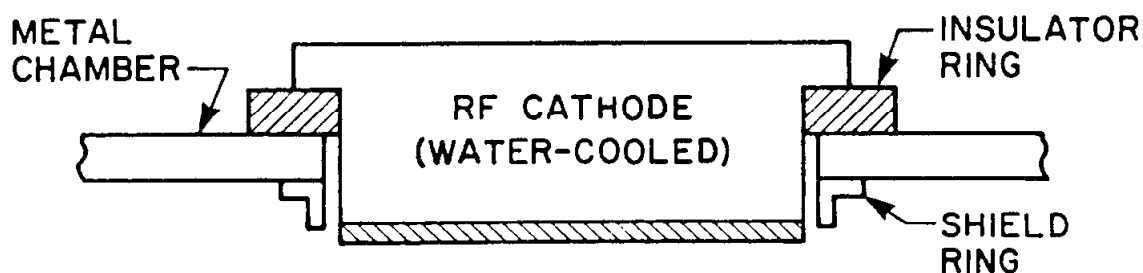


**Figure 12:** Drop-in rf cathode

A large amount of heat may be deposited at the target surface by the bombarding ions, so it is important to have adequate cooling. In extreme cases of high power operation, the target surface temperature may exceed the sublimation temperature (19), and material may be evaporated as well as sputtered. For this reason, with poor thermal conductors it is preferable to use a thin target, although there must be a practical compromise with the useful life of the target plate, and with the need for mechanical strength. Dielectric glasses such as  $\text{SiO}_2$  are typically used in thicknesses of about 6 mm. Lossy materials may be destroyed by self-heating when used as an rf cathode, if not thin enough to allow adequate cooling.

### 5.3.3 RF Power Supply

In most modern equipment, rf power is supplied by a physically separate commercial generator, crystal-controlled, which is coupled to the vacuum deposition or etching apparatus by a coaxial cable. Since the electrical impedance of the discharge is usually much lower than the cable impedance (typically 50 ohm cable), a matching network must be provided to transform the discharge impedance to the cable impedance. This matching network is normally constructed or mounted in intimate contact with the vacuum chamber cover or plate which contains the rf electrode to allow proper shielding from stray radiation. Thus, the coaxial cable is connected to a bulkhead fitting in the shield box covering the matching network/system cover.

In the case of a separately biased substrate electrode, rf power can be supplied in a number of different ways. The most common way is to provide a separate power amplifier, driven by a common exciter, which is then coupled by rf coaxial cable to a matching network at the substrate electrode mounting plate and shielded in a manner similar to the cathode matching network (Fig. 13). This provides the ability to adjust the phase of substrate voltage relative to cathode voltage by introducing an adjustable delay-line between exciter and power amplifier, and an independent control of substrate power. It also adds a degree of rf isolation between the substrate circuit and the cathode circuit, but the two are usually coupled anyway by a common plasma.

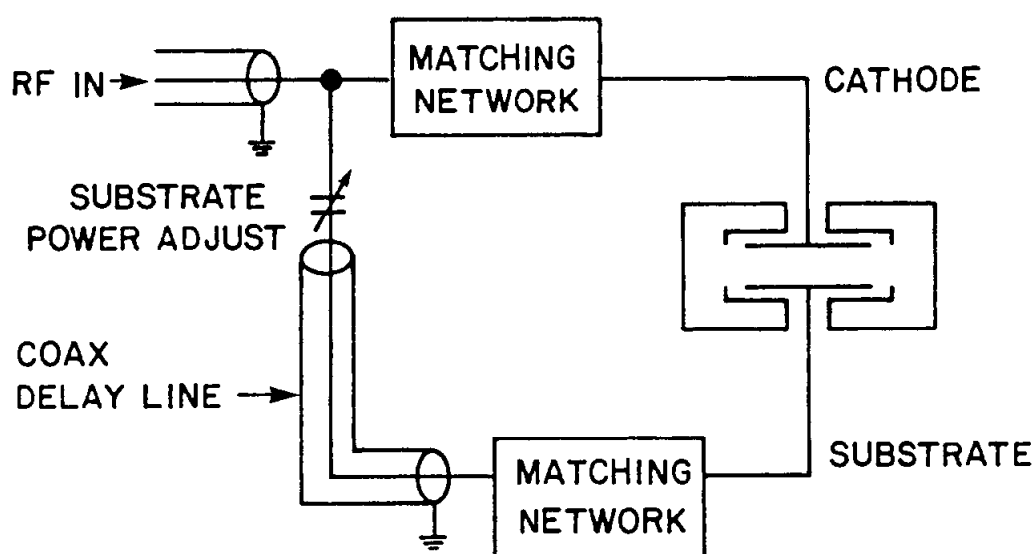


**Figure 13:** Power-splitting rf drive

Less expensive passive power-splitting networks such as the one shown in Fig. 13 can be used, but may result in regions of instability and very sensitive tuning due to the interdependence of cathode and substrate power. A simpler method for substrate bias adjustment which does not require a separate cable and full matching network is the tuned substrate (20) method of Fig. 14. Here there is no independent phase and magnitude adjustment, but a useful range of magnitude of substrate bias can be obtained simply by adjusting the impedance between substrate and ground. It is important to minimize the stray capacitance in the substrate assembly and to minimize wall area to get the greatest possible range of substrate bias.

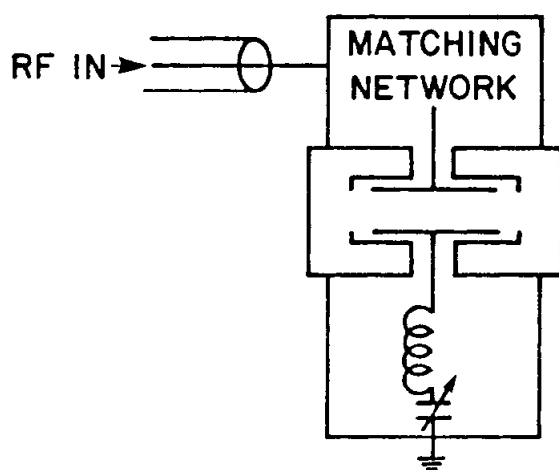


**Figure 14:** Tuned substrate bias adjustment

### 5.3.4 Matching Networks

In order to deliver rf power effectively through a coaxial transmission line, it is necessary to transform the load impedance to match the coaxial line impedance (usually 50 ohms resistive). A very commonly used network for this purpose is shown in Fig. 15. Over a wide range of frequencies, the load impedance is capacitive, dominated by the

cathode sheath charge storage, and by the stray capacitances of the electrode structure itself.

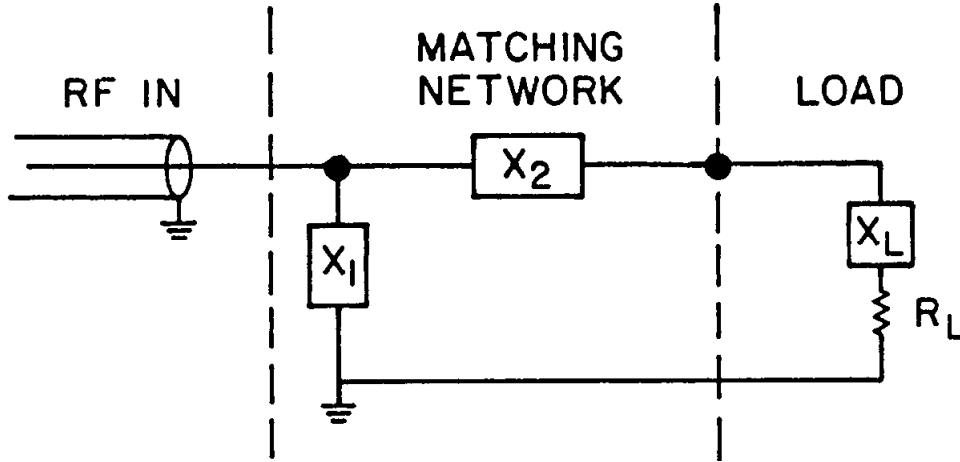


**Figure 15:** Common L-type matching network

The equations that predict the appropriate series and shunt elements for this matching network to transform a load whose series equivalent representation is  $R_L$  and  $X_L$ , are given as follows:

$$X_2 = -X_L + \sqrt{(R_L R_0 - R_L^2)}$$

$$X_1 = \frac{-R_0}{\sqrt{\left(\frac{R_0}{R_L}\right) - 1}}$$

$R_0$  is the coaxial line impedance, usually 50 ohms. The elements  $X_1$  and  $X_2$  are as shown in Fig. 15 and are usually capacitive and inductive, respectively. The signs associated with these reactances are positive for inductive and negative for capacitive elements. It is important to note that the network cannot transform loads with resistive (series) parts which are in excess of the coaxial line impedance. This is not usually the case, but if it should be, the L-network can be reversed.

Values for the discharge load impedance have been measured by various researchers (21,22). These values can be used to predict values for the matching network, by adapting them to a specific system geometry (electrode areas, stray capacitances and inductances), and using the equations given above.

## 5.4 RF SPUTTER-DEPOSITION

### 5.4.1 Direct rf Sputter-Deposition

The widest use of rf sputter deposition has been the direct sputtering of insulating compounds, such as  $\text{SiO}_2$ ,  $\text{Al}_2\text{O}_3$ , BN,  $\text{Si}_3\text{N}_4$ ,  $\text{Ta}_2\text{O}_5$ ,  $\text{HfO}_2$ , and other oxides and glasses. These have been studied for a variety of uses. The high dielectric constant materials are attractive for capacitors (23) and the low dielectric constant materials are useful for thin

film circuit applications on silicon integrated circuits as well as on other substrates. Another common use is for protective coatings.

In many cases the target materials can be obtained in reasonably pure form as a glassy or sintered disk, which may be attached to a metal electrode as described in section 5.3.2. This is the case with  $\text{SiO}_2$ ,  $\text{Al}_2\text{O}_3$ ,  $\text{Cr}_2\text{O}_3$ , and glasses such as Pyrex ®, which are easily joined to a metal backing plate. In other cases, the brittleness of the target material may create mechanical problems either initially, or during use. These problems are not unique to rf sputtered materials. However, one problem that is unique to rf sputtering is the problem of dielectric heating by the rf current in the target. If the material is inherently lossy at the rf frequency used, then heat will be developed which can cause destructive failure of the target itself or of the joint to the backing plate. Materials which have been rf sputtered successfully in spite of their relatively high loss factor at 13.56 MHz are Pyrex ®, graphite, and silicon.

As with dc sputtering, argon is most frequently used as the sputtering gas for the same reasons. The mass of argon is high enough so that there is little interaction of the rf field with argon ions at 13.56 MHz. Tsui (24) has calculated this interaction and shown that light gases such as helium will interact with the rf field at 13 MHz sufficiently to cause a significant spread in the arrival energies of the ions, but not much for argon. Xenon, Neon, and Krypton have all been used by experimenters, but do not appear to have sufficiently higher sputtering yields to justify the higher costs in some cases, nor even a higher yield in others.

#### 5.4.2 Film Composition

Since there are practically no elemental insulators of interest, most insulator sputter-deposition applications involve compounds, usually oxides or nitrides, and occasionally carbides or high resistivity semiconductor compounds where there may be significant difficulty in carrying out dc sputtering, or where the lower pressure discharge is attractive to enhance film purity and reduce backscattering. Complex compounds are rarely transferred from the target to the substrate in exactly the original composition. Nevertheless, the film composition in many cases is sufficiently close to that of the target that no adjustment is necessary for useful properties. This is the case with  $\text{SiO}_2$  and  $\text{Al}_2\text{O}_3$ . In other cases where one component is particularly unstable, eg. glasses containing lead oxides, a significant loss of one component may be found, requiring either that the substrate be cooled, or that excess material be introduced either in the target or in the gas stream. Often, the addition of oxygen to correct stoichiometry, or for other reasons results in a reduction of the target removal rate. This is evident in the sputtering of  $\text{SiO}_2$ ,  $\text{Al}_2\text{O}_3$ , and other materials. Figure 16 shows the effect of oxygen additions on the deposition rate of  $\text{SiO}_2$  (25). This depression of deposition rate has been observed for other compounds as well (26). The mechanism has not been confirmed, but it has been suggested that the oxygen restores surface stoichiometry of the target, thereby increasing the binding energy of surface atoms compared to that of a disturbed surface.

#### 5.4.3 Substrate Bias Effects

Bombardment of growing films is well known from dc sputtering work to be useful in controlling film properties (27), so it is no surprise that the same is true of rf sputtered films. In the case of dc sputtering, one can easily control the resputtering bias down to

the floating potential (usually a few volts) with the dc power supply. In the case of rf sputtering, the actual bias between film and plasma is not easily measurable directly, and is very dependent on the chamber geometry as discussed in section 5.2.4. With a simple diode system using a large area ratio between "anode" (substrate + wall) and cathode, there will be a minimum dc bias developed providing that the substrate connection to ground (wall) is a low-inductance connection. This is not always the case. Many commercial systems have a rather long stem connection to the substrate table, and simple external "grounding" of this stem with a wire or strap does not produce the desired electrical condition. Indeed, it is sometimes possible to increase the bias by such action, because the inductance represented by the ground strap and stem actually resonates with the sheath capacitance in series to produce a large rf current flow, resulting in a large sheath voltage. Even if the substrate is dc-grounded, the plasma potential will be forced up to satisfy equilibrium conditions. For this reason, it is difficult to guarantee near-zero bombardment of the substrate in an rf sputter-deposition system, as might be desirable for depositing crystalline materials.

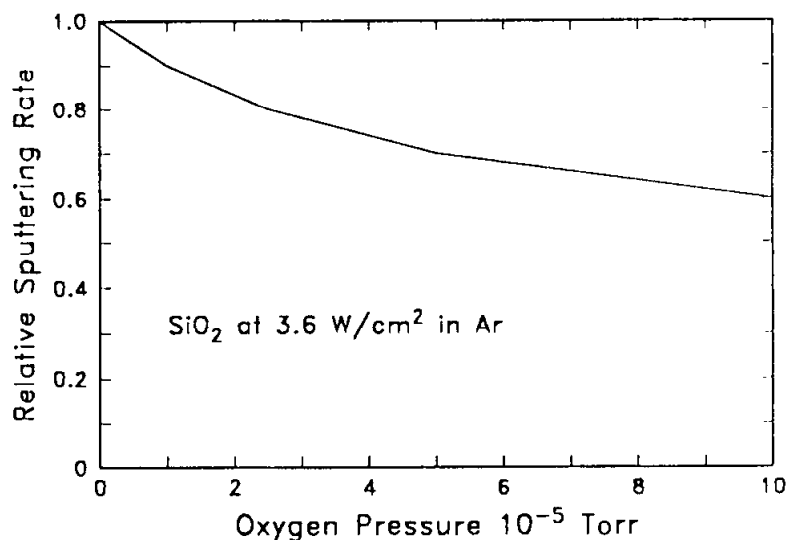


**Figure 16:** Effect of oxygen on sputtering rate (Jones, ref. 25)

More often, however, it is desirable to increase the bias at the substrate, which can be done by the methods mentioned in section 3.1. In the case of rf sputtered  $\text{SiO}_2$ , substrate bias has been found to improve dielectric breakdown (28), decrease chemical etch rate (26), and can be used for planarization (29). Also, bias has been found to relate to stress (30), and to trapped gas (31).

#### 5.4.4 Material Transport and Uniformity

The physics governing the emission and transport of material is the same for both rf and dc sputtering. With rf sputtering, however, the lower pressure range which is normally used reduces the number of collisions in transit, so that the efficiency of transport is usually higher than for dc diode sputtering and the energy of arrival of species is higher because of the fewer collisions.

The use of an axial magnetic field to enhance the plasma density has been found to increase the rate of deposition (3) for a fixed rf power input. This is due to operating at

a more energy-efficient point of the sputter yield vs energy curve (lower voltage). However, the axial magnetic field has been observed to create a radially non-uniform plasma density, which results in more intense plasma near the perimeter of a circular target. The target becomes more like a ring source as a result, and the deposition pattern reflects that change, rising toward the edge. The pattern can be flattened by increasing the separation between target and substrate, which creates more edge loss. If the system is scaled to a larger diameter, then the required spacing for best uniformity is increased. This is not true of the case without axial magnetic field, where the optimum spacing is almost independent of target diameter.

## **5.5 SPUTTER ETCHING APPLICATIONS**

### **5.5.1 Comparison to dc Sputter-Etching**

Sputter-etching using rf power removes material by the same fundamental mechanisms as with dc sputter-etching. However, rf sputter-etching can be used with insulators as well as with metals, and as with rf sputter-deposition, lower pressures can be used, allowing easier transport of material (less backscattering (32)). The equipment used is different only in that the cathode should be adequately shielded and stray capacitance should be minimized. For minimum backscattering, a "catcher" plate (17) may be used, spaced as closely as possible. The "catcher" should have many deep cavities, such as a honeycomb structure, and should be well grounded with low-inductance wide straps or foils to prevent self-bias.

### **5.5.2 Surface Cleaning**

Probably the simplest and earliest applications of rf sputter-cleaning is the removal of surface oxides on metals for contact purposes. This has been shown to be exceptionally effective for making low-resistance contact between successive aluminum thin-film wiring layers on semiconductor devices. Bauer (33) showed that the measured distribution of contact resistances shifted dramatically downward when rf sputter-cleaning was done in-situ prior to evaporation of the next aluminum contact film. This has been shown to be due to the removal of a native oxide layer of 2 to 3 nm thickness. The residual gas level present during the sputter-cleaning and immediately after is critical, as the water-vapor or oxygen can quickly re-form the native oxide.

There are many other examples of the use of rf sputter-cleaning for both oxide removal and for adhesion of subsequent layers. Since the treatment is usually for a short time, cooling of the substrate is not necessary, but can be a problem in some cases of temperature-sensitive substrates. The author has found that a temperature of 200 °C is reached in a time of 3 minutes for silicon substrates 0.38 mm thick subjected to an input rf power density of 0.4 W/cm<sup>2</sup> in 8 mT Ar.

### **5.5.3 Patterning**

The sputter-yield of most materials is not widely different, so that it is necessary usually to use a masking material that has a thickness comparable to the thickness of the material being etched, or greater. Sputter-yields of a number of materials of interest is shown in Table 1 (34). Some of the material will be re-deposited on the mask edges, and

can remain when the mask is removed if it is sufficiently thick and survives the mask removal process. For this reason, patterning of thick layers by sputter-etching is not usually practical and is better accomplished by reactive ion etching. In addition, heat developed by the sputter-etching can harden the mask material and make it difficult to remove.

**Table 1:** Relative sputtering rates of some materials (34).

Material	Sputter Etch Rate (Ar <sup>+</sup> , 500 eV, 1 mA/cm <sup>2</sup> ) Å/ min
Al <sub>2</sub> O <sub>3</sub>	80-130
Cr <sub>2</sub> O <sub>3</sub>	50
FeO	450-490
SiO <sub>2</sub>	260-400
Y <sub>2</sub> O <sub>3</sub>	75
AZ1350 resist	200-250
In <sub>2</sub> O <sub>3</sub> /SnO <sub>2</sub>	80-200
Si <sub>3</sub> N <sub>4</sub>	250
LiNbO <sub>3</sub>	390-420
Si	200-380

#### 5.5.4 Uniformity

In general, uniform removal across the diameter of a parallel-plate diode etcher is readily obtained, provided that the pressure-spacing product is not too low. The usual problem is near the edge of the electrode, where the ground shield configuration can increase the etch rate by "focussing" the ion flux. Extending the ground shield above the plane of the electrode by a few mm usually improves the situation. This cuts off the "focussed" ions.

### 5.6 PRACTICAL MATTERS

#### 5.6.1 Power Measurements and Power Loss

Power is usually measured with coaxial line elements in the coaxial feed to the matching network. Of necessity, the power measurement includes losses in the matching network which can sometimes be significant. Excessive power loss can occur in rf sputtering equipment, usually due to poor matching network design, possibly aggravated by high stray capacitance in the cathode design. Loss is almost always concentrated in the matching network inductance, although connecting straps and associated hardware may also be a problem. It is common practice to water-cool the inductor in high power applications. In general, one should avoid the use of stainless steel screws in any rf current-carrying path. Brass screws are usually quite adequate. The inductor carries not only the discharge rf current, but also the rf current to the electrode shield. The shield current is often much greater than the discharge current.



A reasonable measurement of the loss can be made using an rf voltage probe on the cathode connection and plotting power input vs rf voltage with the discharge on and without a discharge. A discharge can be suppressed by working at atmospheric pressure or at very low pressure, although it is sometimes difficult to completely stop the discharge at the chamber base pressure. An example of such a measurement is shown in Fig. 17 for a small sputtering system. The difference between the curves at constant voltage is (approximately) the net power delivered to the discharge, and the lower curve represents the power loss at a given voltage.

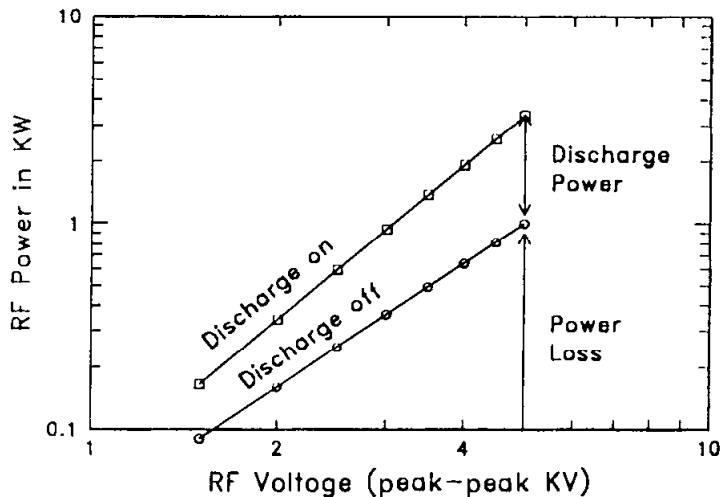


**Figure 17:** Measurement of rf Power Losses

### 5.6.2 Current Measurement

It is not possible to measure the ion current in an rf discharge directly in the cathode circuit, since the dielectric target is insulating and it is masked by displacement current and electron current. Langmuir probes have been used by many investigators, but it is difficult to prevent rf current flow in the probe circuit. A small probe area and effective decoupling of the discharge from the wires are essential. To this end, thick glass tubing can be used for shielding the wires. Equally important are a very low capacitance feed-through and a good rf inductor in series to prevent rf current flow to ground in the probe circuit.

The ion current density can be estimated from the power delivered to the discharge and the sheath voltages, assuming a simple diode system of unequal areas. A rf probe in the plasma can sense the rf plasma potential. Power can be apportioned to each sheath according to the sheath rf voltage and the sheath area, correcting for voltage drop in the dielectric target. Then ion current should be approximately the ratio of sheath power density divided by sheath peak voltage.

RF current transformers can be obtained to measure rf current flowing into the cathode or substrate electrode terminals. Using this current, and subtracting stray capacitance currents (from discharge-off measurements) gives the net rf current into the electrode. RF current into the cathode sheath can be used to calculate the rf voltage drop in the dielectric target plate.

### 5.6.3 Voltage Measurement

Sometimes a dc voltmeter is connected to the cathode circuit through a suitable rf isolation inductor. This voltage may indicate the target surface potential through surface leakage at the target edge, but it is often unreliable for small shield gaps.

RF voltage is usually measured with a capacitance divider probe located as close as possible to the rf feedthrough. The voltage so measured has two principal errors; first the rf drop in the target plate and second the inductive voltage drop in the conductor between the measuring point and the cathode electrode. The voltage drop in the target plate is a capacitive drop and therefore normally adds to the target surface potential, and the voltage drop in the conductor is an inductive drop which normally reduces the rf voltage. If the conductor is long enough, then it can actually reduce the voltage to zero, or even reverse the phase. Calibration for these errors can be done but involves making internal rf voltage measurements. Many applications do not require absolute calibration, so that the rf voltage measurement is used as a control monitor to reproduce conditions.

### 5.6.4 Rate Measurement

Deposition rates are usually not possible to measure in an rf system with a conventional crystal rate monitor, unless the monitor can be closely coupled to ground and provided with special shielding. If the substrate is biased, such a monitor does not represent the net flux of material, but can be proportional to the incident flux. Another method useful for transparent films on reflective substrates is to measure reflectance variation to sense the optical thickness, such as is commonly done in the optical coating industry. This method is non-intrusive and can be quite accurate.

### 5.6.5 RF Leakage

All rf sputtering or etching equipment should be provided with complete electrostatic confinement of the discharge and its electrical connections to prevent unauthorized or unsafe leakage of rf energy. This usually means that the vacuum chamber should be metal, or surrounded by metal screen, and that the matching network components be contained in a metal box in intimate contact with the chamber walls or electrode plate. A low-inductance path must be provided for rf return currents within the discharge chamber. If, for example, a substrate electrode is attached to a chamber bottom plate, which is prevented by an O-ring from making metal-to-metal contact with the chamber, then rf currents cannot return inside the vacuum chamber to the cathode plate, and will seek alternative paths externally, usually resulting in instrument rf noise as well as perceptible rf voltage differences at the gap.

## 5.7 REFERENCES

1. G.S.Anderson, W.N.Mayer and G.K.Weohner J. Appl. Phys. 33: 2291 (1962). J. Vac. Sci. Tech. 4: 33 (1967).
2. G.K.Weohner Advances in Electronics and Electron Physics, vol. 7 (Academic Press Inc., New York) p. 239 (1955).
3. P.D.Davidse and L.I.Maissel Trans. 3rd Int. Vac. Cong. 3: (1965).

4. L.I. Maissel and R. Glang, Handbook of Thin Film Technology (McGraw Hill, New York, 1970).
5. J.L. Vossen "Control of Film Properties by rf-Sputtering Techniques" J. Vac. Sci. Tech. 8: 5 (1971)
6. B.N. Chapman, Glow Discharge Processes; Sputtering and Plasma Etching (John Wiley & Sons, New York, 1980).
7. G.N. Jackson, "R.F. Sputtering" Thin Solid Films 5: 209-246 (1970).
8. H.S. Butler and G.S. Kino Phys. Fluids 67: 1346-1355 (1963).
9. H.R. Koenig and L.I. Maissel, "Application of RF Discharges to Sputtering" IBM J. Res. Dev. 14: 168-171 (1970).
10. J.W. Coburn and E. Kay, J. Appl. Phys. 43: 4965 (1972).
11. C.M. Horwitz "Rf Sputtering-Voltage Division Between Two Electrodes" J. Vac. Sci. Technol. A1: 60-68 (1983).
12. V.A. Godyak and A.A. Kuzovnikov, Sov. J. Plasma Phys. 1: 276-280 (1975).
13. V.A. Godyak, "Steady-State Low Pressure RF Discharge" Sov. J. Plasma Physics 2: 78-85 (1976).
14. S.E. Savas, "Estimation of Ion Impact Energies and Electrode Self-bias Voltage in Capacitive rf Discharges" MRS Symposium, Anaheim (1987).
15. M.S. Barnes, T.J. Colter and M.E. Elta, "Large-signal Time Domain Modelling of Low-pressure rf Glow Discharges" J. Appl. Phys. 61: 81-89 (1987).
16. K. Suzuki, K. Ninomiya, S. Nishimatsu, J.W. Thoman Jr. and J.I. Steinfeld "Analytical Investigation of Plasma and Electrode Potentials in a Diode Type rf Discharge" Jap. J. Appl. Phys. 25: 1569-1574 (1986).
17. L.I. Maissel, C.L. Standley and L.V. Gregor, "Sputter Etching of Heterogeneous Surfaces" IBM J. Res. and Dev. 16: 67 (1972).
18. L. Holland, T.I. Putner and G.N. Jackson J. Sci. Instruments 1: 32 (1968).
19. D.H. Grantham, E.L. Pradis and D.J. Quinn, "High-Rate rf Sputtering System" J. Vac. Sci. Tech. 7: 343-346 (1970).
20. J.S. Logan, "Control of rf Sputtered Film Properties Through Substrate Tuning" IBM J. Res. Develop. 14: 172-175 (1970).
21. J.S. Logan, N.M. Mazza and P.D. Davidse, "Electrical Characterization of Radio-Frequency Sputtering Gas Discharge" J. Vac. Sci. Tech. 6: 120-123 (1969).
22. A.J. van Roosmalen, W.G.M. van den Hoek and H. Kalter, "Electrical Properties of Planar rf Discharges for Dry Etching" J. Appl. Phys. 58: 653-658 (1985).
23. W.B. Pennebaker, "RF Sputtered Strontium Titanate Films" IBM J. Res. Dev. 13: 686-695 (1969).
24. R.T.C. Tsui, "Calculation of Ion Bombarding Energy and Its Distribution in rf Sputtering" Phys. Rev. 168: 107-113 (1968).
25. R.E. Jones, H.F. Winters and L.I. Maissel, "Effect of Oxygen on the rf Sputtering Rate of SiO<sub>2</sub>" J. Vac. Sci. Tech. 5: 84 (1968).
26. D.M. Mattox and G.J. Kominiak "Physical Properties of Thick Sputter-Deposited Glass Films" J. Electrochem. Soc. 120: 1535-1539 (1973).

27. L.I. Maissel and P.M. Schaible, "Thin Films Deposited by Bias Sputtering" J. Appl. Phys. 36: 237-242 (1965).
28. H.-U. Schreiber and E. Froschle, "High Quality RF-Sputtered Silicon Dioxide Layers" J. Electrochem. Soc. 123: 30-33 (1976).
29. C.Y. Ting, V.J. Vivalda and H.G. Schaeffer, "Study of Planarized Sputter-deposited SiO<sub>2</sub>" J. Vac. Sci. Tech. 15: (1978).
30. J.S. Logan, F. Jones, J. Costable and J.E. Lucy, "Radio Frequency Sputter Deposition of SiO<sub>2</sub> Films at High Rate" J. Vac. Sci. Technol. A5: 1879-1882 (1987).
31. W. Hoffmeister and M. Zuegel, "Determination of the Argon Content of Sputtered SiO<sub>2</sub> Films by X-Ray Fluorescence" Thin Solid Films 3: 35-40 (1969).
32. J.L. Vossen, J.J. O'Neill Jr., K.M. Finlayson and L.J. Royer, "Backscattering of Material Emitted from RF-Sputtering Targets" RCA Review 31: 293-305 (1970).
33. H.J. Bauer, "In-situ Sputter Cleaning of Contacts for Multilayer Chip Metallization" Proc. of Eighth Int. Vacuum Congress 1: 649 (1980).
34. "Periodic Table of the Elements with Ion Beam Etch and Sputter Rates" Commonwealth Scientific Corp., Alexandria, Virginia (1985).

---

## Magnetron Plasma Deposition Processes

---

**Stephen M. Rossnagel**

### 6.1 INTRODUCTION

Magnetron sputtering devices have become very widely used and accepted in the past decade. Magnetrons are routinely used to rapidly deposit thin metal films in a broad range of applications, from architectural glass and food packaging to thin film microelectronics. Magnetron-like effects are also used in high-rate sputter and reactive etching devices. Magnetrons, as they are currently used for plasma-based sputtering applications, were developed approximately 20 years ago. Perhaps the most useful description available has been the work of Thornton and Penfold (1), in Vossen and Kern's book dating from the late '70s.

Magnetrons are a class of cold cathode discharge devices used in generally a diode mode. The plasma is initiated between the cathode and the anode at pressures in the mTorr range by the application of a high voltage, which can be either dc or rf. The plasma is sustained by the ionization caused by secondary electrons emitted from the cathode due to ion bombardment which are accelerated into the plasma across the cathode sheath. What differentiates a magnetron cathode from a conventional diode cathode is the presence of a magnetic field. The magnetic field in the magnetron is oriented parallel to the cathode surface. The local polarity of the magnetic field is oriented such that the  $\mathbf{ExB}$  drift paths of the emitted secondary electrons form a closed loop (Fig. 1). Due to the increased confinement of the secondary electrons in this  $\mathbf{ExB}$  drift loop compared to a dc or rf diode device, the plasma density will be much higher, often by an order of magnitude or more, than a conventional rf or dc diode plasma. The result of the high plasma density and its proximity to the cathode is a high current, relatively low voltage discharge. Typical discharge parameters for a magnetron might be a voltage of 500V and a current of 5 Amperes, whereas a non-magnetized diode might operate at 2500V and 0.5 amperes.

Due to the effective trapping of the energetic secondaries close to the cathode, a high plasma density can be sustained at significantly lower chamber pressures than a similar

power rf or dc diode plasma. A magnetron operates at a pressure ranging from about 1-2 mTorr (0.3 Pa) to 30-40 mTorr (4-5.5 Pa), whereas a typical rf diode might operate at 15-200 mTorr (2 to 25 Pa). The low operating pressure results in a significant reduction in gas scattering between the sputtered atoms and the background gas. The result of this reduction is an effective increase in the average kinetic energy of the sputtered atom (less thermalization) and an increase in the probability of atom transport from the cathode to the substrate.

The result of the high discharge currents is the ability to sputter the cathode at a high rate. Deposition rates on surfaces within 5-10 cm. from the cathode may be as high as several microns/minute for high sputter yield materials. Usually, the typical limiting factor to the maximum deposition rate in a magnetron device is the ability to cool the cathode.

Magnetrons have been developed in a wide range of geometries; each of which satisfies the requirement that the  $\mathbf{ExB}$  drift path forms a closed loop. Three basic classes of geometries exist: the planar, the cylindrical and the conical designs. The planar design (Fig. 1(a)) is available in a circular geometry at diameters of from 5 to a few 10's of cm. The rectangular or "racetrack" magnetron (Fig. 1(b)) has been developed at lengths exceeding the meter range. The cylindrical geometry is characterized by a central, cylindrical cathode with an axial magnetic field. (Fig. 1(c)). The electric field in this case is radial, and the resultant  $\mathbf{ExB}$  drift path forms a band around the cathode. These devices need not have a circular cross-section, but have been designed in a flattened mode, where the original circular cross-section is replaced by an almost rectangular cross-section with rounded ends. The third geometry is the conical design (Fig. 1 (d)), which is somewhat similar to the circular planar device. These devices have a cathode surface which is tilted slightly and typically have an opening on the central axis. Often an anode of some sort is placed in this central opening, which helps eliminate the bombardment of the sample with energetic electrons.

While new magnetron designs and applications have been continuously developed over the past 15 years, relatively little work has been published on the fundamental aspects of magnetron operation. This may be due in part to the high level of some of the earlier publications (see ref. 1, for example). It may also be due to the sophisticated engineering work that has gone into the design of magnetron cathodes: i.e., the cathodes function very well, and little effort has gone into process diagnostics. It becomes apparent, after closer examination, that aspects of how magnetrons operate can be exceedingly complex. The various processes of plasma formation, energetic bombardment of the cathode, transport of the sputtered atoms and film deposition are often inter-related in non-trivial ways. One of the goals of this chapter is to identify some of these interactions.

Magnetrons are also routinely used to reactively deposit compound films, such as nitrides and oxides. This topic will be treated at great length in Chap. 9, and will not be included here.

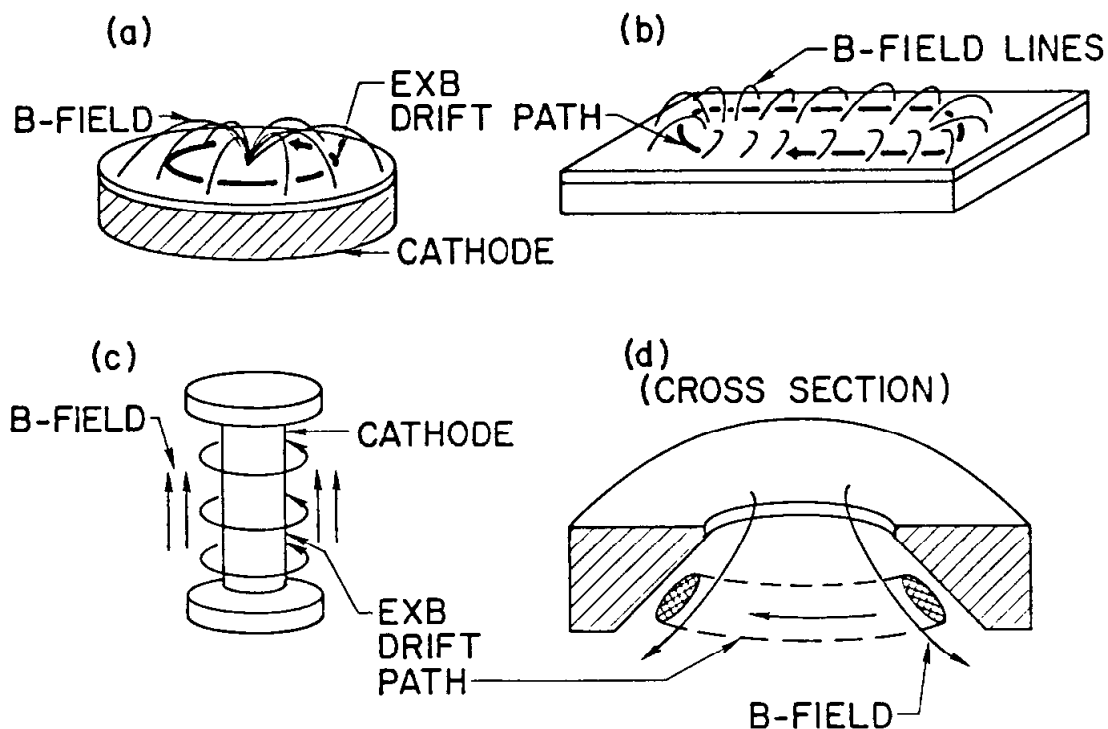


**Figure 1:** (a) circular planar magnetron, (b) rectangular planar magnetron, (c) cylindrical post magnetron, and (d) conical magnetron.

To define more closely some of the basic physical effects present in magnetron sputtering devices, numerous diagnostic experiments have been reported. Among the techniques used are optical emission spectrometry (2,3) mass spectrometry, the use of electrostatic (Langmuir) (4-6) and magnetic probes (7), gas pressure probes (8,9) energetic neutral and negative ion detectors (10,11), current collection techniques both at the cathode and the film surfaces (12), measurements of the deposition and composition of films around the chamber (13,14), electrical measurements of the current and voltage of the discharge itself (1,15,16), measurement of the energy distribution of the incident, bombarding ions (17), measurement of the kinetic energy or effective heating energy of the depositing atoms (18,19), as well as other less direct techniques. The combination of results from each of these experiments will be useful in discussing the inter-relations among the various phenomena in the magnetron device.

It has been popular in the past to break up the sputter deposition of films into the sputtering process at the cathode, transport from the cathode to the substrate, and the deposition process at the substrate. Indeed, this book is partitioned along these same lines. These topics are then treated individually and independently. The results of some

of these diagnostic measurements suggest that this type of delineation may not be appropriate, at least under some conditions, and that significant inter-relationships are present between these three general categories.

## 6.2. EXPERIMENTS

For the purposes of this discussion, the general experiment to be described is a conventional, circular, planar magnetron cathode. Some of the reported experiments, however, have used other cathode arrangements, such as the cylindrical post cathodes or conical (S-Gun-type) of cathode. In general, the results should be fairly consistent from one type of cathode to another. A metal target is mounted on the cathode (typically Cu, Al, W, Mo, etc.) which is sputtered in a dc mode from an inert gas plasma of typically Ar, Ne or Kr. The cathode dimensions range from 5 to 50 cm. diameter. The background pressure of the gas is generally a few to a few tens of mTorr (.3 to 4 Pa) and is supplied through mass-flow controllers. For many of these experiments, the chamber has been stripped of additional fixtures, such as shutters, ground shields and other shielding. In addition, in many cases a separate anode has not been used, effectively causing the chamber walls to function as the anode. The cathode is supplied by a highly regulated DC supply, operated in constant voltage, current or power modes. The chamber in which the magnetron is located is large compared to the dimensions of the magnetron.

In normal operation, the chamber is evacuated to  $10^{-7}$  Torr or so, and backfilled to the desired mTorr pressure. A negative voltage on the order of a few hundred volts is applied to the cathode. This leads rapidly to the formation of a plasma, from which several amperes of ions (for the larger cathodes) are accelerated to the cathode, causing physical sputtering. The sputtered atoms then transit the plasma, and may eventually form films on nearby surfaces.

### 6.2.1 Sputtering at the Cathode Surface

Physical sputtering by energetic ions has been the subject of an earlier chapter (Chap. 3). Magnetrons typically operate with either an applied dc or an effective dc bias (rf mode) of a few hundred volts. Using an inert gas, such as Ar, which will typically be singly ionized, the ions bombarding the cathode are then at energies equivalent to the discharge voltage (in eV). At these energies, the sputtering process is primarily by means of direct knock-on collisions. Sputter yields for most gas-cathode combinations range from 0.1 to 3. This is indicative of a relatively inefficient process: for each incident ion of, let's say, 500 eV, one or two atoms with an average energy of 6-10 eV are ejected. A large fraction of the incident energy is lost to cathode heating. In general, the functional limit to high power, high rate magnetron sputtering is almost always the ability to cool the cathode. Given a maximum water flow-rate and a few simple approximations, the maximum deposition rate in a system can be estimated simply from the consideration of cathode cooling and the melting or damage point of the cathode.

There are several other significant effects that may be observed at the cathode. The first is due to the contamination or poisoning of the cathode when used in a reactive gas. If the gas reacts with the cathode to form a stable, or low sputter yield compound (such as an oxide), the sputtering and electrical characteristics of the discharge will be changed dramatically. This topic will be discussed more fully in Chap. 9. The second major effect is often observed when sputtering from alloy or compound targets. Due, not only to the



difference in the sputtering yield of the constituents, but also to thermodynamic considerations, the composition of the target can change dramatically from bulk. This effect has been discussed at length in Chap. 4.

A third, more subtle modification of the cathode may occur due to gas-scattering induced redeposition of the sputtered atoms back onto the cathode surface. In an alloy, depending on the relative masses of the sputtered atoms, as well as the chamber pressure, gas composition and discharge power, a non-stoichiometric redeposition of sputtered atoms may over time subtly alter the target composition. This is likely to be most significant in cases where one component of the alloy has a much different mass than the other component, such as AlCu or TiW.

### 6.2.2 Gas Rarefaction Effects

One effect of the rather large sputtered particle fluxes present near a magnetron cathode is to perturb the local background gas. Hoffman first systematically studied this effect with observations on the non-uniformity of the particle density and direction, designated as the sputtering wind (8). In that study, the pressure increase observed in the static (non-pumped) mode was indicative of gas heating within the chamber. In the dynamic, pumped mode, a decrease in chamber pressure was noted, also indicative of increases in gas temperature (and hence effective pumping speed). Earlier indications also pointed to an effect of the discharge on the effective gas density in the cathode region (20). A systematic study of the effect of the energetic particle species in the magnetron on the gas density and temperature has shown large changes in the gas density as a function of the power (or current) of the magnetron discharge (9). The gas density was sampled by a tube placed parallel to the magnetron cathode, located a distance of a few centimeters from the cathode. The apparent pressure observed in the tube can be converted to a gas density using the thermal transpiration model of Takaishi and Sensui (21). As a function of increasing magnetron discharge current, the gas density in the near cathode region falls drastically (Fig 2.) although the chamber density is unperturbed. (The chamber is large compared to the size of the cathode.)

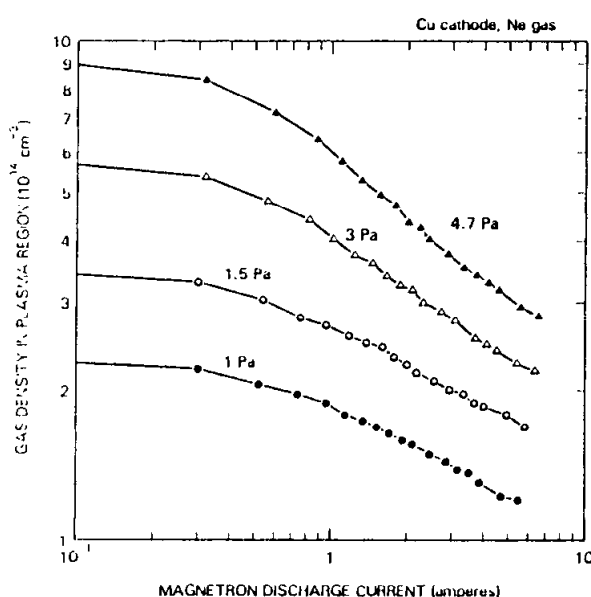


**Figure 2:** Gas density in the plasma region calculated from measured pressure and model of Takaishi and Sensui (21) for a Cu cathode and Ne gas.

The reduction in gas density is consistent with an increase in the gas temperature, caused by the various energetic processes occurring in the magnetron plasma. The two most likely sources for the energy are the energetic sputtered flux from the cathode and incident, bombarding ions which are reflected and neutralized at the cathode surface. The magnitude of the density reduction is dependent on the background gas species, and also on the cathode material, and tends to be largest for high mass gas atoms and high sputter yield targets. The momentum-transfer cross section for the sputtered atoms with kinetic energy of a few eV is a factor of 5-10X larger than for the energetic reflected neutrals from the cathode, whose energy is in the several hundred eV range (22). The mean free path for the sputtered atoms is in the 1-5 cm range at chamber pressures of 30 to 5 mTorr, which is generally smaller than the cathode-to-sample distances in many systems. This suggests that the energetic sputtered flux is the dominant source for the gas heating and that the reflected neutrals from the cathode are more likely to travel to the sample surface or chamber walls.

A model was suggested for the gas heating induced by the thermalization of the energetic, sputtered atom flux (9). The model calculated the effective gas temperature in the cathode region for a known sputtering flux (as a function of discharge current), allowing the energy to be thermally conducted away by the gas to the chamber walls. The model reduced at large discharge currents to:

$$n_H = \left( \frac{2n_o T_o \pi f K}{E_a Y_v \sigma} \right)^{0.5} \times I^{-0.5} \quad (1)$$

where  $n_H$  is the gas density in the plasma region,  $I$  is the discharge current,  $n_o$  is the original chamber gas density,  $T_o$  is the wall temperature,  $K$  is the thermal conductivity of the gas,  $E_a$  is the average energy per sputtered atom,  $Y_v$  is the voltage-dependant sputter yield,  $\sigma$  is the cross-section for momentum transfer of the sputtered atom, and  $f$  is a constant indicating how many mean-free-paths were considered as the thermalization distance. A value of  $f = 3$  was used.

This relation suggests that gas species with high thermal conductivities (He and Ne) will show significantly less density reduction as a function of discharge current, as the energy is more efficiently coupled away to the walls. Also, cathode species with large sputter yields or large average kinetic energy for the sputtered atoms will show significantly more density change with increasing current. This was confirmed for a range of materials and gases (9). The model was used to predict the density changes as a function of increased discharge current by simple substitution of values. The results, shown in Fig. 3, are suggestive that the thermalization of the energetic, sputtered flux is indeed the cause of the significant density changes observed.

The thermalization process, or the cooling of the energetic, sputtered atoms by gas collisions, has been treated by means of calculation and experiment. One interesting experiment measured the Doppler broadening of the emission from the sputtered metal atoms as a function of distance from the cathode (19). The results were generally consistent with the 2 theoretical models available at the time. It should be noted, however, that each of the theoretical treatments in the past has not accounted for the major changes observed in gas temperature and density observed more recently.

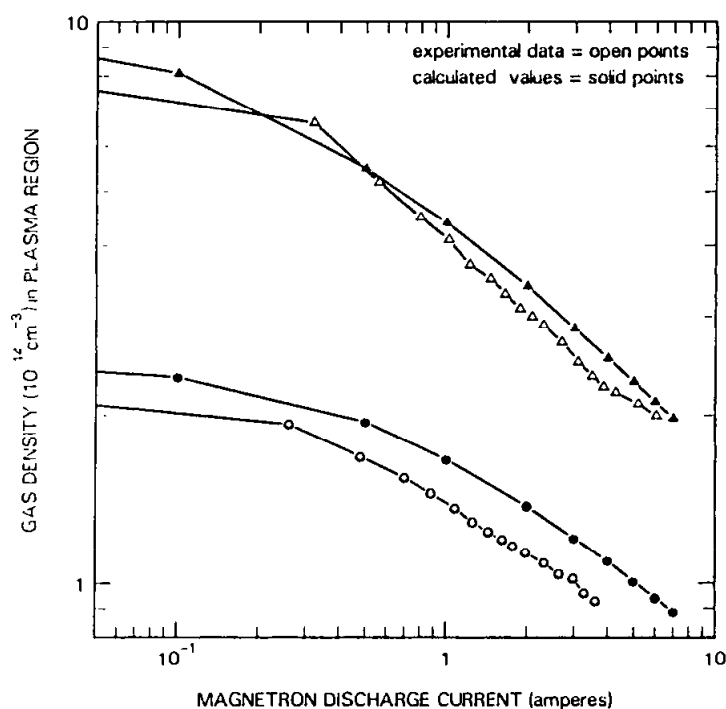


**Figure 3:** Comparison of experimental data and the thermal conduction model for the case of a Cu cathode and Ar gas. The sampling position was 5.3 cm from the cathode.

### 6.2.3 Plasma Measurements:

As listed above, a long list of plasma diagnostic measurements have been reported. Rather than exhaustively chronicle each report, a short list of representative studies will be discussed.

Measurements of the electron temperature and density have been made with small Langmuir probes inserted into the plasma (4-6). In one of these studies, the probes were oriented perpendicular to the cathode surface, and scanned up to the sheath edge (Fig. 4). The results showed electron temperatures in the 2-10 eV range, and electron densities in the  $10^{10}$  to  $10^{11} \text{ cm}^{-3}$  range for low discharge currents. At constant current, these results were strongly dependant on the gas pressure. The electron temperature decreased as pressure was increased, while the electron density increased with increasing pressure. Few measurements were taken at high power, due to thermal damage of the probe. It was not possible to sample a broad range in discharge currents without the use of several probes of varying dimensions. Calculations of the discharge current, using the measured electron temperature and density and the pre-sheath Bohm criteria, were consistent to the experimental results, within experimental error. This suggests that the plasmas are bounded by conventional positive space-charge sheaths.

A magnetron is characterized by an  $\mathbf{E} \times \mathbf{B}$  drift current, located near the cathode surface. The magnitude of this drift current has been measured by observing the magnetic field induced by the current loop in a circular, planar device (7). The magnitude of the drift current is typically 3-9 times the total discharge current, and depends on cathode species, gas species and chamber pressure (Fig. 5). This result is consistent with Bohm diffusion, rather than classical collision-dominated electron diffusion across magnetic fields, being the dominant charge-transport mechanism.

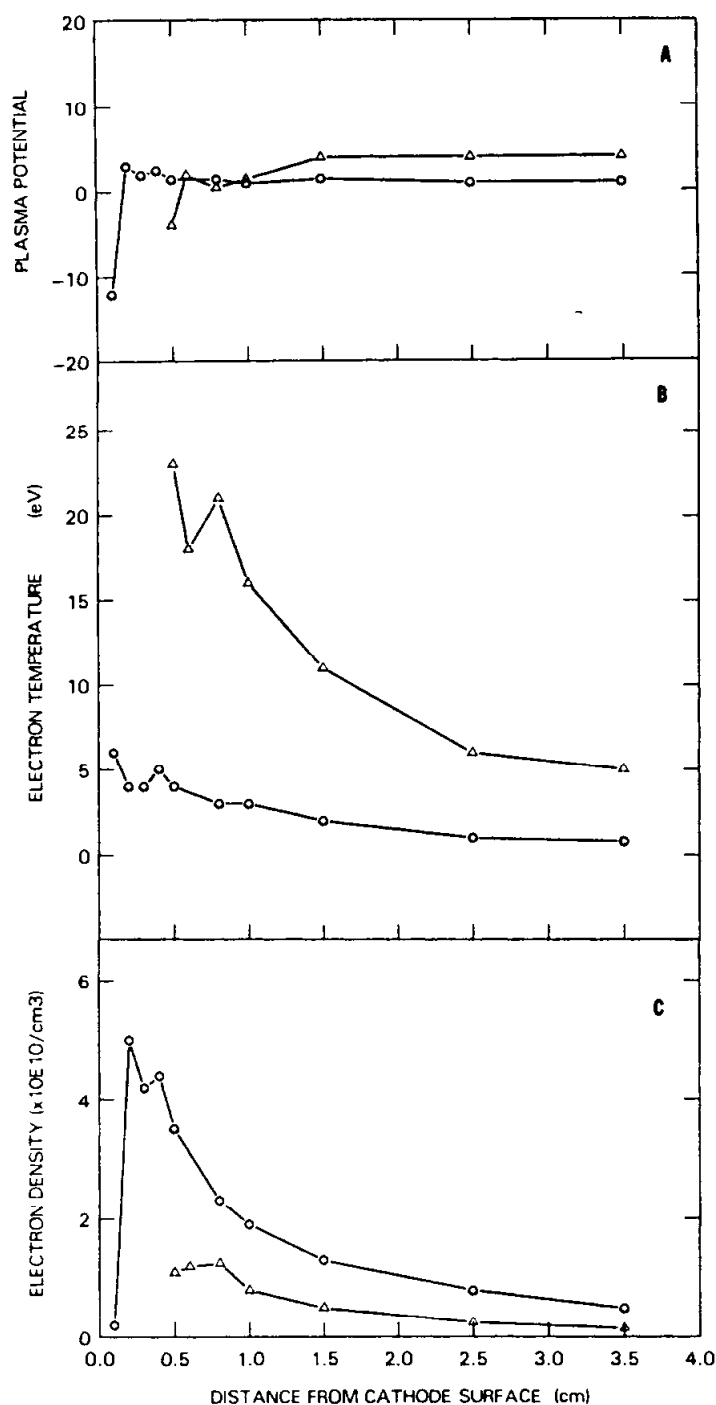


**Figure 4:** Results of Langmuir probe measurements in a magnetron discharge at 5 and 30 mTorr as a function of distance from the cathode.

The sheath thickness was measured roughly with the Langmuir probe. However, a more accurate measurement has been made using a long-focal length, traveling microscope. This device was focussed to the center of the etch track, oriented parallel to the cathode surface. The apparent dark space thickness could then be measured with the graticle, and calibrated against an object of known size. The dark space thickness was found to decrease rapidly as a function of increasing discharge power (23). In particular, a large, exponential dependence of this thickness on discharge voltage was observed, also dependent on the chamber pressure (Fig. 6).

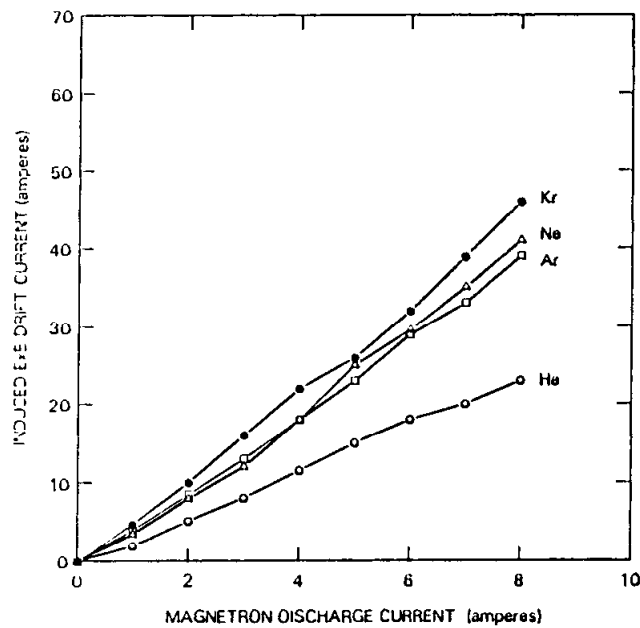


**Figure 5:** Induced drift current as a function of discharge current for a circular planar magnetron for inert gas species at 20 mTorr with a W cathode.

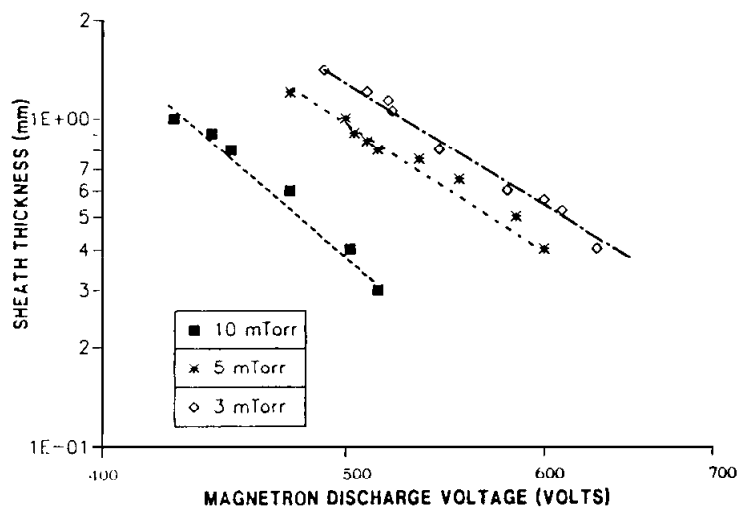


**Figure 6:** The natural log of the optically measured sheath thickness as a function of the natural log of the discharge voltage for three pressures of Ar.

From this data, the discharge voltage and sheath thickness can be related by:  $d = cV^{-m}$ , where  $c$  is a constant and  $m$  is an exponent between -3 and -6. The sheath thickness, current and voltage in a magnetron would be expected to follow Child's Law, which is of the form:

$$I \propto \frac{V^{3/2}}{d^2} \quad (2)$$

When the voltage dependance of the sheath is substituted into Eqn. (2) a relation is found

$$I \propto kV^n \quad (3)$$

where  $n$  is on the range of 7.5 to 13.5 for this case. This relation is quite similar to the empirical current-voltage relations observed in magnetrons.

#### 6.2.4 Interactions: Effects on Plasma

The significant modification of the gas density near the cathode due to the energetic sputtered atoms has implications to both the deposition process as well as to the plasma. In particular, it was first suggested by Hoffman that this phenomena should have an effect on the current-voltage relation in the magnetron (8). The probability of ionization of a gas atom, whether by an energetic secondary electron from the cathode or by an electron from the tail of the Maxwellian distribution, will be directly proportional to the local gas density. As that density is reduced due to rarefaction by the thermalization of the hot sputtered atoms, increased discharge currents must require additional energy, as the plasma is becoming effectively more resistive.

In addition, the results of electrical and optical measurements on the plasma described earlier suggest that the plasma is a conventional space-charge limited plasma whose primary electron conduction process is Bohm Diffusion, rather than the classical collision-dominated electron conduction process across field lines. Bohm Diffusion is characterized by collective, turbulent motions of the electrons. The apparent motion of the secondary electrons in a magnetron, therefore, is probably not a simple cycloidal hopping of the electron around the  $E \times B$  drift path, but more probably a turbulent, buffeted, attenuated drift as the energetic secondary electron rapidly loses its energy sustaining the electron temperature of the plasma. It is then possible that a significant number of the ionizing collisions in the plasma occur between electrons in the tail of the Maxwellian distribution and gas atoms. The probability of this type of collision has been calculated, and can be compared to the discharge current, as recombination at these pressures and plasma densities is low.

The discharge current can then be approximated as: (16)

$$I \propto 2n_e n_g \sigma (m/2\pi kT_e)^{0.5} v_i^2 \exp(-mv_i^2/2kT_e) \quad (4)$$

where  $v_i$  is the minimum electron velocity for ionization,  $n_e$  is the electron density,  $kT_e$  is the electron temperature and  $m$  is the electron mass. The current to the cathode can also be approximated by Bohm pre-sheath flow. The current density of ions to the sheath edge is given by: (24)

$$j = 0.6n_e(kT_e/m_i)^{0.5} \quad (5)$$

where  $m_i$  is the ion mass. The result of this type of calculation is a relation between the local gas density and the electron temperature and density. Combining these relations

leads to an inter-relation between the electron temperature and the gas density of the form:

$$n_g = \frac{G}{\sigma v_i^2 (m_i m)^{0.5}} kT_e \exp\left(\frac{mv_i^2}{2kT_e}\right) \quad (6)$$

where  $G$  is now a geometrical constant related to the cathode size.

The discharge voltage can be described in terms of discharge current and the plasma impedance, which was found to be related to Bohm Diffusion. The voltage is found to increase as a function of the square root of the electron temperature. A comparison of the calculated and experimental discharge voltages is shown in Fig. 7 (16).

The magnetron plasma can be viewed in somewhat dynamic terms, effectively dependant on the interaction of the sputtered atoms on the background gas and the plasma. At a given discharge current (i.e. ion flux to the cathode) there is an emerging flux of energetic, several eV sputtered atoms which enters the plasma region near the cathode. As a result of collisions between these sputtered atoms and the background gas, the net, local gas density is rarefied from its original, pre-plasma value. Therefore, the electron temperature of the plasma must be sufficiently high (at this current) to cause a level of ionization consistent with the discharge current. To increase the discharge current requires overcoming the additional rarefaction caused by the additional sputtered atoms at higher current. This is done by adding additional energy to the plasma through a higher voltage on the cathode. This relatively simplistic, yet consistent process, allows a number of conclusions and predictions to be made about the operating levels of a magnetron device and the effects of changing pressure, cathode or gas species, system geometry, magnetic field, etc.

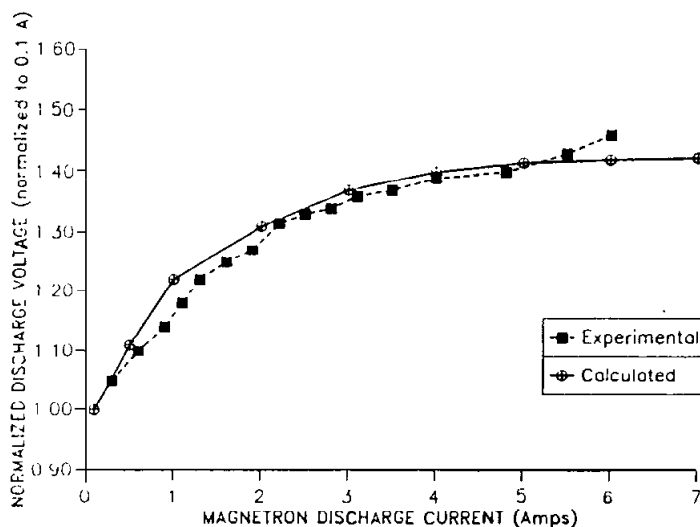


**Figure 7:** Observed and calculated relative voltage increases as a function of magnetron current for the case of Ar gas and a Cu Cathode at a pressure of 30 mTorr. The curves are normalized to the experimental "turn-on" voltage, which is the minimum stable voltage for operation of the discharge.

The sputter yield is quite dependent on the cathode material. Some materials, such as Cu or Au, have relatively high yields at ion energies of a few hundred eV. Other materials, often the refractory materials or compounds, have relatively low yields. In addition, not only is the yield strongly dependent on the gas species (and mass), but the thermal conductivity of the gas can vary dramatically with gas choice. Combining these effects, the expected flux of sputtered atoms as well as the effect of those atoms on the local gas density near the cathode should be strongly dependent on the choice of gas and cathode species. However, using the model described above (Eq. 1), the magnitude of the gas rarefaction should be easily predicted.

We have suggested that the rate of ionization of the background gas, and hence the discharge impedance and voltage will be strongly perturbed by this effect. In cases where the gas rarefaction effect is strongest (high sputter yields, or low thermal conductivity of the gas), the voltage should rise to a larger degree with increasing current than in equivalent cases with smaller gas rarefaction effects. As a means of comparison, consider the generally accepted empirical current-voltage relation often used with magnetrons (1)

$$I = k V^n \quad (3)$$

where  $k$  is a constant and  $n$  is an exponent in the range of 5 to 20 or so. In cases where the voltage increases slowly with current, the exponent,  $n$ , is large.

Following the discussion of voltage increases related to the magnitude of the gas rarefaction, the exponent,  $n$ , should be large in cases of relatively low gas rarefaction, and small in cases of high levels of rarefaction. An example is for the case of sputtering Cu and Al in Ar. Due to the higher sputter yield of Cu, the exponent in the I-V relation should be smaller for Cu than for Al. This is indeed the case, as shown in Fig. 8. Similar arguments can be made for a variation in either gas species or chamber pressure. In each case the general result observed is that large voltage increases (with increasing current) correlate with a high level of gas rarefaction due to the thermalization of the sputtered atoms.

An extreme case of this can be seen for the case of He gas and a W or Mo target. In these cases, the sputter yields are extremely low. In addition, the thermal conductivity of the gas is very high. These two effects together suggest that the voltage will increase exceedingly slowly as a function of current. Indeed, measurements have shown the exponent in the I-V relation to be in the range of 35-70. Often in these plasmas, the current can be increase an order of magnitude or more by increasing the voltage less than 5 volts. It should be noted, however, that in this particular case, the sample undergoes extreme levels of energetic particle bombardment due to the low mass of the gas atoms and the long mean free path of reflected, energetic particles.

### 6.2.5 Interactions: Effects on Sputtered Material

Usually, the general goal of using magnetron devices in a sputtering mode is for the deposition of films. Atoms sputtered from the cathode may deposit on sample surfaces, forming a thin film of a composition near that of the cathode. The sputtered atoms, however, must transit the region between the cathode and the substrate; a region composed



of both the plasma and a large number of neutral gas atoms. The sputtered atoms, depending on the pressure and the distance between the cathode and the substrate, may undergo from zero to many hundreds of collisions. Each collision changes the velocity and direction of the sputtered atom, and usually results in a general cooling (thermalization) of the sputtered atom, while at the same time increasing the average temperature of the background gas.

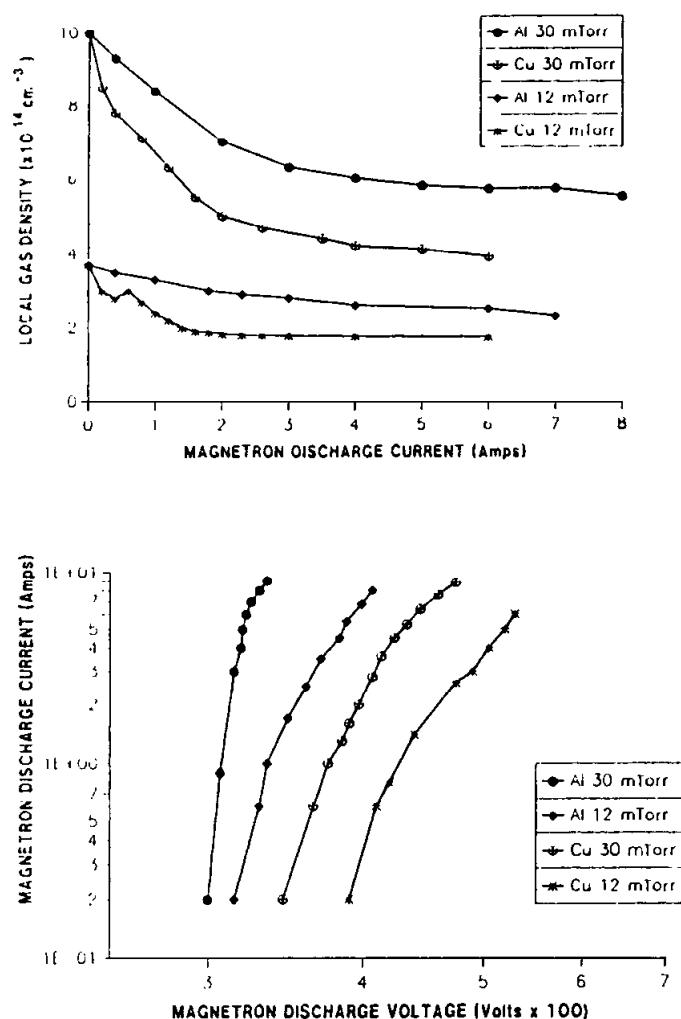


**Figure 8:** (a) Observed gas density reductions for Cu and Al cathodes in Ar at 30 mTorr as a function of discharge current. (b) Experimental current-voltage traces for the same case as (a) plotted logarithmically.

Several authors have treated the transport of atoms from a sputtering source by computational means. The deposition profiles for simple annular targets have been calculated by Gnaedinger (25) and further modified by Este and Westwood (26) for rectangular targets. Gras-Marti et al (27) has analytically treated some of the scattering processes occurring during transport, and a papers by Motohiro and Taga (28) and Somekh (29) has treated the topic with Monte-Carlo-like techniques. In addition, the so-called "throwing power", or the ability to coat the sides of objects has been treated qualitatively (30).

Experimentally, a study was undertaken to measure the probability of atom transport by measuring the resulting deposition profiles for a fixed number of sputtered atoms

(13,14). The atoms sputtered from a magnetron cathode may deposit on the substrate plane, the side areas of the chamber, the fixtures and shutters in the chamber, or even back onto the magnetron cathode. Atoms deposited onto the etch track of the cathode will most likely be resputtered rapidly. However, atoms deposited in areas on the cathode but not in the etch track have a lower probability of being resputtered due to the lower bombardment rates. In general, thick deposits can be formed in the central, "dead" regions of the cathode and also near the cathode edge.

The results of this study for the case of Cu and Al cathodes can be given in tabular form, in Tables 1 and 2. The probabilities are found by dividing the total number of deposited atoms on a surface by the total estimated number of sputtered atoms. There are certain systematic sources of error (14), but these are usually less than 20%. The redeposition of atoms to the cathode may cause a slow change in the composition of films sputtered from alloy targets. It will also be sensitive to the local gas density and the target-to-sample distance. In addition, as the local gas density is strongly perturbed by the rate of emission of energetic sputtered atoms, the redeposition on the cathode will also be dependant on the operating power of the magnetron. This can be seen in Fig. 9, in which the redeposition on the cathode drops off significantly at higher discharge powers, as the local gas density which causes the scattering and redeposition is reduced. Thus, one would expect compositional changes when sputtering from alloy targets as a function of chamber pressure, throw distance as well as power. These are indeed observed, and are the subject of a related work (31).

**Table 1:** Deposition probabilities for various surfaces within the chamber for a Cu cathode in Ar as a function of chamber pressure and throw distance.

<u>1000 Watts</u>				
Gas	P (Pa)	Sample	Magnetron	Side areas*
5 cm	0.7	.63	.031	.16
	2.6	.49	.11	.20
	4	.53	.14	.22
9.5 cm	0.7	.48	.031	.24
	2.6	.47	.13	.24
	4	.45	.18	.18
14.5 cm	0.7	.39	.045	.25
	2.6	.35	.16	.30
	4	.31	.18	.35
<u>200 Watts</u>				
5 cm	4	.53	.23	.13
<u>3000 Watts</u>				
5 cm	4	.48	.09	.24

\* The side areas include only those areas adjacent to the magnetron cathode, parallel to the cathode surface. It does not include all wall areas.

**Table 2:** Deposition probabilities for various surfaces within the chamber for an Al cathode in Kr, Ar and Ne as a function of pressure and throw distance.

Throw	P (Pa)	Sample	Magnetron	Side Areas*
<u>5 cm Throw</u>				
Kr	0.7	.52	.10	.16
	2.6	.45	.18	.17
	4	.38	.34	.13
Ar	0.7	.60	.12	.10
	2.6	.46	.26	.12
	4	.42	.32	.09
Ne	0.7	.80	.08	.05
	2.6	.56	.16	.10
	4	.52	.27	.11
<u>9.5 cm Throw</u>				
Kr	0.7	.35	.18	.20
	2.6	.27	.35	.24
	4	.22	.39	.20
Ar	0.7	.44	.13	.10
	2.6	.45	.35	.15
	4	.36	.40	.17
Ne	0.7	.40	.10	.20
	2.6	.42	.36	.18
	4	.40	.34	.09

\* This is the area adjacent to the cathode, parallel to the cathode surface. It does not include all of the chamber walls.

Various optical techniques have been used to monitor the magnitude and energy of the atoms during transit from the cathode to the anode. Laser Induced Florescence (LIF) has been used for ion beam sputtering experiments (32) and also for selected plasma-based studies (33). Observations of the optical emission from the plasma region are also reported. In one particular case, the temperature of the sputtered atoms could be deduced from the Doppler broadening of the observed emission (19). Conventional optical emission spectroscopy (OES) has also been used to monitor the relative levels of sputtered atoms in the plasma. The emission intensity is generally proportional to the electron density,  $n_e$ , the species density,  $n_s$ , and some function of the electron temperature, cross section for excitation, and de-excitation probability (3):

$$I_{\text{emis}}^s = n_e n_s A \int \rho_e(E) v \sigma_s(E) dE = A n_s n_e f(T_e, \sigma_s) \quad (6)$$

where  $A$  is a geometry-dependent constant, and  $f(T_e, \sigma_s)$  is defined as the excitation rate of the species, which is dependent on the the electron energy ( $E$ ) distribution,  $\rho_e(E)$ , or temperature  $kT_e$ , electron velocity  $v$ , and cross section for excitation,  $\sigma_s(E)$ . The last term is usually assumed, for convenience, to be constant over the range of interest in plasmas of this type.

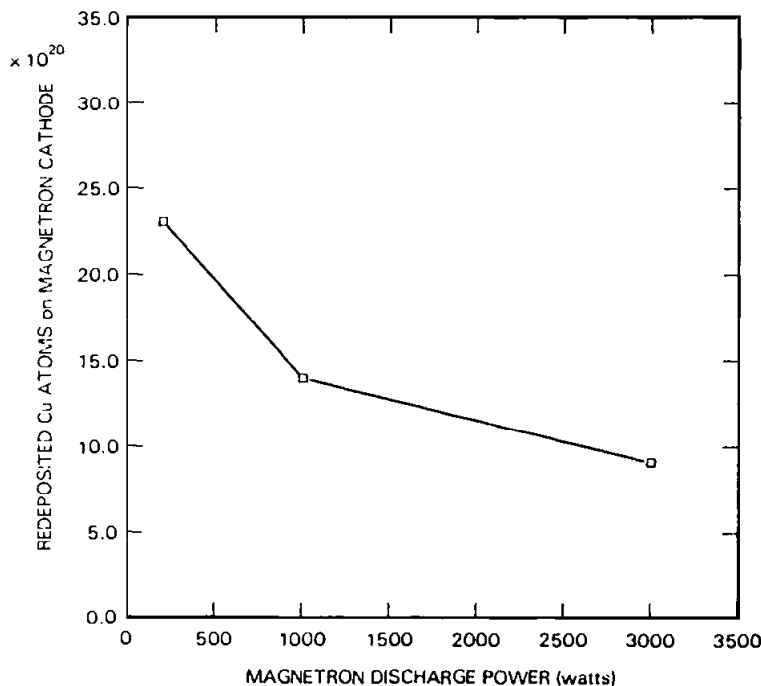


**Figure 9:** The probability of redeposition (in percent) for Cu atoms back onto the magnetron cathode for Ar gas as a function of discharge power.

The emission intensity of various species present in the discharge can be measured as a function of discharge current (2,3). It is reasonable to assume that the electron density is roughly proportional to the discharge current. From this assumption, the emission levels from the background gas species would be expected to scale with the discharge current to approximately the first power (3). This is observed at low discharge powers (Fig. 10), but as power is increased, the intensity becomes proportional to the discharge current to the  $1/2$  power. This change can be attributed to the rarefaction effect described earlier, in which the energetic, sputtered atoms cause a reduction in the local gas density due to the thermalization process. As found in Eq. 1, the gas density is proportional at high power to the discharge current to the  $-1/2$  power. When combined with Eq. 4, the observed slope at high power can be predicted.

The density of the sputtered atoms should be directly proportional to the discharge power, or approximately proportional to the discharge current. Again making the assumption that the electron density is proportional to the discharge current, the intensity of the sputtered atoms would be expected to be proportional to the discharge current to the 2nd power (using Eq. 6). The observed values (Fig. 10) appear to approach the second power at low powers, and fall to approximately the 1.3 power at high discharge powers. This may be indicative of gas rarefaction effects, but may also be due to a lack of a direct proportionality between the electron density and discharge current. (Note: if the electron density scales with the discharge current to less than the first power, as might be expected, the difference is exaggerated in the case of sputtered or ionized, sputtered atoms.) The density of ionized, sputtered atoms should be proportional to the discharge power (number of sputtered atoms) times the electron density (probability for ionization). Thus, one might expect that the intensity of ionized, sputtered atoms would scale with discharge current to approximately the third power. The results (Fig. 10(c)) show an exponent of approximately 2.5. The intensities for these particular species are quite low, however, due to the high excitation energies required.

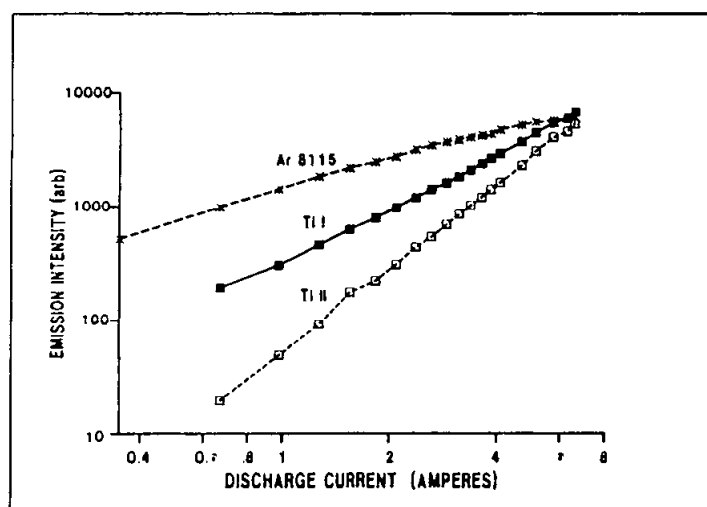


**Figure 10:** Experimentally observed optical emission intensity for lines from (A) Ar ground state, (B) Ti ground state, (C)  $\text{Ti}^+$  for magnetron sputtering of Ti in Ar at 7 mTorr. Data are plotted as a function of discharge current.

The general result, however, is that the source of individual emission lines in a plasma may be identified by their dependence on the discharge current. In addition, using this type of diagnostic technique to monitor a deposition process must be done very carefully, and generally only over a small range of discharge parameters.

### 6.2.6 Interactions at the Sample Surface

It has routinely been observed that the various physical and electrical characteristics of the deposited films are strongly sensitive to the gas pressure in the chamber, the rate of deposition, and the substrate temperature. An example of this interrelationship is Thornton's version of Movchan and Demichishin's structure zone diagram (34,35). (See, for example, Fig. 1 of Chap 22.) In general, it has been postulated that low pressures correlate with increased energetic particle bombardment of the growing film, causing changes in the grain size, stress and impurity incorporation levels (36). This has been the subject of numerous studies, and will not be redescribed here. Many of the explained effects, however, rely on the bombardment of the film with energetic, neutral particles that originate at the cathode surface during the sputtering process. These energetic neutrals are elastically reflected, Auger neutralized ions that have been accelerated to high energy to the cathode or target surface and may reflect with up to several hundred eV of kinetic energy. In addition, a significant component of energetic neutral bombarding species may be attributable to the formation of negative ions at the cathode surface, with the subsequent acceleration across the cathode sheath and charge neutralization in the plasma. This second species is often observed when sputtering in the presence of oxygen, as well as in the case of materials from the far left side of the periodic table. The negative ion species are

usually well collimated in a plasma-sputtering device, whereas the reflected neutrals may have a more isotropic distribution.

Substrate heating during sputter deposition with a magnetron is a combination of many factors. As is the case with all vapor phase depositions, the heat of condensation (3-8 eV/atom) must be considered. Due to the low operating pressure of the magnetron, a significant fraction of the initial kinetic energy of the sputtered atom may still be present for the depositing atoms. This contribution can range up to 20 eV/atom for refractory materials, but is typically closer to 4-8 eV/atom for other metals. The reflection of ions as neutrals from the cathode may also contribute significantly to the energy deposited at the film. This is particularly significant for low mass gas species in combination with high mass cathode species, where the reflection coefficients can be quite large and the sputter yields quite low. Finally, there can also be heating contributions from optical emission from the plasma as well as bombardment with hot gas atoms.

Thornton built a small detector to measure the net energy arriving during film deposition. The detector is based on a thin foil substrate which is thermally isolated from its mount. A thermocouple monitors changes in the foil temperature, which in conjunction with the deposition rate, can be converted into an energy arrival rate per depositing atom. A summary of the results is shown in Table 3, which has been collected from published data (18).

**Table 3:** Measured and calculated energy arrival rates for Ar sputtering (18).

Metal	Atomic Weight	Planar Mag. eV/atom	Cylindrical eV/atom	Theoretical est. eV/atom
Al	27.0	11	13	13
Cr	52.0	16	20	16
Ni	58.7	15	15	19
Cu	63.5	12	17	12
Mo	95.9	42	47	26
In	1158	15	20	9
Ta	181	96	107	38
W	184	98	100	40
Pt	195	48		30

A second detector has been developed to measure the presence of only the energetic species during a sputter deposition. The device is similar to the work of Brodie, Lamont and Jepson (37) and others (38), and is shown in Fig. 11. The device shields out energetic electrons by means of a magnetic field and a collector biased more negative than the cathode (10). A grid (G-1) allows the introduction of ions from the plasma when biased negatively, or repels the ions when biased more positive than plasma potential. A second grid (G-2) near the collector allows for the emission or suppression of secondary electrons caused by energetic bombardment of the collector. The current to (or from) the collector is then indicative of the magnitude of energetic particle bombardment and the secondary

electron yield. By reversing the potential on G-2 with respect to the collector, the secondary electron coefficient can be deduced. Observed currents at the collector with a positive potential on G-2 are then due to the emission of electrons caused by energetic neutral bombardment or photons. The secondary electron yield due to 'neutral' bombardment has been rarely measured in the past, and may or may not be related to an Auger process (24). For the purpose of this study, however, the yields have been routinely measured, and appear to be similar to the yields for ions at comparable energies.

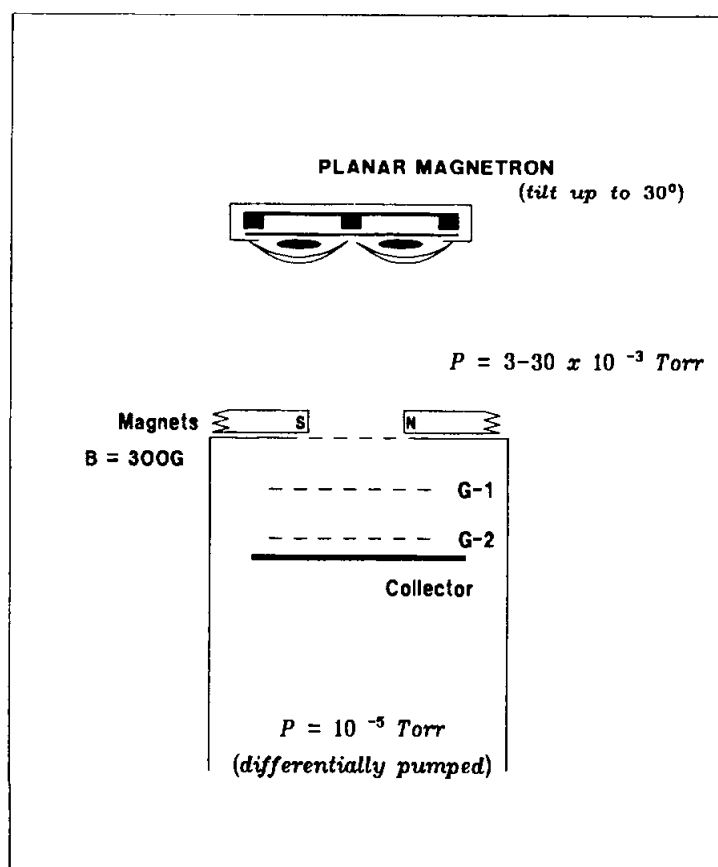


**Figure 11:** Schematic of energetic neutral detector used for magnetron studies (10,11).

Assuming the secondary electron yield does not depend on kinetic energy in the 20-600 eV range, the flux of energetic neutral particles can be determined in a quantitative manner with this device, as can the average secondary electron yield. In addition, a quartz crystal rate monitor has been positioned immediately adjacent to the energetic neutral detector to measure the net arrival rate of depositing atoms. By comparison of these two signals, the arrival rate ratio of energetic-to-depositing atoms can be determined, although the actual energy of the energetic species cannot be measured (10).

Both the deposition rate of condensing atoms and the arrival rate of the energetic species depends on the chamber pressure. An increase in chamber pressure results in a reduction of both signals due to gas scattering. (Fig. 12). In addition, as might be expected following the earlier discussions of gas rarefaction effects, the arrival rates of both species are dependant on the discharge power, which alters the local gas density due to the thermalization process. (Fig. 13). The ratio of energetic-to-depositing atoms has been

found, however, to vary slowly, if at all, with chamber pressure. In many cases, the energetic-to-depositing atom ratio has been found to decrease as the chamber pressure is reduced, rather than increase as might be expected from the effects on the film properties. Upon consideration of the cross sections for collisions (22), however, this result is not too surprising. The sputtered atoms have an average kinetic energy of a few eV and a mean free path on the order of a few centimeters at the operating pressures used. The reflected, neutrals often have energies exceeding 100 or more eV, and thus have a significantly smaller cross section and longer mean free path. Therefore, changes in chamber pressure in the mTorr range will be much more significant to the mean free paths of the low energy sputtered atoms, rather than the reflected, higher energy neutrals.

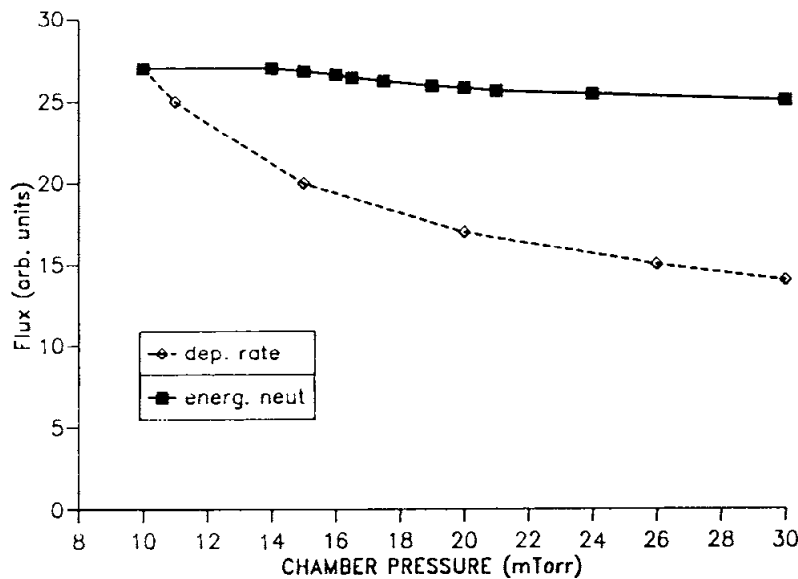


**Figure 12:** Arrival rates of energetic neutral particles and depositing atoms in arbitrary units as a function of chamber pressure for the case of a Al cathode in Ne gas at a constant discharge current.

The relative arrival rates of energetic neutrals to depositing atoms are strongly dependent on the cathode and gas species. The probability of reflection for a primary ion bombarding the cathode surface has been calculated by Eckstein and Biersak (39), and is greatest for the case of light ions bombarding heavy cathodes. The sputter yield of the cathode is also dependent on the choice of species, and tabulations are available (40). The results of measurements with the energetic neutral detector should scale with predictions made from a comparison of the sputter yield and the reflection coefficient, although the effect of gas scattering as well as emission profiles for the various species must also be considered.



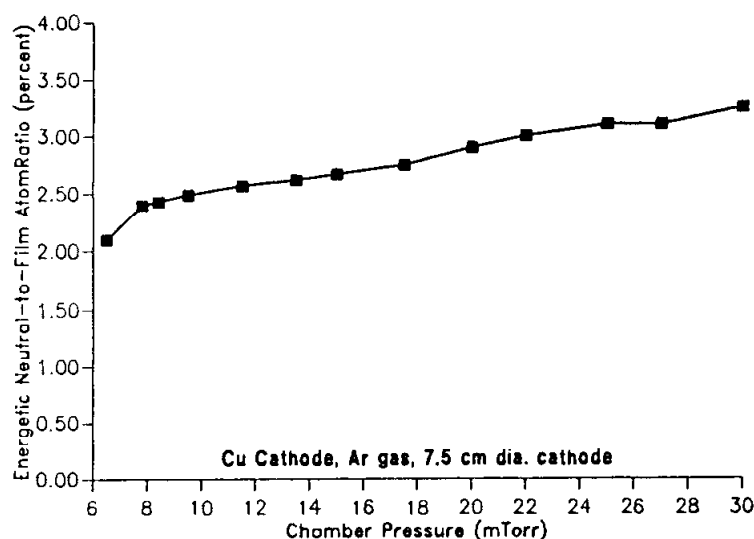


**Figure 13:** Relative arrival rate ratio of energetic-to-depositing atoms at the sample as a function of chamber pressure for the case of Cu cathode in Ar at 14 mTorr.

### 6.3 SUMMARY

An extended series of diagnostic measurements on magnetron sputtering devices has pointed out some of the complexities in understanding the various inter-relations between the sputtering process, the plasma formation, the sample and the background gas. The interaction between the sputtered atoms and the background gas, routinely described as a thermalization process, might more aptly be described as a gas heating process. This heating and rarefaction has numerous implications as to how the plasma is formed and its impedance, as well as the transport and deposition of sputtered atoms on surfaces around the chamber. The bombardment of the sample with energetic species is also a critical effect, which strongly affects the properties of the depositing films. While the bombardment rates can vary extensively as a function of cathode and gas species, little significant pressure dependence has been observed in the bombardment rate, suggesting the need to modify currently accepted explanations for changes in the properties of the sputtered materials as a function of discharge pressure. In addition, the presence of negative ions formed at the cathode surface and possibly due to residual gas impurities has been observed. Previous studies have neglected this effect, which will have strong implications not only on film properties, but on the transfer of a process from one chamber to another. This result also suggests that it is desirable to have a low base pressure and a high pumping speed to reduce the effects of impurities.

Other results of these studies are more conventional. The plasma in a magnetron is characterized by Bohm Diffusion, and is surrounded by positive space charge sheaths. The ExB drift currents are not substantial, and the resulting effects on the magnetic field are extremely low. The optical emission from the plasma is reasonably described by a simple model relating the electron density to the discharge current.

## 6.4 REFERENCES

1. J.A. Thornton and A. Penfold, in Thin Film Processes ed. by J.L. Vossen and W. Kern, (Academic, New York, 1987) p76.
2. S. Schiller, U. Heisig, K. Steinfeld, J. Strümpfel, R. Voight, R. Femdler and G. Teschner, On the investigation of DC plasmotron discharges by optical emission spectrometry, Thin Solid Films, 96: 235 (1982).
3. S.M. Rossnagel and K.L. Saenger, Optical emission in magnetrons, J. Vac. Sci. Technol. A7: (1989, in press).
4. S.M. Rossnagel and H.R. Kaufman, Langmuir probe characterization of magnetron operation, J. Vac. Sci. & Technol. A4: 1822 (1986).
5. J.A. Thornton, Magnetron sputtering: basic physics and application to cylindrical magnetrons. J. Vac. Sci. Technol. 15: 171 (1978).
6. B. Singh, presented at AVS National Symposium, Reno, Nevada, (1984) unpublished.
7. S.M. Rossnagel and H.R. Kaufman, Induced drift currents in magnetrons, J. Vac. Sci. Technol., A5: 88 (1988).
8. D.W. Hoffman, A sputtering wind, J. Vac. Sci. Technol. A3: 561 (1985).
9. S.M. Rossnagel, Gas density reduction effects in magnetrons, J. Vac. Sci. Technol. A6:19 (1988).
10. S.M. Rossnagel, Energetic particle bombardment of films during magnetron sputter deposition, J. Vac. Sci. Technol., A7: (1989, in press).
11. S.M. Rossnagel and J.J. Cuomo, Negative ion effects during magnetron and ion beam sputtering of  $\text{YBa}_2\text{Cu}_3\text{O}_x$ , AIP Conf. Proc 165: (1988) 106.
12. B. Window and N. Savvides, Unbalanced magnetrons as sources of high ion fluxes. J. Vac. Sci. Technol. A4: 453 (1986).
13. S.M. Rossnagel, Magnetron plasma diagnostics and processing implications, J. Vac. Sci. Technol., A6: 1821 (1988).
14. S.M. Rossnagel, Deposition and redeposition in magnetrons, J. Vac. Sci. Technol., A6: 3049 (1988).
15. W.D. Westwood, S. Maniv and P.J. Scanlon, The current-voltage characteristic of magnetron sputtering systems, J. Appl. Phys., 54: 6841 (1983).
16. S.M. Rossnagel, Current-voltage relations in magnetrons, J. Vac. Sci. Technol., A6: 223 (1988).
17. N. Howosokawa, T. Tsudaka and M. Kitahara, in Vide Suppl. 201: 11 (1980).
18. J.A. Thornton and J.L. Lamb, Substrate Heating rates for planar and cylindrical post magnetron sputtering sources, Thin Solid Films 119: 87 (1984).
19. L.T. Ball, I.S. Falconer, D.R. McKenzie and J.M. Smelt, An interferometric investigation of the thermalization of copper atoms in a magnetron sputter discharge, J. Appl. Phys. 59: 720 (1986).
20. D.W. Hoffman, Thin Solid Films 107: 353 (1983).
21. T. Takaishi and Y. Sensui, Trans. Faraday Soc. 59: 2509 (1963).

22. R.S. Robinson, Energetic binary collisions in rare gases, J. Vac. Sci. and Technol. 16: 185 (1979).
23. S.M. Rossnagel and H.R. Kaufman, Charge transport in magnetrons, J. Vac. Sci. & Technol. A5: 2276 (1987).
24. B. Chapman, in Glow Discharge Processes, (J. Wiley and Sons, New York, 1980).
25. R.J. Gnaedinger, Jr., Some calculations of the thickness distribution of films deposited from large area sputtering sources, J. Vac. Sci. Technol. 6: 355 (1969).
26. G. Este and W.D. Westwood, J. Vac. Sci. Technol. A2: 1238 (1984).
27. A. Gras-Marti and J.A. Valles-Abarca, Evolution towards thermalization and diffusion of sputtered particle fluxes: spatial profiles, J. Appl. Phys. 55: 1370 (1984).
28. T. Motohiro and Y. Taga, Monte Carlo simulation of the particle transport process in sputter deposition, Thin Solid Films 112: 161 (1984).
29. R.E. Somekh, The thermalization of energetic atoms during the sputtering process, J. Vac. Sci. Technol., A3: 1285 (1983).
30. W. Stowell, J. Foster, W. Berner, C. Wan, D. Chambers and H. Hanes, Throwing power and shadowing effect in planar magnetron sputtering process, J. Vac. Sci. Technol. A3: 572 (1985).
31. S.M. Rossnagel, I. Yang and J.J. Cuomo (submitted to Thin Solid Films)
32. D.M. Gruen, M.J. Pellin, C.E. Young and W.F. Calaway, Laser spectroscopy of sputtered atoms, J. Vac. Sci. Technol. A4: 1779 (1986).
33. G.S. Selwyn, J. Vac. Sci. Technol., A6: (1988) 2041.
34. J.A. Thornton, J. Vac. Sci. Technol. 11: 666 (1974).
35. B.A. Movchan and A.V. Demichishin, Study of the structure and properties of thick vacuum condensates of nickel, titanium, aluminum oxide and zirconium oxide. Fiz. Metal. Metalloved. 28: 653 (1969).
36. J.A. Thornton and D.W. Hoffman, J. Vac. Sci. Technol. A3: 576 (1985).
37. I. Brodie, L.T. Lamont, Jr. and R.L. Jepsen, Phys. Rev. Lett. 21: (1968) 1224.
38. Y. Shintani, K. Nakanishi, T. Takawaki and O. Tada, Jap. J. Appl. Phys. 14: (1975) 1875.
39. W. Eckstein and J.P. Biersak, Z. Phys. B - Condensed Matter 63: (1986) 471.
40. H.R. Kaufman and R.S. Robinson Operation of Broad Beam Ion Sources (Commonwealth Scientific, Alexandria VA 1988).

---

## Broad-Beam Ion Sources

---

**Harold R. Kaufman and Raymond S. Robinson**

### 7.1 INTRODUCTION

Broad ion beams have transverse dimensions that are much larger than the Debye shielding length. The origins of most broad beam ion sources can be traced back to the late 1950's, when electric space propulsion programs were started in several countries. These programs included a wide range of ion source concepts (1).

The broad-beam ion sources presently of most interest use electron-bombardment to generate ions and dc electrostatic acceleration to accelerate the ions into a beam. The electron bombardment is provided with either a dc or rf discharge. The electrostatic acceleration is provided most often by electric fields between closely spaced grids. For a broad beam of ions to be generated in this manner, multiple grid apertures must be operated in parallel. Gridless ion sources have become available in the last several years. The electric field to accelerate ions in these sources is generated by an electron current, of roughly the same magnitude as the ion beam current, interacting with a magnetic field. The ion beam current densities possible with this acceleration process are much greater than those possible with gridded sources, particularly at low ion energies.

The primary use of gridded, broad-beam sources has been in thin film research applications, which started about 1970, and increased rapidly thereafter (2,3). This rapid growth resulted from the advantages of these ion sources compared to competitive processes. These advantages include ions that are accelerated into a beam with a well-defined and controlled direction, density, and energy. Further, the ion generation is removed from, and independent of, target processes. Both control and process definition are more difficult with competitive plasma processes.

The early thin-film applications of gridded ion sources were limited to etching and deposition. In many recent applications the objective can be better described as property modification or enhancement, rather than simply etching or deposition (4).

Until recently, the few successful production applications have usually involved products of very high unit cost, so that the use of highly skilled operators could be justified

(5). The shift to conventional production applications was delayed by the complicated operation and maintenance of early gridded ion sources, which frequently resulted from inappropriate designs derived from the space-propulsion program. Ion sources suited to a production environment, both gridded and gridless, have been available for several years and have resulted in substantial increases in production applications (6,7). The review of technology presented herein will emphasize recent developments.

## 7.2 GRIDDED ION SOURCES

### 7.2.1 General Description

The schematic diagram of a gridded broad-beam ion source and its controller (power supplies) is shown in Fig. 1. The working gas is introduced into the discharge chamber, where energetic electrons from the cathode strike and ionize atoms or molecules of the working gas. The ions that approach the ion optics (the screen and accelerator grids) are extracted from the discharge chamber and accelerated into the ion beam. The apertures in the grids are aligned so that the screen grid protects the accelerator grid from direct impingement during normal operation. Electrons from the neutralizer both charge and current neutralize the ion beam. The actual recombination of these electrons with ions is normally a negligible process.

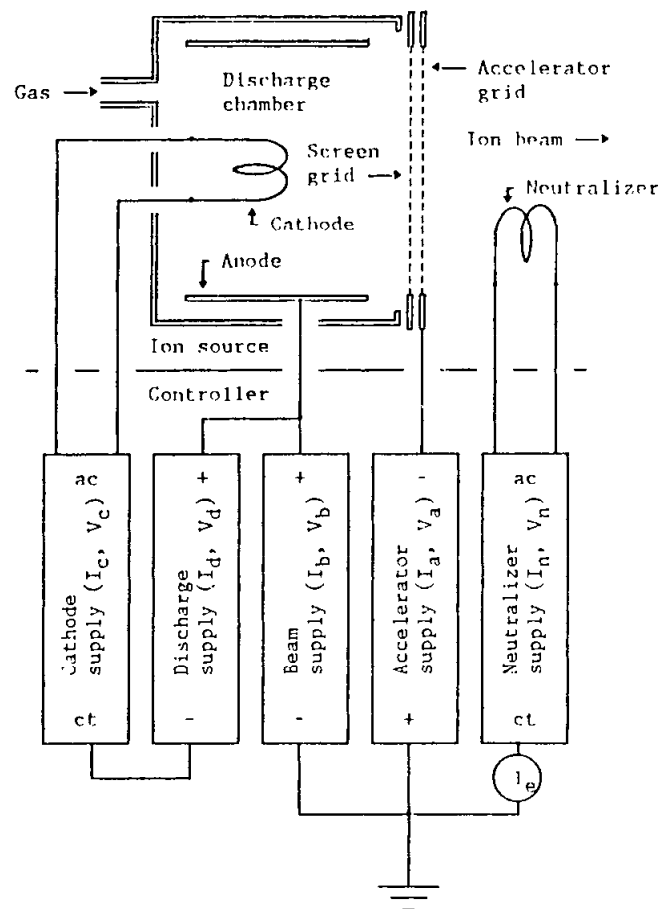


**Figure 1:** Schematic diagram of gridded, broad-beam ion source and controller.

The function of the discharge chamber is to generate ions efficiently, controllably, and with little need for maintenance. A variety of discharge chamber configurations have been used, and all use a magnetic field to contain the energetic electrons emitted from the cathode and thereby improve the efficiency. Both permanent magnets and electromagnets are used to provide the magnetic field. If an electromagnet is used, an additional power supply is required to energize the electromagnet.

The maximum ion beam current,  $I_b$ , that can be accelerated by the ion optics is given approximately by

$$I_b \simeq (\epsilon_0/9)A_b(e/m)^{1/2}V_t^{3/2}/l_g^2 \quad (1)$$

where  $\epsilon_0$  is the permittivity of space,  $A_b$  is the beam area,  $e/m$  is the charge-to-mass ratio of the accelerated ions,  $V_t$  is the total voltage ( $V_b + V_a$ ), and  $l_g$  is the gap between the screen and accelerator grids. This equation is derived from Child's law (8), but is only approximate because the effective area for ion extraction is less than the total beam area and the effective acceleration distance is greater than the gap between the grids. The actual beam current is usually only 20-50% of the approximate value given by Eq. (1).

Because the ion-beam current varies as  $V_t^{3/2}$ , the maximum beam current that can be extracted without direct impingement of energetic ions on the accelerator grid depends strongly on the beam voltage,  $V_b$ .

The cathode and neutralizer in Fig. 1 are of the hot-filament type. The electron emission for either of these functions can be supplied instead by a hollow cathode (9), which requires a separate gas flow, usually argon, krypton, or xenon.

### 7.2.2 Present Technology

The most common working gas for gridded sources is argon. Reactive gases such as nitrogen and oxygen are frequently used, and even more reactive gases incorporating chlorine or fluorine are sometimes used.

The discharge chamber and the ion optics are two major components of the ion source that have been involved in recent technology developments. Most recent improvements in discharge chamber configurations have resulted in reduced maintenance requirements. These improvements have typically used anodes that contain sputtered material and are easily removed for cleaning.

RF discharges for the generation of ions have been the subject of increased interest for thin-film applications. The types presently being investigated include inductively coupled (10), capacitively coupled (11), and microwave (12). (The inductively coupled type has been used previously in the electric space propulsion field.)

The primary advantage of an rf discharge in thin-film applications should be decreased maintenance when the ion source is operated with reactive gases. If rf discharges are to be used in a significant number of thin film applications, this decreased maintenance must be obtained without excessive contamination from the ion source during

normal operation and without excessive sensitivity to the normal industrial operating environment.

Over the past decade, improvements in ion optics have permitted increased beam current capacity at moderate beam voltages, often with increased reliability and decreased maintenance. Assuming circular ion optics, the ion-beam current can be shown to be proportional to the square of the ratio of beam diameter to grid gap,  $(d_b/l_g)^2$ . Assuming the same voltages are used, if one set of ion optics is to have a larger ion-current capacity than another set, the ratio  $d_b/l_g$  must be larger for that set. If this ratio is the same, the beam current capacities of the two ion optics sets will be approximately the same, regardless of any difference in physical size.

The ion current densities that are obtainable depend on the grid spacing ( $l_g$  in Eq. (1)) and the voltages used. Note that the ion-beam current is very sensitive to total voltage. A quoted ion-beam current or current density therefore has little meaning without the corresponding ion energy. For example, higher beam currents can always be obtained at high beam voltages,  $V_b$ , of 1500-2000 V. Such high voltages and ion energies can, however, cause excessive damage to substrates and photoresist in etching applications and are relatively inefficient in terms of material removed per unit beam energy in either etching or deposition applications.

To fully utilize a small grid spacing, small grid apertures and grid thicknesses should be used. As the grid spacing is reduced, then, the reduced aperture diameters and reduced grid thicknesses result in an increasingly fragile grid structure. The limit is not a clearcut one, but the increasing difficulty in handling and maintaining fragile grids does result in a practical limit on the minimum grid spacing. Graphite grids tend to present more handling and maintenance problems than molybdenum grids in a production environment.

The trend is toward larger ion sources for larger production capability. To maintain a small grid gap,  $l_g$ , over a large beam diameter,  $d_b$ , requires careful thermo-mechanical design. The largest value of  $d_b/l_g$ , hence the largest beam current capability at moderate beam voltages, is presently obtained with dished molybdenum grids (7).

An example of present production capability is an ion source with a beam diameter of about 0.4 m (7). Ion-beam currents of 4-5 A are possible - up to 4 A without exceeding 1000 eV (a beam voltage,  $V_b$ , of 1000 V). These large ion-beam currents permit a substantial increase in processing capability. A cutaway sketch of a large ion source is shown in Fig. 2. Ease of maintenance and reliable operation are crucial for a production environment. The discharge chamber anode covers and protects the magnet and pole-piece structure, so that this structure does not accumulate debris and require cleaning. The anode is also readily removable for cleaning.

The ion optics are dished molybdenum. As described previously (5), alignment of the ion optics for broad beam sources has been a major maintenance and reliability problem. A large number of ion optics that require a manual alignment procedure have been used in the past. The serious nature of the alignment problem is indicated by the fact that most of these ion optics have, after extended service, accelerator-grid apertures that have been worn into noncircular shapes by operation while misaligned. Ion optics can be designed to obtain precise alignment from a straightforward assembly procedure;(13) thus bypassing manual alignment altogether.

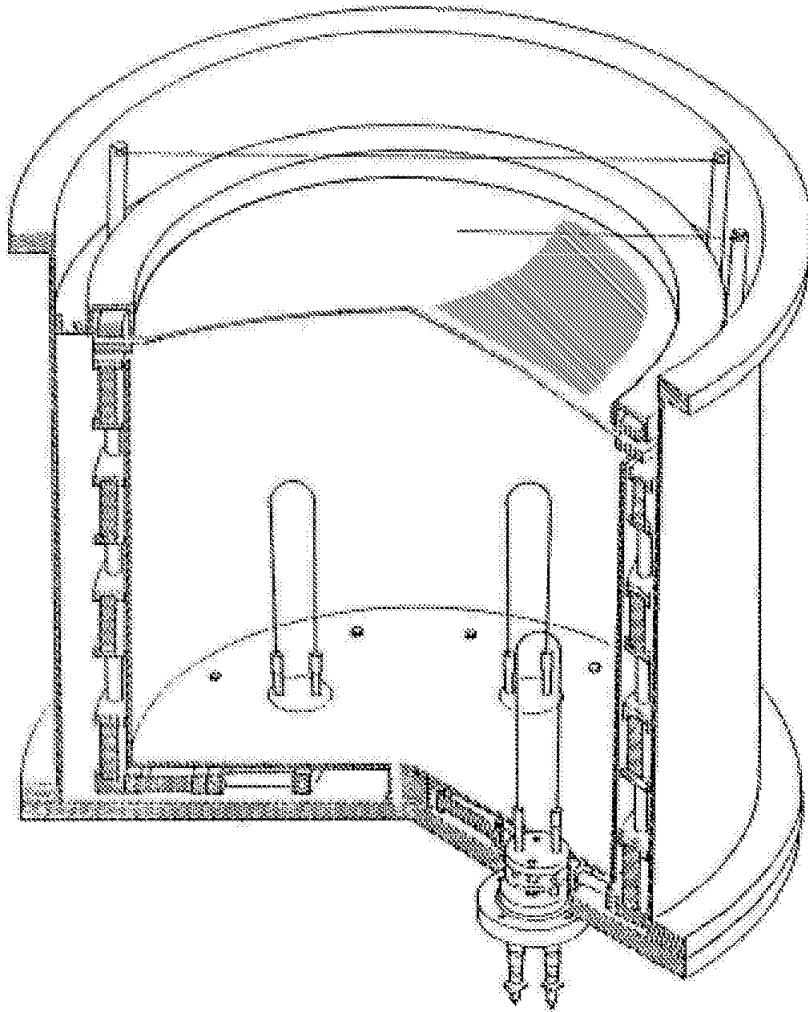


**Figure 2:** Cutaway sketch of large production ion source.

### 7.3 GRIDLESS ION SOURCES

#### 7.3.1 General Description

The schematic diagram of a gridless broad-beam ion source and its controller is shown in Fig. 3. The electron emission from the cathode is controlled with the cathode supply. The anode potential is determined by the anode current, the strength of the magnetic field, and the gas flow. An electromagnet is shown in Fig. 3, but a permanent magnet can also be used, thereby eliminating one of the power supplies shown. A gas flowmeter is included because the voltage of the anode supply is normally controlled by the gas flow at a particular beam current. The cathode supply is customarily an ac supply when filament cathodes are used; however, hollow cathodes are also used as electron sources. As mentioned above, the gases used for hollow cathodes in industrial applications have been inert gases.



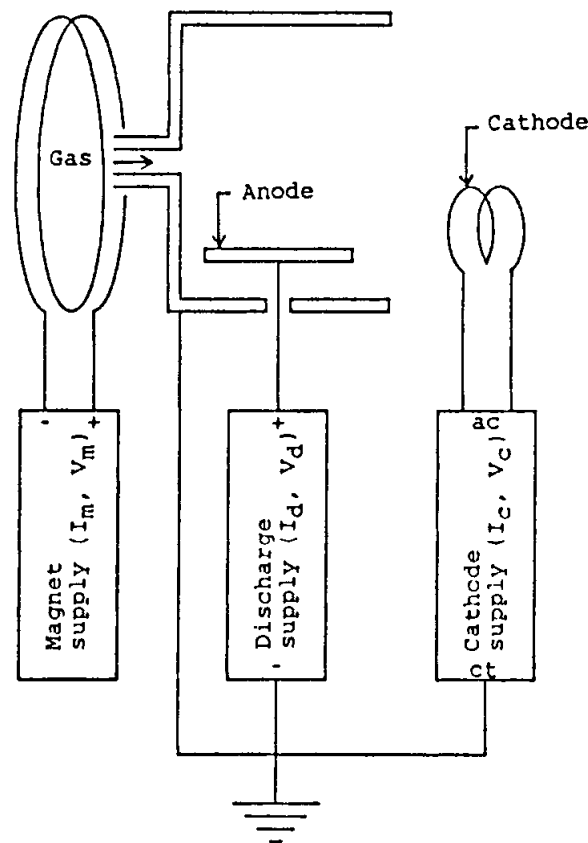


**Figure 3:** Schematic diagram of a gridless, broad-beam ion source and controller.

A gridless ion source can be described as a plasma device operating in approximately the glow-discharge regime. The ions are electrostatically accelerated into a beam with the accelerating electric field established by an electron current of comparable magnitude to the ion beam current, interacting with a magnetic field. One component of the electron motion is counter to the ion flow. Another component is normal to that direction. The current associated with this normal component is called the Hall current. In gridless ion sources there is a complete, or closed, path for the Hall current. In addition, for the ions to be accelerated into a beam, rather than much more diffusely, the ion cyclotron radius must be much larger than the total acceleration length.

Even when operating properly, though, the ions in a gridless ion source are generated over an extended region with varying potentials, resulting in beam ions with a range of energy, typically  $\pm 30\%$  of the mean ion energy. This is much more than the several Volt variation of potential in the discharge chamber of a correctly operating gridded ion source.

The positive space charge and current due to the ions in this beam are neutralized by some of the electrons that leave the cathode. Most of the electrons from the cathode flow back toward the anode and both generate ions and establish the potential difference that accelerates these ions. The excess electron emission from the cathode is approximately sufficient to current-neutralize the ion beam when the electron emission equals the anode current. The cathode is operated in excess of this current in many thin film applications.

There are several types of gridless ion sources. Two basic geometries are described herein. The end-Hall type, named because the beam exits the acceleration region at the end (axis) of the magnetic field, and the closed-drift type, in which the ion-acceleration channel is annular, rather than circular as it is in the end-Hall. There can be a number of variations within these two general categories that emphasize particular operating or performance characteristics. Usually, but not always, closed paths for the circulating Hall current are provided with axially symmetric electrodes and magnetic pole pieces.

The cross section of a closed-drift ion source is shown in Fig. 4 along with a schematic electrical diagram. The magnetic field direction is generally radial. The electrons from the cathode flow back through the annular channel to the anode. In passing through the radial magnetic field, a circulating Hall current is generated in the annular channel.

Most closed-drift ion sources have had dielectric channel walls and a channel length at least equal to the channel width, as indicated in Fig. 4 (1,15-17). In addition, the electron cyclotron orbit is small compared to the acceleration length.

The electric field that accelerates the ions is generated in the radial magnetic field of a closed drift ion source, and is the result of the reduced plasma conductivity across magnetic-field lines. The strong-field approximation is appropriate for the field strengths used in the closed drift source. The ratio of conductivities parallel and transverse to the magnetic field is then

$$\sigma_{\parallel}/\sigma_{\perp} = (\omega_c/\nu_e)^2 \quad (2)$$

where  $\omega_c$  is the electron-cyclotron (angular) frequency and  $\nu_e$  is the electron collision frequency. The electron collision frequency is determined by the plasma fluctuations associated with anomalous diffusion when conduction is across a strong magnetic field. Using Bohm diffusion to estimate this frequency,

$$\sigma_{\parallel}/\sigma_{\perp} = 256 \quad (3)$$

Because Bohm diffusion is typically accurate only within a factor of several, the ratio of Eq. (2) should be treated as correct within an order of magnitude. It should still be expected that

$$\sigma_{\parallel} \gg \sigma_{\perp} \quad (4)$$

Analysis of the closed-drift acceleration process shows that two distinctly different acceleration processes can take place. In one case the electrons in the acceleration region were assumed to be at a negligible temperature (zero). The potential variation throughout the acceleration region then was found to be smooth and continuous. As a result of the continuous and extended acceleration process, this type has been called a closed-drift extended-acceleration (CDEA) source (18). If, however, the electrons were assumed to heat up as they flowed from the ion exit to the ion formation region, then a near-discontinuous potential jump occurred at the positive end of the acceleration channel. The remainder of the acceleration was assumed to take place in an axial length of the or-

der of the local electron-cyclotron orbit. Accelerators that operate with this type of acceleration are called anode-layer accelerators (19).

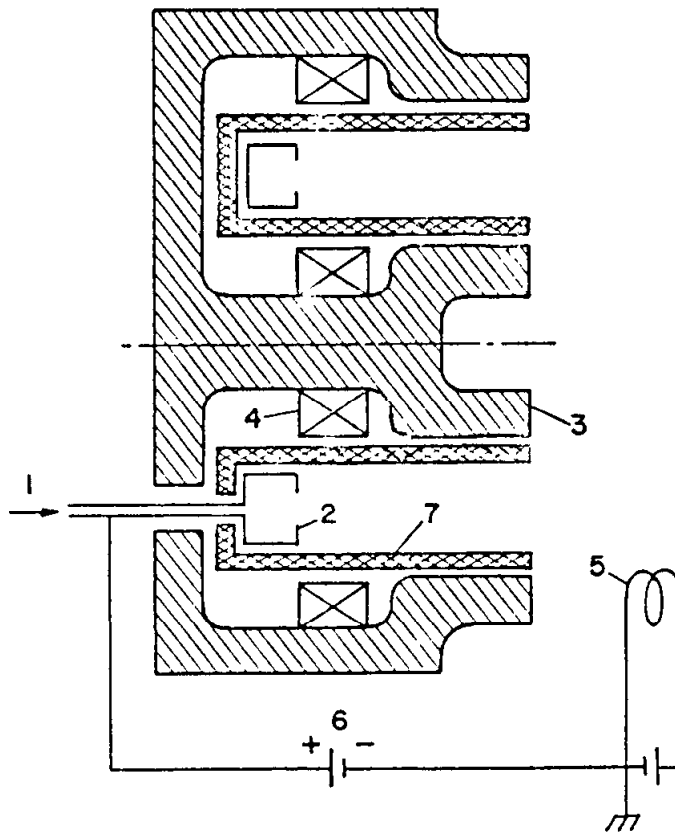


**Figure 4:** Closed-drift extended-acceleration (CDEA), thruster (single stage). (1) Gas feed; (2) anode distributor; (3) magnetic circuit, pole pieces; (4) magnetic winding; (5) cathode neutralizer; (6) discharge power supply; (7) insulator (Ref. 14).

Except for certain geometrical considerations the operation of the end-Hall source can be described in the same general manner as the closed-drift ion source. The cross section of an end-Hall ion source is indicated in Fig. 5. The neutral atoms or molecules of the working gas are introduced to the ion source through a port. Electrons from the cathode approximately follow magnetic field lines back to the discharge region enclosed by the anode and strike atoms or molecules therein. Some of these collisions produce ions. The mixture of electrons and ions in the discharge region forms a plasma. Because the density of the neutral atoms or molecules decreases rapidly downstream of the anode (toward the cathode) most of the ionizing collisions with neutrals occur in the region surrounded by the anode.

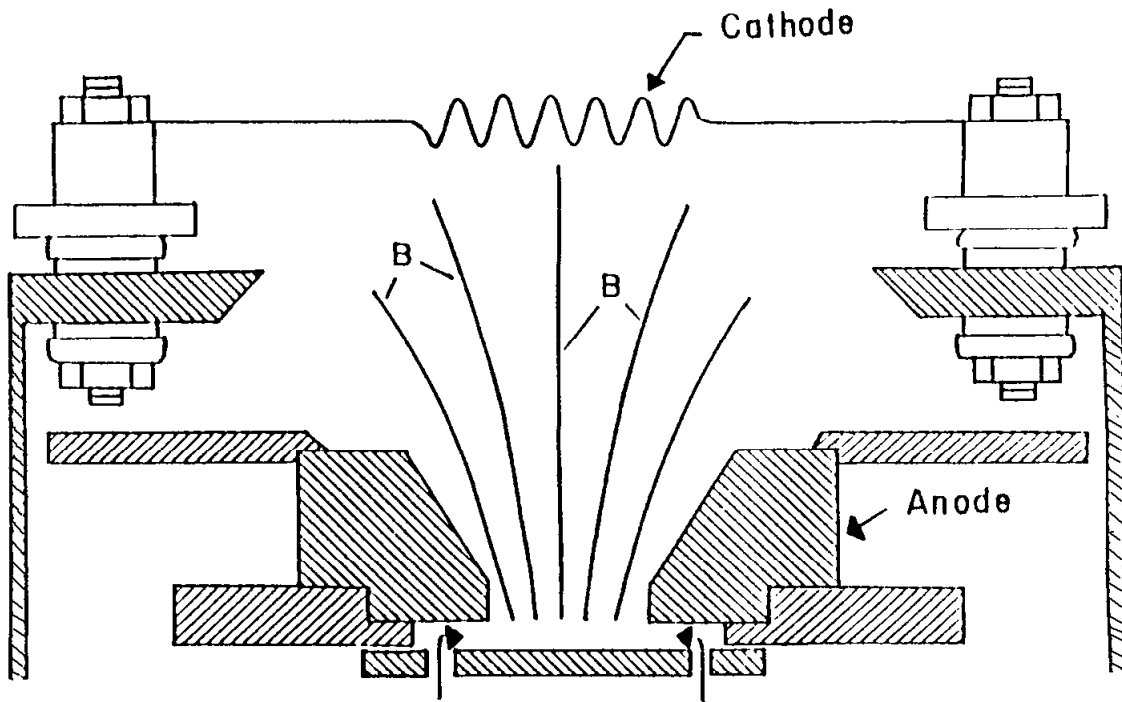


**Figure 5:** Cross section of an end-Hall ion source.

From the difference in conductivity parallel and normal to the magnetic field (Eq. (4)), it would be expected that the magnetic field lines in Fig. 5 would approximately determine the equipotential contours in the plasma. Further, the field lines closer to the anode would be more positive in potential. Radial surveys of plasma potential made using a Langmuir probe show some potential increase when moving from the axis to a magnetic field line close to the anode, but the increase is only a fraction of the total anode-cathode potential difference. The bulk of this difference appears in the axial direction. That is, parallel to the magnetic field, where, from Eq. (4), the potential difference would be expected to be small.

The time-averaged force of a nonuniform magnetic field on an electron moving in a circular orbit can be calculated. For a variation of field strength in only the direction of the magnetic field, this force is parallel to the magnetic field and toward decreased field strength (opposite the field gradient). Assuming an isotropic distribution of electron velocities, two-thirds of the electron energy is associated with motion normal to the magnetic field, and therefore interacts with this field. For a uniform plasma density, the potential difference in the plasma can then be obtained by integrating the electric field required to balance the magnetic-field force on the electron, which gives

$$\Delta V_p = (kT_e/e) \ln(B/B_0) \quad (5)$$

where  $k$  is the Boltzmann constant,  $T_e$  is the electron temperature in K,  $e$  is the electronic charge, and  $B$  and  $B_0$  are the magnetic-field strengths in two locations. With  $B > B_0$ , the plasma potential,  $V_p$ , at  $B$  is greater than that at  $B_0$ .

Axial surveys (6) of plasma potential in the end-Hall source are found to be in approximate agreement with Eq. (5). There is an additional effect of plasma density on potential, and a more complete description of the variation of plasma potential with magnetic-field strength must also include this effect.

### 7.3.2 Present Technology

The only gridless ion sources that are commercially available for thin film applications are the end-Hall type. These gridless ion sources can be used for beam currents up to about one Ampere, and can readily be developed for larger currents. Typical ion energies range from about 30 eV to a little over 100 eV.

End-Hall ion sources have been used in thin-film and surface processing applications for a comparatively short time (6). The high-current, low-energy capabilities of these sources make them particularly suited to thin film property modification or enhancement, such as increasing hardness, passivating surfaces, producing a preferred crystal orientation, activating surface chemical reactions or improving step coverage. They are also suited to a production environment because they are simple to operate, mechanically rugged, and reliable. Oxygen and nitrogen are probably the most frequently used gases in these ion sources.

### 7.4 CONCLUDING REMARKS

Gridded ion sources with the reliability, ease of maintenance, and large processing capability should find greatly increased use in production applications.

Hall-effect ion sources generate ion beams with fairly well-controlled direction, a controllable energy range and current density. The major advantage of these sources is the ability to generate large ion currents at low energy. These sources should find increased application in thin film and surface processing, especially in production, where a simple, reliable source of large ion currents can have a significant impact.

### 7.5 REFERENCES

1. G.R. Seikel, Generation of Thrust - Electromagnetic Thrusters, in NASA-University Conference on the Science and Technology of Space Exploration, Vol. 2: NASA SP-11, Nov. 1962, pp. 171-176; W. D. Rayle, Generation of Thrust - Electrostatic Thrusters, *ibid.*, pp. 177-182; M. C. Ellis, Jr., Survey of Plasma Accelerator Research, *ibid.*, pp.361-381.
2. D. T. Hawkins, Ion Milling (Ion-Beam Etching), 1954-1975: A Bibliography, J. Vac. Sci. Technol. 12: pp. 1389-1398 (1975).
3. D. T. Hawkins, Ion Milling (Ion-Beam Etching), 1975-1978: A Bibliography, J. Vac. Sci. Technol. 16: pp. 1051-1071 (1979).

4. J. M. E. Harper, J. J. Cuomo, R. J. Gambino, and H. R. Kaufman, Modification of Thin Film Properties by Ion Bombardment During Deposition, in Ion Bombardment Modification of Surfaces: Fundamentals and Applications ed. by O. Auciello and R. Kelly, Elsevier Science Publishers B. V., Amsterdam, pp. 127-162 (1984).
5. H. R. Kaufman, Broad-Beam Ion Sources: Present Status and Future Directions, J. Vac. Sci. Technol. A4: pp. 764-771 (1986).
6. H. R. Kaufman, R. S. Robinson, and R. I. Seddo, End-Hall Ion Source, J. Vac. Sci. Technol. A5: pp. 2081-2084 (1987); J.J. Cuomo and H.R. Kaufman, US Patent 4,541,890, Oct. 3, 1985.
7. H. R. Kaufman, W. E. Hughes, R. S. Robinson, and G. R. Thompson, Thirty-Eight Centimeter Ion Source, presented at the 7th International Conference on Ion Implantation Technology, June 7-10, 1988, Kyoto, Japan.
8. C. D. Child, Discharge from Hot CaO, Phys. Rev. 32: pp. 492-511 (1911).
9. H. R. Kaufman, Technology of Electron-Bombardment Thrusters, in Advances in Electronics and Electron Physics 36: ed. by L. Marton, pp. 265-373, Academic Press, New York (1974).
10. J. Freisinger, J. Krempel-Hesse, J. Krumeich, H. W. Loeb, and A. Scharmann, Rf-Ion Source RIM 10 for Material Processing with Reactive Gases, presented at International Conference on Gas Discharges and Their Applications, Venice, 19-23 September 1988.
11. R. Lossy and J. Engemann, Characterization of a Reactive Broad Beam Radio-Frequency Ion Source, J. Vac. Sci. Technol. B6: pp. 284-287, (1988).
12. L. Mahoney, M. Dahimene, and J. Asmussen, Low Power, 3.2 cm, Efficient Microwave Electron Cyclotron Resonant Ion Source, Rev. Sci. Instrum. 59: pp. 448-452 (1988).
13. H. R. Kaufman and R. S. Robinson, patent pending.
14. H.R. Kaufman, Technology of Closed Drift Thrusters, AIAA J. 23: pp. 78-87 (1985).
15. G. R. Seikel, and E. Reshotko, Hall Current Ion Accelerator, Bull. Amer. Phys. Soc. Ser. II, 7: p. 414 (1962); E.C. Lary, E. C., R. C. Meyerand, Jr., and F. Salz, Ion Acceleration in Gyro-Dominated Neutral Plasma-Theory, *ibid.*, p. 441; Salz, F., Meyerand, R. G. Jr., and Lary, E. C., Ion Acceleration in a Gyro-Dominated Neutral Plasma-Experiment, *ibid.*, p. 441.
16. E.A. Pinsley, C. O. Brown, and C.M. Banas, Hall-Current Accelerator Utilizing Surface Contact Ionization, J. of Spacecraft and Rockets 1: pp. 525-531 (1964).
17. C. O. Brown and E. A. Pinsley, Further Experimental Investigations of a Cesium Hall-Current Accelerator, AIAA J. 3: pp. 853-859 (1965).
18. I. A. Morozov, Yu. V. Esipchuk, G. N. Tilinin, A. V. Trofimov, Yu. A. Sharov, and G. Ya. Shchepkin, G. Ya., Plasma Accelerator with Closed Electron Drift and Extended Acceleration Zone, Sov. Phys. Tech. Phys. 17: pp. 38-45 (1972).
19. N. A. Bardadymov, A. B. Ivashkin, L. V. Leskov, and A. V. Trofimov, Hybrid Closed Electron Drift Accelerator, Abstracts for IV All-Union Conference on Plasma Accelerators and Ion Injectors, Moscow, pp. 68-69 (1978).

---

## Reactive Ion Etching

---

**Gottlieb S. Oehrlein**

### 8.1 INTRODUCTION

Wet etching processes in many semiconductor manufacturing steps have been replaced by plasma assisted etching procedures. The most important driving force behind the rapid introduction of plasma-based etching technology into current semiconductor manufacturing has been the achievement of etch directionality and the ability to faithfully transfer lithographically defined photoresist patterns into underlying layers. In addition, plasma based dry etching processes are superior to wet etching because of cleanliness, compatibility with automation and vacuum processing technologies, such as molecular beam epitaxy. Plasma-based etching techniques include ion milling, sputter etching, reactive ion beam etching, plasma etching, and reactive ion etching, several of which have been reviewed in this book. This chapter is devoted to a survey of reactive ion etching [1].

Reactive ion etching (RIE) is a plasma-based dry etching technique characterized by a combination of physical sputtering with the chemical activity of reactive species. This enables the achievement of material selective etch anisotropy.

#### 8.1.1 Basic RIE Apparatus and Reaction Steps

A basic reactive ion etch system is schematically illustrated in Fig. 1. The following processes take place in the system during ion enhanced etching:

- a. Active species generation: In RIE a glow discharge is used to generate from a suitable feed gas (e.g., carbontetrafluoride -  $\text{CF}_4$  - in the case of silicon and silicon dioxide) by electron-impact dissociation/ionization the gas phase etching environment which consists of radicals, positive and negative ions, electrons, and neutrals.
- b. Formation of a dc bias for ion acceleration: The material to be etched is placed on a high-frequency-driven (commonly 13.56MHz) capacitatively coupled electrode. Since the electron mobility is much greater than the ion mobility,

after ignition of the plasma the electrode acquires a negative charge (the corresponding voltage is called self-bias voltage). Therefore, the electrode and material placed on the electrode will be exposed to energetic, positive ion bombardment.

- c. Transport of plasma-generated reactive intermediates from the bulk of the plasma to the surface of the material being etched: This occurs by diffusion which, for particular structures such as narrow deep trenches, can limit the etch rate.
- d. Adsorption step: Reactive radicals (F atoms) adsorb on the surface of the material (Si) to be etched. This step can be strongly enhanced by concurrent ion bombardment which serves to produce "active sites" since it aids in the removal of the fluorinated surface layer which otherwise passivates the Si surface.

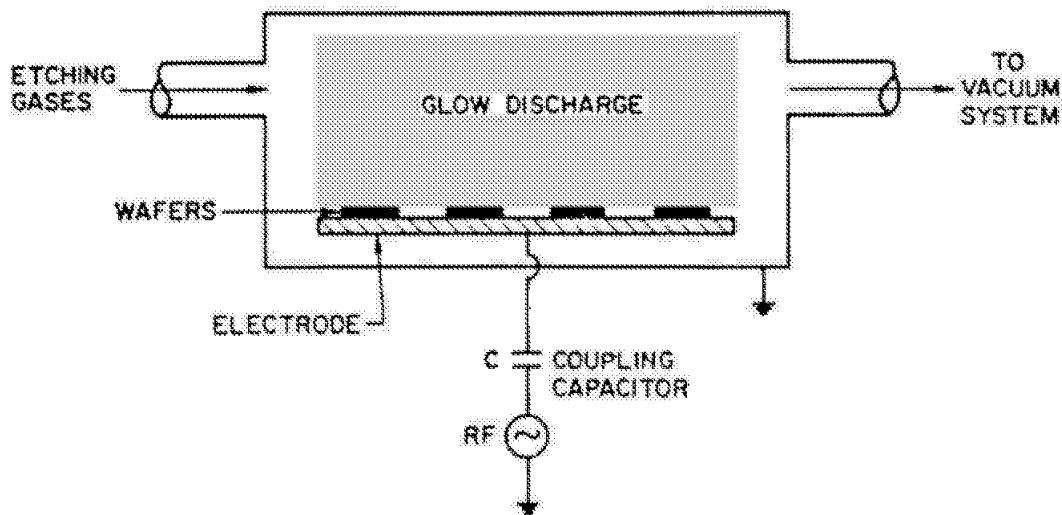


**Figure 1:** Schematic diagram of apparatus used for reactive ion etching in semiconductor processing.

- e. Reaction step: A reaction between the adsorbed species and the material to be etched must take place. In the case of fluorine-based etching of silicon chemical reactions between the fluorine atoms and the surface produces either volatile species ( $\text{SiF}_4$ ) or their precursors ( $\text{SiF}$ ,  $\text{SiF}_2$ ,  $\text{SiF}_3$ ). Because of the plasma-induced formation of reactive radicals, e.g., fluorine atoms, etc., the reaction rate is very large relative to reaction rates in non-plasma environments. The reaction step can be greatly enhanced by ion bombardment. For instance, chlorine atoms are known to adsorb readily on silicon surfaces but the spontaneous etch rate in a glow discharge without ion bombardment is very slow. Ion bombardment makes it possible for adsorbed chlorine atoms to attack more efficiently the backbonds of silicon and form a volatile  $\text{SiCl}_4$  molecule.
- f. Desorption of volatile reaction product: The desorption of the reaction product into the gas phase is one of the most critical steps in the overall etching reaction. This requires that the reaction product has a high vapor pressure at the substrate temperature which, in RIE, is typically below  $100^\circ\text{C}$ . The removal



of reaction product from the surface can be greatly accelerated by ion bombardment via sputtering.

- g. Pumpout of volatile reaction product: This requires that the desorbed species diffuse from the etching surface into the bulk of the plasma and are pumped out. Otherwise plasma induced dissociation of product molecules will occur and redeposition can take place.

Table 1 is a (non-critical) collection of typical RIE parameters reported in the literature [1] and is primarily intended to provide the reader with a rough idea of the magnitude of these quantities.

**Table 1:** Typical characteristics of low pressure plasmas used for reactive ion etching.

<u>Quantity</u>	<u>Typical Values</u>
rf Power Density	0.05-1.0 W/cm <sup>2</sup>
rf Frequency	10 kHz - 27 MHz (commonly 13.56 MHz)
Pressure	0.01-0.2 Torr
Gas Flow	10-200 sccm
Wafer Temperature	-120°C up to 300°C
Gas Temperature	300-600 K
Electron Temperature	3-30 eV (bulk of plasma)
Ion Energies	≈ .05 e V (bulk of plasma) 10-500 eV (after traversing cathode sheath)
Gas Number Density	3.5x10 <sup>14</sup> – 7x10 <sup>15</sup> cm <sup>-3</sup>
Ion Density	10 <sup>9</sup> -10 <sup>10</sup> cm <sup>-3</sup>
Electron Density	Similar to ion density
Ion Flux	10 <sup>14</sup> – 10 <sup>15</sup> cm <sup>-2</sup> sec <sup>-2</sup>
Radical Flux	10 <sup>16</sup> cm <sup>-2</sup> sec <sup>-1</sup>
Neutral Flux	3.6x10 <sup>18</sup> – 7.2x10 <sup>19</sup> cm <sup>-2</sup> sec <sup>-1</sup>

### 8.1.2 RIE PROCESSES IN SEMICONDUCTOR TECHNOLOGY

Although the physical and chemical processes underlying reactive ion etching are still only incompletely understood, RIE has been very successful in meeting the etching requirements of today's semiconductor technology in regard to etch directionality and etch selectivity [2]. With etch directionality (or etch anisotropy) the ratio of vertical to horizontal etch rate of a material immersed in a plasma is conventionally denoted. The etch selectivity between two materials is the ratio between their etch rates under the same conditions. Etch selectivity is much more difficult to achieve in reactive ion etching than in wet etching, since the substantial ion bombardment involved in RIE makes chemical differences between different materials less important in the etching process.

In Table 2 etching steps in silicon device processing which are currently performed using reactive ion etching or plasma etching are listed. Many of the processes listed are non-critical etches and the desired objectives are relatively easy to achieve. The demands on etch directionality are highest in the formation of deep ( $\approx 6 \mu\text{m}$  and greater) trenches for storage capacitors in the silicon substrate. The most challenging applications from the point of view of etch selectivity are (a) the formation of contact holes through oxide to silicon and silicided junctions and (b) polysilicon/polycide gate definition and stopping on a thin ( $\leq 10\text{nm}$ ) oxide. Other etching steps are associated with different challenges, e.g. the patterning of Al(Cu) in chlorine discharges [3]. Copper is added at the percent level to Al in order to increase the electromigration resistance of Al lines.  $\text{AlCl}_3$  has high volatility at room temperature and aluminum etches easily in chlorine;  $\text{CuCl}$  has low volatility and Cu related residues can form. In order to remove the  $\text{CuCl}$  effectively both a higher temperature and significant ion bombardment are needed. These critical applications have been well researched and a great deal of understanding has been obtained. In this article we will use these prototypical applications to highlight our current understanding of etch selectivity and etch directionality mechanisms in RIE. The considerations presented in this article apply to etching applications characterized by similar requirements but not covered because of space limitations, e.g. RIE of compound semiconductors, polymers, etc.

**Table 2:** Common applications of plasma/reactive ion etching in silicon technology.

<u>Application</u>	<u>Etch Step</u>
Device Formation	Polysilicon/polycide gate; sidewall; storage node; emitter contact.
Isolation	Deep trench; shallow trench or recessed oxide.
Interconnections	Contacts; metal; interlevel vias.
Other	Multilayer resist definition; resist strip; backside strip; planarization.

This chapter is a brief review of reactive ion etching as applied to pattern transfer, primarily in silicon technology. Most of the past (and present) efforts to understand plasma-based dry etching processes have been directed to the investigation of halogen-based etching of silicon and silicon related materials and our knowledge of those systems has reached a level of maturity which is far greater than of other etchant-substrate systems. Several of the topics covered also are of particular interest to this author and, for the sake of convenience, I have disproportionately drawn on experimental results of my collaborators in the description of these topics. Rapid progress is being made in all aspects of plasma based etching; therefore this review focuses on concepts, rather than listing data obtained on all different systems. Although the detailed plasma chemistry of rf discharges used for etching materials of interest to compound semiconductor technology, packaging, etc., is different from the one described here, many of the basic processes are similar. Many of the considerations presented in this article can therefore be cautiously adapted to plasmas utilized for the patterning of different materials.

## 8.2. ETCH DIRECTIONALITY

### 8.2.1 General Considerations

Etch directionality is due to directed energy input into an etching reaction at a surface and can be accomplished by ion, electron or photon bombardment of a surface exposed to a chemical etchant. The achievement of etch directionality in the case of RIE is due to energetic ion bombardment. An important clarifying experiment was performed by Coburn and Winters [4]. They exposed a silicon surface to a well-defined dosage of chemical etchant,  $\text{XeF}_2$ , and simultaneous energetic Ar ion bombardment. A key result of their studies has been that the silicon erosion rate obtained for a silicon surface simultaneously exposed to the  $\text{XeF}_2$  chemical etchant and to the Ar ion beam is much greater than the sum of the etch rates for exposure to the ion beam and chemical etchant separately. This synergism can explain the etch anisotropy obtained under these conditions. Recent photoemission work by McFeely et al. [5] has shed some light on the mechanism of ion enhanced etching for the  $\text{XeF}_2/\text{Si}$  system: It was observed that a silicon-fluorine reaction layer much thicker than a monolayer was formed. Volatile  $\text{SiF}_4$  was seen trapped in the reaction layer. A preponderance of  $\text{SiF}_3$  was observed which suggested that the reaction to form  $\text{SiF}_4$  from  $\text{SiF}_3$  was the rate limiting step of the etching reaction. It was observed that when the reaction layer was bombarded with Ar ions the Ar ion beam tended to drive a disproportionate reaction in which involatile  $\text{SiF}_3$  molecules on the Si surface were converted into  $\text{SiF}_2$  and volatile  $\text{SiF}_4$  etch product.

Several mechanisms have been proposed for ion-induced reactions resulting in enhanced etching [6,7]. Some of the primary models are:

- a. Chemically enhanced physical sputtering [8]  
In this model the modified surface layer has a larger sputtering yield than the unmodified surface, e.g.  $\text{SiF}_x$  – species are less tightly bound than Si and have a greater sputtering yield.
- b. Damage model [9]  
Lattice damage produced by ion bombardment increases the reaction rate of etchant species with the substrate relative to undamaged material.
- c. Chemical sputtering model [10]  
In this model ion bombardment induced collision cascades supply energy to the reaction layer which is used to increase the mobility of molecules which will form volatile products and desorb into the gas phase.

There are other models or variants of above models. Depending on the particular etchant-substrate under consideration a different ion-enhancement mechanism may be dominant. For instance, it appears that the lattice damage model is not important for the fluorine-silicon system [11], while there is evidence of its importance for the fluorine-tungsten system [11,12].

### 8.2.2 Fluorine- vs. Chlorine- vs. Bromine-Based Plasmas

Etching of Si can be accomplished using F-, Cl-, and Br-based chemistries and the etch products are volatile  $\text{SiF}_4$ ,  $\text{SiCl}_4$  and  $\text{SiBr}_4$ , respectively. Most studies have focused on halocarbon chemistries, specifically  $\text{CF}_4$ . Mogab studied the etching of Si in a  $\text{CF}_4$  plasma with negligible ion bombardment of the Si substrate [13]. He measured the in-

tensity of the 704nm atomic fluorine related optical emission. A one-to-one correspondence of Si etch rate and atomic fluorine emission as the rf power was varied was observed, showing that F atoms are directly involved and their gas phase density controls the rate of the Si etching process for simple  $\text{CF}_4$  plasmas. Etching of silicon in fluorine-based plasmas results normally in a large undercut of the masking layer, indicating a large chemical etch rate. Because of this fluorine-based plasmas have not commonly been used for anisotropic etching of silicon. However, Tachi and his coworkers showed recently that the horizontal silicon etch rate using an  $\text{SF}_6$  plasma can be dramatically reduced by cooling the substrate to a temperature of  $-120^\circ\text{C}$  and near-ideal etch profiles can be obtained [14]. The low substrate temperature was thought to suppress spontaneous chemical etching reactions occurring on the sidewalls of the trench. Ion assisted etching reactions which dominate at the bottom of the trench were not affected by the low substrate temperature and the vertical silicon etch rate increased as the temperature was decreased, possibly due to condensation of etchant.

Chlorine and bromine based chemistries are primarily used to achieve anisotropic etch profiles in single crystal silicon. Etch directionality for these etchants may be explained by the observation that crystalline silicon and silicon dioxide are not spontaneously etched by chlorine and bromine atoms [15]. Chlorine molecules dissociatively chemisorb on single crystal silicon at room temperature and form an ordered chlorine overlayer. Cluster calculations have shown that chlorine atoms on a silicon surface have to overcome an energy barrier of  $\approx 10\text{eV}$  in order to attack the backbonds of silicon surface atoms in order to form  $\text{SiCl}_4$  [16]. No energy barrier for fluorine to penetration of the silicon surface was found, indicating that sub-surface  $\text{SiF}_x$  species will form spontaneously. The size of the halogen relative to the silicon atom plays an important role. The results of the calculations are consistent with the absence of spontaneous etching of silicon exposed to chlorine atoms. Chlorine based etching of undoped silicon and equivalent etching conditions have been described as ion-initiated etching in contrast to fluorine-based etching which is ion-assisted [9]. Etching of silicon using  $\text{Cl}_2/\text{Ar}$  RIE results in very directional profiles [17]. It is possible that sidewall passivation is absent under these conditions, although it is not possible to rule out a sidewall passivation layer formed by redeposition of masking material.

In contrast to undoped silicon, highly doped silicon (dopant concentration  $\approx 10^{20}\text{cm}^{-3}$ ) etches spontaneously in a  $\text{Cl}_2$  discharge. Schwartz et al. [17] observed horizontal etching of a buried highly As-doped silicon layer in a low pressure (10 mTorr)  $\text{Cl}_2$  discharge (see Fig. 2). However, for a  $\text{CCl}_4$  discharge or undoped silicon the etching was perfectly directional. Mogab et al. observed that etching of doped polycrystalline silicon in a 300mTorr  $\text{Cl}_2$  plasma resulted in an isotropic profile [18]. Directional etching could be achieved by adding  $\text{C}_2\text{F}_6$  to  $\text{Cl}_2$  and forming a sidewall passivation layer. The doping effect and the concept of sidewall passivation will be discussed in the following sections.

Mixed halocarbon etching gases containing chlorine and bromine are often used for anisotropic etching, e.g.  $\text{CClF}_3$ ,  $\text{CCl}_2\text{F}_2$ ,  $\text{CCl}_3\text{F}$ ,  $\text{CF}_3\text{Br}$ . The fluorine-carbon bond is stronger than the chlorine-carbon or bromine-carbon bond. Electron-impact dissociation of the mixed halocarbons produces primarily chlorine or bromine atoms and the etching characteristics using these discharges are chlorine- or bromine-like. For example, Matsuo [19] used a 30mTorr  $\text{CF}_3\text{Br}$  plasma to directionally etch silicon using an oxide mask, whereas a  $\text{CF}_4$  plasma using similar conditions resulted in nearly isotropic etching characteristics. The concentration of chlorine and bromine can be increased by adding oxygen

to the mixed halocarbon gases [9]. However, this will also result in oxidation of the fluorocarbon recombinant ( $\text{CF}_3$ ) and reduce the tendency for polymer formation and sidewall passivation.

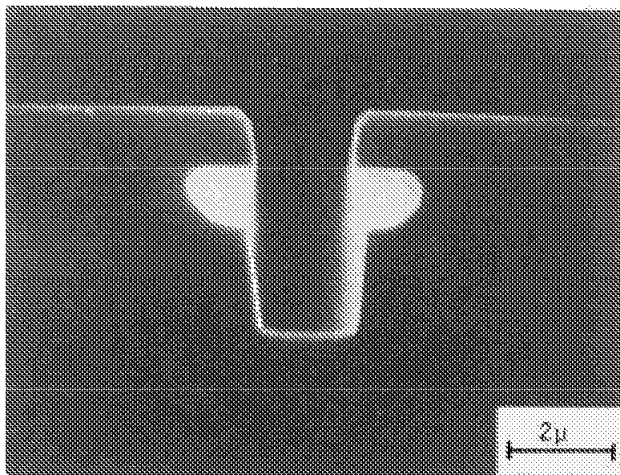


**Figure 2:** Scanning electron micrograph illustrating the lateral etching of a highly As doped Si layer in a  $\text{Cl}_2/\text{As}$  plasma. The etching parameters were: 2mTorr  $\text{Cl}_2$ /8mTorr Ar, 11sccm  $\text{Cl}_2$ , 27.12 MHz, 0.67W/cm<sup>2</sup> (From Ref. 17).

### 8.2.3 Doping Effect

The Si etch rate depends on the electronic properties of the Si substrate (doping effect). N-type silicon (e.g. P, As, etc. doped) etches faster than intrinsic silicon which etches faster than p-type silicon (B, Ga, etc. doped). The dopant concentration of silicon needs to be greater than  $\approx 10^{19}\text{cm}^{-3}$  in order to observe a doping dependence of the etch rate. Figure 3 is from the work by Lee et al. [20] who measured the chemical etch rate of silicon per gas phase fluorine atom as a function of rf power. Heavily As-doped silicon (n-type) etched faster than intrinsic silicon which etched faster than heavily B-doped silicon (p-type). The increase in the silicon etch rate per gas phase fluorine atom with rf power was thought to be due to heating of the silicon substrates. The doping effect is not chemical in nature since it is absent if the dopants are not electrically activated [18]. The doping effect depends on the electronic structure of the surface and has been explained by band bending effects at the semiconductor surface [20]. Coulomb attraction between uncompensated donors, such as  $\text{As}^+$ , and chemisorbed halogens, e.g.  $\text{F}^-$ , enhances the Si etch rate for n-type Si. On the other hand, Coulomb repulsion between uncompensated acceptors, e.g.  $\text{B}^-$ , and chemisorbed halogens, such as  $\text{F}^-$ , inhibits the Si etch rate for p-type Si. A detailed study of the doping effect for silicon has recently been completed by Winters et al. [21].

The doping effect decreases with ion-bombardment and is difficult to observe for reactive ion etching conditions as a doping dependence of the vertical etch rate [22]. Its technological significance lies in the fact that it makes the control of profile shapes in trench etching difficult. Trench formation in silicon technology, e.g., for capacitor and device isolation applications, commonly involves etching through Si layers of different doping levels. Since the lateral etch rates (chemical etching only) of the differently doped Si layers are not the same, non-ideal trench profiles due to different, doping-level dependent amounts of mask undercutting would result (see Fig. 2). The solution to this problem has been sidewall passivation.

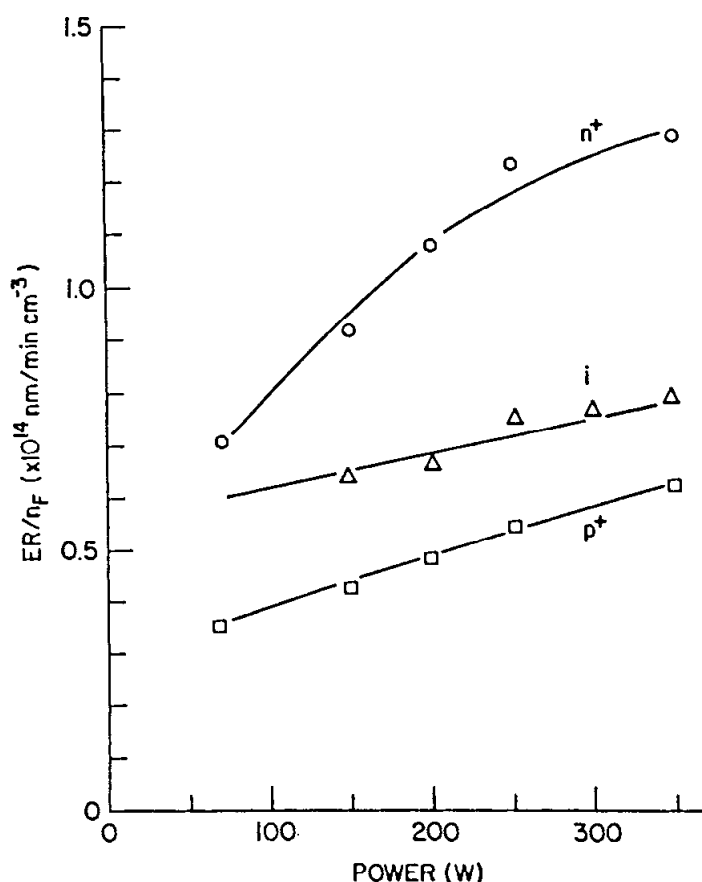


**Figure 3:** Doping effect in plasma etching. The chemical etch rate per fluorine gas phase atom for n-type, p-type and undoped silicon is shown as a function of rf power. The experimental conditions were: 13.56MHz rf, Al cathode, 76.8%CF<sub>4</sub>/19.2%O<sub>2</sub>/4%Ar, 50sccm total flow, 25mTorr (from Ref. 20).

#### 8.2.4 Etch Directionality Through Sidewall Passivation

Sidewall passivation layers (see Fig. 4) are key to achieving etch directionality in many dry etching processes [9,23]. The glow discharge chemistry is chosen so that etch inhibiting films can form as long as they are not exposed to ion bombardment, which leads to the dissolution of these films. Sidewalls of trenches are not exposed to ion bombardment and will be covered by the etch-inhibiting films and prevent mask undercutting. The bottom of the trench which is exposed to ion bombardment is free from passivating film and etching reactions can proceed.

Sidewall passivation makes it possible to achieve etch directionality for etchant/substrate systems which normally exhibit isotropic etching characteristics, e.g. fluorine-based etching of silicon using a SF<sub>6</sub> discharge. In Fig. 5 secondary electron micrographs of silicon trenches formed by SF<sub>6</sub>/O<sub>2</sub> RIE using various percentages of O<sub>2</sub> are displayed [24,25]. Reactive ion etching of silicon using pure SF<sub>6</sub> results in a large undercut of the oxide mask and nearly isotropic etch profiles (see Fig. 5(a)). As SF<sub>6</sub> is diluted with oxygen the etch profiles become more and more directional and the undercut of the oxide mask is reduced (Figs. 5(b) through 5(f)). The simplest explanation for the observed etching behavior is that in the absence of ion bombardment, i.e. at the trench sidewall, oxidation of silicon takes place rather than fluorine attack and concomitant

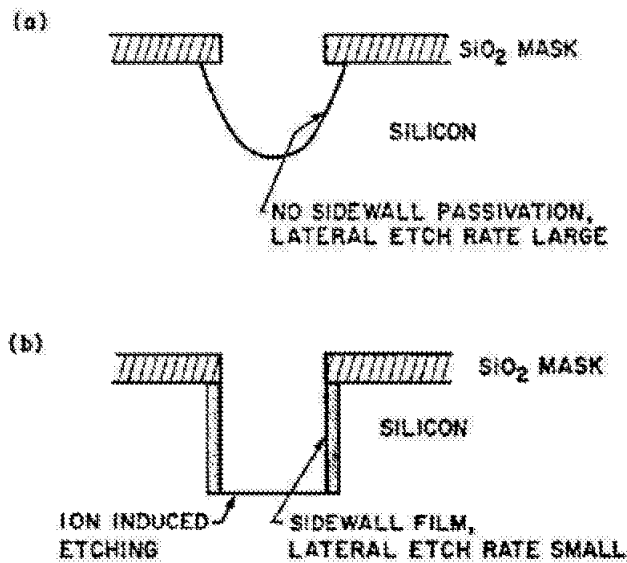


**Figure 4:** Schematic of the concept of sidewall passivation enabling directional etching without undercut of etch mask.

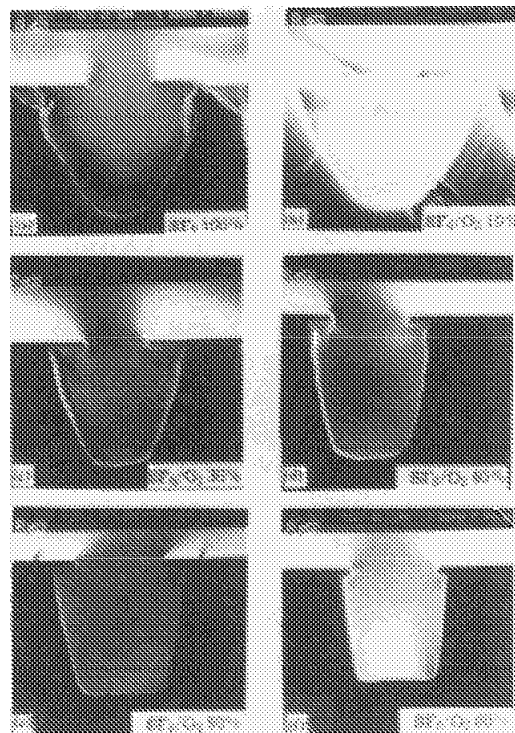


**Figure 5:** Secondary electron micrographs of Si trenches formed by reactive ion etching at 25mTorr using  $\text{SF}_6/\text{O}_2$  gas mixtures illustrating the reduction in mask undercut and improvement in etch directionality with increasing oxygen content. The etching was performed using 200W 13.56MHz rf power, a pressure of 25mT and a gas flow of 100sccm and a quartz covered cathode was used. The opening in the oxide mask is  $3\text{ }\mu\text{m}$  wide; the etch time was 10 min for all trenches (from Ref. 24).

etching. The sidewall of the trench is protected from etching by the resulting "sidewall film". For bombarded surfaces (bottom of the trench) the fluorine attack of silicon is enhanced, oxidation of silicon is reduced and etching can proceed. Without oxygen in the feed gas the protective sidewall film can not be formed and the trench etch profile is nearly isotropic. The composition of the sidewall film formed in  $\text{SF}_6/\text{O}_2$  RIE has recently been determined using in-situ angle resolved X-ray photoemission [24]. Regular arrays of trenches were illuminated with X-rays at grazing incidence which caused shadowing of the trench bottoms and no X-ray induced photoelectron emission from those areas. The contribution of the sidewall film was differentiated from the oxide mask by exploiting electrostatic charging differences due to the photoemission process. The composition of the sidewall passivation layer could thus be determined in-situ. For the  $\text{SF}_6/\text{O}_2$  trench etching process it was found to be a fluorinated oxide-like layer with an oxygen/silicon ratio of 1.7 and a fluorine/silicon ratio of 1.0. The sidewall passivation layer could be dissolved in buffered hydrofluoric acid and was removed with the oxide mask.

Passivation of sidewall features is observed for most reactive chemistries. The sources of sidewall passivation material can be suitable precursors formed in the plasma gas phase, erosion and redeposition of masking material or formation of etch products with low volatility and redeposition. Conceptually it appears simplest to add the sidewall passivation forming gas directly to the primary etching gas, e.g. adding  $\text{O}_2$  to  $\text{SF}_6$ ,  $\text{C}_2\text{F}_6$  to  $\text{Cl}_2$  [18], etc. and control the amount of sidewall passivation by the mixing ratio. However, addition of the sidewall forming gases changes the etch rate, mask selectivity, etc. of the process and requires process modifications, e.g. the formation of very thick masking layers for trench etching. For example, addition of 50%  $\text{O}_2$  to  $\text{SF}_6/\text{O}_2$  decreases the silicon etch rate and the etch selectivity to the oxide mask by a factor of  $\approx 5$ . Often too little sidewall passivation is formed using the gas mixing method and horizontal etching still occurs (see Fig. 5 (f)). In many etching processes the supply of sidewall passivation material is therefore enhanced (or sometimes solely controlled) by indirect processes where passivation material is provided by eroding the etch mask, e.g. argon and xenon have been added to the etching gases in order to cause enhanced sputtering of the photoresist or oxide masking layer and subsequent redeposition.

In order to improve control of the etch profile, methods to decouple the etching process from the formation of sidewall passivation have been suggested. Tsujimoto et al. [26] have used a gas and bias voltage chopping method to enable anisotropic etching of silicon and tungsten. They sequentially generated  $\text{SF}_6$  etching and  $\text{NH}_3$  sidewall film formation plasmas, respectively. At the beginning of each etching cycle the dc bias was increased to enable etching of the passivation film deposited onto the bottom of the feature. The advantage of this method is thought to be that the  $\text{NH}_3$  sidewall film formation processes are independent of and do not disturb the  $\text{SF}_6$  etching plasma.

### 8.2.5 Aspect Ratio Dependence of Etch Rate

As lithographic capabilities improve feature sizes in semiconductor technology will continue to shrink. In trench etching the trench width (or opening) will therefore decrease while the etch depth of the trench will remain the same or become even greater. The aspect ratio (depth/width) therefore increases. Reactive ion etching of trenches with submicron openings and high aspect ratio is more difficult than formation of trenches with



smaller aspect ratio. For a given (sub-micron) opening width the etch rate decreases as a function of the aspect ratio (or depth of the trench) which increases the demands on etch selectivity with respect to the mask. This effect has been examined by Chin et al. [27] and their results are displayed in Fig. 6. The etch rate decreases almost linearly as the aspect ratio increases and is determined by the aspect ratio, regardless of the opening size (for opening widths less than 1 micron). This phenomenon has been attributed to a diverging electric field in the trench [27], diffusion effects on the supply of reactant to the bottom of the trench and consumption of reactant at the trench sidewalls. At this time the dominant mechanism which causes this effect has not been established.

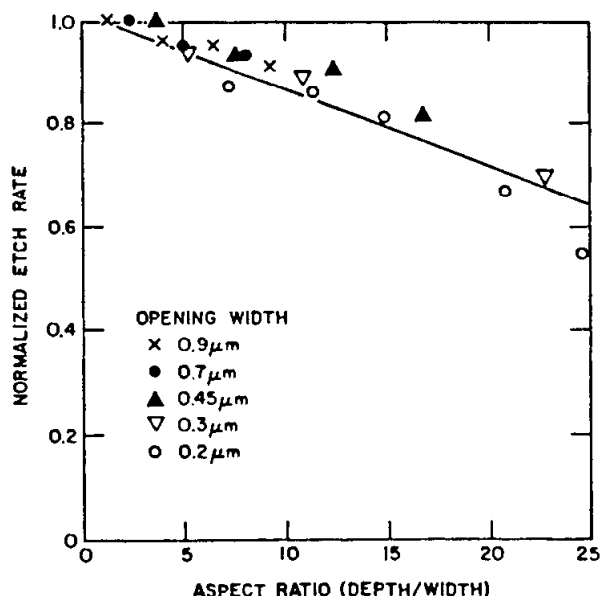


**Figure 6:** Aspect ratio dependence of the silicon etch rate in submicron trench etching ( $\text{CCl}_2\text{F}_2/\text{O}_2$  gas mixture, oxide mask, from Ref. 27).

### 8.3 PLASMA CHEMICAL CONSIDERATIONS

A large variety of fluorine, chlorine, bromine and oxygen based etching plasmas with a profusion of gas additives are used in the semiconductor industry (see Table 3). In most cases a specific etching gas mixture (or "recipe") is based on a great deal of empirical evidence obtained for a particular etching application rather than real fundamental understanding of the relevant plasma chemistry. However, certain basic insights have proven to be helpful in formulating etching gas mixtures [28]. The most studied and best understood etching gas mixtures are  $\text{CF}_4/\text{O}_2$  and  $\text{CF}_4/\text{H}_2$  plasmas.

#### 8.3.1 Effect of Oxygen Addition

The addition of small amounts of  $\text{O}_2$  to a  $\text{CF}_4$  plasma is known to increase the fluorine atom concentration in the discharge dramatically [29-31]. This is due to reaction of oxygen with  $\text{CF}_x$  radicals to form  $\text{CO}$ ,  $\text{CO}_2$ , and  $\text{COF}_2$  and produce more free fluorine. This effect, in combination with the lowering of the concentration of  $\text{CF}_x$  radicals by oxygen reaction (e.g.  $\text{CF}_3$ ), reduces the recombination of F atoms with  $\text{CF}_3$  and increases the steady-state F atom density. The consumption of unsaturated  $\text{CF}_x$  species by oxygen has the additional effect of suppressing polymer formation on surfaces which proceeds from unsaturated intermediates, such as  $\text{CF}_2$ . As oxygen is added to  $\text{CF}_4$  the fluorine atom

**Table 3:** Materials and reactive gases used for reactive ion etching in silicon technology.

<u>Material</u>	<u>Reactive Chemistries</u>	<u>Remarks</u>
Silicon	CF <sub>4</sub> /O <sub>2</sub> , SF <sub>6</sub> , NF <sub>3</sub> , Cl <sub>2</sub> , BCl <sub>3</sub> , CCl <sub>4</sub> , HBr, CF <sub>3</sub> Br,	Anisotropy difficult Directional, good SiO <sub>2</sub> selectivity. Directional.
Oxide	F <sub>4</sub> /H <sub>2</sub> , CHF <sub>3</sub> /C <sub>2</sub> F <sub>6</sub> , CHF <sub>3</sub> /CO <sub>2</sub>	Etch selectivity to Si.
Nitride	CF <sub>4</sub> , CHF <sub>3</sub> , SF <sub>6</sub> , NF <sub>3</sub> ,	Characteristics intermediate to Si; SiO <sub>2</sub> .
TiSi <sub>2</sub>	CCl <sub>2</sub> F <sub>2</sub> , CCl <sub>4</sub>	Control of oxygen impurities.
WSi <sub>2</sub>	CF <sub>4</sub> /O <sub>2</sub> , SF <sub>6</sub>	
W	CF <sub>4</sub> /O <sub>2</sub> , SF <sub>6</sub>	
Al	Cl <sub>2</sub> , BCl <sub>3</sub> , CCl <sub>4</sub> , SiCl <sub>4</sub>	Removal of native oxide.
Al(Cu)	Cl <sub>2</sub> , BCl <sub>3</sub> , CCl <sub>4</sub> , SiCl <sub>4</sub> ,	Cu removal, removal of native oxide.
Polymers	O <sub>2</sub> , O <sub>2</sub> /CF <sub>4</sub>	

concentration increases at first (up to  $\approx 20\%$  O<sub>2</sub> addition) and subsequently decreases again due to dilution. These fluorine-rich plasmas are used for isotropic etching of silicon. The etching of silicon in CF<sub>4</sub>/O<sub>2</sub> glow discharges is also of interest scientifically since it displays nicely how gas phase processes can control the etching behavior for certain conditions whereas surface processes will limit the etch rate for slightly different experimental conditions. Figure 7, from the work of Mogab et al. [29], shows the etch rate of silicon as a function of the fluorine concentration in the gas phase measured by optical emission. The fluorine concentration in the gas phase was varied by adding oxygen to the CF<sub>4</sub> plasma. Depending on the amount of oxygen added to the plasma two different Si etch rates can be observed for the same fluorine concentration. The Si etch rate is determined by the concentrations of both fluorine and oxygen atoms in the gas phase because they compete for active Si surface sites. Mogab et al. [29] proposed that increased oxidation of the Si surface for increasing oxygen percentages in the feed gas is responsible for the lower Si etch rates observed for high fluorine concentrations if simultaneously the oxygen concentration is large. Recently the etching behavior of silicon in CF<sub>4</sub>/O<sub>2</sub> was reexamined and in-situ X-ray photoelectron spectroscopy was used to characterize the silicon surfaces after etching [32]. Photoelectron spectroscopy showed that a SiF<sub>x</sub>O<sub>y</sub> reaction layer was formed on the Si surface and that the composition of the layer changed from primarily SiF-bonding to SiO-bonding as the percentage of O<sub>2</sub> in CF<sub>4</sub>/O<sub>2</sub> was increased. Simultaneously the layer grew in thickness. The silicon etch rate is plotted versus the SiF<sub>x</sub>O<sub>y</sub> layer thickness in Fig. 8 [32]. The percentage of O<sub>2</sub> in CF<sub>4</sub>/O<sub>2</sub> for which a particular etch rate and film thickness value was obtained is also indicated. As oxygen is added to pure CF<sub>4</sub>, the etch rate increases and the film thickness decreases. Both of these effects should be a result of the rise in fluorine atom gas phase concentration (see Fig. 7) which was also observed in this study [32]. For O<sub>2</sub> percentages greater than 5% O<sub>2</sub> the film thickness increases, the Si etch rate reaches a maximum near 7.5% O<sub>2</sub> and subsequently decreases. The Si etch rate for oxygen concentrations greater than 7.5% correlates to and appears to be controlled primarily by the thickness of the SiF<sub>x</sub>O<sub>y</sub> layer,

rather than by the F atom concentration in the gas phase which increases up to 15%O<sub>2</sub> addition. Progressively thicker films on Si are formed as a result of increased oxidation and decreased fluorination of the Si surface as the percentage of O<sub>2</sub> in CF<sub>4</sub>/O<sub>2</sub> is increased. For the same SiF<sub>x</sub>O<sub>y</sub> layer thickness different Si etch rates can be observed. These results show that for low oxygen concentrations the etch rate is controlled by the arrival rate of fluorine to the surface and responds to increases of the gas phase fluorine concentration. For high oxygen concentrations the etch rate is limited by oxidation of the silicon surface and correlates well to the thickness increase of the surface reaction layer.

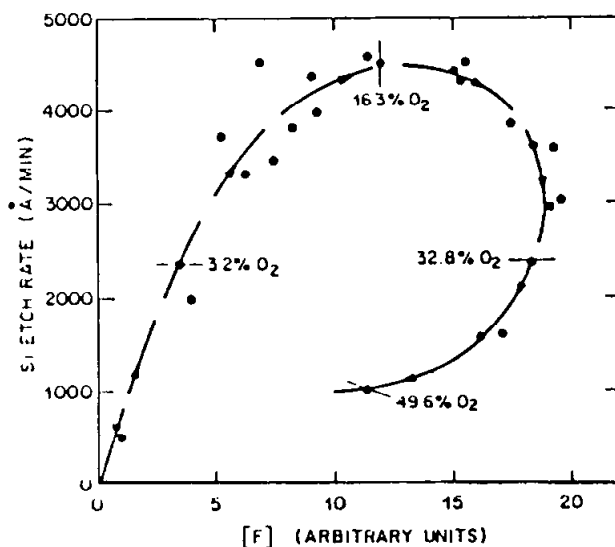


**Figure 7:** Etch rate of silicon versus fluorine concentration in gas phase determined by optical emission spectroscopy. Percentages of O<sub>2</sub> in CF<sub>4</sub>/O<sub>2</sub> are indicated. The experimental conditions were: 350mTorr, 200sccm total flow, 200W rf, 100°C sample temperature, samples grounded (from Ref. 29).

Similar effects of oxygen addition may occur for chloro- and bromocarbon plasmas (e.g., CF<sub>3</sub>Cl, CF<sub>2</sub>Cl<sub>2</sub>, CCl<sub>4</sub>, CF<sub>3</sub>Br) where an increase in the Cl or Br concentration and a decrease in the formation of polymer may result [9].

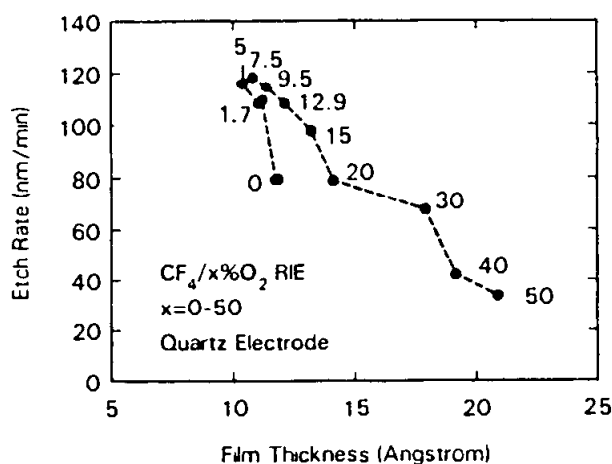


**Figure 8:** Silicon etch rate as a function of the SiF<sub>x</sub>O<sub>y</sub> layer thickness. The numbers next to the data denote the percentage x of O<sub>2</sub> used in CF<sub>4</sub>/O<sub>2</sub> RIE. The fluorine atom gas phase concentration is at a maximum at 15% oxygen addition. Experimental conditions: 200W 13.56MHz RIE, 25mTorr, 100sccm total flow, quartz cathode (from Ref. 32).

### 8.3.2 Effect of Hydrogen Addition

The addition of small amounts of hydrogen to  $\text{CF}_4$  plasmas reduces the concentration of free fluorine because of HF formation. A lower fluorine atom concentration decreases the importance of recombination of fluorine with  $\text{CF}_3$  radicals and a discharge rich in unsaturated fluorocarbons, such as  $\text{CF}_2$ , is produced. These species are precursors of polymeric fluorocarbon films which deposit on the inner surfaces of the plasma chamber. If the hydrogen concentration is too high polymerization occurs on all surfaces and etching stops. Similar effects can be achieved by adding  $\text{CH}_4$ ,  $\text{C}_2\text{H}_4$ ,  $\text{CHF}_3$ , etc. or alternatively  $\text{C}_2\text{F}_6$ ,  $\text{C}_3\text{F}_8$ , etc. to  $\text{CF}_4$  discharges. These fluorine deficient discharges are important since they enable selective etching of  $\text{SiO}_2$  (see section on selective etching).

A useful indicator of the predominance of etching over deposition (polymerization) is the fluorine/carbon ratio of the discharge [33]. In this model the theoretical F/C ratio for the discharge is calculated, i.e. the F/C ratio is 4 for  $\text{CF}_4$ , 3 for  $\text{C}_2\text{F}_6$ , etc.. Hydrogen addition lowers the F/C ratio by reacting with fluorine atoms to form HF, oxygen addition increases the F/C ratio by CO,  $\text{CO}_2$  formation, mixing of  $\text{CF}_4$  with  $\text{CH}_4$  lowers the F/C ratio, loading with an etchable material which consumes fluorine lowers the F/C ratio, and so forth. For a silicon substrate, etching is observed for F/C ratios greater than 3 whereas fluorocarbon film deposition is observed for F/C ratios of less than 2. At intermediate F/C ratios the changeover from deposition to etching depends on the degree of ion bombardment possible under the particular etching conditions, with greater ion bombardment inducing etching.

It appears that the effect of hydrogen addition on mixed halocarbon based plasmas (such as  $\text{CClF}_3$ ) is similar to effects observed with  $\text{CF}_4$  plasmas. For  $\text{CClF}_3$  it has been shown that hydrogen addition results in a discharge with very similar characteristics to a  $\text{CF}_4/\text{H}_2$  discharge, e.g. for silicon the deposition of a chlorofluorocarbon film is observed [34] and  $\text{SiO}_2/\text{Si}$  etch selectivity is achieved [35].

### 8.3.3 Other Gas Additives

Noble gases such as argon and helium are often added to stabilize plasmas or for cooling purposes (He for high pressure plasmas). Argon addition can also cause inert ion bombardment of a surface and result in anisotropic etching (e.g.,  $\text{Ar}/\text{Cl}_2$  RIE of Si). The consequences of diluting a reactive gas with a noble gas are not easily understood. The addition of a chemically inert gas may significantly change the electron energy distribution in a plasma and alter the reactive species population in the discharge. This effect is observed when the ionization potential of the chemically inert additive is very different from the ionization potentials of the plasma species of the primary gas. An altered reactive species make-up of the discharge, e.g. enhanced dissociation, can also be due to more complex effects. For example, Gottscho et al. [36] examined the mixing of  $\text{BCl}_3$  with He, Ar and Kr using laser induced fluorescence. They found that energy transfer from noble gas metastable states to  $\text{BCl}_3$  states to cause enhanced dissociation of  $\text{BCl}_3$ .

### 8.3.4 Loading Effect

The "loading" effect refers to a significant depletion of the etchant species in the gas phase due to consumption in the etching process. Depending on the gas phase mean free path, the number and structure of specimens being etched the loading effect may be both

global, i.e. the reactant concentration in the reactor is uniformly lowered, and local. Mogab analyzed the relationship between etch rate ER and area A of wafer load and found this expression [13]:

$$ER(A) = \frac{(k_{etch}/k_{loss})G}{1 + (k_{etch}\rho A/k_{loss}V)} \quad (1)$$

where  $k_{etch}$  and  $k_{loss}$  are the first order rate constants for etching and etchant loss in an empty reactor, respectively,  $G$  is the rate of production of etchant species,  $\rho$  the number density of substrate molecules, and  $V$  the volume of the reactor. For a large wafer load area  $A$  equation (1) becomes  $ER(A) = GV/\rho A$  and the etch rate varies inversely with the wafer load area  $A$ . The importance of the loading effect is decreased by making  $k_{loss}$  large relative to  $k_{etch}$ , i.e. by consuming etchant species through processes other than reaction with the wafer load, e.g. rapid pumping.

The local loading effect is important for patterned wafers (pattern sensitivity) and is difficult to minimize. In this case the reactant concentration varies locally due to consumption by a reactive material and non-consumption by a non-reactive material. Figure 9 shows results of the work by Selwyn [37] who measured the spatially resolved oxygen

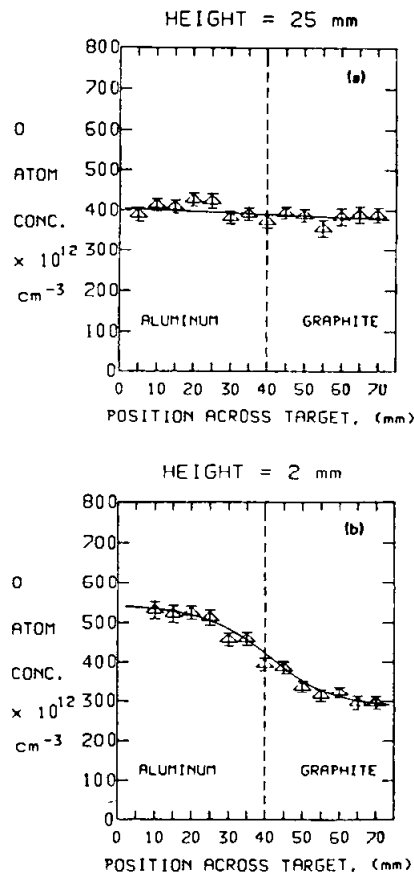


**Figure 9:** Spatial variation of the oxygen atom density (as determined by two-photon laser-induced fluorescence) as a function of horizontal sample position in the O<sub>2</sub>/Ar plasma (27 mTorr O<sub>2</sub> and 80 mTorr Ar). The aluminum cathode was partially covered with graphite and the interface between the two halves is shown by the dashed line. In (a) data obtained at a height of 25mm above the substrate are shown, whereas the data in (b) were obtained 2mm above the substrate. In (a) the O atom concentration is rather uniform. In (b) an O atom gradient exists which is thought to arise from the consumption of O atoms by the etching of graphite (from Ref. 37).

atom concentration in an oxygen plasma over graphite and aluminum surfaces using laser induced fluorescence. At 25mm above the target only a minor variation is observed between the graphite (loaded) and the aluminum (unloaded) portions of the electrode. At a height of 2mm above the samples a strong gradient in oxygen atom concentration can be observed above the two sections of the electrode, which is apparently due to the consumption of oxygen atoms by the etching of graphite. The gradual decrease in oxygen atom concentration observed between the Al and graphite sections of the cathode is indicative of diffusional processes in the plasma. At a height of 25mm above the electrode diffusion/mixing processes have eliminated the O atom concentration gradient.

## 8.4 ETCH SELECTIVITY

### 8.4.1 General Considerations

Etch selectivity of a film being etched is required with respect to the etch mask and - if present - to the underlayer. Etch selectivity to the underlayer is more critical since in most cases the mask will be removed after the etching step whereas the underlayer becomes part of the completed device. Commonly a certain amount of overetching (i.e. etching beyond the time when complete removal of the film being patterned is first signalled by endpoint detection - see section 7) needs to occur in order to account for non-uniform etch rates throughout the reactor and ensure complete removal of the film everywhere on the wafer.

Etch selectivity of a material A over a material B in reactive ion etching is due to rate differences of the elementary steps taking place at the surfaces of these materials. These are a) the adsorption step, b) the reaction step, and c) the desorption step. The following mechanisms can be responsible for the achievement of etch selectivity:

- a. Selective formation of an etch inhibiting layer on one material. Due to the simultaneous presence of different plasma gas phase species several processes occur in parallel at surfaces immersed in a processing plasma. For example, in fluorocarbon-based plasma etching of silicon and silicon dioxide it is known that fluorine induced etching occurs in parallel with, and competes with, fluorocarbon film deposition. If the processing conditions are chosen such that etching and deposition are nearly balanced for a material A (i.e.  $\text{SiO}_2$ ), this balance may be tilted to deposition for a different material B (i.e. Si) because of a different net adsorption rate for the gas phase precursor of the passivating film (due to higher sticking coefficients, different reactivity, etc. with the surface of B). This is the basis for selective etching of silicon dioxide over silicon in a fluorocarbon plasma, such as  $\text{CHF}_3$ , and will be discussed in more detail later.
- b. Non-reactivity of material B in plasma environment, e.g. ashing of photoresist on a silicon dioxide film in an oxygen discharge. The photoresist layer will volatilize by forming C-O, H-O, etc. related species, but the  $\text{SiO}_2$  layer is not attacked by the oxygen plasma.
- c. Non-volatility of reaction product, e.g. ashing of photoresist on silicon in an oxygen discharge and formation of involatile silicon dioxide. The photoresist reacts with oxygen to form volatile species whereas silicon reaction with the oxygen plasma causes the formation of an involatile reaction product.

In many practical situations a combination of these factors may determine the achieved etch rate ratio. A very useful indicator of the possible plasma etch selectivity is the volatilization ratio of two materials exposed to controlled atom or molecular beams. Experimentally it has been found that these non-plasma etch rate ratios are relevant to plasma etching environments without ion bombardment. For instance, Flamm and his coworkers have determined an etch rate ratio of silicon to silicon dioxide exposed to fluorine atoms of 41:1 [38]. A similar Si/SiO<sub>2</sub> etch rate ratio can be achieved in a glow discharge of SF<sub>6</sub> which provides a fluorine-rich plasma with a low dc self-bias voltage [24,25].

The effect of ion bombardment is to accelerate the same elementary surface processes that are responsible for the achievement of etch selectivity, i.e. the adsorption, reaction and desorption steps (see section 1). This reduces the importance of "bottlenecks" in the overall etching reaction. It is not surprising therefore that ion bombardment nearly always decreases the possible etch rate ratio of chemically different materials exposed to a reactive plasma from the "intrinsic" value.

#### 8.4.2 Silicon Dioxide to Silicon Etch Selectivity

The important case of etching selectively silicon dioxide over silicon in a fluorocarbon plasma is discussed now in some detail. For SiO<sub>2</sub> and Si no acceptable etch selectivity can normally be obtained in a CF<sub>4</sub> discharge. Heinecke discovered that addition of H<sub>2</sub> to CF<sub>4</sub> makes it possible to minimize the etching of Si as compared to the etching of SiO<sub>2</sub> [39]. This approach was subsequently investigated further and optimized by Ephrath et al. [40] for RIE applications. Lehmann et al. [41] used CHF<sub>3</sub> and obtained similar results. As hydrogen is added to a CF<sub>4</sub> plasma the Si etch rate decreases monotonically as the percentage of H<sub>2</sub> is raised and eventually stops. The percentage of hydrogen where Si etching stops depends on the plasma etching process parameters, e.g. the total gas flow, pressure, etc., but is typically  $\approx 30\text{--}60\%$  H<sub>2</sub> in CF<sub>4</sub>/x%H<sub>2</sub>. For a CF<sub>4</sub>/H<sub>2</sub> composition sufficient to stop the etching of Si only a small decrease of the silicon dioxide etch rate ( $\approx 20\%$  of maximum etch rate) is observed [40]. The role of hydrogen in controlling the Si etch rate is twofold. (i) Atomic H scavenges atomic F in the gas phase to form HF molecules and the Si etch rate which depends on the F concentration is consequently reduced. (ii) More important in slowing down the Si etch rate and achieving SiO<sub>2</sub>/Si etch selectivity is the selective formation of a fluorocarbon film on the Si surface as a result of hydrogen addition to a CF<sub>4</sub> plasma. For suitably chosen RIE processing conditions the fluorocarbon film is not formed on SiO<sub>2</sub>, allowing etching of SiO<sub>2</sub> to proceed [42,43]. This is shown in Fig. 10. Carbon 1s X-ray photoemission spectra are displayed for SiO<sub>2</sub> and Si surfaces after reactive ion etching in CF<sub>4</sub>/40%H<sub>2</sub> plasmas, a gas mixture used to selectively etch SiO<sub>2</sub> over Si (etch rate ratio  $\approx 20:1$ ) [40]. The photoemission peaks are due to the fluorocarbon film which covers the silicon substrate after reactive ion etching. The chemical groups giving rise to the photoemission peaks are C – CF<sub>x</sub>, CF, CF<sub>2</sub> and CF<sub>3</sub> (in order of increasing binding energy). An additional shoulder centered at a binding energy of 284eV is apparent also in the carbon 1s spectrum for silicon. The chemical origin of the 284eV component is silicon-carbon bonding and arises from bonds localized at the fluorocarbon film/silicon interface [42,44]. The formation of a silicon-carbon bond is a critical step in the formation of a fluorocarbon film on silicon since the silicon-carbon bond is the "bridging bond" between the silicon substrate and the fluorocarbon layer. The importance of surface carbon contamination of silicon in the achievement of SiO<sub>2</sub>/Si etch selectivity was first observed by Coburn in Auger studies [45].

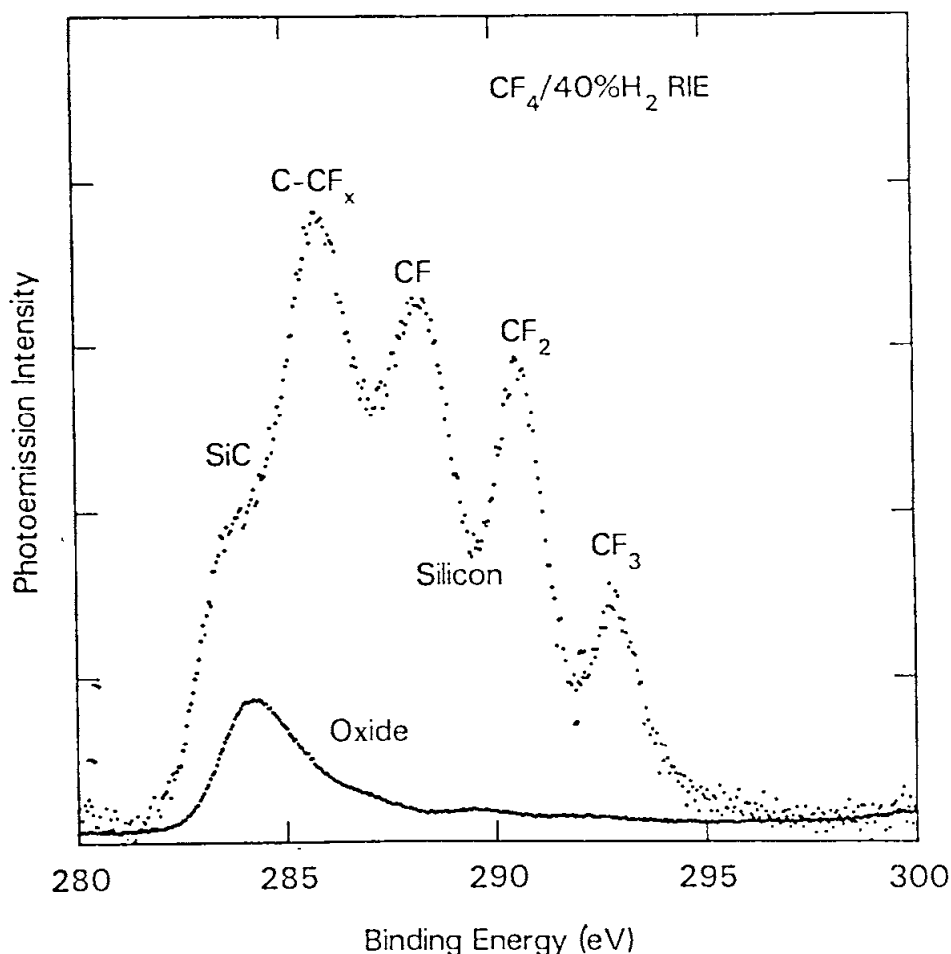


**Figure 10:** A comparison of carbon 1s X-ray photoemission spectra measured for Si and  $\text{SiO}_2$  after  $\text{CF}_4/40\%\text{H}_2$  reactive ion etching. The etching was performed using 200W rf power, a pressure of 25mTorr and a gas flow of 40sccm. The samples were transferred in vacuum from the RIE chamber to the surface analysis chamber. The peaks observed for silicon are due to a fluorocarbon film which is absent for reactive ion etched  $\text{SiO}_2$  (from Ref. 51).

In the lower panel of Fig. 11, the fluorocarbon steady-state film thickness is shown as a function of the hydrogen percentage in the  $\text{CF}_4/\text{H}_2$  discharge for silicon and oxide. Whereas the fluorocarbon film thickness on silicon increases roughly linearly with hydrogen addition to  $\text{CF}_4$ , little fluorocarbon is formed on  $\text{SiO}_2$  for all hydrogen concentrations. In the upper panel of Fig. 11 inverse Si and  $\text{SiO}_2$  etch rates are shown. The  $\text{SiO}_2$  etch rate remains nearly unaffected by the addition of  $\text{H}_2$  to  $\text{CF}_4$  and the Si etch rate drops off significantly. Silicon etch rate suppression relative to  $\text{SiO}_2$  and fluorocarbon film thickness increase on Si relative to  $\text{SiO}_2$  show a very similar behavior as a function of  $\text{H}_2$  addition to  $\text{CF}_4$ , showing that the Si etch rate and the achieved  $\text{SiO}_2/\text{Si}$  etch selectivity is controlled by the fluorocarbon film thickness. The fluorocarbon film interrupts the chain of elementary surface processes necessary for Si etching to proceed. The film decreases, and eventually completely prevents, the supply of fluorine to the silicon/fluorocarbon film interface [42,43]. Silicon etching stops because the fluorocarbon film limits the fluorine attack necessary to sustain silicon etching.



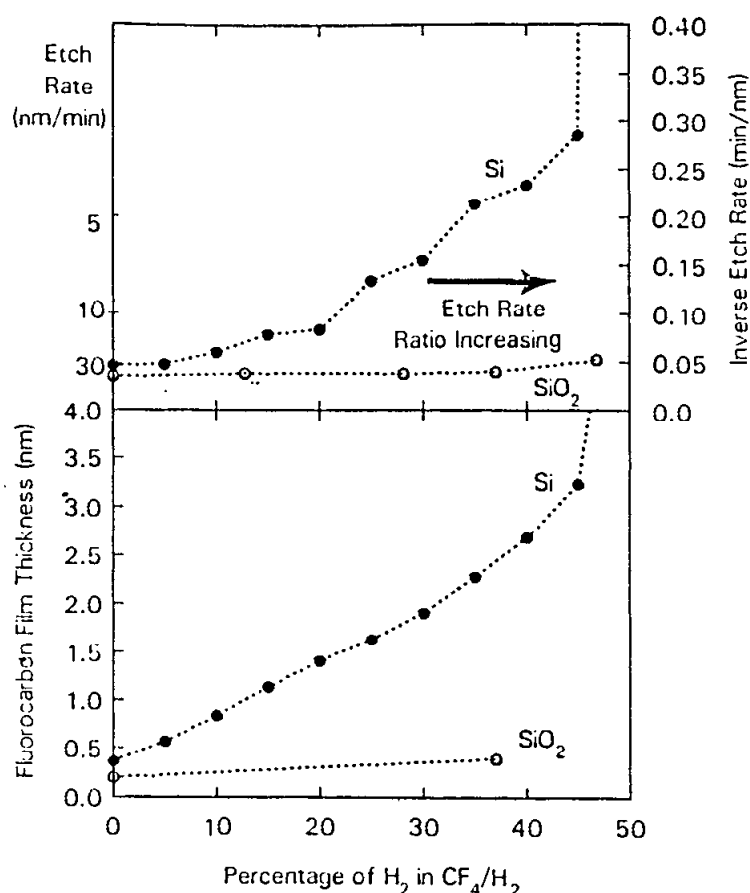


**Figure 11:** Upper panel: Inverse Si and SiO<sub>2</sub> reactive ion etch rates in a CF<sub>4</sub>/H<sub>2</sub> plasma as a function of percentage of hydrogen. A total gas flow of 40sccm was used, the pressure 25mTorr, and 200W rf power supplied to the teflon covered cathode. The cathode diameter was 12 inches. As hydrogen is added the SiO<sub>2</sub>/Si etch rate ratio is seen to increase. Lower panel: Fluorocarbon film thickness on Si and SiO<sub>2</sub> measured after 5 min of reactive ion etching using identical conditions. The similarity of the two plots is strongly suggestive that the suppression of the silicon etch rate (and the achievement of SiO<sub>2</sub>/Si etch selectivity) is due to the selective formation of the relatively thick fluorocarbon film on silicon (from Ref. 51).

Hydrogen addition to CF<sub>4</sub> plasmas is required since laser induced fluorescence/optical emission studies have shown that atomic hydrogen reacts with CF<sub>3</sub> to form HF and CF<sub>2</sub> [46,47]. The increase in the density of CF<sub>2</sub> radicals, the fluorocarbon film precursor [48], enhances the formation rate of the fluorocarbon film. Since hydrogen also lowers the atomic fluorine concentration via HF formation, the revolatilization of the fluorocarbon film by fluorine-based etching is reduced as the hydrogen percentage in the CF<sub>4</sub>/H<sub>2</sub> gas mixture is increased.

Etch selectivity is a consequence of the presence of oxygen in SiO<sub>2</sub> which minimizes fluorocarbon film growth on the oxide (see Fig. 10). The absence of the fluorocarbon film on oxide makes etching of silicon dioxide possible. Qualitatively, the absence of fluorocarbon film on SiO<sub>2</sub> is rather plausible. During etching of silicon dioxide, oxygen is continuously present on the etching surface which can react with the fluorocarbon film

precursor(s) to form volatile  $\text{CO}$ ,  $\text{CO}_2$  and  $\text{COF}_2$ . However, the microscopic processes which lead to the fluorocarbon film absence on  $\text{SiO}_2$  are likely to be complex and are very difficult to study experimentally. Virtually no experimental data which shed light on the mechanistic details of these processes in realistic etching plasmas are available at this time.

Etch selectivity of  $\text{SiO}_2$  with respect to other substrates using the same discharge chemistry (25mTorr RIE conditions) has been shown to be due to the same selective fluorocarbon film formation mechanism. For example, the photoresist etch rate decreases in a fashion similar to that of silicon as  $\text{H}_2$  is added to  $\text{CF}_4$  [40]. Using photoresist patterned  $\text{SiO}_2/\text{Si}$  specimens it has been shown that the photoresist mask and the Si contact hole are covered by the same fluorocarbon film following RIE [49]. The same conclusion was reached for  $\text{TiSi}_2$  and Ti substrates using the  $\text{CF}_4/\text{H}_2$  gas mixture [50,51]. The latter case is significant since  $\text{TiF}_x$  species have very low volatility ( $\text{TiF}_3$  has a boiling point of  $1400^\circ\text{C}$ ) and a  $\text{TiF}_x$  surface passivation layer may have been expected as responsible for  $\text{SiO}_2/\text{Ti}$  etch selectivity.

### 8.4.3 Silicon to Silicon Dioxide Etch Selectivity

High etch selectivity of silicon over silicon dioxide is required in the formation of silicon trenches using oxide masks, the patterning of poly-Si gate contacts over the gate oxide and a great number of other steps. In the definition of the poly-Si gate the requirement is to stop on a thin ( $\leq 10\text{nm}$ ) gate oxide since otherwise the underlying shallow source-drain junctions in the Si substrate would be rapidly etched. As indicated by the "intrinsic" Si/ $\text{SiO}_2$  etch rate ratio for fluorine atoms of 41 [38], high Si/ $\text{SiO}_2$  etch selectivities of 30 and greater are possible using fluorine- and also chlorine-based plasmas, e.g.  $\text{SF}_6$  and  $\text{Cl}_2$  discharges enable the achievement of excellent Si/ $\text{SiO}_2$  etch selectivity. In fact, thin oxide layers, e.g. the native oxide on silicon, can completely prevent etching of the silicon [18] or, if non-uniformly etched, cause the formation of surface roughness in the silicon layer ("black" silicon or sometimes called "grass"). The native oxide has to be removed initially using a short oxide etch, e.g. a  $\text{CF}_4$  plasma. The primary difficulty in etching poly-Si and crystalline Si is control of the etch profile (see section on etch anisotropy). Chlorine-based chemistries have been used for directional silicon etching, e.g.  $\text{Cl}_2$ ,  $\text{CCl}_4$  [17] (which is not recommended since it has  $\approx 5$  times worse selectivity to the oxide than a  $\text{Cl}_2$  plasma and is a carcinogen),  $\text{CCl}_2\text{F}_2$ ,  $\text{CCl}_2\text{F}_3$ ,  $\text{Cl}_2/\text{SF}_6$  mixtures, and so forth which provide good etch directionality. Silicon etching processes using only chlorine, e.g.  $\text{Cl}_2$ , are characterized by a slow etch rate. The addition of a small percentage of  $\text{SF}_6$  to  $\text{Cl}_2$  increases the etch rate without loss of directionality, presumably because of sidewall passivation by chlorine [52]. For critical applications "mixed" processes are used where certain characteristics, e.g. high etch rate, directionality and selectivity relative to the photoresist mask, are optimized in the first part of the etching process and other characteristics, e.g. etch selectivity to the  $\text{SiO}_2$  substrate, low damage, etc., are achieved in the final part of the process.

## 8.5 CONTAMINATION & DAMAGE ISSUES

### 8.5.1 Survey of RIE Damage Effects

The detrimental impact of reactive ion etching on the electrical properties of devices has been an area of considerable concern and is thought to be due to RIE related surface

contamination and substrate displacement damage [53]. Etch-selectivity is often due to the deposition of etch inhibitors, which will remain on the exposed material after completion of the dry etching step (see the section on  $\text{SiO}_2/\text{Si}$  etch selectivity) and interfere with device processing following RIE. Bombardment damage is a concern since, although ion energies are typically below 500eV in RIE, the fluence is high ( $\approx 10^{15}$  ions/cm<sup>2</sup>sec) and lattice damage may be introduced. Displacement damage will alter the near-surface region of the material which is exposed to the plasma and change its electrical properties.

The term "RIE damage" has been used for a variety of undesirable RIE effects such as:

- a. **Surface residues**  
These can be intrinsic to the etch process, i.e. related to the chemistry of discharge such as the fluorocarbon film, or due to the formation of involatile products with film impurities, e.g.  $\text{CaF}_2$  from Ca in quartz etching. They can be extrinsic to the etch process, e.g. depend on the particular etching chamber configuration (aluminum electrode vs. teflon electrode).
- b. **Impurity penetration (implantation, diffusion)**  
Plasma related impurities can penetrate the substrate during RIE, either as a result of direct implantation or diffusion. Hydrogen is of particular concern [54]. Substrate temperature control during RIE is also of great importance.
- c. **Lattice damage**  
Point defects or extended defects can be introduced into the substrate by RIE. For silicon exposed to  $\text{CF}_4$  plasmas, point defects known from radiation damage studies have been observed, e.g. carbon-carbon-silicon self-interstitial complexes [55,56].
- d. **Dopant loss or loss of dopant activity**  
After  $\text{CHF}_3$ - and  $\text{CF}_4/\text{H}_2$ -based oxide RIE, loss of the electrical activity of dopants in the near-surface region of the Si substrate has been observed [57]. This is in part due to hydrogen-boron interaction in which a hydrogen atom which penetrated the silicon during RIE bonds to the dangling Si bond at the substitutional B site and renders the dopant electrically inactive [57].
- e. **Heavy metal contamination**  
Transition metal contamination (nickel, iron and chromium) of semiconductors is caused primarily by sputtering of stainless steel parts of the chamber and subsequent contamination of the semiconductor [58]. These impurities diffuse very readily into the semiconductor and introduce energy levels near the middle of the energy gap which act as recombination centers and reduce the minority carrier lifetime. Heavy metal contamination is reduced by increasing the grounded/powered electrode area ratio which lowers the plasma potential.
- f. **Surface roughness**  
This effect can be extrinsic, e.g. micromasking due to Al sputtering and redeposition in fluorine containing plasmas [59] or possibly intrinsic, e.g. etching of rough overlayer and replication of roughness in the underlayer.
- g. **Gate oxide breakdown or introduction of traps [60,61].**  
Gate oxide breakdown has been observed as a result of RIE and the origin of the effect is not well understood. In one model oxide breakdown is thought to

be caused by the transient surge current as the rf power is turned off and the coupling capacitor discharges [60].

- h. **Mobile ion contamination [62].**  
Etching of the electrode material, e.g. teflon which often contains significant concentrations of sodium, exposes sodium at the surface of the electrode. In a fluorine-based discharge sodium does not form a volatile product and can contaminate the wafer being etched.
- i. **Post-RIE Corrosion [63]**  
In chlorine-based etching of aluminum, residues containing chlorine will remain after RIE. Upon exposure to atmosphere HCl is formed and corrosion of the Al lines takes place. The chlorine-containing residues are removed by post-RIE plasma/wet cleaning treatments.

These material modifications impact the performance of electronic devices built from RIE damaged materials. For example, surface residues and lattice damage have been shown to change the Schottky barrier height and reduce the forward leakage current of Schottky barriers formed on dry etched silicon [64]. Surface residues and dopant deactivation caused by contact hole etching through  $\text{SiO}_2$  to the Si substrate have resulted in a high contact resistance of ohmic contacts fabricated on the exposed Si surface [57]. Surface roughness, gate oxide breakdown and mobile ion contamination reduce the quality of silicon dioxide layers which were either present during the RIE step or subsequently thermally grown on dry etched Si. In the latter case the interface state density was increased and the breakdown strength of the oxides was reduced as compared to controls. The amount of change depended on the voltage applied during etching [65]. Silicon lattice damage and heavy metal contamination reduce the minority carrier lifetime of silicon.

### 8.5.2 Silicon Surface Modifications Due to Selective $\text{SiO}_2$ /Si RIE

It is important to differentiate between surface modifications which are essential to meeting the objectives of the RIE process and those which occur coincidentally, without any obvious function in the etching process. In the latter case it will be possible to eliminate these material modifications by improved RIE process/chamber design. In this section surface and near-surface substrate modifications caused by a prototypical RIE process, namely  $\text{CF}_4/\text{H}_2$ -based (or  $\text{CHF}_3$ -based) selective etching of  $\text{SiO}_2$  over Si, are described [66,67]. This etching situation encompasses essential possible concerns with RIE, since a critical, active surface region of a Si device is exposed to the plasma.

The changes in the silicon near-surface region incurred as a result of selective oxide removal by  $\text{CF}_4/\text{H}_2$  RIE are schematically depicted in Fig. 12 [54]. This picture is based on these measurements: i) In ion channeling and X-ray photoemission studies a fluorocarbon film was detected on the silicon substrate. The thickness of the film is limited to less than  $\approx 5\text{nm}$ . ii) A thin  $\text{SiO}_2$  layer is present underneath the C,F-film which is formed after air exposure of the etched specimens. iii) A heavily damaged Si layer ( $\approx 3\text{--}5\text{nm}$  thick) is formed near the Si surface. In ion channeling, this layer causes a more intense and wider Si surface peak. Raman scattering due to the destruction of crystalline long range order has also been observed for dry-etched Si, demonstrating the existence of a disordered, amorphous-like region near the surface. iv) The existence of sub-surface silicon carbon bonding was established by X-ray photoemission spectroscopy. v) Hydrogen at depths in excess of  $\approx 30\text{nm}$  was detected in dry etched specimens by nuclear

reaction profiling. By Raman scattering the stretching modes of Si-H centers were observed. By substituting deuterium for hydrogen in reactive ion etching and using secondary ion mass spectrometry, deuterium at concentrations of  $10^{17}$  atoms/cm<sup>3</sup> has been detected at a Si depth of more than 200nm from the surface after 1min of plasma exposure. vi) Transmission electron microscopy studies revealed no extended Si defects for pure CF<sub>4</sub> or CF<sub>4</sub>/20%H<sub>2</sub> RIE. For CF<sub>4</sub>/40%H<sub>2</sub> or pure H<sub>2</sub> RIE extended lattice defects were observed after overetching [68]. The extended defects consisted of {111} planar defects distributing to a depth of 30nm from the Si surface. Hydrogen was shown to play a critical role in the formation of extended Si defects as a result of RIE [69].

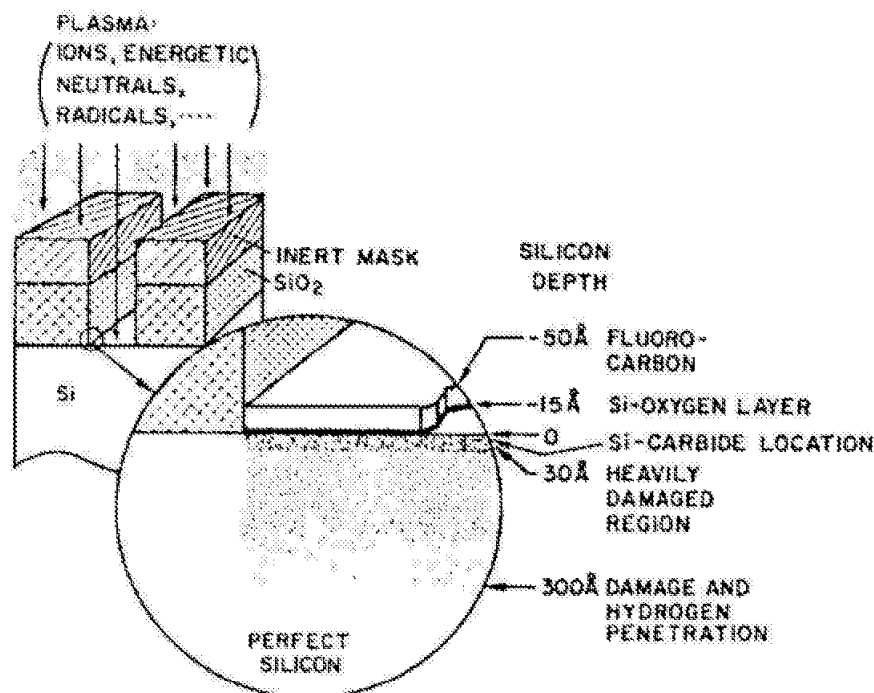


**Figure 12:** Schematic view of changes of the near-surface properties of the silicon substrate resulting from a SiO<sub>2</sub> to Si selective reactive ion etch process using CF<sub>4</sub>/40%H<sub>2</sub>. The etching was performed using 200W rf power, a pressure of 25mTorr and a gas flow of 40sccm. The Si substrate was exposed for 1min to the plasma. After RIE and prior to surface analysis the Si sample was exposed to air which caused the growth of the thin oxide layer underneath the fluorocarbon film (from Ref. 54).

The performance of electronic devices formed on CF<sub>4</sub>/H<sub>2</sub> RIE modified silicon (as shown in Fig. 12) is dramatically different from control samples. Data obtained with Schottky barriers demonstrated the following: (i) The leakage current measured was severely reduced for reactive ion etched silicon relative to control specimens. The reduction of the leakage current correlated with the thickness of the C,F-film overlayer [70]. (ii) The ideality factor  $n$  was 3.7 for the Si samples exposed for 15 seconds to the plasma, largely due to an increase in the density of surface states by more than an order of magnitude as compared to controls [70]. (iii) In DLTS measurements performed with CF<sub>4</sub>/H<sub>2</sub> dry etched p-type silicon, five hole traps located at 0.18, 0.21, 0.33, 0.43 and 0.48eV above the valence band were observed [71]. None of the observed hole traps could conclusively be related to a known defect structure, although it appeared that the 0.33eV level was due to a defect consisting of two carbon atoms. For n-type Si four electron traps located at 0.14, 0.17, 0.27 and 0.35eV below the conduction band edge were observed as a result of CF<sub>4</sub>/H<sub>2</sub> RIE [72]. The 0.17 and 0.27eV traps appeared to

be hydrogen related. Complementary information was obtained by minority carrier lifetime measurements using MOS-structures formed with  $\text{CF}_4/\text{H}_2$  dry etched Si [73]. These showed a severely reduced Si minority carrier lifetime due to defects in the substrate. Both hydrogen and accumulation of carbon in the vicinity of the surface [73] were thought to be responsible for the electrical degradation. The published electrical measurement data are consistent with the picture of RIE induced surface modifications of Fig. 12 as regards both the C,F-overlayer (reduction in diode leakage) and subsurface damage (reduced Si minority carrier lifetime, increased surface state density and deep level traps).

### 8.5.3 Etch Rate Dependence of Lattice Damage

The residual lattice damage level in a substrate is a strong function of the maximum ion energy as determined by the sheath potential and pressure, the ion flux, the types of species present in the discharge (e.g., hydrogen), the presence/absence of passivation layers, and so forth. However, the primary variable which controls the amount of residual damage in a substrate after RIE is the substrate etch rate. Upon exposure of a substrate to the reactive ion plasma, damage will be introduced into the substrate and accumulate. At the same time, reactive ion etching of the substrate occurs which consumes the damaged layer. Initially the degree of disorder in the near-surface substrate region will increase with etching time. The time necessary to reach a steady-state and a constant damage level will vary with the etch rate. These competitive effects were considered in reference [66] and it was shown that for a location  $x_1$  fixed with respect to the substrate surface, the impurity (or damage) concentration will have reached its maximum possible value to within 1% after a time  $t_{\max}$ :

$$t_{\max} \geq \frac{2.69\Delta R_p + R_p - x_1}{\text{ER}} \quad (2)$$

with  $\Delta R_p$  being the straggle and  $R_p$  the projected range of the impinging ions. The etch rate is denoted by ER. A good approximation for the low ion energies of interest in RIE is the assumption that the range stragglings equals the numerical value of the projected range. For the present example they are set equal to 2.3nm. The location  $x_1$  within the substrate for which the time evolution of residual damage is examined is set equal to the projected ion range  $R_p$ . Equation (2) becomes

$$t_{\max} \approx \frac{6\text{nm}}{\text{ER}} \quad (3)$$

This expression is used to evaluate the maximum RIE related impurity concentration as a result of ion implantation for different typical RIE applications. Table 4 shows that for rapid etching conditions of 600nm/min, representative of silicon etching in a  $\text{SF}_6$  discharge, steady-state is reached within 0.6sec. If a dose rate of  $10^{15}$  ions/cm<sup>2</sup>sec which is typical of RIE plasmas is assumed, that all ions are retained by the sample and that the residual damage profile coincides with the impurity profile, we find that the maximum retained dose is  $6 \times 10^{14}$  ions/cm<sup>2</sup>. For a slower etch rate of 60nm/min, which is more typical of a  $\text{CF}_4$  discharge, the time to steady-state is 6sec and the maximum possible retained dose is  $6 \times 10^{15}$  ions/cm<sup>2</sup>. For a very slow etch rate of 0.6nm/min, which is characteristic of selective etching conditions, the time to reach steady-state is 600sec and the maximum possible retained dose is  $6 \times 10^{17}$  ions/cm<sup>2</sup>. These considerations indicate that,

depending on the substrate etch rate, the importance of RIE induced damage will vary for different etching applications. For high etch rates little residual damage should be observed. Indeed little Si substrate damage is observed after  $\text{SF}_6$  based RIE (rapid Si etch rate). Residual damage will be important primarily for conditions of slow or negligible etching, such as for selective etching conditions. As seen in section 5.2, major Si near-surface modifications can occur during a selective etching process with negligible etching of the Si substrate.

**Table 4:** Example of the etch rate dependence of the concentration of residual RIE induced substrate impurities (or substrate lattice damage).

<u>Etch Rate</u> (nm/min)	<u>Time to Reach</u> <u>Steady-State</u> (sec)	<u>Maximum Dose</u> <u>Retained</u> ( $\text{cm}^{-2}$ )	<u>Remark</u>
600	0.6	$6 \times 10^{14}$	$\text{SF}_6$ based RIE of silicon.
60	6	$6 \times 10^{15}$	$\text{CF}_4$ based RIE of silicon.
0.6	600	$6 \times 10^{17}$	$\text{CHF}_3$ based RIE of silicon.

#### 8.5.4 Post-RIE Surface Recovery Treatments

The example of the contact hole etching process described in section 8.5.2 indicates that in many cases a reactive ion etching step has to be followed by a surface cleaning step. In general the goal is the removal of etch passivation layers, such as the fluorocarbon film in silicon dioxide etching, chlorine-containing residues for aluminum etching to prevent long-term corrosion, sidewall passivation films in silicon trench etching, the annealing of lattice damage (if introduced), and so forth. Typically RIE induced lattice damage is not dealt with explicitly since device processing invariably involves heat treatments which will anneal out any lattice damage (e.g., thermal oxidation, ion implantation anneal, etc.). On the other hand RIE passivation films have to be removed explicitly as part of the RIE process. In the simplest case the passivation film is removed with the masking layer, e.g. sidewall passivation layers are often due to erosion and redeposition of masking material and the same treatment, such as an acid dip for an oxide mask, which removes the masking layer removes the sidewall passivation film. In other instances a special surface cleaning process has to be introduced, such as a plasma clean in a different plasma etching system. For example, the fluorocarbon film, which is crucial to the achievement of  $\text{SiO}_2/\text{Si}$  etch selectivity, is difficult to remove using solvents. It is commonly removed by volatilization in an oxygen discharge which also causes the formation of a thin silicon-dioxide layer on the silicon surface. It would be desirable to conduct the fluorocarbon removal treatment in the same chamber as used for the oxide etching process in order to minimize sample handling, e.g. an in-situ  $\text{O}_2$  clean. Unfortunately, as the oxygen discharge cleans the wafer surface it volatilizes simultaneously fluorocarbon films from the walls of the etching chamber (deposited during the oxide etching step). This produces an oxygen discharge containing a significant density of atomic fluorine and causes etching of the exposed contact hole silicon surface. This is not acceptable for critical applications. In those circumstances the fluorocarbon layer removal treatment has to be undertaken in a different plasma etching chamber not used for fluorine-based etching.

## 8.6 REACTOR, EQUIPMENT CONSIDERATIONS

### 8.6.1 Reactor Types

A great number of different reactor types are used for plasma etching. These include the barrel etchers (the name derives from the shape) and downstream plasma etchers in which the plasma is excited using microwaves and which are characterized by minimal ion bombardment and purely chemical etching. Such systems are often used for photoresist stripping and other applications where high selectivity and low radiation damage are key requirements and the isotropic nature of the etch is not a problem. In applications where ion bombardment is required, parallel plate reactors can be employed. In symmetrical parallel plate systems, where the rf driven and grounded electrodes are of equal size and the plasma is truly confined between the electrodes, the plasma potential is high and both electrodes are bombarded by energetic ions. The wafer is placed on the grounded electrode (anode coupled system) and is bombarded by energetic ions because of the high plasma potential. A disadvantage of this system is that the wafer can easily be contaminated by material sputtered off the counter-electrode. Asymmetrical systems, in which the rf powered electrode is small relative to the grounded surface area, are called reactive ion etchers (or reactive sputter etchers) and are more commonly used. These systems are characterized by a low plasma potential ( $\approx 30\text{V}$ ) and a large self-bias voltage on the rf driven electrode ( $\approx 300\text{--}500\text{eV}$ ). Because of the low plasma potential relatively little sputter contamination from grounded surfaces occurs. The two most popular types of reactors used for reactive ion etching have these geometries: (i) The cathode is a horizontal plate and the walls of the chamber act as the anode of the system (see Fig. 1). These reactors can be either batch or single wafer etchers. (ii) The cathode has the shape of a hexagon which is surrounded by the cylindrical chamber walls which form the anode ("hexode" reactor). Hexode reactors are designed for high throughput batch processing.

Most industrial RIE reactors use 13.56 MHz rf power. This frequency is greater than the ion plasma frequency  $\omega_i = \sqrt{e^2 n_i / \epsilon m_i}$  where  $e$  is the electronic charge,  $n_i$  and  $m_i$  the ion density and ion mass, respectively, and  $\epsilon$  the permittivity of vacuum [74]. Consequently ions can not follow the applied rf field and respond only to the time average of the voltage at the cathode, i.e. the self-bias voltage. At a frequency of 100 kHz ions can follow the applied rf field and the ion bombardment of the cathode increases relative to high frequency excitation. This effect has been exploited in the triode configuration where 100kHz excitation is supplied to the cathode to maximize ion bombardment and 13.56MHz is supplied to an annular electrode surrounding the chamber to produce reactive ions.

### 8.6.2 Reactor Materials

Since both the electrodes and the walls of the reactor can become sources of sputtered material which may deposit on the wafer being etched, the choice of the wall/electrode materials is of critical importance. For example, in RIE batch reactors using fluorine chemistries the choice of an aluminum electrode results in very undesirable etch characteristics. Since  $\text{AlF}_3$  is involatile, Al sputtered from the cathode is deposited onto the wafer surface during processing. The deposition of Al results in micromasking and surface roughening of the wafer surface as a result of etching [59]. Micromasking and surface roughening can be avoided by using electrode materials which form volatile products with the etching gas, e.g. silicon, quartz, graphite, teflon, etc. for use with fluorine based



chemistries. These electrode materials give rise to different problems: Since fluorine will etch these materials and thus is consumed, the atomic fluorine density in the gas phase will be lowered. The etching of quartz or graphite will change the oxygen or carbon content of the gas phase. These electrode effects can significantly alter the plasma chemistry. For example the few percent of oxygen added to the gas phase by the etching of a quartz electrode in a fluorocarbon plasma prevents the formation of fluorocarbon films on bombarded surfaces and makes it impossible to achieve etch selectivity of silicon dioxide over an underlayer based on fluorocarbon film passivation of the underlayer. In this application an electrode made of graphite, teflon or equivalent is needed instead. The secondary electron emission coefficient of electrode surfaces may also influence the nature of the discharge. These problems are minimized for single wafer reactors where primarily the wafer being etched faces the glow discharge.

In reactive ion etching the plasma potential is low, so ions striking the walls of the reactor have much reduced energies compared with those striking the cathode and little material will be sputtered. However, for stainless steel walls any sputtering will free Fe, Cr and Ni and these impurities introduce deep levels into silicon which degrade the minority carrier lifetime. Even very low concentrations of these heavy metals can make the semiconductor unusable and therefore no stainless steel parts should be in direct contact with the plasma.

### **8.6.3 Chamber Cleanliness, Process Reproducibility Issues**

The addition of small amounts of contaminants to a plasma can significantly change the etching characteristics of a given process. The best studied case is the effect of small amounts of water to the etching of Al in chlorine plasmas [63]. Aluminum films are covered by their native oxide and etching of  $\text{Al}_2\text{O}_3$  is very difficult as compared to Al; the etching of Al lines proceeds therefore in a two-step process. First the native oxide is removed using considerable ion bombardment and oxygen scavengers, such as  $\text{BCl}_3$ . Subsequently the etching of Al takes place. The etching of the native oxide is greatly retarded or made irreproducible if small amounts of water are present in the chamber; the water will react with the oxygen scavengers. Since the presence of water is primarily due to exposure of the chamber to room ambient between runs and the adsorption of moisture by the chamber walls, many dry etching chambers used in manufacturing employ load locks which eliminate this problem.

The etching process itself can lead to chamber contamination and process irreproducibility. For example, if fluorocarbon gases are used to selectively etch  $\text{SiO}_2$  the same insulating fluorocarbon film which serves as an etch stop layer is deposited at a much greater thickness on the grounded inner surfaces of the reactor. The presence of this film changes the etching characteristics of the plasma since it has an effect on both the electrical properties (by changing the powered/grounded electrode area ratio via insulation of the chamber walls) and chemical characteristics (due to fluorine consumption/recycling by interaction of the film with reactive plasma species) of the discharge. The best procedure appears to be to "condition" the chamber after each clean-up by running the process plasma for some time and depositing a film onto the walls of the system. The oxide etching characteristics will then be stable in subsequent runs. After a certain number of runs the fluorocarbon film on the chamber walls has grown thick enough to loose adhesion and cause particulates. In order to prevent this, the chamber needs to be cleaned by volatilizing the fluorocarbon film using an oxygen dis-

charge. The cycle is then repeated. Similar tool cleaning schedules need to be observed for other etching processes.

#### 8.6.4 Single Wafer vs. Batch Reactors

Batch reactors commonly work at lower pressure and lower power densities than single wafer reactors and the etch rates are smaller. High throughput is achieved with large batch sizes, e.g. up to 24 6-inch Si wafers for commercial systems. Directional etching of materials requiring significant ion bombardment to induce etching, e.g. silicon dioxide, is possible because of etching at low pressure (10-100 mTorr). Increases in semiconductor wafer size to 6-inch and greater and the demand for greater process automation, for instance microprocessor controlled cassette-to-cassette loading/unloading, and improved process control, such as individual end point detection, have made single wafer etching reactors more desirable for many etching applications than batch reactors. In order to achieve adequate throughput, high etch rates ( $\approx 1 \mu\text{m}/\text{min}$ ) are required for single wafer reactors. Since the arrival rate of reactive species at the wafer surface controls the etch rate, a high reactive species generation rate is a prerequisite. The generation rate  $R$  of a reactive specie in a glow discharge by electron impact is given by [75]

$$R = kn_e N \quad (4)$$

where  $k$  is the reaction rate constant for ionization (or dissociation),  $n_e$  the electron number density and  $N$  the neutral gas number density. The reaction rate constant depends on the electron energy distribution  $f(\epsilon)$

$$k = \int_0^\infty \sqrt{\frac{\epsilon}{2m}} \sigma(\epsilon) f(\epsilon) d\epsilon \quad (5)$$

where  $\epsilon$  is the electron energy,  $m$  the electron mass,  $\sigma(\epsilon)$  the cross section as a function of energy. Increases in either the rate coefficient  $k$ , the number density  $n_e$  of electrons or the gas number density cause a larger generation rate of reactive species. Different reactor designs optimize different factors.

The approach used in the past for single wafer reactors was to operate at a high gas pressure ( $\approx 1$  Torr and greater) using a small interelectrode gap (less than 1 cm) and high rf input power to achieve high generation rates of reactive species and the required etch rates. High pressure single wafer reactors are characterized by a) a high neutral flux to ion flux ratio and b) little energetic ion bombardment because of ion-neutral collisions in the sheath region. Anisotropic etching in those systems is due to sidewall passivation.

Directional etching of materials where sidewall passivation is difficult to achieve or etching of materials requiring a significant sputtering component (e.g., involatile CuCl removal for Al etching, etching of silicon dioxide) cannot be accomplished in high pressure single wafer reactors and low pressure RIE batch reactors have been used for those applications. However, with the current trend to single wafer reactors a great deal of development effort has gone into producing low pressure single wafer etchers ( $p < 10 \text{ mTorr}$ ) with adequate throughput which would perform tasks currently accomplished in RIE batch reactors. High etchant specie(s) production rates can be achieved at low gas pressure by increasing the electron concentration  $n_e$  in equation 4 using mag-

netic confinement to reduce the loss of electrons to the walls of the system. Two primary technologies of low pressure single wafer reactors are currently available commercially; magnetrons (closely related to conventional RIE reactors) and electron cyclotron resonance systems.

In magnetron ion etching (MIE) magnetic field lines parallel to the cathode surface (produced either by permanent magnets inside the cathode or external electromagnets) and electric field lines normal to the cathode surface (due to the cathode dc bias) confine electrons on cycloidal trajectories near the cathode [76]. The probability of an electron undergoing dissociative/ionizing collisions with gas phase species is thus enhanced and, e.g. the ion/neutral ratio can be  $\approx 50$  times greater in MIE than in RIE. The mobility of electrons towards the cathode is decreased because of this confinement, causing the self-bias voltage to be lower than in conventional RIE. A large flux of low energy ions is thus produced in magnetrons at low pressure whereas in RIE a small flux of high energy ions is produced for the same input power. Anisotropic etching is easier to achieve in low pressure single wafer reactors than in high pressure single wafer reactors because of a) a high ion-to-neutral flux ratio and b) the reduced probability of ion-neutral collisions in the sheath region at low pressure.

In electron cyclotron resonance (ECR) systems a discharge is produced by microwave excitation (commonly 2.45 GHz) [77] (see also Chap. 11). A magnetic field of  $\approx 1$  kGauss is applied which decreases as a function of distance from the location of the electromagnets. At certain locations the field is 875 Gauss and a resonance between the cyclotron motion of the electrons in the magnetic and microwave field occurs. At resonance the electron cyclotron resonance frequency  $\omega_{ce} = eB/2\pi m$  is equal to the microwave frequency (where  $e$  is the electronic charge,  $B$  the magnetic flux and  $m$  the electron mass). Electrons at resonance convert efficiently microwave energy into ionization and dissociation of gas species. The wafer is placed below the discharge chamber and can be rf or dc biased to control the energy of impinging ions. In electron cyclotron resonance reactors the generation of ions and radicals is effectively decoupled from their acceleration and energy gain which potentially enables far greater control of the etching process than possible in RIE.

Low pressure single wafer reactors are much more demanding in terms of pumping equipment and wafer cooling than RIE systems or high pressure single wafer reactors. For high pressure single wafer reactors a mechanical pump is typically sufficient and wafer cooling is not an issue because of the high working pressure. For RIE an additional Roots blower and a turbopump is required to maintain pressures down to 10mTorr at adequate gas flows. Because of the relatively low etch rates the temperature rise of the wafers during etching is in most cases limited to  $\approx 100^\circ\text{C}$ . The pressure for MIE processing is near 1mTorr and for ECR etching it can be even lower. Moderate gas flows at these low pressures demand very high pumping speeds, e.g. for a flow of 30sccm a 1500 liter/sec turbopump may need to be employed. Wafer cooling is a critical issue both because of the achievement of high etch rates, significant ion bombardment and low pressure operation. Backside helium cooling using either a wafer clamp or an electrostatic chuck is necessary in order to control the etching process and prevent damage to the wafer such as resist reticulation.

## 8.7 END POINT DETECTION and PLASMA DIAGNOSTICS

### 8.7.1 General Considerations

The most direct need for plasma diagnostic techniques [78-80] arises in the determination of the etch end point for a given process. In addition plasma diagnostic techniques are used for process monitoring and provide information on the types of species present in a reactive ion etching plasma, their concentration, their energy content, and so forth. For etch endpoint detection and plasma diagnostic measurements laser interferometry, optical emission spectroscopy and mass spectrometry are the most commonly used techniques. The first two techniques require only a suitably located optical window on the chamber, are easily implemented and enable the obtaining of a great deal of information about etching plasmas. Langmuir probe measurements, laser induced fluorescence (LIF), coherent anti-stokes spectroscopy (CARS), ellipsometry and infrared/visible region absorption spectroscopy have been used to obtain important insights into reactive ion plasmas but are experimentally more demanding than the former techniques and they have primarily been used for plasma research. These latter techniques will not be covered in this article. In the future some of these techniques may be used for endpoint detection for systems where laser interferometry and optical emission methods fail. Selwyn [81] was able to detect the presence of As in the gas phase during etching of GaAs and Si using laser induced fluorescence. He suggested the use of LIF for detecting the etch endpoint in the removal of a boron-doped silicon layer on top of arsenic-doped silicon or vice versa.

### 8.7.2 Laser Interferometry, Reflectance

In this technique the laser light reflected from the surface of a wafer being etched is measured. For transparent films, e.g.  $\text{SiO}_2$ , an oscillating signal is observed for the reflected laser light intensity which is due to interference of the reflected light from the film surface and the substrate surface. The spacing between adjacent maxima (or minima) is  $\delta d = \lambda/2n$ , where  $\lambda$  is the wavelength of the laser light and  $n$  the refractive index of the transparent layer. Etch rates can be determined in real time. For nontransparent films, e.g. metals, a change in reflectivity is observed upon complete removal of the metallic film. For patterned wafers without an etch stop layer the pattern can be used as a diffraction grating and the depth of the etched pattern can be determined in-situ. There are two principal drawbacks to these techniques. Firstly, they usually require the presence of a special test site since the features being etched, e.g. contact holes into an  $\text{SiO}_2$  film, are too small for measurements. Secondly, information about the etch endpoint is obtained only for one specific area on the wafer, which can cause difficulties in batch processing.

### 8.7.3 Optical Emission Spectroscopy

Optical emission spectroscopy is the most widely used technique for etch end point detection [78,79,80,82]. The change in emission from a characteristic species is observed as etching of a film is completed. Either the decrease in emission of a suitable etch product specie or the increase in etchant specie at the end of the etching process is monitored. Table 5 lists for some important electronic materials and commonly used etching gases emission lines employed for etch end point detection. The sensitivity of this technique depends on how much etchant is consumed or how much film material is etched per unit time. If the etch rate is too slow or the size of the etched pattern too small, e.g. con-

tact hole etching into SiO<sub>2</sub> layers, this technique may not be suitable for end point detection.

**Table 5:** Table 5: Common optical emission lines used for end-point detection. This table was compiled from data provided in references [78, 82].

<u>Material</u>	<u>Etchant Gas</u>	<u>Emitting Species</u>	<u>Wavelength (nm)</u>
Silicon	CF <sub>4</sub> /O <sub>2</sub> ;SF <sub>6</sub>	F (Etchant)	704
	CF <sub>4</sub> /O <sub>2</sub> ;SF <sub>6</sub>	SiF (Product)	440;777
	Cl <sub>2</sub> ;CCl <sub>4</sub>	SiCl (Product)	287
SiO <sub>2</sub>	CHF <sub>3</sub>	CO (Product)	484
Si <sub>3</sub> N <sub>4</sub>	CF <sub>4</sub> /O <sub>2</sub>	N <sub>2</sub> (Product)	337
	CF <sub>4</sub> /O <sub>2</sub>	CN (Product)	387
	CF <sub>4</sub> /O <sub>2</sub>	N (Product)	674
W	CF <sub>4</sub> /O <sub>2</sub>	F (Etchant)	704
Al	CCl <sub>4</sub> ;Cl <sub>2</sub> ;BCl <sub>3</sub>	Al (Product)	391;394;396
	CCl <sub>4</sub> ;Cl <sub>2</sub> ;BCl <sub>3</sub>	AlCl (Product)	261
Resist	O <sub>2</sub>	O (Etchant)	777;843
	O <sub>2</sub>	CO (Product)	484
	O <sub>2</sub>	OH (Product)	309
	O <sub>2</sub>	H (Product)	656

## 8.8. CURRENT TRENDS

A decade ago the primary focus of the RIE research and development efforts was the empirical search for plasma etching processes which would satisfy the etch directionality and etch selectivity requirements of semiconductor device and circuit fabrication. Within the last few years, research and development efforts on reactive ion etching have evolved to address the following topics:

- a. Enhanced plasma generation schemes for high rate low pressure etching. Magnetron ion etchers and electron cyclotron resonance single wafer etchers are results of this research and development activity and were discussed in section 8.6. Microwave multipolar plasma reactors equipped with confinement magnets which surround the etching chamber and use ECR sources [83], and the rf driven double cathode etcher [84] are different developments with the promise of high-rate etching at low pressure.
- b. RIE process-integration (process clustering). The goal is to effectively integrate RIE into the overall fabrication sequence, e.g. by connecting deposition and etching chambers by clean, evacuated transport chambers. Process clustering requires clean, damage-free etching processes (see section 5) and dry surface cleaning methods.

- c. Real-time control of RIE processes.  
Because of the use of large silicon wafers and increasing process complexity the value of partially processed wafers is going up rapidly. This justifies considerable investment in real-time process monitoring equipment (beyond endpoint detection) which will detect equipment/process malfunctioning in real-time and "save" wafers. Better process diagnostics and understanding will enable the design of feedback loops and real-time process control.
- d. Improved fundamental understanding and computer models of RIE processes.  
The "output" of a RIE process depends in a non-linear way on a great number of "input" parameters (rf power, frequency, reactant gas composition, pressure, chamber residence time, etc.). We also lack a valid model for the processes occurring in glow discharge etching plasmas. This situation requires extensive experimentation in the development of suitable etching processes. It is expected that accurate computer models of plasma etching processes based on an improved understanding of the science of rf discharges will aid significantly in optimizing their use for electronic materials processing or other applications. A three-fold approach is being pursued in order to reach this goal.

First, measurements are being performed on real rf plasma systems in order to address the question as to what kind of phenomena are occurring. Although there is a great need for new diagnostic techniques, in particular for the study of plasma-surface interactions, certain important glow discharge parameters have been determined for particular plasma-substrate systems. Significant progress has been made in determining atom, radical and ion concentrations and their energies, the electron density and its energy distribution, processes occurring selectively on certain surfaces and not on others, e.g. a material A versus a material B, bottom of a trench versus the sidewall, and so forth. There is an increased emphasis on performing the measurements non-intrusively and in-situ. Multiple techniques are being used to measure the same quantities, e.g. microwave interferometry and Langmuir probes are being used to measure electron densities. New diagnostic techniques are being developed in order to measure the desired glow discharge parameters. For example, two groups independently developed a photoemission optogalvanic method which can be used to characterize in real-time, in-situ the surfaces of semiconductors and metals exposed to a plasma [85].

The second required research component are model system studies, since real glow discharges make well-controlled experiments difficult. Due to the coupling of most parameters in a plasma, a controlled change in one quantity invariably changes other quantities and it is difficult to assess the relative importance of the change of a specific quantity in producing a new result. The goal of the model system studies is to investigate the interaction of fluxes of atoms and radicals with well-specified surfaces, alone or in combination with ion (mass/energy analyzed), electron and photon bombardment, measure the energy dependence of the cross sections for the production of important species found in glow discharges, perform controlled experiments to establish the rate and importance of plasma and surface chemical reactions, and so forth.

The third component needed is numerical modelling [86]. Values of the controllable plasma operating parameters such as rf power and frequency, type of gas, gas pressure, and so forth and the results of the model system approach on cross sections, sticking coefficients, reaction rates etc. are used as inputs of a computer model of a glow discharge for a specific application. A model of the plasma etching process requires treatment of both the discharge physics and chemistry (gas phase and surface) which are coupled [86]. The output of the numerical model can be compared to the results of measurements performed on real systems. For prototypical plasma processes, such as Si etching using SF<sub>6</sub>, numerical models are already quite advanced and increasingly accurate [87].

The near future may see the utilization of computer models of RIE discharges in the design of etching processes for new materials. Two-dimensional modelling may be used instead of the demanding experimental approach to optimize etch uniformity. Accurate computer models should also contribute to the scale-up of plasma reactors, e.g. ECR-based systems, and the control of the etching process.

Acknowledgement: I would like to thank T. D. Bestwick for a critical reading of this article and many helpful suggestions.

## 8.9 REFERENCES

1. Reactive ion etching is covered in these books:  
J. W. Coburn, Plasma Etching and Reactive Ion Etching, (American Vacuum Society Monograph Series, New York, 1982);  
B. Chapman, Glow Discharge Processes, John Wiley & Sons, New York (1980);  
T. Sugano, "Applications of Plasma Processes to VLSI Technology", John Wiley & Sons, New York (1985);  
VLSI Electronics Microstructure Science, Vol. 8, Plasma Processing for VLSI, eds. N. G. Einspruch and D. M. Brown, (Academic Press, New York, 1984);  
The Electrochemical Society (Pennington, NJ) and the Materials Research Society (Pittsburgh, PA) organize regularly symposia on Plasma Processing and publish proceedings. Recent volumes are: Proceedings of the Sixth Symposium on Plasma Processing, edited by G. S. Mathad, G. C. Schwartz and R. A. Gottscho (The Electrochem. Soc., Pennington, 1987) and Plasma Processing, eds. J. W. Coburn, R. A. Gottscho, and D. W. Hess, (Materials Research Society, Vol. 68 of the Symposia Proceedings Series, Pittsburgh, 1986).  
Of great interest is also the series of international symposia on plasma chemistry, e.g. the most recent proceedings volume is: Proceedings 8th Int. Symposium Plasma Chemistry/Tokyo 1987, eds. K. Akashi and A. Kinbara, (Int. Union of Pure and Appl. Chemistry, 1987).
2. See e.g., S. Wolf and R. N. Tauber, Silicon Processing for the VLSI Era (Lattice Press, Sunset Beach, 1986).
3. G. C. Schwartz, in Proceedings of the Fifth Symposium on Plasma Processing (Electrochem. Soc., Pennington, 1985), pp. 26.
4. J. W. Coburn and H. F. Winters, J. Appl. Phys. 50: 3189 (1979).
5. F. R. McFeely, J. F. Morar, and J. A. Yarmoff, in Proceedings of the Sixth Symposium on Plasma Processing, edited by G. S. Mathad, G. C. Schwartz and R. A.

- Gottscho (The Electrochem. Soc., Pennington, 1987), pp. 619; F. R. McFeely, J. F. Morar, N. D. Shinn, G. Landgren, and F. J. Himpsel, Phys. Rev. B30: 674 (1984).
6. J. W. Coburn, H. F. Winters, and T. J. Chuang, J. Appl. Phys. 48: 3532 (1977).
  7. H. F. Winters, J. W. Coburn, and T. J. Chuang, J. Vac. Sci. & Technol. B1: 469 (1983).
  8. J. L. Mauer, J. S. Logan, L. B. Zielinski, and G. C. Schwartz, J. Vac. Sci. & Technol. 15: 1734 (1978).
  9. D. L. Flamm and V. M. Donnelly, Plasma Chem. Plasma Process. 1: 317 (1981).
  10. Y.-Y. Tu, T. J. Chuang, and H. F. Winters, Phys. Rev. B23: 823 (1981).
  11. H. F. Winters and J. W. Coburn, in Plasma Synthesis and Etching of Electronic Materials, eds. R. P. H. Chang and B. Abeles, (Materials Research Society, Vol. 38 of the Symposia Proceedings Series, Pittsburgh, 1985), pp. 189.
  12. A. Bensaoula, J. Stozier, A. Ignatiev and J. Wolfe, Plasma Processing, eds. J. W. Coburn, R. A. Gottscho, and D. W. Hess, (Materials Research Society, Vol. 68 of the Symposia Proceedings Series, Pittsburgh, 1986), pp. 429.
  13. C. J. Mogab, J. Electrochem. Soc. 124: 1262 (1977).
  14. S. Tachi, K. Tsujimoto, and S. Okudaira, Appl. Phys. Lett. 52: 616 (1988).
  15. R. A. Haring, A. Haring, F. W. Saris, and A. E. de Vries, Appl. Phys. Lett. 41: 174 (1982); A. W. Kofschoten, R. A. Haring, A. Haring, and A. E. de Vries, J. Appl. Phys. 55: 3813 (1984).
  16. M. Seel and P. S. Bagus, Phys. Rev. B23: 5464 (1981); *ibid* B28: 2023 (1983); *ibid* B29: 1070 (1984).
  17. G. C. Schwartz and P. M. Schaible, J. Vac. Sci. & Tech. 16: 410 (1979).
  18. C. J. Mogab and H. J. Levinstein, J. Vac. Sci. & Technol. 17: 721 (1980).
  19. S. Matsuo, Appl. Phys. Lett. 36: 768 (1980).
  20. Y. H. Lee and M.-M. Chen, J. Vac. Sci. Technol. B4: 468 (1986).
  21. H. F. Winters and D. Haarer, Phys. Rev. B36: 6613 (1987).
  22. Y. H. Lee, M. M. Chen, and A. A. Bright, Appl. Phys. Lett. 46: 260 (1985).
  23. See e.g., M. Sekine, T. Arikado, H. Okano, and Y. Horiike, in Proceedings of the 8th Symposium on Dry Process, (Inst. Electr. Eng., Tokyo, 1986), pp. 42.
  24. G. S. Oehrlein, K. K. Chan, M. A. Jaso, and G. W. Rubloff, J. Vac. Sci. & Technol. (to be published, 1989).
  25. For a study of the etching characteristics of SF<sub>6</sub>/O<sub>2</sub> plasmas see: M. Pons, A. Inard, and D. Henry, Supplement a la Revue Le Vide, Les Couches Minces 237: 264 (1987).
  26. K. Tsujimoto, S. Tachi, K. Ninomiya, K. Suzuki, S. Okudaira and S. Nishimatsu, in Ext. Abstracts of the 18th Int. Conf. Solid State Devices and Materials, (Tokyo, 1986), pp. 229.
  27. D. Chin, S. H. Dhong, and G. J. Long, J. Electrochem. Soc. 132: 1705 (1985).
  28. For an excellent discussion see reference 9.
  29. C. J. Mogab, A. C. Adams, and D. L. Flamm, J. Appl. Phys. 49: 3796 (1978).



30. R. D'Agostino, F. Cramarossa, S. De Benedictis and G. Ferraro, J. Appl. Phys. 52: 1259 (1981).
31. V. M. Donnelly, D. L. Flamm, W. C. Dautremont-Smith, and D. J. Werder, J. Appl. Phys. 55: 242 (1984).
32. G. S. Oehrlein, S. W. Robey, and J. L. Lindström, Appl. Phys. Lett. 52: 1170 (1988).
33. J. W. Coburn, and H. F. Winters, J. Vac. Sci. & Technol. 16: 391 (1979).
34. G. S. Oehrlein, C. M. Ransom, S. N. Chakravarti, and Y. H. Lee, Appl. Phys. Lett. 46: 686 (1985).
35. R. S. Bennett, Electrochem. Soc. Extended Abstracts 82-2: 283 (1982).
36. R. A. Gottscho and G. R. Scheller, in Proceedings of the Sixth Symposium on Plasma Processing, edited by G. S. Mathad, G. C. Schwartz and R. A. Gottscho (The Electrochem. Soc., Pennington, 1987), pp. 201.
37. G. S. Selwyn, J. Appl. Phys. 60: 2771 (1986).
38. D. L. Flamm, V. M. Donnelly, and J. A. Mucha, J. Appl. Phys. 52: 3833 (1981).
39. R. A. H. Heinecke, Solid State Electronics 18: 1146 (1975).
40. L. M. Ephrath, J. Electrochem. Soc. 126: 1419 (1979); L. M. Ephrath, and E. J. Petrillo, J. Electrochem. Soc. 129: 2282 (1982).
41. H. W. Lehmann and R. Widmer, J. Vac. Sci. & Technol. 15: 319 (1978).
42. G. S. Oehrlein, and H. L. Williams, J. Appl. Phys. 62: 662 (1987).
43. G. S. Oehrlein, S. W. Robey, and M. A. Jaso, in Plasma Processing, D. Apelian and J. Szekely, eds., (Materials Research Society Symposia Proceedings, Vol. 98, Pittsburgh, 1987), pp. 229.
44. G. J. Coyle, Jr. and G. S. Oehrlein, Appl. Phys. Lett. 47: 604 (1985).
45. J. W. Coburn, J. Appl. Phys. 50: 5210 (1979).
46. P. J. Hargis and M. J. Kushner, Appl. Phys. Lett. 40: 779 (1982).
47. Eric Kay, in Methods and Materials in Microelectronic Technology, ed. J. Bargon, (Plenum Publish. Corp., New York, 1984), pp. 243.
48. M. M. Millard and E. Kay, J. Electrochem. Soc. 129: 160 (1982).
49. G. S. Oehrlein, K. K. Chan, and M. A. Jaso, J. Appl. Phys. 64: 2399 (1988).
50. S. W. Robey, M. A. Jaso, G. S. Oehrlein, J. Appl. Phys. (to be published 1989).
51. G. S. Oehrlein, S. W. Robey, J. L. Lindström, K. K. Chan, M. A. Jaso, and G. J. Scilla, J. Electrochem. Soc. (to be published 1989).
52. M. Mieth, Semiconductor International (May 1984 Issue), pp. 222.
53. For reviews see e.g., S. W. Pang, Solid State Technolog. 27: 249 (1984); S. J. Fonash, Solid State Technolog. 28: 201 (1985).
54. G. S. Oehrlein and Y. H. Lee, J. Vac. Sci. & Technol. A5: 1585 (1987).
55. G. A. Northrop and G. S. Oehrlein, Materials Science Forum 10-12: 1253 (1986).
56. J. Weber and M. Singh, Appl. Phys. Lett. 49: 1617 (1986).
57. J. C. Mikkelsen, Jr. and I.-W. Wu, Appl. Phys. Lett. 49: 103 (1986); X. C. Mu, S. J. Fonash, and R. Singh, Appl. Phys. Lett. 49: 67 (1986).

58. L. M. Ephrath and R. S. Bennett, J. Electrochem. Soc. 129: 1822 (1982).
59. G. S. Oehrlein, R. G. Schad, and M. A. Jaso, Surf. Interf. Analysis 8: 243 (1986).
60. T. Watanabe and Y. Yoshida, Solid State Technol. 27: 213 (1984).
61. D. J. DiMaria, L. M. Ephrath, D. R. Young, J. Appl. Phys. 50: 4015 (1979).
62. S. P. Murarka and C. J. Mogab, J. Electron. Materials 8: 763 (1979).
63. D. W. Hess and R. H. Bruce, in Dry Etching for Microelectronics, ed. R. A. Powell, (Elsevier, New York, 1984), pp. 1.
64. S. J. Fonash, S. Ashok, and R. Singh, Appl. Phys. Lett. 39: 423 (1981); C. M. Ransom, T. I. Chappell, L. M. Ephrath, and R. S. Bennett, Electrochem. Soc. Extended Abstracts 83-1: 282 (1983).
65. S. W. Pang, D. D. Rathman, D. J. Silversmith, R. W. Mountain, and P. D. DeGraff, J. Appl. Phys. 54: 3272 (1983).
66. G. S. Oehrlein, R. M. Tromp, J. C. Tsang, Y. H. Lee, and E. J. Petrillo, J. Electrochem. Soc., 132: 1441 (1985).
67. G. S. Oehrlein, G. J. Coyle, J. C. Tsang, R. M. Tromp, and Y. H. Lee, in Plasma Processing, eds. J. W. Coburn, R. A. Gottscho, and D. W. Hess, (Materials Research Society, Vol. 68 of the Symposia Proceedings Series, Pittsburgh, 1986), pp. 367; G. S. Oehrlein, R. M. Tromp, Y. H. Lee, and E. J. Petrillo, Appl. Phys. Lett., 45: 420 (1984).
68. S. J. Jeng and G. S. Oehrlein, Appl. Phys. Lett. 50: 1912 (1987).
69. S.J. Jeng, G. S. Oehrlein, G. J. Scilla, Appl. Phys. Lett. 53: 1735 (1988).
70. P. Spirito, C. M. Ransom, and G. S. Oehrlein, Solid State Electronics 29: 607 (1986).
71. C. M. Ransom, in "Tegal Eleventh Annual Plasma Seminar", (Tegal Corp., Novato, 1985), pp. 31.
72. Y. Kawamoto, and N. Hashimoto, in Proceedings Second Symposium Dry Process, (Inst. Elect. Eng. Japan, Tokyo, 1980), pp. 63.
73. Y. Ozaki, and K. Ikuta, Jap. J. Appl. Phys. 23: 1526 (1984).
74. D. L. Flamm, J. Vac. Sci. & Technol. A4: 729 (1986).
75. A. T. Bell, J. Macromol. Sci. Chem. A10: 369 (1976).
76. Y. Horiike, H. Okano, T. Yamazaki, and H. Horie, Jap. J. Appl. Phys. 20: L817 (1981); H. Okano and Y. Horiike, in Plasma Processing, eds. J. Dieleman, R. G. Frieser, and G. S. Mathad (Electrochem. Soc., Pennington, 1982), PV 82-6, pp. 206; I. Lin, J. Appl. Phys. 58: 1638 (1985); A. A. Bright, S. Kaushik, G. S. Oehrlein, J. Appl. Phys. 62: 2518 (1987).
77. K. Suzuki, S. Okudaira, N. Sakudo, and I. Kanomata, Japan. J. Appl. Phys. 16: 1979 (1977); K. Suzuki, K. Ninomiya, and S. Nishimatsu, Vacuum 34: 953 (1984).
78. W. R. Harshbarger, in VLSI Electronics Microstructure Science, Vol. 8, Plasma Processing for VLSI, eds. N. G. Einspruch and D. M. Brown, (Academic Press, New York, 1984), 411.
79. R. A. Gottscho, and T. A. Miller, Pure Appl. Chem. 56: 189 (1984).

80. G. S. Selwyn, in Proceedings of the Sixth Symposium on Plasma Processing, edited by G. S. Mathad, G. C. Schwartz and R. A. Gottscho (The Electrochem. Soc., Pennington, 1987), pp. 220.
81. G. S. Selwyn, Appl. Phys. Lett. 51: 167 (1987).
82. P. J. Marcoux and P. D. Foo, Solid State Technol. 24: 115 (1981).
83. Y. Arnal, A. Durandet, J. Pelletier, M. Pichot, and L. Vallier, in Supplement a la Revue Le Vide, les Couches Minces 237: 73 (1987).
84. R. W. Boswell, R. K. Porteous, A. Bouchoule, and P. Ranson, in Supplement a la Revue Le Vide, les Couches Minces 237: 78 (1987).
85. G. S. Selwyn, B. D. Ai, and J. Singh, Appl. Phys. Lett. 52: 1953, (1988); S. W. Downey, A. Mitchell, and R. A. Gottscho, J. Appl. Phys. 63: 5280 (1988).
86. D. B. Graves and K. F. Jensen, IEEE Transactions on Plasma Science PS-14: 78 (1986); J. P. Boeuf, Phys. Rev. A36: 2782 (1987); A. D. Richards, B. E. Thompson, and H. H. Sawin, Appl. Phys. Lett. 50: 492 (1988).
87. H. H. Sawin (private communication) and E. Gogolides, J.-P. Nicolai, and H. H. Sawin (to be published).

---

## Reactive Sputter Deposition

---

**William D. Westwood**

### 9.1 INTRODUCTION

Reactive sputter deposition involves the sputtering of a metal, alloy or compound in a reactive gas mixture in order to deposit a compound thin film composed of the sputtered material and the reactive species. A wide variety of compounds have been formed in this way, with a wide range of properties. In some cases, these compounds are difficult or impossible to form by other means, particularly at low substrate temperature. The process of reactive sputter deposition can be very complex, and involves the sputtering process, the physics of the plasma discharge, transport of the sputtered and gas species, the kinetics of film growth and chemical interactions at the target and film surfaces. These all interact in some way and therefore can affect the properties of the film.

Films can be reactively sputter deposited in a number of ways, using rf-diodes, triodes, ion beam and dual ion beam systems, magnetrons and modified magnetrons. Of particular interest in this chapter will be the magnetron techniques.

There are many applications for reactively sputter deposited films. Perhaps the most common example is TiN coatings for wear resistance, and also diffusion barriers. Other examples include SiO<sub>2</sub> dielectric coatings, Si-H solar cells, In-Sn-oxide transparent conductors and the new high T<sub>c</sub> superconductors. While there is a large volume of literature on reactive sputtering, there are only a few reviews of the topic (1-3).

### 9.2 PLASMA-BASED SPUTTERING TECHNIQUES: HYSTERESIS EFFECTS

A typical reactive sputter deposition system might be composed of a metallic sputtering target, such as Al or Ti, sputtered in a predominantly inert gas plasma at a pressure between 0.1 and 10 Pa (1 Pa = 7.5 mTorr). Without the introduction of a reactive species, oxygen or nitrogen, for example, the films deposited by the sputtering process would be metallic. Upon introduction of a reactive gas species, those atoms will combine with the sputtered atoms from the target to form a compound thin film. At low levels of the reactive species, the films will be only partially reacted. At sufficiently high flow levels of the reactive species, the films will be fully reacted. However, even higher levels of the

reactive species will cause compound formation on the target or cathode surface. This compound formation on the cathode will persist as the flow of reactive gas is reduced, until at a significantly lower flow level the metal cathode is exposed by physical sputtering. This general phenomena is qualitatively known as a hysteresis effect.

The two regimes of operation, i.e. metallic cathode sputtering and compound-coated cathode sputtering, can be described by the plotting of the hysteresis effect between the flow rate,  $f_r$  of the reactive species and the chamber pressure,  $P$ . A generic example is shown in Fig. 1, which would apply, for example, to the case of the sputtering of an Al cathode in Ar with the addition of  $O_2$  to the chamber. A constant pressure,  $P_a$  is maintained by the flow  $f_a$  of the non-reactive gas (Ar in this case) into the continuously pumped chamber. The sputtering of the Al target in the Ar alone would result in the deposition of a pure Al film. The dashed line in Fig. 1 shows the linear increase in  $P$  which would result simply from increasing the argon flow  $f_a$ . This follows the relation  $Q = S \times P$ , where  $Q$  is the total flow rate of gas and  $S$  is the pumping speed.

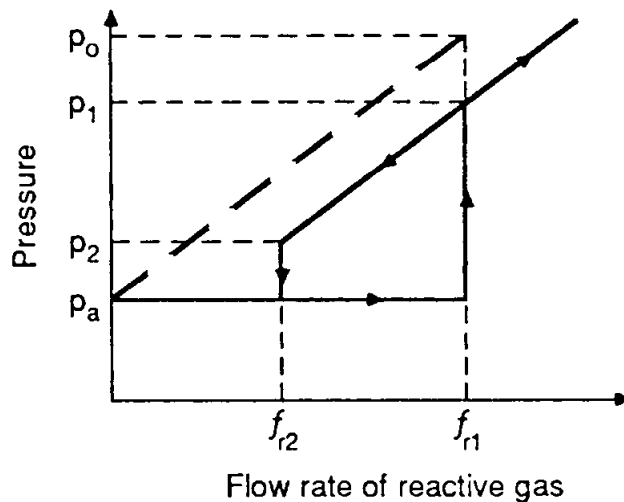


**Figure 1:** Generic hysteresis curve for system pressure,  $P$ , as a function of reactive gas flow rate,  $f_r$ .

The hysteresis curve represents two stable states of a system with rapid transitions between the two states. In state A, there is negligible change in the total pressure as the reactive gas flow,  $f_r$ , is varied; in state B, the pressure rises linearly with reactive flow rate, but is lower by  $\Delta P$  than the total pressure in the absence of sputtering. In state A, essentially all of the reactive gas is being incorporated in the deposited film and the atomic ratio of the reactive gas to sputtered metal in the film increases with  $f_r$ . Thus, state A can be considered as a regime in which the sputtered metal is doped with reactive gas. In state B, a constant volume of reactive gas is consumed, independent of  $f_r$ , and there is an excess of reactive gas so the formation of a stable compound is favored.

The transition from state A to state B is due to the formation of a compound on the surface of the sputtering target. In most cases the sputtering yield for metal atoms from the target will decrease once a compound forms on the target surface. Some of the energy of the incident ion on the target must go to sputtering the other component of the compound. For example, if an  $Al_2O_3$  film is formed on the cathode surface, only 40% of the atoms sputtered from the surface would be Al atoms. Thus, if the discharge power is kept constant as the transition from state A to state B occurs, the sputtering rate of Al would decrease by a minimum of 60%. The greater the ratio of the sputter yields of the metal

atoms from the element and compound, the smaller will be the value of  $\Delta P$  in Fig. 1, and the more rapid the transition from state A to state B. In addition, the deposition rate in state B will be significantly below the deposition rate in state A.

The hysteresis effect is strongly dependent on the pumping speed of the vacuum system. In a series of experiments, Okamoto and Serikawa (5) varied the pumping speed,  $S$ , by a factor of 20 to change the flow of Ar from 5 to 100 SCCM for the reactive sputtering of Si in Ar/N<sub>2</sub>. At an Ar flow of 5 SCCM, a well defined hysteresis curve was obtained (Fig. 2) with  $f_{r1} = 8$  SCCM and  $f_{r2} = 5.5$  SCCM with a reduction in the deposition rate from 15 to 3 nm/min. At successively higher Ar flows, the hysteresis effect was diminished until at 100 SCCM Ar flow, there was no effect. However, the deposition rate decreased continuously to approximately 6 nm/min. The Si<sub>3</sub>N<sub>4</sub> films had reached their desired composition as  $f_r = 25$  SCCM. Although  $S$  was increased by a factor of 20, the value of  $f_r$  required to make Si<sub>3</sub>N<sub>4</sub> only increased by a factor of 3. They also showed that the deposition rate depended only on  $P - P_o$  and not on the argon flow.

The effect of pumping speed on the shape of the pressure hysteresis curve was also explored by Kadlec et al (6) for the reactive sputtering of TiN. In their diode system, the critical pumping speed for N<sub>2</sub> was about 200 l/s: for higher values no hysteresis was observed. Danroc et al (7) reported the change in shape of the hysteresis curve during the reactive sputtering of TiN, as a function of both the pumping speed and the location of the N<sub>2</sub> inlet. The width of the hysteresis curve decreased as the nitrogen inlet was moved closer to the pump throat. Since much of the N<sub>2</sub> passes directly to the pump, this is equivalent to either reducing the effective flow of nitrogen or else reducing the gettering rate by the sputtered Ti.

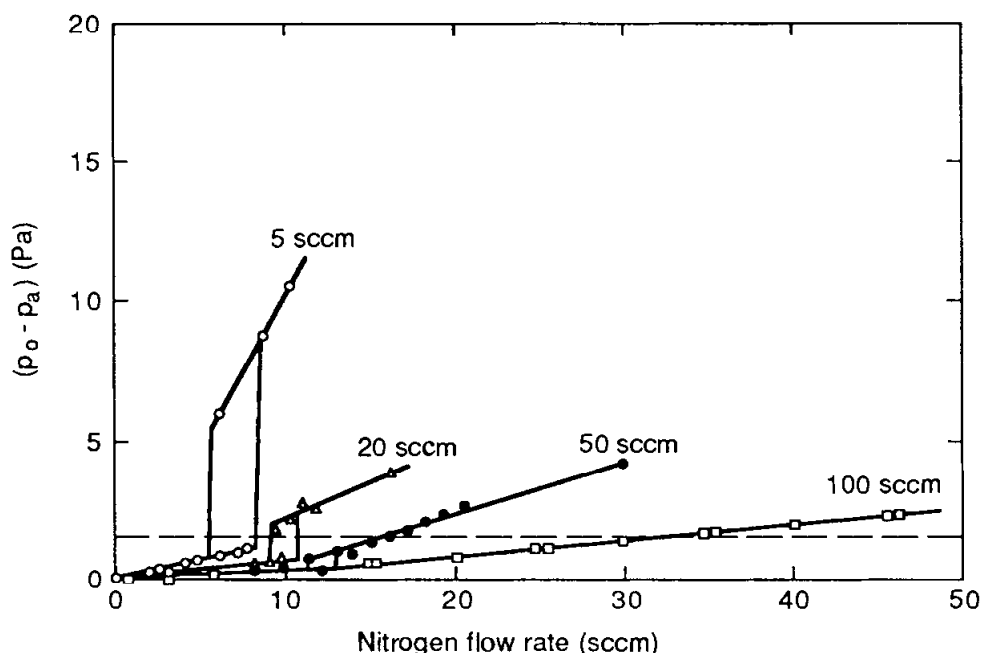


**Figure 2:** Variation of pressure with N<sub>2</sub> flow rate for different flow rates of Ar during rf planar magnetron sputtering of Si (5). The dashed line shows the value of  $(P_o - P_a)$  at which the films were Si<sub>3</sub>N<sub>4</sub>.

As might be expected, the film deposition rate also shows a hysteresis-like effect as a function of the flow of the reactive gas. The pressure-flow hysteresis curve is shown in Fig. 3(a) for the case of reactive sputtering of Ti in Ar/O<sub>2</sub> mixtures. The effect on the sputtering yield is shown in Fig. 3(c), and the effect on the net deposition rate in Fig. 3(b). This type of behavior is characteristic of most reactive sputter deposition systems.

In addition, due to the change in the surface composition of the target in states A and B, there may often be a change in the discharge voltage and current at constant discharge power. In many cases, such as reactively sputtering Al in Ar/O<sub>2</sub>, the voltage drops significantly going from state A to state B. This may be due to changes in the secondary electron coefficient of the cathode. For example, a thin aluminum-oxide layer on the cathode may have a significantly larger secondary electronic coefficient than pure Al. The additional electrons can cause additional ionization in the plasma, resulting in a higher ion flux to the cathode, and hence a lower discharge voltage at constant power. For the Al - O<sub>2</sub> system, the voltage changes can be as high as several hundred volts. However, other systems have much smaller voltage shifts, and some systems, such as Ti - O<sub>2</sub> have been reported to increase, rather than decrease the discharge voltage upon transition from state A to state B. This may be indicative of negative ion effects, which will be discussed below.

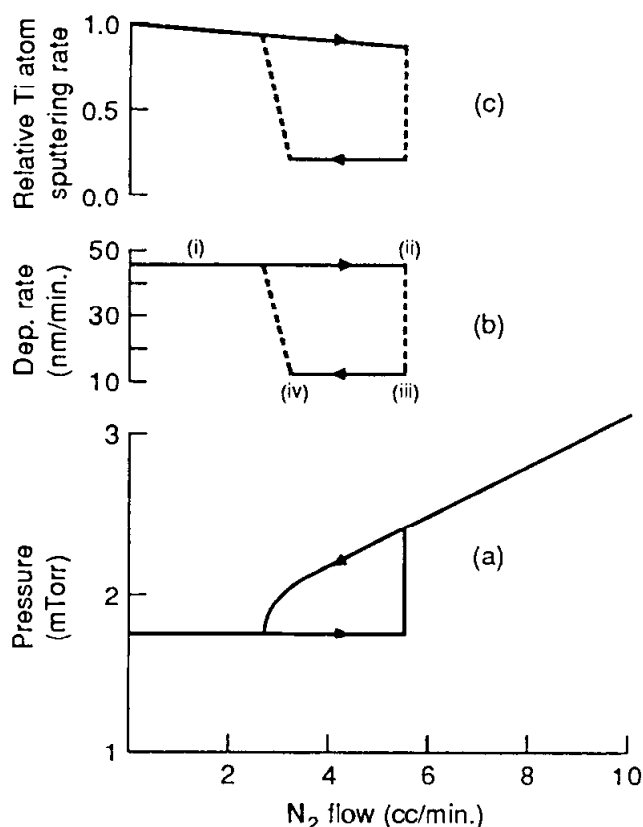


**Figure 3:** Changes in (a) total pressure, (b) deposition rate and (c) relative Ti sputtering rate for a 5x8 inch planar magnetron Ti target sputtered in Ar/N<sub>2</sub> mixtures at a constant power of 800W.

### 9.3 REACTION KINETICS: MODELS

The main cause of the hysteresis effect has been attributed to the formation of a compound layer on the surface of the sputtering target or cathode. The getter-pumping effect of the freshly-deposited metal films is reduced by the reduction in metal atom sputtering rate, causing the partial pressure of the reactive species (and the total pressure of the chamber) to increase. Conversion back to the metal mode (state A) occurs only when the flow of reactive gas is reduced to the point where it can no longer maintain the compound layer, which is being continuously sputtered. However, a detailed model of the reaction kinetics is more difficult because all the parameters interact and their behavior in the sputtering environment is not well known.

The first attempt at a model describing this basic phenomena was proposed by Heller (8), addressing the case of rf etching in oxygen. In this model, an equilibrium oxide thickness resulted from a balance between the sputtering rate and the target oxidation rate, assumed to be logarithmic. The basic premise was that these two rates were independent, which is not generally true. Goranchev, et al.(9) introduced the concept of a partial surface coverage,  $\Theta$ , of the target by oxide and pointed out that  $\Theta$  depended on both the gas flow and the sputtering power. However, this dependence is even more complex, as the sticking coefficient,  $\eta$  for the reactive gas can vary rapidly with  $\Theta$ . Harra and Haywood (10) reported changes in the sticking coefficient  $\eta$  of two orders of magnitude for the case of reactive sputtering of Ti in  $N_2$  as a function of  $N_2$ /Ti flux ratio. Such rapid changes mean there may be a substantial gradient in  $\eta$  and  $\Theta$  over a sputtering target, as was shown by Schiller et al (11) for the case of magnetron sputtering.

A number of models describing aspects of the transition from state A to state B have been introduced (8-17). More recent models have been developed by Berg et al. (18), by Larsson et al (19) and by Penfold (20). These models use the consumption rate due to the gettering effect as well as exhaustion by the pump. In the first case, the system-wide balance of atoms can be explicitly solved by 8 coupled equations, and complex hysteresis phenomena modeled. However, each of these models require assumptions about variations in sputter yields under different conditions and variations in  $\Theta$  on different surfaces. By making suitable assumptions, the hysteresis curve behavior is predicted for reactive sputtering of Ti in  $N_2$ . These are steady-state models, so that a series of operating characteristics are developed and the path between them developed as a function of the  $N_2$  flow rate. Although this type of approach should apply to any reactive sputtering system, evaluation of the operating characteristics still requires assumptions about the values of the parameters in the models. In the  $N_2$  reactive sputtering case, these appear to change fairly slowly with increased nitrogen levels. This does not appear to be the case for  $O_2$ . This means that various feedback-control systems (to be discussed below) may be more successful in nitrogen-based systems than in oxygen-based systems.

### 9.4 SPUTTERED SPECIES

#### 9.4.1 Cluster Emission

In the metallic cathode mode (state A), the sputtered atoms consist mainly of individual, neutral atoms. However, some clusters may be ejected, both as neutral and charged species (21). The bonding between the metal atoms is sufficiently strong that some fraction of the bonds may hold together (i.e. form a cluster) during the sputtering



process. The bonding between a metal atom and a reactive gas atom, however, can be stronger than the bonds between the metal atoms, and as a result a cluster of metal and reactive gas atoms may result from the sputtering process. Of course, individual metal and reactive gas atoms will also be sputtered and a variety of charge states may occur.

By combining quartz micro-balance measurements of the deposition rate and atomic absorption and emission analysis of Al, Stirling and Westwood (22) showed that clusters must be responsible for the majority of the depositing flux for the reactive sputtering of Al in  $O_2$ . This conclusion was reached by the observation that the spectroscopic signal for Al became undetectable upon the transition from state A to state B. Later studies (23,24) found a similar effect when a  $NiFe_2O_4$  target was sputtered in  $Ar/O_2$ . While Ni and Fe atoms were still sputtered, they accounted for less than 10% of the depositing atoms.

A similar conclusion was reached by Betz and Husinsky (25) using Laser Induced Fluorescence (LIF) during the sputtering of Cr by  $Ar^+$  in a background pressure of oxygen. Upon undergoing the transition from the metallic to the compound cathode form, the deposition rate decreased by a factor of 4, while the Cr atom LIF signal decreased by a factor of 130. Since less than 25% of the deposited film could be accounted for by Cr atoms alone, they concluded that  $Cr_xO_y$  clusters were being formed.

To obtain stoichiometric or fully reacted films by sputtering a bulk compound target, it is usually necessary to add additional reactive gas to the chamber. In the case of oxides, there can be sufficient oxygen present in the background water vapor in the chamber, but this is likely to cause non-reproducible results. Since a reactive gas must usually be added in these cases, either a compound, bulk target or a metallic target may be used. Control of the gas supply for the reactive species will be required in either case, although the flow rates in the metallic case will be significantly higher. There are, of course, advantages to operating in the metallic mode. For example, by controlling the gas species and flow, the same Al target may be used to deposit Al,  $Al_2O_3$  and AlN films. Metal targets are generally easier to fabricate at high purity, and they usually have better thermal conductivity than the compound. They are thus easier to cool, allowing higher power levels, and hence higher deposition rates. Finally, metallic targets can be operated in either a dc or rf mode, whereas the compound targets often require rf.

#### 9.4.2 Negative Ion Emission

During the sputtering process at the cathode surface, there is a probability that some of the sputtered species will be emitted as ions. Due to the high positive potential of the sheath, positive ions formed at the cathode surface will most likely remain on the surface. Negative ions, however, will be accelerated by the high field ( $\approx 5000V/cm$ ) and enter the plasma. In ion beam sputtering systems, to be discussed later, the electric field is very weak ( $\approx 5V/cm$ ) and the negative ions do not gain more than a few eV of energy. Harper et al (26) showed that in a plasma sputtering case, the negative ions would gain the full discharge voltage crossing the sheath, and hence have long mean free paths. (The cross section for collision decreases as the particle energy increases.) It was also suggested that due to the low electron affinity (1-2 eV), the extra electron on the negative ion may be quickly stripped upon entering the plasma, which typically has an electron temperature of several eV.

A result of the formation of negative ions during sputtering is sputtering of substrate. This was observed by Hanak (27) for  $F^-$  ions from a  $MgF_2$  target, and also by Cuomo et al. (28) for the sputtering of alloy targets of Au and rare earth metals. In the latter case, a model was proposed that treats the target like an ionic solid. To remove an electron from the first target, A, requires an energy equal to the ionization potential,  $E_i$ . To form a negative ion,  $B^-$ , energy is gained equal to the electron affinity of B,  $\chi$ . Thus, the total energy required,  $E_i - \chi$ , is a measure of the difficulty of transferring an electron from A to B. If this value was less than 3.4 eV,  $Au^-$  ion were observed in sufficient quantities to etch the substrate.

Later work by Kester and Messier (29) characterized a large number of oxide targets (Table 1), and found negative ion emission even though the energy difference was greater than the empirical 3.4 eV described above. Other studies have shown that the negative ions formed have energies equal to the target potential (30).

Two principle effects can be present due to the formation of large numbers of negative ions during sputtering. The first is a significant change in the net deposition rate. The sputtering caused by the negative, (now neutralized) ions causes an effective reduction in the film deposition rate, as compared to the case without negative ion formation. Secondly, the composition of the deposited film may be dramatically altered as the lower sputter yield components are preferentially sputtered from the depositing film.

Significant changes in composition have been observed in the high  $T_c$  oxide films when deposited by sputtering. Films deposited using  $MBa_2Cu_3O_{6-7}$  where M is a rare earth such as Y, Yb Er, etc., tend to be deficient in both Cu and often in the rare earth component due to negative ion sputtering (31,32). This is not surprising, upon viewing Table 1, as the yield of  $O^-$  ions can be quite large. A variety of solutions have been identified to avoid this problem. Lee et al. (33) mounted two planar magnetron targets opposite to each other and mounted the samples off to one side. This solution has been used in various geometrical forms by others. It was first used to improve ZnO films (34). Clarke (35) has used an S-gun composed of elemental tile segments oriented in conical array. The separation of the compounds, as well as the geometrical dispersion of the negative ions has allowed the deposition of good films. Other approaches forgo the use of oxide targets completely, sputtering from multiple targets of elemental, or simple alloy composition (36).

The occurrence of negative ions during sputtering must be considered when any electronegative species, such as O or F, is present either in the target or the reactive gas. In addition, the presence of O in the residual gas of the chamber, perhaps in the form of OH, can lead to negative ion formation which can change over time as the system is conditioned. Tominaga et al (37) documented the effects of energetic particle bombardment during the sputtering of Al in Ar/ $N_2$  mixtures to form AlN. The film structure was different in regions opposite the magnetron plasma ring in front of the target. Using a time-of-flight method, they concluded that the energetic species were NO and OH, due to residual water vapor in the chamber. A similar conclusion was reached during the sputtering of AlCu in Ar, where significant changes in the morphology of the films opposite the etch track were traced to negative ion formation due to background gases (38).

**Table 1:** Observed effects of energetic particle bombardment resulting from sputtered negative ions ( $O^-$  in all cases except for  $NO^-$  and  $OH^-$  in ref (d); s = strong effect; w = weak effect, p = possible effect. The lowest values of  $E_i - \chi$  are given.

Material	$E_i - \chi$ (eV)	Effects	Ref.
BaTiO <sub>3</sub>	3.74	s	29,30
LiNbO <sub>3</sub>	3.92	s	29,30
SrTiO <sub>3</sub>	4.23	s	29,30
SrZrO <sub>3</sub>	4.23	s	29,30
Sr <sub>2</sub> Nb <sub>2</sub> O <sub>7</sub>	4.23	s	29,30
CaTiO <sub>3</sub>	4.65	s	29,30
Bi <sub>4</sub> Ti <sub>3</sub> O <sub>12</sub>	5.35	s	29,30
TiO <sub>2</sub>	5.35	w	29,30
ZrO <sub>2</sub>	5.37	w	29,30
SnO <sub>2</sub>	5.88	p	29,30
PbO	5.94	p	29,30
PbTiO <sub>3</sub>	5.94	s	29,30
PbZrO <sub>3</sub>	5.94	p	29,30
Ta <sub>2</sub> O <sub>5</sub>	6.41	s	29,30
WO <sub>3</sub>	6.51	w	29,30
ZnO		s	30
YBa <sub>2</sub> Cu <sub>3</sub> O <sub>6</sub>		s	32,33
AlN( +H <sub>2</sub> O)		s	37

Clearly, the types and energies of the species reaching the substrate during reactive sputter deposition in a plasma may differ from the simple sputtering model. In that case, individual atoms leave the target with a few eV of kinetic energy and lose much of this energy through gas phase collisions prior to deposition. Highly energetic atoms and molecules may be present due to both negative ion formation or the reflection and neutralization of incident ions at the cathode surface. Clusters of atoms may arrive at the substrate, and these clusters may be positively charged by Penning ionization. In diode and triode systems, energetic electrons will also be present. This will generally not be the case with magnetrons due to the magnetic fields. However, the so-called "unbalanced" magnetrons (39), as well as small, poorly confined targets, will have a loss path for energetic secondary electrons from the cathode surface.

## 9.5 PLASMA-BASED SPUTTERING SYSTEMS

### 9.5.1 Diode Systems

In a diode sputtering system, both the target and the substrate are immersed in the plasma. Ions are extracted from the plasma for sputtering of the target and the pressure is usually high enough (several Pa) that the sputtered atoms are effectively thermalized before reaching the substrate. However, discharge voltages are typically high, 1-3 keV, so that energetic, reflected neutrals, negative ions, and especially secondary electrons may bombard the substrate. The electron current density at the substrate may be as high as

10% of the ion current density at the target. The ion current density is limited by space-charge effects to about  $1\text{mA}/\text{cm}^2$ . The power density at the substrate may be as high as  $1\text{ W}/\text{cm}^2$  and may produce substrate temperatures of several hundred degrees C.

Both rf and dc diodes are used for sputtering, but dc is restricted to sufficiently conducting targets. As pointed out by Maissel (40), the diode discharge provides a very reactive environment. Although the percentage of ionization is low ( $\approx 0.1\%$ ), the flux of excited species to the surface may be quite high relative to the sputtered flux. This is due to the generally low sputtering rates caused by the low ion currents.

The basic diode sputtering arrangement is shown in Fig. 4(a). The two electrodes of approximately equal area are separated by 5 to 10 cm. A minimum pressure is required to maintain a glow discharge in the space between them. This is typically 1 Pa, but much higher pressures may be necessary to attain a current density of  $1\text{mA}/\text{cm}^2$ . The substrate is usually placed on one of the electrodes, but other positions have also been used to avoid the effects of negative ion bombardment.

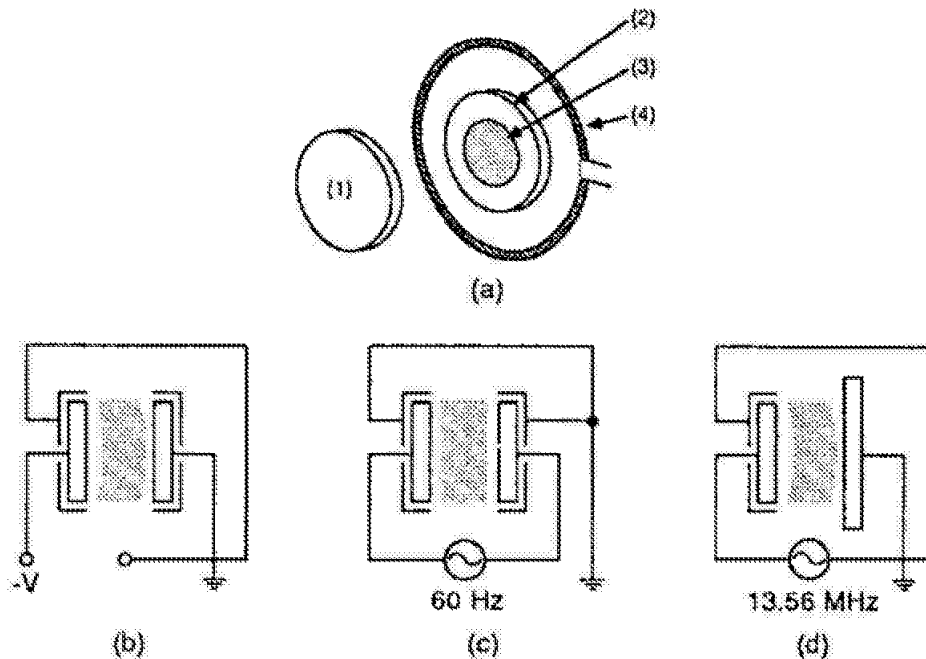


**Figure 4:** General schematic of (a) diode target-substrate orientation, (b) dc-diode electrical circuit, (c) ac sputtering, and (d) rf-diode sputtering at 13.56 MHz.

There are generally three modes of powering a diode discharge. In dc sputtering (Fig. 4(b)), the target is connected to a negative potential and the other electrode is grounded. In this case, the other electrode also functions as the anode. The discharge is established with the applied potential dropped across the dark space in front of the target, which has a thickness of 1-2 cm. Ions accelerated across the dark space sputter the target. However,

due to charge exchange collisions, the average ion energy is typically about 800 eV, even though the target potential may be as high as 5 keV.

In ac sputtering (Fig. 4(c)), a 60 Hz supply is connected between the two electrodes and both are effectively used as targets. Either the same or different materials may be used for the two targets. However, in general this type of system has been used infrequently.

In rf sputtering (Fig. 4(d)), a high frequency generator (usually 13.56 MHz) is connected between the electrodes. The rf voltage is  $V_0 \cos \omega t$  and an average negative potential is developed on the electrodes because of a difference on ion and electron mobilities (40). If the system is symmetric, as in Fig. 4(c), a potential  $-V_0$  is developed on both electrodes. By increasing the effective capacitance of the non-powered electrode (substrate), its potential can be reduced to much lower values, typically -10 to -20 V. Thus, the substrate is usually subjected to ion bombardment. The energy of the ion bombardment is typically the difference between the plasma potential and the floating potential of the substrate electrode. In cases with symmetric electrodes, the plasma potential can be quite high. If the substrate electrode is grounded, along with the chamber walls, the plasma potential can be quite low. Although a net potential of  $-V_0$  is developed on the target, there is no net current flow. Therefore, the target may be either conducting or insulating. This allows a great flexibility in target choice, and has greatly expanded the potential of reactive sputter deposition.

In diode sputtering, the substrate is immersed in the plasma, and is thus exposed to all the species listed in Table 2. Since electrons are accelerated across the dark space, they reach the substrate with high energies. Since ions (eg.  $N_2^+$ ) will reach the substrate with several eV, and excited neutral species may also be present, it is not surprising that the chemical reactivity is high in diode systems.

This reactivity, of course, is desirable in depositing compounds but may be responsible for non-uniform composition of the films across the substrate electrode. For uniform film thickness, the sample is typically located directly in the center of the substrate electrode. However, the reactive gas is usually introduced from the perimeter through some sort of manifold. At a pressure greater than 1 Pa, the mean free path of the reactive gas atoms is less than 1 cm and the reactive gas will then have a high probability of hitting one of the electrode surfaces before it reaches the sample locations. If the sticking coefficient is near unity, due perhaps to the high reactivity of the deposited film and the environment, the gas will be trapped prior to reaching the sample location. For example, if  $N_2$  is added while a Ta target is being sputtered in Ar (41,42), a Ta-N film is deposited. Gettering of the nitrogen reduces the flux towards the center of the substrate, resulting in a radial composition gradient. This gradient will be greatest for the more reactive gases and will also depend strongly on target size and orientation.

In nearly all cases of compound formation by reactive diode sputtering, the target is in state B, the compound state. For most materials, both metallic and compound targets have been used. For some materials, such as  $BaTiO_3$  (43),  $LiNbO_3$  (44) and lead titanate (45), as well as the superconducting oxides, compound targets have generally been used.

**Table 2:** Approximate flux and energy of particles reaching the substrate during sputtering of an oxidized layer on a Zn target in Ar/O<sub>2</sub> discharge (i.e. state B). Magnetron sputtering at 1 Pa is assumed. For diode sputtering, electrons have energy equal to the target voltage and the value for the relative flux is 0.1.

Species	Source	Approximate		Effect of Pressure	
		Relative flux	Energy(eV)	increase on flux	increase on energy
Zn	sp	1	1	↓	↓
O	sp	1	1	↓	↓
O	sp O <sup>-</sup>	0.1	500	↓	↓
ZnO	sp	0.3	1	↓	↓
ZnO <sup>+</sup>	sp+Penning	0.05	1	↓	-
O <sup>-</sup>	sp	0.05	500	↓	↓
Ar	gas	1000	0.03	↑	-
Ar	refl	0.01	100	↓	↓
O <sub>2</sub>	gas	1000	0.03	↑	-
O	refl	0.01	100	↓	↓
Ar <sup>+</sup>	plasma	10	1	↑	-
O <sub>2</sub> <sup>+</sup>	plasma	10	1	↑	-
e	plasma	10	3	↑	-
e	sp	?	500	↓	↓

### 9.5.2 Magnetron Systems

The use of magnetron sputtering systems has expanded greatly since about 1970. The flexible geometry inherent in the design has distinct advantages for reactive sputtering and special modifications have made it possible to reactively deposit thin films at high rates. The basic physical principles of magnetron operation have been discussed in an earlier chapter (Chap. 6) and also have been the subject of numerous papers (46-51). The planar magnetron, both in circular and rectangular geometry, has been the most widely used design for reactive sputtering.

A simple schematic of a planar magnetron is shown in Fig. 5. Although it appears similar to a diode (Fig. 4), the arrangement of the magnetic field makes the discharge operation quite different. In general, a magnetron is arranged with a magnetic field oriented parallel to the cathode surface, such that the path of electrons undergoing ExB drifts is a closed loop. The plasma density is highest in this drift loop due to the trapping of energetic secondary electrons and the subsequent ionization of the background gas atoms. The proximity of the dense plasma to the target electrode allows large ion currents (many amperes) at relatively modest voltages (200-800V) and pressures of 1 Pa and below.

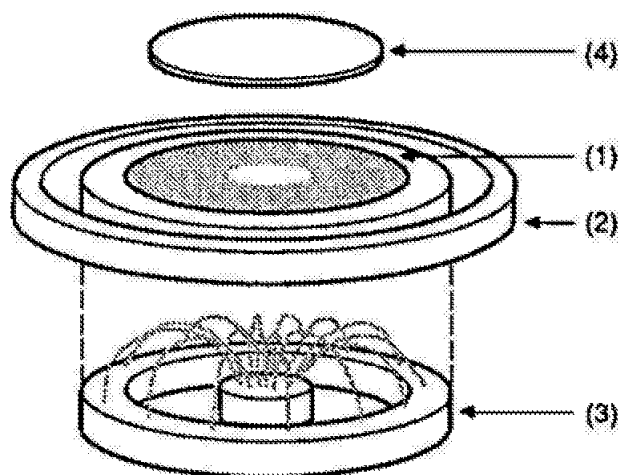


**Figure 5:** Schematic of circular planar magnetron. (1) target, (2) anode (3) magnet providing a field of  $\approx 0.03$  T in front of the target with field lines parallel to the target surface. In operation, the magnetic array is typically paced immediately behind the target. (4) substrate.

As is evident in Fig. 5, the magnetic field on some magnetrons is not strictly parallel to the cathode surface at all locations. In particular, areas near the cathode center and perimeter have a field component perpendicular to the cathode surface. This allows secondary electrons emitted from the cathode surface to intercept the substrate plane in some locations. However, these same regions that have a perpendicular magnetic field component also are characterized by significantly lower plasma density, which results in a reduction in the electron bombardment, as compared to the conventional diode case. The highest ion density occurs at the region of the cathode where the magnetic field is parallel to the surface. These areas are also subject to the most ion bombardments, and the sputtering rate, therefore, is non-uniform across the target surface. The rate is greatest just under the ExB drift path, and is lowest in the edge and central regions of the cathode. In many cases, these regions can experience a net deposition during the sputtering of the cathode (Chap 6).

When a reactive gas (eg.  $N_2$ ) is introduced to the chamber during inert gas sputtering of the cathode, the gettering effects discussed earlier occur and reactive gas (N) atoms must also be sputtered from the cathode surface. The sputter yield of the compound (i.e. reacted) surface is lower than that of the pure metal surface. Where the rate is low, the coverage of N atoms will increase, further decreasing the sputter rate of the target. In the case of a Ti target sputtered in  $Ar/O_2$ , Schiller et al (52) found that the width of the eroded annulus on the target decreases from 30mm to 18 mm as the fraction of oxygen was increased to the values where full oxidation of the target occurred (state B). (Fig. 7). The very low sputter yield of  $TiO_2$  accentuates the non-uniform sputtering rate intrinsic to magnetron sputtering. In the region of lowest rate, the O coverage becomes sufficient to form  $TiO_2$  and the sputtering rate decreases there. However, the rate is high enough in the

region of highest current density to maintain a Ti surface. Thus part of the surface is in state A, while other parts have made the transition to state B. As the flow of reactive gas increases, the whole surface will eventually change to state B, and the total deposition rate falls to a value typical of a  $\text{TiO}_2$  surface layer.

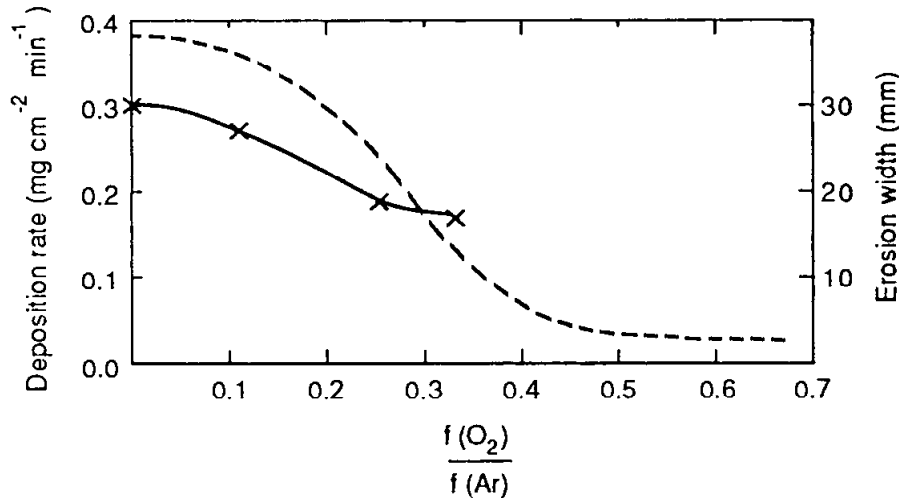


**Figure 6:** Variation of target erosion width (solid line) and mass deposition rate (dashed line) as a function of  $\text{O}_2$  to Ar flow ratio during sputtering of a Ti target (130 mm dia.) at 5 kW. The substrate to target distance was 50 mm. (52).

This transition often results in large changes in the discharge characteristics, as noted earlier. Schiller et al (52) observed a maximum in the voltage as the transition to state B occurred. The result shown in Fig. 7 appears to be more typical: the target voltage required to maintain a constant dc current of 2A decreased from 380 to 260V when the  $\text{Al}_2\text{O}_3$  layer formed on the Al target (53). The decrease is due to the higher secondary electron coefficient,  $\gamma_1$  for  $\text{Al}_2\text{O}_3$  than Al. Only when the  $\text{Al}_2\text{O}_3$  is removed from the target, by reducing the oxygen flow, does the voltage again increase.

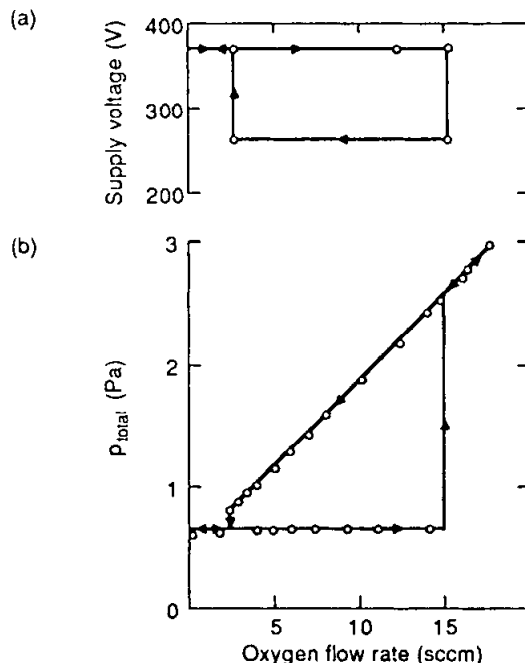


**Figure 7:** (a) voltage required to maintain a dc current of 2A on a 5x8 inch Al planar magnetron target as a function of  $\text{O}_2$  flow rate;  $f(\text{Ar}) = 5$  SCCM. (b) Total pressure change for a constant dc power of 560W. (from ref. 53).



If the compound which forms on the target surface is a conductor, rather than an insulator, the value of  $\gamma_i$  may not change significantly. However, there may still be a change in the discharge characteristics due to the change in both pressure, gas composition and gas rarefaction. Noel et al (54) observed an increase in target voltage for a Ti target as the flow of  $n_2$  increased:  $V_T$  was 40 V higher for the TiN layer than for the Ti target for a constant discharge current of 2 A.

The large, uniform sputtering source in a cylindrical magnetron (see Chap. 6) is not appropriate for doping by reactive sputtering unless the gas can be introduced fairly uniformly over the deposition area. Otherwise, non-uniformity in the film composition must result, especially at high sputtering rates. This is similar to the case of diode sputtering discussed earlier, where substantial doping gradients can result from the strong gettering effects. The magnitude of the effect is enhanced at high discharge current values. The planar magnetron is actually better suited to this type of reactive sputtering (i.e. state A) because the gas can be introduced around the periphery of the target, near the anode or substrate, and the sputtering annulus (etch track) can be quite narrow (Fig. 6). Of course, the gas could also be introduced through the center of the target, where no sputtering takes place. In the sputter-gun arrangement, the anode is located in the center of the target, making the introduction of gas there much easier.

The high values of discharge current possible in magnetrons may not be useful in depositing high resistivity, compound films by reactive sputtering. Arcing is often observed in these cases and this can cause defects in the films and make process control almost impossible. Thornton noted (55) that serious arcing occurred when a Cd cylindrical target was sputtering in Ar/H<sub>2</sub>S even at very low discharge currents (0.2 mA/cm<sup>2</sup>). The arcs contain high electron currents and propagate under the influence of the magnetic field. Este and Westwood (56) observed both pits and Al particles, approximately 1  $\mu$ m in size in Al<sub>2</sub>O<sub>3</sub> films deposited under arcing conditions. A possible cause of these arcs is the rapid accumulation of charge on a small area of dielectric on the target surface. The subsequent breakdown, somewhat like the discharge of a capacitor, dissipates the energy on the ejection of a particle. At a discharge current density of 0.1 A/cm<sup>2</sup>, the 1  $\mu$ m diameter area could receive a charge sufficient to cause the breakdown of the dielectric layer in less than 10 ns.

To avoid, or at least minimize arcing, it is common to use rf, commonly at 13.56 MHz, to power the sputtering cathode, particularly for cathodes which have a high resistivity, such as dielectrics. Thornton (55) argued that the magnetron principle is basically a dc concept and should be much less effective in rf operation. Much like diode sputtering, when powered at rf frequencies, the magnetron cathode develops a negative bias potential on the order of 1/2 the applied peak-to-peak voltage. This is slightly inconsistent with calculations (57) which suggest that the mobility of the electron across field lines should be smaller than the ion mobility. This would result in a positive bias at the cathode. The presence of a negative bias may be indicative of turbulent, Bohm-like transport of the electrons (58), which results in effectively higher mobilities for the electrons than the classical predictions.

Thornton operated both cylindrical and planar magnetrons with Al<sub>2</sub>O<sub>3</sub> targets at 1.8 MHz in Ar and measured the self bias voltage,  $V_{sb}$ , as a function of the rf voltage amplitude  $V_o$ , for different configurations (55). He also measured the discharge current,  $I$  and derived values of  $n$  in the expression  $I = k V_o^n$ . The values of  $V_{sb}/V_o$  and  $n$  are

given in Table 3, and the configurations are shown in Fig. 8. For the usual single-ended operation (Figs. 8(a), (c)), the rf is connected between the target and the chamber, which is itself grounded. This is equivalent to the diode case in Fig. 4(d). The values of  $n$  were low in both cases but  $V_{sb}/V_o$  was 1 in the planar magnetron case whereas it was 0.1 in the cylindrical case. The double ended arrangement (Fig. 8(b)) gave the highest value of  $n$ , provided that the magnetic traps for the two targets were not common. This is the only report in the literature where the current was measured in an rf system. Usually only the power and the various voltages are reported.

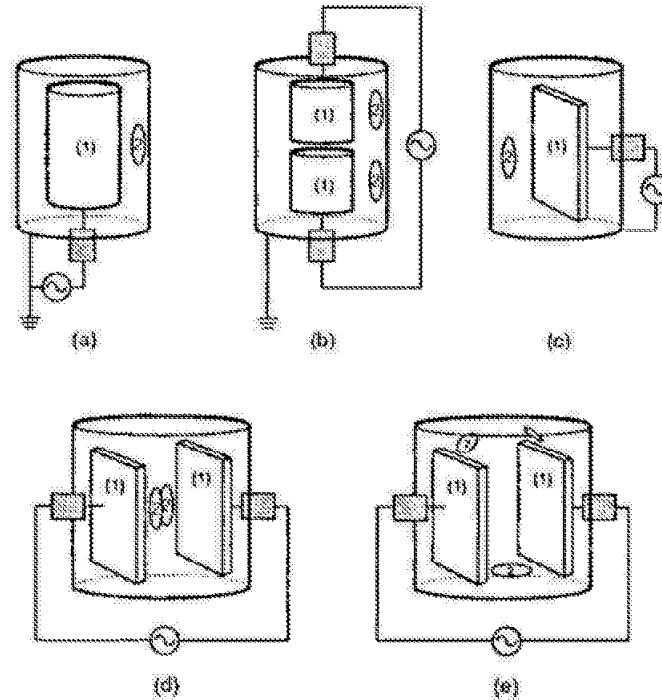


**Figure 8:** Configurations of magnetrons using rf power for sputtering. (1) targets, (2) substrates.

**Table 3:** Values of self bias,  $V_{sb}$  and  $n$  in the expression for the discharge current  $I_{rms} = kV^n$  for the magnetron configurations in Fig. 8 at 1.8 MHz. (from ref. 55)

Configuration	$V_o$ (volts)	$I_{rms}$ (Amps)	$V_{sb}/V_o$	$n$
(a)	300	1	0.1-0.7*	2.2
	600	5		
(b)	400	2		4.5
	550	10		
(c)	1200	1	1	2
	1800	2		

\* B decreased from 0.02 to 0.001

Maniv and Westwood (59) also found  $V_{sb}/V_o$  to be 1 in a planar magnetron. The difference between the cylindrical and planar magnetrons may be due to the magnetic traps. In the cylindrical case, the B field is parallel to the target surface at all points on the surface. In the planar case, the B field intercepts the cathode at the inner and outer edges of the etch track. Here, the electron velocity normal to the surface is not reduced by the B field so that electrons can rapidly follow the rf field, just as in the diode case.

It has been reported that in the rf case, only 50% of the power output from the rf generator resulted in sputtering of the target (59). Este and Westwood (60) measured both the deposition rate and the target power dissipation in a system with two planar magnetrons run in a double ended mode (Fig. 8(d)) with the substrate holder placed between them. The total deposition rate was the sum of the rates on the substrates placed in front of the two targets. For Al targets in noble gases, they found that the deposition rate,  $R_f$  normalized to the rate,  $R_o$  for dc sputtering decreased as the frequency increased beyond approximately 30 kHz (Fig. 9). The same frequency dependence was obtained for the deposition of AlN in a  $N_2$  ambient. Due to arcing, no value could be obtained for  $R_o$  when the high resistivity AlN formed on the target surface. For all frequencies,  $R_f$  was proportional to the total power dissipated in the targets, as measured calorimetrically. Thus, the decrease in  $R_f$  was a result of a decrease in the power actually utilized for sputtering. However, they were unable to determine how the rest of the applied power was dissipated in the system. Heating of the matching networks did not appear to account for more than 20% of the discrepancy.

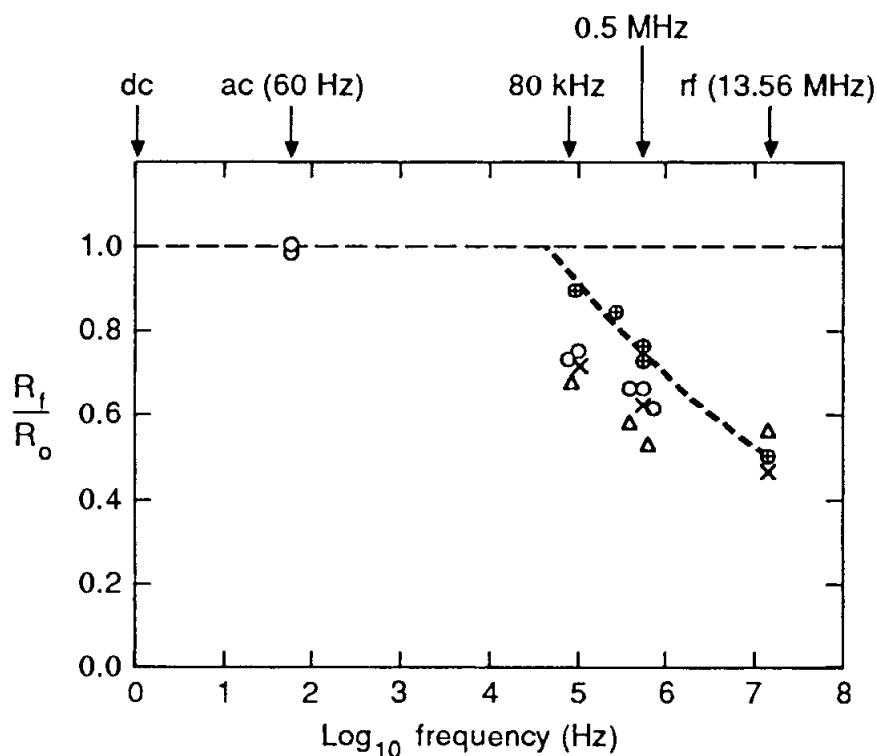


**Figure 9:** Variation with power supply frequency of the relative sputtering rates from the Al targets in Ar (O), Kr (x) and  $N_2$  (⊕) discharges at 0.3 Pa and in Ne (Δ) at 0.6 Pa. The  $N_2$  values are plotted on the assumption that the 13.56 MHz value is 0.5. From ref. 60).

### 9.5.3 Modified Magnetron Systems

If reactive sputter deposition of compounds can be carried out without the formations of an insulating layer on the target surface, it would not be necessary to use rf power supplies and the effective deposition rate would also be greatly increased. To do this, the target must remain in state A, while the reaction which would convert it to state B occurs at the substrate to form the desired compound. There are basically two means of doing this: in the first case, the flux of reactant gas to the target must be decreased relative to the flux to the substrate, while still maintaining a similar reaction rate. In the second case, the flux of sputtered metal atoms to the substrate must be much lower than the total sputtered flux; i.e., the deposition area must be much greater than the area of the target which is sputtered. Various methods for meeting these conditions were discussed by Schiller et al (11).

In one of these methods, a baffle is introduced between the target and the substrate, with the reactive gas only entering the chamber on the substrate side (61), as shown in Fig. 10. The  $O_2$  flux to the target is reduced by the baffle, and oxygen reacts with the metal deposited on the walls of the apertures in the baffle. They were able to deposit transparent, conducting films by sputtering a  $Cd_2Sn$  alloy target. They also observed the maximum in target voltage reported by Schiller (11). By coupling an rf power of 100W to the substrate holder, they obtained films with a 95% transmittance and a resistivity of  $4.5 \times 10^{-4} \Omega cm$ . Both the power density and self bias voltage were very low for resputtering of the film, but the oxygen discharge around the substrate increased the reaction rate and thus increased the process window.

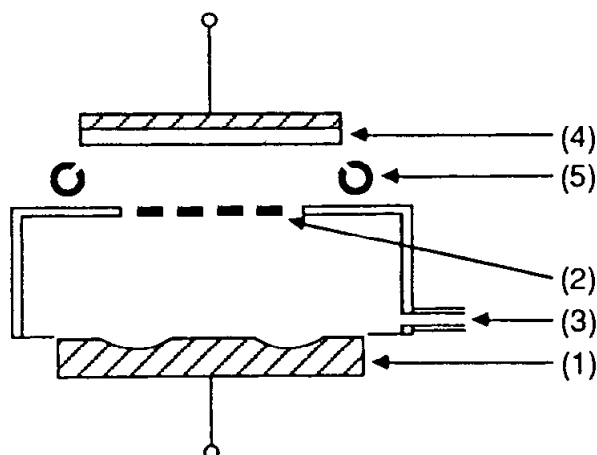


**Figure 10:** Schematic of baffled magnetron sputtering system. (1) target, (2) baffle, (3) Ar inlet, (4) substrate, (5) reactive gas manifold.

Este and Westwood used the baffled magnetron to deposit  $Al_2O_3$  for optical waveguides (56). They investigated the effect of different aperture sizes in the baffle on the value of  $f_{r1}$ , the critical flow rate at which the target converted to state B, and on the deposition rate and uniformity. The results are summarized in Table 4. The critical flow increased only slightly when the apertures in the baffle had a diameter of 4 mm, but it increased 11% when 100W of rf power was coupled to the substrate. Apertures of 2mm diameter increased the critical flow rate by 26%, but then the rf discharge did not make a significant difference. Thus, the smaller apertures gave a larger operating window because the  $O_2$  conductance was lower and more of the sputtered Al flux was deposited on

the aperture walls. However, this was coupled with a 40% decrease in the deposition rate, compared to the large apertures.  $\text{Al}_2\text{O}_3$  films with optical waveguide losses of 1 dB/cm were obtained in all cases, but the flow of oxygen had to be closely monitored.

**Table 4:** Values for  $f_{r1}$  for conversion of the Al target to state B at a dc power level of 1 kW for baffles consisting of apertures in a 5 mm thick plate, with and without rf power coupled to the substrate. The  $\text{Al}_2\text{O}_3$  deposition rate is normalized to the unbaffled rate obtained by rf sputtering the Al target (56).

Aperture dia (mm)	Conductance l/s	rf power (W)	f( $\text{O}_2$ ) sccm	Relative Dep. rate	%flux on aperture walls
none	2	-	8.4	1	-
2	0.15	-	10.6	1.2	58
2	0.15	100	10.7	1.2	58
4	0.3	-	8.5	3	49
4	0.3	100	9.3	3	49

As shown in Table 4, the  $\text{Al}_2\text{O}_3$  deposition rate for the larger apertures was three times the rate obtained for the same total power in an unbaffled magnetron. The higher rate in the baffled case is due, in part, to the 50% efficiency in utilizing the applied rf power discussed above. The optimum arrangement of a baffle will, of course, depend on the reactivity of the system, the specific geometry and the process window required for a particular application. It might seem that an increase in the deposition rate (at constant power) of a factor of 3 would not justify the extra complexity of the baffled magnetrons. However, the use of dc, rather than the rf required in the unbaffled case has a significant advantage: a 20 kW dc power supply and a 2 kW rf power supply are approximately the same size and cost. Jones (62) has recently demonstrated high rate deposition of  $\text{ZrO}_2$ .

Chang and McGarr obtained silicon nitride films using a Si target in a sputter gun configuration (63). As shown in Fig. 11, the Ar enters the system between the central anode and the target face, while the nitrogen is introduced in a manifold in front of the target, directed at the sample surface. For a discharge current of 3A, the target voltage decreased from 800 to 640 V as the nitrogen flow increases from 5 to 9 SCCM, and then remained constant at higher flows. Silicon nitride films were deposited at flows exceeding 9 SCCM with good thickness and refractive index uniformity. The normalized deposition rate for  $\text{Si}_3\text{N}_4$  was  $40 \text{ nm min}^{-1}\text{kW}^{-1}$ . They noted, however, that the placement of the nitrogen manifold was critical.

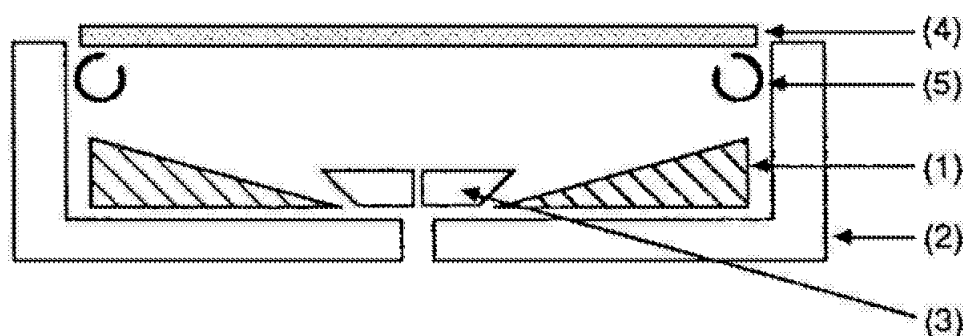


**Figure 11:** Schematic of sputter gun arrangement for reactive sputtering of  $\text{Si}_3\text{N}_4$  (1) Si target, dc powered, (2) magnetic field system for magnetron, (3) anode), (4) close-coupled substrate, and (5)  $\text{N}_2$  dispenser ring (from ref. 63).

In principle, it should be possible to decrease the flux of sputtered atoms to the substrate while maintaining a constant total sputtering flux by increasing the substrate area. Typically, the deposition area is 1-3 times the area of the erosion ring in the magnetrons. Of course, the sputtered atom flux at the substrate could be reduced by increasing the target to substrate separation. However, the deposition rate is decreased and the environment in which the film grows (eg. atom energy) also changes. Moreover, the effective substrate area must be increased to use the sputtered atoms efficiently. For a given substrate size, a number of substrates may be coated in parallel. Generally, the substrate holder must be moved to obtain uniform deposition on each substrate. As shown in Fig. 12(a), a number of substrates can be moved continuously past the target. However, while deposition at substrate position  $S_1$  is due to sputtered atoms travelling almost normal to the target, any deposition at  $S_2$  is due to atoms which have travelled a considerable distance from the target and will, therefore, have much lower energies and a lower flux. Deposition is usually limited to position  $S_1$  by a shield (Fig. 12(b)) to eliminate the low energy flux. The substrates move sequentially past the opening in the shield.

Suppose that this arrangement is used to sputter an Al target in an  $\text{Ar}/\text{O}_2$  mixture with the target in state B (oxidized). If the sputtering rate of Al is  $1\mu\text{m}/\text{min}$  and the rotation rate of the substrate holder is  $1/6\text{ rpm}$ , a 300 nm thick  $\text{Al}/\text{Al}_2\text{O}_3$  film will be deposited on each substrate in one rotation. If the rotation speed is 50 rpm, only a 1 nm thick layer will be deposited per rotation. During the  $5/6$  of the rotation time when no film is being deposited, the layer may react with the  $\text{O}_2$  in the chamber: if there is sufficient  $\text{O}_2$ , the layer may be completely oxidized. Thus the result will be a film consisting of perhaps hundreds of thin layers. This effect is often seen in metal deposition systems, where the oxidation may be due to background water vapor in the system, and the resulting thin film is really a stack of metallic and partially reacted films (64). In general, only the more reactive compounds can be formed with this process. This is usually limited to oxides with heats of formation greater than 9 eV (65), including oxides of Cr, Al, W, Ta and Ti. For nitride formation, bombardment of the growing film by energetic species is required to form compound films. This can be arranged by the addition of an ion beam or a subsidiary discharge.

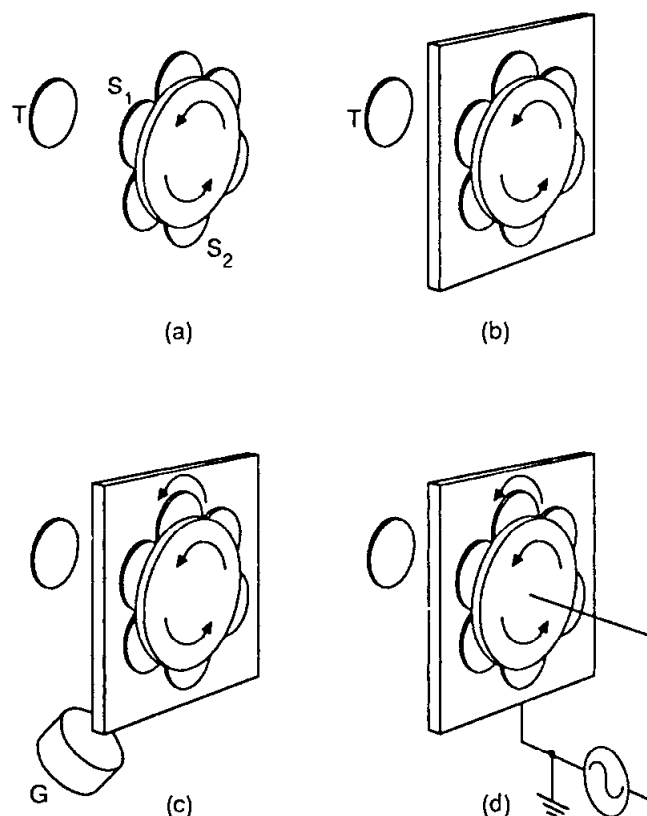


**Figure 12:** Schematic arrangements for deposition on multiple substrates. (a) substrate rotation through whole sputtering flux, (b) deposition limited by shield, (c) increased reactivity on position S<sub>2</sub> by ion bombardment from gun G, (d) increased reactivity produced by discharge between shield and substrate holder.

#### 9.5.4 Monitoring Systems

The control of the reactive gas flow relative to the sputtering rate is clearly very important in determining the operating point for reactive sputtering. In general, it is desirable to operate the target in state A, but as close as possible to the critical flow for transition to state B. If the ratio of the reactive gas flow to discharge power,  $f_r/P$ , increases, the target will convert to state B and the deposition rate may dramatically decrease. If  $f_r/P$  decreases, the film composition could change to a more metal rich mixture, with a consequent change in film properties. As discussed earlier, in many target-gas systems, the response of the magnetron in the reactive gas is not a simple linear function of  $f_r/P$ , and hence the conversion from state A to state B may be rapid and difficult to control. In addition, as the target conditions change, for example due to the erosion of a deeper etch track in the target, the sputtering rate and the sputtered flux distributions for a given power will change, so that the exact nature of the critical reactive gas flow will also change.

In an experimental system, it is relatively easy to do an initial experiment to determine the value of the critical flow at a given sputtering power,  $P$ , and system pressure. The reactive gas flow can then be stopped, and the target will recover to state A. The reactive

gas flow can then be adjusted to just below the critical flow level, and monitored carefully. In manufacturing systems, however, a method of continuously adjusting the operating point to maintain constant deposition rate and film properties is necessary. This involves some means of monitoring any change in the operating point and providing a feedback control to change either the reactive gas flow or the discharge power accordingly. In general, the time response of the power supply is faster than the response of the gas flow controllers.

To monitor the operating point in such a non-linear system requires a sensitive method. If the pressure increases significantly, it will be impossible to recover the operating point without essentially tracing out the hysteresis curves in Fig. 1. This is also clearly unacceptable for the deposition of homogeneous films. The parameters which change rapidly near the critical flow transition are the system pressure and the partial pressure of the reactive gas species, the discharge parameters such as the voltage or current in a dc system or the self-bias voltage in an rf system, and the resultant film properties. An additional, observable change is the emission of light from the plasma, which is indicative of both particle density as well as discharge parameters. All of these parameters have been used as monitors, but their application depends on the particular reaction which is being controlled as well as aspects of the sputtering system.

Affinito and Parsons described the detailed operation of a microprocessor-based control tool for the reactive sputtering of Al in Ar/N<sub>2</sub> (13). The values of chamber pressure, P, and nitrogen partial pressure, p(N<sub>2</sub>), the gas flows, the discharge current and voltage and the optical emission from the Al were all measured. Using the discharge voltage, V<sub>T</sub>, as the experimental variable, they obtained data for several of these parameters (Fig. 13). At low values of V<sub>T</sub>, p(N<sub>2</sub>) was 2 Pa, the discharge current was low and no Al emission was observed. This suggested the target was in state B. When V<sub>T</sub> was increased to 270V, the target converted to state A with a large increase in discharge current, coupled with a strong increase in Al emission and a decrease in p(N<sub>2</sub>). As V<sub>T</sub> increased to 330 V, the current decreased. All points along this apparently negative resistance region were reached through positive resistance steps away from the equilibrium point and back again. These steps had to be much smaller than the width or height of the negative resistance region; otherwise, oscillations developed from which recovery was not possible.

Affinito and Parsons found that they could control the transition from State A to state B in the Al – N<sub>2</sub> case by this feedback control method, but that the same method was not successful when the nitrogen was replaced by oxygen. They developed a model for the change in rate of target coverage caused by a fluctuation in the current (  $\Delta I$  )

$$\Delta\left(\frac{dn_s}{dt}\right) = -\left[\frac{\eta p_r}{I} + \frac{\eta + \eta I}{(1 + \gamma_i)e} \frac{\delta F_i}{\delta p} \frac{\delta p_r}{\delta I}\right] \Delta I \quad (1)$$

where  $n_s$  is the number of reactive gas molecules adsorbed on the target surface,  $p_r$  is the relative gas pressure,  $\eta/p_r$  is a sticking coefficient for chemisorption,  $F_i$  is the fraction of reactive gas ions bombarding the target (eg.  $I(N_2^+)/I$ ) and  $\eta$  is the sticking coefficient for reactive ion species at the target. As discussed above, the meaning of  $p_r$  when the target is in state A is questionable and many of the values of the other parameters are unknown. They proposed that the different behavior of O<sub>2</sub> and N<sub>2</sub> was due to the first term,  $\eta p_r \Delta I / I$  : for molecular N<sub>2</sub> there is no chemisorption ( $\eta = 0$ ), whereas  $\eta$  is definitely



greater than 0 for the case of oxygen. This results in a much faster change in surface coverage for  $O_2$  than  $N_2$ , such that their control system could not respond. The monolayer coverage time for the formation of Al-O compounds at their operating condition was estimated to be 1 ms. The control system in this case would allow only a 10% change in discharge current in that time.

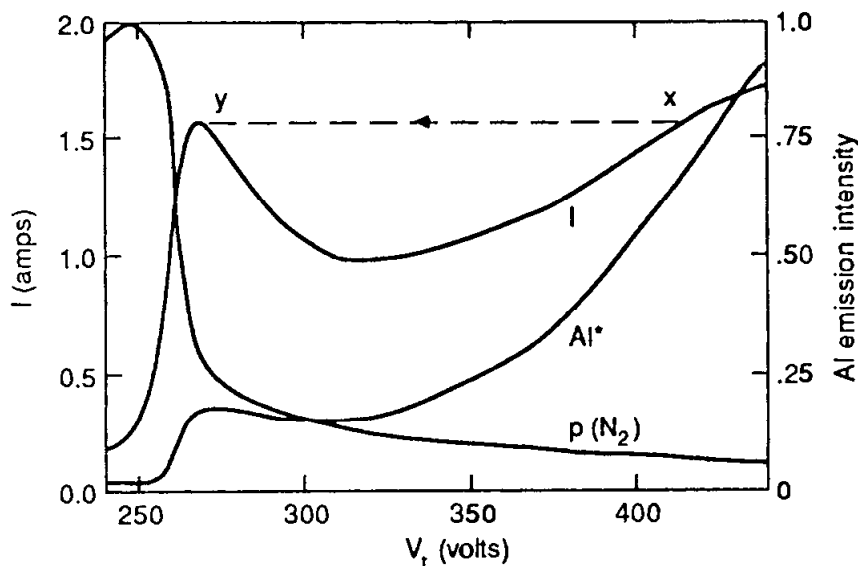


**Figure 13:** Variation of  $I$ ,  $p(N_2)$  and optical emission intensity from excited Al as a function of the voltage on the planar magnetron cathode in Ar/ $N_2$ . The ar flow rate was 1 SCCM and the resulting pressure was 0.93 Pa. The nitrogen flow was 1.5 SCCM. The dashed line from X to Y shows the transition which would occur if  $I$  is the experimental variable (from ref. 13).

Sproul used a residual gas analyzer to monitor  $p(N_2)$  in the production of wear-resistant coatings of TiN, ZrN and HfN (66). Using feedback control from the RGA, he operated continuously at deposition rates within 15% of those for metals in Ar. Because the chamber pressure for sputtering is much higher than for the operation of the RGA, the RGA must be differentially pumped. He later described the advantages of automatic control using a fast feedback loop ( $<0.2$  s) for the deposition of TiN. Hmiel also described an automated system for the deposition of TiN (67). He pointed out that the response time of the control loop depended of the distances between the target, the  $N_2$  inlet and the RGA. When the RGA was too far from the chamber (1 m), the response time was 1.5 s, and stable operation was not obtainable.

Optical emission from the plasma has been successfully used to drive the feedback loop in several cases. In general, these techniques monitor either a reduction in the emission of the metal species or an increase in the emission of the reactive gas species near the critical flow point. The advantage of an optical emission monitor is that it samples from regions where the reaction is actually taking place: there is no need for differentially pumping as in the case of the RGA. This means that the response time can be much faster. A number of authors have reported results with this technique (68-71), and the control hardware is becoming commercially available.

Finally, for transparent conducting films, both the transmittance and the resistivity depend on the operating conditions for the reactive sputtering. Ridge and Howson (72) have reported measurements of indium-tin-oxide on polyester film sheet resistance used as a feedback loop for controlling the discharge. They used a baffled-magnetron device discussed earlier and found an increase in the sheet resistance of a factor of 10x for only a 10% increase in the oxygen flow.

## 9.6 REACTIVE SPUTTER DEPOSITION WITH ION BEAMS

Ion beam systems are, at least conceptually, less complex than plasma-based sputtering systems. Ions are generated in a plasma source located away from the target and are extracted from the source with a given energy and directed at the target with a current density  $J_i$ . Electrons may be mixed with the ions so that no net charge is delivered to the target. This prevents charge build-up, and as such, the insulating targets can be sputtered as easily as conducting targets.

A schematic of an ion beam system is shown in Fig. 14. Kaufman multiple aperture ion sources (see Chap. 7) have been the most widely used for the past 15 years. They can provide a monoenergetic ion beam with diameters up to 40 cm and energies of up to 2000 eV. Other types of sources, the "End-Hall" or closed-drift source (73), the ECR source (74), the saddle-field ion source (75) and the cold-cathode-type source (76) can be used, depending on the application and the gas choice. Often for reactive gases, the hot filaments present in the Kaufman source can be troublesome and other sources may be preferred.

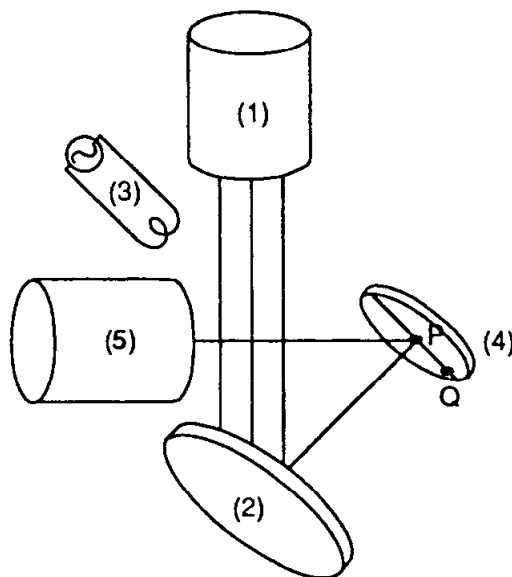


**Figure 14:** Schematic of dual ion beam sputter deposition system.

The use of ion sources for reactive sputter deposition differs from the plasma-based techniques due to the lower pressure of operation of the ion sources. Typical pressures for the plasma systems are a few Pa (5-100 mTorr) and for the ion beam sources are 0.01 to 0.1 Pa ( $7 \times 10^{-5}$  to  $7 \times 10^{-4}$ ). The reduction in pressure means that the sputtered species are not scattered by gas atom collisions following sputtering, and retain their full kinetic en-

ergy. Another significant difference from plasma-based techniques is that there is no potential on the target and therefore negative ions or secondary electrons are not accelerated to the depositing film at high energies. Energetic, reflected neutrals from the target surface, however, will not be scattered in an ion beam system, and thus may have a more significant effect on film properties than in the plasma-based techniques.

The ions from the ion source may be either an inert species, such as  $\text{Ar}^+$ ,  $\text{Kr}^+$ , etc, or mixtures of inert gas and reactive gas species, such as  $\text{O}_2^+$  or  $\text{N}_2^+$ . The ions are usually incident on the target at approximately  $45^\circ$  both for geometric reasons and to maximize the sputter yield. To obtain a symmetric deposition with optimum uniformity, the substrate should lie on the axis of the target and be parallel to it.

For many reactive deposition cases with ion beam sputtering, it is not necessary to add the reactive gas to the primary ion source, but simply to the discharge chamber. The ion source is then operated in a pure inert gas environment, and is less susceptible to internal damage caused by the reactive species. For nitride deposition, however, it was observed to be very difficult to deposit  $\text{Si}_3\text{N}_4$  films by simply bombarding a Si target with  $\text{N}_2^+$  ions, and only for very low deposition rates were the films stoichiometric (77). A second source was introduced, as shown in Fig. 14 which delivered 680 eV  $\text{N}_2^+$  ions to the substrate while the primary ion source sputtered the Si target with  $\text{Ar}^+$ . Provided the  $\text{N}_2^+$  flux was sufficient, the films produced were of the desired  $\text{Si}_3\text{N}_4$  composition.

In a similar experiment, Harper et al (78) investigated the sputter deposition of AlN from an Al target using a dual ion beam approach. The Al target was sputtered with 1.5 keV  $\text{Ar}^+$ , while the second ion source directed  $\text{N}_2^+$  ions from 100 to 500 eV to the sample. Due to a gradient in the current density of the second ion source, it was possible to examine regimes where the  $\text{N}_2^+$  ion flux both exceeded or was smaller than the Al flux. With excess nitrogen ion bombardment, the films formed were AlN, with the excess nitrogen being desorbed. Where the Al flux was larger, the films formed were a mixture of Al and AlN. However, when the same amount of nitrogen was admitted to the chamber without the operation of the second ion source, there was essentially no reaction with the sputtered Al. A similar effect can be inferred from the work of Kitabatake and Wasa (79), who obtained  $\text{Si}_3\text{N}_4$  films using a single source operating in Ar and  $\text{N}_2$ . In this case, the sample was located close to the target such that the ion beam also hit the sample at grazing incidence.

One of the most successful applications of reactive sputter deposition with ion beams has been the deposition of high quality optical films. This is done either in the arrangement of Fig. 14 or with an evaporation source replacing the sputtering target as a source of metal atoms. The films produced with these techniques are superior to films deposited without concurrent bombardment.

## 9.7 CONCLUSIONS

Reactive sputter deposition continues to be an area of intense interest for the production of compound films. While the ion beam experiments have shown excellent results, particularly for the deposition of optical and nitride films, much of the interest has remained in the use of the magnetron-based reactive deposition technique. Numerous studies have reported techniques or models which deal with the basic problem of target poisoning. Some of these techniques, particularly with the deposition of nitrides, have

been very successful. This can probably be traced to the energy requirements to form the nitride. The same cannot generally be said for the reactive deposition of oxides. Generally in this case, process control by feedback techniques has not been successful, at least on a large scale. Individual experiments, using either very large pumping speeds, baffles or some means of optical feedback control have been successful in some cases, but a general solution to this problem still remains elusive.

## 9.8 REFERENCES

1. N. Schwartz and R.W. Berry, Physics of Thin Films ed. by G. Hass and R.E. Thuns, Vol 2, p.363 (Academic, New York, 1964).
2. W.D. Westwood, Prog. in Surf. Sci. 7: 71 (1976).
3. J.A. Thornton, Surface Eng. 2: 283 (1986).
4. W.D. Westwood, Physics of Thin Films vol. 14 (Academic, New York, 1987).
5. A. Okamoto and T. Serikawa, Thin Solid Films 137: 143 (1986).
6. S. Kadlec, J. Musil and J. Vyskocil, Vacuum 37: 729 (1987).
7. J. Danroc, A. Aubert and R. Gillet, Surf. and Coatings Tech. 33: 83 (1987).
8. J. Heller, Thin Solid Films 17: 163 (1973).
9. B. Goranchev, V. Orlinov and V. Popova, Thin Solid Films 33: 173 (1976).
10. D.J. Harra and W.H. Haywood, Supplemento al Nuova Cimento 10: 381 (1967).
11. S. Schiller, U. Heisig, K. Steinfelder and J. Strumpfel, Proc. Int. Conf. on Ion Plating and Allied Techniques, London, p. 211 (1979).
12. K. Steenbeck, E. Steinbeiss, K-D. Ufert, Thin Solid Films, 92: 371 (1982).
13. J. Affinito and R.R. Parsons J. Vac. Sci. Technol. A2: 1275 (1984).
14. C.R. Aita and M.E. Marhic, J. Appl. Phys. 52: 6584 (1981).
15. F. Shinoki and A. Itoh, J. Appl. Phys. 46: 3381 (1975).
16. G. Lemperiere and J.M. Poitevin, Thin Solid Films 111: 339 (1984).
17. D.K. Hohnke, D.J. Schmatz and M.D. Hurley, Thin Solid Films, 118: 301 (1984).
18. G. Lemperiere, Le Vide, Les Couches Minces, 235: 3 (1987).
19. S. Berg, H-O. Blom, T. Larsson and C. Nender, J. Vac. Sci. Technol. A5: 202 (1987).
20. T. Larsson, H-O. Blom, C. Nender and S. Berg, J. Vac. Sci. Technol. A6: (1988).
21. A. Penfold, unpublished (1986).
22. D.E. Harrison, Rad. Eff. 70: 1 (1983).
23. A.J. Stirling and W.D. Westwood, J. Appl. Phys. 41: 742 (1970).
24. A.J. Stirling and W.D. Westwood, Thin Solid Films 7: 1 (1971).
25. A.J. Stirling and W.D. Westwood, Thin Solid Films 8: 199 (1971).
26. G. Betz and W. Husinsky, Nucl. Instrum. Meth. B13: 343 (1986).
27. J.M.E. Harper, J.J. Cuomo, R.J. Gambino, H.R. Kaufman and R.S. Robinson, J. Vac. Sci. Technol. 15: 1597 (1978).
28. J.J. Hanak, Le Vide 175: 11 (1975).

29. J.J. Cuomo, R.J. Gambino, J.M.E. Harper, J.D. Kuptsis and J.C. Webber, J. Vac. Sci. Technol. 15: 281 (1978).
30. D. Kester and R. Messier, J. Vac. Sci. Technol. A4: 496 (1986).
31. K. Tominaga, S. Iwamura, Y. Shintani and O. Tada, Jpn. J. Appl. Phys. 21: 688 (1982).
32. K. Wasa, M. Kitabatake, H. Adachi, K. Setsune and K. Hirochi, AIP Conf. Proc. 165: 38 (1988).
33. S.M. Rossnagel and J.J. Cuomo, AIP Conf. Proc. 165: 108 (1988).
34. W.Y. Less, J. Salem, V. Lee, C. Rettner, G. Lim, and R. Savoy, AIP Conf. Proc. 165: (1988).
35. P.J. Clarke AIP Conf. Proc. (Proceedings of 1988 AVS Topical Symposium on High Temperature Superconductors, in-press, 1989).
36. M.R. Scheuermann, Appl. Phys. Lett. 1987.
37. K. Tominaga, S. Iwamura, Y. Shintani and O. Tada, Jpn. J. Appl. Phys. 22: 418 (1983).
38. S.M. Rossnagel, I. Yang and J.J. Cuomo, Int. Conf. Metallurgical Coatings, San Diego, CA, April, 1989.
39. B. Window and N. Savvides, J. Vac. Sci. Technol. A4: 453 (1986).
40. L. I. Maissel, in Handbook of Thin Film Technology ed. by L.I. Maissel and R.H. Glang, Chap. 4 (McGraw-Hill, New York, 1970).
41. R.W. Berry, US Patent 2,993,266 (1961).
42. W.D. Westwood, N. Waterhouse and P.S. Wilcox, Tantalum Thin Films (Academic, New York, 1975).
43. G.H. Maher and R.J. Diefendorf, IEEE Trans. PHP-8: 11 (1972).
44. S. Fukunishi, A. Kawana, N. Uchida and J. Noda, J. Appl. Phys. Suppl. 2: Pt. I, 749 (1974).
45. Y. Higuma, K. Tanaka, T. Nakagawa, T. Kariya and Y. Hamakawa, Jpn. J. Appl. Phys. 16: 1707 (1977).
46. J.A. Thornton and A.S. Penfold, in Thin Film Processes, ed. by J. Vossen and W. Kern, Chap. II-2, (Academic, New York, 1978).
47. R.K. Waits, in Thin Film Processes, ed. by J. Vossen and W. Kern, Chap. II-4, (Academic, New York, 1978).
48. J.A. Thornton, J. Vac. Sci. Technol. 15: 171 (1978).
49. R.K. Waits, J. Vac. Sci. Technol. 15: 179 (1978).
50. D.B. Fraser, in Thin Film Processes, ed. by J. Vossen and W. Kern, Chap. II-3 (Academic, New York, 1978).
51. D.B. Fraser, J. Vac. Sci. Technol. 15: 178 (1978).
52. S. Schiller, U. Heisig, K. Goedicke, K. Schade, G. Teschner and J. Henneberger, Thin Solid Films 64: 455 (1979).
53. S. Maniv and W.D. Westwood, Surf. Sci. 100: 108 (1980).

54. J.P. Noel, D.C. Houghton, G. Este, F.R. Shepherd and H. Plattner, J. Vac. Sci. Technol. A2: 284 (1984).
55. J.A. Thornton, Thin Solid Films 80: 1 (1981).
56. G. Este and W.D. Westwood, J. Vac. Sci. Technol. A2: 1238 (1984).
57. W.D. Westwood, S. Maniv and P.J. Scanlon, J. Appl. Phys. 54: 6481 (1983).
58. S.M. Rossnagel and H.R. Kaufman, J. Vac. Sci. Technol. A5: 88 (1988).
59. S. Maniv and W.D. Westwood, J. Vac. Sci. Technol. 17: 743 (1980).
60. G. Este and W.D. Westwood, J. Vac. Sci. Technol. A6: 1845 (1988).
61. S. Maniv, C. Miner and W.D. Westwood, J. Vac. Sci. Technol. 18: 195 (1981).
62. F. Jones, J. Vac. Sci. Technol. A6: 3088 (1988).
63. P. Chang and D.M. McGarr, Diagnostic Techniques in VLSI Fabrication, p. 189 (Semiconductor Equipment and Materials Inst. Inc, Mountain View, CA, 1987).
64. G.D. Davis and M. Natan, J. Vac. Sci. Technol. A4: 159 (1986).
65. ref 65 = old 166, look up.
66. W.D. Sproul, AIP Conf. Proc. 149: 157 (1986).
67. A.F. Hmiel, J. Vac. Sci. Technol. A3: 592 (1985).
68. M. Bhushan, J. Vac. Sci. Technol. A5: 2829 (1987).
69. S. Sciller, U. Heisig, K. Steinfelder, J. Strumpfel, R. Voight, R. Fendler and G. Teschner, Thin Solid Films 96: 235 (1982).
70. K. Enjouji, K. Murata and S. Nishakawa, Thin Solid Films 108: 1 (1983).
71. S. Schiller, O. Heisig, C. Korndorfer, G. Beister, J. Reschke, K. Steinfelder and J. Strompfel, Surf. and Coatings Tech. 33: 405 (1987).
72. M.I. Ridge and R.P. Howson, Vacuum 34: 327 (1984).
73. R.S. Robinson and H.R. Kaufman, in Handbook of Ion Beam Processing Technology ed. by J.J. Cuomo, S.M. Rossnagel and H.R. Kaufman (Noyes, Park Ridge, NJ 1989), p. 39.
74. W. Holber, in Handbook of Ion Beam Processing Technology, ed. by J.J. Cuomo, S.M. Rossnagel and H.R. Kaufman (Noyes, Park Ridge, NJ 1989) p. 21.
75. R.K. Fitch, T. Mulvey, W.J. Thetcher and A.H. McIlraith, J. Phys. D. Appl. Phys. 3: 1399 (1970).
76. Cold cathode ion source, model cc-100, Denton Vacuum, Inc., Cherry Hill, NJ 08003.
77. C. Weissmantel, Thin Solid Films 32: 11 (1976).
78. J.M. E. Harper, J.J. Cuomo and H.T. G. Hentzell, Appl. Phys. Lett. 43: 547 (1983).
79. M. Kitabatake and K. Wasa, J. Vac. Sci. Technol. A5: 1793 (1987).

---

## Plasma Enhanced Chemical Vapor Deposition of Thin Films for Microelectronics

---

**Rafael Reif**

### 10.1 INTRODUCTION

Plasma enhanced chemical vapor deposition (PECVD) is an established commercial technique for the deposition of insulating films such as silicon nitride and silicon oxide (1). The major advantage of PECVD is its lower temperature capability compared to that of thermally driven CVD. For example, deposition temperatures of 700 to 900°C are required to deposit silicon nitride films by thermal CVD, while only 250 to 350°C are sufficient to deposit similar films by PECVD (2,3). This lower temperature capability is made possible by the addition of electrical energy to the CVD environment, and the effective substitution of this electrical energy for thermal energy.

PECVD is also being investigated as a potential technique for the deposition of crystalline films such as polycrystalline silicon (4-6), epitaxial silicon (7-9), epitaxial gallium arsenide (10-12), and refractory metal and silicide (13,14) films. More recently, the PECVD of diamond films has also received a great deal of attention (15,16). The driving force for the PECVD of these materials is the same as that for the insulating films; that is, to lower the deposition temperature while maintaining reasonable growth rates and high quality.

This chapter discusses the plasma enhanced chemical vapor deposition technique, emphasizing the issues important to the deposition of thin films for microelectronics. It begins with a review of the basic physics and chemistry of nonequilibrium glow discharges, followed by a discussion of the effects of adding a glow discharge to a chemical vapor deposition (CVD) environment. The latter sections discuss the most important dielectric, semiconductor, and conductor films that have been deposited by PECVD. References (17-24) correspond to other reviews of PECVD.

## 10.2 NONEQUILIBRIUM GLOW DISCHARGES

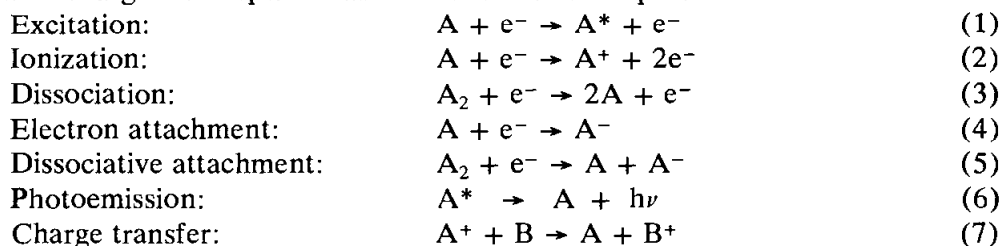
A glow discharge can be defined as a partially ionized gas containing equal volume concentrations of positive and negative charged species (mostly ions and electrons, respectively) and different concentrations of ground-state and excited species (25,26). This partially ionized gas can be generated by subjecting the gas to very high temperatures or to strong electric or magnetic fields. In thermal plasmas, the electrons, ions, and neutral species are in local thermodynamic equilibrium. In nonequilibrium or "cold" plasmas, the electrons and ions are more energetic than the neutral species.

Most of the glow discharges used in microelectronics are generated by subjecting the gas to a radio frequency (rf) electric field, and they are nonequilibrium glow discharges (i.e., "cold" plasmas). The electric field initially accelerates a few free electrons present in the gas. Although the electric field also acts on the ions, they remain relatively unaffected because of their much heavier mass. The accelerated electrons do not lose much energy in elastic collisions with gas species because of the large mass difference. Furthermore, these electrons do not lose much energy in inelastic collisions (e.g., excitation and ionization), until their energies reach the necessary threshold energies (e.g., 11.56 eV for excitation and 15.8 eV for ionization of argon (25)). Consequently, these accelerated electrons gain energy quickly from the electric field.

Once these electrons acquire sufficiently high energies, their collisions with gas species result in excitations and ionizations, the latter generating additional electrons that are, in turn, accelerated by the electric field. This transient process avalanches quickly, creating the steady state glow discharge. In steady state, the glow continuously loses charged species (i.e., electrons and ions) to the electrodes and other surfaces within the chamber, and gains a numerically equal number of electrons and ions from ionizations. Other mechanisms that produce additional electrons, such as secondary electron emission from positive ion bombardment on the electrodes and walls, are known to play a major role in sustaining the glow discharge.

The inelastic collisions between high-energy electrons and gas species give rise to highly reactive species, such as excited neutrals and free radicals, as well as ions and more electrons. In this manner, the energy of the electrons is used to create reactive and charged species without significantly raising the gas temperature. The reactive species produced in the plasma have lower energy barriers to physical and chemical reactions than the parent species and, consequently, can react at lower temperatures. PECVD uses these reactive species to deposit thin films at temperatures lower than those possible with thermally driven CVD. The charged species in the glow discharge may also affect the properties of the deposited films (27,28).

There are many possible inelastic collisions between electrons and gas species in a glow discharge. Examples of those believed to be important in PECVD are listed below:





where A, A<sub>2</sub>, and B are reactants, e<sup>-</sup> is an electron, A\* is reactant A in an excited state, and A<sup>+</sup>, A<sup>-</sup>, and B<sup>+</sup> are ions of A and B.

The rate at which these inelastic collisions create excited species, ions, free radicals, etc., can be estimated by using a reaction rate equation (29). For example, the rate at which A\* is created from reaction (1) can be given by:

$$\frac{d[A^*]}{dt} = k_1[A][e^-] \quad (8)$$

where d[A\*]/dt is the rate of formation of A\*, k<sub>1</sub> is the reaction rate coefficient, [A] is the concentration of species A, and [e<sup>-</sup>] is the electron concentration (30). Similar equations can be used to describe the reaction rates corresponding to reactions in Eqns. (2) through (7).

As discussed above, only high energy electrons can take part in inelastic collisions. In order to take this into account, k<sub>1</sub> in Eqn. (8) needs to be defined in terms of the electron velocity and the inelastic collision cross-section. The cross section of an electron-reactant inelastic collision is proportional to the probability that this inelastic collision will occur and is a function of the electron energy. For example, if the energy of the electron is lower than the required threshold energy, the collision cross section is zero. The rate coefficient k<sub>i</sub> can be calculated by using the following equation (29):

$$k_i = \int_0^\infty \left[ \frac{2E}{m_e} \right]^{1/2} \sigma_i(E) f(E) dE \quad (9)$$

where E is the electron energy, m<sub>e</sub> is the electron mass, σ<sub>i</sub> is the collision cross section of reaction i and is a function of E, and f(E) is the electron energy distribution function and gives the fraction of free electrons having a given energy. The integration is carried out over all possible electron energies. The square root term in Eqn. (9) is the electron velocity.

Some collision cross section data can be found in the literature (31). However, most of the cross sections of interest in microelectronics are not known. A similar situation exists with the electron energy distribution function f(E). It is typical to assume a Maxwell-Boltzmann distribution for f(E), that is, a distribution in which a large fraction of the electrons have energies lower than or equal to the average electron energy, and the fraction of electrons having higher energies decays exponentially with increasing energy. However, the actual electron energy distribution function is not known, and non-Maxwellian distributions have been proposed. Moreover, it is possible that the reactant composition of the gas influences f(E) because the higher-energy electrons lose a significant fraction of their energies in inelastic collisions with these reactants. Consequently, it is difficult to calculate reaction rate coefficients and reaction rates theoretically (32).

The rf glow discharges commercially used in microelectronics operate at frequencies between 50 kHz and 13.56 MHz, and pressures of 0.1-2.0 Torr. The plasma density (i.e. the density of ions and free electrons) is in the range of 10<sup>8</sup> to 10<sup>12</sup> cm<sup>-3</sup>. The degree of

ionization is typically  $\leq 10^{-4}$ , i.e., the principle species in the glow is primarily neutrals. A Maxwell-Boltzmann distribution is usually used to approximate the energy distribution of free electrons. Typical average electron energies are 1-3 eV, but the fastest electrons may reach energies as high as 10-30 eV (33). These high energy electrons make possible the creation, at relatively low temperatures, of the reactive species responsible for film formation. Because the average electron energies are much higher than the ion energies, these are known as non-equilibrium glow discharges; i.e. the PECVD environment is not in thermal equilibrium. Consequently, thermodynamics is of little help in predicting the product of a PECVD reaction.

### 10.3 POTENTIALS IN RF GLOW DISCHARGES

Several potentials are important in the glow discharges used in microelectronics: the plasma potential, the floating potential, and the sheath potential.

The plasma potential ( $V_p$ ) is the potential of the glow region of the plasma, which is normally considered nearly equipotential. It is the most positive potential in the chamber and is the reference potential for the glow discharge.

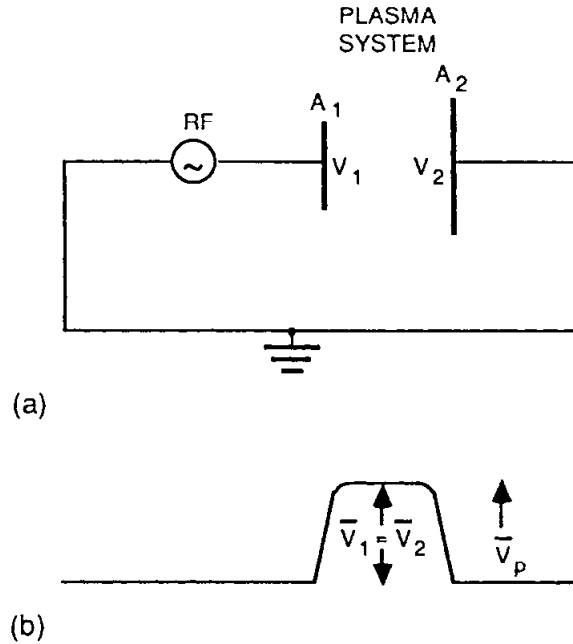
The floating potential ( $V_f$ ) is the potential at which equal fluxes of negative and positive charged species arrive at an electrically floating surface in contact with the plasma. It is approximately given by:

$$V_p - V_f = \frac{kT_e}{2e} \ln\left(\frac{m_i}{2.3m_e}\right) \quad (10)$$

where  $T_e$  is the electron temperature,  $e$  is the unit electron charge, and  $m_i$  and  $m_e$  are the ion and electron mass, respectively (25,34). Equation (10) can be used to estimate the maximum energy with which positive ions may bombard electrically insulated chamber walls. Most sputtering threshold energies are 20 to 30 eV (25). Therefore, a  $V_p - V_f \leq 20$  to 30V would avoid sputtering off the walls, which may lead to film contamination.

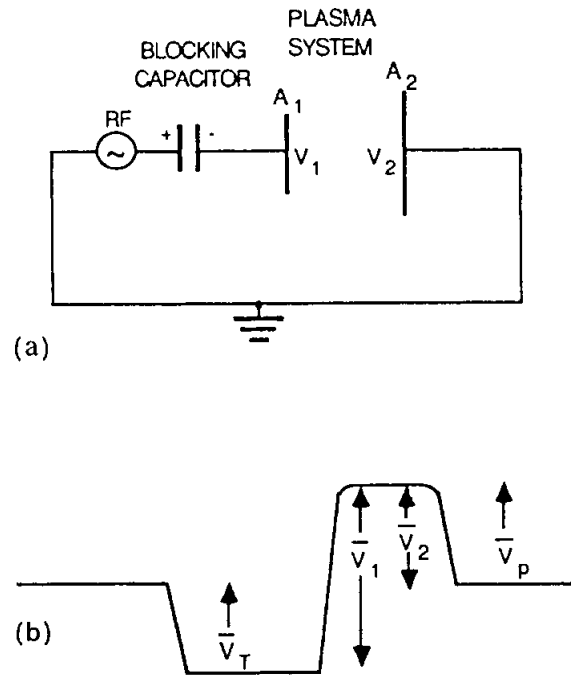
The plasma potential is always positive with respect to any surface in contact with the plasma. This is because the mobility of free electrons in the plasma is much greater than that of ions and, consequently, the initial electron flux to all surfaces is greater than the ion flux. Therefore, the surfaces in contact with the plasma become negatively charged, and a positive space charge layer develops in front of these surfaces. Because there are fewer electrons in the space charge layer, or sheath, fewer gas species are excited by electron collisions. Consequently, fewer species relax and give off radiation, and the sheath region is dark relative to the glow discharge. Positive ions that enter the sheaths from the glow region by random thermal motion accelerate into the electrodes and other surfaces in contact with the plasma. Similarly, secondary electrons emitted from the surfaces (e.g., due to positive ion bombardment) accelerate through the sheaths into the glow region. The maximum energy with which positive ions bombard a surface, and the maximum energy with which secondary electrons enter the glow region, is determined by the difference between the potential of the surface and the plasma potential. Because this is the potential across the sheath, it is usually referred to as the sheath potential.

Figure 1(a) shows schematically an rf generator connected to the electrodes of a plasma system (35).  $A_1, A_2$  are the areas of the electrodes and  $V_1, V_2$  are the voltages across the sheaths in front of the electrodes. An rf generator signal of  $V_{\text{peak}} \sin \omega t$  is assumed in this discussion. As indicated in Fig. 1(b), the average sheath voltages are the same, i.e.  $\bar{V}_1 = \bar{V}_2$ , because the generator is dc coupled to the reactor. Moreover, the average plasma potential is equal to the average sheath potential, i.e.  $\bar{V}_1 = \bar{V}_2 = \bar{V}_p$ . The value of  $\bar{V}_1 = \bar{V}_2 = \bar{V}_p$  varies from about  $0.5V_{\text{peak}}$  in symmetric reactors (i.e. where  $A_1 = A_2$ ), to higher values in asymmetric systems (36). If a "blocking" capacitor is added between the generator and the powered electrode (Fig. 2(a)), no dc current is allowed in the circuit in steady-state. Consequently, the capacitor charges up to a sufficient "self bias" voltage until there is no dc current in the circuit. This average self bias potential is indicated as  $\bar{V}_T$  in Fig. 2(b). It is negative when the smaller electrode is powered (Fig. 2(b)), but positive when the larger electrode is powered (36). The values of  $\bar{V}_1, \bar{V}_2$  and  $\bar{V}_T$  are determined by the ratio of the electrode areas, i.e.  $\bar{V}_1/\bar{V}_2 = (A_2/A_1)^n$  (37, 38).



**Figure 1:** Potential distribution in rf plasma systems without blocking capacitor (35). (a) Electric circuit with rf generator connected to the electrodes of the plasma system. (b) Potential distribution:  $|\bar{V}_1| = |\bar{V}_2| = \bar{V}_p$  is the average plasma potential.

Koenig and Maissel (37) derived this area ratio expression assuming very low pressure operation and theoretically found  $n = 3$  or  $4$ . Experimental data suggest that the ratio  $\bar{V}_1/\bar{V}_2$  is also a function of the gas in the discharge and the peak-to-peak rf voltage applied (39). Moreover, for  $A_2/A_1 \approx 1 - 1.7$ , the value of  $n$  was found to be close to  $4$  (39), but for larger area ratios  $n$  has been found to be closer to  $1$  (34,38,39). In very asymmetric reactors (i.e.  $A_2 \gg A_1$ ),  $|\bar{V}_1| \approx |\bar{V}_T| \approx V_{\text{peak}}$ , while  $\bar{V}_2 = \bar{V}_p \approx 0$ . On the other hand, in symmetric reactors  $|\bar{V}_1| = |\bar{V}_2| = \bar{V}_p = V_{\text{peak}}/2$ . Notice that the sheath potentials and the plasma potential are equal to  $0.5V_{\text{peak}}$  in symmetric systems with or without a blocking capacitor. Tables 1 and 2 summarize the sheath, plasma, and self-bias voltages discussed here.



**Figure 2:** Potential distribution in rf plasma systems with blocking capacitor (35). (a) Electric circuit with rf generator connected to the electrodes of the plasma system through a blocking capacitor. (b) Potential distribution:  $\bar{V}_T$  is the self-bias voltage.

dc coupled		
	symmetric ( $A_1 = A_2$ )	asymmetric ( $A_1 \ll A_2$ )
$\bar{V}_1$	$V_{\text{peak}}/2$	$V_{\text{peak}}/2 < \bar{V}_1 < V_{\text{peak}}$
$\bar{V}_2$	$V_{\text{peak}}/2$	$V_{\text{peak}}/2 < \bar{V}_2 < V_{\text{peak}}$
$\bar{V}_p$	$V_{\text{peak}}/2$	$V_{\text{peak}}/2 < \bar{V}_p < V_{\text{peak}}$
$ \bar{V}_T $	0	0

**Table 1:** Average sheath ( $\bar{V}_1$ ,  $\bar{V}_2$ ), plasma ( $\bar{V}_p$ ), and self bias ( $\bar{V}_T$ ) voltages in dc-coupled reactor. The applied voltage is  $V_{\text{peak}} \sin \omega t$ . Notice that  $\bar{V}_1 = \bar{V}_2 = \bar{V}_p$  and that  $\bar{V}_T = 0$  as there is no blocking capacitor. (see Fig. 1.)

dc coupled		
	symmetric ( $A_1 = A_2$ )	asymmetric ( $A_1 \ll A_2$ )
$\bar{V}_1$	$V_{\text{peak}}/2$	$V_{\text{peak}}/2 < \bar{V}_1 < V_{\text{peak}}$
$\bar{V}_2$	$V_{\text{peak}}/2$	$V_{\text{peak}}/2 < \bar{V}_2 < V_{\text{peak}}$
$\bar{V}_p$	$V_{\text{peak}}/2$	$V_{\text{peak}}/2 < \bar{V}_p < V_{\text{peak}}$
$ \bar{V}_T $	0	0

**Table 2:** Average sheath ( $\bar{V}_1, \bar{V}_2$ ), plasma ( $\bar{V}_p$ ), and self bias ( $\bar{V}_T$ ) voltages in capacitively coupled reactor. The applied voltage is  $V_{\text{peak}} \sin \omega t$ . Under these conditions,  $\bar{V}_1/\bar{V}_2 = (A_2/A_1)^n$ ,  $|\bar{V}_T| = \bar{V}_1 - \bar{V}_2$ , and  $\bar{V}_2 = \bar{V}_p$ . (See Fig. 2.)

#### 10.4 QUALITATIVE MODEL FOR PECVD

In thermally-driven CVD, ground state species containing the elements to be deposited (e.g. silane ( $\text{SiH}_4$ ) and ammonia ( $\text{NH}_3$ ) as parent species for Si and N, respectively, in  $\text{Si}_3\text{N}_4$  depositions) are transported to the vicinity of the wafer surface where they diffuse to the surface, adsorb on the surface, undergo chemical reactions and surface migration, and eventually yield a solid film. Reaction byproducts also form, and they desorb, diffuse away into the main gas stream, and are transported out of the chamber. This sequence of steps is summarized below:

1. Transport of reactants to the growth region
2. Mass transport of reactants to the wafer surface
3. Adsorption of reactants
4. Physical-chemical reactions yielding the solid film and reaction byproducts
5. Desorption of byproducts
6. Mass transport of byproducts to the main gas stream
7. Transport of byproducts away from the growth region

An equivalent circuit representation of this sequence of steps is shown in Fig. 3 (40).

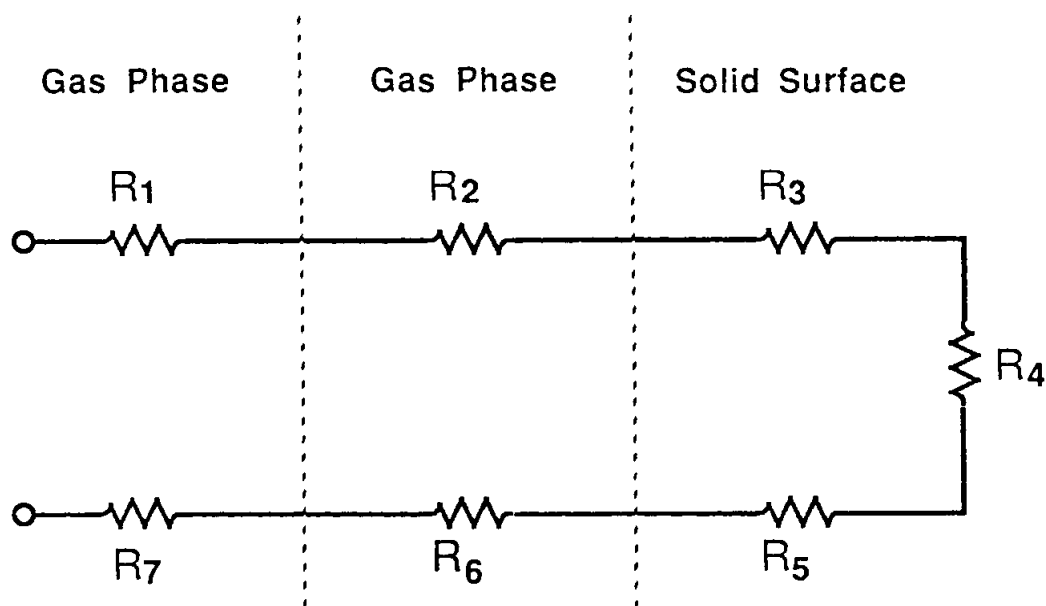
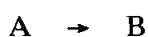
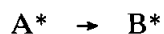
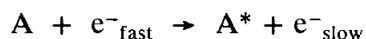


**Figure 3:** Equivalent circuit representation of sequence of steps in thermally-driven CVD (40). The  $R_i$ 's (with  $i = 1 - 7$ ) represent the seven steps described in text.

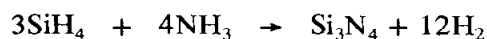
When a plasma is generated in a CVD environment, a fraction of the ground-state parent species in the gas phase undergoes electron impact dissociation and excitation, and highly reactive species are consequently generated. As a result, in addition to the ground state species, these highly reactive species also diffuse to the surface, and undergo similar processes of adsorption, chemical reactions, surface migration, etc. In other words, these highly reactive species follow an alternative deposition pathway which operates in parallel to the existing thermal deposition pathway. An equivalent circuit representation of this situation is shown in Fig. 4. The plasma kinetic pathway often bypasses that of the ground state species because the sticking coefficients of the highly reactive species are closer to unity (26), and the activation energies for chemical dissociation are typically lower. The latter is illustrated in Fig. 5, which compares the activation energy diagram of a ground-state reaction:



which has an activation energy  $\Delta E$ , with that of



which has an activation energy  $\Delta E^*$ . (Strictly speaking, the reaction product  $B^*$  is not the same as  $B$ . For example, the thermal reaction



yields a  $\text{Si}_3\text{N}_4$  film, while the plasma enhanced reaction



yields a SiNH film.)

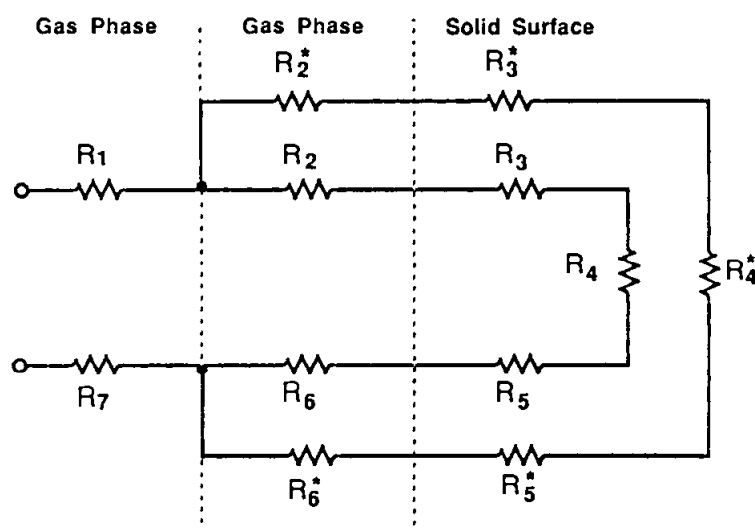


**Figure 4:** Equivalent circuit representation showing the thermal CVD path, and the parallel plasma-enhanced path represented by the  $R_i^*$ 's.

Consequently, the plasma kinetic pathway makes possible a higher deposition rate. Moreover, the ions present in the plasma may bombard the substrate surface, further modifying the kinetic pathway by effecting the breaking down of weakly bonded reactive species, the surface migration of adatoms, and/or removing undesired contaminants. (However, if ion energies, fluxes, and/or doses are too high, they may also affect the film quality.) Temperature is still needed to drive the reaction over  $\Delta E^*$  (Fig. 5), i.e. to provide the energy required to promote surface reactions and desorb byproducts, as well as to lower film contamination.

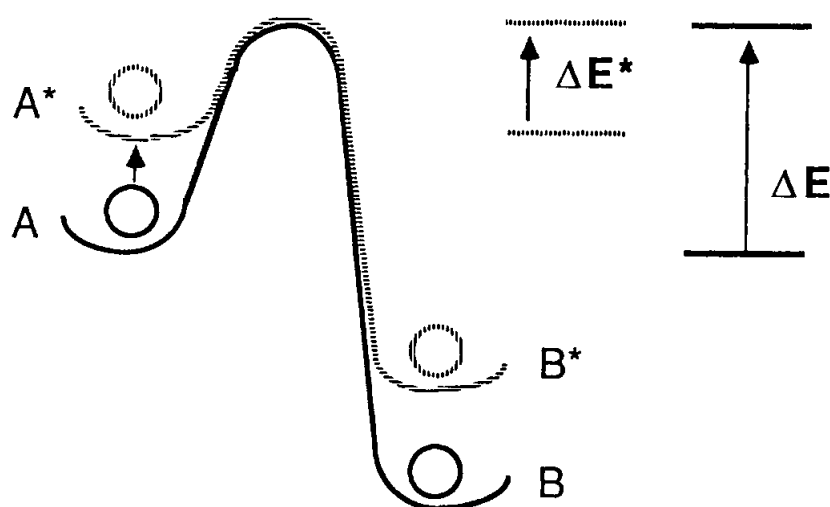


**Figure 5:** Activation energy diagram for a thermally-driven (solid line) and for a plasma-enhanced (dashed line) reaction.

## 10.5 COMMERCIAL PECVD SYSTEMS

The commercial PECVD systems discussed here have been used successfully to deposit silicon nitride, silicon oxynitride, silicon oxide, and hydrogenated amorphous silicon films. Some of these systems are also being used to investigate the deposition of polycrystalline (Si, refractory metal, refractory metal silicide, diamond) and epitaxial (Si, compound semiconductor) films.

The first commercially important PECVD reactor was introduced by Reinberg in 1974 (see Fig. 6) (41). The plasma is generated between the two parallel, circular electrodes. The wafers are loaded onto the lower, electrically grounded, electrode. The upper electrode is connected to the rf generator through an impedance matching network. The reactants are fed in from the gas ring, enter the plasma region (i.e., the region between the electrodes) at its outer edge, and flow radially in toward a pumping port at the center of the lower electrode (42, 43). These reactors are also known as "radial flow" reactors.

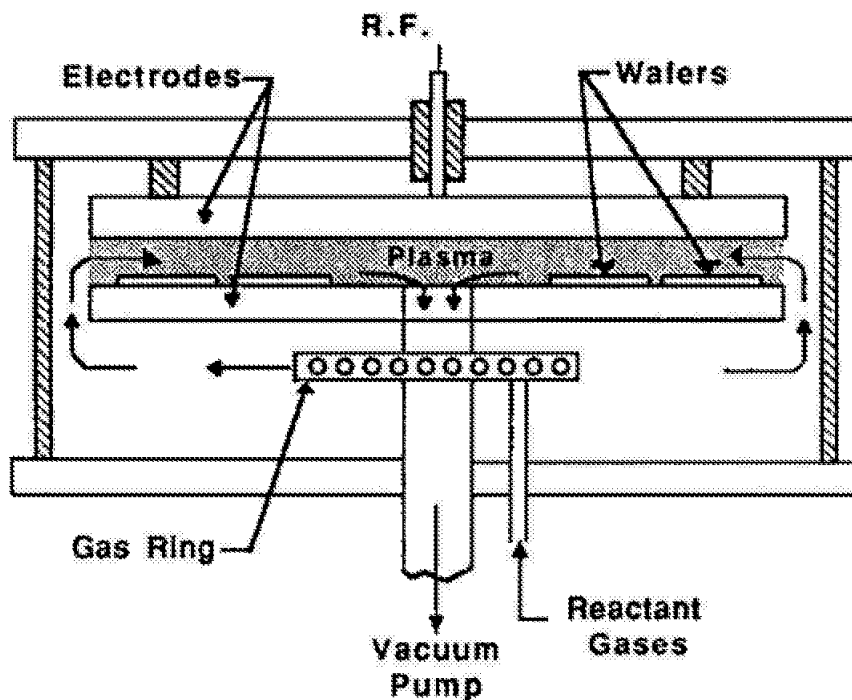


**Figure 6:** Schematic of radial flow reactor designed by Reinberg (41). (Courtesy of the Electrochemical Society, Inc.)

An "inverse" radial flow reactor was introduced by Applied Materials in 1976 (see Fig. 7) (44). The gas inlet is at the center of the lower electrode, with the gas flow directed radially outward. A magnetic drive assembly permits rotation of the lower electrode, thus randomizing the substrate position and optimizing deposition uniformity. An improvement to this design, also introduced by Applied Materials, is shown in Fig. 8 (43). The perforated electrode in this newer design further improves deposition uniformity.



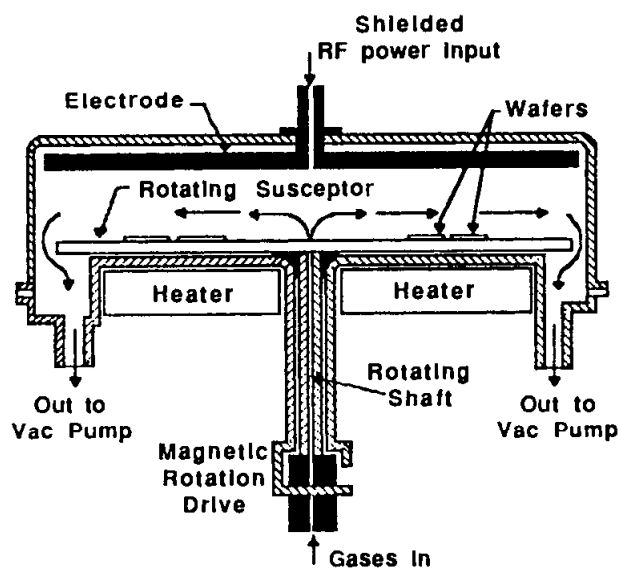


**Figure 7:** Schematic of inverse radial flow reactor (44). (Courtesy of Applied Materials, Inc.)

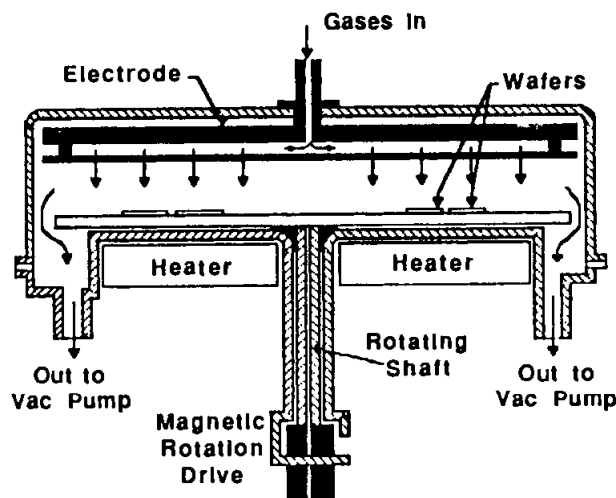


**Figure 8:** Schematic of inverse radial flow reactor with perforated electrode (43). (Courtesy of Applied Materials, Inc.)

A hot-wall, batch PECVD system (see Fig. 9) was introduced simultaneously by ASM America and Pacific Western Systems in the late 1970s (45,46). The deposition chamber consists of a quartz tube placed within a resistively heated furnace. Vertically oriented graphite slabs carry the wafers in slots. Every other slab is connected to the same rf power terminal, as shown in Fig. 9. The glow discharge is generated between adjacent electrodes. The reactants are directed along the axis of the chamber tube and between

the electrodes. The vertical position of the wafers in this "tubular" design makes possible a reduction in the collection of particulates (from wafer handling and flaking off the walls) on the wafer surface. In addition, good ( $\pm 5\%$ ) film uniformity can be achieved over a large batch of wafers (e.g.,  $\approx 90$  125-mm wafers), and the furnace-type heating aids temperature control. Moreover, the plasma excitation technique for these systems makes it possible to pulse the rf power to the electrodes. (The rf power is applied continuously in all other systems.) Pulsing of the rf power improves deposition uniformity in this reactor.

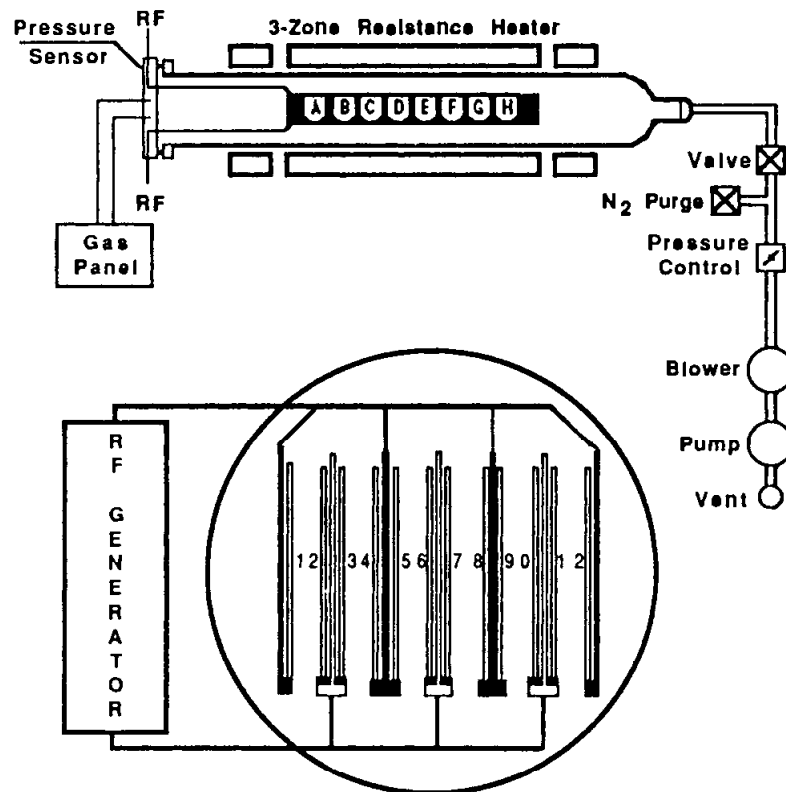


**Figure 9:** Schematic of hot-wall, batch PECVD system (45). (Courtesy of ASM America, Inc.).

Increasing performance demands and larger wafer sizes are driving the equipment technology away from the batch machines described here and into single-wafer processing. Consequently, next-generation PECVD equipment will probably be single-wafer machines.

## 10.6 PECVD OF DIELECTRIC FILMS

The most important PECVD dielectric films in microelectronics today are silicon nitride, silicon oxide, silicon oxynitride, and silicate glasses. Silicon nitride was the first material deposited by the PECVD technique on a large production scale. It is used extensively as a final protective passivation and coating layer for integrated circuits because it is an excellent diffusion barrier against moisture and alkali ions. The PECVD technique

makes possible the low deposition temperature (250 – 400°C) required to deposit a silicon nitride film over wafers containing an aluminum metallization layer. Furthermore, PECVD nitride films with compressive stress can be obtained, and this permits the deposition of relatively thick films. Silane ( $\text{SiH}_4$ ) and ammonia ( $\text{NH}_3$ ) are typically used as sources of silicon and nitrogen, respectively. Silane and nitrogen ( $\text{N}_2$ ) can also be used, but these reactants typically yield silicon-rich films (probably due to the relatively high bond energy of  $\text{N}_2$  (21)), as well as films with low breakdown strengths (47,48). Depositions are normally carried out at pressures of 0.2 to 3 Torr, which yield growth rates of 200 to 500 Å/min. PECVD silicon nitride films contain 15 to 30 at % of hydrogen bonded to either silicon or nitrogen (34,38). Film properties such as refractive index, stress, and optical absorption edge are greatly affected by the concentration and chemical distribution of hydrogen in the film.

The following general trends relating the properties of PECVD silicon nitride films with process parameters and film composition have been observed. These trends are sensitive to reactor geometry and deposition conditions, and are included here only as a guide.

1. The refractive index (1.9-2.2) increases as the Si-H/N-H bond ratio and/or Si/N ratio in the film increases (47, 49).
2. The optical gap is 3-4 eV (compared to 5 eV for stoichiometric  $\text{Si}_3\text{N}_4$ ), and is a function of the silicon content in the film. It decreases with increasing Si/N ratio (47, 49).
3. The resistivity ranges from  $10^5$  to  $10^{19}$  ohm-cm, and decreases with increasing Si/N ratio (47, 50).
4. Breakdown strengths are  $1 - 6 \times 10^6$  V/cm, and are sensitive to film composition, with the silicon-rich films exhibiting the lower breakdown fields (47, 50).
5. Film etch rates are typically used to determine film quality. Plasma silicon nitride etch rates in aqueous HF acid solutions increase with decreasing Si/N ratios down to 0.75, and with increasing H content (47, 51).
6. Stress varies from  $10^{10}$  dyn/cm<sup>2</sup>, compressive, to  $10^{10}$  dyn/cm<sup>2</sup>, tensile, and is a function of substrate temperature, gas composition, operating pressure, rf power, and rf frequency (47,49,52,53). For example, low excitation frequencies (e.g. 50 kHz) usually yield films with small compressive stress ( $\approx 2 \times 10^9$  dyn/cm<sup>2</sup>) (54), while higher frequencies (e.g. 13.56 MHz) may yield films with tensile stress ( $\approx 2 \times 10^9$  dyn/cm<sup>2</sup>) (52). The optimum stress for silicon nitride films used as final passivation layers is  $2 - 5 \times 10^9$  dyn/cm<sup>2</sup>, compressive (54).

More complete reviews of the PECVD of silicon nitride can be found in references (21,42,47,55,56,57).

PECVD silicon oxide films have been proposed as an interconductor dielectric material because of their low deposition temperature (200-400°C) and relatively low dielectric constant (4-6 vs. 6-9 for PECVD silicon nitride (47)). Silane is typically used as the silicon source, while nitrous oxide ( $\text{N}_2\text{O}$ ), nitric oxide ( $\text{NO}$ ), carbon dioxide ( $\text{CO}_2$ ), and oxygen have been used as oxygen sources. Nitrous oxide has been the preferred oxidizer because of the relatively low (1.7 eV) bond dissociative energy of N-O in this molecule (17,18). PECVD silicon oxide films are compressive ( $0.07 - 2.4 \times 10^9$  dynes/cm<sup>2</sup>) independent of rf frequency, and contain 2 to 9 wt % of hydrogen and less than 5 wt % of

nitrogen (54,58). Other properties of PECVD silicon oxide films are refractive index (1.45-1.50), breakdown strength ( $2 - 6 \times 10^6 \text{V/cm}$ ), and resistivity ( $10^{13} - 10^{17} \text{ohm-cm}$ ). A more complete review on the PECVD of silicon oxide films can be found in references (2,21,47,59).

PECVD silicon oxynitride films combine some of the best properties of PECVD silicon nitride and oxide films. The presence of oxygen lowers the dielectric constant of silicon nitride films, while that of nitrogen increases the resistance to sodium ions and moisture of silicon oxide films. Consequently, these films have found applications as interconductor dielectric layers and as surface passivation coating for integrated circuits. The deposition conditions for these films are a combination of those used for silicon nitrides and oxides (60).

Phosphosilicate glass (PSG) and boro-phosphosilicate glass (BPSG) can be readily deposited by PECVD (54). PSG is frequently used as the interconductor layer between polycrystalline silicon and aluminum, and it provides conformal step coverage after heating the wafer until the glass softens and flows. This "reflow" process requires phosphorus concentrations of 6 to 8 wt % and temperatures of 1000 to 1100°C. BPSG is sometimes preferred because it softens and flows at temperatures below 1000°C (61,62).

## 10.7 PECVD OF POLYCRYSTALLINE SILICON FILMS

Polycrystalline silicon (polysilicon) films can be deposited by atmospheric pressure chemical vapor deposition (CVD) (63), low pressure CVD (LPCVD) (64), and molecular beam deposition (MBD) (65) at temperatures over 600°C. Polysilicon is commercially used as the gate electrode and interconnect material in MOS integrated circuits (66), and is being investigated as the active material for thin film transistors (TFTs) (67) and as solar-energy conversion devices (68). The most commonly used deposition technique for integrated circuit applications is LPCVD. This technique has two basic problems: (1) the deposition rate and film structure are a strong function of the deposition temperature, and (2) the thickness uniformity and deposition rate are affected when large quantities of dopant species are introduced in the reactor during growth (4). TFTs are attractive for flat panel displays but require fabrication temperatures much lower than those possible with either CVD, LPCVD, or MBD. PECVD is being studied as an alternative to LPCVD for the fabrication of polysilicon gate electrodes, and as a low temperature fabrication technique for TFTs (67). The potential advantages of PECVD are: (1) less sensitivity to deposition temperature, (2) capability of introducing large quantities of dopant species without affecting the deposition rate, and (3) lower deposition temperature.

Figure 10 shows growth-rate data as a function of deposition temperature for LPCVD and PECVD films deposited in the same reactor (6). As indicated earlier, LPCVD depositions are very sensitive to the substrate temperature. At temperatures below 700°C, the LPCVD process has an apparent activation energy of 48 kcal/mole, which corresponds to the energy required to thermally dissociate the silicon source, silane. At temperatures above 700°C, the growth rate is essentially constant, probably because of mass transport and/or silane depletion limitations in the reactor used (6). PECVD depositions, on the other hand, yield growth rates which are higher and only weakly dependent (7 kcal/mole) on substrate temperature.

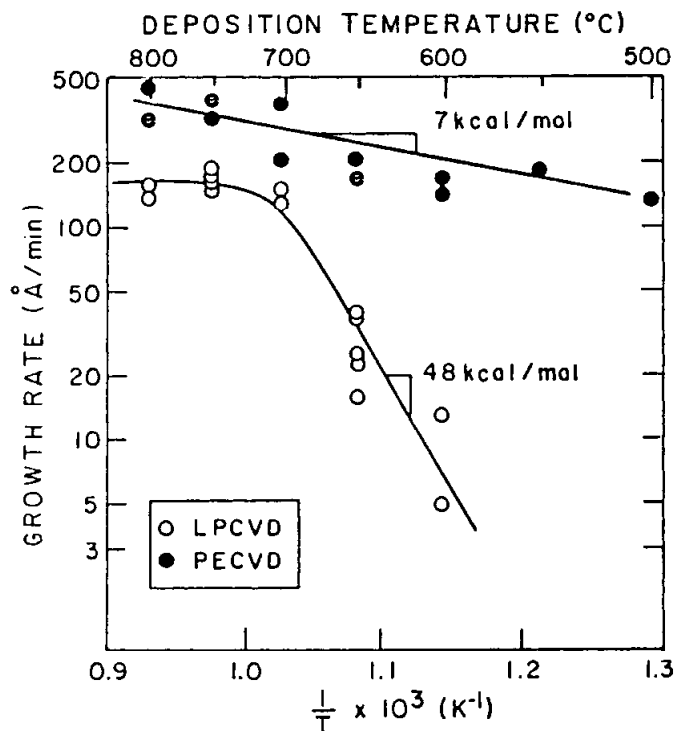


**Figure 10:** Plots of  $\log_{10}$  (growth rate) vs reciprocal temperature for polycrystalline silicon thin films grown on oxidized silicon substrates with and without plasma assistance (PECVD and LPCVD, respectively) (6).

The amorphous-to-polycrystalline transition temperature and the polysilicon structure vary with reactor design and deposition conditions. Polysilicon films have been deposited at 450°C in a silane/argon plasma (69), at 600°C in a silane/hydrogen plasma (70), at 700°C in a silane plasma (6), and at 625°C in a dichlorosilane/argon plasma (4). Grain sizes ranging from 30 Å (71) to 500 Å (72) and deposition rates ranging from 30 Å/min (73) to 3000 Å/min (74) have been reported. Kamins and Chiang (4) found their PECVD polysilicon films to be compressive. They introduced up to  $5 \times 10^{20}$  phosphorous atoms/cm<sup>3</sup> in the films by adding phosphine (PH<sub>3</sub>) to the gas ambient. However, they also introduced in the film up to  $3 \times 10^{20}$  chlorine atoms/cm<sup>3</sup>, which were supplied by the dichlorosilane (SiH<sub>2</sub>Cl<sub>2</sub>) used as the silicon source.

## 10.8 PECVD OF EPITAXIAL FILMS

### 10.8.1 Silicon

Silicon epitaxial layers are commercially deposited by atmospheric or reduced (40-100 Torr) pressure CVD at temperatures of 1050 to 1200°C (75). The relatively high deposition temperature imposes limits on the minimum thickness and conductivity of films deposited on heavily doped substrates because of dopant redistribution during growth. These limitations restrict the levels of integration available for VLSI applications, and evidence the need for a lower temperature technique capable of depositing high quality silicon epitaxial layers. Molecular beam epitaxy (76), ion beam epitaxy (77), ion cluster

beam deposition (78), solid phase epitaxy (79), ultra high vacuum/CVD (80), and photoenhanced CVD (81) have been proposed as possible low temperature alternatives. Another interesting alternative is PECVD.

Silicon epitaxial layers have been deposited by PECVD at a temperature as low as 800°C using a horizontal water-cooled reactor (82). A  $\text{SiH}_4/\text{H}_2$  (27 MHz) discharge produced deposition rates of 200 Å/min at 800°C, silane partial pressures of about 1 mTorr, and operating pressures of 0.2 to 0.6 Torr. The substrate surface was in-situ cleaned by a hydrogen plasma for a few minutes at the deposition temperature immediately before the start of the deposition. The success of these experiments was attributed to this predeposition plasma cleaning step.

Silicon epitaxial layers have also been deposited at a temperature of 750°C using a vertically aligned PECVD system with rf (13.56 MHz) excitation (7,83). The glow discharge was confined between two mesh electrodes perpendicular to the gas flow, and the wafer was located downstream, parallel to the electrodes, and 150 mm below the lowest electrode. These experiments were carried out at much lower operating pressures,  $1 \times 10^{-2}$  and  $3 \times 10^{-3}$  Torr, but yielded higher deposition rates, 1980 and 840 Å/min, respectively. The power level supplied to the discharge was 200 watts. The gas ambient consisted of silane, but germanium was added to the plasma at the beginning of the deposition. The addition of germanium was found to be essential, and it was proposed that it cleaned the wafer surface by removing the native silicon dioxide layer coating the substrate. The addition of germanium, moreover, resulted in the formation of a Si-Ge alloy in the first 1000 Å of the epitaxial film. Predeposition cleaning consisting of HCl gas (850°C, 10 min) was found unsuitable because it produced epitaxial films with hazy surfaces. The films were in-situ doped by adding phosphine diluted in helium to the plasma, but they had to be annealed (1000°C, 60 min) to electrically activate most of the phosphorus in the film.

Silicon epitaxial films have been deposited at temperatures as low as 650°C using a low pressure CVD system both with and without plasma enhancement using silane (84-87). The reaction chamber consists of a quartz tube fitted with a polished flange and sealed to water-cooled stainless-steel flanges using silicone or Kalrez gaskets (see Fig. 11) (87). A graphite susceptor is suspended from the upper flange and it holds a single wafer (50 or 100 mm) in a vertical position facing an infrared lamp array. A 510 l/s turbomolecular pump system permits total flow rates up to 100 sccm while achieving a hydrocarbon free base pressure in the  $10^{-8}$  Torr range. Operating pressures are 1-100 mTorr. The rf power supply is a 1 kW, 13.56-MHz generator coupled to the reactor through an automatic matching network. Plasma powers from 2.5 to 100 W may be used. A dc power supply is additionally used to bias the susceptor relative to ground. This arrangement decouples substrate biasing from rf plasma power or electrode self-bias.

Figure 12 shows Arrhenius plots of  $\langle 100 \rangle$  growth rates with (PECVD) and without (CVD) plasma enhancement for temperatures from 750 to 800°C and a silane total pressure of 6 mTorr (88). The thermal CVD deposition rates range from 500 to 600 Å/min and exhibit an apparent activation energy of about 8 kcal/mole. Low rf power (2.5 W) plasma enhanced depositions are 20% faster in this temperature range. By increasing the plasma power to 20 W, an additional 10% growth rate increase is obtained.

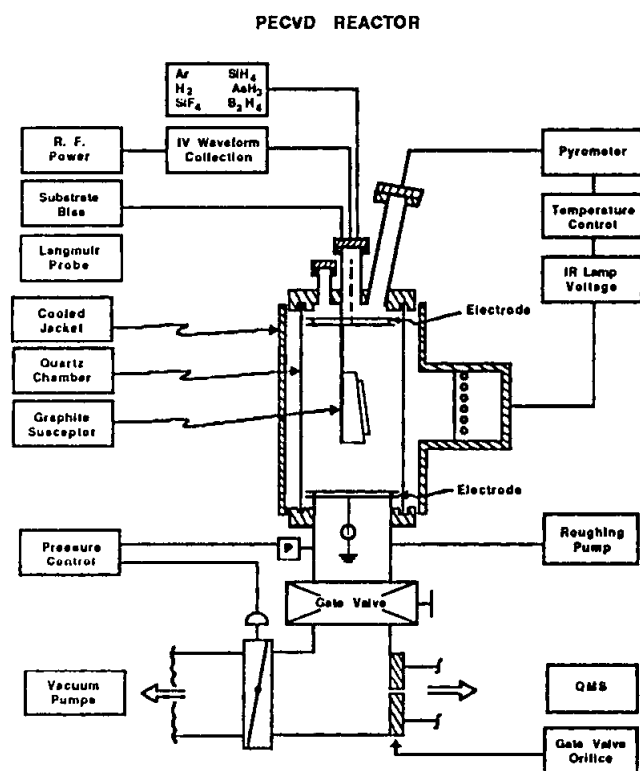


**Figure 11:** Cross-sectional schematic of PECVD epitaxial silicon reaction chamber (87).

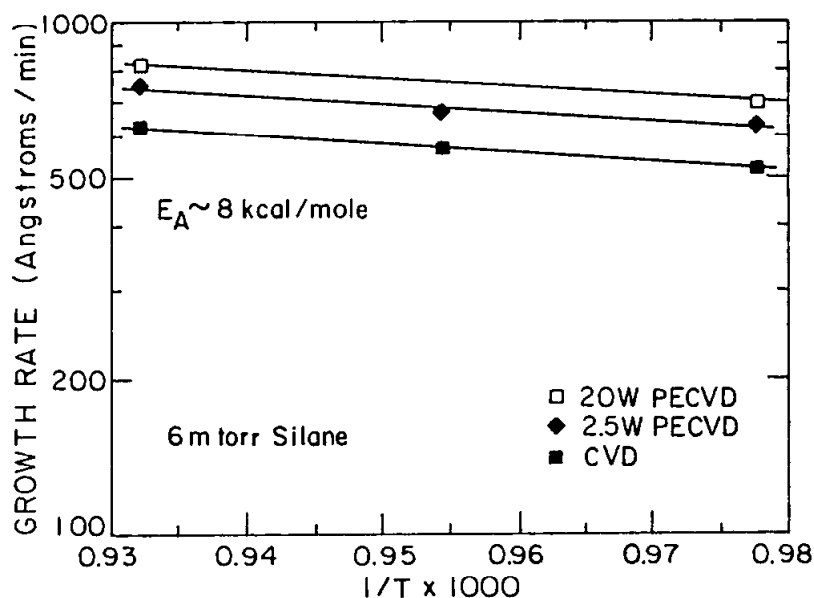


**Figure 12:** Arrhenius plots of <100> growth rates with and without plasma enhancement (PECVD and CVD, respectively) (88).

A predeposition in-situ cleaning of the substrate surface to remove the native silicon dioxide was found essential for achieving epitaxial growth. Surface cleaning was done by sputtering the wafer in a 5-W argon plasma at deposition temperature for 8-16 min with a negative dc bias of 100 V applied to the susceptor (87,89). Lightly doped epitaxial layers deposited on heavily doped silicon substrates by this technique exhibit extremely

abrupt dopant concentration profiles (85). PECVD also makes possible the in-situ incorporation of large quantities of arsenic ( $> 10^{19}\text{cm}^{-3}$ ) in the epitaxial layer without degrading film growth rate and morphology (90).

### 10.8.2 Gallium Arsenide

Several groups have also reported the plasma-enhanced, metal organic CVD (PE-MOCVD) of epitaxial GaAs films (11,12,91-94). Remote plasma configurations are typically used, in which the plasma is confined to a region and separated some distance from the substrate downstream. In these remote plasmas, the growth rate is very sensitive to the distance separating the plasma and the substrate, decreasing as the distance increases. The epitaxial growth rate has also been found to increase with rf power and with substrate temperature. The apparent activation energy from Arrhenius plots is about 13-14 kcal/mole.

## 10.9 PECVD OF REFRACTORY METALS AND THEIR SILICIDES

Refractory metals and their silicides are compatible with high temperature IC processing and have relatively high conductivities (metals:  $\approx 5\mu\Omega\text{-cm}$ , silicides: 16-40  $\mu\Omega\text{-cm}$  (95,96)). Consequently, they are attractive as gate, interconnection, and contact metallization materials in VLSI circuits. These materials can be deposited by physical vapor deposition (PVD) methods such as evaporation (97) and sputtering (98), by chemical vapor deposition (CVD) (99), and by PECVD.

### 10.9.1 Refractory Metals

Tungsten (W) films have been deposited in a radial-flow, parallel plate reactor with rf (4.5 MHz) excitation using tungsten hexafluoride ( $\text{WF}_6$ ) and  $\text{H}_2$  (100,101). Hydrogen was used to scavenge fluorine species, which otherwise etch the tungsten film being deposited. Deposition rates of about 40 Å/min were obtained at a substrate temperature of 350°C, operating pressure of 0.2 Torr, and rf power density of 0.06 W/cm<sup>2</sup>. Auger studies indicated that silicon and oxygen were present in the films. The silicon contamination may have come from silicon tetrafluoride ( $\text{SiF}_4$ ) in the  $\text{WF}_6$  source gas. XPS measurements indicated that the as-deposited (350°C) films have  $\approx 1.1 - 1.5$  at. % fluorine, which drops to  $\approx 0.5$  at. % after heat treatments ( $\geq 650^\circ\text{C}$ ) in forming gas (23). Film resistivity was sensitive to the  $\text{H}_2/\text{WF}_6$  ratio in the ambient, with higher ratios yielding lower resistivities. This is probably because the scavenging of fluorine becomes more effective at higher hydrogen concentrations, and lowers the fluorine contamination in the deposited film. The resistivity of as-deposited films decreased with increasing deposition temperature (probably because of larger grains and/or lower defect concentrations), increasing rf power, and decreasing rf frequency and pressure (23). The resistivity also decreased with post-deposition heat treatments, presumably because of outdiffusion of contaminants (e.g., fluorine), annealing of radiation-induced defects created during deposition, or increases in the size of the grains. Films deposited at 400°C and subsequently annealed at 1100°C for 30 min had their resistivities lowered from 40  $\mu\Omega\text{-cm}$  to 7  $\mu\Omega\text{-cm}$ .

PECVD molybdenum (Mo) films have been deposited from molybdenum hexafluoride ( $\text{MoF}_6$ ) and  $\text{H}_2$  (100,101). These films were heavily contaminated with



fluorine ( $\approx 15$  at. %) and had high resistivities ( $> 10^{-2}\Omega\text{--cm}$  for a  $0.3\text{-}\mu\text{m}$ -thick film). Molybdenum films have also been deposited from molybdenum hexacarbonyl  $[\text{Mo}(\text{CO})_6]$  in a dc discharge onto the cathode of a parallel plate system, but these films contained 20 to 30 wt % carbon (102). A more successful attempt used molybdenum pentachloride ( $\text{MoCl}_5$ ) diluted in  $\text{H}_2$  at a pressure of 1 Torr and temperatures of 170 to  $430^\circ\text{C}$  (13,99). The as-deposited Mo films were amorphous, but crystallized after high temperature annealing. Auger analysis indicated the presence of chlorine and oxygen in the as-deposited films. The chlorine concentration in the films decreased after post-deposition heat treatments. The resistivity of as-deposited films decreased with increasing deposition temperature, probably because the incorporation of unreacted chloride in the film decreased with increasing temperatures. The resistivity of these films decreased significantly after a post-deposition annealing at  $800^\circ\text{C}$  for 20 min in nitrogen, presumably because of crystallization of the films and/or outdiffusion of chlorine. The lowest resistivity obtained for Mo films, after annealing, was  $\approx 10\mu\Omega\text{--cm}$ .

Although the high conductivities of refractory metals are desirable for gate and inter-connection applications, these materials are chemically unstable in oxidizing ambients (95). Consequently, the silicides of these metals have been used, although their resistivities are an order of magnitude higher than those of the refractory metals. PECVD has been used to deposit silicides of molybdenum, tungsten, tantalum, and titanium.

### 10.9.2 Refractory Metal Silicides

Mo-silicide films were obtained by adding  $\text{SiH}_4$  diluted in argon to the  $\text{MoCl}_5/\text{H}_2$  plasma discussed above (13). The film composition was controlled by adjusting the composition of the gas ambient. The resistivity of as-deposited films increased with increasing  $\text{SiH}_4$  flow rate, possibly because of a decrease in the Mo content of the film. The resistivity of these films also increased with increasing hydrogen flow rate, presumably because of a higher concentration of unreacted chloride in the film. The as-deposited films were amorphous and crystallized into the hexagonal structure after a post-deposition annealing in nitrogen at  $1000^\circ\text{C}$  for 20 min. It was proposed that chlorine atoms segregated in the grain boundaries prevented the hexagonal structure from changing to the tetragonal structure associated with sputtered and CVD  $\text{MoSi}_2$  (99). As-deposited ( $400^\circ\text{C}$ ) PECVD resistivities are  $\approx 800\mu\Omega\text{--cm}$  (13).

Tungsten silicides ( $\text{W}_x\text{Si}_{1-x}$ ) have been deposited in a parallel-plate reactor with rf (13.56 MHz) excitation using  $\text{WF}_6$  and  $\text{SiH}_4$  diluted in helium (103). Deposition rates were about 550 to  $600\text{ \AA}/\text{min}$  at a substrate temperature of  $230^\circ\text{C}$ , and an operating pressure between 0.5 and 0.7 Torr. The atomic ratio of W/Si in the film was controlled by the  $\text{WF}_6/\text{SiH}_4$  ratio in the gas ambient. The resistivity of the films decreased with post-deposition heat treatments. This is particularly interesting because the  $\text{W}_x\text{Si}_{1-x}$  films with  $x \leq 0.45$  were amorphous both as deposited and after a post-deposition annealing at  $1100^\circ\text{C}$  for 60 min in nitrogen. Therefore, the decrease in resistivity upon annealing was attributed to outdiffusion of F and H, presumably present in the as-deposited films, and not to the crystallization of the films. The lowest resistivity obtained with these films, after annealing, was about  $40\mu\Omega\text{--cm}$ .

Tantalum-silicide films have been deposited by reacting tantalum pentachloride ( $\text{TaCl}_5$ ) and  $\text{SiH}_2\text{Cl}_2$  in a hydrogen ambient (104). The films were deposited at 1.38 Torr using an inductive-coupled rf (600 kHz or 3.5 MHz) glow discharge. Films deposited at

temperatures below 540°C were amorphous, while those deposited at temperatures above 580°C were crystalline and had a resistivity of  $70\mu\Omega\text{--cm}$ . The film thicknesses were about 2000 to 5000 Å. After annealing at 900°C for 1 hour in an argon ambient, the resistivity decreased to  $55\mu\Omega\text{--cm}$ .

Titanium-silicide films have been obtained by reacting titanium tetrachloride ( $\text{TiCl}_4$ ) and  $\text{SiH}_4$  in an argon plasma (105). The depositions were carried out in a hot-wall, parallel-plate, 300 kHz plasma reactor at 1 Torr and temperatures of 300 and 350°C. The film composition was very sensitive to gas-phase composition. The as-deposited films were amorphous, but crystallized after a 750°C anneal for 1 hour to yield a resistivity of  $20\mu\Omega\text{--cm}$ .

Titanium-silicide films have also been deposited in a PECVD system similar to that shown in Fig. 9 but with a modified version of the boat assembly to prevent arcing (106). The rf generator operates at 50 kHz. Deposition rates of 60 to 80 Å/min are obtained with an rf power of about 100 watts and deposition temperatures of 300 to 500°C. The reactants are  $\text{SiH}_4$  and  $\text{TiCl}_4$  diluted in argon. The as-deposited films are amorphous, but crystallize upon sintering above 600°C. Resistivities as low as  $20\mu\Omega\text{--cm}$  were obtained after annealing at 650°C for 5 min. In depositions carried out at 450°C and 1.75 Torr,  $\text{TiSi}_x$  layers with different silicon compositions were obtained (107). The silicon content was varied from  $x = 1.1$  to 2.0 by varying the  $\text{TiCl}_4/\text{SiH}_4$  flow rate ratio from 0.23 to 0.09.

### 10.10 PECVD OF DIAMOND FILMS

The high thermal conductivity, transparency, hardness, and high-temperature semiconductor properties of diamond make it an attractive material for many possible applications. Consequently, the low-pressure, low-temperature growth of crystals and thin films of diamond has been the subject of intense research recently (15,16). PECVD techniques are being investigated because a critical issue with this material is the need for lower temperature deposition techniques.

Diamond films have been deposited at pressures of 1-50 Torr, substrate temperatures above 700°C, and relatively high ( $>500\text{ W}$ ) rf powers (15,16). Arc, dc, rf, and microwave discharges have been utilized. Methane/hydrogen mixtures are typically used, and growth rates are approximately 1-20  $\mu\text{m}/\text{hour}$ . This material technology is in its infancy, and it is growing at a very fast pace.

### 10.11 OTHER PLASMA DEPOSITION CONFIGURATIONS

Microwave multipolar plasmas (MMP) are 2.45 GHz glow discharges confined by multipolar magnetic fields. The main differences between MMP's and the conventional plasmas discussed here are: (i) in MMP's, plasma excitation and plasma-surface interactions are decoupled, and (ii) there is no self-bias in MMPs, and the substrate bias and ion bombardment energies can be controlled independently. The microwave excitation can be applied in three ways: (i) localized electron cyclotron resonance, (ii) surface wave, and (iii) distributed electron cyclotron resonance (DECR). The latter (DECR) appears

to be the most technologically promising. Silicon epitaxial layers have been deposited by DECR excitation at temperatures as low as 400°C (108).

Magnetically enhanced plasma deposition is another configuration in which a magnet is added to confine the electrons near the electrode thereby increasing the rate of electron dissociation collisions with molecules. As a result, a glow discharge can be maintained at pressures in the 1-10 mTorr range. Silicon oxide, silicon nitride, and silicon oxynitride films have been deposited by this technique, as well as other inorganic and organic films (109).

Afterglow CVD is a remote plasma technique that provides independent control of the generation of active species and the reaction chemistry. In the afterglow technique, only certain desired species are excited by the glow discharge. These are then transported to the vicinity of the wafer where the desired deposition reactions take place. The afterglow technique does not require the wafer to be exposed to the plasma discharge environment. Furthermore, it allows independent optimization of plasma, afterglow, and wafer parameters. This technology is presently being used to deposit silicon oxide films (110).

## 10.12 SUMMARY

This chapter discussed the plasma enhanced chemical vapor deposition technique as applied to thin films for microelectronic applications. In particular, fundamental aspects of nonequilibrium glow discharges were reviewed, as well as the voltage distribution in rf plasma systems. A qualitative model for PECVD was presented, and commercial PECVD systems were briefly reviewed. The PECVD of films of present commercial importance, such as silicon nitride and silicon oxide, was discussed. The state-of-the-art in the development of the PECVD of films such as polycrystalline silicon, epitaxial silicon and gallium arsenide, refractory metals and their silicides, and diamond, was also discussed. PECVD will continue to be the preferred commercial technique for the low temperature deposition of silicon nitride and oxide films, and is showing great promise for the deposition of semiconductor and conductor films.

## 10.13 REFERENCES

1. Gorowitz, B., Gorczyca, T. B., and Saia, R. J., Solid State Technol. 28(6): 197 (1985).
2. Adams, A. C., in VLSI Technology, S. Sze, Editor, Chap. 3, McGraw-Hill, New York, 1983.
3. Adams, A. C., Solid State Technol. 26(4): 135 (1983).
4. Kamins, T. I., and Chiang, K. L., J. Electrochem. Soc. 129: 2326 (1982) and 2331 (1982).
5. Burger, W. R., Donahue, T. J., and Reif, R., in VLSI Science and Technology/1982, C. J. Dell'Oca and W. M. Bullis, Editors, pp. 87-93, The Electrochemical Society, Proc. Vol. 82-7, Pennington, NJ, 1982.
6. Hajjar, J.-J., Reif, R., and Adler, D., J. Electronic Mat. 15: 279 (1986).

7. Suzuki, S., and Itoh, T., J. Appl. Phys. 54: 1466 (1983).
8. Shanfield, S. R., and Reif, R., The Electrochem. Soc. Extended Abstracts, Vol. 83-1, Abs. 144, pp. 230-231 (1983).
9. Comfort, J. H., Garverick, L. M., and Reif, R., J. Appl. Phys. 62: 3388 (1987).
10. Hariu, T., Takenaka, K., Shibuya, S., Komatsu, Y., and Shibata, Y., Thin Solid Films 80: 235 (1981).
11. Pande, K. P., The Electrochem. Soc. Extended Abstracts, Vol. 83-1, Abs. 340, pp. 531-532 (1983).
12. Pande, K. P., and Seabaugh, A. C., J. Electrochem. Soc. 131: 1357 (1984).
13. Tabuchi, A., Inoue, S., Maeda, M., and Takagi, M., Proceedings of the 23rd Symposium on Semiconductors and IC Technology of the Electrochemical Society of Japan, p. 60 (Dec. 1-2, 1982).
14. Hess, D. W., in VLSI Electronics: Microstructure Science, N. G. Einspruch and D. M. Brown, Editors, p. 55, Academic Press, New York, 1984.
15. Chang, C.-P., Flamm, D. L., Ibbotson, D. E., and Mucha, J. A., J. Appl. Phys. 63: 1744 (1988).
16. Meyer, D. E., Ianno, N. J., Woollam, J. A., Swartzlander, A. B., and Nelson, A. J., J. Mater. Res. 3: 1397 (1988).
17. Reinberg, A. R., Ann. Rev. Material Sci. 9: 341 (1979).
18. Reinberg, A. R., J. Electronic Mat. 8: 345 (1979).
19. Ojha, S. M., in Physics of Thin Films, G. Hass, M. H. Francombe, and J. L. Vossen, Editors, Vol. 12, p. 237, Academic Press, New York, 1982.
20. Hess, D. W., in Silicon Processing, D. C. Gupta, Editor, p. 218, American Society for Testing and Materials, 1983.
21. Hess, D. W., J. Vac. Sci. Technol. A2: 244 (1984).
22. Bonifield, T. D., in Deposition Technologies for Films and Coatings, R. F. Bunshah, Editor, p. 365, Noyes Publications, New Jersey, 1982.
23. Hess, D. W., in Reduced Temperature Processing for VLSI, R. Reif, and G. R. Srinivasan, Editors, p. 3, The Electrochemical Society, New Jersey, 1986.
24. Sherman, A., Thin Solid Films 113: 135 (1984).
25. Chapman, B., Glow Discharge Processes, John Wiley, New York, 1980.
26. Rand, M. J., J. Vac. Sci. Technol. 16: 420 (1979).
27. Greene, J. E., and Barnett, S. A., J. Vac. Sci. Technol. 21: 285 (1982).
28. Greene, J. E., Solid State Technology 30(4): 115 (1987).
29. Turban, G., Catherine, Y., and Grolleau, B., Thin Solid Films 60: 147 (1979).
30. Sawin, H. H., Solid State Technol. 28: 211 (1985).
31. Brown, S. C., Basic Data of Plasma Physics, MIT Press, Cambridge, MA, 1966.
32. Kushner, M. J., J. Appl. Phys. 63: 2532 (1988).
33. Hollahan, J. R., and Bell, A. T., Editors, Techniques and Applications of Plasma Chemistry, John Wiley, New York, 1974.
34. Vossen, J. L., J. Electrochem. Soc. 126: 319 (1979).

35. Reif, R., J. Vac. Sci. Technol. A2: 429 (1984).
36. Köhler, K., Coburn, J. W., Horne, D. E., Kay, E., and Keller, J.H., J. Appl. Phys. 57: 59 (1985).
37. Koenig, H. R., and Maissel, L. I., IBM J. Res. Dev., 14: 276 (1970).
38. Coburn, J. W., and Kay, E., J. Appl. Phys., 43: 4965 (1972).
39. Horwitz, C. M., J. Vac. Sci. Technol. A1: 60 (1983).
40. Reif, R., Kamins, T. I., and Saraswat, K. C., J. Electrochem. Soc. 126: 644 (1979).
41. Reinberg, A. R., The Electrochem. Soc. Extended Abstracts, Vol. 74-1, Abs. 6, Spring Meeting (1974).
42. Sinha, A. K., Solid State Technol. 23(4): 133 (1980).
43. Kumagai, H. Y., Proceedings of the Ninth International Conference on Chemical Vapor Deposition, McD. Robinson et al., Editors, pp. 189-204, The Electrochemical Society, Proc. Vol. 84-6, Pennington, NJ (1984).
44. Hollahan, J. R., and Rosler, R. S., in Thin Film Processes, J. L. Vossen and W. Kern, Editors, Academic Press, New York, 1978.
45. Rosler, R. S., and Engle, G. M., Solid State Technol. 24(4): 172 (1981).
46. Weiss, A. D., Semiconductor International 6: 88 (1983).
47. Adams, A. C., in Reduced Temperature Processing for VLSI, R. Reif and G. R. Srinivasan, Editors, p. 111, The Electrochemical Society, New Jersey, 1986.
48. Maeda, M., and Nakamura, H., Thin Solid Films 112: 279 (1984).
49. Samuelson, G. M., and Mar, K. M., J. Electrochem. Soc. 129: 1773 (1982).
50. Sinha, A. K., and Smith, T. E., J. Appl. Phys. 49: 2756 (1978).
51. Chow, R., Lanford, W. A., Ke-Ming, W., and Rosler, R. S., J. Appl. Phys. 53: 5630 (1982).
52. Sinha, A. K., Levinstein, H. J., Smith, T. E., Quintana, G., and Haszko, S. E., J. Electrochem. Soc. 125: 601 (1978).
53. Koyama, K., Takasaki, K., Maeda, M., and Takagi, M., The Electrochem. Soc. Extended Abstracts, Vol. 81-2, Abs. 301, pp. 738-740 (1981). Also in Plasma Processing, J. Dieleman, R. G. Grieser, and G. S. Mathad, Editors, p. 478, The Electrochemical Society, Proc. Vol. 82-7, Pennington, NJ (1984).
54. van den Ven, E. P. G. T., Solid State Technol. 24(4): 167 (1981).
55. Zhou, N. S., Fujita, S., and Sasaki, A., J. Electronic Mat. 14: 55 (1985).
56. Mar, K. M., and Samuelson, G. M., Solid State Technol. 23(4): 137 (1980).
57. Classen, W., et al., J. Electrochem. Soc. 132: 893 (1985).
58. Ritchie, W., and Metz, W., The Electrochem. Soc. Extended Abstracts, Vol. 82-2, Abs. 187, pp. 295-296 (1982).
59. Kaganowicz, G., Ban, V. S., and Robinson, J. W., J. Vac. Sci. Technol. A2: 1233 (1984).
60. Chu, J. K., Sachdev, S., and Gargini, P. A., The Electrochem. Soc. Extended Abstracts, Vol. 83-2, Abs. 321, pp. 510-511 (1983).
61. Avigal, I., Solid State Technol. 26(10): 217 (1983).

62. Tong, J. E., Schertenleib, K., and Carpio, R. A., Solid State Technol. 27(1): 161 (1984).
63. Seto, J. Y. W., J. Appl. Phys. 46: 5247 (1975).
64. Kamins, T. I., J. Electrochem. Soc. 127: 686 (1980).
65. Matsui, M., Shiraki, Y., Katayama, Y., Kobayashi, K. I., Shintani, A., and Maruyama, E., Appl. Phys. Lett. 37: 936 (1980).
66. Mahan, J. E., Newman, D. S., and Gullett, M., IEEE Trans. Electron Dev. ED-30: 45 (1983).
67. Hirai, Y., Osada, Y., Komatsu, T., Omata, S., Aihara, K., and Nakagiri, T., Appl. Phys. Lett. 42: 701 (1983).
68. Seager, C. H., Sharp, D. J., Panitz, J. K. G., and Hanoka, J. I., J. Vac. Sci. Technol. 20: 430 (1982).
69. Morin, F., and Morel, M., Appl. Phys. Lett. 35: 686 (1979).
70. Burger, W. R., Donahue, T. J., and Reif, R., Proceedings of the Fourth European Conference on Chemical Vapor Deposition, J. Bloem et al., Editors, pp. 265-272, Eindhoven Druk B. V. (1983).
71. Hamasaki, T., Kurata, H., Hirose, M., and Osaka, Y., Appl. Phys. Lett. 37: 1084 (1980).
72. Nagata, Y., and Kunioka, A., Appl. Phys. Lett. 38: 142 (1981).
73. Veprek, S., Iqbal, Z., Oswald, H. R., and Webb, A. P., J. Phys. C: Solid State 14: 295 (1981).
74. Usui, S., and Kikuchi, M., J. Non-crystalline Solids 34: 1 (1979).
75. Borland, J. O., and Drowley, C., Solid State Technology 28: 141 (1985).
76. Ota, Y., J. Appl. Phys. 51: 1102 (1980).
77. Zalm, P. C., and Beckers, L. J., Appl. Phys. Lett. 41: 167 (1982).
78. Takagi, T., Yamada, I., and Sasaki, A., Thin Solid Films 39: 207 (1976).
79. Quach, N. T., and Reif, R., Appl. Phys. Lett. 45: 910 (1984).
80. Meyerson, B. S., Appl. Phys. Lett. 48: 797 (1986).
81. Ishitani, A., Ohshita, Y., Tanigaki, K., Takada, K., and Itoh, S., J. Appl. Phys. 61: 2224 (1987).
82. Townsend, W. G., and Uddin, M. E., Solid State Electronics 16: 39 (1973).
83. Suzuki, S., Okuda, H., and Itoh, T., Jap. J. Appl. Phys., 19: Supplement 19-1: 647 (1979).
84. Donahue, T. J., Burger, W. R., and Reif, R., Appl. Phys. Lett. 44: 346 (1984).
85. Donahue, T. J., and Reif, R., J. Appl. Phys. 57: 2757 (1985).
86. Reif, R., J. Electrochem. Soc. 131: 2430 (1984).
87. Comfort, J. H., Garverick, L. M., and Reif, R., J. Appl. Phys. 62: 3388 (1987).
88. Comfort, J. H., and Reif, R., J. Electrochem. Soc. to be published (1989).
89. Yew, T. R., Comfort, J. H., Garverick, L. M., Berger, W. R., and Reif, R., Mat. Res. Soc. Symp. Proc., Vol. 75: p. 705 (1987).

90. Comfort, J. H., and Reif, R., Appl. Phys. Lett. 51: 1536 (1987).
91. Heinecke, H., Brauers, A., Luth, H., and Balk, P., J. Crystal Growth 77: 241 (1986).
92. Pande, K. P., and Aina, O., J. Vac. Sci. Technol. A4: 673 (1986).
93. Huelsman, A. D., Reif, R., and Fonstad, C. G., Appl. Phys. Lett. 50: 206 (1987).
94. Huelsman, A. D., and Reif, R., J. Vac. Sci. Technol. to be published (1989).
95. Murarka, S. P., in Semiconductor Silicon 1981, H. R. Huff et al., Editors, pp. 551-561, The Electrochemical Soc., Proc. Vol. 81-5, Pennington, NJ, 1981.
96. Murarka, S. P., Materials Lett. 38: 142 (1981).
97. Murarka, S. P., J. Vac. Sci. Technol. 17: 775 (1980).
98. Crowder, B. L., and Zirinsky, S., IEEE Trans. Elec. Dev. ED-26: 369 (1979).
99. Inoue, S., Toyokura, N., Nakamura, T., Maeda, M., and Takagi, M., J. Electrochem. Soc. 130: 1603 (1983).
100. Chu, J. K., Tang, C. C., and Hess, D. W., Appl. Phys. Lett. 41: 75 (1982).
101. Tang, C. C., Chu, J. K., and Hess, D. W., Solid State Technol. 26: (3) 125 (1983).
102. Okuyama, F., Appl. Phys. Lett. A28: 125 (1982).
103. Akitmoto, K., and Watanabe, K., Appl. Phys. Lett. 39: 445 (1981).
104. Hieber, K., Stolz, M., and Wieczorik, C., Proceedings of the Ninth International Conference on Chemical Vapor Deposition, pp. 205-212, The Electrochemical Society, Proc. Vol. 84-6, Pennington, NJ (1984).
105. Kemper, M. J. H., Koo, S. W., and Huizinga, F., The Electrochem. Soc. Extended Abstracts, Vol. 84-2: Abs. 377, pp. 533-534 (1984).
106. Rosler, R. S., and Engle, G. M., J. Vac. Sci. Technol. B2: 733 (1984).
107. Hara, T., Ishizawa, Y., Wu, H. M., Hemmes, D. G., and Rosler, R. S., Proceedings of the Tenth International Conference on Chemical Vapor Deposition, G. W. Cullen, Editor, pp. 867-876, The Electrochemical Society, Proc. Vol. 87-8, Pennington, NJ (1987).
108. Burke, R. R., and Pomot, C., Solid State Technology p. 67, February 1988.
109. Leahy, M. F., and Kaganowicz, G., Solid State Technology p. 99, April 1987.
110. Jackson, R. L., Spencer, J. E., McGuire, J. L., and Hoff, A. M., Solid State Technology p. 107, April 1987.

---

# Electron Cyclotron Resonance Microwave Discharges For Etching and Thin Film Deposition

---

**Jes Asmussen**

A recent, important development in low pressure and low temperature plasma processing is the microwave electron cyclotron resonance (ECR) discharge. Its lack of electrodes and its ability to create high densities of charged and excited species at low pressures ( $\leq 10^{-4}$ Torr) make it an attractive processing discharge in etching and thin film deposition applications. This paper reviews the basic physics of ECR discharges and reviews the associated microwave system and applicator technologies. Waveguide and cavity ECR applicators are compared and are described in detail. Several ECR plasma processing reactors are also described. Methods of processing large surfaces are outlined and typical experimentally measured ECR discharge characteristics are also presented.

## 11.1 INTRODUCTION

Microwave discharges have experienced intense interest and use in recent years. Their electrodeless nature together with their ability to create high densities of excited and charged species have made both high pressure and low pressure microwave discharges an attractive technology for many plasma processing applications. By using the appropriate microwave applicators, microwave discharges can be efficiently created and maintained from pressures above several atmospheres (1-3) to sub-mTorr pressures (4-14) resulting in high pressure discharges with high temperatures ( $\geq 1000$ K) for thermal processing applications, and low temperature and low pressure discharges for applications such as thin film deposition and etching. Recent and notable experiments which demonstrate diamond thin film growth in a microwave discharge (15) utilize discharge pressures of 1-100 Torr. These discharge applications lie in the transition between a purely thermal and low temperature discharge.

An important development in low pressure and low temperature microwave plasma processing is the electron cyclotron resonance (ECR) discharge. This technology, borrowed from fusion (16) and electric propulsion (17) plasmas and modified for the requirements of plasma processing (4,5,8-13) can create a variety of low pressure ( $< 0.5$  Torr) discharges. As the name ECR suggests, microwave energy is coupled to the natural resonant frequency of the electron gas in the presence of a static magnetic field. This



resonant frequency occurs when the electron cyclotron frequency equals the excitation frequency. The cyclotron frequency is found as:

$$\omega_{ce} = \frac{eB}{m_e} \quad (1)$$

where  $e$  is charge on an electron,  $B$  is the strength of the static magnetic field, and  $m_e$  is the electron mass. In an actual discharge, this condition can be satisfied in a volume or surface layer within the discharge where the static magnetic field strength is adjusted to resonance, i.e.  $\omega = \omega_{ce}$  and a component of electric field is perpendicular to the static magnetic field. The electrons are accelerated in this ECR volume and in turn ionize and excite the neutral gas. The result is a low pressure, almost collisionless, plasma which can be varied from a weakly to a highly ionized state by changing discharge pressure, gas flow rates and input microwave power. The electrodeless and noncollisional heating nature of the discharge together with the availability of well established, low cost microwave power supplies make ECR plasma sources attractive for many plasma processing applications.

This chapter reviews the basic principles of ECR microwave discharge formation first by describing the physics of coupling microwave energy into the discharge and then briefly describes microwave system and applicator technology. ECR waveguide and cavity applicators are described and several ECR plasma reactor geometries used in etching and film deposition are reviewed. Finally measured characteristics of ECR discharges are presented.

## 11.2 ENERGY COUPLING AND POWER BALANCE IN STEADY STATE MICROWAVE DISCHARGES

A diagram of a generic microwave discharge configuration is shown in Fig. 1. The discharge occupies a finite volume,  $V_L$ , and is bounded by the discharge container walls. In practice the walls are made from a microwave transparent material such as quartz or are conducting waveguide walls. The discharge enclosure may also have an opening which allows the excited species and charged particles to diffuse out of the active discharge into a processing zone. An arbitrary discharge volume is composed of at least three interpenetrating gases, i.e. electron, ion, and neutral gases. A steady time independent density of neutrals, electrons and ions exists at each point within the discharge volume. In Fig. 1 the steady-state electron density is denoted as  $N_{e0}(\vec{r})$  where the  $\vec{r}$  dependence emphasizes that the density is a function of position within the discharge.

The time and spatially varying microwave electric field,  $\vec{E}(\vec{r})e^{j\omega t}$ , which maintains the discharge of Fig. 1, is represented by a dashed line. In general this electric field penetrates the discharge and may have a nonzero value at each point inside the discharge volume. A static but spatially varying magnetic field is also impressed on the discharge volume and in Fig. 1 is displayed as the solid field lines drawn in the shape of a magnetic mirror. ECR layers, which are the thin volumes in the discharge where  $\omega = \omega_{ce}$ , are displayed as the solid, curved lines.

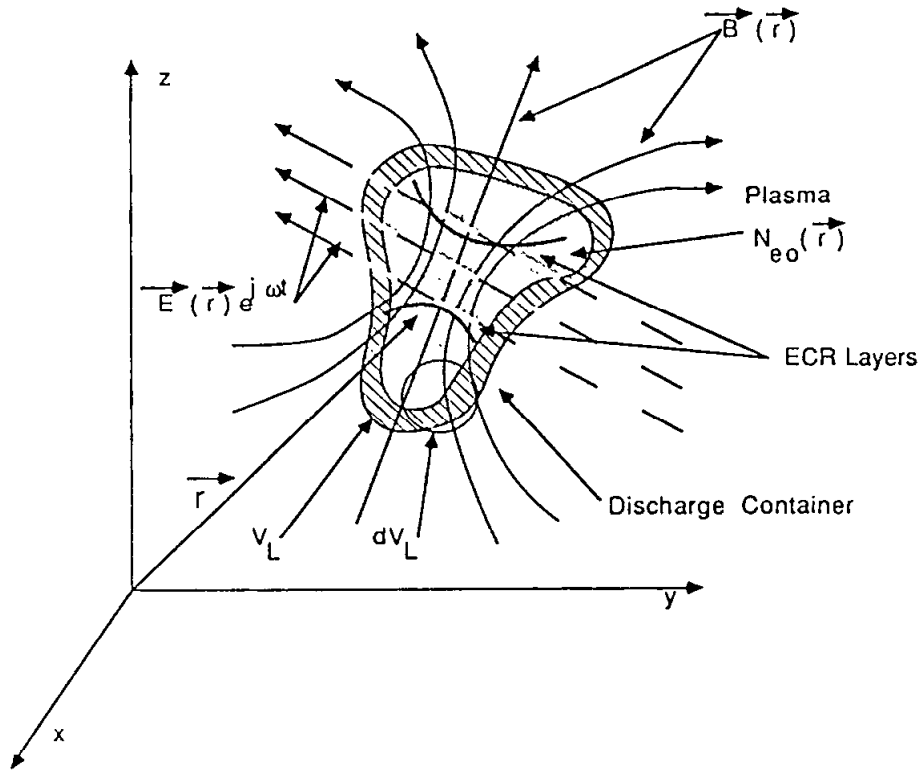


**Figure 1:** A generic microwave discharge immersed in an electromagnetic field and static magnetic field. The circle encloses an arbitrary differential volume  $dV_L$ .

A steady-state microwave discharge is characterized by the equality between the electromagnetic power absorbed by the plasma,  $P_a$  and the power losses,  $P_{loss}$ , in the plasma volume. Expressed as an equation

$$P_a = P_{loss} \quad (2)$$

The left hand term represents the total power delivered to the plasma by the electromagnetic field. The power absorbed in a unit volume is a function of position, and thus absorbed power per differential volume is expressed as

$$\langle P \rangle_{abs}(\vec{r}) = 1/2 \operatorname{Re} [\vec{E}(\vec{r}) \cdot (\vec{\sigma}(\vec{r}) \cdot \vec{E}(\vec{r})^*)] \quad (3)$$

where the discharge complex tensor conductivity  $\vec{\sigma}(\vec{r})$  and the electric field  $\vec{E}(\vec{r})$  are functions of position  $\vec{r}$  in the plasma and  $\langle P \rangle_{abs}(\vec{r})$  has units of power density.

For any differential plasma volume the power input, i.e. equation (3), must equal the power loss, i.e.,

$$\langle P \rangle_{\text{abs}}(\vec{r}) = \langle P \rangle_{\text{loss}}(\vec{r}) \quad (4)$$

where  $\langle P \rangle_{\text{loss}}(\vec{r})$  is the power lost per differential volume at position  $\vec{r}$ . Integrating over the entire plasma volume yields

$$P_a = \int_{V_L} \langle P \rangle_{\text{abs}}(\vec{r}) dV_L = \int_{V_L} \langle P \rangle_{\text{loss}}(\vec{r}) dV_L = P_{\text{loss}} \quad (5)$$

which is, of course, equation (2).

An understanding of the microwave discharge energy absorption and the discharge loss processes can be obtained by investigating the left and right hand sides of equation (5). Considering first the absorption process Eq. (3) includes the microwave energy absorption by both the electron and ion gases. However since the work done on a charged particle by an electric field between collisions varies inversely as the particle mass, the energy imparted to an electron is much greater than the energy imparted to an ion. Therefore direct energy transfer from the field to the ions usually can be neglected (except for ion cyclotron heating) and electromagnetic energy transfer to the discharge takes place through Joule (elastic and inelastic collisional heating) and electron cyclotron heating of the electron gas.

The heating and the energy interchange processes for a small differential volume are shown in Fig. 2. Since direct ion gas heating can be neglected for most plasma processing applications dashed lines are shown between the electric energy source and the ion gas. As shown, the electron gas is heated directly by the electric fields and in turn the heated electron gas transfers its energy to the neutral and ion gases by elastic and inelastic collisions. The neutral and ion gases thus become heated from these electron gas interactions and interchange energy by elastic ion-neutral collisions and transfer energy to the walls by heat conduction and convection.

Referring again to Fig. 2 the power lost per differential volume by the electron gas can be expressed in terms of the removal of energy per unit time from the electron gas by conduction and convection and by elastic and inelastic collisions. That is, per unit volume at position  $\vec{r}$  within the discharge

$$\langle P \rangle_{\text{loss}}(\vec{r}) = (\text{elastic collision losses}) + (\text{inelastic collision losses}) \\ + (\text{conduction and convection losses})$$

In equation form (neglecting electron heat conduction)

$$\langle P \rangle_{\text{loss}}(\vec{r}) = \left[ \left( \frac{5kT_e}{2} \right) \frac{D_a}{\Lambda^2} + \nu_{\text{men}} \left( \frac{2m_e}{M_n} \right) \frac{3k}{2} (T_e - T_n) + \right. \\ \left. eV_i \nu_i + \sum_j eV_{\text{exj}} \nu_{\text{exj}} \right] N_{e0}(\vec{r}) \quad (6)$$

where  $D_a$  = the ambipolar diffusion coefficients,  $T_e$  = the electron temperature,  $T_n$  = the neutral gas temperature,  $k$  = Boltzman's constant,  $\Lambda$  = discharge diffusion length,  $M_n$  = mass of the neutral atoms,  $\nu_i$  = ionization frequency,  $\nu_{men}$  = collision frequency for momentum transfer,  $\nu_{exj}$  = the  $j$ th excitation frequency,  $V_i$  = the ionization potential and  $V_{exj}$  = the excitation potential.

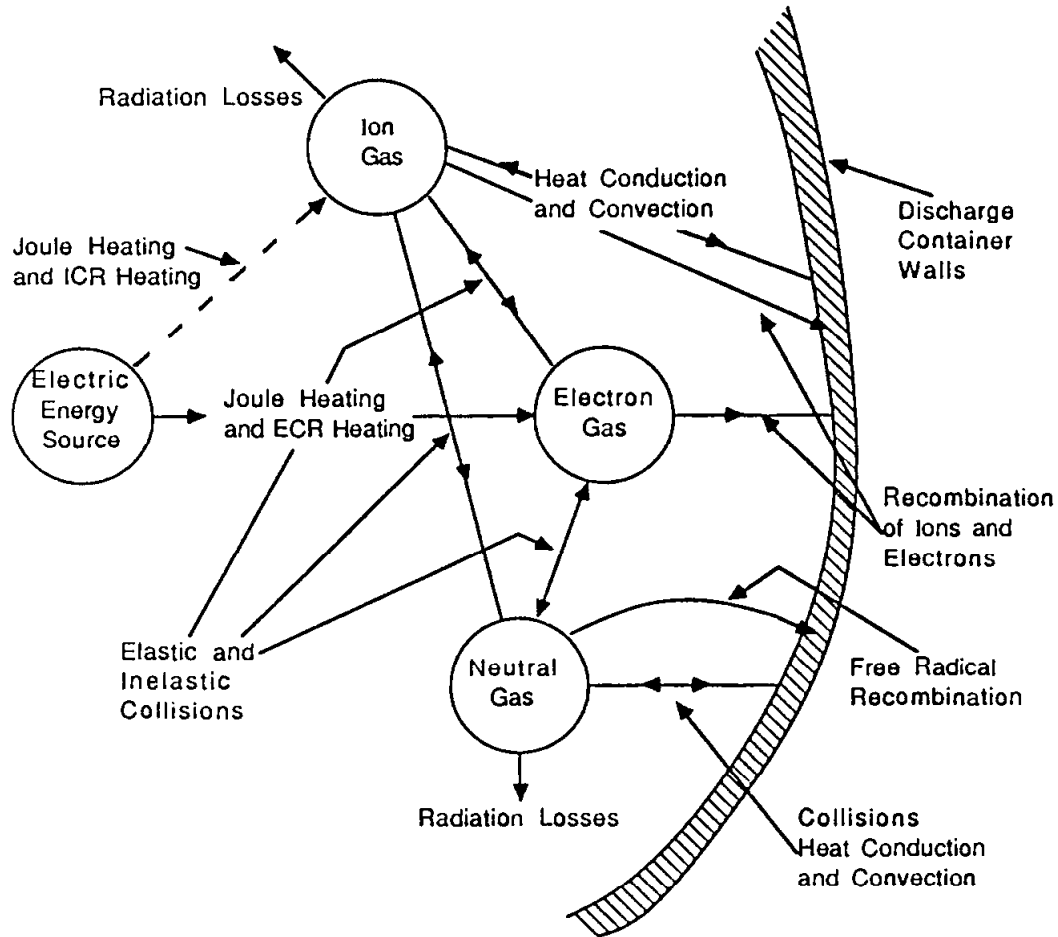


**Figure 2:** Microwave energy transfer in a weakly ionized gas. Energy coupling is shown for the arbitrary differential volume circled in Figure 1.

Integrating Eq. (6) over the entire discharge volume  $V_L$  yields the total power loss in the discharge. Thus it is apparent that discharge losses depend upon discharge geometry, pressure, gas type and the electron density. Since in the steady-state  $\langle P \rangle_{\text{loss}}(\vec{r}) = \langle P \rangle_{\text{abs}}(\vec{r})$ , the electric field required to sustain a discharge is dependent on many different experimental variables and in practice can vary over several orders of magnitude as pressure, gas type, flow rate, etc. are varied. Thus a versatile microwave discharge system must be able to adjust the impressed electric field for a wide range of experimental conditions. This has an important impact on the design of microwave power supplies and applicators.

### 11.3 MICROWAVE ENERGY COUPLING VS PRESSURE IN A UNIFORM MAGNETIC FIELD GRADIENT

Equation (3) can be written entirely in terms of power absorbed by the electron gas (18). Thus in the absence of a static magnetic field the time average absorbed power density is given by

$$\langle P \rangle_{\text{abs}}(\vec{r}) = \frac{N_{\text{eo}}(\vec{r})e^2}{2m_e\nu_e} \left[ \frac{\nu_e^2}{\omega^2 + \nu_e^2} \right] |E(\vec{r})|^2 \quad (7)$$

where  $N_{\text{eo}}(\vec{r})$  = the time independent electron density,  $|E(\vec{r})|$  = the magnitude of the electric field, and  $\nu_e$  = the effective collision frequency for electrons. This expression often is written in terms of an effective electric field, i.e.

$$\langle P \rangle_{\text{abs}}(\vec{r}) = \frac{N_{\text{eo}}(\vec{r})e^2}{m_e\nu_e} |E_e|^2 \quad (8)$$

$$\text{where } |E_e| = \frac{|E(\vec{r})|}{\sqrt{2}} \frac{\nu_e}{\sqrt{\nu_e^2 + \omega^2}} = \text{effective electric field.}$$

If a static magnetic field is present the power absorption includes the ECR heating process. Considering only the simple case of when the time varying electric field is perpendicular to the static magnetic field, the time average power density absorbed by the electron gas is

$$\langle P \rangle_{\text{abs}}(\vec{r}) = \frac{N_{\text{eo}}(\vec{r})e^2\nu_e}{2m_e} \left[ \frac{1}{\nu_e^2 + (\omega - \omega_{\text{ce}})^2} + \frac{1}{\nu_e^2 + (\omega + \omega_{\text{ce}})^2} \right] |E(\vec{r})|^2 \quad (9)$$

The effective electric field is now defined as

$$|E_e|^2 = \frac{\nu_e^2}{2} \left[ \frac{1}{\nu_e^2 + (\omega - \omega_{\text{ce}})^2} + \frac{1}{\nu_e^2 + (\omega + \omega_{\text{ce}})^2} \right] |E(\vec{r})|^2 \quad (10)$$

Specifics of the microwave energy absorption can be understood by examining the process in a simple example gas such as helium. The effective collision frequency at 300 K for helium is given by (18)  $\nu_e = 2.3 \times 10^9 p$  where  $p$  = pressure in Torr. Investigating first the zero magnetic field case, when density and electric field are held constant, Eq.(7) has a maximum, when  $\omega = \nu_e$ . Good microwave energy coupling is directly related to a synchronization between the combined electron-neutral and electron-ion collision processes and the exciting frequency  $\omega$ . Thus good microwave energy coupling is discharge pressure dependent. For a 2.45 GHz excitation frequency maximum power absorption

in helium occurs at approximately seven Torr and discharge pressures of 5-10 Torr provide efficient coupling of microwave energy into a helium discharge. Generalizing this result to other gases with different elastic collision cross sections and accounting for the influence of the discharge walls, the optimum pressure range for efficient discharge breakdown and maintenance with 2.45 GHz microwave energy usually occurs between 0.5-10 Torr (19).

At very low pressure of  $\leq 100\text{mTorr}$  the mean free path of electron-neutral and electron-ion collision becomes very long,  $\nu_e < \omega$  and Eq. (7) becomes

$$\langle P \rangle_{\text{abs}}(\vec{r}) \approx \frac{N_{\text{eo}}(\vec{r})e^2}{2m_e\nu_e} \left[ \frac{\nu_e}{\omega} \right]^2 |E(\vec{r})|^2 \quad (11)$$

High electric fields are required to sustain the discharge since  $\langle P \rangle_{\text{loss}}(\vec{r})$  increases as pressure is reduced. In order to produce the required high electric fields, high incident microwave powers and/or high Q applicators are necessary and therefore it becomes difficult to maintain a discharge at low pressures. However, the presence of an ECR static magnetic field simplifies discharge maintenance (7) below pressures of 20 mTorr.

The influence of an impressed static magnetic field on the energy coupling process can be observed from Eq. (9). At low pressures  $\nu_e \ll \omega$  and Eq. (9) has a pole at  $\omega = \omega_{\text{ce}}$  indicating high power absorption even for every low impressed electric fields. This can be viewed as an increase in the effective electric field at resonance (20). Physically at electron cyclotron resonance the electron velocity perpendicular to the static magnetic increases, as shown in Fig. 3, resulting in an outward, spiralling motion along a magnetic field line. The electron gains energy proportional to the square of time, and in a typical discharge the radius of the electron orbit is limited by an elastic or inelastic collision, a collision with the walls or the electron moving out of the ECR region. Lax, et al. (20) have shown that in the presence of collisions, but with  $\nu_e \ll \omega$ , the energy gain by an ECR accelerated electron between collisions is inversely proportional to  $\nu_e$ . Thus at low pressures even low electric fields can couple large amounts of energy to the electron gas.

A further examination of Eq. (9) reveals the effect of pressure on ECR coupling. It is observed that as pressure increases  $\nu_e \rightarrow \omega = \omega_{\text{ce}}$  and the absorbed power density is equal to Eq. (7). Thus at higher pressures the energy absorption process again becomes collisional and the magnetic field has little influence on heating the electron gas. As pressure increases the transition between purely ECR heating and collisional heating is gradual and in helium gas takes place between 0.5 and 3 Torr. ECR heating at 2.45 GHz is not useful above 3 Torr unless the gas temperature is much higher than 300 K. Thus it is clear that ECR is a coupling technique for low pressure discharges where the electrons can orbit many times between elastic and inelastic collisions.

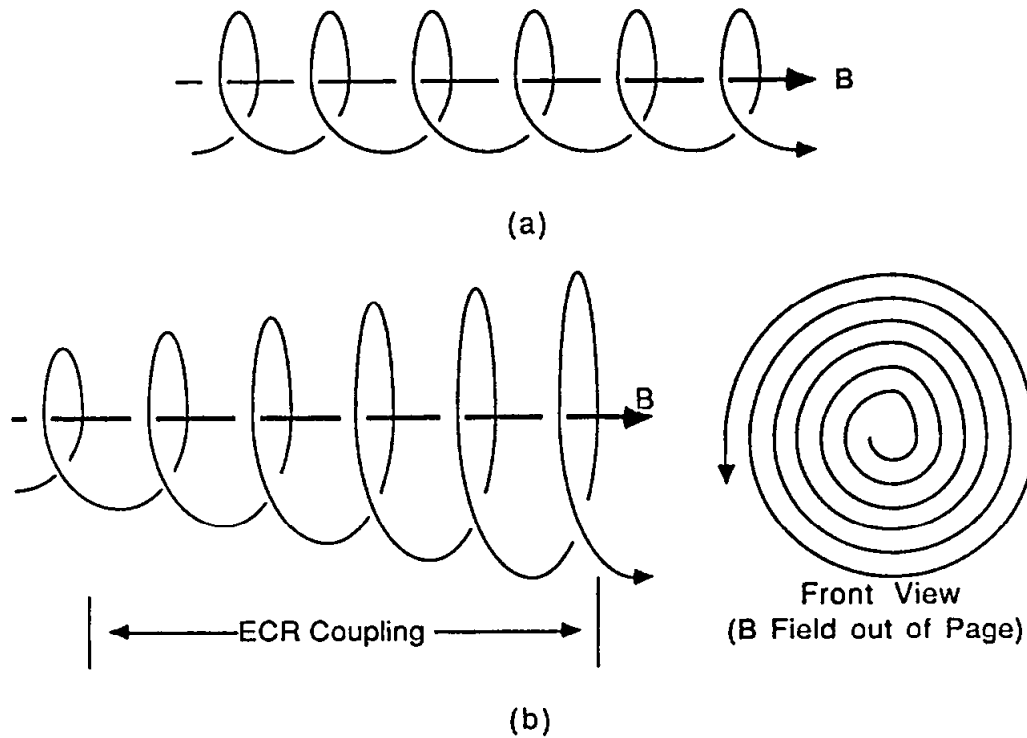


**Figure 3:** Electron motion in a static magnetic field (a) when the electric field is zero and (b) when  $\vec{E} = \vec{E}_0 e^{j\omega t}$  where  $\omega = \omega_{ce}$  and  $\vec{E}_0 \perp \vec{B}$

#### 11.4 MICROWAVE ENERGY COUPLING IN A NONUNIFORM STATIC MAGNETIC FIELD

In practice ECR discharges make use of a nonuniform static magnetic field. This magnetic field is usually mirror-like or cusp-like and is produced by magnetic coils (4,5) or permanent magnets (7,8). In the absence of an accelerating electric field the motion of an electron in such a magnetic field is well known and is shown as the solid trajectory in Fig. 4(a). When moving into a magnetic mirror a charged particle will spiral with ever decreasing transverse orbits into the converging field until it is reflected. It then reverses direction and spirals out of the mirror with increasing orbits. The radii of these orbiting trajectories are small for a typical electron. For example, a 4 eV electron will have a radius of gyration of 0.05 mm in a 875-G field.

If a transverse, time varying microwave electric field is present in the mirror, ECR acceleration of the electron takes place when the electron passes through a region where  $\omega = \omega_{ce}$ . This accelerating region is usually very thin (often less than one mm thick) and is referred to as an ECR surface or layer shown as the shaded region of Fig. 4(b). If the electron is outside this region, as Eq. (9) indicates, little microwave energy is coupled to the electron. However, an average electron can experience many oscillations of electric field during the time it spends in the ECR layer. Thus at low pressure considerable energy can be imparted to electrons in this layer with only a small electric field (10-100v/cm). Writing Eq (5) for a low pressure ECR discharge yields:

$$P_a = \int_{V_L} \langle P \rangle_{\text{abs}}(\vec{r}) dv = \int_{V_L - V_{\text{ECR}}} \langle P \rangle_{\text{abs}}(\vec{r}) dv + \int_{V_{\text{ECR}}} \langle P \rangle_{\text{abs}}(\vec{r}) dv \approx \int_{V_{\text{ECR}}} \langle P \rangle_{\text{abs}}(\vec{r}) dv \quad (12)$$

where  $V_{\text{ECR}}$  = the volume of the ECR layer. As described by Eq. (12) when  $v_e \ll \omega$  collisional energy coupling throughout the discharge volume can be ignored and microwave energy transfer occurs within the ECR volume. Since the ECR coupling takes place within small, thin volumes, energy coupling occurs with high power densities. This ECR layer, which serves the function of a hot cathode filament in dc discharges, provides the high energy electrons required to sustain the discharge at low pressures.

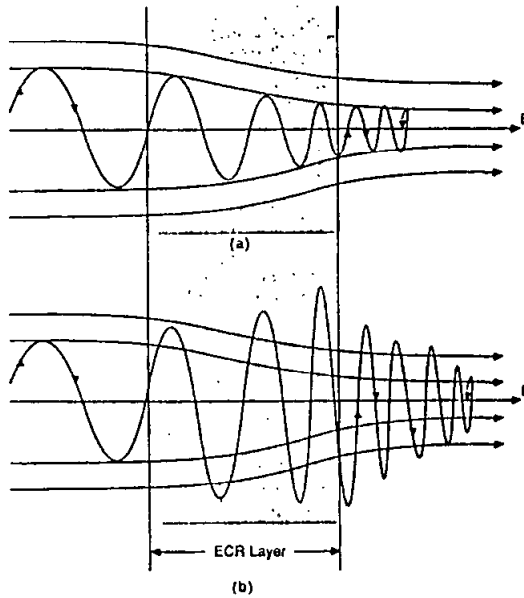


**Figure 4:** Electron motion in a mirror-like static magnetic field (a) without an accelerating electric field (b) with a perpendicular electric field  $\vec{E}_0 e^{j\omega_{\text{cc}}t}$  where the shaded region represents the ECR layer.

Upon leaving the ECR zone the accelerated electrons possess energies usually greater than 10 eV. They move through the discharge volume and excite, dissociate, and ionize neutrals and ions. Because of these high energy electrons and because of an ECR acceleration process that tends to favor higher energy electrons, it is expected the ECR discharges will have a non-Maxawellian electron energy distribution. The shape of the distribution will be dependent upon the intensity of the electric field and the location, shape, thickness, and total volume of the ECR layer in the discharge. Thus it appears that it may be possible to "engineer" the electron distribution in ECR discharges. Knowledge of how electrons are accelerated in the ECR layer is essential to understanding the ECR discharge. However, in most plasma processing applications high energy electrons and multiply charged species are not desired (as they may be in certain ion source applications (14)). Thus a careful management of electron acceleration is important.

### 11.5 MICROWAVE SYSTEM CONSIDERATIONS

ECR discharges are often required to operate with different gases, variable gas mixtures and flow rates over a wide range of operating ( $10^{-5}$  to over 0.1 Torr). Thus the microwave discharge system must be adaptable for many different experimental conditions and should be able to efficiently produce a stable, repeatable and controllable discharge for many experimental situations including discharge start up and adjustment for final processing operation. Further, considering that the ECR system will be placed in



an industrial setting, it must be able to be operated as part of a larger production facility. Thus the ECR system must be adaptable to automatic control without the need of a highly trained microwave engineer. These design requirements have an impact upon the entire microwave system and thus some basic considerations of microwave ECR systems are reviewed.

A generic microwave plasma processing system and its equivalent circuit are shown in Fig. 5. It consists of several interconnected components: (1) a power source, usually a constant frequency but variable power microwave oscillator, (2) transmission lines, often waveguide or coaxial cable, (3) a microwave applicator, and (4) the microwave plasma load. An example experimental microwave system is displayed in Fig. 6. It consists of a variable power 2.45 GHz, CW microwave power source, circulator and matched dummy load, directional couplers, attenuators and power meters that measure incident power  $P_i$  and reflected power,  $P_r$ , and the microwave applicator and plasma load. The microwave power coupled into the plasma loaded applicator is given by  $P_t = P_i - P_r$ .

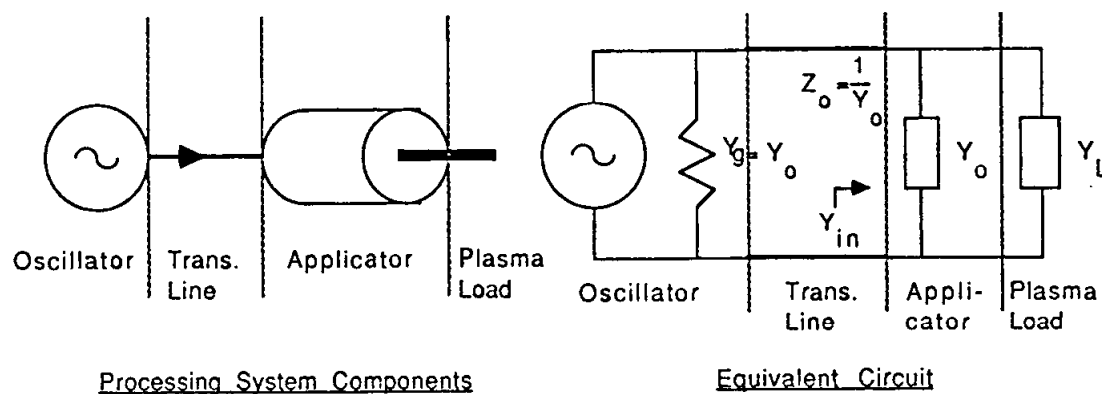


**Figure 5:** Generic microwave processing system and its equivalent circuit.

An efficient plasma processing system is designed for maximum power transfer between the microwave oscillator and the plasma-loaded applicator. This occurs when the output admittance of the microwave oscillator  $Y_g$  (See Fig. 5) and the input admittance of the plasma loaded applicator  $Y_{in}$  are equal to the transmission line characteristic admittance  $Y_0$ .

The power coupled into the applicator  $P_t$  divides itself between the power absorbed in the conducting applicator walls  $P_b$ , and the power delivered to the discharge load  $P_a$ ; i.e.  $P_t = P_b + P_a$ . These two quantities can be related to the applicator fields, the intrinsic resistance  $R$  of the applicator walls, the discharge volume and the complex conductivity of the discharge. The exact division of the power  $P_t$  between the walls and the discharge load depends on the relative losses in the discharge versus the losses in the applicator walls. Applicator design should attempt to minimize  $P_b$ , for all operating conditions.

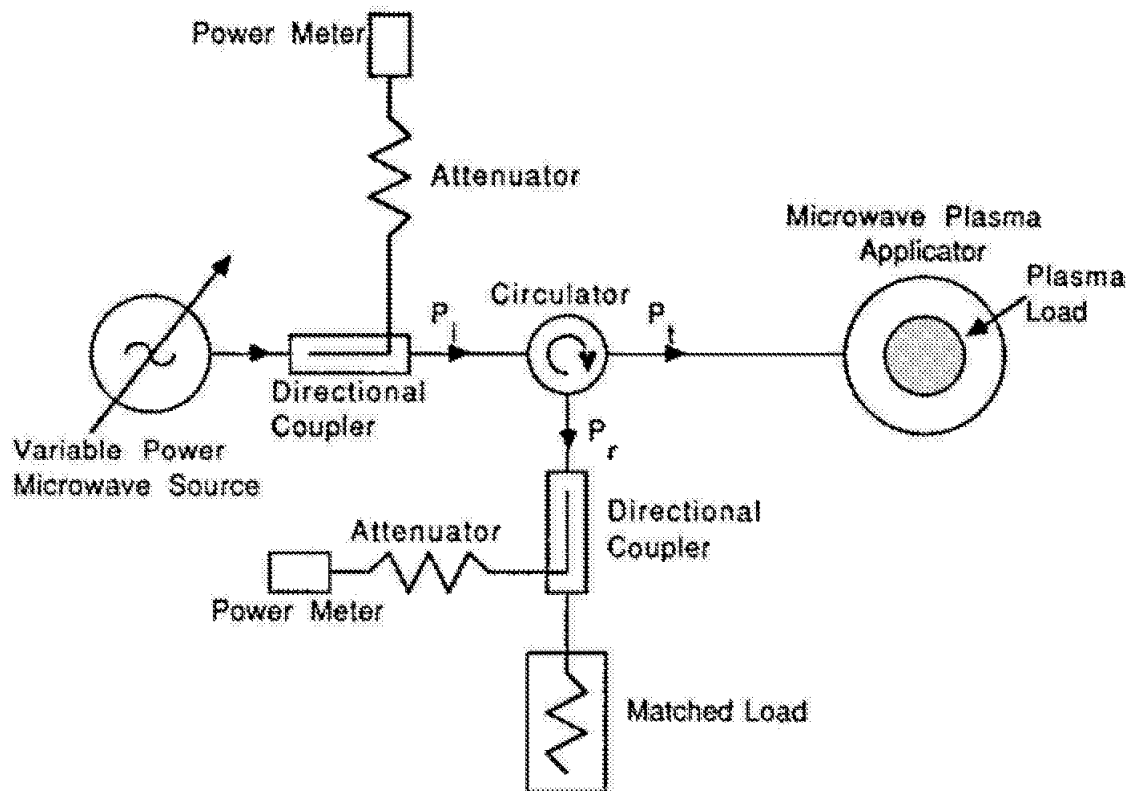


**Figure 6:** Example experimental microwave system.

A major difficulty in the design of a microwave ECR system is the variable, nonlinear often reactive discharge load. As shown in Sect. 11.2, this load depends on many different experimental conditions such as gas type, mix and flow rate, discharge pressure, etc. At present ECR discharge models can not accurately predict discharge impedance and hence cannot aid in the design process. In addition, similar to lower frequency rf discharges, the applicator/discharge possesses stable and unstable operating conditions (21-24). These must be accounted for and understood (25). Finally from efficiency considerations it is desirable to match (tightly couple) the microwave oscillator to the plasma load. However, under matched conditions the variable plasma load may cause the power oscillator frequency and output power to vary resulting in further system instabilities. Thus it is often desirable to electrically separate the microwave power oscillator and the plasma load with a circulator as shown in Fig. 6.

While ECR processing technology must still be considered in the development stage certain desirable system features are apparent. These are as follows:

1. a well filtered, variable power but constant frequency microwave power supply;
2. the use of a circulator to allow the oscillator to work into a matched load independent of discharge variations; this circulator also protects the oscillator from large reflected power conditions that may occur from an unmatched applicator;

3. the ability to accurately measure incident and reflected power;
4. a variable, automatic method of matching the applicator/discharge for the numerous discharge conditions that may occur;
5. a microwave system and applicator/discharge designed to facilitate maintenance.

### 11.6 FUNDAMENTAL ECR APPLICATOR CONFIGURATIONS

The microwave applicator performs several functions in a specific plasma processing application. These are: (a) to impedance match and focus the microwave energy into the discharge, (b) to efficiently produce high densities of excited and charged species, (c) to produce controllable and uniform densities of excited and charged species over a desired processing area (usually 10 to 30 centimeters in diameter) and (d) to process (etch, deposit, etc.) without producing material damage to the product. Several typical conventional applicator types are displayed in Fig. 7. As shown, they are nonresonant waveguide, single mode and multimode resonant cavities and are specially designed surface-wave applicators.

At low pressures a high Q applicator is required unless an ECR layer exists within the discharge. The ECR layer provides good, stable discharge coupling with low electric fields reducing the required circuit Q and simplifying the coupling and matching of the discharge. Thus even waveguide applicators can sustain a low pressure ECR discharge. However if coupling efficiency and operation over a wide pressure and power range are desired the waveguide applicators are often supplemented by additional external matching (external to the applicator) stubs or screw tuners. These external matching devices produce a standing wave between the discharge and the tuner increasing coupling to the discharge and reducing the reflected power. Thus the applicator and matching network together become a resonant, cavity-like applicator. Under these conditions ECR cavity applicators (7,8,13,26) have advantages over ECR waveguide applicators. Internally tuned resonant cavities excited at 2.45 GHz are able to create well matched ( $P_r \approx 0$ ) discharges with high densities over a wide range of input powers (100-1500W) and can even operate without ECR at higher pressures (1-3).

ECR applicators can be divided into two groups (a) waveguide applicators and (b) cavity applicators and ECR magnetic field configurations can be grouped into mirror and multicusp geometries. Each of these is briefly reviewed below.

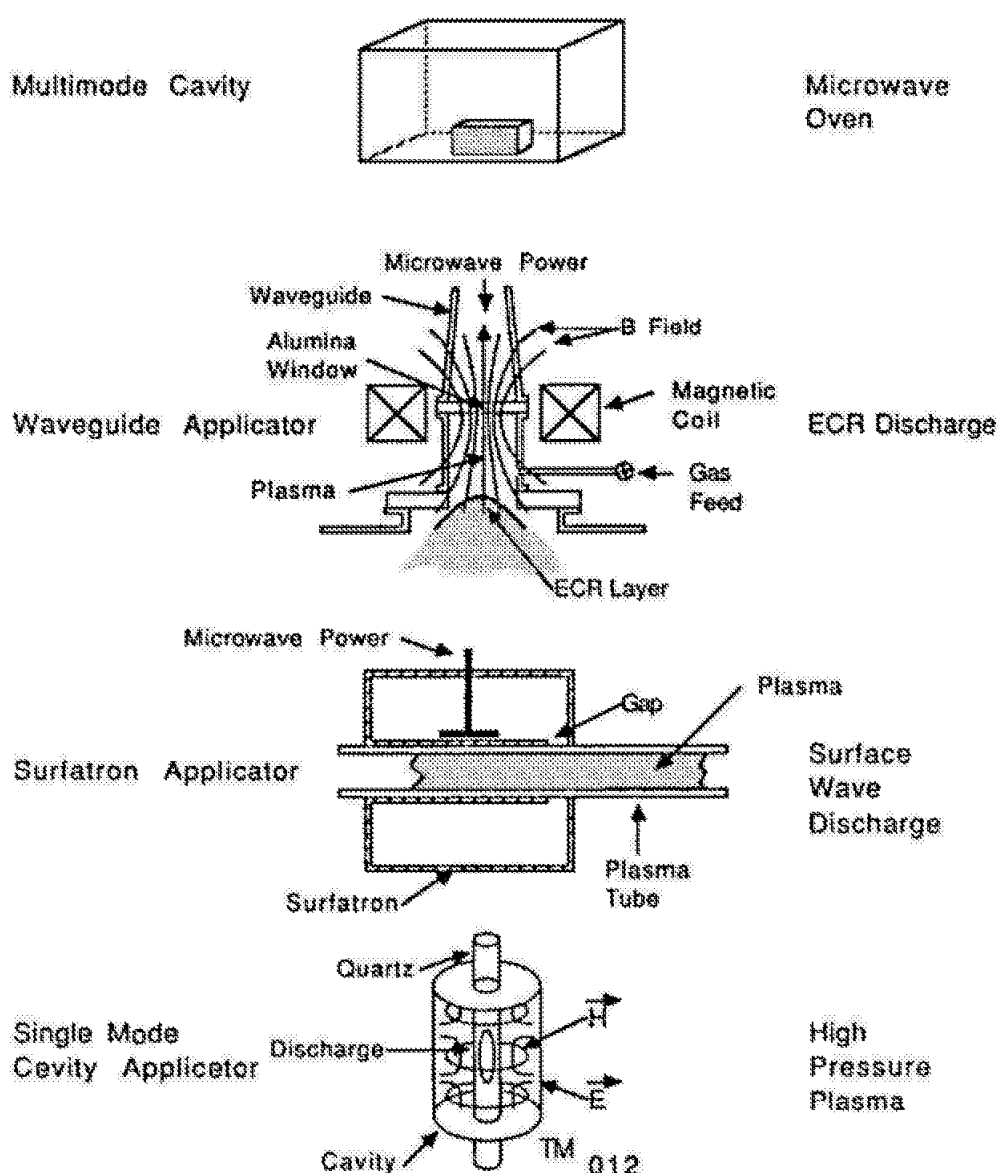


**Figure 7:** Types of applicators.

### 11.6.1 Waveguide Applicators

Typical examples of ECR waveguide applicators are displayed as the waveguide applicator (27) shown in Fig. 7 and the two applicators (28,29) shown in Fig. 8. Although often described as distinctly different and unique discharge configurations (and sometimes even described as a cavity), they are the same basic discharge configuration. In each, electromagnetic energy is coupled into the discharge zone from a standard rectangular or circular waveguide excited by an incident, electromagnetic wave. The discharge, which is located at the end of the waveguide, is defined by either a 4-9 cm diameter quartz tube or a waveguide window and surrounding, cylindrical metal enclosure. Process gases are fed radially into the discharge zone, and after microwave

excitation the ionized and excited neutral species pass out the open end of the discharge zone into a plasma processing region.

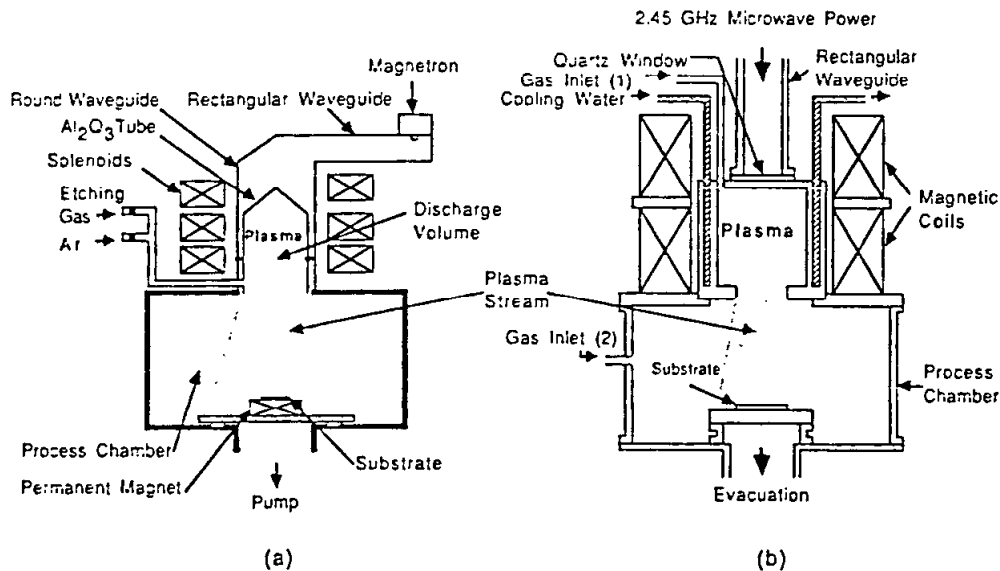


**Figure 8:** Examples of waveguide, magnetic mirror ECR applicators used in (a) etching (5,28) and (b) low temperature chemical vapor deposition (29).

The applicator discharge zone is surrounded by one or more coils which produce an axial, mirror-like magnetic field. With the proper current bias and coil spacing the magnetic field can be adjusted to produce an axially variable 875-G ECR layer across the discharge cross section. This surface which is clearly displayed in Fig. 7 is a zone of intense electron acceleration. The axial magnetic field strength is adjusted so that the magnitude is the greatest at the microwave input end and decreases vs axial position toward the discharge output. This magnetic field geometry, often called a magnetic beach, positions the intense ECR surface away from waveguide windows or other coupling surfaces. These applicators can be used with external matching networks and a variable ECR surface to provide improved coupling over many pressure and input power conditions.

This type of ECR/magnetic mirror-like waveguide applicator produces a neutralized beam of electrons and ions and was originally investigated as an electric space engine (17). The ECR accelerated electrons immediately experience a longitudinal force due to the diverging magnetic field. Thus electrons are pushed out of the high magnetic field region and as they pass into the low magnetic field regions their transverse kinetic energy is converted into longitudinal kinetic energy. In the steady state ions are attracted to the electrons by Coulomb forces and hence are also accelerated out of the discharge with the electrons. Thus a neutralized beam of electron-ion pairs flows out of the diverging magnetic field and impinges on the substrate. This beam may or may not be useful depending

upon the application. Recently (30) it has been shown that the directed ion energy can be influenced by the magnetic field gradient. Apparently ECR discharges with different field gradients will produce ion beams with different energies.

### 11.6.2. Cavity Applicators

An alternate ECR discharge configuration (6-8,12,13,31-35) called the microwave plasma disk reactor (MPDR), utilizes a tunable microwave cavity and a radially inhomogeneous multicusp magnetic field to couple microwave energy into the discharge. It is designed to create a cylindrical disk discharge zone which occupies only a fraction of the cavity volume but provides a large surface for ion extraction or plasma processing (7). The reactor concept can be configured to operate at very low pressures with ECR rare earth magnets or at moderate to high pressures (10 mTorr - 500 Torr) without magnets. It is the low pressure ECR configuration that is described here.

An example of a 10 cm prototype plasma/ion source is displayed in Figs. 9 and 10. It consists of a 17.8 cm i.d. brass cylinder [1] forming the outer conducting shell of the cavity applicator. The sliding short [2], the water-cooled, removable end-plate [3a and 3b] and the cylinder [1] form the cavity excitation zone. A disk-shaped quartz tube [4] confines the working gas to region [5] where the microwave fields produce a disk-shaped plasma adjacent to a screen [8]. The input gas is introduced into the discharge region [5] through eight pin hole openings (not shown) in the annular ring [6] and the gas feed tube [7].

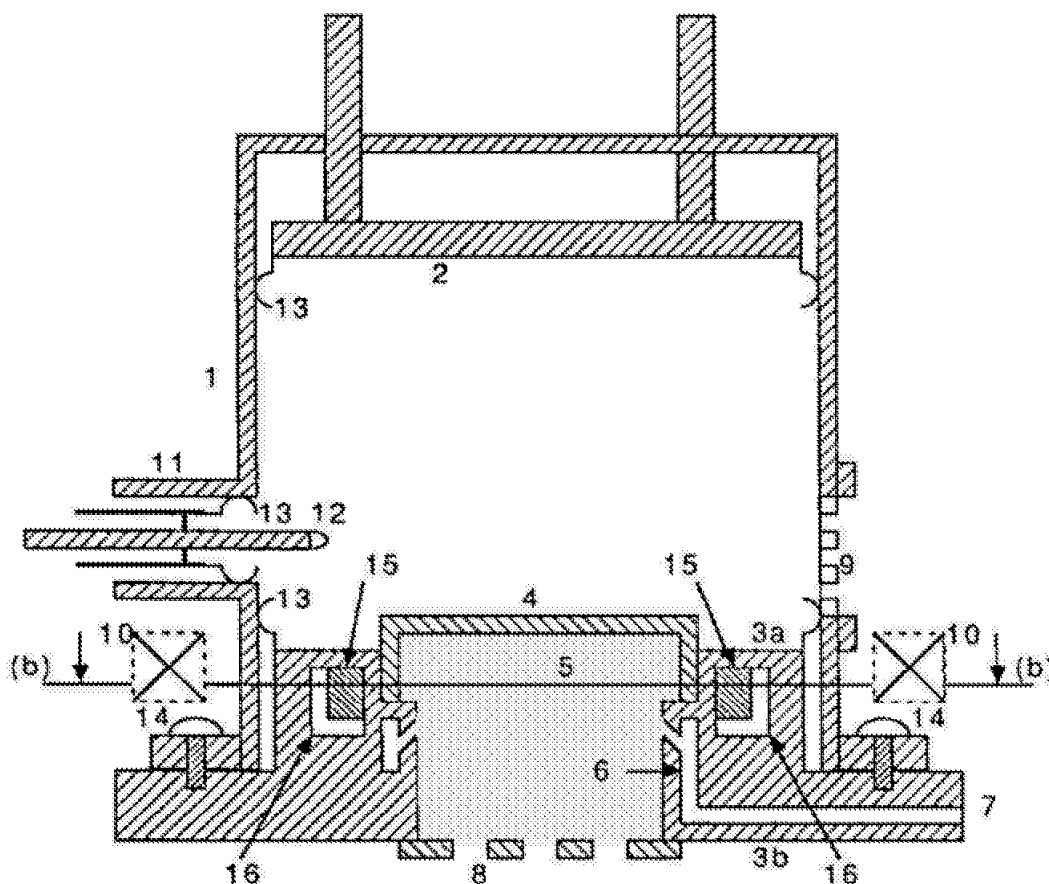


**Figure 9:** Cross sectional view of cavity ECR applicator.

A screened port [9] is cut in the cavity sidewall for viewing the discharge. Microwave power is coupled into the cavity through a coaxial input port [11] via the length-adjustable coaxial input probe [12]. Four threaded bolts [14] firmly hold the end plate [3b] onto the cylinder [1] during cavity excitation.

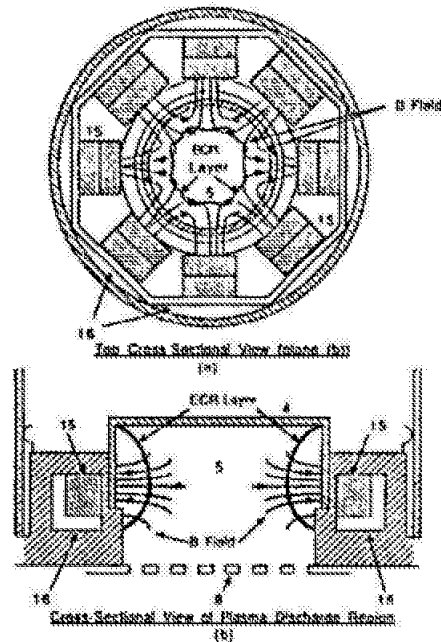


**Figure 10:** Additional cross sectional views of cavity ECR applicator. (a) cross-sectional view of plane (b) of Fig. 9 and (b) enlarged cross-sectional view of the discharge region.

The end plate consists of two separate pieces bolted tightly together. The piece [3a] adjacent to the interior of the cavity is made from brass, while the piece [3b], which is exposed to the discharge and the downstream vacuum, is machined from nonmagnetic stainless steel. As shown in Fig. 10 these two cylindrical pieces enclose sixteen 2.54 x 2.54 x 1 cm magnets [15]. Eight pairs of magnets [15] are equally spaced on a circle around and adjacent to the radial gas feed ring [6] and quartz discharge chamber [4]. The magnet pairs are arranged on a soft iron keeper [16] with alternate poles forming a multicusp, octapole, static magnetic field across a radial plane as shown in the cross-sectional view of Fig. 10. The magnetic field strength produced by these magnets is zero at the center and increases in the radial direction. Each magnet pole pair produces a pole-face maximum field strength of approximately 3 kG which is well in excess of the 875-G required for ECR at the cavity excitation frequency of 2.45 GHz. The strength and position of these magnet pairs produces a radial magnetic field surface in excess of 875-G approximately 1 cm inside the discharge zone and thus, as shown in Fig. 10, results in an undulating three-dimensional radial ECR surface inside the quartz chamber. The keeper [16] has an L-shaped cross section and is placed on the outer radius and under the magnet pairs, reducing the fringing static magnetic field in the plasma processing zone.

The cavity excitation region is defined by the brass cylinder [1], the sliding short [2] and the end-plate [3] and during ignition the screen [8] or during operation the discharge which forms in the volume [5]. The cavity can be single mode ( $TE_{111}$  or  $TE_{211}$ ) or controlled multimode excited. External matching stubs are not required since the internal adjustments of sliding short and probe match the plasma loaded applicator to the input transmission line. An important feature of this applicator is its ability to impress a high, tangential, standing wave electric field against the top volume of the discharge without reflecting power from the applicator. Thus even for high density discharges an evanescent

electric field is coupled into the discharge. The cavity can be operated either with or without the screen [8].

The multicusp magnetic field geometry is considerably different than the ECR waveguide magnetic mirror geometry. In this geometry the electrons move through the discharge following magnetic field lines and reflect off adjacent magnetic cusps. As they pass through the ECR layers they are accelerated by the impressed electric fields. Thus the high energy electrons follow this reflection and acceleration process until they elastically or inelastically collide with the larger neutrals or ions and diffuse and recombine on the walls. It is these inelastic collisions that provide the excitation, ionization and dissociation throughout the discharge volume. The high energy electrons are not all pushed out of the discharge by the magnetic field but many are bounced back forth perpendicular to the discharge axis. The low magnetic field region in the center of the discharge allows low energy electrons and ions to diffuse out of the discharge zone. In addition, one or more magnetic coils [10] (shown in Fig. 9 with dashed lines) can be added to this geometry. These coils with just a few hundred gauss will move and modify the ECR surfaces and if desired can be used to accelerate a neutralized beam of charged particles out of the discharge.

### 11.7 MICROWAVE PLASMA PROCESSING REACTORS

One of the benefits of investigating microwave discharge applications is the potential to evolve new and useful plasma reactor configurations. These new reactors make use of the microwave discharge's ability to create high densities of excited, charged and free radical species without having the disadvantages of large sheath potentials and contamination from electrodes. It is expected that one or more microwave plasma reactor configurations will one day take their place along side barrel and parallel-plate rf plasma reactors as important industrial machines for a variety of plasma processing applications.

Several potentially important microwave plasma reactor processing configurations are shown in Fig. 11. In each, a generic microwave discharge applicator is the source of chemically active species. It is useful to note that, while applicators can be interchanged (i.e. waveguide interchanged with cavity, etc.), the basic plasma processing geometry remains the same. However, the exact processing characteristics and rates will be influenced by the specific applicator.

As shown in Fig. 11 there are three important reactor variations: (a) the substrate (or processed surface) is placed entirely inside the active microwave discharge, (b) the substrate is located downstream from the discharge in a processing chamber and (c) a hybrid reactor where the substrate is again placed downstream in a processing chamber but where rf and/or dc energy creates a new discharge adjacent to the substrate. The screen, shown in reactor (b) and (c) separating the process chamber from the discharge, is optional. Its removal may allow microwave energy and energetic charged particles to impact on the substrate while increasing the density of excited species in the chamber. On the other hand placing a conventional single or double grid in the opening converts this ECR system into a broad beam ion source (7,8,26,36-38).



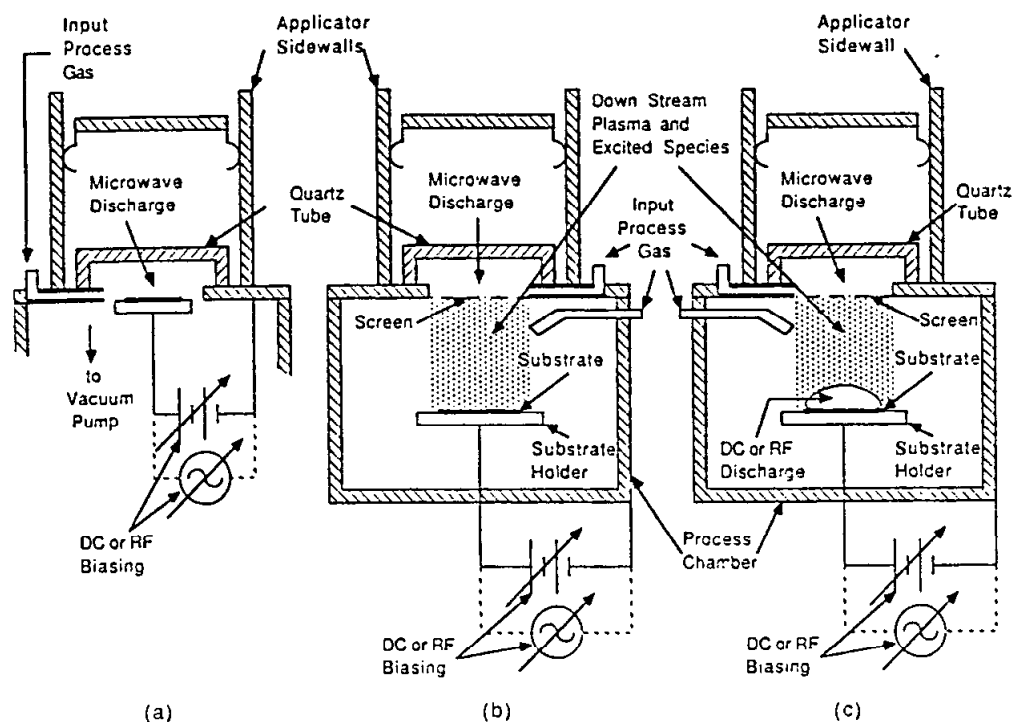


**Figure 11:** Microwave plasma processing configurations.

Each of these configurations has important similarities and differences. In each, the substrate can be independently biased with dc or rf potentials. In (a) the substrate surface is biased relative to the active microwave discharge while in (b) the bias is applied relative to the chemically active species (ions, radicals, etc.) diffusing into the processing chamber. For example in oxide growth applications the material surface can be biased (12) positive to attract negative ions and electrons. In etching applications the material surface can be biased negative attracting positively charged species (5,13,41). This configuration is essentially an electrodeless, high plasma density version of triode etching. The independent biasing allows more control over the sheath potential and hence etching profile than does conventional parallel plate reactive ion etching.

In reactor (c), rf and dc energy is supplied to create a separate discharge adjacent to the substrate surface. The microwave discharge provides a preionization and excitation of the process gas before the final formation of the process discharge above the substrate. The three reactors allow numerous processing possibilities including the cases where gases

are either passed entirely through the discharge, or independently pass through the discharge and directly into the process chamber.

The desirability of using one reactor vs another involves several trade-offs. In reactor (a) the placement of the substrate directly inside the discharge has the advantage of high processing rates due to high densities of excited species with the potential disadvantage of processing damage caused by high energy charged particles and direct microwave interactions with the substrate. In addition, substrate size is limited by the applicator size and discharge nonuniformities. Thus the ability to uniformly process large surfaces in this reactor depends on applicator type.

Reactors (b) and (c) allow chemically active species to diffuse from the applicator into a larger, often lower pressure processing chamber. Thus the specific production non uniformities of the applicator can be smoothed out by diffusion processes (free fall, ambipolar, etc.) in the process chamber. The chamber diffusion can be engineered by controlling pressure and diffusion length or by the use of multipolar plasma confinement (10,11,27,39).

An example of a multipolar processing chamber is shown in Fig. 12. The chamber is lined with closely spaced permanent magnets producing a multicusp magnetic field entirely enclosing the chamber. As shown, one or more plasma applicators can be connected to the chamber as sources of excited species. This multipolar processing chamber produces a well behaved uniform plasma at the expense of reducing excited species densities, usually by a factor of 10 or more, and thus a reduction of process rates. Surrounding the chamber with rare earth magnets and connecting several separate applicators or directly coupling microwave energy into the chamber (11) can improve densities and processing rates but only with the addition of overall system complexity.

In reactor (c) a separate rf or dc discharge is produced above the substrate. The properties of this discharge depend upon both the microwave and rf (dc) inputs. This configuration has the potential advantages of low sheath potentials, improved uniformity and control over the processing surface, and the introduction of new chemistry (40) due to the hybrid excitation of the final process discharge.

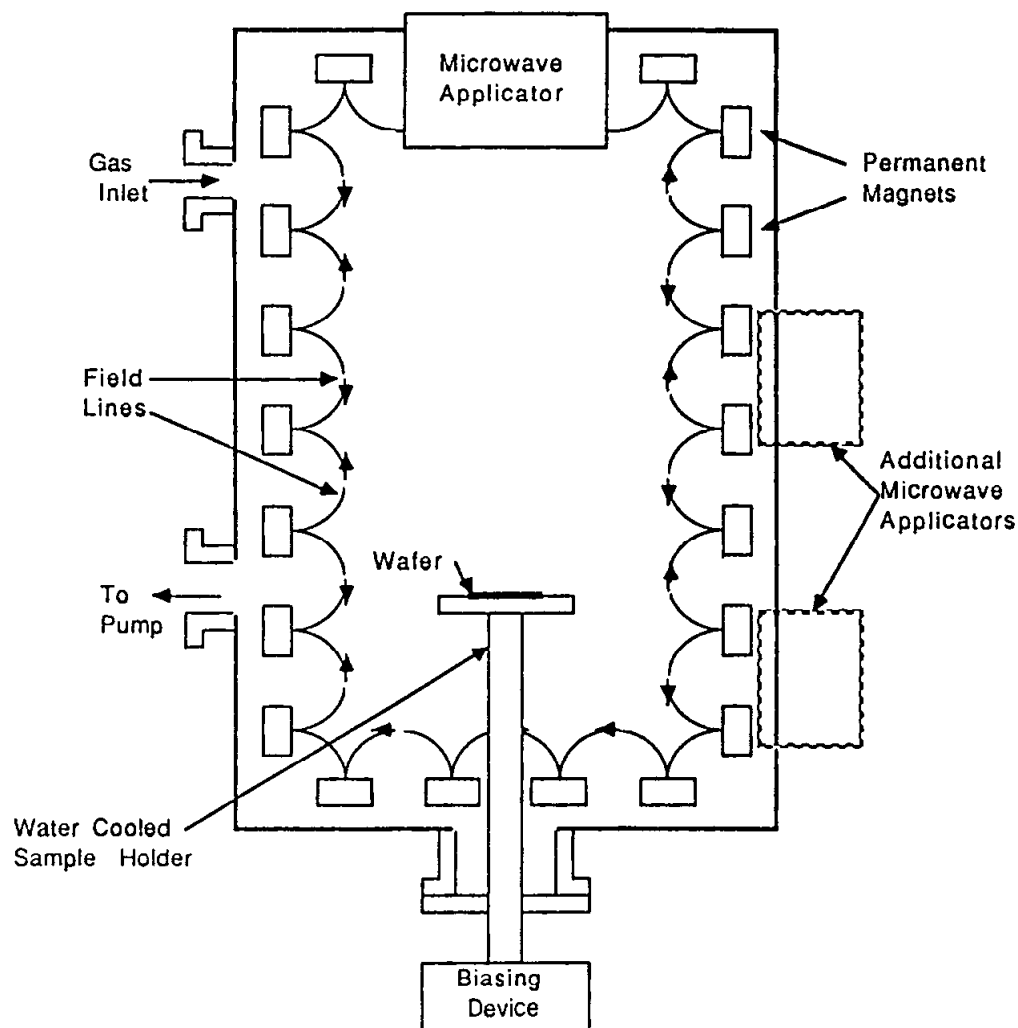


**Figure 12:** Multipolar Microwave Plasma Processing Chamber

### 11.8 DISCHARGE CHARACTERISTICS

Conventional wisdom suggests that plasma electron and ion densities within microwave discharges are limited to less than a critical density given by

$$n_e = 1.2 \times 10^{-2} f^2 \quad (13)$$

where  $n_e$  is given in electrons/ $\text{m}^3$  and  $f$  is the excitation frequency. This implies that with 2.45 GHz excitation plasma densities are limited to a maximum of  $7.2 \times 10^{10}/\text{cm}^3$ . In practice waveguide applicators produce slightly higher densities (5,10,11) and cavity applicators are capable of producing densities of 10 to 50 times the critical density at the low ECR operating pressures, and densities above 100 critical densities at high pressures (1-3). The ability to produce high densities no doubt is due to evanescent wave penetration in the plasma. This type of coupling is greatly enhanced in cavity applicators because of their ability to impress an intense, standing wave electric field against the discharge without reflecting power from the applicator.

Single (5) and double (13,26,41) Langmuir probe measurements of electron density within and downstream from the discharge have confirmed that ECR discharges are capable of generating high densities of ions and electrons. For example over the 0.1-10 mTorr pressure range in argon gas charge densities increase with pressure (constant input power) and input power (constant pressure), and the degree of ionization increases as the pressure is reduced. Numerous measurements (13,26,41) performed in discharges with different diffusion lengths indicate that electron and ion densities vary between  $3 \times 10^{11}$  and  $5 \times 10^{12} \text{ cm}^{-3}$  as power and pressure are varied from 0.1-10 mTorr. and the degree of ionization increases to 20-25% at the low pressures. Measured electron temperatures and density profiles obey Schottky ambipolar and free fall diffusion theories (41) inside the discharge and in the processing chamber. This approximate, but preliminary, knowledge of discharge behavior gives the impression that discharge optimization for uniformity, efficiency and control can be engineered by size and type (i.e. multipole, etc.) of the process chamber.

## 11.9 DISCUSSION

ECR discharges have been demonstrated as a useful, electrodeless, high density source of excited and charged species over  $10^{-4} - 10^{-2}$  Torr pressure regimes. ECR/microwave technology allows a number of different design approaches. That is, there are several different processing configurations possible. Both waveguide and cavity applicators have been employed, ECR magnetic fields can be produced with coils or rare-earth magnets, etc. Both low energy plasma or neutralized electron-ion beams can be produced for surface processing. Thus specific applications may have one or more acceptable ECR approaches and/or very specific reactors can be designed for particular applications.

The utility of the ECR discharge has been demonstrated in etching, thin film and broad ion beam applications. Using the configuration of Fig. 11(b), anisotropic etching of Si has been demonstrated without high plasma sheath potentials (5,10,13). Etch rates as high as  $0.4 \mu\text{m} / \text{min}$  with an anisotropy of 0.8-0.9 have been achieved over 3-6 inch wafers in  $\text{SF}_6/\text{Ar}$  mixtures (11,41). Using ECR discharges as the plasma for a broad beam ion source beam current densities  $> 5 \text{ mA}/\text{cm}^2$  have been achieved in argon and oxygen (26,38). Numerous thin film deposition applications including diamond thin film deposition, have also been demonstrated (12,29,42-44).

Considerable work remains on discharge characterization. It is important to determine the number and the energy of ECR accelerated electrons, the shape of the electron energy distribution, the density of doubly ionized species (14), the energy of neutralized electron-ion beams (30) and the relationship between the shape of the ECR zones and the plasma properties such as excitation and ionization efficiency, etc. Such information can be related to reactor design and process chemistry.

Since ECR discharges are a relatively new technology, damage to etched surfaces and thin films either has not been or is in the process of being evaluated. The fact that microwave discharges can be produced without large plasma potentials is a definite advantage over rf parallel plate discharges. Thus surface damage produced by high plasma potentials should not be a problem. However there are other sources of process damage that may occur. These are damage caused by high energy electrons and ions produced and accelerated in magnetic mirror fields, damage caused by direct microwave radiation

and damage produced by ultraviolet and other plasma radiation. Thus process damage produced by ECR discharges must be evaluated for each specific application and for each type of applicator.

Finally, it is noted that the technology of producing high density microwave discharges over cross sections of less than 4 – 5cm<sup>2</sup> has been well established for many years. The present challenge for microwave discharge technology is to produce high density, uniform microwave discharges over surfaces areas of 300-500 cm<sup>2</sup> without damage to process products. Such discharges would have important applications for processing six to eight inch wafers. An additional important challenge is to design ECR plasma sources to operate in the very low pressure environments of MBE machines. These plasma sources, if retrofitted into existing MBE machines, would advance the scientific investigation of low temperature ion, plasma and free radical chemistry in MBE environments.

#### 11.10 REFERENCES

1. J. Asmussen, R. Mallavarpu, J. R. Hamman and H. C. Park, Proc. IEEE 62: 109 (1974).
2. R. Mallavarpu, M. C. Hawley and J. Asmussen, IEEE Trans. Plasma Sci. PS-6: 341 (1978).
3. S. Whitehair, J. Asmussen and S. Nakanishi, J. of Propulsion and Power 3: 136 (1987).
4. G. Loncar, J. Musil and L. Bardos, Czech. J. Phys. B30: 688 (1980).
5. K. Suzuki, S. Okudairo, N. Sadudo and I. Kanomata, Jap. J. Appl. Phys. 16: 1979 (1977).
6. J. Root and J. Asmussen Rev. Sci. Instrum. 56: 154 (1985).
7. M. Dahimene and J. Asmussen, J. Vac. Sci. Technol. B4: 126 (1986).
8. J. Asmussen and M. Dahimene J. Vac. Sci. Technol. B5: 328 (1987).
9. T. Sugano, Applications of Plasma Processes to VLSI Technology, (J. Wiley, New York, 1985).
10. C. Pomot, B. Mahi, B. Petit, Y. Arnal and J. Pelletier, J. Vac. Sci. Technol. B4: 1 (1986)
11. R.R. Burke and C. Pomot, Solid State Technol. 67 (1988).
12. T. Roppel, D.K. Reinhard and J. Asmussen, J. Vac. Sci. Technol. B4: 295 (1986).
13. J. Hopwood, M. Dahimene, D.K. Reinhard and J. Asmussen, J. Vac. Sci. Technol., B6: 268 (1988).
14. R. Geller, IEEE Trans. NS-26: 2120 (1979).
15. M. Kamo, Y. Sato, S. Matsumoto and N. Setaka, J. Crys. Growth. 62: 642 (1983).
16. W.B. Ard, M.C. Becker, R.A. Dandl, H.O. Eason, A.C. England and J.R. Kerr, Phys. Rev. Lett. 10: 87 (1963).
17. D.B. Miller and G.W. Bethke, AIAA Jour. 4: 835 (1966).
18. B.E. Cherrington, Gaseous Electronics and Gas Lasers, (Pergammon Press, New York, 1979).

19. A.D. MacDonald, Microwave Breakdown in Gases, (J. Wiley and Sons, New York, 1966).
20. B. Lax, W.P. Allis and S.C. Brown, J. Appl. Phys. 21: 1297-1304 (1950).
21. G.I. Babet, J. Inst. Elect. Eng. 94: 27 (1947).
22. T.B. Reed, J. Appl. Phys. 32: 821 (1961).
23. J. Taillet, Am. J. Phys. 37: 423 (1960).
24. A.J. Hatch and L.E. Heuckroth, J. Appl. Phys. 41: 1701 (1970).
25. R.M. Fredericks and J. Asmussen, J. Appl. Phys. 42: 3647 (1971).
26. J. Mahoney, M. Dahimene and J. Asmussen, Rev. Sci. Instrum. 59: 448 (1988).
27. L. Pramathoid, R. Debrie, Y. Arnal and J. Pelletier, Phys. Lett. 106A: 301 (1984).
28. K. Ninomiya, K. Susuki and S. Nishimatsu, Jap. J. Appl. Phys. 22: 139 (1983).
29. S. Matsuo and M. Kiuchi, Jap. J. Appl. Phys. 22: L210 (1983).
30. M. Matsuoka and K. Ono, Appl. Phys. Lett. 50: 1864 (1987).
31. J. Asmussen and J. Root, U.S. Patent No. 4,507,588 (26 March 1985).
32. J. Asmussen and D.K. Reinhardt, U.S. Patent No. 4,585,668 (29 April 1986).
33. J. Asmussen and D.K. Reinhardt, U.S. Patent No. 4,630,566 (23 December 1986).
34. T. Roppel, D.K. Reinhardt and J. Asmussen, U.S. Patent No. 4,691,662 (8 September 1987).
35. J. Asmussen, D.K. Reinhardt and M. Dahimene, U.S. Patent No. 4,727,293 (23 February 1988).
36. N. Sakudo, K. Tokiguchi, H. Koike and I. Kanomata, Rev. Sci. Instrum. 48: 762 (1977).
37. M. Miyamura, O. Tsukakoshi and S. Komiya, J. Vac. Sci. Technol. 20: 986 (1982).
38. K. Tokiguchi, N. Sakudo and H. Koike, Rev. Sci. Instrum. 57: 1526 (1986).
39. R. Limpaecher and K.R. Mackenzie, Rev. Sci. Instrum. 44: 726 (1973).
40. J.E. Heidenreich and J.R. Paraszczak, J. Vac. Sci. Technol. B5: 347 (1987).
41. J. Hopwood, D.K. Reinhardt and J. Asmussen, J. Vac. Sci. Technol. (to be published).
42. T. Ono, C. Takahashi and S. Matsuo, Jap. J. Appl. Phys. 23: L534 (1984).
43. K. Wakita and S. Matsuo, Jap. J. Appl. Phys. 23: L556 (1984).
44. H. Kwarada, K.S. Mar and A. Hiraki, Jap. J. Appl. Phys. 26: L1032 (1987).

## 12

---

# Hollow Cathode Etching and Deposition

---

**Chris M. Horwitz**

### 12.1 INTRODUCTION

The hollow cathode is an enhanced-discharge configuration which permits high intensity, low voltage discharges to be obtained at low pressures. In this, it is similar to other configurations such as the magnetron and microwave ECR in providing enhanced operation in comparison with the standard radio-frequency sputtering diode. We will see that the hollow cathode can also yield a very high power efficiency, and that its symmetric construction can minimize high-energy electron bombardment of the substrates as well as minimizing particulate contamination. All of the above factors are important in modern semiconductor device processing: low operating pressures permit accurate pattern transfer (1,2); low voltages minimize surface contamination "damage" (3,4,5); high power efficiency minimizes heatsinking requirements (6,7); the absence of high-energy electrons improves dielectric layer properties (8,9); and low particle generation improves overall system performance (10,11).

It must be pointed out that the "hollow cathode" described in this chapter differs from hollow cathodes which are used as electron sources; such sources are often formed from small tubes of refractory metal and are operated in inert gas discharges at red heat (12,13). Here the hollow cathode is formed partly from the semiconductor wafers being processed, and it is thankfully not necessary to operate them at red heat to obtain the performance described here.

This chapter provides an overview of hollow cathode operation, starting with the fundamentals of discharge confinement and basic machine design. Some more complex applications of these principles, related to semiconductor processing, are then described.

## 12.2 DISCHARGE CONFINEMENT EFFECTS

### 12.2.1 Diode

Reactive sputtering rates depend on rates of reactant arrival at target surfaces; i.e., upon reactant pressures. Such reactants, formed by discharge dissociation of the input gas, are active chemical species capable of etching or depositing in the presence of energetic discharge processes such as ion bombardment. Low reactant partial pressure, whether due to low gas flow, or to inefficient breakup of the input gas into active constituents, results in low etch and deposition rates. Discharge confinement improves this availability in two ways; firstly, by simply constraining reactants, forcing them to spend their (often short) lifetimes close to the active target area. Secondly, discharge confinement could increase the discharge ionization level. Discharge ionization can be enhanced if the energetic particles produced by discharge heating (e.g., see Ch.6) are retained in the discharge region, again by simple mechanical confinement. In addition the correct choice of confining electrode polarity can result in trapping of energetic electrons. Such increases in discharge ionization would yield increased rates due both to increased reactant supply, and to increased ion bombardment of the target.

Examples of unconfined and confined diode systems are shown in Fig. 1. The upper unconfined diode corresponds to those described in earlier chapters. The central "guard-confined" diode has a target surrounded by material at the guard (i.e., chamber) potential

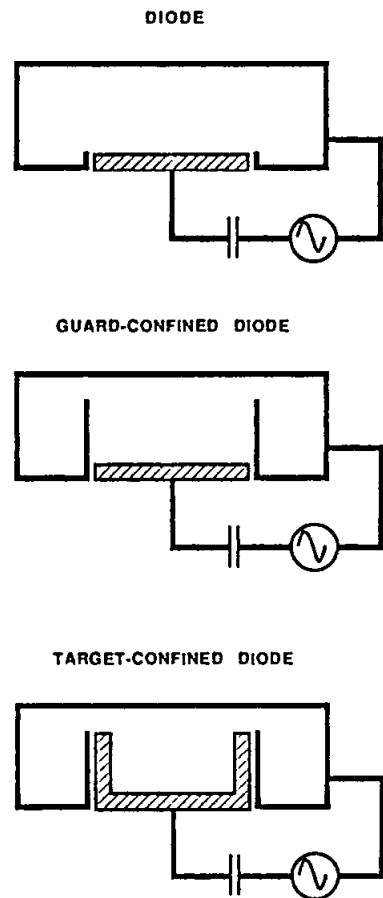


**Figure 1:** Diode configurations. Top: standard system. Center: Confinement at the chamber (guard) potential. Bottom: Confinement at the target potential and guarded on the outside.



and often exhibits increased rates. For instance, etch rate increases of a factor of 2, at constant target voltage and power input have been obtained in  $\text{CF}_4$  gas (2, 14). Such rate increases can be attributed to reactant trapping; the fairly constant input power indicates that discharge ionization is not affected by such guard-confinement of a diode.

The lower diagram in Fig. 1 shows a diode target which is confined by material at the target potential. Surrounding this is a guard at chamber potential, limiting the discharge to the central target area. Not only are neutral reactants confined by the arrangement; the extended target area is bombarded by more of the available ions in the glow region, while repelling electrons from its surface for most of the radio-frequency cycle. This "target-confinement" of a diode results in substantial improvements in deposition rate and in power efficiency of the discharge, but instability has made this discharge type hard to use in practice (15).

Common to all diode-confinement schemes is the area ratio problem illustrated in Fig. 2. The upper part of the diagram shows a 50 mm dia. target confined by a 15 mm high, 90 mm dia. chamber. This small chamber has a (chamber:target) area ratio of  $A_2/A_1 = 7.6$ , implying that ion bombardment of the target is significantly more energetic than that of the chamber walls (16). Thus, in this case the chamber walls are not heavily attacked by sputter-etch processes. Scale-up of the target area to a more practical 200 mm diameter, with all other diameters similarly scaled, results in the geometry illustrated in the lower part of Fig. 2. The nominal chamber:target area ratio is 6, again high. However, the intense glow region delineates the areas to be included in this area calculation (16) resulting in the effective area ratio tending towards unity in the scaled up diode. An area ratio of exactly one results in equal bombardment of the two "electrodes", chamber and target; hence often in the use of sacrificial materials opposing a diode target.

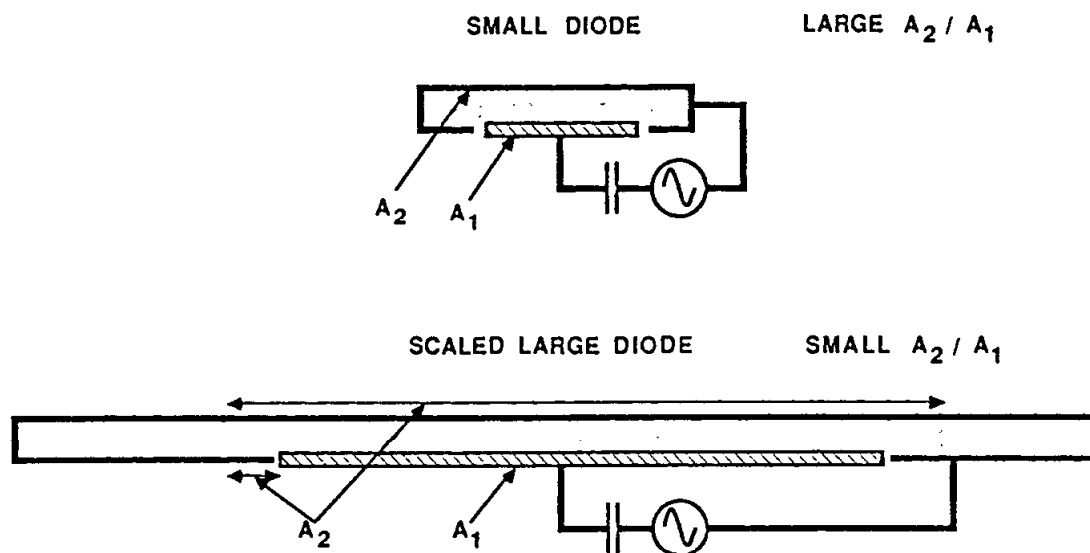


**Figure 2:** Effective area ratios in small and large diodes. The lower diode has all radii increased by a factor of 4. The intense glow region does not fill the entire volume of the larger chamber.

### 12.2.2 Hollow Cathode

A simple hollow cathode is formed by confining a diode target with a similar opposing diode target (Fig. 3 and top, Fig. 4). This confinement allows an increase in utilization of the available ions in the glow region, as did the target-confined diode. In addition, the hollow cathode so formed allows each target to repel secondary electrons ejected from the opposing target, forming an "electron mirror" (17). Such secondary electrons, formed by ion impact on a target and then accelerated by the sheath into the discharge glow region, would otherwise be lost at low pressures (2). Application of this electron mirror concept to the hollow cathode indicates that while guard-confinement of a hollow cathode (center, Fig. 4) may increase rates due to retention of reactants and other active neutral discharge components, target-confinement (bottom, Fig. 4) should give the larger improvement due to its more efficient trapping of electrons by the negatively biased targets.

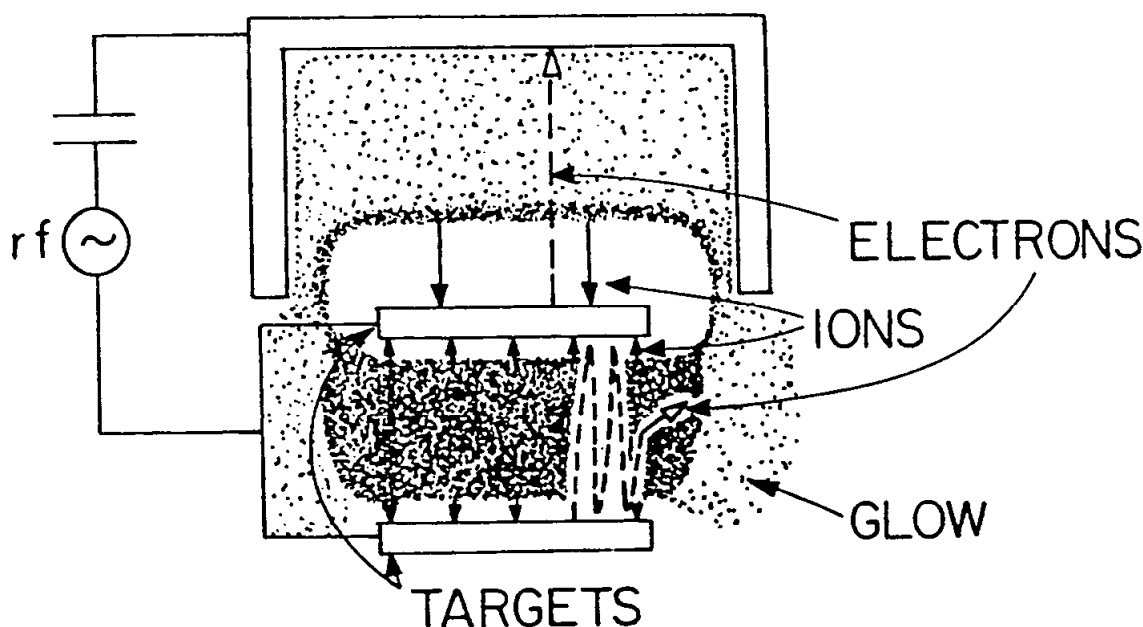


**Figure 3:** Secondary electrons, liberated from hollow cathode targets by ion bombardment, can be trapped in an electron mirror.

These general conclusions are borne out by the experimental data. As an example, Si deposition rates from  $\text{SiH}_4$  gas are given for various confinement methods in Fig. 5 as a function of target voltage and in Fig. 6 as a function of power input (15). In both cases, the least-confined system (the diode) exhibits the lowest rate, while the most-confined system (the target-confined hollow cathode) exhibits the highest rate. All other systems, including the unstable target-confined diode, have intermediate performance. The impact of confinement is greatest at low pressures; Fig. 7 shows that while the etch efficiency of a guard-confined hollow cathode is about three times that of a diode at 1 Pa  $\text{CF}_4$  pressure, the two systems' efficiencies become similar at 10 Pa  $\text{CF}_4$  pressure (14).

**Figure 4:** Hollow cathode configurations: Top: standard system. Center: Confinement at the chamber (guard) potential. Bottom: Confinement at the target potential, guarded on the outside.

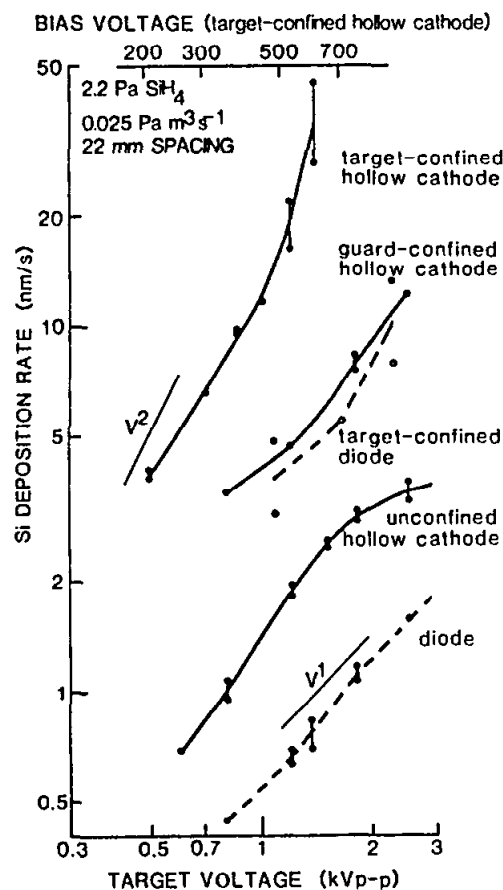
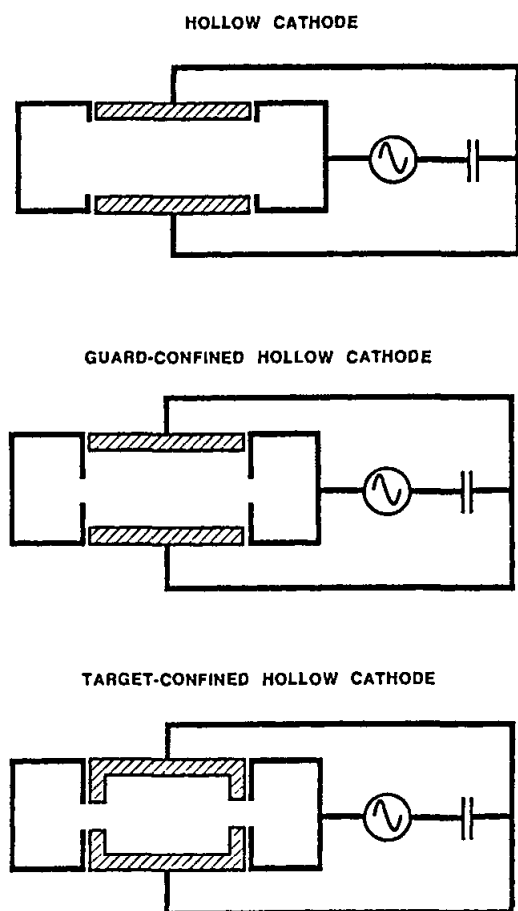


**Figure 5:** Voltage dependence of deposition rate from silane in diodes (dashed lines) and hollow cathodes (solid lines), with various degrees of confinement. The target confined diode results are sketchy due to discharge instability.

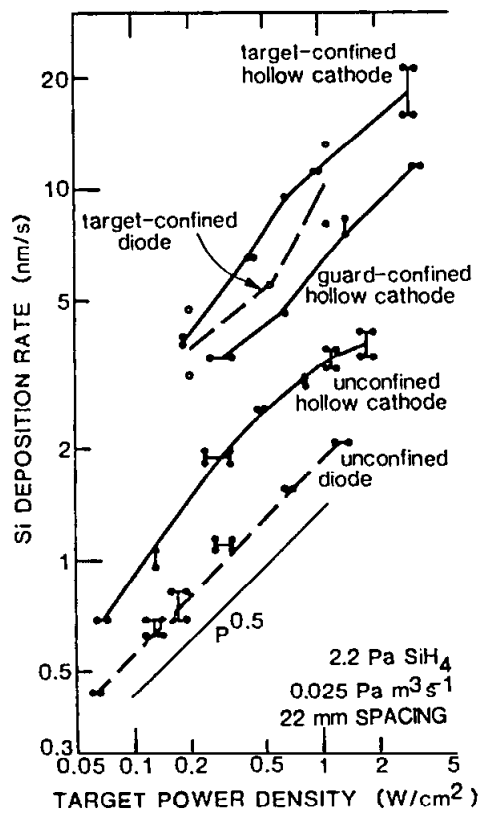


**Figure 6:** Power dependence of deposition rate from silane for diodes (dashed lines) and hollow cathodes (solid lines), with various degrees of confinement.

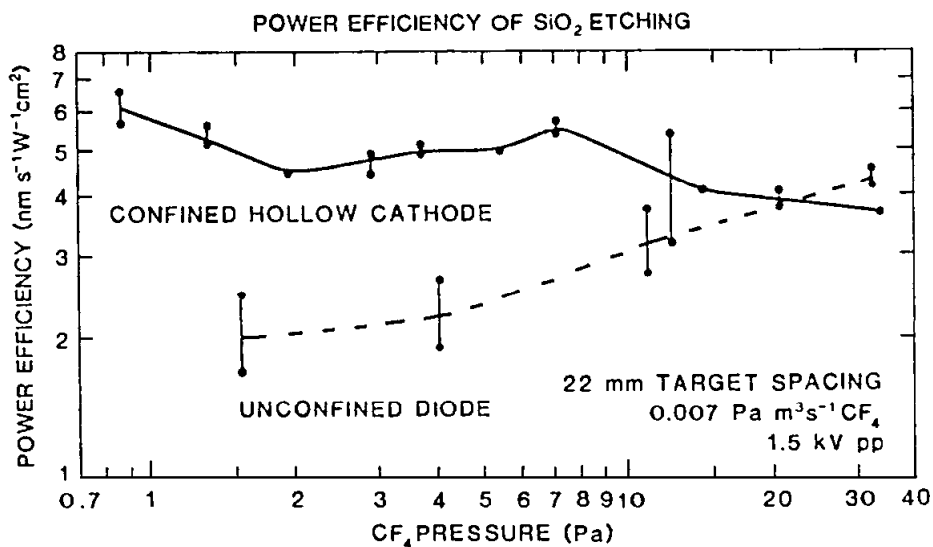


**Figure 7:** Power efficiency of  $\text{CF}_4$  etching as a function of pressure for a diode and hollow cathode. Power efficiency is given here as ( $\text{SiO}_2$  etch rate) / (surface power density).

There are minor differences in the confined behaviors of  $\text{CF}_4$  and  $\text{SiH}_4$  discharges; while guard-confinement of a diode has no effect on  $\text{SiH}_4$  discharges, it has a slight power-reducing, rate-increasing effect on  $\text{CF}_4$  discharges. In addition, guard-confined

$\text{CF}_4$  diode discharges were unstable at pressures lower than 6 Pa, whereas only the target-confined diode was unstable in  $\text{SiH}_4$ .

The experimental data shows that confinement of a diode, while conferring some benefits, is not as effective as hollow cathode configurations in obtaining higher rates for a given target voltage and input power density. In particular, hollow cathode guard confinement improves both reactant trapping and discharge ionization by providing a mechanical barrier to the escape of energetic particles. The opposing grounded surface in a diode discharge is probably serving both as a heatsink and as a center for recombination and polymerization of reactants, on balance extracting energy from the diode discharge region and preventing guard confinement from conferring substantial benefits. This energy loss mechanism may also explain the observed instability of confined diode discharges.

Target confinement of the hollow cathode can result in a different type of instability from that seen in diodes; the discharge may exit from the central region in a "plume" at low pressure and/or at high input power. This plume can be suppressed with a small axial magnetic field of 10-50 Gauss, as shown in the "Super-confined Hollow Cathode" of Fig. 8, permitting stable high-efficiency operation at low pressures and at high input power densities.

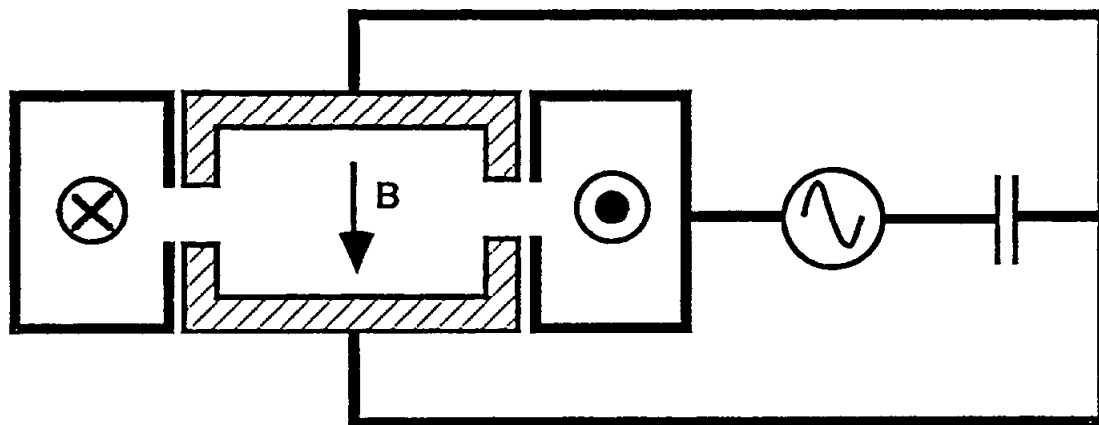


**Figure 8:** "Super-confined" hollow cathode using a magnetic field and target confinement to obtain a high efficiency low-pressure discharge.

The hollow cathode, like the diode, cannot be scaled in target area indefinitely without regard to the effective area of exposed chamber wall. However very little work has been done on the nature of this effective chamber area, and on the significance of area ratios in the hollow cathode case. Our work to date indicates that scaling of the hollow cathode to large target sizes is easier than in the diode.

## 12.3 ETCHED SIDEWALL ANGLE CONTROL

### 12.3.1 Mechanism

The angle of an etched sidewall on a surface structure must be controlled in many applications. One example is in via and contact hole etching, where angles of  $10^\circ - 20^\circ$  from the vertical permit good metal coverage (18). Here we discuss a method of sidewall angle control employing a metal compound of low volatility (e.g.  $\text{MgF}_2$ ) which is coated onto surfaces while they are etched. This metal compound is normally present in monolayer quantities, and as will be shown in section 14.4.2, is compatible with standard device processing. As will be seen the process is applicable to a wide variety of etcher configurations, although it has mostly been used with the hollow cathode.

If a conformal uniform-thickness layer is being continuously applied over a surface which is also subject to directional ion-assisted etching, horizontal areas will be etched to completion faster than angled areas, where the effective layer thickness is greater (Fig.9, Ref.19). Defining the angle between the substrate and the incident ion direction as  $\Theta$ , the effective layer thickness is proportional to  $\sin \Theta^{-1}$ , hence rises as the angle  $\Theta$  falls. At large angles  $\Theta$  (i.e. for horizontal surfaces, normal to the ion direction), this coating typically etches rapidly and so does not greatly subtract from the substrate etch rate. However, at a sufficiently small angle  $\Theta$  to the ion direction, the effective layer thickness will be so large that the substrate etch rate is reduced to zero. At this angle the conformal deposition rate of this layer is precisely equal to its directional etch rate, resulting in the formation of a stable, very thin equilibrium layer. At this equilibrium angle no further etching of the substrate can take place.

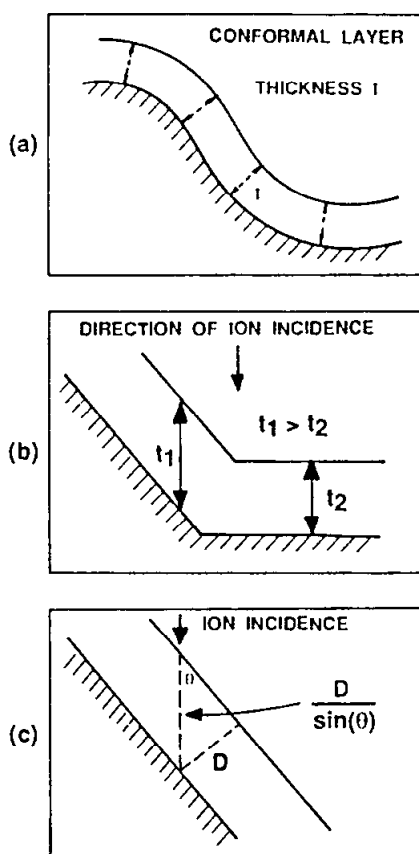


**Figure 9:** Mechanism of angle control using a surface coating. (a) Conformal surface coating: (b), (c) Effective coating thickness along ion etch direction is larger on angled surfaces. At the angle where effective etched thickness equals deposited thickness in any given time period, an equilibrium state is reached.

The above mechanism implies that the etched angle is dependent on the nature of the coating material and on its deposition rate, but not on the material being etched. This surprising result is borne out by experiment, where both Si and SiO<sub>2</sub> layers are etched to very nearly identical angles in the presence of metallic compound deposition (19-21). Another useful attribute of this angle-control mechanism is its independence of other discharge parameters, allowing independent control of etch selectivity and etched angles (22). We have found that a wide variety of metal and gas combinations result in useful angle control properties, as illustrated in Figs. 10 and 11; in general the metal compound must have a low vapor pressure to have a significant angle-control effect, but not so low that its effect is too localized.

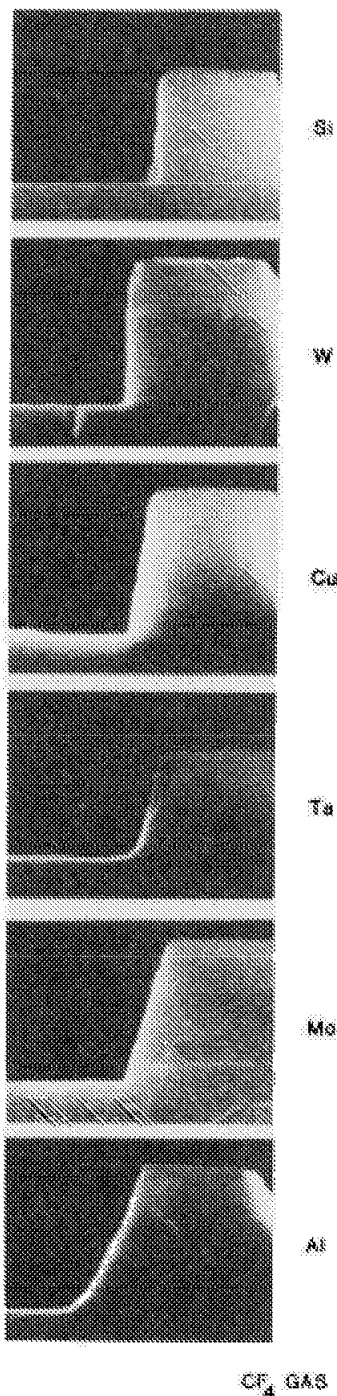


**Figure 10:** Effect of upper target material on etched angles in SiO<sub>2</sub> and Si at 1.7 kV<sub>p-p</sub> in a 2.2 Pa, 0.006 Pa m<sup>3</sup>s<sup>-1</sup>CF<sub>4</sub> hollow cathode discharge. Heatsunk samples; MgF<sub>2</sub> mask removed. Top layer is 0.6 μm thermal SiO<sub>2</sub>.

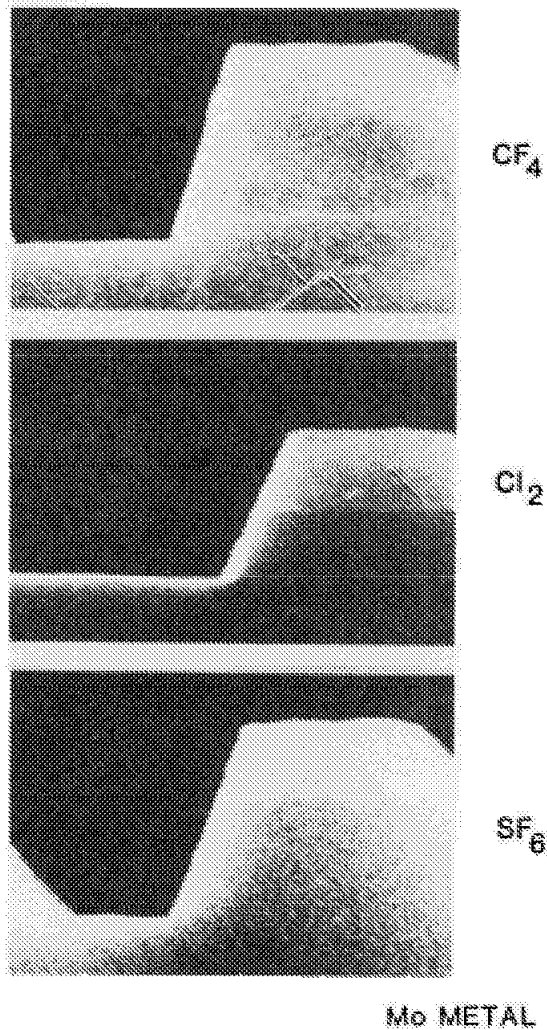


**Figure 11:** Effect of etch gas on etched angles at 1.7 kV<sub>p-p</sub> with a Mo upper hollow cathode target. Heatsunk samples; MgF<sub>2</sub> mask removed. Top layer is 0.6 μm thermal SiO<sub>2</sub>. CF<sub>4</sub> and Cl<sub>2</sub> at 2.2 Pa, SF<sub>6</sub> at 1.1 Pa pressure.

### 12.3.2 Special Machine Designs

Metal compounds may be added to the discharge gas in a variety of ways. If the operating pressure is high, or the compounds in use have a moderately low vapor pressure (as with Mo-F combinations), a source of metal from a subsidiary discharge at the side of the etching chamber will result in good angle uniformity (Fig. 12(a)). Sources of metal closer to the etched substrates permit a wider choice of materials and operating pressures; Figure 12(b) shows that an opposing hollow cathode target may be partly metallic. However this permits etched angle control only through target changes. Another relatively inflexible method relies on a small (chamber:target) area ratio, causing ion bombardment of the chamber to a lesser extent than the target, but nevertheless sufficient to sputter a controlled amount of chamber metal material into the discharge (Fig. 12(c)).

The "trielectrode" hollow cathode (Fig. 12(d)) has three main electrodes; central targets, metallic ring targets, and the chamber walls. This configuration provides a source of metal close to the targets, while permitting etched angle control by adjustment of the metal ring target discharge current. These ring targets also contribute to discharge confinement and hence to discharge power efficiency (ref. 21). Although the rf generator is shown connected only to the central targets, and only the dc supply to the ring targets, in fact a fraction of the central target rf voltage appears on the ring targets. External capacitors can be connected between the ring targets and the chamber or central



electrodes to adjust the value of this ring rf voltage; a high ring voltage results in low input power density for a given etch rate, but also in a high rate of metal supply to the discharge.

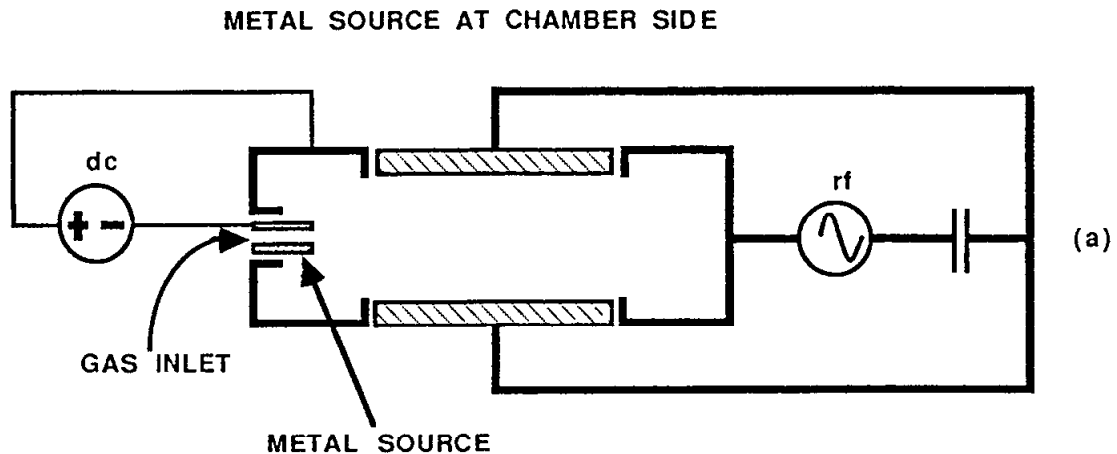


**Figure 12:** Methods of incorporating a metal source in hollow cathode discharges.

## 12.4 ETCHING PERFORMANCE

### 12.4.1 $\text{SiO}_2$ Selectivity and Etching

As in diode reactors, the hollow cathode allows  $\text{SiO}_2$  to be selectively etched using controlled polymer deposition during the etch process. Addition of hydrogen to  $\text{CF}_4$  etch gas encourages formation of this polymer on photoresist and on silicon, thereby retarding the etch rates of these materials relative to that of  $\text{SiO}_2$  (22,23,24). Thus  $\text{SiO}_2$  films formed on Si and masked by patterned photoresist can be etched, without excessive erosion of the mask or of the underlying silicon, in a high selectivity process. One limit to the attainable material selectivity is gas flow reproducibility; excessive hydrogen flow, beyond the so-called "polymer point", results in the deposition of a thick continuous polymer

film. This is to be avoided as much as the lower selectivity obtained at low hydrogen flow. The precision to which gas flow must be controlled can be derived from the rate of change of selectivity with hydrogen flow; a small rate of change indicates a small (and desirable) sensitivity to hydrogen flow. Figure 13 shows how the etch selectivity of  $\text{SiO}_2$  relative to Si varies with hydrogen flow in the hollow cathode. Figure 13(b) also shows the performance of a diode etcher (23,24). In these graphs the hydrogen flow is shown on a logarithmic scale and in arbitrary units to allow comparisons of curve shapes to be made; the relative positions of the curves on this axis have no significance.

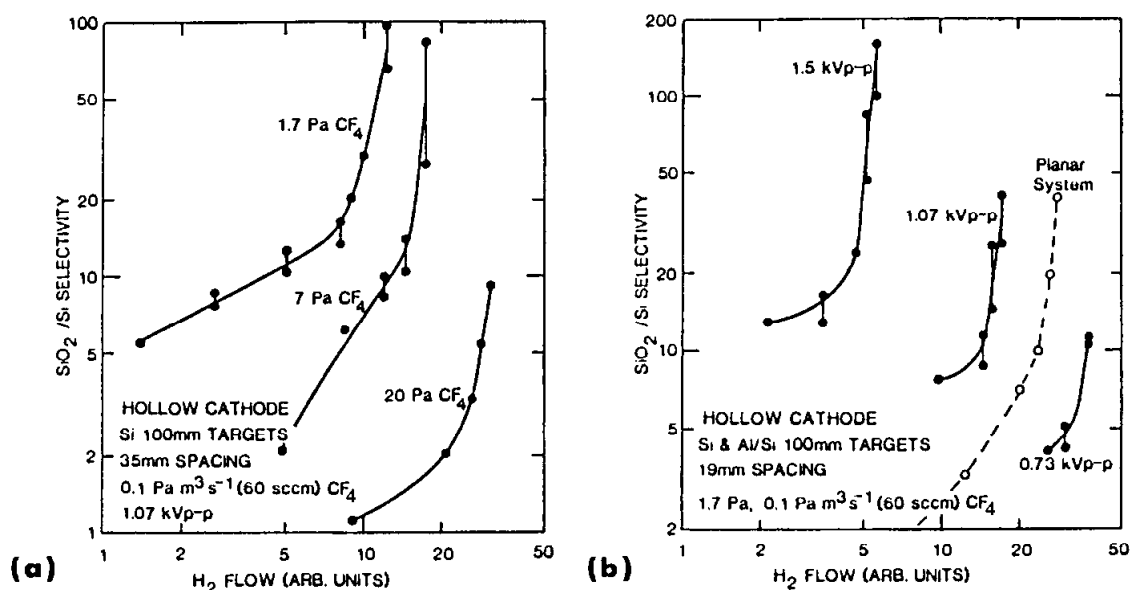


**Figure 13:** The effect of hydrogen on the  $\text{SiO}_2/\text{SiO}$  selectivity for the hollow cathode. Curve positions on the  $\text{H}_2$  flow axis have been shifted for clarity. (a) non heatsunk samples;  $\text{CF}_4$  pressure as parameter. (b) Heatsunk samples; target voltage as parameter. The Planar System (diode) curve is replotted from refs. 23, 24.

All the curves in Fig. 13 exhibit regions of low slope, hence of a desirable low sensitivity to hydrogen flow. Beyond a "knee" region the slope increases, making accurate process control more difficult. The value of selectivity at that knee position can be used to compare different operating conditions; for instance at 20 Pa operating pressure, a knee selectivity of roughly 2 is obtained, whereas at 1.7 Pa pressure the knee selectivity is 15, demonstrating one benefit of low-pressure operation (Fig. 13(a)). The knee selectivity varies even more rapidly with target voltage; a doubling from 0.73 kV<sub>p-p</sub> to 1.5 kV<sub>p-p</sub> increases knee selectivity from about 4 to 18, at low operating pressure (Fig. 13(b)).

Selectivity at the curve knees in Fig. 13 is clearly related to the etch selectivity of  $\text{CF}_4$  in the absence of hydrogen. Although high inherent  $\text{CF}_4$  selectivity can be obtained

in both diode and hollow cathode reactors (25,26), Figure 14 shows that hollow cathode selectivities are greater than those of diodes over a wide pressure range, for a fixed 50 mm dia. target geometry and operating voltage. Rates and input powers are shown in Fig. 14(a) for unconfined and in Fig. 14(b) for glass-ring-confined targets (14). Both figures demonstrate a large  $\text{SiO}_2/\text{Si}$  etch rate ratio for hollow cathode configurations. This behavior enables the larger hollow cathode system used for Fig. 13 to yield selectivities in pure  $\text{CF}_4$  of the order of 10 at high target voltage and low pressure. This is high enough for many integrated circuit applications and is also well above the selectivity of 1.3 reported for a diode system in 4.7 Pa  $\text{CF}_4$  and at 800 V<sub>p-p</sub> (Fig. 13(b)) (23,24). Clearly high target voltage by itself does not make  $\text{CF}_4$  gas selective. It is the combination of low operating pressure and high input volume power density (i.e., high energy input per input gas molecule) that seems to result in a desirable polymer deposition process.

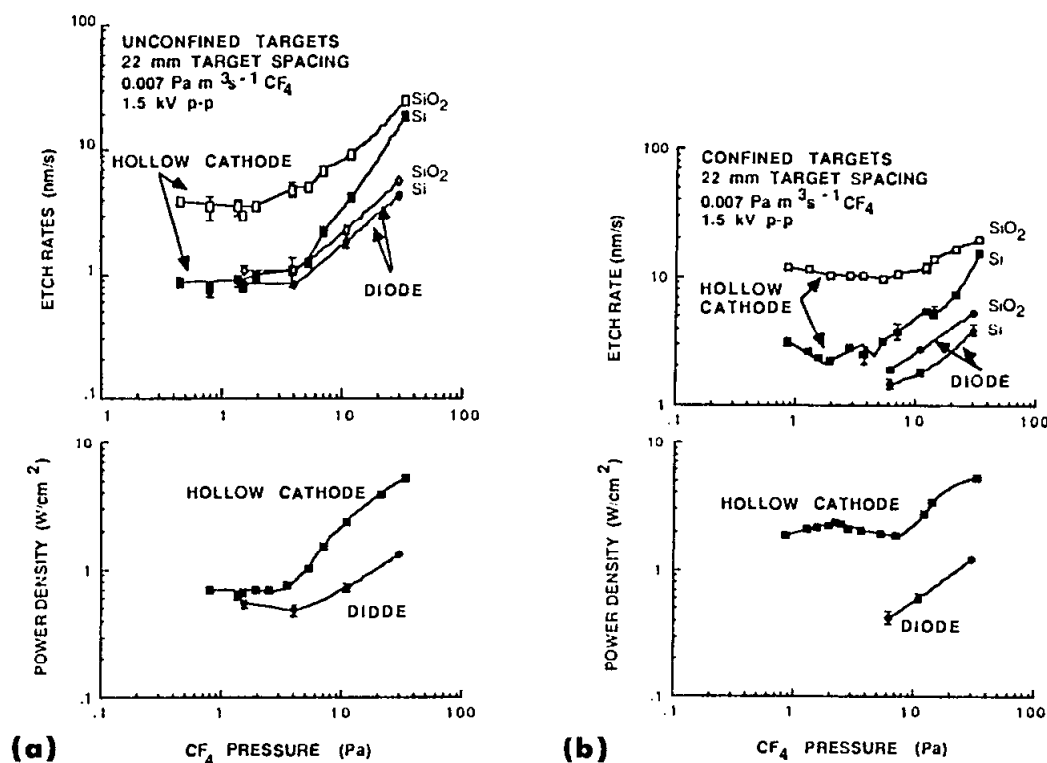


**Figure 14:**  $\text{SiO}_2$  and Si etch rates and power densities in  $\text{CF}_4$  discharges. (a) Unconfined targets;  $\text{SiO}_2/\text{Si}$  selectivity is higher in the hollow cathode than in the diode, even at similar target voltage and surface power density. (b) Guard-confined targets; the hollow cathode again exhibits higher selectivity than the diode.

High selectivities are limited not only by gas flow repeatability but also by pattern sensitivity of etching rates. The centers of large apertures etch slowly, probably because of their large polymer acceptance angle (Fig. 15). Another possible explanation may be a local chemical interaction between the plasma and the resist, but the low resist etch rate makes this unlikely. This behavior appears to be the reverse of high-pressure reactor performance, where small opening sizes etch more slowly. The effect can be observed after overetch of an oxide film with large pattern openings; close to the pattern edges silicon is etched deeper than at the pattern center. For instance, with 1.6  $\mu\text{m}$  resist and 1  $\mu\text{m}$  oxide thicknesses, an overetch of 300% at a selectivity of 150 to 300 results in silicon etch depths of 3 to 10  $\mu\text{m}$  within 10  $\mu\text{m}$  of the pattern edges. However, in the remaining

areas of the pattern an etch depth of 1 nm is obtained. This pattern sensitivity can be minimized by (a) requiring uniform pattern hole sizes; or (b) operating at selectivities of 100 or below, where this effect has not been observed in patterns as wide as 70  $\mu\text{m}$ .

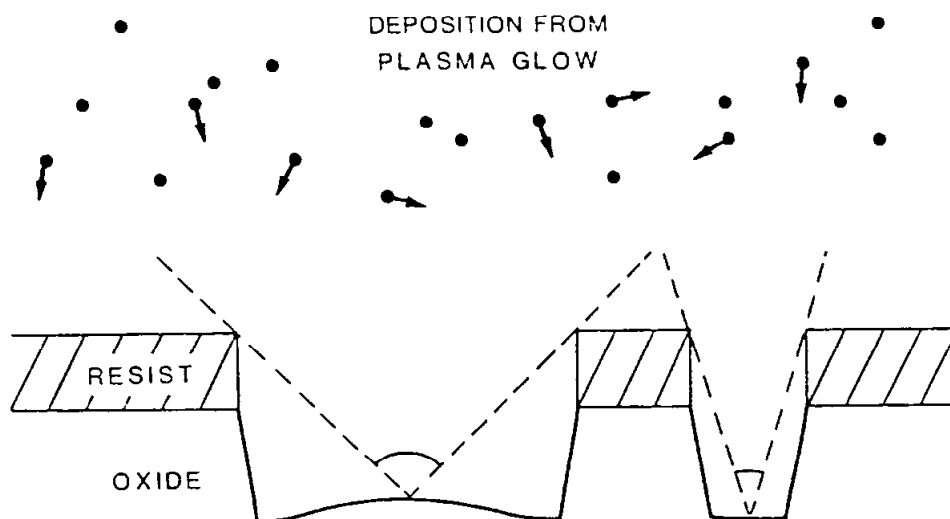


**Figure 15:** Preferential etching of small apertures at high selectivity. Wide structures have large polymer acceptance angles and have low central etch rates.

Another practical limit to selectivity is the tolerable level of polymer deposition. In the trielectrode chamber (Fig. 12(d)), the rf voltage on the ring can be set at the level where ring etching begins to dominate over polymer deposition, without dc supply current flow. Application of dc current to the rings then permits adjustment of the metal ring sputtering rate. In this case, polymer deposition is inhibited on all central target and ring areas, resulting in polymer film buildup only on chamber surfaces remote from the etched substrate wafer. This "clean" environment for the etched wafer compares with standard unconfined and guard-confined systems, which permit polymer buildup opposite the etched wafer (Fig. 1), and on the periphery of the etched wafers (Fig. 4). Thick polymer deposits can flake on exposure to air, resulting in undesirable particle deposition on etched wafers (10, 11). Only three chamber types discussed here are capable of inhibiting polymer buildup around the etched wafers; symmetric diodes with large etched target areas surrounding the wafers, the trielectrode hollow cathode (Fig. 12(d)), and the hollow cathode surrounded by a reduced-area chamber (Fig. 12(c)). These chamber types offer longer periods between cleanup cycles than the other hollow cathode and diode systems, and the possibility of more prolonged operation at high selectivity levels.

Etch uniformity is of greatest importance in cases where the  $\text{SiO}_2$  layer thickness is identical in all etched apertures on a wafer. Then even a low-selectivity process could in principle be stopped exactly at the point where all  $\text{SiO}_2$  had been cleared from those apertures, provided that this low selectivity process exhibited uniform etching over the wafer surface. In practice the  $\text{SiO}_2$  layer thickness often varies from aperture to aperture because contacts must be made to different layers in a chip, at differing levels. Thus etch uniformity cannot be exactly traded off against selectivity; in chips with varying oxide

thicknesses uniformity must be less important than selectivity. Hollow cathode uniformity can be adjusted with gas pressure and target spacing; the trielectrode hollow cathode uniformity can also be varied with the level of ring electrode excitation. In general wide electrode spacing results in low etch rates at the substrate edge in comparison with the central etch rate, probably because energetic particle loss at the discharge edge results in lower discharge intensity there. Closer electrode spacing aids confinement processes and results in lower losses and in higher edge etch rates. These trends are illustrated in Fig. 16, which shows etch rates across a 100mm dia. wafer (clamped by a 90 mm I.D. polyimide-coated metal ring) in a trielectrode hollow cathode. Target spacings were varied by changing the height of the surrounding chamber walls; at a wide target spacing of 34 mm the edge etch rate is lower than that in the center, as expected. Closer spacings, to a minimum target separation of 14mm, demonstrate a general trend towards higher edge etch rates, resulting in  $\pm 1\%$  etch rate uniformity being obtained between 21 and 24 mm target spacing.

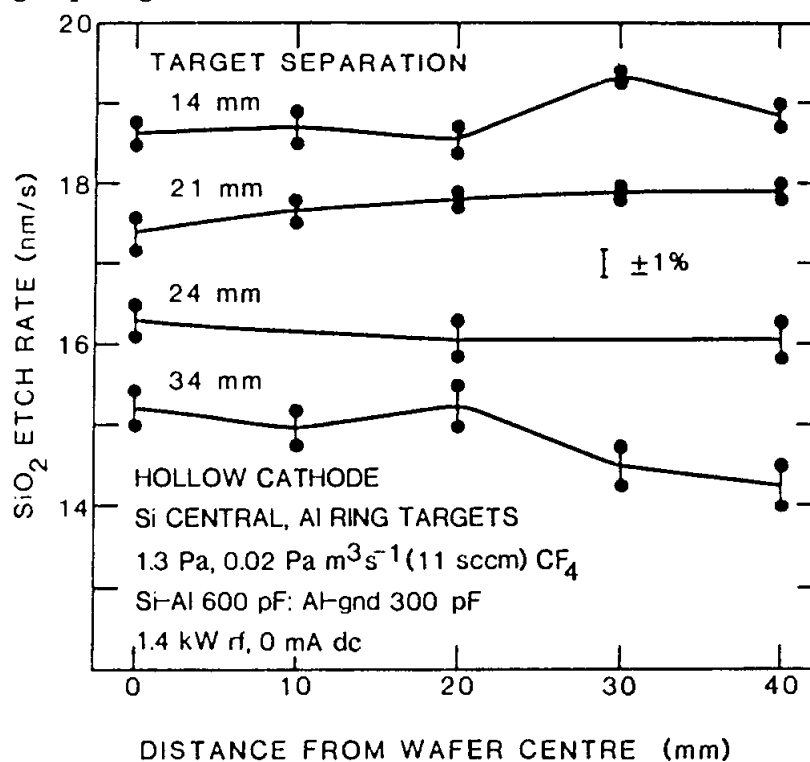


**Figure 16:** Etch uniformity across a 100-mm wafer for various target separations using a trielectrode chamber. The input rf power was kept constant; the rf voltage falls sharply at small separations. The wafer was clamped by a ring of 45-mm radius.

Silicon etch uniformity is of interest because of its impact on etch selectivity. Often the silicon etch rate variation across a wafer is far greater than that of  $\text{SiO}_2$ . Silicon etch rates are affected not only by ion bombardment (which is the dominant etch mechanism for  $\text{SiO}_2$ ), but by neutral fluorine concentration and by polymer deposition rate. At low polymer generation rates (i.e. with only  $\text{CF}_4$  etch gas) the electrode spacing for best silicon etch uniformity is typically a little larger than that for  $\text{SiO}_2$ ; and uniformities to within a few percent are normal at the optimum spacing. However with  $\text{H}_2$  added, silicon etch uniformity is controlled by polymer deposition which, in the trielectrode system, depends on metal ring target voltage more than on target spacing. Thus the best silicon etch uniformity, hence the best selectivity uniformity, is obtained when the metal ring voltage

is close to that of the target. This would be achieved by ensuring close capacitive coupling between the central targets and the ring targets, and can result in very high input power levels for a given  $\text{SiO}_2$  etch rate. High  $\text{SiO}_2$  etch rates are more easily obtained under the looser coupling between ring and central targets indicated in Fig. 16, which results in higher silicon etch rates at the edge than in the center. The resultant difference in edge and center selectivities is plotted in Fig. 17, which shows a highest central selectivity of 150-300, and an edge value of 50. The lowest selectivities are obtained in pure  $\text{CF}_4$ ; 15 at the center, falling to 10 at the edge. At the highest selectivities in this system the  $\text{SiO}_2$  etch rate remains high at  $15\text{nm/s}$  ( $0.9\text{ }\mu\text{m/min}$ ), and uniform to within  $\pm 1\%$  from center to edge.

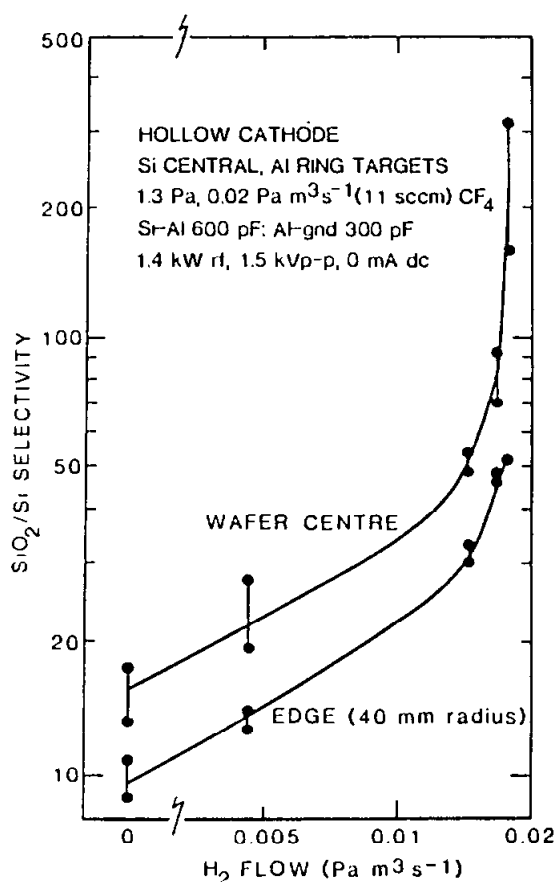


**Figure 17:** Etch selectivity at center and edge of trielectrode hollow cathode with 21-mm target separation.

The etched  $\text{SiO}_2$  angle depends on metal ring target etch rates; with 200 mA ring dc applied current and Al metal electrodes a  $75^\circ \pm 5^\circ$  angle is obtained between 0 and 40mm radius (i.e., to within 5mm of the wafer clamp edge). Thus our Al-containing angle control compounds appear to have adequate range with this operating pressure and target geometry.

#### 12.4.2 Device Processing; $\text{SiO}_2$ Etch

The previous sections have shown that low  $\text{CF}_4$  pressures and high target voltages allow a highly selective  $\text{SiO}_2$  etch to be obtained with added hydrogen, and that angle control can be obtained with added metal. As an example of such conditions, Fig. 18 shows the performance of a guard-confined hollow cathode as a function of hydrogen gas partial pressure.  $\text{SiO}_2$  etch rates of  $1 - 1.5\text{ }\mu\text{m/min}$  were obtained at selectivities of 15 - 20, while the amount of Al metal on the target opposing the patterned wafer resulted in

a  $70^\circ$  etched angle from the horizontal. The compatibility of this high-rate, high-voltage, angle-controlled etch with CMOS device processing was demonstrated as follows:

(a) Etched contact holes in  $\text{SiO}_2$  must yield low contact resistances to the underlying Si or poly-Si substrate. The quality of the etched Si surface can be inferred from previous studies, which have shown that the quality of thermal oxide grown on a previously etched Si wafer falls as  $\text{CF}_4$  etch voltage rises. This indicates that high voltage  $\text{CF}_4$  discharges cause surface roughness and/or leave chemical residues on Si surfaces (4). Surprisingly, the addition of hydrogen to these discharges resulted in higher surface quality (27). It is worth noting the effect of discharge chemistry on these "damage" levels; a gas without carbon such as  $\text{SiF}_4$  resulted in very low damage levels at the highest voltages tested.

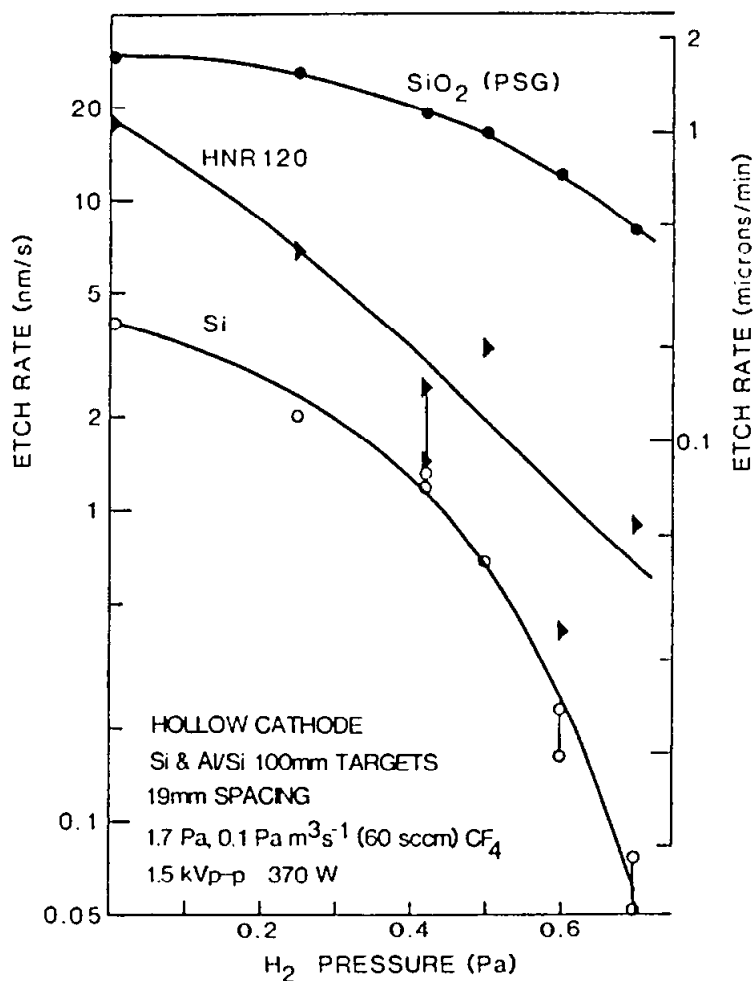


**Figure 18:** Selective etching of heatsunk substrates in a guard-confined hollow cathode chamber. HNR 120 is a negative photoresist, and PSG is phosphosilicate glass (similar to  $\text{SiO}_2$  in our apparatus). CMOS device wafers were processed between 0.4 and 0.6 Pa hydrogen pressure.

Our measured contact resistances correlate well with the above data on damage levels in grown oxides. Intermediate contact resistances to  $p^+$  doped Si and to  $n^+$  poly-Si, counterdoped with  $p^+$  dopant were obtained at completion of the selective  $\text{CF}_4/\text{H}_2$  etch (Fig. 19, "no final etch" points on left-hand side). Although such resistances may be tolerable in low-current CMOS circuits, they are not as low as can be obtained with wet oxide etching in HF, indicating the presence of residues and/or surface roughness. This "damage" may be removed by etching off a thin Si surface layer in several ways (28-30). In the present case pure  $\text{CF}_4$  was used to remove about 10 nm of silicon in a non-selective final etch step, resulting in poor resistances at high applied voltages, but in excellent

contact resistances at low applied voltages (Fig. 19). This is again in agreement with the oxide damage studies.

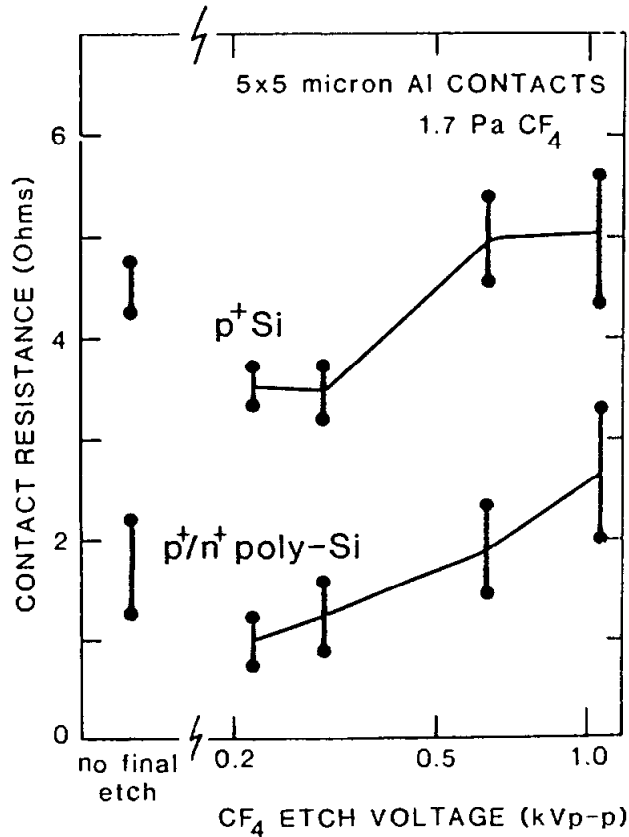


**Figure 19:** Contact resistances after various CF<sub>4</sub> etch treatments following a selective CF<sub>4</sub>/H<sub>2</sub> etch. Errors shown are one  $\sigma$  over ten readings. Silicon etch depths were  $\approx 10\text{nm}(100\text{\AA})$

The above data relates to contact resistances between Al and the relatively lightly doped materials with p-type (boron) doping. In silicon this doping level gave a sheet resistivity of  $100\ \Omega/\text{square}$ . The n<sup>+</sup> - type polysilicon, and n<sup>+</sup> -type silicon doped to a  $10\ \Omega/\text{square}$  level gave contact resistances between  $0.8$  and  $1.1\ \Omega$  in  $5 \times 5\ \mu\text{m}$  (nominal) contact holes, independent of post processing etch treatment and roughly equal to the value obtained with wet HF etching.

(b) Field-effect devices, such as those used in CMOS logic, can be damaged by changes in the properties of gate oxides. Rapid target potential changes can result in high-voltage gate oxide stress, and in device breakdown (31); in the present study target voltages were ramped and controlled by computer, with no sudden changes permitted. The device yield figures which are listed below indicate that our process has not induced gate breakdown.

Gate oxides can also be modified by injected charges arising either from charged particle bombardment or from discharge UV/Xray irradiation (32); these charges could induce a shift in device threshold voltages. Threshold voltages of n-channel devices with  $100\ \text{nm}$  oxide thickness showed no detectable deviation (within the  $\pm 20\ \text{mV}$  scatter) between our high-rate hollow cathode process and the control wafers. p-channel thresholds also showed no detectable deviation from the control wafers, within their larger scatter of  $\pm 50\text{mV}$ .

(c) The sidewall angle etch process relies on novel chemistry and leaves a thin layer, of the order of one monolayer thickness, on etched sidewalls. To test whether this layer causes any yield or long-term reliability problems, CMOS clock generator chips, using



devices with 100 nm oxide thickness and 5  $\mu\text{m}$  minimum gate length, were fabricated using the high-rate hollow cathode process for the final contact hole etch. Control wafers were etched in a commercial planar etch system, then given a phosphosilicate glass reflow to obtain sloped sidewalls. All wafers were then metallized, sintered, and overcoated. The control wafer yields were in the normal range for this device of 52% to 69%; hollow cathode wafer yields were between 67% and 82% even after over-etching by up to 200%, indicating adequate etch selectivity for these devices, and showing a 15% yield improvement over the control wafers. When placed on life test for 1000 hours with 5V supply and at 125°C, no failures occurred in the 89 chips tested.

The above data demonstrates the viability of high-rate, controlled-angle and selective hollow cathode etching in standard CMOS processing. Lately the angled hollow cathode etch has been applied to front-surface texturing of solar cells (33). A hollow cathode silicon trench process (see following section) has also been used to form high-efficiency solar cell diode structures. Our processes have been compatible with all of these devices, without special post-etch treatments.

### 12.4.3 Si Etching

Limited work on silicon etching has been performed in the hollow cathode to date, in comparison with oxide etching and with silicon deposition. The results reported here relate to process selectivity and to isolated Si beam formation, and have been obtained during the fabrication of small isolated bipolar devices (34). Throughout this discussion the mask material is patterned  $\text{SiO}_2$ .

Silicon may be etched selectively relative to  $\text{SiO}_2$  in gases with greater fluorine content than  $\text{CF}_4$ . An example is  $\text{SF}_6$ , where selectivities of around 5 can be obtained at high pressure and at high etch rate (Fig. 20). Here the observed selectivity is a result of the high reactivity of Si with free F atoms, and non-directional (isotropic) etching is obtained under these conditions. At a lower target voltage of 200  $\text{V}_{\text{p-p}}$ , a selectivity of 200 can be obtained, again with isotropic Si etching. Such behavior is similar to that of  $\text{SF}_6$  in diode systems (35). High selectivity in a directional etch requires gases containing Cl, in which ion bombardment is required to induce Cl-Si reactions. One example is shown in Fig. 21, where a selectivity of almost 10 is obtained at a relatively high  $\text{Cl}_2$  operating pressure and etch rate. As with  $\text{SF}_6$ , selectivities against oxide rise as target voltage is lowered; in 10 Pa  $\text{Cl}_2$  we have measured a selectivity of 15 at 1.4  $\text{kV}_{\text{p-p}}$ , rising to 32 at 1  $\text{kV}_{\text{p-p}}$ .

The above etch results relate to "simple" discharge etch processes, without competitive deposition. As in silicon dioxide etching where polymer deposition enables high selectivity to be obtained without etch rate and target voltage tradeoffs, silicon etch processes can benefit from controlled deposition of a layer containing silicon dioxide. The silicon for this layer can be sourced from the etched target or from the etch gas (36), and the rate of oxide layer growth controlled by the oxygen content of the discharge gas. Because the deposition of this layer is from an approximately isotropic source in the discharge it deposits easier on tall masked structures than in deep trenches. This enables etch selectivity to be increased during trench etching, protecting mask layers from erosion

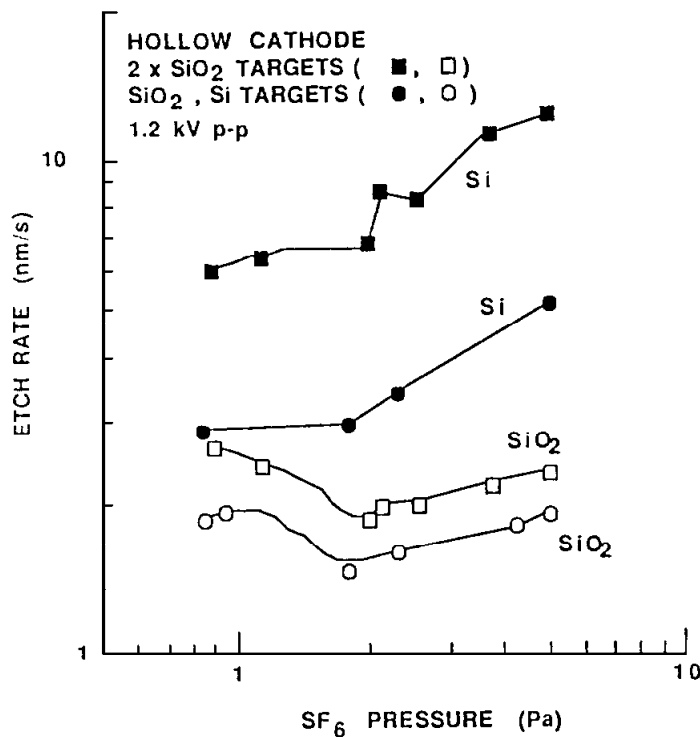


**Figure 20:** Silicon and SiO<sub>2</sub> hollow cathode etch rates in SF<sub>6</sub> discharges. High Si etch rates and Si/SiO<sub>2</sub> selectivities are obtained in an "unloaded" system with two SiO<sub>2</sub> targets.

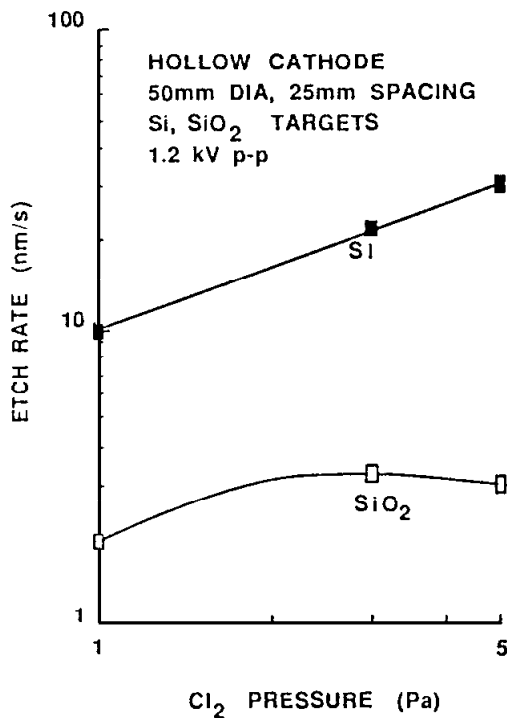


**Figure 21:** Silicon and SiO<sub>2</sub> hollow cathode etch rates in Cl<sub>2</sub> discharges, as a function of Cl<sub>2</sub> pressure. Note the high Si etch rates; 16.7 nm/s is one micron/minute.

during the final etch stages but allowing the native Si oxide layer to be broken through cleanly in the initial etch phase. The results shown in Fig. 22 for an SiCl<sub>4</sub>/H<sub>2</sub>/O<sub>2</sub> gas mixture show that selectivities of 10-20 are obtained up to the high- O<sub>2</sub> flow point where an oxide coating would form on all exposed flat surfaces. Deep trench etching would

commence at such selectivity levels, then operate at increased  $O_2$  flow to permit accurate control of the trench bottom shape while protecting the top mask (Fig. 23). As in diode etching (37-38), low  $O_2$  gas flow allows mask faceting and etch-back; intermediate  $O_2$  flow protects the mask, but results in straight trench walls which increase ion bombardment and etching at the trench sides; and high  $O_2$  flow gradually narrows the top mask aperture, resulting in sloped trench sides and a smooth trench profile.

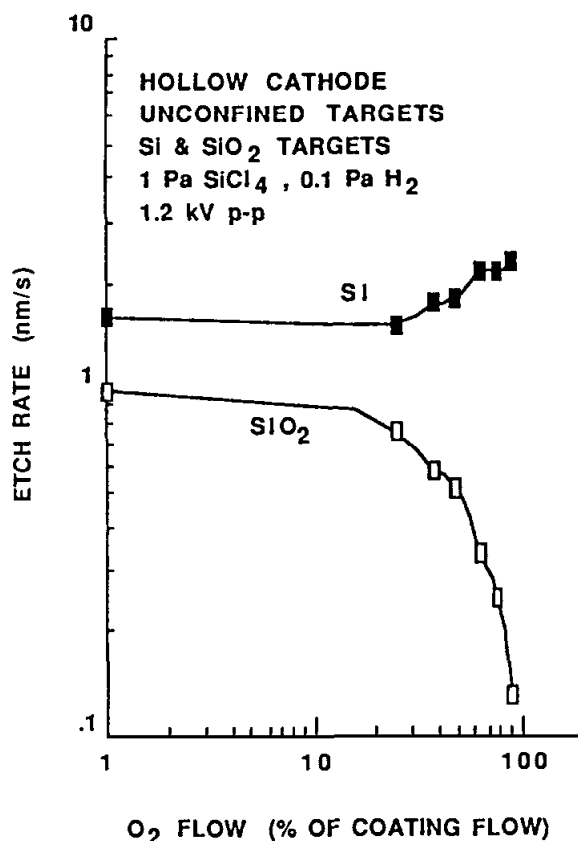


**Figure 22:** Silicon and  $SiO_2$  hollow cathode etch rates in a  $SiCl_4/H_2/O_2$  gas mixture, as a function of  $O_2$  gas flow. "100%"  $O_2$  flow is just sufficient to cause deposition of a  $SiO_x$  film on flat exposed target surfaces. Trench bottoms are shadowed from this deposition, and are not coated until higher  $O_2$  flows are reached. Typical etches begin at low flow, rising to above "100%" during the etch.

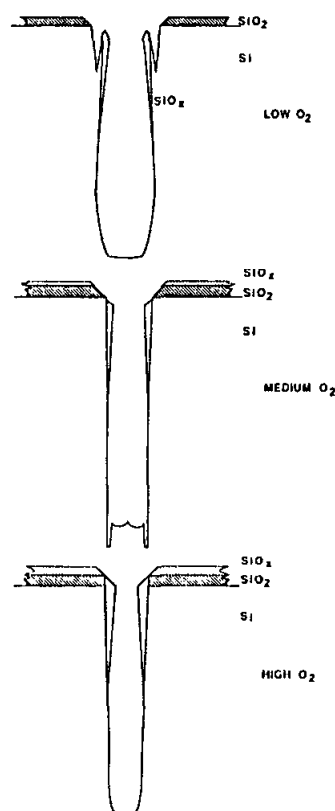


**Figure 23:** Silicon trench etch profiles. Top: low  $O_2$  levels result in mask faceting and Si edge erosion. Center: medium  $O_2$  levels facet the mask and form bottom trenches. Bottom: high  $O_2$  levels form rounded trench bottom profiles.

The deposited oxide may be removed in a selective wet etch. For instance, 100:1 diluted HF etches the deposited oxide 70 times faster than thermal oxide, allowing thermal oxide masks to be retained if needed (Fig. 24). The deposited oxide may however be retained if isolated silicon beams are required; it acts as a good etch mask against isotropic  $\text{SF}_6$  etching. A cantilever structure so formed is shown in Fig. 25, before insulator refill around the Si beam.

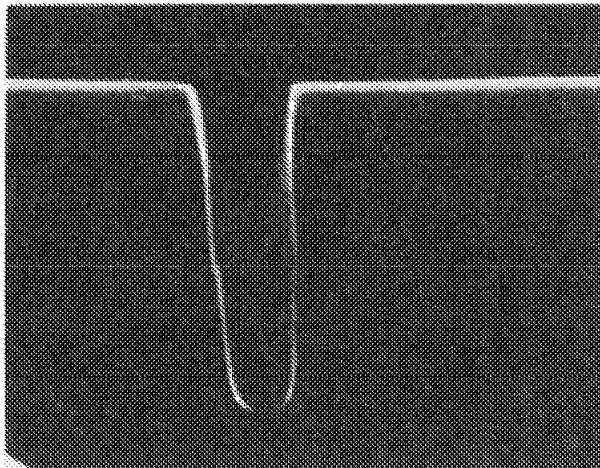
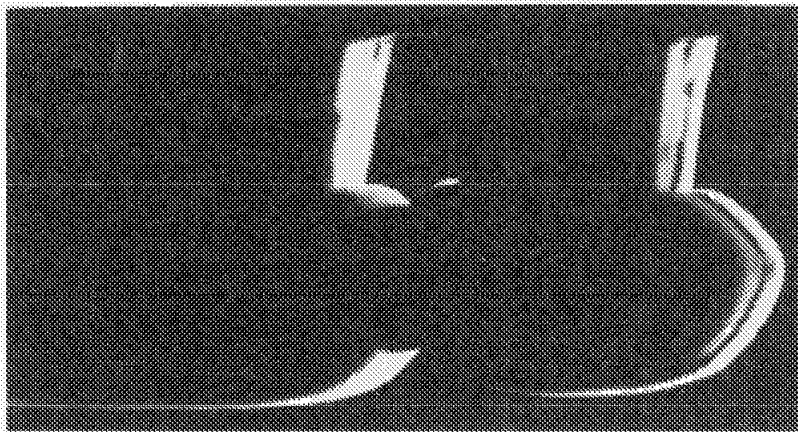


**Figure 24:** Silicon trench etched in the hollow cathode using low initial  $\text{O}_2$  gas flow, rising to high levels later in the etch.  $\text{Cl}_2$  etch gas; deposited oxide removed, 0.5-micron thermal oxide mask remaining; 20  $\mu\text{m}$  deep trench.

———— 10 microns



———— 10 microns

**Figure 25:** Single-crystal Si cantilever beam after trench etch,  $\text{SF}_6$  "cutoff" etch, and oxide removal; before insulator refill.

## 12.5 Si DEPOSITION PERFORMANCE

### 12.5.1 Substrate Processes

Previous sections have shown how controlled deposition can benefit etch processes. In this section the benefits of controlled etching during film deposition will be investi-

gated, using silicon deposition from silane as a model. In our discharges the film deposition of interest occurs on ion-bombarded targets, resulting in many film-forming and film-modifying processes:

(a) The discharge glow region can form Si nuclei, resulting in particles which fall or diffuse to the wafer surface. Such "homogeneous nucleation" in the gas results in a rough film if the particles are large in comparison with the scale of redistribution processes on the substrate.

(b) The input  $\text{SiH}_4$  gas, or a fragment of it such as  $\text{SiH}_2$ , may adsorb on the target surface. Thermally activated processes could further break this adsorbate down, depositing Si. Such thermally activated "heterogeneous nucleation" is often the primary mechanism of chemical vapor deposition, but on our room-temperature substrates is negligible.

(c) The surface adsorbates in (b) may be broken down by the energy liberated during ion impact, resulting in Si film formation. In the present case this growth process dominates over (a) (homogeneous nucleation) at low silane pressures.

(d) Ion impact during film deposition redistributes film atoms, removing voids and densifying the film (39). However, interstitials are created which result in a compressive film stress (40), which in some cases has been observed to increase with the square root of the ion energy (41). Films under high compressive stress can fail even during deposition, through loss of adhesion to the substrate and subsequent peeling. High stress can also lead to peeling of the film during high temperature ( $1000^\circ\text{C}$ ) doping operations. Film stress can be lowered by deposition above room temperature or by annealing, both of which permit relaxation of strain by thermal diffusion of atoms to low energy sites. The Si films in this study tolerate  $1000^\circ\text{C}$  thermal treatments after a  $600^\circ\text{C}$  anneal cycle.

(e) Ion impact also results in sputter etching and redeposition, which "facets" sharp edges and fills in deep holes, resulting in planarization of the growing film (8,9,42).

(f) High-energy ion impact (above 2000 eV) forms interstitials at depths of 10 nm and deeper, below the target surface. Such "ion implantation" in the present case should result in little alteration of film chemistry. However, it should be noted that the hydrogen derived from our silane input gas may have a greater range than the larger ions (43).

(g) Electron bombardment of a growing insulator film results in inferior electronic performance due to trap formation (8,9,32). Although these can be annealed out, the hollow cathode electron mirror phenomena should minimize such trap formation.

(h) Traps may also be formed in insulators by UV and Xray irradiation (32). It is possible that systems with high power efficiency (such as the confined hollow cathodes) have advantages over reactors with lower power efficiency in this regard.

### 12.5.2 Experimental Results

In our experiments with hollow cathode discharges the dominant deposition mechanism can be deduced by comparing deposition rates on adjacent substrates. Target substrates are exposed to deposition from the glow as well as to ion bombardment,

whereas surrounding guard surfaces are only exposed to glow deposition processes. A comparison of target and guard deposition rates at two pressures (Fig. 26) shows that at 20 Pa the guard rate is 27% higher than the average target rate, implying that deposition of silicon is primarily from the discharge glow. High pressure ion bombardment appears to serve more as an agent of etching than of deposition. At a low 1.34 Pa pressure the situation is reversed with a guard rate equal to 55% of the average target rate. Hence at low pressure, ion-induced deposition coupled with ion-induced etching become the dominant film forming mechanisms. Films deposited at low pressures should thus be somewhat smoother than those deposited at high pressures, due to a greater "heterogeneous nucleation" contribution.

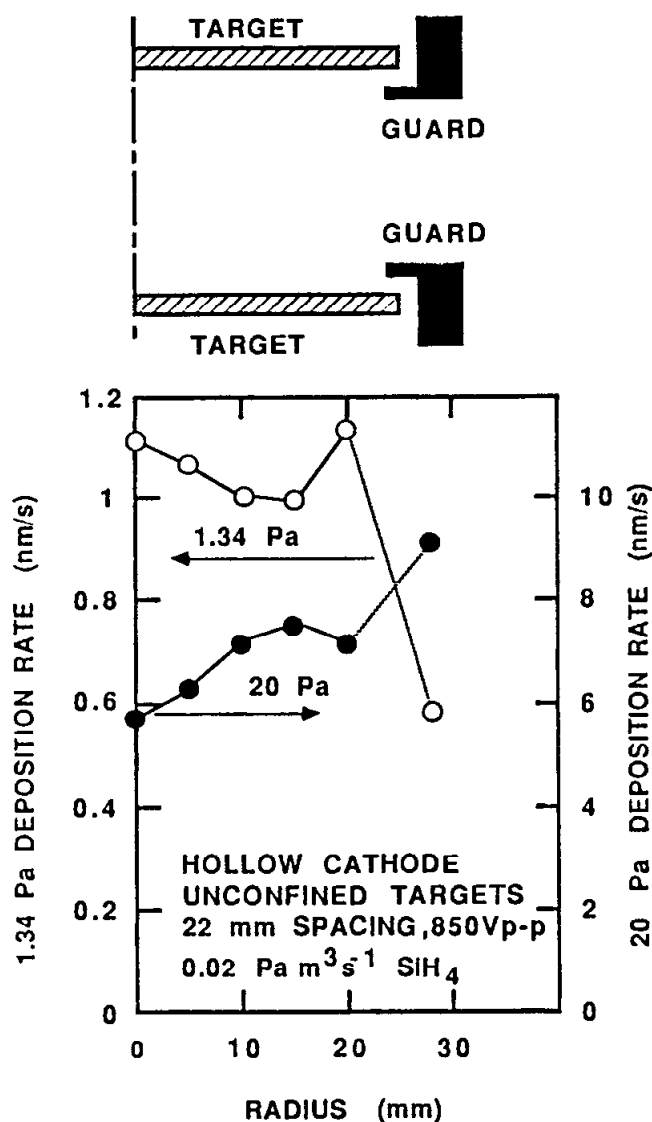


**Figure 26:** Deposition rate as a function of substrate position at two silane pressures. The upper drawing of (half of) the targets shows the 27mm samples to be on the guard. Uniformity between 0 and 21 mm radius is  $\pm 6\%$  ( $1\sigma$ ) in both cases.

Independent of the deposition mechanism, the step coverage of a growing film is controlled by its (deposition/etching) rate ratio. Large ratios imply that etching due to ion bombardment is swamped by deposition processes, resulting in little film redistribution after initial deposition, and so in poor coverage over steps in the substrate. An example of the resulting re-entrant film profiles, and of void formation, is given in Fig. 27 for a relatively thick (2 micron) film. Such poor deposition conditions are generally obtained at high pressures and at high gas flow rates, where copious chemical reactants are available for film deposition processes. At low pressures (Fig. 28), or at low input gas

flow rates (Fig. 29), etching processes become more effective (15). The results of this etching, and subsequent redeposition of etched material on other parts of the substrate, are better filling of hollows in the substrate and of voids in the growing film; and formation of etched facets on upper exposed portions of the growing film. Sufficiently thick films become planarized by this faceting process (21).

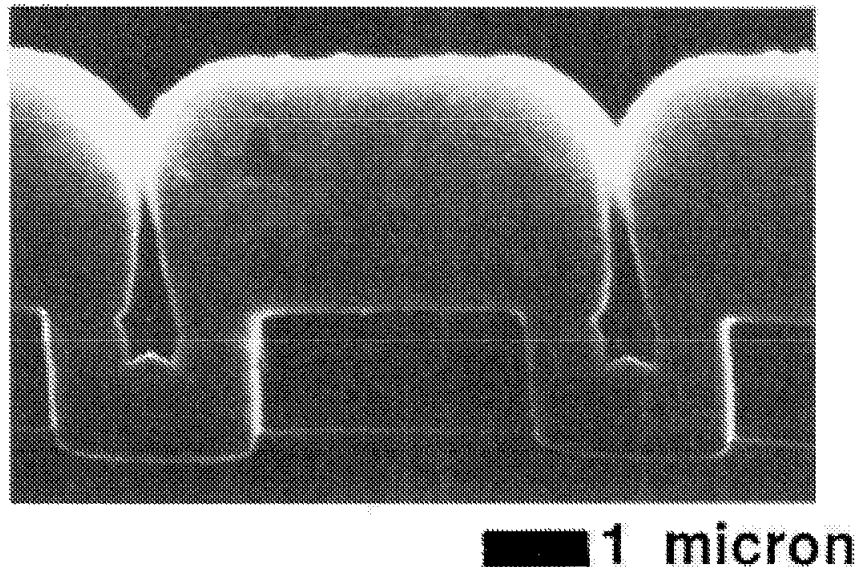


**Figure 27:** Voids and re-entrant profiles in a directionally-deposited film. Si film deposited over  $\text{SiO}_2$  grating steps ( $\text{SiO}_2$  removed in HF). Unconfined hollow cathode; 3.5  $\text{kV}_{\text{p-p}}$ , 10 Pa  $\text{SiH}_4$ , 2 micron nominal Si film thickness.

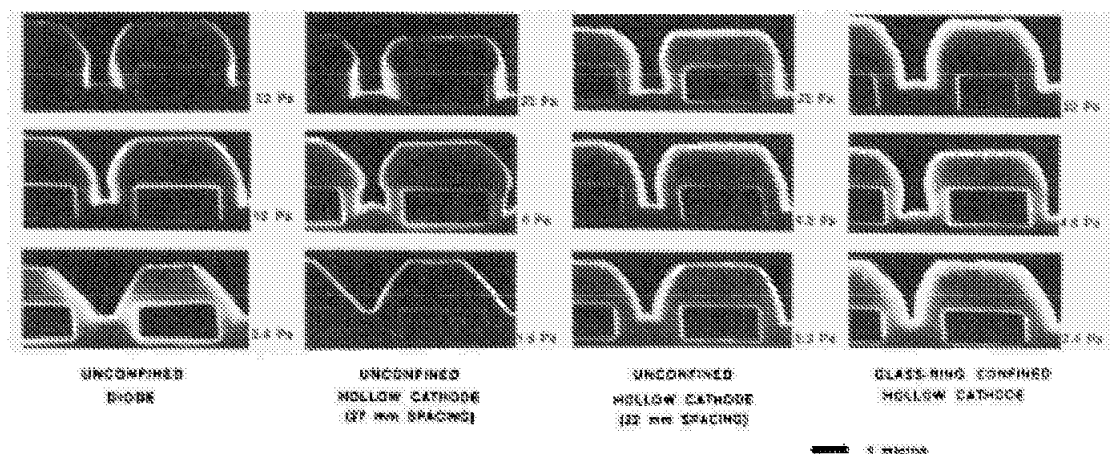


**Figure 28:** Deposited silicon profiles over  $\text{SiO}_2$  grating steps with  $\text{SiO}_2$  etched away. Left; diode; Center; unconfined hollow cathodes; Right; glass-ring-confined hollow cathode. This latter is similar to a guard-confined hollow cathode. Silane pressures shown to the right of each picture. For these studies, a high silane flow (about  $0.04 \text{ Pa m}^3\text{s}^{-1}$ ), and 3.5  $\text{kV}_{\text{p-p}}$  was used.

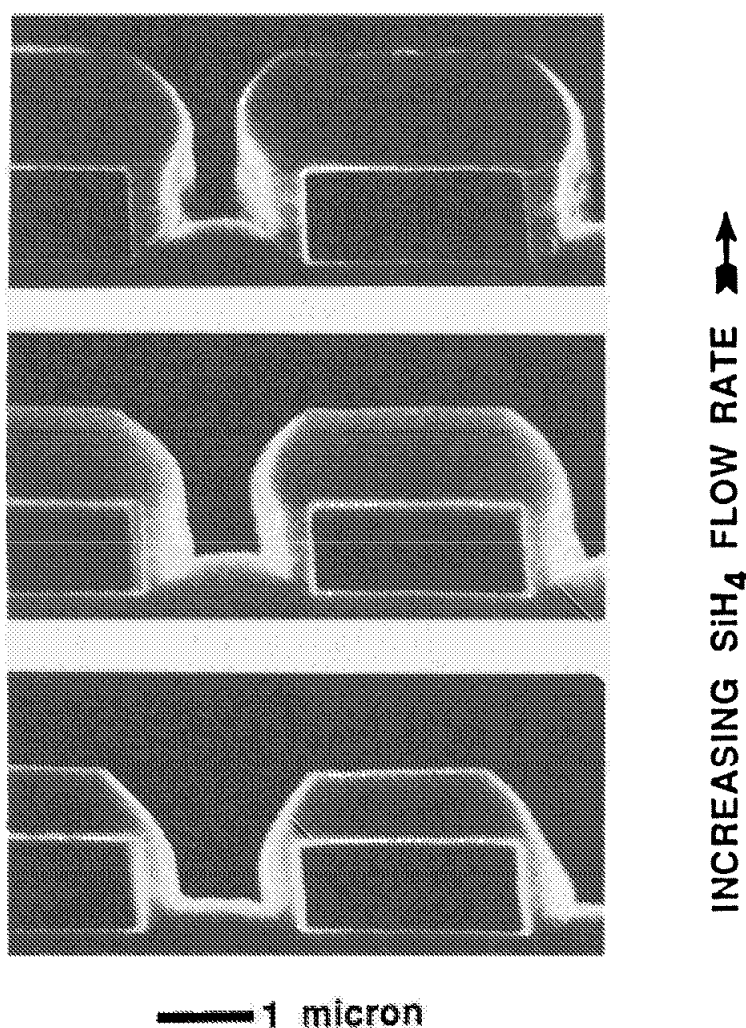


**Figure 29:** Flow rate dependence of deposited silicon profiles at 22 Pa silane fill pressure, in an unconfined hollow cathode with remote gas injection. Deposition rates increase by about a factor of 5 from bottom to top of the figure. Flow rates (from bottom): 0.004, 0.016, 0.085 Pa m<sup>3</sup>s<sup>-1</sup> of SiH<sub>4</sub>, with 3.5 kV<sub>p-p</sub> target voltage.

## 12.6 CONCLUSIONS

Our understanding of discharge behavior and of confinement effects is by no means complete. We do not understand why oxide etching is inherently more selective in hollow cathodes than in diode reactors. In addition the relationship between ion bombardment and target areas, familiar in the diode situation, is not yet clarified for hollow cathodes. Further work in these areas will doubtless clarify the interrelationships between these enhanced discharge systems, and their simple diode precursor. However, confined rf discharges, and especially those incorporating hollow cathodes, permit high deposition rates to be maintained at low pressures, with low target voltages and low rf input power densities. This capability, combined with competitive deposition as in the case of an etch process, or competitive etching as in the case of a deposition process, gives a wide degree of control over the shapes that can be formed in electronic substrate materials.



**12.7 REFERENCES**

1. G. C. Schwartz, L. B. Rothman, and T. J. Schopen, J. Electrochem Soc. 126: 464 (1979).
2. C. M. Horwitz, J. Vac. Sci. Technol. A1: 1795 (1983).
3. L. M. Ephrath and D. J. Di Maria, Solid State Technol. 24: 184 (April 1981).
4. S. W. Pang, C. M. Horwitz, D. D. Rathman, S.M. Cabral, D. J. Silversmith and R. W. Mountain, in Proc. 4th ECS symp. on Plasma Processing, (Electrochemical Society, Pennington, NJ, 1983) 83-10: pp.84 - 92.
5. F.H.M. Sanderson and J. Dielman, 3rd Int'l. Symp. on Dry Etching and Plasma Deposition, 26-29 Nov. 1985; Le Vide - Les Couches Minces 229: 45, (1985).
6. E. J. Egerton, A. Nef, W. Millikin, W. Cook, and D. Baril, Solid State Technol. 25: 84, (1982).
7. I.Hussla, K.Enke, H.Grunwald, G.Lorenz and H.Stoll, J. Phys.D: Appl. Phys. 20: 889 (1987).
8. Y. Hazuki and T. Moriya, in Proc. 1985 Symp. on VLSI Technol Kobe, Japan, IEEE Cat. No. 85 CH2125-3 (IEEE, NJ, 1985) pp. 20-23.
9. H. Okabayashi, in Proc.1984 Symp.on VLSI Technol, San Diego, USA, IEEE Cat.No.84 CH2061-0 (IEEE, NJ, 1984) pp 20-23.
10. C.J. Mullins, Microelectron. Manufact. Test. 9: 1, (1986).
11. G. O. Fior, L. N. Giffen, and W. W. Palmer, Solid State Technol. 31: 109 (1988).
12. J. J. Cuomo and S. M. Rossnagel, J. Vac. Sci. Technol. A4: 393 (1986).
13. Y. S. Kuo, R. F. Bunshah, and D. Okrent, J. Vac. Sci. Technol., A4: 397 (1986).
14. K. E. Davies and C. M. Horwitz, "Diode and Hollow Cathode Etching in CF<sub>4</sub> ", submitted to J. Vac. Sci. Technol. (1988).
15. C. M. Horwitz, "Silicon Deposition in Diode and Hollow-Cathode Systems", submitted to J. Vac. Sci. Technol. (1988).
16. C. M. Horwitz, J. Vac. Sci. Technol. A1: 60 (1983).
17. M. E. Pillow, Spectrochim. Acta 36: 821 (1981).
18. J. S. Chang, Solid State Technol. 27: 214 (1984).
19. M. Gross and C. M. Horwitz, "Modelling of Sloped Sidewalls Formed by Simultaneous Etching and Deposition", (1988).
20. C. M. Horwitz, Appl. Phys. Lett. 44: 1041, (1984).
21. C. M. Horwitz, S. Boronkay, M. Gross and K. E. Davies, J. Vac. Sci. Technol. A6: 1837 (1988).
22. C. M. Horwitz, J. Vac. Sci. Technol. B3: 419 (1985).
23. L.M. Ephrath, J.Electrochem. Soc. 126: 1419 (1979).
24. L. M. Ephrath and E. J. Petrillo, in Proc. 3rd. ECS Symp. on Plasma Processing, (Electrochemical Society, Pennington, NJ, 1982) 82-6: pp. 217-233.
25. C. M. Horwitz, Appl. Phys. Lett. 43: 977 (1983).
26. C. M. Horwitz and J. Melngailis, J. Vac. Sci. Technol. B1: 1408 (1981)

27. S. W. Pang, Solid State Technol. 27: 249, (1984); S. W. Pang, D. D. Rathman, D. J. Silversmith, R. W. Mountain, and P. D. De Graff, J. Appl. Phys. 54: 3272, (1983).
28. H. -O. Blom, H. Norstrom, M. Ostling, P. Wiklund, R. Buchta, and C. S. Peterson, J. Vac. Sci. Technol. A4: 752, (1986).
29. S. J. Fonash, Solid State Technol. 28: 201, (1985).
30. G. S. Oehrlein, J. G. Clabes, and P. Spirito, J. Electrochem. Soc. 133: 1022 (1986).
31. T. Watanabe and Y. Yoshida, Solid State Technol. 27: 263 (1984).
32. D. J. DiMaria, L.M. Ephrath, and D. R. Young, J. Appl. Phys. 50: 4015, (1979).
33. S. Narayanan, M. Gross, C. M. Horwitz, and M. A. Green, "High Efficiency Processing/Texturing of Polycrystalline Solar Cells", B-1p-9 in 3rd. Int'l. Photovoltaic Science and Eng. Conf (PVSEC-3), Tokyo, Nov. 3-6, 1987.
34. M. Gross, private communication, 1986.
35. R. A. Gdula, Ext. Abstr. 608, Fall Mtg. of Electrochem. Soc., Los Angeles, October 14-19, 1979, pp.1524-1526.
36. C. M. Horwitz, IEEE Trans. on Electron Devices, ED-28: 1320 (1981).
37. K. Hirobe, K. Kawamura, and K. Nojiri, J. Vac. Sci. Technol. B5: 594 (1987).
38. G. K. Herb, D. J. Reiger, K. Shields, Solid State Technol. 30: 109 (1987).
39. J. E. Yehoda, B. Yang, K. Vedam, and R. Messier, J. Vac. Sci. Technol., A6: 1631 (1988); K.-H. Müller, Phys. Rev. B35: 7906 (1987).
40. K.-H. Müller, J. Vac. Sci. Technol. A3: 2089 (1985); J. Appl. Phys. 59: 2803 (1986); J. Appl. Phys. 62: 1796 (1987).
41. H. Windischmann, J. Appl. Phys. 62: 1800 (1987).
42. C. Y. Ting, V. J. Vivalda, and H. G. Schaefer, J. Vac. Sci. Technol. 15: 1105 (1978).
43. J. M. Heddleson, M. W. Horn, S. J. Fonash, and D. C. Nguyen, J. Vac. Sci. Technol. B6: 280, 1988.

# 13

---

## Ion Plating

---

**Donald M. Mattox**

### 13.1 INTRODUCTION

"Ion Plating" is a generic term applied to atomistic film deposition processes in which the substrate surface and the growing film are subjected to a flux of energetic bombarding particles sufficient to cause changes in the film formation process and the properties of the deposited film. This broad definition does not specify the source of the depositing film particles, the source of bombarding particles nor the environment in which the deposition takes place. The principal criterion is that energetic particle bombardment is used to modify the film formation process and film properties (1-4).

Most recently the term ion plating has been applied to processes where the surface to be coated is in contact with a plasma and the term "Ion Assisted Deposition" (IAD) or Ion Beam Enhanced Deposition (IBED) is used where the substrate is bombarded by an energetic ion beam in a vacuum environment during deposition (e.g. 5,6). There are several other modifying terms which are sometimes used with ion plating such as: "sputter ion plating" and "chemical ion plating" which specify the origin of the depositing species (sputtered material or chemical vapor precursor gases respectively) and "reactive ion plating" used for the deposition of films of compound materials.

Generally, the energetic particles used for bombarding surfaces and growing films are gaseous ions and arise from: i) biasing (dc or rf) a surface in contact with a plasma so that it is bombarded by ions from the plasma, ii) extraction of ions from a confined plasma and accelerating them to a high energy through a grid system into a vacuum environment (ion beam) (7) or iii) reflected high energy neutrals which arise from ion bombarding a surface in a low pressure environment (8,9) such that the reflected neutrals are not thermalized by collisions in the gas phase.

The energetic particles may also be of a condensible species and arise from: i) sources such as are used for isotope separation (10-13), i) acceleration of negative ions from a negatively biased compound or alloy sputtering target (14), i) ions from vacuum or plasma arcs (15) or i) special ion sources (16). In this chapter we will be primarily concerned with the coating of a substrate surface in contact with a plasma where the ion are extracted from the plasma using a DC or RF bias on the substrate or substrate fixturing. However energetic particle bombardment from any source will have the same effects.

### 13.2 PROCESSING PLASMA ENVIRONMENT

Plasmas are gaseous media which contain enough ions and electrons to be electrically conductive (e.g. 17). Energy is introduced into the plasma by the acceleration of electrons in a DC, RF or microwave electric field. These energetic electrons then fragment, excite and ionize atoms or molecules by collisions. A processing plasma is a plasma that is used in materials processing (18). In many if not most cases the processing plasma is a weakly ionized plasma such that there are many more neutral particles than ions in the gas phase and there is a large number of radical species compared to ions when a molecular gas is used. In a processing system the local plasma densities and properties may vary significantly due to electrode configurations, presence of fixturing and other geometrical factors.

In film processing utilizing plasmas the depositing (condensible) species usually traverse the plasma before condensing on the substrate. In doing so some of the species may be fragmented and/or ionized in the plasma. In addition to ionization and excitation by electron-atom collisions the atoms/molecules may be excited or ionized by collision with an excited metastable species in the plasma (Penning ionization) (i.e. Cu by Ar\*). However in the usual ion plating configuration (low density - weakly ionized plasma) little ionization of the condensible species is to be expected (19).

For reactive deposition processes the gaseous reactive species may be "activated" in the plasma to become more chemically reactive. This activation may be in the form of fragmentation (formation of radicals), ionization, atomic excitation and/or increased kinetic energy ("temperature"). Plasma activation of a reactive species is also used in the "Activated Reactive Evaporation" deposition process (20) and Plasma Enhanced Chemical Vapor Deposition (PECVD) (21). A plasma may also be used to form radical species which polymerize to form polymer films of organic and inorganic materials.

In film deposition processes the substrate may be in contact with the plasma in the region of plasma generation (plasma chamber) or may be exposed to the plasma in a "downstream" location. Figure 1 shows some configurations that allow a substrate to be bombarded from a plasma. Figure 2 shows a simple ion plating system using a DC diode gas discharge and a thermal vaporization source (3). Figure 3 shows an ion plating system utilizing a dc diode discharge and a sputtering source (Sputter Ion Plating - SIP) (22). This system allows almost complete coverage of the part except for the point of suspension and high voltage contact.

Plasma enhancement techniques may also be used to locally increase the plasma density. This plasma enhancement may be accomplished by using local RF fields (23), thermo-electron emitting surfaces (24), hollow cathode electron emitters (25-27), deflection of secondary electrons in e-beam evaporation, localized higher gas pressure, etc.

The plasma density may also be increased by the use of magnetic fields which cause the electrons to spiral around the magnetic field lines thus increasing their path length (as in, for example, magnetron configurations) (28). Some of the most dense plasma sources have been developed for the magnetic fusion community (29). Many of these sources use RF power input or thermo-electron emitting surfaces (30) along with confining magnetic fields.

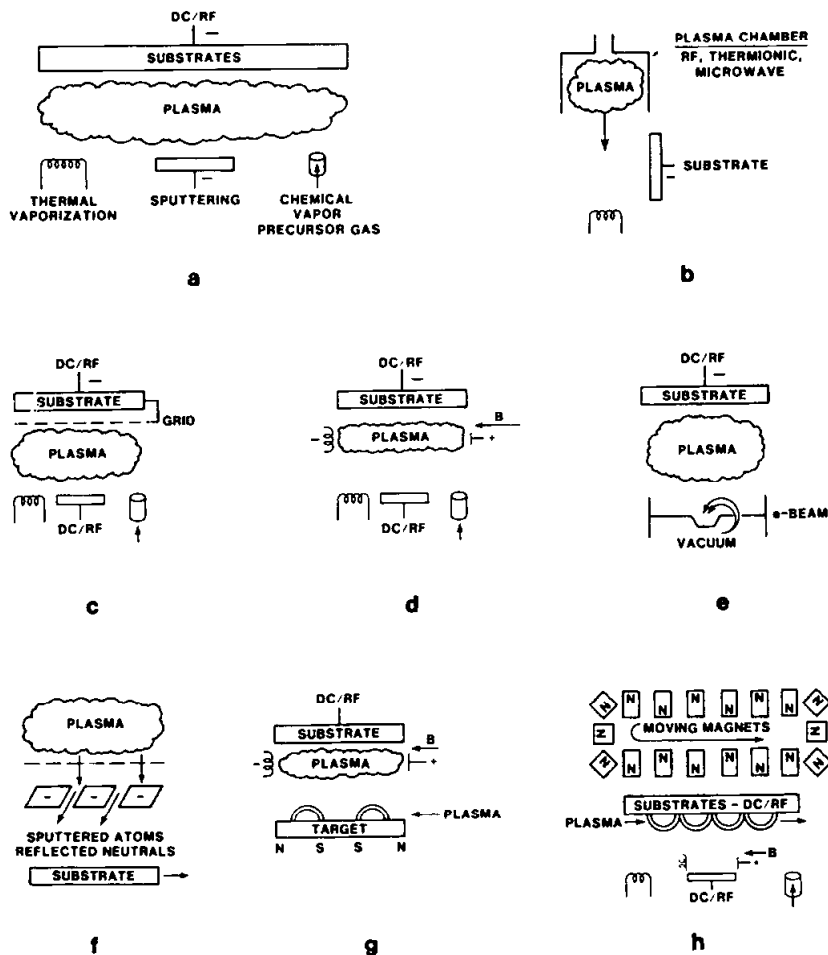


**Figure 1:** Some configurations for bombarding a surface from a plasma by using accelerated or reflected high energy particles. a) diode, b) "downstream configuration", c) grid to allow bombardment of complex surfaces or insulators, d) thermo-electron sustained plasma with magnetic enhancement/confinement, e) e-beam evaporation with a differentially pumped vacuum chamber, f) utilizing reflected high energy neutrals and sputtering, g) magnetron sputtering source and h) moving magnetron plasma to allow uniform bombardment of substrate surface.

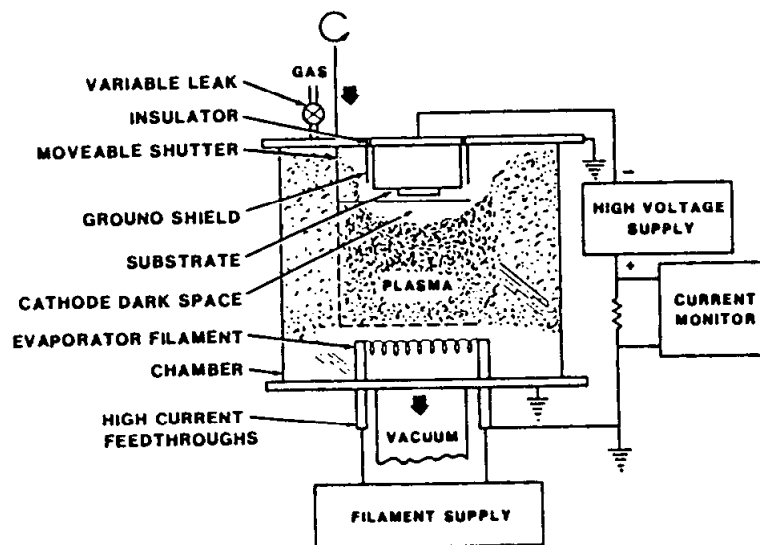


**Figure 2:** An ion plating configuration using a DC diode discharge and a thermal vaporization source (3)

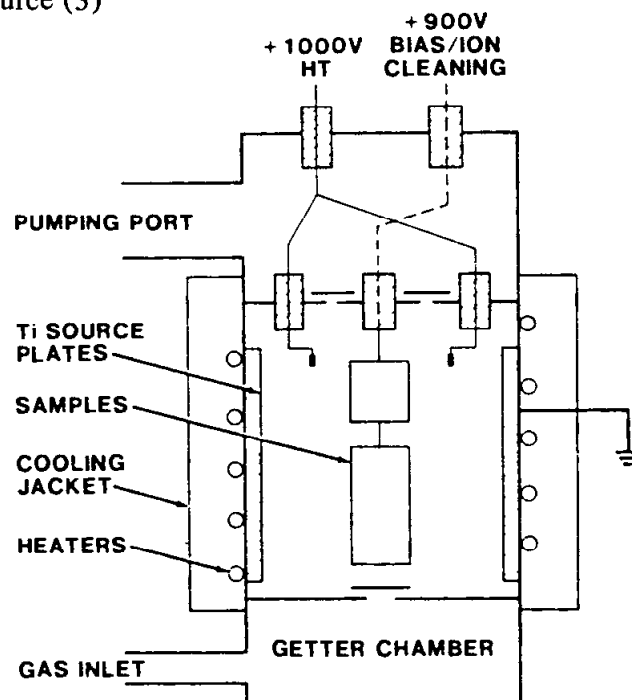


**Figure 3:** An ion plating configuration using a DC diode discharge and a sputtering vapor source at ground potential (SIP)(22).

### 13.3 BOMBARDMENT EFFECTS ON SURFACES AND FILM GROWTH

The physical effects of energetic particle bombardment on surfaces and depositing film material are very dependent on the mass, flux, angle of incidence, and energy of the

bombarding particles and the atomic mass of the target material. Also of importance is the flux of non-energetic particles i.e. depositing or adsorbing species. In many cases these fluxes are not determined or controlled except by the deposition parameters.

Figure 4 depicts the effects on the surface and the subsurface region of bombardment by energetic species. Surface effects include: 1) desorption of weakly bonded surface species, 2) ejection of secondary electrons, 3) reflection of the energetic species as high energy neutrals, 4) sputter ejection (physical sputtering) of surface atoms by momentum transfer through collision cascades, 5) redeposition of sputtered species by collisions in the gas phase or by ionization and acceleration back to the surface and by "forward sputter deposition" due to the ejection angle on a rough surface, 6) enhanced surface mobilities of atoms on the surface and 7) enhanced chemical reaction of adsorbed species on the surface to produce a modified surface (e.g. plasma anodization) or volatile species ("reactive ion etching" {RIE} or "reactive plasma cleaning") or, in the case of depositing species, "reactive deposition".

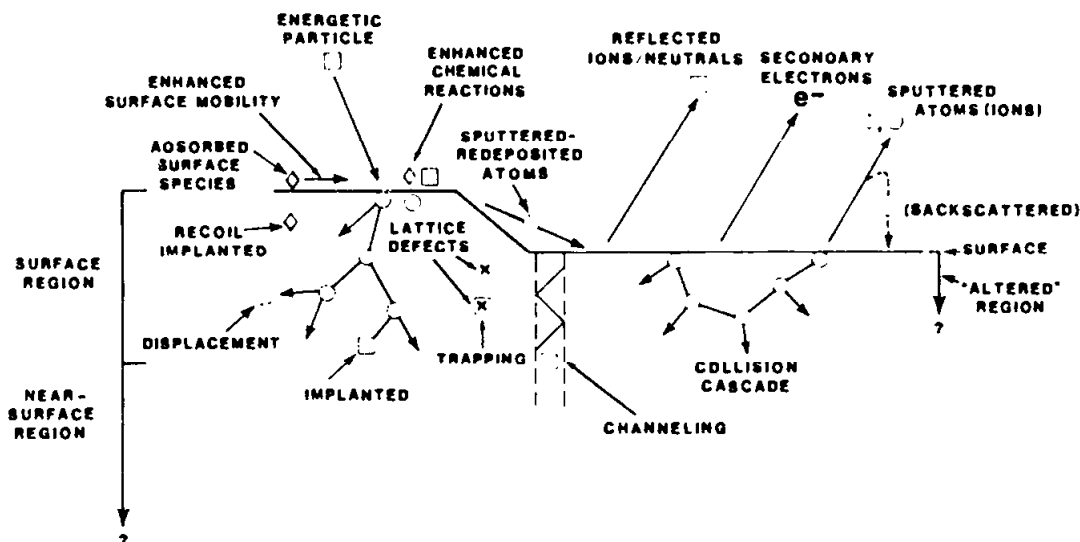


**Figure 4:** Schematic depiction of the energetic particle bombardment effects on surfaces and growing films. See text for discussion.

In the subsurface region: 1) the impinging particles may be physically implanted, 2) the collision cascades cause displacement of lattice atoms and the creation of lattice defects, 3) surface species may be "recoil implanted" into the subsurface lattice, 4) mobile species may be trapped at lattice defects and 5) much of the particle kinetic energy is converted into heat (31,32). Lattice channeling processes can carry these effects deeply into the surface.

The desorption of weakly bound surface species by bombardment is important to plasma cleaning and may be used to reduce the incorporated contaminants in deposited films (33). The desorption may also be useful in desorbing unreacted species in reactive

deposition processes giving rise to more stoichiometric and chemically stable deposits (34).

In the case of dc diode discharges, secondary electrons are accelerated away from the cathode and give rise to ionization in the plasma and to electron bombardment of surfaces in the system. This electron heating may be detrimental to thin film processing and may be reduced or eliminated using magnetron configurations. In addition to being necessary for sustaining the discharge in dc diode discharges, secondary electrons may also assist in the chemical reaction of reactive species on the bombarded surface.

When surfaces are subjected to bombardment by high energy ions a portion of the particles are reflected as high energy neutrals (8,9). If these high energy particles are not thermalized by collisions in the gas phase (35,36) they bombard the growing surface of a depositing material giving rise to such film properties as residual compressive stress (e.g. 37,38).

The physical sputtering of a surface may lead to surface texturing which give a roughened surface (e.g. 39-41). Preferential crystallographic sputtering will result in some crystalline orientations being etched at a faster rate than are others giving rise to "sputter etching". Preferential atomic sputtering can cause changes in the chemical composition of alloy and compound surfaces (42,43).

Energetic particle bombardment of surfaces can also introduce lattice defects into surfaces (44-48). Defect densities of 10-20 atomic percent have been measured using desorption techniques. On semiconductor surfaces these defects may act as electron traps when an interface is formed (49). In semiconductor device fabrication these types of defects must be avoided during surface cleaning and film formation (50).

The heating and formation of lattice defects in the near-surface region increases diffusion and chemical reaction in that region. The implantation of a mobile bombarding species into a surface increases the chemical potential between the surface and the bulk thereby increasing the diffusion rate of mobile species (e.g. hydrogen) into the bulk of the material.

When a reactive species is present, concurrent energetic particle bombardment enhances chemical reactions with the surface. The nature of this enhancement is poorly understood since heating, physical collisions, molecular fragmentation of adsorbed species and the presence of energetic electrons (secondary electrons) may each play a role. The existence of bombardment enhanced chemical reactions is well established in etching studies where the reaction products are volatile (51-53), in reactive plasma cleaning (54) and the same effects are found in reactive film deposition processes where the reaction products are non-volatile (55).

### **13.4 VAPORIZATION SOURCES FOR ION PLATING**

Vaporization sources for ion plating can be of any form including: 1) thermal evaporation/sublimation, 2) physical sputtering, 3) molecular dissociation of a chemical precursor gas or 4) vacuum and plasma arcs.



Thermal vaporization (evaporation or sublimation) can be from resistively heated sources for materials which have a high vapor pressure at temperatures of about 1400°C and below. High current - low voltage electron bombardment may also be used to vaporize these materials (56) and has the added advantage that the dense electron cloud can ionize a portion of the vaporized material which can then be accelerated ("film ions")(57-62). High energy focussed electron beams can be used to vaporize refractory materials into a plasma; however, these sources generally require a differentially pumped vacuum system so that the high voltage (cathodic) thermo-electron emitter can be isolated from the plasma (3).

Sputtering sources can be fabricated from all of the conventional sputtering configurations (63). In the magnetron sputtering configurations it may be desirable to have an auxiliary plasma near the substrate to provide ions for bombardment in that region.

Chemical precursor gases may be introduced through a plasma chamber (64,65) or directly into the plasma (66-68). Ionization of the fragments allow them to be accelerated to the substrate where their properties are dependent on the ionization and acceleration conditions. This is a means for making "i-C" and "i-BN" materials (69).

Vacuum arcs utilize material arc-vaporized from a solid cathode or from a molten anode to supply the ions for sustaining the plasma (no supporting gas). In these types of arcs there is a high ionization efficiencies (15, 70-72). The addition of a gas to the plasma environment allows reactive deposition (73).

### **13.5 BOMBARDMENT EFFECTS ON FILM PROPERTIES**

Concurrent energetic particle bombardment during atomistic film deposition may modify many film properties (e.g. 74-77). The amount of modification will depend on both the mass, energy and flux of the bombarding species and the mass and flux of depositing species. In the case of reactive deposition the availability of "activated" species and the effect of adsorbed surface species may also be important. The following are some of the film properties that can be modified by controlled concurrent bombardment during deposition.

#### **13.5.1 Film Adhesion**

The adhesion of a deposited film to a surface depends on the deformation and fracture modes associated with the failure (78,79). Energetic particle bombardment prior to and during the initial stages of film formation may enhance adhesion by: removing contaminant layers, changing the surface chemistry, generating a microscopically rough surface, increasing the nucleation density by forming nucleation sites (defects, implanted and recoil implanted species), increasing the surface mobility of adatoms and by creating lattice defects. Introducing thermal energy directly into the surface region promotes reaction and diffusion. These effects will also improve surface coverage and thus decrease the number of interfacial voids which result in easy fracture and poor adhesion. Film adhesion may be degraded by the diffusion and precipitation of gaseous species at the interface. The adhesion may also be degraded by the residual film stress due either to differences in the coefficient of thermal expansion of the film and substrate material in high temperature processing or the residual film growth stresses developed in low temperature processing.

### 13.5.2 Film Morphology, Density

Physical sputtering and redeposition, increased nucleation density and increased surface mobilities of adatoms on the surface under bombardment conditions may be important in disrupting the columnar microstructure that develops during low temperature atomistic deposition processes (80-85, also Chap. 22). Figure 5 shows the fracture cross-section and surface morphology of RF sputter deposited chromium films at zero bias and with a -500 volt bias during deposition. Note that the bombardment completely disrupted the columnar microstructure. Bombardment-related effects may also improve the surface coverage and decrease the pinhole porosity in a deposited film. This increased film density is reflected in film properties such as: better corrosion resistance, lower chemical etch rate, higher hardness, lower electrical resistivity (metals) and the increased index of refraction (optical coatings). However it has been found that if the bombarding species is too energetic and the substrate temperature is low, high gas incorporation gives rise to voids (e.g. 86). Some investigators have used the parameter "resputtering rate" (deposition rate with and without an applied bias) as the parameter for disruption of the columnar morphology: however this parameter does not take into consideration the backscattering from the gas phase which will be greater the higher the gas pressure and so must be used with caution.

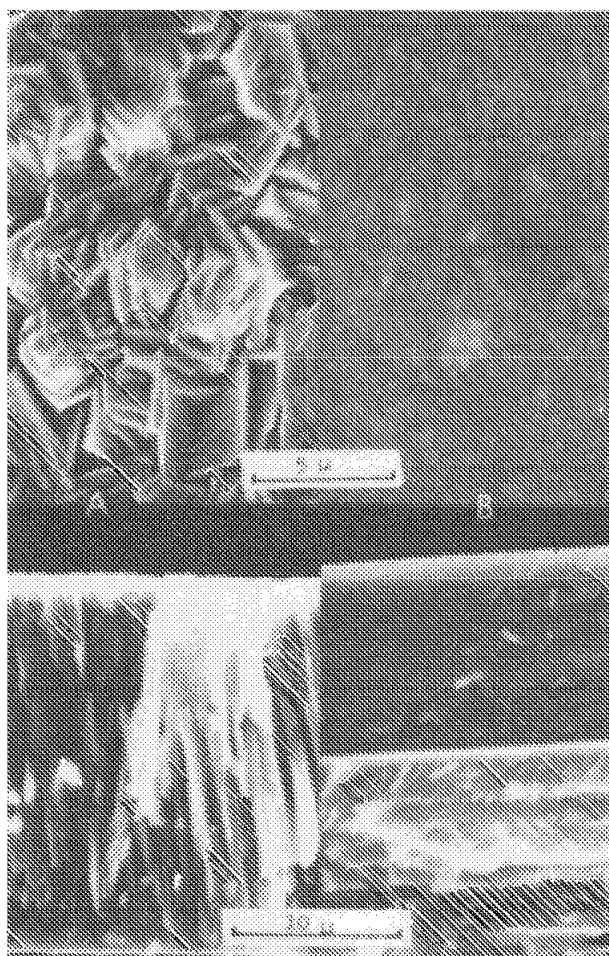


**Figure 5:** Fracture cross-section (bottom) and surface morphology (top) of a thick RF sputter deposited chromium deposit (80). A) without bias (no bombardment) and B) with concurrent bombardment (-500 v bias on the substrate).

### 13.5.3 Residual Film Stress

Invariably atomistically deposited films have residual growth stresses which may be tensile or compressive in nature and may approach the yield or fracture strength of the materials involved. The origin of these stresses is poorly understood although several phenomenological models have been proposed (87). Generally, vacuum deposited films and sputter-deposited films prepared at high pressures have tensile stresses which may be anisotropic with off-normal angle of incidence depositions (88). In low pressure sputter deposition and ion plating, energetic particle bombardment may give rise to high compressive film stresses due to the recoil implantation of surface atoms (38, 89-92). Studies of deposited films with concurrent bombardment have shown that the conversion of tensile to compressive stress is very dependent on the ratio of bombarding species to depositing species (93,94). In plasma processing the residual film stress may be very sensitive to the substrate bias (80) and gas pressure (38) during deposition in a plasma environment.

Figure 6 shows the residual stress and gas content in sputter deposited chromium films as a function of substrate bias. Where rather thick films of high modulus materials are involved these stresses must be controlled or spontaneous failure (adhesion, cracking, blistering) will occur (79).

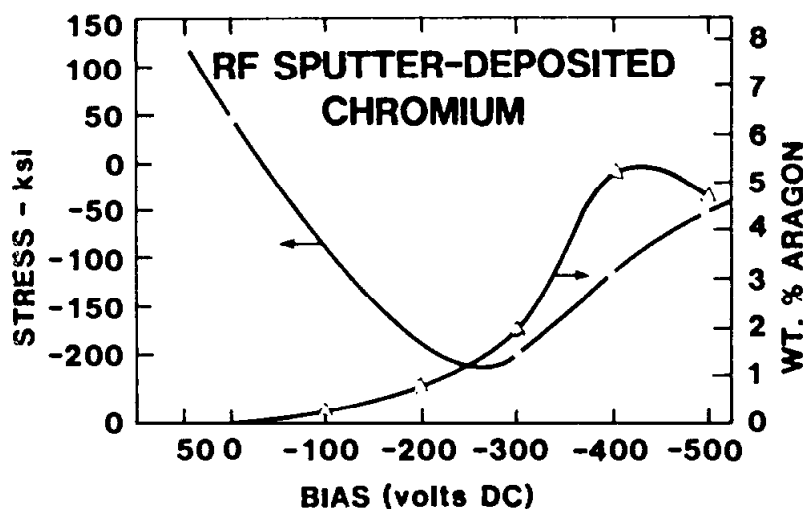


**Figure 6:** Residual stress and gas content of an RF sputter deposited chromium deposit as a function of substrate bias during RF sputter deposition (80)

The lattice strain associated with the film stress represents stored energy and this energy along with a high concentration of lattice defects may lead to: 1) lowering of the recrystallization temperature in crystalline materials, 2) a lowered strain point in glassy materials, 3) a high chemical etch rate, 4) electromigration problems, 5) void growth in metallization lines by creep and 6) other such mass transport effects.

#### 13.5.4 Crystallographic Orientation

Under proper bombardment conditions the crystallographic orientation of the deposited material is developed such that the more dense crystallographic planes are parallel to the bombarding direction (95,96). This effect is attributed to the channeling of the bombarding species into the film thus decreasing the sputtering rate under this orientation. Under more energetic bombardment condition however the crystallographic orientation is disrupted due to the formation and consolidation of defects.

#### 13.5.5 Gas Incorporation

When a depositing film is bombarded during deposition by energetic gaseous particles the incorporated gas content is dependent on the particle energy, substrate temperature, film material and bombarding species. Generally low mass bombarding particles are more easily incorporated than are large mass particles. The gas incorporation increases with energy of the bombarding species to the point which etching causes gas desorption. Under some conditions very high concentrations of normally insoluble gas may be incorporated into the depositing film by concurrent bombardment during deposition. An example is the incorporation of 20-40 atomic percent hydrogen and helium in gold (97,98) and the incorporation of krypton in amorphous metals films (99). This incorporation is probably due, in part, to the high lattice defect concentration in the bombarded material which traps mobile species (45-48). At very high gas contents the gas may precipitate into voids. Gas incorporation can be minimized by using low energy bombarding species (i.e. less than 100 eV), an elevated substrate temperature during deposition (300-400 °C) and/or using higher atomic mass bombarding species (Kr, Xe).

#### 13.5.6 Surface Coverage

The macroscopic and microscopic surface coverage of a deposited film on a substrate surface may be improved by the use of concurrent bombardment during film deposition. The ability to cover complex geometries depends mostly on scattering of the depositing material in the gas phase (36, 101, 102). If gas scattering is extensive then gas phase nucleation will occur and the resulting deposit will be poorly consolidated. If a plasma is present and the substrate is at a negative potential the gas phase nucleated materials will become negatively charged and repelled from the substrate. In addition, bombardment will heat, densify and consolidate the deposited material into a high quality film over the whole surface. On a more microscopic scale, sputtering and redeposition of the depositing film material will lead to better coverage on micron and submicron sized features (86, 103-105) and reduced pinhole formation. On the atomic scale the increased surface mobility, increased nucleation density and erosion/redeposition of the depositing adatoms will disrupt the columnar microstructure and eliminate the porosity along the column boundaries. In total, the use of gas scattering, along with concurrent bombardment, increases the surface covering ability and decreases the microscopic porosity of the deposited film material as long as gas incorporation does not generate voids.

#### 13.5.7 Other Properties

Many other properties of the film material may be changed and improved by bombardment during deposition. They include: 1) electrical resistivity of metal films, 2)

hardness of hard-coatings, 3) chemical etch rate, 4) corrosion resistance, 5) pinhole density, 6) index of refraction of dielectric coatings, 7) color of TiN films, etc.

### 13.6 PROBLEM AREAS

A major problem area in using plasmas for thin film deposition is how to obtain a uniform plasma density over a surface so that uniform bombardment and reactive gas availability can be attained. Plasma non-uniformity can arise from a number of sources including: 1) geometrical arrangement of power input electrodes and substrate fixturing, 2) substrate geometry, 3) the presence of surfaces that allow recombination and loss of species in the nearby plasma and 4) in the case of reactive deposition, reactive surfaces that deplete the supply of reactive gas at the growing film surface.

As a general rule the best plasma system design is one that is geometrically symmetric. The SIP system shown in Fig. 3 is a good example of this approach. However, in many instances a symmetric geometry is difficult to attain. The use of magnetron configurations is an example. The use of a magnetic field to confine electrons and increase the local plasma density in one region leads to a decrease in plasma density in other regions. Figure 7 shows an example of how two independently sustained plasmas may be used to allow magnetron sputtering of a source and the use of a hot filament sustained plasma in the vicinity of the substrate to provide a plasma from which ions can be extracted to bombard the substrate and film.

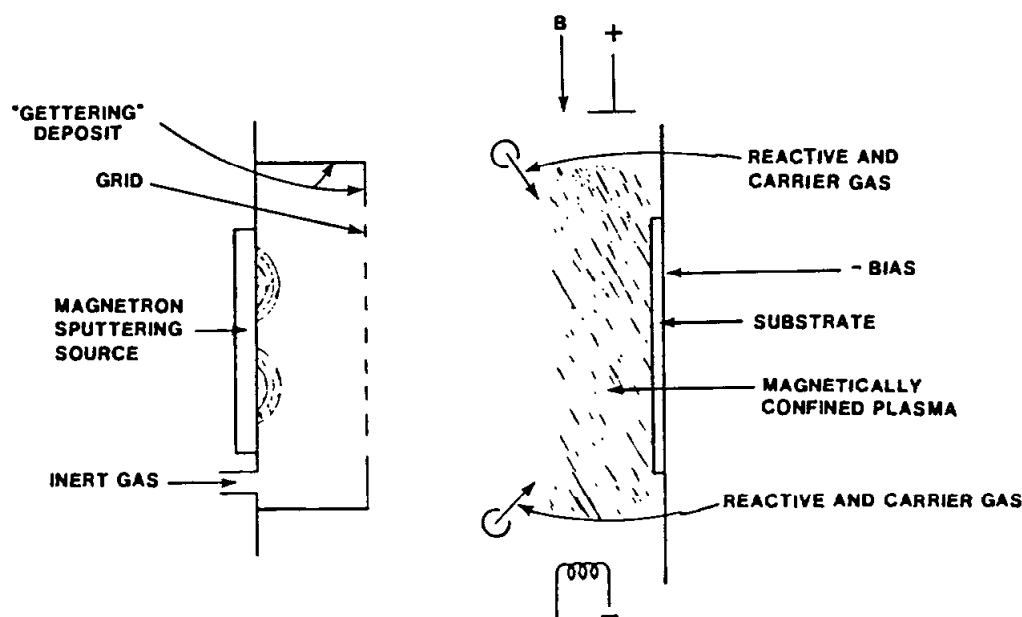


**Figure 7:** Ion Plating system utilizing a magnetron sputtering source and an auxiliary plasma for supplying the ions for bombarding the substrate and depositing film.

If the part has a very complex configuration the electric field around points and corners focus the bombardment giving high erosion rates and heating in these areas. A thin region gives poor thermal conductance and results in heating. Holes and reentrant features give low field gradients. In these regions heating will be high and erosion will be low

giving poor cleaning and allowing reaction with contamination. Excessive heating can sometimes be alleviated by "pulse processing" where the substrate bias is periodically turned on and off.

In some cases high transparency grids at the substrate potential may be used to surround the substrate to give a more uniform bombardment over a complex surface. This is the basis of the equipment used in the "Ion Vapor Deposition (IVD)" process (106) and in the "barrel-plating" ion plating configuration (107). Figure 8 shows a barrel-plating configuration used to coat small parts which are tumbled in the rotating cage. A grid configuration may also be useful in coating dielectric materials where charge buildup may be a problem or in coating moving substrates where electrical contact may be a problem.

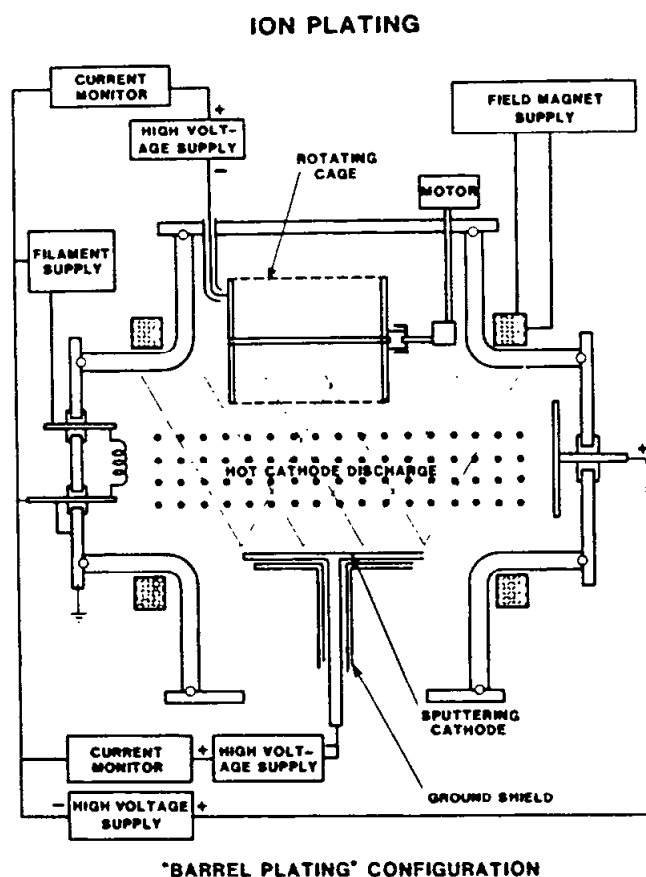


**Figure 8:** Ion plating "barrel plating" configuration using a rotating cage to contain the parts (106).

Generally the equipment used for ion plating is the same as that used for sputter deposition except that the substrate is the sputtering target and another vaporization (deposition) source has been added. Because of the high "throwing power" conditions often used in ion plating systems the insulators of electrical feedthroughs must be carefully shielded from deposition or else they will become shorted. These conditions may also lead to gas phase nucleation of particles which will deposit on the system walls (called "black sooty crap" - BSC by the operators). This material has a very low density and if the material is pyrophoric (Ti, Zr etc) the BSC may ignite if disturbed in air. In such a case system cleanup should be done wet.

As with any plasma process, wall effects enhance the desorption of contaminants. This contamination, when introduced into the plasma, is "activated" and can be an important source of contamination which must be controlled.

When using plasmas and bombardment effects there are many processing variables that are unknown. Processing unknowns include: 1) the portion of the substrate current that is due to secondary electron emission, 2) the flux and energy spectrum of the ions and electrons and 3) the flux, adsorption and surface coverage of the neutral gaseous species. Generally no attempt is made to determine these process variables during the processing but rather they are controlled by controlling other processing variables such as: 1) system geometry, 2) deposition rate, 3) gas pressure, 4) gas composition, 5) gas flow rate(s), 6) substrate and system temperatures, 7) contaminants in the plasma and 8) substrate power input per unit area (voltage and current).

### 13.7 APPLICATIONS

There are many applications of the ion plating process some of which are:

- Obtaining good adhesion - Ag on steel for mirrors, soft metals on surfaces for space lubrication, Ag on Be for diffusion bonding, Cu & Au on Ta and Mo for subsequent brazing, Cu-on- ceramic metallization
- Metallization - Al, Ag, Au on plastics and semiconductors
- Good surface coverage on complex surfaces - TiN on tool bits, injection molds and jewelry items; semiconductor metallization
- Good reaction and stoichiometry - TiN on tool bits, injection molds (hardness, wear); jewelry items (TiN - color)
- Corrosion protection - Al on U, steel & Ti (galvanic); C and Ta on biological implants
- Abrasion resistance -  $MgF_2$  coatings on plastics, i-c
- Deposition of diffusion barriers - HfN & TiN on semiconductor devices

### 13.8 SUMMARY

Like any deposition technique the ion plating process has its advantages and disadvantages. They include:

- Advantages:
  - Excellent surface covering ability (throwing power) under the proper conditions
  - Ability to have an in-situ cleaning of the substrate surface
  - Ability to obtain good adhesion in many otherwise difficult systems
  - A great deal of flexibility in tailoring film properties by controlling bombardment conditions
  - Equipment requirements are roughly equivalent to those of sputter deposition
- Disadvantages:
  - Many processing parameter that must be controlled
  - Processing may be very dependent on substrate geometry and fixturing

- Obtaining uniform bombardment and reactive species availability over a complex surface may be difficult
- Gas incorporation may be excessive
- High compressive stresses may be generated in the bombarded film
- Substrate heating may be excessive
- Contaminants are desorbed from surfaces and "activated" in the discharge and can contaminate deposited material

In order to achieve the desired film property modification there must be an appreciable ratio of bombarding particles to depositing species. This ratio must be much higher to disrupt the columnar morphology than is necessary to change the film stress. The necessary bombardment conditions for each application are usually determined empirically and controlled by controlling the processing geometry and parameters. A typical condition to control film stress might be a substrate bias of -50 to -100 volts DC, a current density of 1mA/cm<sup>2</sup> and a deposition rate of 10 nanometers per second. For columnar structure disruption and maximum covering ability a "resputtering rate" might be as high as 30%.

High voltage pulsing of substrates immersed in plasmas is being studied as a way to modify surfaces by ion bombardment (108). This technique could be used in ion plating to allow periodic bombardment of the depositing film material. The ion plating process provides an alternative film deposition technique which should be evaluated for specific applications.

### 13.9 REFERENCES

1. D.M. Mattox US Patent 3,329,601 (1974).
2. D.M. Mattox, J. Electrochemical Technol. 2: 295 (1964).
3. D.M. Mattox J. Vac. Sci. Technol. 10: 47 (1973).
4. N.A.G. Ahmed, Ion Plating Technology - Developments and Applications, John Wiley (1987).
5. P.J. Martin, R.P. Netterfield, W.G. Sainty and C.G. Pacey, J. Vac. Sci. Technol. A2: 341 (1984).
6. J.M.E. Harper, J.J. Cuomo and H.R. Kaufman, J. Vac. Sci. Technol. 21: 737 (1982).
7. H.R. Kaufman, J. Vac. Sci. Technol. 15: 272 (1978).
8. W.W.Y. Lee and D. Oblas, J. Appl. Phys. 46: 1728 (1975).
9. H.D. Hagstrum, in Inelastic Ion Surface Collisions edited by N.H. Tolk, J.C. Tully, W. Heiland and C.W. White, Academic Press, pp. 1-25 (1977).
10. L. Valyi, Atom and Ion Sources, John Wiley (1977).
11. M.R. Shubaly, Nucl. Instrum. Meth. Phys. Res. B26: 195 (1987).



12. T.E. Romesser, V. Vanek, J.Tang, D. Dixon, J. Bayless, M. Musetto, C. Strawitch and L. Higgins "A Large Area Plasma Source" IEEE Conf Record 1983 IEEE International Conference of Plasma Science 83CH1847-3, US Doe Contract No. DE-ACO3-77ET33006.
13. V.S. Letokhov, Sov. At. Energy. (Translation) 62:(4) 297 (1987).
14. J.J. Cuomo, R.J. Gambino, J.M.E. Harper, J.D. Kuptsis and J.C. Webber, J. Vac. Sci. Technol. 15: 281 (1978).
15. R.L. Boxman and S. Goldsmith, Surf. Coat. Technol. 33: 153 (1987).
16. John Melngailis, "Focussed Ion Beam Technology and Applications" J. Vac. Sci. Technol. B5: 469 (1987).
17. Brian Chapman Glow Discharge Processes, John Wiley (1980).
18. John A Thornton, Thin Solid Films 107: 3 (1983).
19. F. Plas, J. Guille and J. Machet, Le Vide, Suppl. 196: 45 (1979)
20. R.F. Bunshah: please see Chap. 18, this volume.
21. S. Veprek, Thin Solid Films 130: 135 (1985).
22. M.H. Jacobs, Surf. Coat. Technol. 29: 221 (1986).
23. Yoichi Murayama and Toshihiro Takao, Thin Solid Films 40: 309 (1977).
24. D.M. Goebel, Y. Hirooka and T.A. Sketchley, Rev. Sci. Instrum. 56: 1717 (1985).
25. Harold R. Kaufman and Raymond S. Robinson, J. Vac. Sci. Technol. A3: 1774 (1985).
26. Yu Shen Kuo, R.F. Bunshah and D. Okrent, J. Vac. Sci. Technol. A4: 397 (1986).
27. S. Komiya and K. Tsuruoka, J. Vac. Sci. Technol. 12: 589 (1975).
28. J.A. Thornton, Surf. Eng. 2: 283 (1986).
29. A. Theodore Forrester, Large Area Ion Beams: Fundamentals of Generation and Propagation, John Wiley, (1988).
30. D.M. Goebel, G. Campbell and R.W. Conn, J. Nucl. Mat. 121: 277 (1984).
31. A. Mathews and D.T. Gethin, Thin Solid Films 117: 261 (1987).
32. A. Mathews, Vacuum 32: 311 (1982).
33. L.I. Maissel and P.M. Schaible, J. Appl. Phys. 36: 237 (1965).
34. Michael H. Jacobs "Process and Engineering Benefits of Sputter Ion Plated Titanium Nitride Coatings" in Surface Modification and Coatings, edited by Richard D. Sisson, Jr. ASM Conference Proceedings, 291 (1986).
35. R.E. Somekh, J. Vac. Sci. Technol. A2: 1285 (1984).
36. A. Bessaudou, J. Machet and C. Weissmantel, Thin Solid Films 149: 225 (1987).
37. J.A. Thornton and D.W. Hoffman, J. Vac. Sci. Technol. A3: 576 (1985).
38. R.E. Cuthrell, D.M. Mattox, C.R. Peebles, P.L. Dreike and K.P. Lamppa, J. Vac. Sci. Technol. A6: 2914 (1988).
39. R.S. Berg and G.J. Kominiak, J. Vac. Sci. Technol. 13: 403 (1976).
40. Zbigniew W. Kowalski, J. Mat. Sci. Lett. 6: 69 (1987).
41. G.K. Wehner, J. Vac. Sci. Technol. A3: 1821 (1985).

42. G. Betz, Surf. Sci. 92: 283 (1980).
43. J.B. Malherbe, S. Hofmann and J.M. Sanz, Appl. Surf. Sci. 27: 355 (1986).
44. R. Miranda and J.M. Rojo, Vacuum 34: 1069 (1984).
45. D. Edwards, Jr and E.V. Kornelsen, Rad. Effects 26: 155 (1975).
46. E.V. Kornelsen, Rad. Effects 13: 227 (1972).
47. E.V. Kornelsen and A.A. Van Gorkum, Rad. Effects 42: 93 (1979).
48. A.A. Van Gorkum and E.V. Kornelsen, Rad. Effects 42: 113 (1979).
49. L.J. Brillson, Thin Solid Films 89: 461 (1982).
50. J.L. Vossen, J.H. Thomas III, J.-S. Maa and J.J. O'Neill, J. Vac. Sci. Technol. A2: 212 (1984).
51. M.W. Geis, G.A. Lincoln, N. Efremow and W.J. Piacentini, J. Vac. Sci. Technol. 19: 1390 (1981).
52. Harold F. Winters, J.W. Coburn and T.J. Chuang, J. Vac. Sci. Technol. B1: 469 (1983).
53. J.W. Coburn and H.F. Winters, Nucl. Instrum. Met. Phys. Res. B27: 243 (1987).
54. G.J. Kominiak and D.M. Mattox, Thin Solid Films 40: 141 (1977).
55. J.M.E. Harper, J.J. Cuomo and H.T.G. Henzell, Appl. Phys. Lett. 36: 56 (1980) also Appl. Phys. Lett. 37: 540 (1980).
56. S. Komiya and K. Tsuruoka, J. Vac. Sci. Technol. 12: 589 (1975).
57. D.T. Larson and H.L. Draper, Thin Solid Films 107: 327 (1983).
58. G. Mah, P.S. Mcleod and D.G. Williams, J. Vac. Sci. Technol. 11: 663 (1974).
59. P.S. Mcleod and G. Mah, J. Vac. Sci. Technol. 11: 119 (1974).
60. Carl Schalansky, Z.A. Munir and D.L. Walmsley, J. Mat. Sci. 22: 745 (1987).
61. Hans K. Pulker, US Patent 4,254,159 (Mar 3, 1981)
62. Helmut Kaufmann, US Patent 4,346,123 (Aug 24, 1982)
63. Please see Chaps 3 and 4.
64. Toshio Mori and Yoshikatsu Namba, J. Vac. Sci. Technol. A1: 23 (1983).
65. S. Shanfield and R. Wolfson, J. Vac. Sci. Technol. A1: 323 (1983).
66. D.M. Mattox, US Patent 3,329,601 (July 1974)
67. Robert Culbertson, US Patent 3,604,970 (1971)
68. K.P. Paude and A.C. Seabaugh, J. Electrochem. Soc. 131: 1357 (1984).
69. C. Weissmantel, "Preparation, Structure and Properties of Hard Coatings on the Basis of i-C and i-BN" Ch 4 in Thin Films from Free Atoms and Particles, edited by Kenneth J. Klabunde, Academic Press 1985
70. J.E. Daalder, J. Phys. D: Appl. Phys. 9: 2379 (1976).
71. R.L. Williamson, F.J. Zanner and W.A. Hareland " Monochromatic Imaging Studies of Low Pressure Arcs Burning on Molten Inconel 718 Alloy Electrodes During Vacuum Arc Remelting" Presented to the 9th International Vacuum Metallurgy Conference, San Diego CA April 11-15, 1988 and to be published in the proceedings.

72. F.J. Zanner and L.A. Bertrum, IEEE Trans on Plasma Science Vol PS-11: 223 (1983).
73. S. Boelens and H. Veltrop, Surf. Coat. Technol. 33: 63 (1987).
74. D.M. Mattox and G.J. Kominiak, J. Vac. Sci. Technol. 9: 528 (1972).
75. R.D. Bland, G.J. Kominiak and D.M. Mattox J. Vac. Sci. Technol. 11: 671 (1974).
76. G.J. Kominiak and D.M. Mattox, J. Electrochem. Soc. 120: 1535 (1973).
77. J.E. Harper, J.J. Cuomo, R.J. Gambino and H.R. Kaufman "Modification of thin film properties by ion bombardment during deposition" Ch. 4 in Ion Bombardment Modification of Surfaces - Fundamentals and Applications ed. by Orlando Aucello and Roger Kelly, Elsevier (1984).
78. D.M. Mattox, "Thin film adhesion and adhesive failure - A perspective" in Adhesion Measurement of Thin Films, Thick Films and Bulk Coatings ed. by K.L. Mittal ASTM STP 640, American Society for Testing and Materials, 54 (1978).
79. D.M. Mattox and R.E. Cuthrell, MRS Symposium Proceedings, Adhesion in Solids, Vol 119: ed. by D.M. Mattox, J.E.E. Baglin, R.E. Gottschall and C.D. Batich, 141 (1988).
80. R.D. Bland, G.J. Kominiak and D.M. Mattox, J. Vac. Sci. Technol. 11: 671 (1974).
81. J.A. Thornton, Thin Solid Films 40: 335 (1977).
82. J.A. Thornton, Annual Rev. Mat. Sci. 7: 239 (1977).
83. J.A. Thornton, J. Vac. Sci. Technol. A4: 3059 (1986).
84. R. Messier, A.P. Giri and R.A. Roy, J. Vac. Sci. Technol. A2: 500 (1984).
85. R. Meissier and J.E. Yehoda, J. Appl. Phys. 58: 3739 (1985).
86. J.K.G. Panitz, B.L. Draper and R.M. Curlee "Comparison of the Step Coverage of Aluminum Coatings Produced by Two sputter Magnetron Systems and a Dual Beam In System" Presented to the 1988 ICMC Conference and to be published in Thin Solid Films.
87. E. Klokholm and B.S. Berry, J. Electrochem. Soc. 115: 823 (1968).
88. J.D. Finnegan and R.W. Hoffman, Trans. 8th Nat. Vac. Symp. Pergamon Press, 935 (1961).
89. D.W. Hoffman and J.A. Thornton, J. Vac. Sci. Technol. 16: 134 (1979).
90. A.G. Blachman, J. Vac. Sci. Technol. 10: 299 (1973).
91. J.A. Thornton, J. Tabcock and D.W. Hoffman, Thin Solid Films 64: 111 (1979).
92. J.A. Thornton and D.W. Hoffman, J. Vac. Sci. Technol. 18: 203 (1981).
93. J.A. Thornton and D.W. Hoffman, J. Vac. Sci. Technol. A3: 576 (1985).
94. D.W. Hoffman and M.R. Gaerttner, J. Vac. Sci. Technol. 17: 425 (1980).
95. D.R. Brighton and G.K. Hubler, Nucl. Instrum. Meth. Phys. Res. B28: 527 (1987).
96. D. Dobrev, Thin Solid Films 92: 41 (1982).
97. E. Kay, F. Parmigiani and W. Parrish, J. Vac. Sci. Technol. A5: 44 (1987).
98. D.M. Mattox and G.J. Kominiak, J. Vac. Sci. Technol. 8: 194 (1971).
99. H.T. Weaver, J. Appl. Phys. 42: 2356 (1971).

100. J.J. Cuomo and R.J. Gambino, J. Vac. Sci. Technol. 14: 152 (1977).
101. K.S. Fancey and J. Beynon, Vacuum 34: 591 (1984).
102. K.S. Fancey and A. Mathews "Ion Plating Processes: Design Criteria and System Optimization" Presented to the 1988 ICMC and to be published in Thin Solid Films.
103. Y. Homma and S. Tsunekawa, J. Electrochem. Soc. 132: 1466 (1985).
104. David W. Skelly and Lothar A. Gruenke, J. Vac. Sci. Technol. A4: 457 (1986).
105. H.P. Bader and M.A. Lardon, J. Vac. Sci. Technol. A3: 2167 (1985).
106. D.E. Muehlberger "Application of Ion Vapor Deposited Aluminum Coatings" in Ion Plating and Ion Implantation: Application to Materials, ed. by R.F. Hochman, Conference Proceedings American Society for Metals, 75 (1986).
107. D.M. Mattox and F.N. Rebarchik J. Electrochem. Technol. 6: 374 (1968). save J.R. Conrad, J.L. Radtke, R.A. Dodd, F.J. Worzala and N.C. Tran, J. Appl. Phys. 62: 4591 (1987).

---

## **Ionized Cluster Beam (ICB) Deposition Techniques**

---

**Isao Yamada**

### **14.1 INTRODUCTION**

Ionized Cluster Beam (ICB) techniques utilize small clusters of atoms, rather than individual atoms, to form thin films on substrates. Clusters of atoms can have unique physical and chemical properties, quite unlike the atomic fluxes and unlike the liquid or bulk states of the film. As a result of the unique properties of small clusters, numerous new applications in plasma physics, atomic and molecular physics, surface science, and thin film formation become available. The clusters used in this work number from a few hundred to a few thousand atoms. In a cluster this size, a large percentage of the atoms are located at or within a few layers of the cluster surface. Therefore, the overall structure of the cluster is dominated by the surface atoms, and we should consequently expect that the physical and chemical properties of the cluster are much different from those of bulk and liquid (1).

The ICB deposition technique has several features which can be attributed both to the unique properties of small clusters and to aspects of the cluster acceleration process (2,3). One of the most significant properties of the ICB deposition technique is an apparent enhancement of the surface adatom migration or diffusion in the depositing film. The ICB deposition process also allows the gradual increase in cluster (or atom) energy. The effective kinetic energy for each depositing atom can be increased easily from thermal energies up into a range similar to sputtering. This great sensitivity will be quite important to modifying or tailoring the properties of thin films.

The importance of low energy ion beams for film formation can be easily understood when we recognize that the binding energies of the atoms in a solid are in the range of a few eV per atom. For atoms evaporated from thermal sources, the kinetic energies correspond roughly to the temperature of the source and are approximately 0.01-0.1 eV, or much less than binding energies of the film atoms. A strong effect can be expected, however, as the result of bombarding by accelerated ion or neutral atom beams, even at energies of only a few eV which correspond to binding energies. The clusters in the ICB technique initially have thermal energies on the order of 0.1 eV per atom. For a cluster of a few hundred to a thousand atoms, this corresponds to less than 100 eV per cluster. If the cluster is ionized and accelerated by a few hundred to many thousands of volts, the average energy for each atom can be increased from the initial thermal energies up to the

binding energy of the film atoms and beyond. By working with these high acceleration potentials, space charge problems are strongly reduced, and high fluxes can be achieved.

## 14.2 EXPERIMENTAL TECHNIQUES

In the Ionized Cluster Beam technique, small clusters of a few hundred atoms each are formed in a source, using techniques somewhat similar to evaporation. As the clusters leave the source, they drift through the vacuum chamber under conditions of pressure low enough that there are no collisions with gas atoms or other clusters. Upon reaching a surface, the clusters condense to form a film. Often the clusters are intentionally ionized in the drift region and accelerated by electric fields to the sample. This acceleration increases the net kinetic energy of the cluster, and can have an effect on the properties of the depositing film.

The design of an ICB system is broken up into four regions. These are the source region, where the clusters are formed; the ionization and acceleration region; a drift region; and finally the substrate. A typical schematic of the ICB system is shown in Fig. 1. These systems operate typically in the  $10^{-5}$  to  $10^{-7}$  Torr region ( $10^{-3}$  to  $10^{-5}$  Pascals).

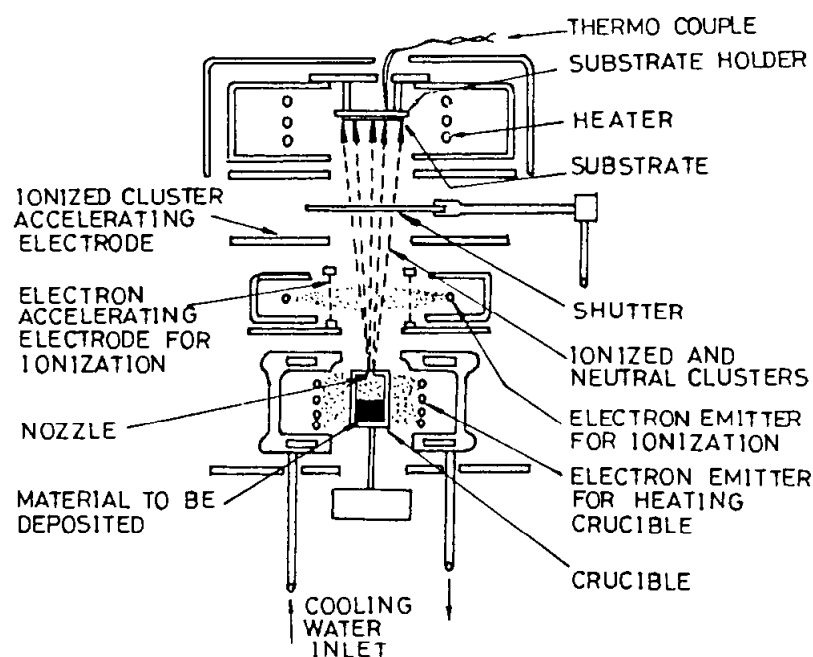


**Figure 1:** A typical Ionized Cluster Beam (ICB) system. The vacuum system and chamber, as well as the power supplies are omitted for clarity.

In the source region, the clusters are formed by an adiabatic expansion and condensation process (4,5). The nozzle diameter  $D$  of the crucible has to be larger than the mean free path  $\lambda$  between vapor atoms in the crucible (Fig. 2). This causes a viscous flow in the nozzle region. In the case where the nozzle diameter is smaller than the mean free path of the vapor atoms (molecular flow), there are few, if any, collisions between atoms in the nozzle region and agglomeration or clustering of the vapor atoms will not occur. The ratio of the vapor pressure  $P_0$  in the crucible to the vapor pressure  $P$  outside the crucible (in the chamber) must be larger than  $10^2 - 10^5$ . Therefore, if film deposition

in the  $10^{-7}$  to  $10^{-5}$  Torr range is desired, it is necessary to operate the inner pressure in the crucible in the range of  $10^{-2}$  to 1 Torr. To cause a sufficient number of collisions in the nozzle to form clusters, it is necessary to make the nozzle thickness-to-diameter ratio ( $L/D$ ) in the range of 0.5 to 2.0. This serves to keep the ratio of the chamber pressure  $P$  to the crucible pressure  $P_0$  high, allowing for low pressure depositions. A simple nozzle shape is cylindrical, with a diameter  $D$  and length of 1-2 mm, which is sufficient to form a beam of clusters with a high drift velocity. Multiple nozzle sources may also be used for uniformity and throughput considerations. The range of the source temperature is determined in order to produce the vapor pressure  $P_0$  of the order of  $10^{-2}$  to a few Torr. The crucible can be heated by either resistive heating, electron bombardment heating or by hybrid methods according to the application purposes.

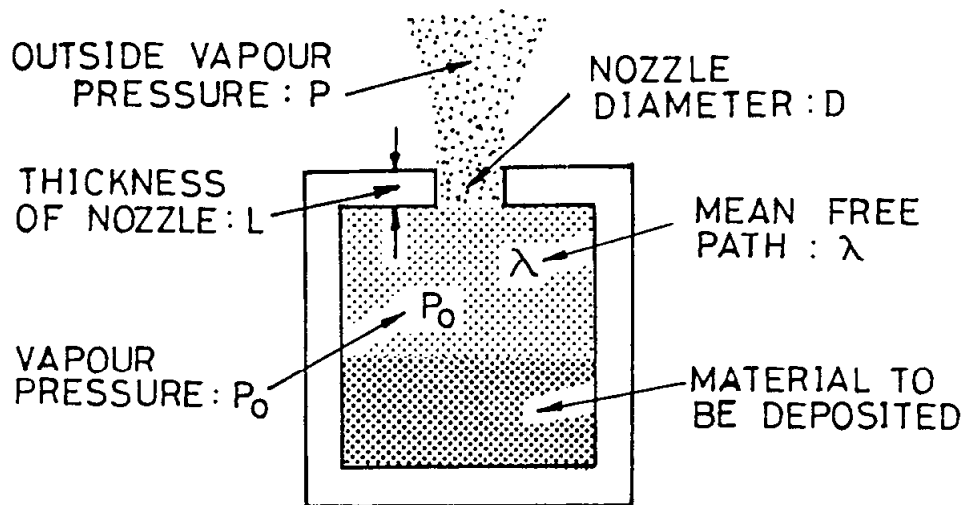


**Figure 2:** A schematic of the nozzle region for an ICB source. Typical parameters are a nozzle diameter,  $D$ , of 2 mm, the nozzle thickness,  $L$ , of 0.5 mm, the internal vapor pressure,  $P_0$ , of a few Torr, the mean free path for the vapor atoms,  $\lambda = 0.2$  mm and a chamber pressure of  $10^{-5}$  Torr. The crucible can be heated by a number of means, and is generally constructed of graphite and refractory metals.

The kinetic energy of the clusters upon leaving the source region can be considerably higher than for either single atoms or simple groups of atoms evaporated from an open hearth at the same temperature. The kinetic energy is also dependent on the nozzle dimensions. An example of this is shown in Fig. 3 for the case of Ag clusters. For the top curve, the nozzle was opened to 8 mm, which is effectively equivalent to an open hearth.

The clusters are ionized by an electron impact in an ionization electrode region located just above the expansion nozzle. The ratio of number of ionized clusters to the total number of clusters can be adjusted by changing the electron emission current  $I_e$  in the ionization region. In general, the clusters only become singly ionized by this technique due to the low currents. The degree of ionization is defined as the percent of the total cluster flux which is ionized. In a typical system, (6) the degree of ionization obtained for a single nozzle is 5-7% at  $I_e = 100$  mA, 7-15% at  $I_e = 150$  mA and 30-35% at  $I_e = 300$  mA. The ionized clusters are accelerated by the electric field caused by the potential  $V_a$  on the accelerating electrode located just outside the ionization region. Typically this electrode would operate at a potential of a few hundred to several thousand volts negative w.r.t. the system ground. The accelerated ionized clusters bombard the substrate together with

neutral clusters which are not ionized in the ionization electrode system. The ionized clusters have a kinetic energy corresponding to the acceleration voltage, whereas the neutral clusters have a kinetic energy corresponding to the ejection velocity. The trajectory of the ionized clusters is controlled to obtain a wide and uniform bombardment on the substrate by optimizing the aspect ratio ( $L/D$ ) of the nozzle or by adjusting the acceleration voltage applied to the acceleration electrode. The uniform radiation by cluster ions of the depositing film is critical in cases where the film properties are dependent on the bombardment by the ions.

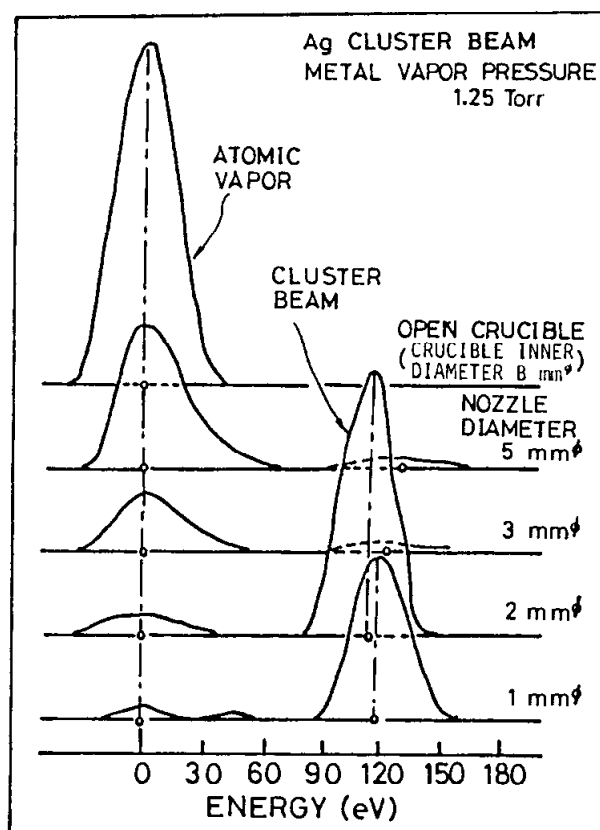


**Figure 3:** The energy distribution measured using an electrostatic,  $90^\circ$  energy analyzer for Ag clusters for various nozzle diameters. The internal vapor pressure in the crucible was held constant at 1.25 Torr.

The shape and spacing of the acceleration electrodes can be optimized by modeling the ion trajectories through the acceleration region to give the best beam uniformity. One acceleration design is shown in Fig. 4, consisting of a grid, an ionization electrode (part of the electron source for ionization of the clusters), an intermediate electrode and the acceleration electrode. It should be noted that the optimum voltage on each electrode is interrelated. The best or optimum focussing conditions result in a broad, uniform beam at the sample.

Typically these substrate mounts are radiation-heated, and contain a thermocouple for the measurement of sample temperature. It is also usually desirable to measure the current to the sample as a means of monitoring the deposition process. There can also be rate monitors of various designs in the sample region.



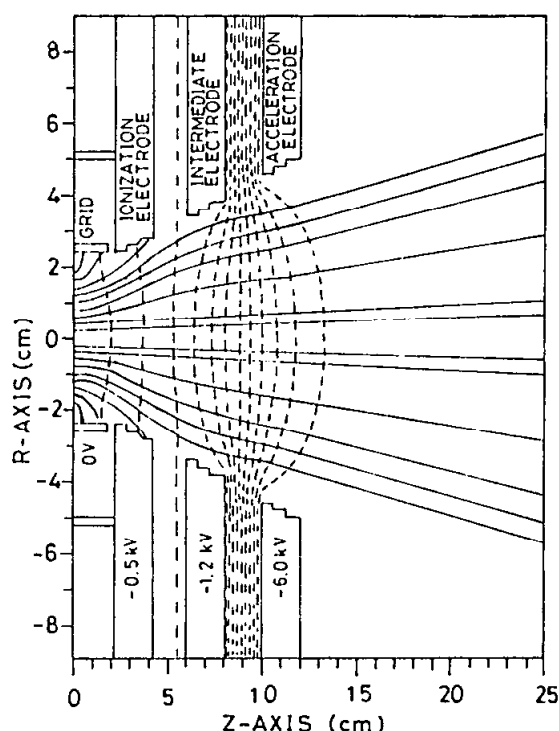


**Figure 4:** Trajectories for Ag clusters in a multiple-aperture acceleration system. In this case, the optimum voltage is applied to the intermediate electrode.

By introducing a reactive species during ICB operation, it is possible to reactively deposit compound thin films. This allows the deposition of oxide, nitride, hydride or carbide films, for example, while still using relatively simple elemental sources. During a reactive ICB deposition (RICB), an appropriate reactive gas is introduced into the chamber at a pressure of  $10^{-5}$  to  $10^{-4}$  Torr (7). In this low pressure region, no plasma is produced in the acceleration or drift regions, as is the case with Activated Reactive Evaporation (ARE) (8) or ion plating techniques. At higher pressures where a plasma is formed, the clusters are rapidly destroyed by collisions with energetic particles. This eliminates the advantages of using the cluster technology. The chemical reactions at these pressures all take place at the depositing film surface on the sample. The deposition rate of clusters must be carefully controlled along with the partial pressure of the reactive gas to control the film stoichiometry.

Multiple ICB source operation is possible due to the low chamber pressure during operation. (Fig. 5) (9). Multiple source operation is applicable for the deposition of alloys, and in particular those alloys whose components have radically different melting points and vapor pressures. A good example of a relevant compound is GaAs. In a multiple-source system, the sources operate completely independently, and can be used simultaneously to form compounds, or in sequence to form multilayer or superlattice films.

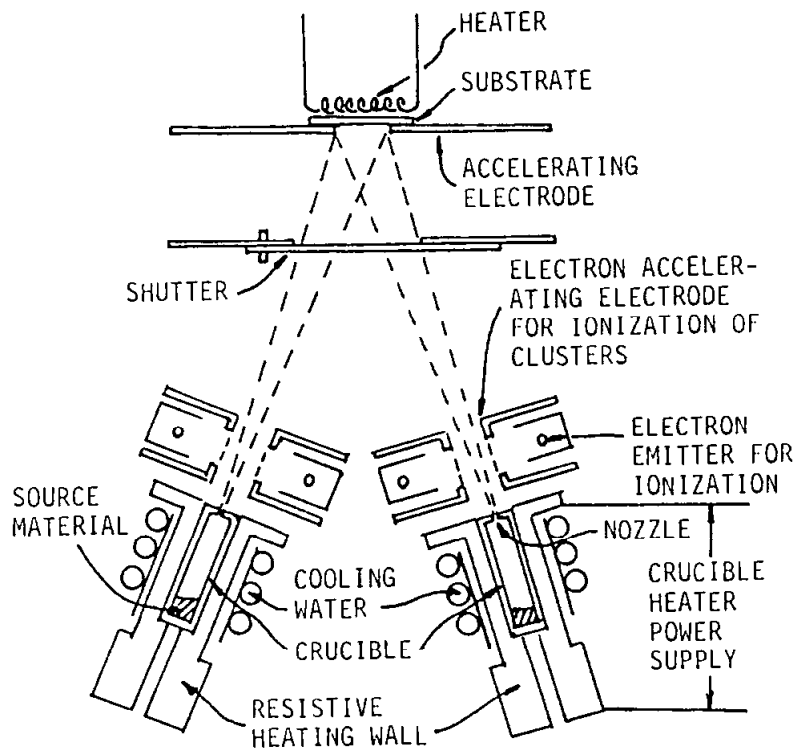


**Figure 5:** A typical arrangement for a ICB deposition with two sources. Each of the sources is completely independent during operation.

### 14.3 FILM DEPOSITION WITH ICB

Films deposited by conventional evaporation often differ radically from films of the identical material deposited by physical sputtering, even though in both cases the depositing atoms are arriving at the surface singly or in very small groups. It is therefore not too surprising that films deposited by the ICB technique can have very different qualities than either evaporated or sputtered films. In addition, it should be obvious that by changing the kinetic energy of the cluster from effectively a hundred eV or so to many thousands of eV, the physical properties of the deposited films can also be drastically altered.

The surface binding energy of the adsorbed atom, the nucleation density or critical size for surface nucleation and the level of surface mobility of the adsorbed atom are all critical to the film formation process. The sticking coefficient is a term describing the effective probability of the arriving, condensing atom to be adsorbed on the substrate surface. Such factors as the substrate temperature, the arrival rates of condensing atoms and energetic ions, the presence of impurities and the crystalline orientation of the surface, and even the presence of electric charge on the arriving species will influence the film growth process.

In the case of ICB, a number of features are quite different from conventional evaporation, and these features must be included in discussions of the basic film deposition and modification mechanisms. Clearly there is a significant difference compared to evaporation in the arrival of atoms in the form of large clusters to the film surface. In addition,

the additional kinetic energy of the clusters, when ionized and accelerated, must be considered, as must the possible effects of the electronic charge those clusters carry. Some of the effects that can be attributed to the ICB technique include: (a) creation of activated centers for nuclear formation, (b) sputtering or in-situ cleaning, (c) substrate surface heating (higher effective surface temperature), (d) very shallow ion implantation, and (e) enhancement of adatom migration.

The use of ionized clusters in the ICB technique has certain advantages over both conventional evaporation and sputter deposition as well as low energy ion beam deposition. One fundamental difference is the low effective charge-to-mass ratio. Generally only one atom in a cluster of many hundred atoms is ionized. Therefore, space charge effect-based problems that can occur with low energy ion beam deposition techniques are significantly reduced. In addition, the charging problems that can occur with highly ionized ion beams can be reduced or eliminated. The other basic phenomena of critical value to the ICB technique is the reduced internal binding of the cluster atoms. Due to this lower level of interatomic binding, upon collision of the cluster with the sample the cluster atoms are more easily dislodged from the cluster for the purpose of surface diffusion. One result of this effect is the ability to deposit epitaxial thin films at substrate temperatures significantly below those of conventional evaporation techniques.

The initial kinetic energy of the ionized cluster upon impact with the surface can result in several phenomena, including: (a) an increase in the local temperature at the point of impact, (b) a possible implantation of cluster atoms into the bulk of the film, (c) at high enough energies, physical sputtering or desorption from the surface, (d) increased surface diffusion of the surface and cluster atoms, and (e) the creation of activated sites or defects to be nucleation points for film growth. The presence of ions in the arriving particle flux to the surface can have a great influence on critical parameters in the condensation process, such as coalescence and nucleation, and chemical reactions of the condensing atoms with bulk or gas phase atoms.

The magnitude of these effects can be modified by adjusting the acceleration voltage and the content of the ionized clusters in the total flux. An optimum value of the kinetic energy of ionized and accelerated particles in film formation is estimated to be in the range of a few to a hundred eV/atom under the good quality film deposition conditions. However, some amount of defects and displacements of atoms are often effective at the initial stage of film formation. Therefore energies above the damage threshold can often be of great value to film formation. In addition, the optimum energy may vary according to the required characteristics characteristics of the film, such as mechanical properties, optical properties, or morphology and the combination of deposit and substrate materials.

#### **14.3.1 Kinetic Energy Range of ICB and Effects of the Kinetic Energy**

The clusters have been analyzed in-flight by electron diffraction techniques and found to have an amorphous structure. The constituent atoms are considered to be loosely coupled to one another compared to those in the crystalline state. An ionized cluster accelerated to an appropriate energy will break up upon striking the sample surface with the kinetic energy distributed for the most part evenly to the individual atoms. The migration of the atoms on the substrate surface has an important role in the film formation kinetics. Moreover, the ICB deposition process allows the production of equivalently low energy and high intensity ion beams without space charge problems.

The degree of surface disorder during the deposition process can have a significant effect on the film nucleation process. The surface crystallinity of Si substrates bombarded by Al clusters was measured by ion channeling after the Al film was removed by chemical etching. A Si substrate bombarded by a 500 eV Ar ion beam to a dose of  $2 \times 10^{15}$  ions/cm<sup>2</sup> was also examined for comparison. Figure 6 compares the number of displaced atoms for the same cases (10). The results show that the displacement of surface atoms induced by the Al ICB bombardment is much smaller than that caused by the Ar ion bombardment. Actually, the disorder caused by ICB bombardment is much smaller than that produced by the naturally occurring oxidized layer. It can be concluded that the kinetic energy of the individual atoms in an accelerated cluster as it impacts the surface appear no larger than the order of a few 10's of eV per atom.

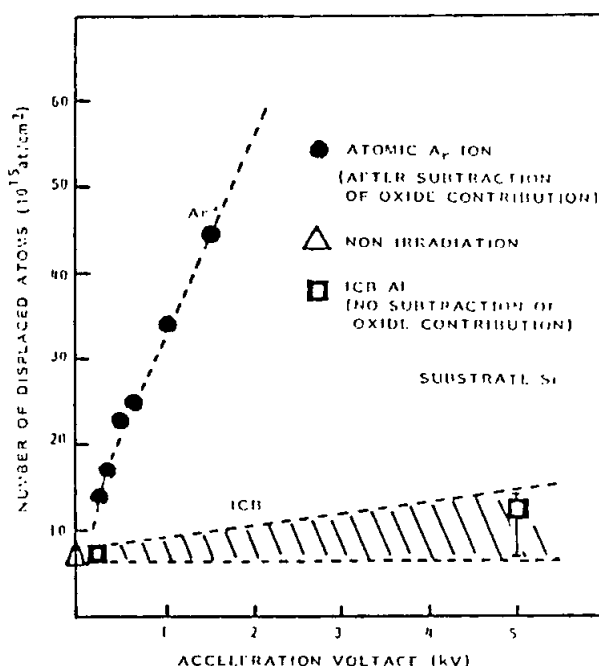


**Figure 6:** Comparison of the number of displaced Si surface atoms for Si surfaces bombarded by Ar ions at 500 eV and Al ICB clusters.

For an actual film deposition by using the ICB technique, the kinetic energy of the accelerated clusters produces effects such as the following: (1) formation of preferential nucleation sites, (2) surface cleaning by desorption or sputtering, (3) very shallow ion implantation, (4) surface heating at equivalently high temperature, and (5) adatom migration. These effects have been confirmed experimentally.

The spatial density of the nuclei at early stages of film growth has been observed to be dependant on the kinetic energy of the incoming clusters with ICB. By increasing the kinetic energy of the ionized clusters, the density of nuclei is increased monotonically at first and then becomes constant. Fig. 7 shows a plot of the number of nuclei as a function of the acceleration voltage on the cluster. The increase in the density of nuclei at higher acceleration voltages is attributed to the effect of ion bombardment. At a high deceleration voltage (on the sample) greater than 300 V, the increase of nuclei density is considered to be due to electron bombardment. The spatial density of nuclei on the surface is considered to be determined mainly by such factors as the deposition rate, the presence of charges, structural defects, ion bombardment, and statistical fluctuations in the supersaturation conditions. In these experiments the deposition rate and the ionization ratio were kept constant. Therefore it is reasonably assumed that ion bombardment and the resulting creation of surface defects produced the increased number of nuclei (11).

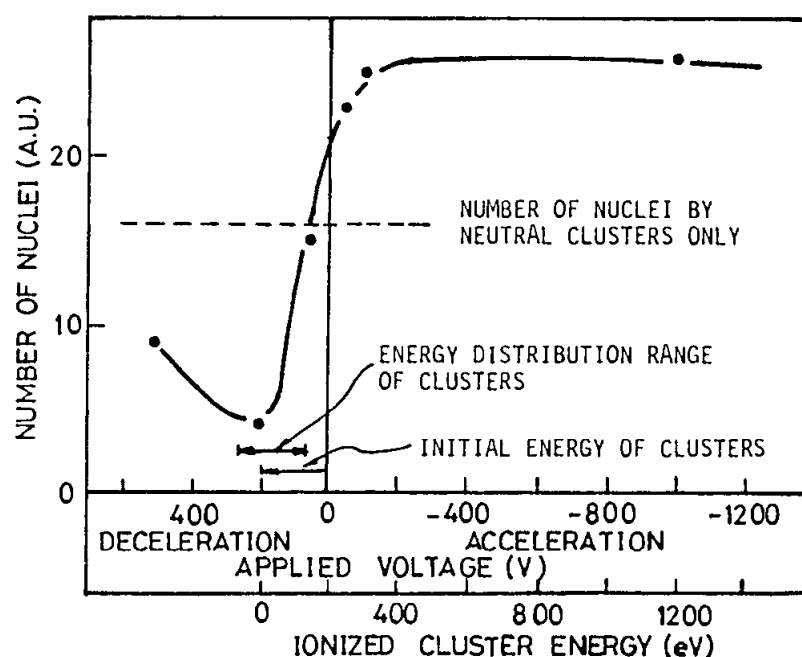


**Figure 7:** A plot of the number of nuclei (per unit area) as a function of acceleration voltage for the clusters. The initial energy of the clusters is approximately 100 eV.

Surface cleaning or sputtering effects can also be clearly seen by comparing the Si epitaxial growth in an ultra high vacuum (UHV) and a high vacuum chambers. In the epitaxial growth of Si on an atomically clean and well-ordered silicon surface in the UHV chamber, only a 200 V acceleration voltage was sufficient to deposit partially epitaxial films at a substrate temperature ( $T_s$ ) of 500°C. By increasing the acceleration voltage, an improvement of the crystalline quality could be obtained. For the identical deposition case in the high vacuum chamber, the results were quite different. The chamber was evacuated by an oil diffusion pump to a base pressure of  $10^{-7} - 10^{-6}$  Torr. In this system, an acceleration voltage of at least 6 kV was necessary before the deposited films attained a degree of epitaxy. An amorphous or polycrystalline structure is formed in a range of 0 - 4 kV. In this deposition, no special cleaning process except for chemical cleaning was used prior to the deposition. In this case, higher acceleration voltage is required in order to sputter the native oxide and to remove adsorbed residual gas atoms on the substrate surface during the deposition. From the Rutherford backscattering spectra using 185 keV  $H^+$ , it was found that the film prepared with clusters accelerated to 6 keV has no oxygen at the interface between the film and the substrate (12).

To measure the enhancement of the surface mobility for a condensing atom, the very early stages of film deposition were examined. In this experiment, Au was deposited onto a silicon oxide (SiO) film which had been deposited on an NaCl substrate. The substrate surface was partially covered with a cleaved NaCl plate to study shadowing at the cleaved edge. The average spacing between the SiO and the NaCl cover was about 80  $\mu\text{m}$ . The gold was deposited both by the ionized-cluster beam technique and by conventional vacuum deposition. Fig. 8 shows electron micrographs of the deposited Au film near the edge of the penumbra. In the case of ionized-cluster beam deposition, the deposited gold particles were observed to have migrated under the cleaved NaCl cover.

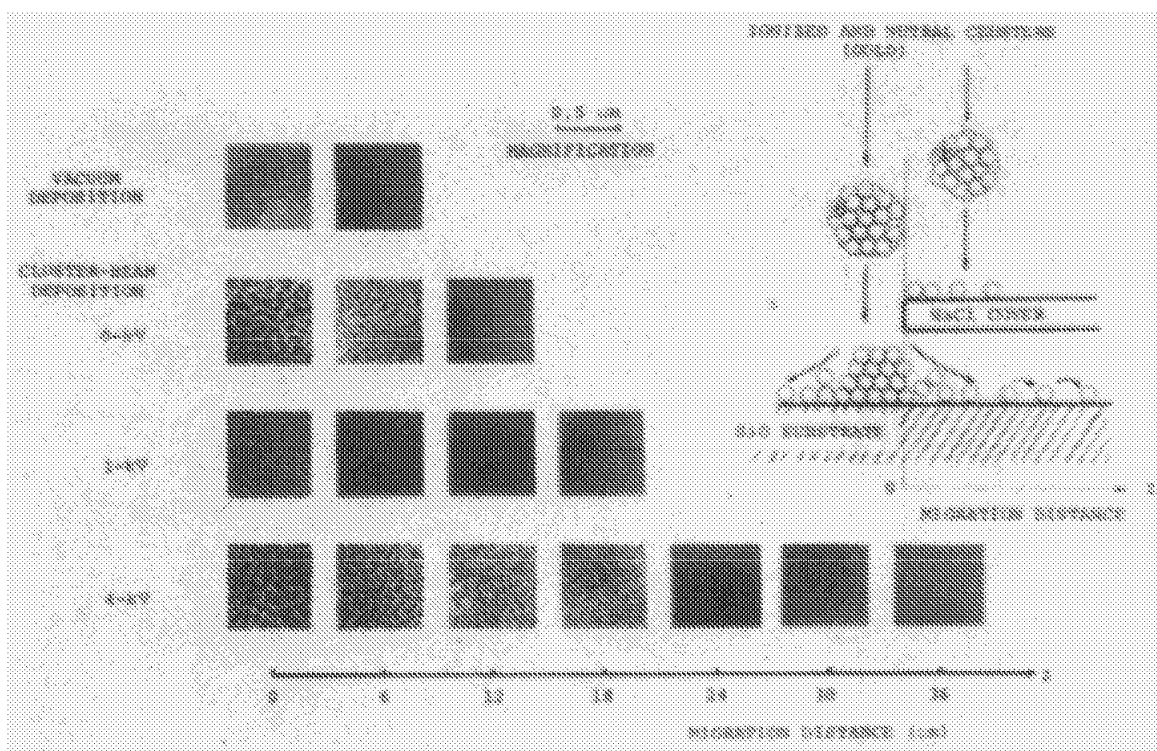


**Figure 8:** Electron micrographs of the deposited film clusters under an overhanging edge as a function of cluster acceleration voltage.

Even when the acceleration voltage was zero, the migration distance of the deposited particles was greater than in conventional evaporation technique. The increased migration distance could be the result of the breaking up of deposited clusters into atoms upon impact with the film surface.

These and related results strongly suggest that the acceleration of the clusters during ICB influences the dynamic processes in the film formation. These dynamic processes include the breaking of clusters into atoms upon bombarding the substrate surface, sputtering of impurities from the substrate surface, formation of activation centers for nuclear formation, adatom migration, and shallow implantation. In ICB deposition these processes can be controlled by changing the acceleration of ionized clusters and the content of ionized clusters in the total flux, and consequently the physical properties of the deposited films can be controlled.

#### 14.3.2 Film Deposition by Reactive ICB Techniques

Compound films, such as oxides, nitrides or hydrides, can be deposited by introducing the appropriate reactive gas species into the vacuum chamber during the ICB deposition process. The partial pressure of the reactive gas is typically on the order of  $10^{-5}$ – $10^{-4}$  Torr. A fraction of the reactive gas introduced into the chamber is ionized and dissociated in the ionization region of the ICB source. These species can become active and may contribute to the reaction at the film surface.

Reactive ICB (RICB) deposition mechanisms have been studied (13) by examining the deposition of amorphous, hydrogenated silicon (a-Si:H). In this case, silicon clusters were deposited in a hydrogen ambient at  $10^{-5}$  Torr. At this pressure range, there are few gas phase collisions of the hydrogen molecules with the Si clusters, and the reactions take place predominantly at the film surface. The reaction rate appeared to increase with the acceleration voltage on the clusters. Since the background gas pressure before introducing the hydrogen gas was  $5 \times 10^{-7}$  Torr, the main particles impinging on the substrate surface are ionized and neutral silicon clusters from the ion source, and the mixed hydrogen gas and doping gases that are introduced into the chamber through the leak valves. Some fraction of the hydrogen molecules are ionized and dissociated in the ionization section of the cluster beam. Therefore, the flux of hydrogen to the sample surface consists of a range of atoms, molecules and ions. Under typical deposition conditions, the arrival rate of Si atoms (within the clusters) was on the order of  $10^{15} - 10^{16}$  atoms  $\text{cm}^{-2} \text{sec}^{-1}$ , as calculated from the measured silicon ion-current to the substrate. The ratio of the hydrogen atoms to the hydrogen molecules was estimated from the change of H and  $\text{H}_2$  peaks in a mass spectrum when the electrical input power into the source was varied. From these measurements, the bombardment rate of  $\text{H}_2$  molecules to the sample was approximately  $10^{16}$  molecules  $\text{cm}^{-2} \text{sec}^{-1}$  and the bombardment rate of dissociated hydrogen atoms was estimated to be  $10^{15}$  atoms  $\text{cm}^2 \text{sec}^{-1}$ . The rate of impinging hydrogen ions is three orders of magnitude smaller than that of molecular hydrogen. It is not clear yet which state of hydrogen is dominantly involved in the hydrogenation process, but it seems reasonable to consider that hydrogen atoms could have a considerable influence in providing uniform hydrogenation. For doped film formation, the hydrogen gas was mixed with phosphine or diborane on the order of 5000 ppm sequentially in the same chamber. No problems arose as a result of the residual reactive gas used in previous processes. Doped films of either p or n type could be reproducibly deposited at practical deposition rates. Subsequent structural analysis showed that the films mainly consisted of monohydrides. The density of monohydrides can be increased by accelerating the Si clusters to a higher acceleration voltage. For both this case and the parallel case of oxide and nitride RIBC deposition, operation at a gas pressure of less than  $10^{-5} - 10^{-4}$  Torr was sufficient to cause sufficient surface chemical reactions to form the compound films without forming a plasma within the chamber.

#### 14.3.3 Film Deposition by Simultaneous Use of ICB and Microwave Ion Sources

Concurrent ion bombardment by means of an ion source during the deposition with ICB techniques was first proposed in 1973 (14). Along these lines, the simultaneous use of a microwave ion source and an ICB source has been developed. This technique is attractive because the reactive gas ion energy and the current can be controlled independently from the ICB source operation. Therefore, the reactivities of the gases can potentially be enhanced by this method.

Fig. 9 shows a schematic diagram of the simultaneous system consisting of the microwave ion source and the ICB source. The details of the microwave ion source are not important to this discussion and have been described elsewhere (15). The microwave source requires permanent magnets around the discharge chamber. The source operation can be set to the Electron Cyclotron Resonance (ECR) condition which results in a very high density plasma. The gas ions are extracted by the extraction electrode applied at  $V_{\text{ex}} = 3 - 15$  kV and the extracted ions are then subsequently decelerated down to 500 eV by the retarding field produced between the source and the substrate holder.

This system was used for the deposition of AlN films. High purity Al metal and  $N_2$  gas were used as source materials. Sapphire (0001) and p-type Si (111) were used as substrates. The substrate temperature ( $T_s$ ) was  $100^\circ\text{C}$ . The films deposited with neutral  $N_2$  (rather than accelerated ions) were opaque and not characteristic of reacted AlN. Films deposited with concurrent  $N_2^+$  were clear and had high optical transmittance. Measurements by Rutherford Backscattering Spectroscopy (RBS), suggested a composition ratio in these cases of AlN.

As an example of oxide film formation using this same technique,  $Al_2O_3$  films have been deposited. For the case of neutral Al-clusters and  $O_2$  gas, the transmittance of the film is low particularly at small wavelengths, suggesting that pure  $Al_2O_3$  has not been formed.

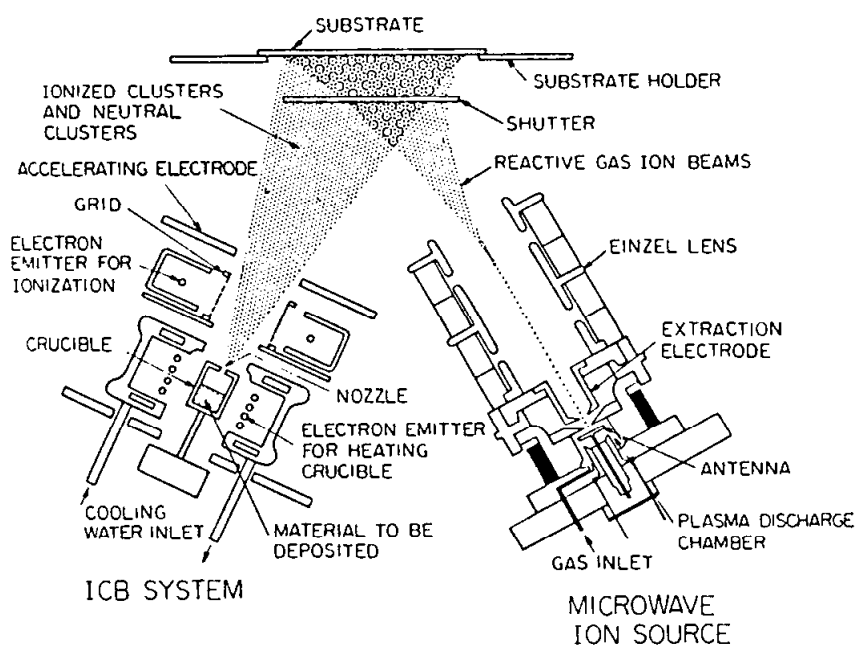


**Figure 9:** Schematic of the ICB deposition system with simultaneous ion bombardment from a microwave ion source.

On the other hand, the films deposited with neutral Al clusters and  $O_2$  ions had significantly higher transmittances. Also, in the case of the film deposited with both  $O_2$  ions and ionized Al-clusters the film was transparent and its transmittance approached that of the sapphire substrate. It was found from RBS measurements that the composition ratio of oxygen to Al in these last films was 0.67, and that stoichiometric  $Al_2O_3$  films were formed. The film prepared at an incident energy of 500 eV for  $O_2$  ions and an acceleration voltage of 0.5 kV for Al clusters was found to be thermally stable even after annealing at  $1000^\circ\text{C}$ . The refractive index ( $n$ ) is found to increase with increasing ion energy. In addition, the same increase in refractive index for ionized, accelerated clusters compared to neutral clusters was found in this case as was found in the case of AlN (above). The etching rate of these films in 5% HF solutions is found to decrease as a function of increased cluster acceleration voltage. In particular, in the case of using both  $O_2$  ions and ionized Al-clusters, the film prepared at an incident energy of 500 eV was



not etched at all in the 5% HF solution. This indicates that the higher incident energy such as 500 eV may increase the packing density of the film.

#### 14.4 SUMMARY

The deposition of thin films by means of beams of large clusters of atoms rather than individual atoms has been shown to have numerous advantages over other deposition techniques. The clusters are generally formed by condensation during the expansion of a vapor through an aperture into high vacuum. Ionization of the clusters in flight and subsequent acceleration of the clusters to the film surface has also been found to be a sensitive technique for the modification of the properties of the deposited film. These techniques are equally applicable to reactive deposition of compound materials, in which clusters of one species are deposited in the presence of background gas atoms and ions of a reactive species.

The critical features of the ICB technique are the control of the cluster kinetic energy through ionization and acceleration, and the subtle characteristics of the clusters themselves. The clusters are characterized by lower levels of inter-atomic bonding than the solid phase. This reduced bonding apparently allows increased surface mobility of the atoms upon arrival at the film surface, compared to conventionally evaporated films. One result of these effects is a greatly lowered temperature for the deposition of epitaxial films, compared to evaporative or MBE techniques.

The control of the cluster kinetic energy, through partial ionization of the clusters and subsequent acceleration by an electric field, results in a broad degree of control in the effective kinetic energy of each of the atoms that arrives at the film surface. In addition, due to the high mass-to-charge ratio of the clusters, such aspects as space charge limited current flow are avoided in most cases and charging effects are reduced significantly. The broad range of energy control is not possible in other techniques such as evaporation or sputtering.

The Ionized Cluster Beam techniques have been shown to be valuable additions to the realm of thin film deposition techniques. The processes are well characterized and reliable equipment is available from a number of sources. The films deposited by these techniques are often superior to those deposited by either evaporation or sputtering, and the range of control of the process exceeds other techniques by a great margin. It is hoped that the technique will find greater acceptance and recognition in the future as its features become even more advanced and more and more of the thin film community becomes familiar with the technology.

#### 14.5 REFERENCES

1. J. Borel and J. Buttet (ed.), Small Particles and Inorganic Clusters. Surf. Sci. 106: (1981).
2. P.P. Kulik, G.E. Norman and L.S. Polak, Khimiya Vysokikh Energii 10: p. 203 (1976).
3. T. Takagi, Thin Solid Films 92: p. 1 (1982).

4. T. Takagi, I. Yamada, M. Kumnori and S. Kobiyama. Proc. 2nd Int. Conf. Ion Sources, Vienna (Osterreichische Studiengesellschaft fur Atomenergie, Vienna, 1972)) p. 790.
5. T. Takagi, I. Yamada and A. Sasaki, J. Vac. Sci. Technol. 12: p. 1128 (1975).
6. T. Takagi, I. Yamada and A. Sasaki, Inst. Phys. Conf. Ser. 38: p. 142 (1978).
7. T. Takagi, I. Yamada, K. Matsubara and H. Takaoka, J. Cryst. Growth 45: p. 326 (1978).
8. R.F. Bunshah in Deposition Technologies for Films and Coatings ed. by R.F. Bunshah (Noyes, N.J. 1982) 5.
9. T. Takagi, K. Matsubara, N. Kondo, K. Fujii and H. Tokaoka, Jpn. J. Appl. Phys. 19: Supple. 19-1, p.507 (1980).
10. I. Yamada and T. Takagi, Nucl. Instrum. Methods Phys. Res. B21: p. 120 (1987).
11. I. Yamada, H. Takaoka, H. Inokawa, H. Usui, S.C. Cheng and T. Takagi, Thin Solid Films 92: p. 137 (1982).
12. I. Yamada, F.W. Saris, T. Takagi, K. Matsubara, H. Takaoka and S. Ishiyama, Jpn. J. Appl. Phys. 19: p. 181 (1980).
13. I. Yamada, I. Nagai, H. Horie and T. Takagi, J. Appl. Phys. 54: p. 1583 (1983).
14. K. Fujime, T. Ueda, H. Takaoka, J. Ishikawa and T. Takagi, Proc. Int. Workshop on Ionized Cluster Beam Technique, Tokyo and Kyoto, Japan, p. 195 (1986).
15. J. Ishikawa, Y. Takeiri and T. Takagi, Rev. Sci. Instrum. 55: p. 449 (1984).

---

## The Activated Reactive Evaporation (ARE) Process

---

**Chandra V. Deshpandey and Rointan F. Bunshah**

### 15.1 INTRODUCTION

A major advance in the technology for the deposition of refractory compounds such as carbides, oxides, nitrides and sulfides has been the development of and advances in plasma-assisted deposition processes (1). The plasma-assisted chemical vapor deposition (PACVD) or plasma-enhanced chemical vapor deposition (PECVD) process has found extensive applications in the microelectronics industry (see Chap. 10). Remarkable advances have also been made in the plasma-assisted physical vapor deposition (PAPVD) processes and applications have been developing in such areas as microelectronics, tribology, and superconducting films.

Evaporative deposition and sputter deposition are the two basic physical vapor deposition (PVD) processes. The vapor species are produced by thermal means in evaporation; and by momentum transfer in sputtering. Ion plating, in which ions are created from the background gas during evaporation and accelerated to the sample, is a hybrid process where the primary emphasis is on the changes in the microstructure, the surface coverage, the composition and the residual stresses of the deposited film produce by ion bombardment during growth. (Please see Chap. 13 for an extensive discussion of ion plating processes.) The substrate-film interface can also be significantly affected by the ion bombardment in the initial stages of deposition.

The increasing use of plasmas in deposition technology in the past few years has stemmed from the stringent requirements of low temperature processing in modern microelectronics and optoelectronic industries. The plasma is a convenient *insitu* source of activated gas atoms and molecules, and energetic neutrals and ions, which can be used to overcome the activation energy barrier for a particular chemical reaction. It thus becomes possible to synthesize a given compound in a plasma environment at a relatively low substrate temperatures, compared to a non-plasma, thermal process. A variety of plasma assisted techniques and modification have therefore been developed to deposit required films under the given processing constraints (1, and Chap. 13).

Evaporation-based plasma assisted techniques offer the control and flexibility necessary to deposit thin and thick films of alloys, compounds, and novel metastable materials (2). In this chapter, we shall examine the development and current status of the activated reactive evaporation (ARE) process for the deposition of a variety of compound films.

### 15.1.1 Historical Developments

The need for good quality compound films was felt early during the development of optical interference filters. This provided the stimulus for research and development of suitable techniques to synthesize these films with controlled optical properties. Consequently reactive evaporation, flash evaporation of compounds and reactive, as well as plasma enhanced reactive evaporation processes were developed. A brief review of the development of these processes is given below.

The historical origins of the reactive evaporation processes go back to 1907 when Soddy (3) found that calcium vapor reacted with gases other than inert gases. The use of reactive evaporation processes in the deposition of oxide films dates to the pioneering work of Brismaid et al (4) in 1957 and Auwarter (5) in 1960 who studied the deposition of oxide films by the reaction between metal or suboxide vapors and oxygen gas. Auwarter (5) also suggested that the reactivity can be enhanced by separate ionization of the oxygen gas molecules using an electrical discharge, prior to interaction with the metal atoms.

Other work on reactive evaporation processes without ionization of the reactive gas is:

- (a) Herrick and Tevebaugh (6) deposited copper oxide films by vaporization of copper from resistance heated sources in an oxygen atmosphere (1963).
- (b) Novice et al (7) and Schilling (8) deposited  $\text{Al}_2\text{O}_3$  films by reactive evaporation from a resistance heated aluminum sources in the presence of oxygen (1964).
- (c) Ritter (9) produced thin films of  $\text{SiO}_2$  and  $\text{TiO}_2$  by reactive evaporation of Si, Ti, SiO and TiO from resistance heated sources in the presence of  $10^{-4}$  to  $10^{-3}$  Torr partial pressure of oxygen (1966).
- (d) Ferrieu and Pruniaux (10) produced  $\text{Al}_2\text{O}_3$  by reactive evaporation of Al in an atmosphere of water vapor at  $10^{-1}$  Torr in the reaction zone (1969).
- (e) Rairden (11) prepared thin films of NbN and TaN by evaporation of Nb and Ta from an electron beam heated source in an  $\text{N}_2$  partial pressure of  $10^{-4}$  to  $10^{-3}$  Torr, and AlN by evaporation of Al in  $\text{NH}_3$  atmosphere (12) (1969).
- (f) deKlerk and Kelly (13) produced CdS and ZnS films by co-evaporation from two independent sources of Cd and S and condensation on a substrate at temperatures between 50 and  $200^\circ\text{C}$  (1965).
- (g) Learn and Haq (14) produced  $\beta\text{-SiC}$  by reactive evaporation of Si in a  $\text{C}_2\text{H}_2$  atmosphere (1970).

(h) Itoh and Misawa (15) produced TiC by evaporation of titanium from an electron-beam-heated source in  $\text{CH}_4$  or  $\text{C}_3\text{H}_8$  as the reactive gas. They also deposited AlN films by reaction between aluminum atoms and  $\text{NH}_3$  gas (1974).

(i) Abe et al (16) deposited TiC films by reaction between titanium atoms evaporated from a resistance-heated filament and  $\text{C}_2\text{H}_2$  or  $\text{C}_2\text{H}_4$  as the reactive gases (1982).

Examples of reactive evaporation processes where the reactive gas was ionized in a separate chamber (located inside or outside the vacuum system) are:

(a) Auwarter (5) studied the deposition of thin films oxides of Si, Zr, Ti, Al, Zn, Sn by reactive evaporation of the metal from resistance heated sources in a partial pressure of oxygen gas. Ionization of the oxygen gas outside the reaction zone by glow discharge between two electrodes is claimed to increase the "affinity" between the gas ion and the metal compound, i.e., enhance the probability of formation of metal compounds. Deposition rates of about  $0.2\mu\text{m min}^{-1}$  were obtained.

(b) Wank and Winslow (17) deposited films of AlN by evaporating films of Al from an rf heated BN crucible and reacting the Al deposited on the substrate with  $\text{N}_2$  gas which has been dissociated by 60 Hz a.c. discharge at the end of the gas feed tube. Deposition rates of  $0.1$  to  $0.2\mu\text{m min}^{-1}$  were obtained (1968).

(c) Kosicki and Khang (18) produced GaN thin-films by depositing pure Ga from a resistance heated source onto a substrate in the presence of activated  $\text{N}_2$  gas. The  $\text{N}_2$  gas was made chemically active by partial dissociation in a microwave discharge located away from the source and the substrate. Deposition rates of  $0.2$  and  $0.3\mu\text{m min}^{-1}$  were obtained (1969).

(d) Heitmann (19,20) used a hollow cathode discharge in a glass chamber to ionize oxygen gas and deposit films of  $\text{SiO}_2$ ,  $\text{SiO}_x\text{N}_y$  and  $\text{TiO}_2$  (1971).

(e) More recently, Kuster and Ebert (21) have used a modification of the method by Heitmann to deposit  $\text{TiO}_2$  layers and study their optical properties. These researchers refer to this process as the Activated Reactive Evaporation Process (1980).

(f) In an excellent and detailed paper by Ebert (22), the deposition of  $\text{TiO}_2$ ,  $\text{BeO}$ ,  $\text{In}_2\text{O}_3$ ,  $\text{SnO}_2$ , and  $\text{SiO}_2$  coatings using ionized oxygen gas is described (1982).

At this time it should be pointed out that there is an important distinction between the Reactive Evaporation processes using an ionized gas stream (as detailed above) and the Activated Reactive Evaporation (ARE) process. In the ARE process, ionization of both the metal vapor and the reactive gas or gas mixture occurs in the Reaction Zone which is defined as the space between the metal vapor source and the substrate, unlike the other plasma enhanced evaporation processes discussed above where only the reactive gas is separately ionized. This characteristic of the ARE process and its significance in film growth by this techniques will be discussed in depth in a later section.

## 15.2 EVAPORATION PROCESSES FOR THE DEPOSITION OF COMPOUND FILMS

Evaporation processes for the deposition of compounds can be subdivided into two types: (a) direct evaporation where the evaporant is the compound itself and (b) reactive evaporation where metal or compounds of a metal in a low valance state is evaporated in the presence of a reactive gas to form a compound, e.g., Si or SiO evaporated in the presence of  $O_2$  to form  $SiO_2$ , or Ti evaporated in the presence of  $N_2$  to form TiN.

### 15.2.1 Direct Evaporation

Evaporation can occur with or without dissociation of the compound into fragments. The observed vapor specie show that a few compounds evaporate without dissociation. Examples are SiO,  $MgF_2$ ,  $B_2O_3$ ,  $CaF_2$ , and other Group IV divalent oxides (SiO homologs like GeO and SnO).

In the more general case, when a compound is evaporated or sputtered, the material is not transformed to the vapor state as compound molecules but as fragments thereof. This compound fragmentation step is very difficult to characterize and control. Subsequently, the fragments have to recombine most probably on the substrate to reconstitute the compound. Therefore, the stoichiometry of the film depends on several factors including the deposition rate and the ratios of the various molecular fragments, the impingement rate of other gases present in the environment, the surface mobility of the fragments (which in turn depends on their kinetic energy and substrate temperature), the mean residence time of the fragments on the substrate, the reaction rate of the fragments on the substrate to reconstitute the compound and the impurities present on the substrate. For example, it was found that direct evaporation of  $Al_2O_3$  resulted in a deposit which was deficient in oxygen, i.e., which had the composition  $Al_2O_{3-x}$ . This  $O_2$  deficiency could be made up by introducing  $O_2$  at a low partial pressure into the environment (23).

In other cases, the situation is more complex (24).  $ZrB_2$  films produced by direct evaporation of  $ZrB_2$  billets from an electron beam heated source either at high or low deposition rates ( $2.14$  and  $0.11 \mu m \text{ min}^{-1}$  thickness per minute respectively) consisted entirely of the  $ZrB_2$  phase. In contrast, in similar experiments with high rate evaporation of  $TiB_2$ , the deposits consisted of a mixture of  $TiB_2$  and TiB phases with the amount of the TiB phase increasing with higher deposition temperatures. Low rate evaporation of  $TiB_2$  produced  $TiB_2$  deposits exclusively.

### 15.2.2 Reactive Evaporation Processes

**15.2.2.1 Using a Compound Evaporant.** The above problem related to stoichiometry of the films when deposited by direct evaporation process can be to a certain extent circumvented by introducing the reactive gas at a controlled rate during evaporation to raise the partial pressure to about  $10^{-3} - 10^{-4}$  Torr. The film stoichiometry is improved due to gas absorption by growing film. The stoichiometry of the films is also enhanced due to: (25) (i) the possibility of collisions between oxygen and evaporating vapor molecules in transit, and (ii) reaction between the vapor and oxygen molecule at the surface. Although composition is improved, it is difficult to ensure exact stoichiometry of the film by this process.

**15.2.2.2 Using a Metal Evaporant.** Another variant of the reactive evaporation process involves evaporating the metal in a partial pressure of the reactive gas. However, high substrate temperature and low deposition rates are some of the constraints associated with the process of reactive evaporation with metals (26). These limitations can be addressed in terms of thermodynamic and kinetic considerations.

### 15.3 THERMODYNAMIC AND KINETIC FACTORS IN REACTIVE EVAPORATION PROCESS

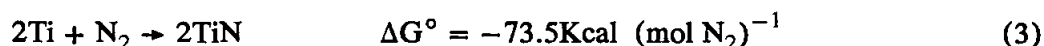
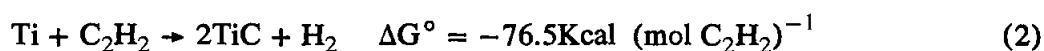
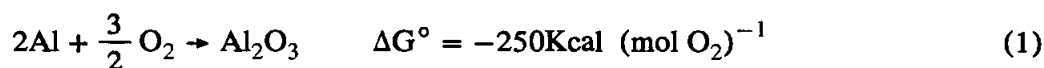
The chemical reaction forming a compound by reactive evaporation process can, in general, be represented as:



As with all chemical reactions, thermodynamic and kinetic constraints apply to deposition of compounds by the above type of reaction. Let us analyze these constraints and how they impose limitations on compound growth by reactive evaporation process.

#### 15.3.1 Thermodynamic Factors

Reactions between metal and gas to form a given compound must have negative free energy of formation. Let us consider the reaction involved in the synthesis of some oxides, carbides and nitrides by reactive evaporation process in view of the thermodynamic criteria given above. Given below (27) are the reactions forming  $\text{Al}_2\text{O}_3$ ,  $\text{TiC}$  and  $\text{TiN}$ , all at 298 K:



As can be seen from the above reactions, the thermodynamic criterion of negative free energy of formation is satisfied for the respective compounds.

Although formation of these compounds is thermodynamically favored, the observed rate at which the respective films are formed in reactive evaporation is extremely low. This process limitation can be addressed in terms of reaction kinetics in a reactive evaporation process.

#### 15.3.2 Kinetic Factors

The question of reaction kinetics in reactive evaporation processes can be treated in exactly the same manner as for reactions occurring in heterogeneous systems of condensed phases (26). The model for heterogeneous metallurgical reactions involves the following: (i) transport of the reactants to the reaction interface; (ii) transport of reaction products away from the reaction interface; (iii) the chemical reaction at the reaction interface; (iv) the nucleation of new phases; (v) heat transfer to or away from the

reaction interface. Any of these can be rate-limiting steps and can control the overall rate of the reaction.

The possible rate-controlling steps in a reactive evaporation process are: (a) the supply of reactants, (b) the collision frequency between reactants, (c) the rate of the chemical reaction at the reaction interface and (d) the rate of removal of products from the interface. It may be noted that the physical location of the reaction interface may be the substrate surface, the surface of the evaporation billet, the gas phase or a combination of these.

It is easy to satisfy conditions (a), (b) and (d) above in reactive evaporation processes. However, condition (c), i.e. the rate of reaction, often becomes the rate-governing step. In reactive deposition processes, another important factor is the deposition rate, which in turn is dependent on the arrival rate of metal atoms or complex species as well as gas atoms on the substrate surface. Thus, Abe et al (16) found that titanium carbide with carbon-to-titanium ratio of 1.0 could be formed by reaction between titanium atoms and  $C_2H_2$  and  $C_2H_4$  molecules on the substrate at  $300 - 500^\circ C$  only if the deposition rate was  $.3 - 1.5 \text{ \AA/s}$ . At higher rates, from  $2 - 4 \text{ \AA/s}$ , the ratio of carbon to titanium decreased from 1 to 0.2.

However, the reaction between titanium vapor atoms and  $C_2H_2$  gas did not occur readily, i.e. condition (c) was the rate-controlling step due to the inability of the reactants to overcome the activation energy barrier. The problem was solved by imparting sufficient energy to the reactants, i.e. titanium vapor atoms and  $C_2H_2$  gas molecules, to overcome the activation energy barrier by exciting them to high energy levels through the creation of a plasma in the reaction zone between the source and the substrate (28,29). Thus condition (c), i.e. the rate of reaction, was no longer the rate-governing step.

## 15.4 ROLE OF PLASMA IN EVAPORATION BASED PROCESSES

As illustrated in the previous section, the presence of a plasma can enhance the reaction rate. The second major role of the plasma in this process is to modify the growth kinetics and hence the structure/morphology of the deposits.

### 15.4.1 Influence of Plasma on Growth Kinetics of the Deposits

In order to understand the role of plasma on overall growth kinetics of the depositing film, one has to consider its influence on the three characteristic steps involved in the formation of the deposit: i) creation of the vapor phase, ii) transport of vapor phase, and iii) film growth on the substrate (30).

**15.4.1.1 Plasma-Source Reactions in ARE Processes.** In the ARE process, the vapor species are generated by thermal energy imparted to the source. The evaporation rate varies directly as the vapor pressure of the target element which in turn is dependent on the temperature of the target surface. The plasma has little or no influence on the evaporation rate. Therefore the vapor generation rate in the ARE process is plasma independent.

**15.4.1.2 Plasma Volume Reactions.** Collision of vapor/gas molecules with electrons during transport from source to substrate gives rise to a variety of chemical reactions in



that region. These reactions play a dominant role in producing various molecular precursors which in turn govern the growth and properties of the depositing film (31). The important factors affecting the plasma volume chemistry are the electron density, electron energy and distribution function. To obtain the desired control of the plasma volume chemistry, film growth and properties, it is therefore imperative that one should be able to control properties of the plasma independently of the deposition parameters. It is in this respect that the ARE type of processes derives its advantage over the other plasma assisted processes (32). For example, the electron number density can be controlled as a separate variable by use of a thermionic emitter. In addition, the electron energy can be adjusted by selecting the appropriate accelerating voltage.

**15.4.1.3 Plasma Substrate Reactions.** Substrates exposed to a plasma (glow discharge) are bombarded by energetic neutrals, ions and electrons. The nature and energy of the bombarding species are primarily dependent on the process parameters and geometrical location of the substrate within or outside the plasma zone (33,34). Such bombardment can initiate a variety of reactions which may lead to substrate heating, substrate surface chemistry changes, gas incorporation in the growing film, as well as modification of the film morphology, crystallite size and orientation and defect level. At significantly higher energies, as may be present with intentional substrate bias, removal of the deposited atoms by sputtering may become important.

In a plasma-based physical sputter deposition process, ion bombardment of the deposited films occurs due to the difference between the sample potential (floating, grounded or biased) and the plasma potential. The plasma potential depends on a number of parameters, including the energy distribution and density of the electrons as well as the geometrical orientation of the chamber and electrodes (35,36). The effect of the plasma on the three general deposition steps outlined above can vary significantly between plasma deposition processes (37). Such differences are manifest in terms of the types and concentration of the metastable species, ionized species, and energetic neutrals which in turn influence the reaction paths or steps involved in the overall reaction for film formation and the physical location of these reactions sites. The advantages and limitations of various plasma assisted deposition techniques can be addressed in terms of the differences in plasma interaction at the source, during transport and at the substrate in the respective processes. The advantages and limitations of the various plasma assisted processes are due to: i) interdependency of the above three plasma interactions and ii) the coupling of the plasma parameters and processes parameters. For an ideal plasma assisted process, one should be able to control each of the above reactions independently of each other.

A summary of the plasma interactions, the parameters controlling these interactions and their effect on structure properties of films by ARE process is given in Table 1.

## **15.5 IMPLEMENTATION OF THE ACTIVATED REACTIVE EVAPORATION PROCESS**

### **15.5.1 Basic ARE Processes**

The two variants of the basic ARE process are (a) the Activated Reactive Evaporation (ARE) process with electron beam evaporation source, (b) the ARE process with resistance heated source. Both of these processes are schematically shown in Fig. 1.

**Table 1:** Influence of plasma on three steps of film deposition by ARE process.

GROWTH STEP	PLASMA INTERACTION	ADVANTAGE
Source reactions	no effect on source	absence of source poisoning allows high rate deposition
Transport reactions	Independent control of electron density, energy	1. Better control of film composition 2. Low substrate temperature 3. Synthesize new structures
Substrate reactions	Substrate bombardment controlled independently of source.	Substrate can be located out of plasma region

In ARE using an e-beam source, the metal is evaporated by an electron beam in presence of a reactive gas. The plasma is generated by accelerating the secondary electrons from the plasma sheath above the molten pool towards a probe biased to a small a.c. or positive d.c. potential. This technique has been successfully used to deposit carbides, (28) nitrides, (38,39) oxides, (40,41) sulphides, (42,43) as well as carbonitrides of titanium, (44).

Nath and Bunshah modified the ARE process for use with resistance heated sources. The metal is evaporated from a resistance heated source in the presence of the reactive gas (45). The plasma is generated by accelerating the thermionically emitted electrons from a heated filament towards a positively biased anode. A transverse magnetic field is applied to cause the electrons to travel in spiral paths thereby increasing the probability of ionization. This technique has been successfully used to deposit transparent conducting coatings of indium oxide, indium tin oxide, zinc oxide, etc.

### 15.5.2 Modification of the Basic ARE Process

There are several modifications of the basic ARE process as illustrated in Fig. 2 (26).

### 15.5.3 Low Pressure Plasma Deposition (LPPD) Process

Using electron beam evaporation sources, the electric field may be generated for a conducting substrate by biasing the substrate positively instead of using a positively biased interspace electrode. In this case, it is called Low Pressure Plasma Deposition (LPPD) by Nakamura et al (46). However, this version has a disadvantage over the basic ARE process since one does not have the freedom of choice to ground the substrate, let it float or bias it negatively.

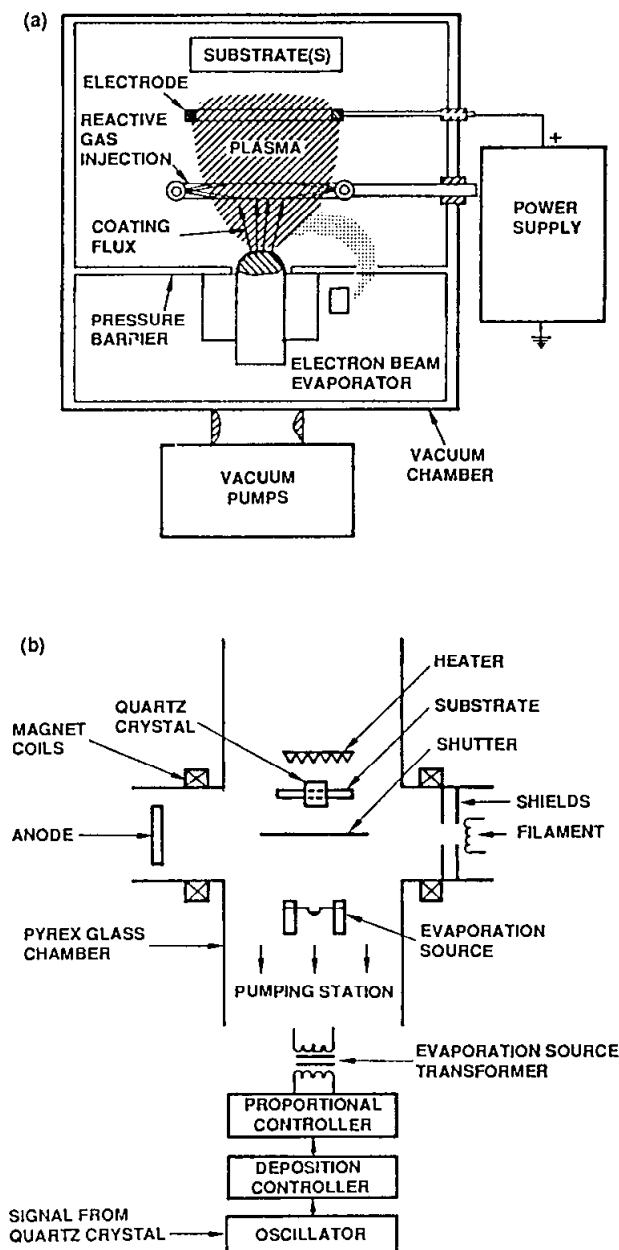


**Figure 1:** Schematic of the activated reactive evaporation system: (a) using an electron beam evaporation source, and (b) using a resistance heated evaporation source.

If the substrate is biased in the ARE process, it is called biased ARE, or BARE (47). This bias is usually negative to attract the positive ions in the plasma. Kobayashi and Doi (48) reported the same process in 1978 and called it reactive ion plating.

Murayama (49) used an electron beam heated source with a negatively biased substrate and rf activation of the reactants by means of a coil electrode of aluminum wire in the reaction zone to deposit oxide and nitride films.

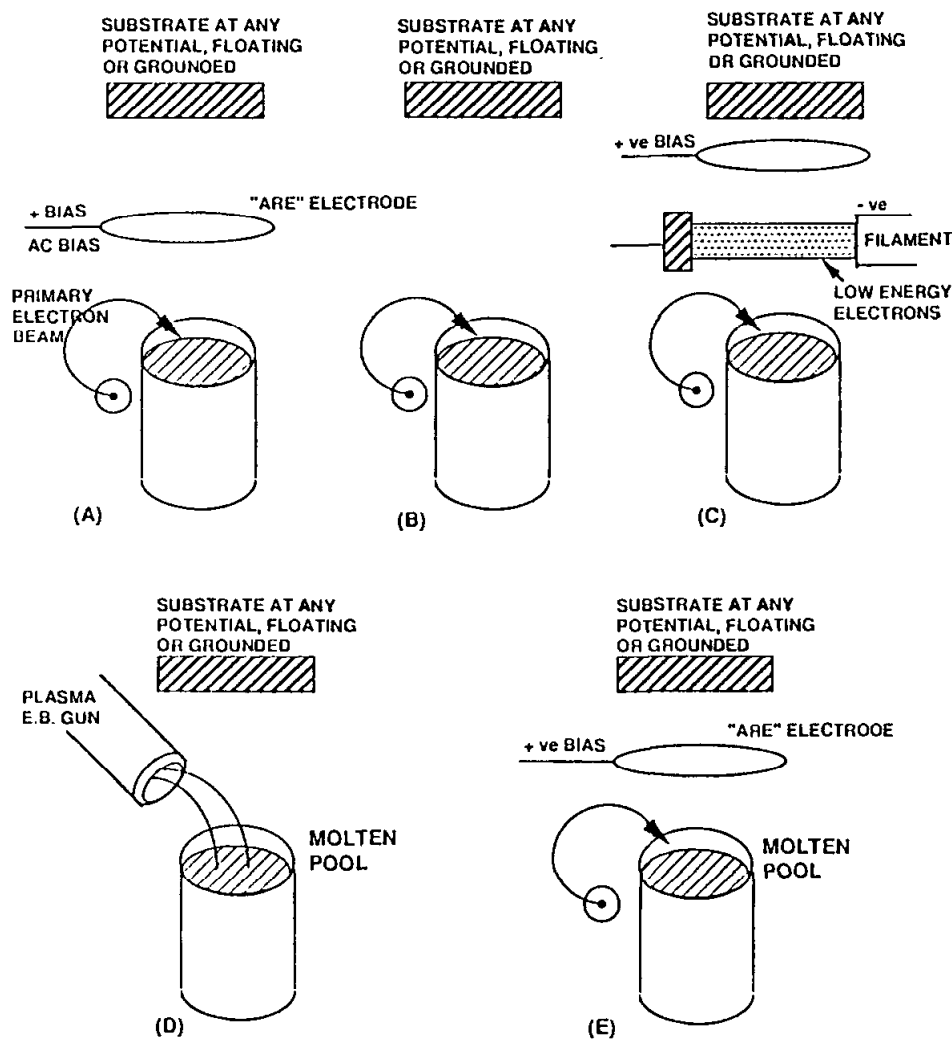


**Figure 2:** (a) The basic ARE process and (b)-(e) later variations: (b) low pressure plasma deposition process; (c) enhanced ARE process; (d) ARE process with hot hollow cathode electron beam gun or cold cathode discharge electron beam gun; and (e) biased ARE or reactive ion plating process.

#### 15.5.4 Processing Using Plasma Electron Beam Guns

A plasma electron beam gun can be used in place of the thermionic electron source to increase the level of ionization in the ARE process. The advantage of these guns is that they provide an abundant supply of low energy electrons and are relatively rugged and long-lived. These are two types of plasma-based electron sources that could be used (50). They are:

- The Cold Cathode Plasma Electron Beam - This plasma electron beam gun has a cylindrical cathode cavity made from a metal mesh or sheet containing the ionized plasma from which electrons are extracted through a small aperture in one end. The cathode is maintained at a negative potential, e.g., -5 to -20 kV, relative to the workpiece and remainder of the system, which are at ground potential (50). Zega

et al (51) used a cold cathode discharge electron beam gun to deposit titanium nitride films.

- The Hot Hollow Cathode Discharge - The hollow cathode discharge applied to vacuum processing has been reported by Morley (52). Here the cathode operates at an elevated temperature and must be constructed of refractory materials. A gas, often argon or krypton, is introduced into the system through the tubular-shaped cathode. The internal walls of the hollow cathode are heated to thermionic emission temperatures (2000K) by the ion bombardment. A low voltage, high amperage d.c. power source is utilized. Often rf power from a commercial welding starter is coupled to the gas to initiate the discharge. The high current glow discharge that occurs is analogous to that experienced in vacuum arc melting at higher pressures. When a axial magnetic field is imposed on the emitted plasma, it then forms a high power density, well-collimated beam. The hollow cathode discharge beam is operationally stable and efficient over the pressure range from  $10^{-4}$  to  $10^{-1}$  Torr. A more detailed description of physical aspects, operational characteristics, and cathode design has been given by Morley (52). The hot hollow cathode has been used by Komiya et al (53), for example, to deposit TiC films.

### **15.5.5 Activated Reactive Evaporation Process Using an Arc Evaporation Source**

The evaporation of metals using a low voltage arc in the presence of a plasma and a negatively biased substrate is used by Snaper (54) and Dorodnov (55) to deposit nitride and carbide films, with  $N_2$  and hydrocarbon reactive gases respectively. (For a discussion of vacuum arc technology, please see Chap. 18). Since arcs naturally operate at low voltages, ionization processes are very efficient and a reaction plasma is very easily created.

## **15.6 RECENT DEVELOPMENTS IN THE ARE PROCESS**

In the last few years new techniques based on ARE are being developed for the synthesis of novel and unique materials. The emphasis of such developments is generally on two aspects: i) new approaches to produce the vapor species and ii) new plasma excitation techniques and development of modified plasma excitation geometries.

### **15.6.1 New Approaches to Produce the Various Species**

The basic process involves evaporation of the constituent metal alloy, or compound using e-beam or resistance/induction heated sources. However, it is difficult to use this approach with certain materials such as boron and carbon. Two possible solutions can be used to overcome these difficulties: 1) use of a low melting point compound of the respective element, and 2) use of a pulsed laser beam where the pulse rate and pulse width can be appropriately adjusted to control the rate of material generation and fragmentation. Moreover, in many cases, the energy of the laser beam can also be used as a source for plasma excitation.

Both these approaches have been explored. A process developed by Bunshah et al (56) for the synthesis of cubic boron nitride involve boric acid as an evaporant, which can be easily evaporated from a resistance heated tungsten boat. In addition to the ease of

evaporation, this process also excludes the toxicity problems associated with fine boron particles which can be produced during e-beam evaporation of boron. A similar approach can be extended to evaporation of carbon using a low melting point carbon compound such as adamantane. It is likely that many new materials hitherto difficult to synthesize may possibly be deposited using this route. Moreover, this novel approach may contribute to further development in reactive MBE processes and processes involving organometallic compound reactants.

The use of pulsed laser beams in an ARE type of process has been demonstrated in recent literature on high  $T_c$  superconducting films (57). Films with high  $T_c$  (90 K) and high critical current density ( $0.7 \times 10^6 \text{ A/cm}^2$  at 77K) have been produced (58). It is claimed that pulsing of the laser beam avoids fractionation of the compound and hence good control of film stoichiometry is achieved. It is also suggested that the photon energy is sufficient to activate the reactive gas/metal species thereby increasing their reactivity leading to increase in oxygen concentration in the deposited films.

### 15.6.2 New Plasma Excitation Modes and Geometries

As discussed earlier the attributes of the ARE processes are due to the possibility to control the plasma parameters independently of the deposition process. However, improvement in excitation and confinement of the plasma as well as control and optimization of plasma parameters in the ARE processes are likely to enhance the process capabilities. Recent developments include i) the use of inductively coupled rf with parallel plate rf geometries, and ii) the use of multiple filaments and anodes with magnetic confinement. These enhancements have led to substantial improvements in film properties as well as process control. Examples are high rate deposition of a-Si-H films (59), transparent conducting films on polymeric substrates (60) and  $\text{TiS}_x$  and  $\text{MoS}_x$  (61,62) films with variable  $x$  values.

Two additional modes of ionization are being explored. Currently an auxiliary rf excitation source similar to that reported by Oeschner (63) is being developed for use in ARE. It is believed that the high electron density and energy selectivity offered by this source is likely to enhance advantages of the ARE processes for compound synthesis. Also, work is underway to integrate Electron Cyclotron Resonance excitation at microwave frequencies with the ARE process. ECR plasmas are characterized by a very high level of ionization and excitation, and may greatly enhance the uses of ARE for the deposition and synthesis of films.

## 15.7 STRUCTURE AND PROPERTIES OF THE FILMS

The physical and chemical properties of films critically depend on structure and morphology, defects, and the impurity content.

The influence of process parameters on the film growth can be understood in terms of their effects on sticking coefficient, surface mobility of adatoms, nucleation density as well as the thermodynamic and kinetic factors determining the various chemical reactions occurring at the substrate, especially in the case of deposition of compound films. Plasma parameters influence film growth and properties in two ways:

1. By controlling the plasma volume chemistry thereby producing molecular precursors which determining the reaction path leading to the formation of one compound on the substrate;
2. By enhancing the energy of the condensing species thereby modifying the nucleation and growth of the films.

The interaction between deposition parameters and plasma or ion bombardment on film properties is indeed complex. This topic will be covered in more detail in Chaps. 19-21.

### **15.8 MATERIALS SYNTHESIZED USING THE ACTIVATED REACTIVE EVAPORATION PROCESS**

A variety of compounds such as carbides, nitrides and oxides of refractory metals, sulphides, alloyed carbides, carbonitrides, superconducting coatings such as Nb<sub>3</sub>Ge have been deposited using this technique. A representative list of the compounds synthesized using the ARE technique is given in Table 2.

In recent years, ARE and related processes have been successfully used to synthesize novel materials (64). Of particular industrial interest are cubic boron nitride, (65) diamond and high temperature superconducting films (66). The principal attributes of the process are related to its ability to control stoichiometry, structure and properties of the films as well as its ability to provide high deposition rates at low substrate temperatures.

### **15.9 FUTURE OUTLOOK AND PERSPECTIVE**

With increasing demand for low temperature processing and requirements for new materials, plasma assisted processing is likely to remain a major research area. Modified and novel plasma excitation techniques such as auxiliary rf ion/plasma source/microwave excitation in conjunction with the basic ARE set-up is likely to further enhance its processing capability.

Apart from process development research, interest needs to be directed towards understanding the plasma chemistry and its role in film growth and properties. *In situ* diagnostic studies using optical emission spectroscopy, mass spectroscopy and plasma mass spectroscopy, and other sophisticated tools such as coherent anti-Stokes Raman spectroscopy and laser induced fluorescence spectroscopy are necessary to develop quantitative models of film growth by the ARE and related processes. Such studies are not only important in understanding the basic film chemistry, growth and properties but also in developing appropriate modifications of the process to optimize the properties of deposited coatings.

### **15.10 CONCLUSIONS**

The ARE process has demonstrated its versatility in the synthesis and deposition of thin films of simple and complex refractory compounds and at low temperatures which makes it compatible with many of the operations in microelectronics, optoelectronics and optical coatings. Further areas of application may be magnetic and ferroelectric films.

This process is used currently in industry in one or more of its variants to deposit TiN coatings on cutting tools. With the advent of reliable rate monitors, gas flow control systems, feed back loops and computer controlled processing, the ARE process should find its way into many other areas, including the synthesis of new and novel materials.

**Table 2:** Examples of some compounds synthesized and deposition rates obtained using ARE, reactive sputtering, and PACVD.

<u>Compound</u>	<u>ARE</u> $\text{\AA min}^{-1}$	<u>Reactive</u> $\text{\AA min}^{-1}$	<u>PACVD</u> $\text{\AA min}^{-1}$
Carbides TiC, HfC, ZrC, VC	2000-3000	400-500	150-400
Nitrides TiN, HfN, ZrN	2000-3000	300-400	60-150
Oxides TiO <sub>2</sub> , ZrO <sub>2</sub> Al <sub>2</sub> O <sub>3</sub> , SiO <sub>2</sub>	1000-2000	200-800	200-300
Sulphides TiS <sub>2</sub> , MoS <sub>2</sub> MoS <sub>3</sub>	1000-2000		
<u>Novel Materials</u>			
Superconducting materials Nb <sub>3</sub> Ge, CuMO <sub>6S8</sub>	1000-1500		
Photovoltaic materials a-SiH, CuInS <sub>2</sub>	1500-2000	50-200	
Optoelectronic materials Indium-tin-oxide, zinc oxide	500-1000		
Cubic BN	1000-1500		
Diamond			1000 $\text{\AA hr}^{-1}$
carbon	300	200	

### 15.11 REFERENCES

1. C. Deshpandey and R. F. Bunshah, Thin Solid Films 163: 131 (1988).
2. B. Chapman, Glow Discharge Processes (Wiley and Sons Inc., N.Y., 1980).
3. V. Soddy, Proc. R. Soc. London 78: 429 (1907).



4. S. Brinsmaid, W. J. Keenan, G. E. Koch, and W. F. Parsons, US Patent 2,784,115, March 5, (1957).
5. M. Auwarter, U. S. Patent 2,920,002 (1960).
6. C. S. Herrick and A. D. Tevebaugh, J. Electrochem. Soc. 110: 199 (1963).
7. M. A. Novice, J. A. Bennett, and K. B. Cross, J. Vac. Sci. Technol. 1: 73A, (1964).
8. R. B. Schilling, Proc. IEEE 52: 1350 (1964).
9. E. Ritter, J. Vac. Sci. Technol. 3: 225 (1966).
10. E. Ferrieu and B. Pruniaux, J. Electrochem. Soc. 116: 1008 (1969).
11. J. R. Rairden, Electrochem. Technol. 6: 269 (1968).
12. J. R. Rairden, in Thin Film Dielectrics ed. by F. Vratny (Electrochem. Soc. , New York, 1969) p. 279.
13. J. DeKlerk and E. F. Kelley, Rev. Sci. Instrum. 36: 506 (1965).
14. A. J. Learn and K. E. Haq, Appl. Phys. Lett. 17: 26 (1970).
15. A. Itoh and S. Misawa, Proc. 6th Intl. Vacuum Congress, Kyoto, in Jpn. J. Appl. Phys. Suppl. 2, Part 1: 467 (1974).
16. T. Abe, K. Inagawa, K. Obara, Y. Murakami, Proc. 12th Symp. on Fusion Technology, Zurich, September 13-17 (1982).
17. M. T. Wank and D. K. Winslow, Appl. Phys. Letts. 13: 286 (1968).
18. B. B. Kosicki and D. Khang, J. Vac. Sci. Technol. 6: 592 (1969).
19. W. Heitmann, Appl. Opt. 10: 2414 (1971).
20. W. Heitmann, Appl. Opt. 10: 2685 (1971).
21. H. Kuster and J. Ebert, Thin Solid Films 70: 43 (1980).
22. J. Ebert, SPIE 325: 29 (1982).
23. D. Hoffman and D. Liebowitz, J. Vac. Sci. Technol. 9: 326 (1972).
24. R. F. Bunshah, R. J. Schramm, R. Nimmagadda, B. A. Movchan and V. P. Borodin, Thin Solid Films 40: 169 (1977).
25. L. Holland, Vacuum Deposition of Thin Films (Chapman and Hall, London, 1956).
26. R. F. Bunshah, Thin Solid Films 107: 21 (1983).
27. L. I. Quill in The Chemistry and Metallurgy of Miscellaneous Materials and Thermodynamics (McGraw Hill Inc., New York, 1950).
28. R. F. Bunshah and A. C. Raghuram, J. Vac. Sci. Technol. 9: 1385 (1972).
29. R. F. Bunshah, US Patent 3,791,852, Feb. 2 (1974).
30. C. Deshpandey and R. F. Bunshah, J. Vac. Sci. Technol. A3: 553 (1985).
31. C. Deshpandey, B. P. O'Brien, H. J. Doerr, R. F. Bunshah and D. Hofmann, Surf. Coat. Technol. 33 (1987).
32. C. Deshpandey and R. F. Bunshah in Physics of Thin Films ed. by M. H. Fromcombe and J. L. Vossen (Academic Press, New York, 1987).
33. L. Holland, J. Vac. Sci. Technol. 14:5 (1977).
34. L. Holland, Surface Technology, 11: 145 (1980).

35. J. A. Thornton in Deposition Technologies for Films and Coatings ed. by R. F. Bunshah et al (Noyes, Park Ridge, N.J. 1982).
36. J. A. Thornton, Thin Solid Films 107: 3 (1983).
37. C. Deshpandey and R. F. Bunshah, to be published in Jour. of Materials Education.
38. A. K. Suri, R. Nimagadda and R. F. Bunshah, Thin Solid Films 72: 529, (1980).
39. P. Lin, C. Deshpandey, H. J. Doerr and R. F. Bunshah in Quarterly Progress Report ed. by F. A. Nichols and A. R. Michaels, TRIB-ECUT, 86-1 and 86-2, Argonne National Laboratory, Argonne, Illinois, U. S.
40. R. F. Bunshah and R. J. Schram, Thin Solid Films 40: 211 (1977).
41. M. Colen and R. F. Bunshah, J. Vac. Sci. Technol 13: 536 (1976).
42. K. C. Chi, R. O. Dillan, R. F. Bunshah, S. Alterovitz and J. A. Wollam, Thin Solid Films 54: 259 (1978).
43. H. S. Randhawa, D. Brock, R. F. Bunshah, B. Basol and O. M. Stafsudd, Sol. Energy Materials 6: 4456 (1982).
44. B. E. Jacobson, C. Deshpandey, A. A. Karim, H. J. Doerr and R. F. Bunshah, Thin Solid Films 118: 293 (1984).
45. P. Nath and R. F. Bunshah, US Patent 4,336,277, June (1982).
46. K. Nakumara, K. Inagawa, K. Tsusoka, and S. Komiya, Thin Solid Films 40, 155 (1977).
47. R. F. Bunshah, Physical Vapor Deposition of Metals and Alloys and Compounds, New Trends in Materials Processing, American Society of Metals, Metals Park Ohio (1976) p. 200.
48. M. Kobayashi and Y. Doi, Thin Solid Films 54: 67 (1978).
49. Y. Murayami, J. Vac. Sci. Technol. 12: 818 (1975).
50. R. F. Bunshah in Deposition Technologies for Films and Coatings ed. by R.F. Bunshah et al (Noyes, Park Ridge, NJ 1982).
51. S. Zega, M. Kornmann and J. Amiquet, Thin Solid Films 54: 51 (1978).
52. J. R. Morley, Trans. Vac. Met. Conf., American Vacuum Society (1966) pg. 166, 186.
53. S. Komiya, N. Umezu and T. Narusawa, Thin Solid Films 54: 51 (1978).
54. A. Snaper, US Patent: 3,125,848, Dec. 7, 1971 and US Patent: 3,836,451, Sept. 17 (1974).
55. A. M. Dorodnov, Sov. Phys. 23: 1058 (1978).
56. R. F. Bunshah, K. L. Chopra, C. Deshpandey and R. F. Vankar, US Patent: 4,714,625, (1987).
57. D. Wu, D. Dijkkamp, S. B. Ogale, A. Inain, E. W. Chase, P. F. Miceli, C. C. Chang, J. M. Tarascon and T. Venkatesan, Appl. Phys. Letts. 51(11): 861 (1987).
58. A. Inam, M. S. Hedge, X. D. Wu, T. Venkatesan, D. England, P. F. Miceli, E. W. Chase, C. C. Chang, J. M. Taraskan and Y. B. Watchman, Appl. Phys. Letts. 53: (10), 908 (1988).

59. C. Y. Chen, M. S. Thesis, Dept. Mat. Sci. & Eng. University of California, Los Angeles, CA (1987).
60. B. P. O'Brien, M. S. Thesis, Dept. Mat. Sci. & Eng. University of California, Los Angeles (1987).
61. D. Zender, C. Deshpandey, B. Dunn and R. F. Bunshah in Proc. 5th Intl. Conf. on Solid State Ionics Part I, ed. by J. B. Boyle, L. C. DeJonghe and R. A. Huggins, (North Holland, Amsterdam, 1986) p. 813.
62. H. Shin, H. J. Doerr, C. Deshpandey, B. Dunn and R. F. Bunshah, to be published in Thin Solid Films.
63. Prof. H. Oeschner, University of Kaiserslauten, FRG, Private Communication, to be published.
64. C. Deshpandey and R. F. Bunshah, Thin Solid Films, 163: 131 (1988).
65. P. Lin, C. Deshpandey, H. J. Doerr, R. F. Bunshah, K. L. Chopra and V. D. Vankar, Thin Solid Films 153: 487 (1987).
66. S. Prakash, C. Deshpandey, R. F. Bunshah, to be published.

---

## **Formation of Thin Films by Remote Plasma Enhanced Chemical Vapor Deposition (Remote PECVD)**

---

**Gerold Lucovsky, David V. Tsu and Robert J. Markunas**

### **16.1 INTRODUCTION**

Much of the stimulation for research in the area of Plasma Enhanced Chemical Vapor Deposition, PECVD, comes from a more general interest in the low temperature processing of electronic materials, where low temperature usually means temperatures below about 500°C. In this chapter we emphasize the deposition of silicon containing dielectric materials, i.e., silicon oxide, nitride and oxynitride alloys, as well as hydrogenated amorphous silicon. These materials are currently utilized in several different types of device structures, but also have the potential for additional applications in more advanced and emerging microelectronic structures that require, for example, low temperature dielectrics. The limited use of the PECVD dielectric materials can, in part, be related to the nature of the deposition process reaction pathways in the conventional (and commercialized) Direct PECVD process that promote: (a) deviations from oxide or nitride compound stoichiometry, i.e., Si-Si bonds in addition to the Si-O and/or Si-N bonds; and (b) significant incorporation of bonded hydrogen, 2-10 at.% in the oxides, and as high as 20 to 40 at.% in the nitrides (1,2). The Direct PECVD dielectrics have nevertheless been used in applications such as in passivation and in field oxides, where deviations from compound stoichiometry and hydrogen incorporation are not deleterious to device operation. In contrast, Direct PECVD of a-Si:H (also called Glow Discharge decomposition or simply GD in the amorphous silicon literature) is the preferred method (3) for the a-Si:H films used in photovoltaic cells (4), xerographic photoreceptors and thin film transistors (TFT's) (5). In these applications, controlled incorporation of hydrogen at the 10-15 at.% level is essential for reducing the densities of intrinsic bonding defects, e.g., dangling bonds (3), to the low levels required for satisfactory device operation (3-5).

The deposition of oxide and nitride films on a substrate separated from the existing plasma was apparently first used by Alt et al (6) in 1963, although the description of the

method was not reported until 1965 (7). A 500 kHz power supply was used to dissociate  $O_2$  flowing into a reaction chamber into which tetraethoxysilane was introduced. In 1966, Secrist and MacKenzie (8) described the use of a 2.45 GHz discharge to activate  $O_2$  and deposited a variety of films, including  $SiO_2$ .

In 1977, Shiloh et al (9) deposited  $Si_3N_4$  by exciting  $N_2$  in a 2.45 GHz microwave cavity from where it flowed into a heated tube into which  $SiH_4$  was introduced;  $I_2$  vapor was used to provide a gaseous source of Si from Si powder.

However, a much greater interest in the Remote PECVD (RPECVD) technique is marked by the publication in 1982 of several reports. The common intent was to deposit films at low substrate temperatures and with minimum introduction of damage, either structural or electrical, to the substrate. Kato et al (10) introduced an  $Ar/SiH_4$  mixture into a 2.45 GHz discharge to deposit a-Si at a distance of 15 cm from the cavity center. Clark and Anderson (11) deposited  $Si_3N_4$  on GaAs substrates using an rf (13.56 MHz) discharge to excite a  $N_2/H_2$  mixture which flowed into the substrate chamber with an  $Ar/SiH_4$  mixture introduced into a gas dispersal ring above the substrate. Meiners (12) deposited  $SiO_2$  films on InP substrates using a 13.56 MHz discharge; he added  $N_2$  to the  $O_2$  in the discharge to increase deposition rates. The excited gas was mixed with a  $SiH_4/N_4$  mixture in a heated tube and gases flowed over the heated substrate to the pump. Bardos, et al (13) compared the efficiency of microwave (2.45 GHz) and rf (13.56 MHz) discharges for the production of excited molecular  $N_2$  for  $Si_3N_4$  deposition by RPECVD.

Since 1982, many papers have been published on the deposition of a-Si,  $SiO_2$  and  $Si_3N_4$  films by RPECVD. It is not the intention here to review this literature in detail, but to discuss the possible reaction paths for film deposition. To provide an explanation of these processes and their consequences, we will use results obtained over several years in our laboratories as examples. This should make it easier for the reader to follow the discussion of the processes without having to consider possible effects of the many experimental arrangements which have been investigated in different laboratories.

This chapter begins with a discussion of the CVD process, focusing on the plasma enhanced procedures that have been applied for the deposition of the electronic materials discussed above. We identify the differences between the conventional Direct PECVD process and the Remote PECVD process, that is the subject of this chapter. We then discuss the Remote PECVD process in greater detail, emphasizing: (a) the deposition processes relative to selective excitation of the different gas reactants and/or diluents; (b) the design of deposition chambers used to implement these procedures or protocols; (c) the reaction pathways for deposition of hydrogenated amorphous silicon, and the silicon dielectrics; (d) selected vibrational, optical and electronic properties of the deposited films; (e) applications of these Remote PECVD films in device structures; and finally (f) new directions in Remote PECVD research, including the extension of the approach to additional electronic materials.

## 16.2 BACKGROUND - CVD PROCESSES

The CVD process is defined as the deposition of a thin solid film from a chemical reaction involving gas species at a heated substrate (14). For all CVD processes, the determinant factors in film formation are: (a) the rate of delivery of the process gases to the substrate; (b) the chemical reaction rates for film formation at the substrate surface; and

(c) the rate of removal of reaction by-products (14). In general, the transport of the gases is determined by the process pressure and the gas flow rates. Diffusion of source gases to, and by-product gases away from the deposition surface is enhanced at low pressures (below about 1 Torr). In hot wall CVD reactors, the temperature of the gas,  $T_g$ , is the same as that of the substrate,  $T_s$ . The operation of hot wall reactors at high pressures, e.g., at one atmosphere, can result in homogeneous gas phase reactions, sometimes resulting in the production of unwanted powder species. Powder formation can be eliminated by minimizing homogeneous gas phase reactions either by: (a) diluting the reactant gases with inert gases, thereby reducing the partial pressures, and the collision rates necessary for these reactions; or (b) using cold wall reactors in which only the substrate is heated. In cold wall reactors, the reactant gases generally do not react homogeneously in the gas phase to form the thin film material, but require either: (a) an additional energy input to increase their reactivity (14); or (b) a pre-activated nucleation surface site in order to be able to take part in heterogeneous surface reactions leading to film deposition (15-16). The basic or elementary CVD process is one in which all the additional energy is supplied at the heated substrate, and where the rate of reaction is then determined by the temperature of that substrate; i.e.,  $T_s$ . There are no inherent restrictions on the nature of the heterogeneous chemical reactions that are used in CVD processes (14); they can be oxidation, pyrolysis, etc. We designate this type of process as thermal CVD. This definition is used to differentiate the thermal CVD processes from other CVD processes in which different source of energy, such as rf or microwave plasmas, are employed to activate the chemical reaction pathways leading to film deposition.

In general and depending on the particular reactants employed, thermal CVD processes for stoichiometric, hydrogen-free silicon oxides and nitrides, and for poly- or single crystal silicon, require relatively high substrate temperatures, in excess of 500°C, and generally in the range of 600 – 900°C (14). These temperatures are too high for many projected VLSI and ULSI devices because of thermal budget limitations (17,18). One approach to reducing substrate temperatures is to increase the reactivity of the process gases before their arrival at the deposition substrate. This can be accomplished by supplying energy to the reactants through excitation in the gas phase, e.g., using energetic electrons produced in either radio-frequency (rf) or microwave discharges, or using photons.

Our discussion of the enhancement mechanisms for CVD, will be limited to the plasma enhanced techniques, and in particular to plasmas generated by rf power. We note that the one important difference between rf and microwave discharges is in the energy distribution of the plasma-generated electrons (19), which results in significant differences in the specific nature of the plasma-activated species that take part in film deposition. We will not focus on this aspect of PECVD process. What concerns us instead is not exactly how the activated species are generated, but where they are generated with respect to the substrate, and which of the reactant gases are directly subjected to plasma excitation. The "where" and "which" represent the differences between two different plasma enhanced processes, Direct and Remote PECVD, which involve respectively either direct or remote plasma excitation of the process gases.

The distinction between Direct and Remote PECVD is made primarily on the basis of which of the gas reactants and diluents are directly plasma excited (2). In the Direct process, all process gases are exposed to a common rf plasma. In diode type rf reactors, the substrate is attached to one of the rf electrodes, usually the grounded electrode, and

is immersed in the plasma glow. Silicon oxide and nitride films produced in this way usually display significant departures from compound stoichiometry, and also contain large amounts of bonded hydrogen, 5-30 at.% (1). In contrast, in the Remote PECVD process, not all of the reactant gases are plasma excited and the substrate is removed from the glow region of the plasma. These restrictions on which of the gases are plasma excited, and on the placement of the substrate outside the plasma glow region tend to limit the number of possible reaction pathways and thereby lead to increased control over stoichiometry and hydrogen incorporation (or elimination) in the deposited films. There is another and non-conventional Direct PECVD process technique where very high levels of dilution of the reactant gases by noble gases, approaching 10,000:1 in some cases, can also restrict the process of plasma excitation to a specific subset of the process gases, and therefore also limit the number of reaction pathways. We will not discuss this process in any detail, but instead refer the reader to the literature (20).

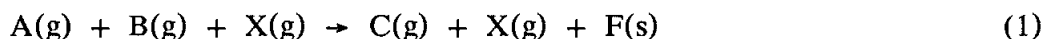
Finally, we note that there are several hybrid PECVD processes that combine some of the properties of the Direct and Remote processes. For example, in reactors of the triode design, the substrate sits below a grid which replaces one of the rf electrodes so that the substrate is not exposed directly to the plasma glow. This technique has been used primarily in the deposition of a-Si:H (21). Another technique uses microwave power, and also accomplished deposition outside the plasma. In this process, designated electron cyclotron resonance (ECR) microwave PECVD, the plasma is magnetically contained so that deposition occurs outside the glow region (22). In both these techniques, all the process gases are subjected to the plasma excitation. We refer the reader to another chapter in this volume for a discussion of the ECR PECVD process (23).

The initial attempts at rf excited Remote PECVD are described in Refs. 6-12,24,25. These papers provide the basis for the more recent and extensive studies pursued jointly in the Department of Physics at North Carolina State University and the Semiconductor Research Group at the Research Triangle Institute (2,26-28). These results form the body of this paper are discussed in detail in the sections that follow. Our emphasis is on the deposition process, rather than the film properties. However, we include short discussions of both film properties and device applications to complement the discussions of the deposition processes.

## 16.3 THE REMOTE CVD DEPOSITION PROCESS

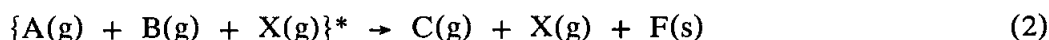
### 16.3.1 Overall Deposition Reactions

Consider first a symbolic representation of an elementary CVD process that: (i) uses two different reactant gases, A(g) and B(g); (ii) has a gaseous reaction by-product, C(g); and (iii) generates a thin film solid material, F(s). The reaction leading to thin film formation is given by:

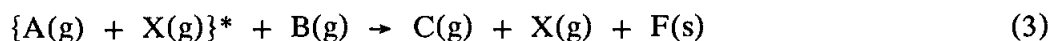


where X(g) is an inert diluent; e.g., one of the noble gases. It should be noted that throughout this chapter, reaction pathways are designated by an arrow ( $\rightarrow$ ). The pathways listed here have been simplified in that the specific quantities of each of the species have been omitted. To distinguish between the Remote and Direct PECVD processes,

we use a starred bracket  $\{ \}^*$  to indicate those gases that are directly plasma excited. For the same reaction as in Eqn. (1), the Direct PECVD process is defined by



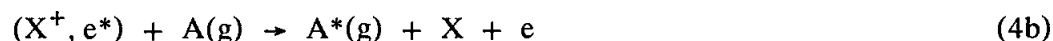
and the Remote PECVD process by



We also consider a second class of Remote PECVD processes where neither of the two reactant gases is directly plasma excited, but where at least one of the molecular species, e.g.,  $A(g)$ , is activated by electrons, ions, or metastable atoms extracted from a remote noble gas plasma. An illustration of this type of process reaction is given in Eqns. (4a), (4b) and (4c):

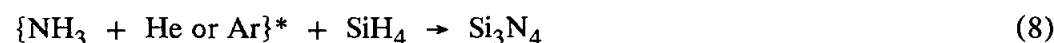


where  $X$  is a noble gas, e.g., He, Ar, etc., and  $X^+$  and  $X'$  are respectively, noble gas ions and metastables, and  $e^*$  are defined as energetic electrons generated in the remote plasma as opposed to those electrons formed as a result of a reaction (29). For a deposition process reaction that is driven by electron and/or ion excitation, we invoke the following two symbolic reaction equations:

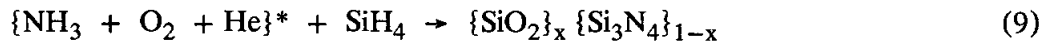


where  $A^*(g)$  is a reactive species activated: (a) through an inelastic collision with a plasma generated electron or ion (30); or (b) at an active surface site created by one of the plasma extracted species (15,16).

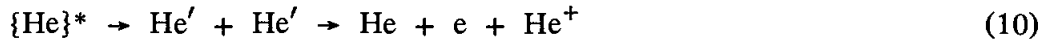
We now list the overall Remote PECVD process reactions that have been used to produce silicon dielectric films (2,26,28,31-33). We first indicate the films grown by the process described by Eqn. (3) that utilizes plasma excitation of noble gas/nitrogen containing molecule and/or noble gas/oxygen containing molecule mixtures:



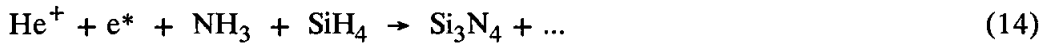
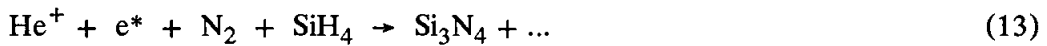
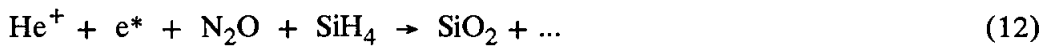
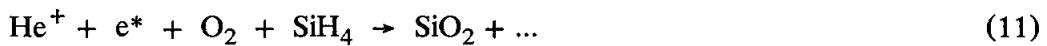




Thin film dielectrics have also been grown by the process described by Eqns. (4a-4c) (33-35), where the deposition process is initiated by extraction of excited species from a He or Ar plasma (30,33-35). For reaction processes involving remote He plasmas, the most probable activating species based on reported cross-sections for excitation are low energy electrons (30) and/or He ions which can result from both direct electron impact ionization as well as by the Penning ionization of He metastables as defined by:



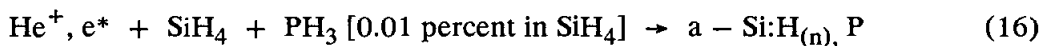
Although there are many channels operative in the production of  $\text{He}'$  metastables, e.g., by the direct electron impact, by the cascading of excited He atoms into the metastable state by photon emission, etc., the mechanism represented by Eqn. (10) is an effective way to consume the He metastable species (29). Using electrons and/or positive He ions as activators, the overall reactions for this second class of remote PECVD processes are given by:



Films of intrinsic and doped hydrogenated amorphous silicon have also been grown by this type of process (36-39). The overall reactions here are: (a) for intrinsic a-Si:H thin films,



(b) for n-doped a-Si:H films,



The Remote PECVD process has also been used to grow epitaxial films of Si and Ge (27), as well as carbon films, including diamond and diamond-like materials (40). The process protocols are essentially the same as that given in Eqn. (15), and the noble gases that have been used for the formation of epitaxial Si and Ge layers include Ar and He (27). For the discussion of these processes and the results obtained, we refer the reader to the literature (27,40).

### 16.3.2 Deposition Chamber Design and Process Variables

To produce films by Remote PECVD, the reaction chamber design must make provision for the special requirements of this process, specifically for: (a) selective excitation of the process gases; and (b) film deposition on a substrate outside the plasma glow region. We discuss the deposition chamber designs that have been employed in the Remote PECVD studies (26,41). The chamber designs, along with the operating pressures and relative gas flow rates, are designed to promote the reaction pathways indicated above, Eqns. (5-16), and in addition to eliminate, or minimize any direct plasma excitation of the  $\text{SiH}_4$  reactant. Figure 1 shows a recent experimental chamber design with a second down-stream gas dispersal ring (41). The range of processing conditions used in the majority of the reported Remote PECVD studies is indicated below (26-28,31-33, 35-39,41,42):

- Chamber pressure prior to deposition:  $< 5 \times 10^{-9}$  Torr
- Operating pressure for depositions: 100-300 mTorr
- Substrate temperatures: 100 – 500°C
- Gas Flow rates: [ X =  $\text{O}_2$ ,  $\text{N}_2\text{O}$ ,  $\text{N}_2$ ,  $\text{NH}_3$  ] :
  - X/He or Ar Mixtures: 100-200 sccm
  - He: 100-200 sccm
  - X: 100-200 sccm
  - $\text{SiH}_4$  [10% in Ar] : 1 sccm [10 sccm of Ar/ $\text{SiH}_4$  mixture ]

The low initial base pressure is required to insure the chemical cleanliness of the chamber; it is achieved after a thermal bakeout at 150 – 200°C that is designed to remove residual gas contaminants, primarily water vapor, from the chamber walls and fixtures. Water vapor can combine with silane via a homogeneous gas phase reaction to produce a silicon dioxide powder, which is detrimental to the thin film depositions. The operating pressure of 100-300 mTorr promotes the collision that are required for thin film deposition at rates between about 0.05-0.1 and 2-5.0 Å/s (2). The relative flow rates of reactant and diluent gases provide a range in which stoichiometric compound and alloy films have been grown, and in which bonded hydrogen incorporation can be controlled. The range of substrate temperatures does not vary deposition rates significantly, but has a profound effect on the amount of bonded hydrogen retained in some of the deposited films, primarily in the oxides, nitrides and a-Si:H alloys (31,37-39,42). More detailed discussions of the effects of processing variables on the film properties are given in the references cited above.

We now describe the way the chamber design in Fig. 1 is designed to implement the sequential steps of the Remote PECVD process. The Remote PECVD process can be described in terms of four discrete and separate process steps (2): (a) remote plasma excitation of a subset of the reactants and diluents; (b) transport of plasma generated reactive species from the glow region into the reaction chamber; (c) mixing of the plasma extracted reactive species with the remaining process gases; and (d) deposition of a thin film on a heated substrate remote from the plasma glow. The chamber designs provide:

(i) a fused silica tube in which process gases can be inductively rf plasma excited; (ii) one or more gas dispersal rings by which the remaining process gases can be introduced into the reaction chamber; (iii) a heated substrate for film deposition that is outside the plasma glow region. Backstreaming of gases, introduced through the dispersal rings, into the plasma region is minimized by the high flow velocity of the gases travelling through the rf excitation tube (43) and the small diffusion length for molecular migration established by the relatively high operating pressure (43).

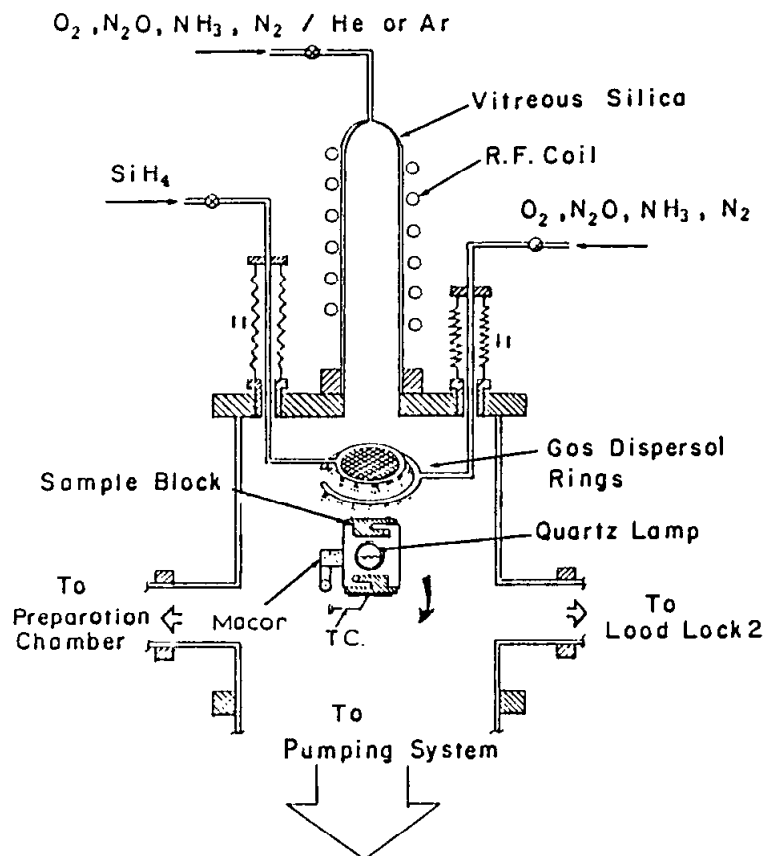


**Figure 1:** Deposition chamber for Remote PECVD with two downstream gas dispersal rings (41).

## 16.4. CHEMICAL REACTION PATHWAYS IN THE REMOTE PECVD PROCESS

### 16.4.1 The Deposition Analysis System

Figure 2 is a schematic representation of a system that has been used to study deposition reaction pathways (43). This system contains the gas feed and processing features of the chamber shown in Fig. 1, plus two additional tools for monitoring the process reaction pathways, optical emission spectroscopy (OES) and mass spectrometry (MS). The system consists of the following: (a) a fused silica feed gas tube with provision for remote plasma excitation by an inductively coupled rf field; (b) two downstream gas dispersal rings to introduce additional process gases; (c) provision to perform optical studies (e.g., OES) in the plasma, or downstream regions; (d) provision to sample process and by-product gases at different positions in the chamber using MS; (e) a movable, heated

substrate for film deposition; and (f) a load lock substrate introduction chamber. In addition, studies have been performed in a mode where metallic screens with different bias potentials could be interposed in the gas stream in order to determine the extent to which ions and/or electrons play a role in particular deposition process reactions. Reaction pathways have been studied for the deposition of hydrogenated amorphous silicon, silicon dioxide and silicon nitride.

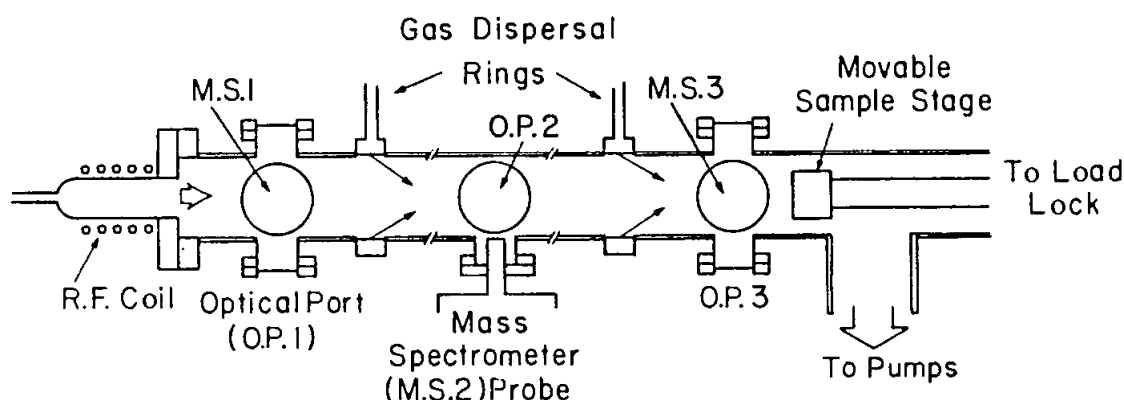
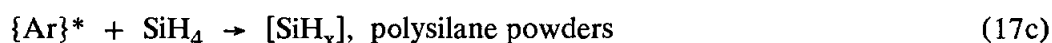


**Figure 2:** Schematic representation of the deposition/analysis system used to study reaction pathways in the Remote PECVD process (38,42,53).

#### 16.4.2 Deposition of Hydrogenated Amorphous Silicon

We have deposited a-Si:H films using two different excitation mechanisms (36-39); these are described by the reactions given below:



We have studied the He driven deposition more extensively because it generates a thin film of device grade a-Si:H with no other solid or powder reaction by-products (45). The Ar process generates polysilane powder via a homogeneous gas phase reaction in addition

to thin films of a-Si:H via a heterogeneous surface reaction similar to the one present in the He process (37-39). The studies of the He-driven process include (45): (a) OES studies of the spectral emission from He plasmas; (b) MS studies of the species extracted from the He plasmas; and (c) MS studies of silane under three different conditions: (i) when it is the only gas flowing; (ii) when it is mixed with neutral He; and (iii) when it is mixed with the species extracted from a He plasma. The results of these studies indicate the following (45): (a) OES identifies the formation of metastable He' species by rf plasma excitation; (b) MS and biased grid studies demonstrate that the primary species transported from the plasma are He<sup>+</sup> ions, He neutrals and electrons, and that the He<sup>+</sup> ions and electrons are the SiH<sub>4</sub> activators; (c) MS studies do not show either a fragmentation of silane or the creation of higher silane species, such as disilane, etc., by mixing the silane with either neutral He, or the species extracted from the He plasma. The conclusion drawn from these observations is that the precursor for film deposition of a-Si:H is an excited SiH<sub>4</sub> molecular species, and that this is produced by an interaction with electrons, and/or He<sup>+</sup> ions (30). Additional insight into this process is gained by studying the substrate temperature dependence of the deposition rate as shown in Fig. 3, and the substrate temperature dependence of the bonded hydrogen incorporation as shown in Fig. 4.

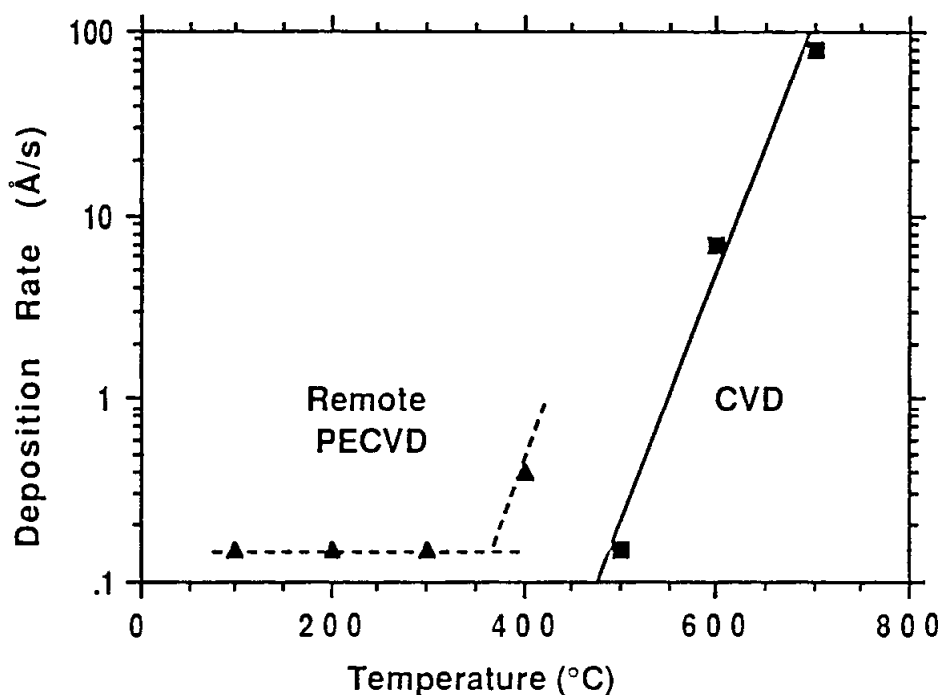


**Figure 3:** Deposition rate versus substrate temperature for: (a) deposition of a-Si:H alloys by Remote PECVD (3,49); and (b) silicon thin films by CVD (46,47).

Figure 3 shows the deposition rate for a-Si:H is independent of  $T_s$  for temperatures between about 100°C and 300°C, but that it rises significantly for  $T_s > 400^\circ\text{C}$ . We have made several observations: (a) the temperature dependence of the deposition rates for "homogeneous" chemical vapor deposition (HOMOCVD) (46,47) and for Remote PECVD (48) display similar behavior; (b) in addition to this similarity, the absolute values of the deposition rates are also about the same; and (c) for  $T_s > 350^\circ\text{C}$ , the Remote PECVD deposition rate increases with about the same activation energy as the

HOMOCVD and thermal CVD processes; however, the deposition rate for the Remote PECVD process is about two orders of magnitude greater than the thermal CVD rates (46-48) at a given temperature.

Figure 4 compares the total bonded hydrogen concentrations, associated with the spectral features characteristic of monohydride and polyhydride bonding environments; e.g.,  $\text{SiH}$ ,  $\text{SiH}_2$  and  $[\text{SiH}_2]_n$ , for films grown by Glow Discharge (GD) (3,49) and Remote PECVD (36). For  $T_s$  greater than about  $70^\circ\text{C}$ , the amount of incorporated hydrogen is always less in the Remote PECVD films. Studies of the distribution of the hydrogen between mono- and polyhydride bonding groups also indicate qualitative differences between the Remote PECVD films and the films grown by GD or HOMOCVD (3,37-39,46,47,50). The most notable difference is in the temperature at which polyhydride groups become the dominant bonding configurations. This occurs for  $T_s$  below about  $200^\circ\text{C}$  in the GD and CVD films (3,46,47,50), whereas in the Remote PECVD films, monohydride bonding dominates for temperatures down to about  $50 - 100^\circ\text{C}$  (36-39).

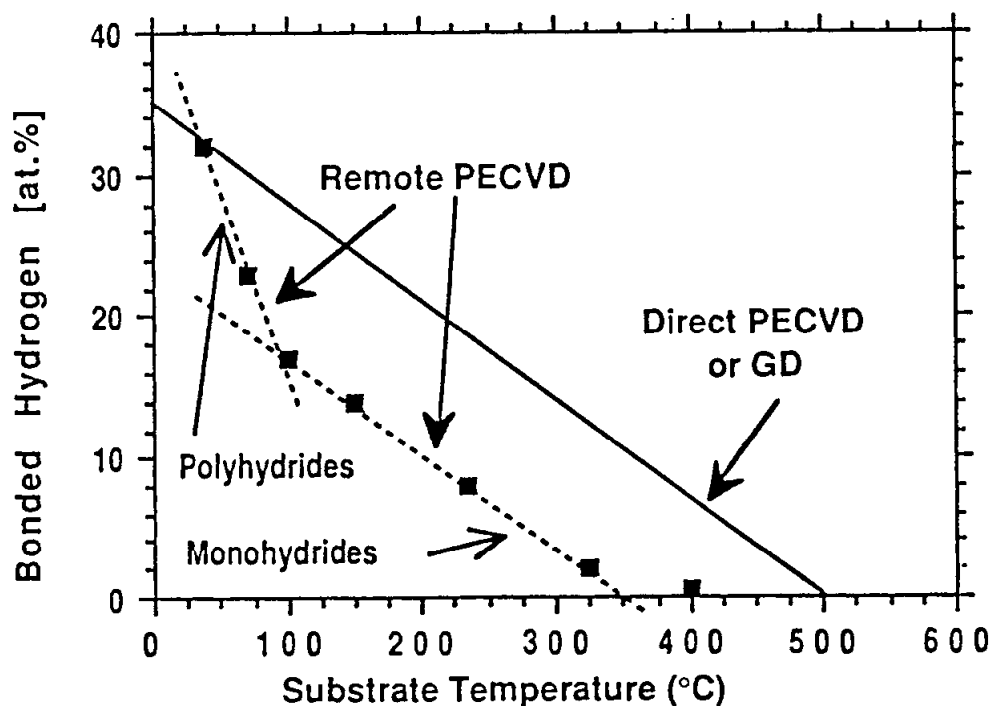


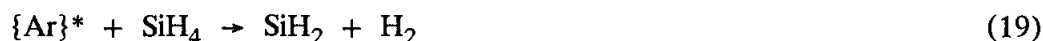
**Figure 4:** Bonded hydrogen incorporation in Remote PECVD and GD a-Si:H alloys as a function of substrate temperature (3,46,47,49).

The conclusion that is drawn from the comparisons displayed in Figs. 3 and 4 is that in the Remote PECVD process, the precursor species for film growth is different than in HOMOCVD, ordinary thermal CVD and GD with silane. It has been established that the silane molecule undergoes fragmentation into radicals, molecular fragments, ions, etc., in the CVD, HOMOCVD and GD processes (3,46,47,49), whereas in Remote PECVD, there is no evidence from MS for silane fragmentation (45). We believe that the active precursor species for film deposition in Remote PECVD is an excited molecule,  $\text{SiH}_4^*$

(45). This is also supported by the very large cross section reported for excitation of  $\text{SiH}_4$  by low energy electrons ( $E < 15\text{eV}$ ) (30).

In addition, it has been shown that the incorporation of hydrogen in a-Si:H deposited by GD (49) and reactive magnetron sputtering (51) derives from a surface that is saturated with hydrogen where the amount of hydrogen retained in the film is determined by substrate temperature (3,51). The comparisons in Fig. 4 lead to the conclusion that the starting point for film growth in Remote PECVD is different from the GD process, specifically, below  $350^\circ\text{C}$  the surface is not saturated with hydrogen, but has a smaller hydrogen coverage determined by the exothermic CVD reaction of the excited silane molecules at the growth surface.

The situation is qualitatively different when species extracted from an argon plasma are used. In this instance, it has been reported that in addition to thin film formation with similar bonded hydrogen incorporation, there is also a homogeneous gas phase reaction that produces polysilane powders of the general composition  $\text{SiH}_x$ , with  $x < 2$  (36-39). The formation of the solid films of a-Si:H is accomplished via a deposition reaction pathway similar to the remote He excitation pathway described above, but the concurrent powder formation implies a parallel reaction pathway in which there is also gas phase dissociation of the silane, presumably by  $\text{Ar}^+$  ions. The reactions for the powder formation process are given by a sequence of attachment reactions of the general form (52):



The differences between the He and Ar processes then derive from differences in cross sections for the fragmentation process that generates the polymerization initiator,  $\text{SiH}_2$ .

### 16.4.3 Deposition of Silicon Based Dielectrics

**16.4.3.1 Silicon Dioxide ( $\text{SiO}_2$ ):** It has been reported that the deposition rate for  $\text{SiO}_2$  does not correlate with the plasma generation of atomic oxygen or molecular oxygen ions,  $\text{O}_2^+$ , and that the most probable active oxygen species is then a molecular metastable,  $\text{O}_2'$  (53). It has also been established that atomic oxygen metastables,  $\text{O}'$ , are not generated in rf plasmas (54), so that even though these species are known to be long lived, they are not generated in sufficient number to be important in the deposition of  $\text{SiO}_2$  by Remote PECVD. The assumption that  $\text{O}_2'$  metastables are the active species is consistent with earlier experimental observations in Ref. 12. Combining the use of MS and OES, the following reaction pathway has been found (53):



It is also reported that departures from oxide stoichiometry, as Si-Si and Si-H bonds, are correlated with high He dilution ratios, He/ $\text{O}_2$  of about 100 or greater (42,53). At these high dilutions, OES indicates that He metastable production in the plasma phase has increased significantly and dominates the plasma glow. Under these conditions,  $\text{He}^+$  ions

and energetic electrons generated via Penning ionization can excite the silane and open up an additional parallel reaction pathway for an amorphous silicon alloy constituent. The composition of the resulting film will be determined by the relative reaction rates for the two processes; deposition of  $\text{SiO}_2$  which requires both  $\text{SiH}_4^*$  and  $\text{O}_2'$  and deposition of a-Si:H that simply requires  $\text{SiH}_4^*$ . This explanation is suggested by the data in Fig. 5, where the deposition rate for  $\text{SiO}_2$  is displayed as a function of the He dilution of the  $\text{O}_2$  source gas.

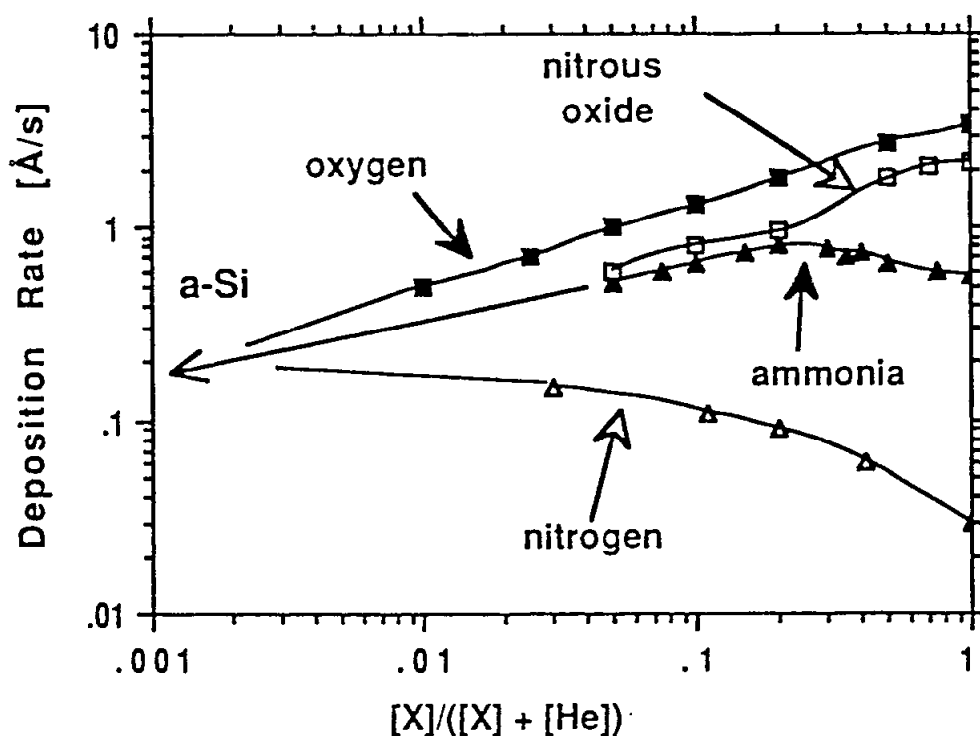


**Figure 5:** Deposition rate versus gas dilution for silicon oxide films grown from  $\text{O}_2$  and  $\text{N}_2\text{O}$  (33,42,55) source gases, and for silicon nitride films grown from  $\text{NH}_3$  and  $\text{N}_2$  source gases (31,57). The source gases in each case are labelled **X** on the figure.

It has also been shown that an important source of OH contamination in oxide films derives from the purity of the oxygen feed gas [the likely contaminants are  $\text{H}_2\text{O}$  and  $\text{CH}_4$ ] (42). This has been established by comparing the OH and OD infrared absorption bands in  $\text{SiO}_2$ :(OH) films grown from  $\text{SiH}_4$  and  $\text{SiD}_4$  process gases. In addition, SiOD groups are also found in the films grown from the  $\text{SiD}_4$  process gas, indicating that OD groups are also generated in the heterogeneous reaction between the  $\text{SiD}_4$  and the  $\text{O}_2$ . The generation of OH groups by the intrinsic mechanism appears to be correlated with the deposition rate, the higher the deposition rate the greater the SiOH incorporation. The incorporation of OH groups has been minimized by using: (a) down stream excitation of the oxygen as opposed to plasma excitation of oxygen along with the He (53); and (b)  $\text{N}_2\text{O}$  gas, rather than  $\text{O}_2$ , as the source of the oxygen atoms (55). There are also reported studies of the reaction pathways in the completely downstream excitation process in which active species extracted from a He plasma are mixed with both the reactant gases,  $\text{SiH}_4$  and  $\text{O}_2$ , or  $\text{SiH}_4$  and  $\text{N}_2\text{O}$  (55). The reaction pathways in these



processes appear to be essentially the same as in the processes discussed above, i.e., they involve a surface reaction between excited  $\text{SiH}_4$  molecules and  $\text{O}_2'$  metastables.

#### 16.4.3.2 Silicon Nitride: $\text{Si}_3\text{N}_4$

**(a) The Ammonia Process:** Studies of the reaction pathways using the  $\text{NH}_3$  reactions as described by Eqns. (8 and 14), have indicated the following (56): (i) for pure  $\text{NH}_3$  plasmas, the films contain Si-NH bonds, and the OES studies indicate NH and H species in the plasma; (ii) for intermediate and high dilutions of  $\text{NH}_3$  with He, to about 95% He, the films contain decreasing amounts of Si-NH, and the OES studies show the same NH and H species; (iii) for still higher dilutions >95 % He, stoichiometric nitride films can be grown. This corresponds to a narrow window, wherein the OES indicates significant decreases in NH emission, the presence of increasing N emission, and strong He emission. Finally, (iv) at the highest He dilutions >98 % He, He emission dominates and the films display significant departures from stoichiometry, containing both Si-Si and SiH bonding configurations. These observations establish that: (a) plasma generated NH species are the precursors for Si-NH bonds in the deposited films; (b) plasma generated N species are the precursors for "Si-N-Si" bonding arrangements; and (c), paralleling the reactions pathways for a-Si:H, silicon suboxides with SiH bonds,  $\text{He}'$  metastables are the precursors for departures from nitride stoichiometry and SiH incorporation in the resulting subnitrides.

Additional support for this model of two parallel deposition pathways, one for SiN or SiNH groups and a second for Si-Si and SiH groups, is derived from comparisons between films grown from  $\text{NH}_3$  /He and  $\text{NH}_3$ /Ar mixtures (31,57). In both instances the deposition rate drops with increasing dilution. For the films grown from  $\text{NH}_3$ /Ar mixtures, the decrease in deposition rate is also correlated with the occurrence of SiH bonding in the deposited thin films. The limiting deposition rates for  $T_s = 250^\circ\text{C}$  are only a small range from about  $0.56 \text{ \AA/s}$  for the deposition of silicon diimide films using pure  $\text{NH}_3$ , with a saturation of SiNH bonding groups,  $\text{Si}(\text{NH})_2$ , to about  $0.81 \text{ \AA/s}$  for mixed nitride/diimide alloys deposited with  $\text{NH}_3$  fractions of about 0.20, and finally to about  $0.5 \text{ \AA/s}$  for nitrides films with small amounts of bonded hydrogen (less than 5 at.%) and deposited with  $\text{NH}_3$  fractions of about 0.05. There is a qualitatively different result for the deposition rate versus dilution for films grown from  $\text{N}_2$ /He gas mixtures; this is discussed below.

**(b) The Nitrogen Process:** The deposition rate for films grown from  $\text{N}_2$ /He gas mixtures for  $T_s = 400^\circ\text{C}$  increases with He dilution (31,57). This again is a manifestation of two different reaction pathways. In this instance the deposition rate for the silicon nitride material is smaller than the deposition rate for hydrogenated amorphous silicon material. As the He dilution increases, the deposition rate monotonically increases from about  $0.02 \text{ \AA/s}$  at the nitride end point to about  $0.25 \text{ \AA/s}$  at the a-Si:H end point. If the film deposition depended solely on the presence of activated nitrogen species, we would expect the deposition rate to fall to zero as the source gas is depleted of  $\text{N}_2$ . Because this behavior is not observed, it shows that there is a smooth transition between the nitride deposition channel, which depends on the presence of nitrogen, and the a-Si:H deposition channel, which, as discussed above, is heralded by the presence of strong He emission lines. This explanation is supported by Infrared (IR) and Auger electron Spectrometry (AES) measurements which indicate the incorporation of both Si-Si and SiH bonds dilution levels greater than about 0.1. Films of silicon nitride have also been deposited with downstream injection of nitrogen; in this case the formation of stoichiometric nitrides required very

high  $N_2$  flow rates that correspond to N/Si ratios in the gas phase of greater than 100 (57).

**16.4.3.3 Silicon Oxynitrides**  $[(SiO_2)_x(Si_3N_4)_{1-x}]$ . The deposition rate for the silicon oxynitride films grown from  $O_2/NH_3/He$  gas mixtures also reflects a two channel mechanism in the deposition process (32). This is based on the absence of a linear correlation between the relative oxide and nitride bonding groups, and the fraction of  $O_2$  or  $NH_3$  in the feed gas mixture (32). The deposition rate for the "oxide-bonding" component is higher than that of the "nitride-bonding" component, and as a result of this the cross over point between oxide and nitride rich alloys occurs when the relative oxygen concentration in the feed gas is about 10% of its maximum value rather than 50% as would occur for equal deposition rates. We have just developed a second process for silicon oxide deposition based on  $N_2O$  as a reactant gas (55). This process is characterized by lower deposition rates than the  $O_2$  process, and therefore offers the potential of being combined with  $NH_3$  in a way in which the relative concentrations of oxygen and nitrogen in the deposited oxynitride films are closer to the relative concentrations of the respective oxygen and nitrogen containing feed gases.

## 16.5 SELECTED BULK PROPERTIES OF DEPOSITED THIN FILMS

We will present a short discussion of selected bulk properties of the a-Si:H and the silicon based dielectrics. Details are found in the references cited above. For a-Si:H, the studies have included chemical, optical and electronic properties (36-39), whereas for the silicon dielectrics the major emphasis has been on properties that yield information relative to the chemical bonding and composition (31,32,42).

### 16.5.1 Hydrogenated Amorphous Silicon

The primary tool for determining the chemical bonding in the films has been IR spectroscopy. Once a calibration scheme has been established (3), this turns out to be the most convenient way to determine the bonded hydrogen concentrations. The results of our IR studies are included in Refs. 36-39. There are two important observations relative to the differences between bonded hydrogen incorporation in a-Si:H alloys grown by Remote PECVD and Direct PECVD (or GD): (a) the amount of bonded hydrogen is lower in the Remote PECVD a-Si:H alloys by about a factor of at least two over the transition temperature range between 100°C and 400°C ; and (b) the way the bonded hydrogen is incorporated in the structure in the Remote PECVD films is very different. For example, for the temperature range between 100°C and 325°C , the dominant hydrogen bonding group in the Remote PECVD films is the monohydride (SiH) group, whereas in the Direct PECVD (or GD) films, polyhydride bonding groups such as  $SiH_2$  and  $[SiH_2]_n$  dominate for deposition temperatures less than about 200°C (3,36-39,50).

There have been other studies of electronic, optical and photoelectronic properties (36-39). The main differences between the Remote PECVD and GD materials are in the electronic properties of films deposited below about 200°C , and in excess of 300°C. The electronic properties of the GD films degrade significantly for  $T_s$  below 200°C (3), and in addition these low  $T_s$  films cannot be doped, whereas the Remote PECVD films show only very small degradations in electronic properties and doping efficiencies at  $T_s$  as low as 100°C to 125°C (30-32). These differences are correlated with the differences in bonded hydrogen incorporation as mentioned above, and are consistent with other

studies which have attributed defect generation to changes in the film morphology due to polyhydride incorporation (3). In a complementary way the GD films grown with  $T_s$  between about 300°C and 400°C display much better electrical properties than a-Si:H grown by Remote PECVD for the same  $T_s$  range.

### 16.5.2 Silicon Dielectrics

The silicon dielectric thin films have been studied for the most part by techniques which elucidate various aspects of the chemical bonding: (a) by IR absorption to detect the presence of bonding groups containing hydrogen, i.e., SiH, SiOH and SiNH, and to detect departures from oxide stoichiometry; (b) by ellipsometry to measure the index and to estimate density; and (c) by Auger Electron Spectroscopy and X-ray Photoelectron Spectroscopy (AES and XPS, respectively) to determine stoichiometry, and in the case of the oxynitride alloys to determine the oxygen to nitrogen atom ratio. The details of these measurements and the results are included in Refs. 31, 32 and 42. In summary, the major advantages of the Remote PECVD process over the Direct PECVD of dielectrics identified in these studies are: (i) increased control of bonded hydrogen incorporation and stoichiometry by processing variables including relative dilution of gas mixtures and  $T_s$ ; and (ii) the resulting ability to produce hydrogen free (defined by the limit of IR detection of about 0.5 to 1.0 at.%) dielectric films at substrate temperatures in the range of 100°C to 550°C. In addition there have been interesting and informative comparisons made between the properties of SiO<sub>2</sub> films deposited by Remote PECVD, and grown via high temperature thermal oxidation of silicon (700 – 1150°C); the results of these comparisons indicate that the local atomic structure and its relationship to the film density are different in the thermal and Remote PECVD oxides, but that these differences do not reflect on the electrical behavior of the films. Details of these comparisons are in Ref. 56 and 57.

## 16.6 REMOTE PECVD DIELECTRIC FILMS IN DEVICE STRUCTURES

### 16.6.1 Silicon Dielectrics in MOS Capacitors and FETs

There have been only a limited number of studies in which Remote PECVD dielectrics have been used in device structures. The two most notable examples are the use of a tri-layer oxide/nitride/oxide dielectric that was used for gate electrodes for a field effect transistor device based on (In,Ga)As (26). Three layers were used in the following way: (a) the oxide layers formed a barrier to prevent electron injection into the nitride layer; and (b) the nitride layer acted as a diffusion barrier to any transport of positive ions through the structure. Devices formed in this way displayed a transconductance of about 75 mS/mm, and showed less than a 5% drift during 24 hours stress bias testing.

In addition, there have been several studies using SiO<sub>2</sub> and silicon oxynitride layers in MOS and MIS capacitor studies (2,59). For structures using Remote PECVD oxide layers deposited for  $T_s$  between 250°C and 400°C onto crystalline silicon substrates, the following results were obtained: (a) breakdown fields were in excess of about 8x10<sup>6</sup> V/cm; (b) densities of interfacial traps were generally less than 5x10<sup>10</sup>cm<sup>-2</sup>eV<sup>-1</sup>, with some devices displaying levels less than 10<sup>10</sup>cm<sup>-2</sup>eV<sup>-1</sup> (59). Using silicon oxynitrides, in place of the oxides has the effect of reducing the break-down field by about 25% to about 6x10<sup>6</sup> V/cm. The achievement of the low interfacial trapping state densities depends critically on the processing of the silicon surface; details are discussed in Ref. 59.

### 16.6.2 Amorphous Silicon Devices

The electronic and optical properties of Remote PECVD intrinsic and n-doped a-Si:H alloys deposited at temperatures between about 125°C and 275°C are similar to the properties of the so-called device or PV (photovoltaic) grade GD material (3,36-39). However, these films have not been used in device structures, e.g., p-i-n solar cells or TFT's.

## 16.7 RECENT DEVELOPMENTS IN REMOTE PECVD

### 16.7.1 Integrated Processing with in situ Process Diagnostics and in-situ Surface Analysis

*In-situ* analysis and *in-situ* diagnostics have been on going themes of the research activities at both North Carolina State University (NCSU) (41,44) and at the Research Triangle Institute (RTI) (59). The rationale behind the use of *in-situ* techniques is fairly straightforward. In some instances there are narrow windows in processing variables whereby some type of spectroscopic feedback can be used to maintain film composition and purity. One example is the use of OES to monitor the emission spectrum from He/NH<sub>3</sub> discharges to define the regime wherein atomic N spectral features are present, and thereby indicate that hydrogen free films with nitride stoichiometry can be deposited. With regard to *in-situ* surface analysis, this has been used in two ways: (a) to determine the character of silicon surfaces prior to dielectric film deposition for MOS structures (41,59); and (b) to determine oxide and nitride stoichiometry in deposited dielectrics (41).

The research performed at NCSU has used multi-chamber systems with in situ diagnostics and/or analysis (34), while the RTI approach has been with both in situ and free standing analysis, and with UHV transfer accessibility to the free standing instrumentation.

### 16.7.2 Other Material Systems

In addition to the materials described above, the Remote PECVD process has been used to deposit Group IV crystalline semiconducting films. This was done primarily at the RTI. Materials so far deposited include Si, Ge and Diamond (27,41). Preliminary studies indicate that films of compound semiconductors, e.g., GaN and BN (60) can also be grown by this approach.

There are also plans to extend the approach to other deposition chemistries employing different types of feed gases, e.g., halogenated silanes, SiH<sub>2</sub>Cl<sub>2</sub>, and organometallics, Si(CH<sub>3</sub>)<sub>4</sub> as sources of silicon atoms, and thereby extending the technique to additional materials such as multicomponent or mixed oxides, and metals and metal alloys.

### 16.7.3 Subcutaneous Oxidation Processes During Remote PECVD

We have recently discovered that there can be oxidation reactions occurring at a semiconductor substrate during the Remote PECVD process, particularly during the

deposition of  $\text{SiO}_2$  thin films (61). We have found evidence for this process occurring for both Si and GaAs substrates. In the case of deposition of silicon oxides and oxynitrides on to silicon, the oxide that forms on the silicon substrate is self-limiting and grows to a thickness between 25 and 30 Å. We have not as yet determined the thickness or composition of the native oxide formed on GaAs, although preliminary studies of the oxide character by AES indicate it has more  $\text{Ga}_2\text{O}_3$  character than arsenic oxide character. These subcutaneous oxidation processes have important implications for the fabrication of device structures. In the case of Si/silicon oxide or oxynitride interfaces, the subcutaneous oxide does not prevent the formation of electronic grade device structures with low densities of interface traps, high breakdown fields, etc.. In fact, the subcutaneous oxide could possibly be the factor that promotes the excellent interfacial properties. In contrast, the subcutaneous oxidation of GaAs clearly degrades MOS/MIS device characteristics. We cannot form good GaAs MOS/MIS structures unless there is a 20-50 Å pseudomorphic silicon layer grown on the GaAs substrate prior to oxide deposition. This silicon layer must be thick enough so that it is not fully consumed in a subcutaneous oxidation process during the deposition. Similar considerations apply to the formation of germanium MOS/MIS structures. On the other hand, we have observed that oxide films could be directly deposited on (In,Ga)As substrates, with the resulting semiconductor/dielectric interface displaying excellent device characteristics (26). This means that subcutaneous oxidation of the (In,Ga)As is qualitatively different from the subcutaneous oxidation of GaAs.

The subcutaneous process proceeds in much the same way as a thermal oxidation or anodization process, i.e., active oxygen species (presumed to be atomic) are transported through the depositing oxide layer to the semiconductor surface and promote the oxidation process reactions at that surface. This means that the boundary between the semiconductor and the dielectric material is not the starting semiconductor surface, but rather is buried beneath that surface. This phenomenon clearly needs additional study, since it is one of the important considerations for device fabrication.

## 16.8 SUMMARY

We have described the important differences between conventional or Direct PECVD and rf-excited Remote PECVD for the deposition of a-Si:H alloys and for silicon dielectrics. We have shown that the two PECVD processes are fundamentally different with regard to the multiplicity of deposition pathways, which in turn has a significant effect on the ability to use process variables to control film composition and purity. In the direct process the simultaneous plasma excitation of all reactant gases and diluents opens many possible reaction pathways and thereby makes it virtually impossible to restrict deposition reactions to those which promote only the desired thin film bonding chemistry. There is one counter-example of a direct process for  $\text{SiO}_2$  deposition where very high levels of silane dilution (up to 104:1 of He:silane) suppress plasma excitation of the silane gas and thereby restrict deposition pathways according (20).

## ACKNOWLEDGEMENTS

The authors acknowledge support for their contributions to this research from The Office of Naval Research, The National Science Foundation, The Semiconductor Research Corporation, and The Solar Energy Research Institute. In addition one of us

(DVT) acknowledges additional support from The Standard Oil Company of OHIO (now British Petroleum/North America) and the Microelectronics Center of North Carolina.

## 16.9 REFERENCES

1. A.C. Adams, Plasma deposition of inorganic films. Solid State Technology 26: 135 (1983).
2. G. Lucovsky and D.V. Tsu, Plasma enhanced chemical vapor deposition: Differences between direct and remote plasma excitation. J. Vac. Sci. Technol. A5: 2231 (1987).
3. J.C. Knights and G. Lucovsky, Hydrogen in amorphous semiconductors. in CRC Critical Reviews in Solid State and Materials Sciences 9: 211 (1980).
4. D.E. Carlson, Solar energy conversion. in The Physics of Hydrogenated Amorphous Silicon I, ed. by J.D. Joannopolous and G. Lucovsky (Spring-Verlag, Berlin, 1984), p. 203.
5. W.E. Spear and P.G. LeComber, Fundamental and applied work on glow discharge material. in The Physics of Hydrogenated Amorphous Silicon I ed. by J.D. Joannopolous and G. Lucovsky (Spring-Verlag, Berlin, 1984), p. 63.
6. L.L. Alt, S.W. Ing and K.W. Laendle, J. Electrochem. Soc. 110: 465 (1963).
7. S.W. Ing and W. Davern, J. Electrochem. Soc. 112: 285 (1965).
8. D.R. Secrist and J.D. MacKenzie Ceram. Bull. 45: 784 (1966).
9. M. Shiloh, B. Gayer and F.E. Brinchman, J. Electrochem. Soc. 124: 295 (1977).
10. I. Kato, S. Wakana, S. Hara and H. Kezuka, Jpn. J. Appl. Phys. 21: L470 (1982).
11. M.D. Clark and C.L. Anderson, J. Vac. Sci. Technol. 21: 453 (1982).
12. L.G. Meiners, Indirect plasma deposition of silicon dioxide. J. Vac. Sci. Technol. 21: 655 (1982).
13. L. Bardos, J. Musil and P. Taras, J. Phys. D: Appl. Phys. 15: L79 (1982).
14. W. Kern and V.S. Ban, Chemical vapor deposition of inorganic thin films. in Thin Film Processes, ed. by J.L. Vossen and W. Kern (Academic Press, New York, 1978), p. 258.
15. R.J. Buss, Pauline Ho, W.G. Breiland and M.E. Coltrin, Reactive sticking coefficients for silane and disilane on polycrystalline silicon. J. Appl. Phys. 63: 2808 (1988).
16. S.G. Brass and Gert Ehrlich, Activation Chemisorption: Internal degrees of freedom and measured activation energies. Phys. Rev. Lett. 57: 2532 (1986).
17. R. Rosenberg, Materials and processing science: Limits for microelectronics. AIP Conference Proc. 167: AVS Series, ed. by G.W. Rubloff (in Press).
18. J.F. Gibbons S. Reynolds, C. Gronet, D. Vook, C. King and W. Opyd, Limited reaction processing: Flexible thermal budgeting. AIP Conference Proc. 167: AVS Series, ed. by G.W. Rubloff (in Press).
19. M.R. Wertheimer and M. Moisan, Comparison of microwave and lower frequency plasmas for thin film deposition and etching. J. Vac. Sci. Technol. A3: 2643 (1983).

20. J. Batey and E. Tierney, Low-temperature deposition of high quality silicon dioxide by plasma enhanced chemical vapor deposition. J. Appl. Phys. 60: 3136 (1986).
21. A. Matsuda and K. Tanaka, Investigation of the growth kinetics of glow-discharge hydrogenated amorphous silicon using a radial separation technique. J. Appl. Phys. 60: 2351 (1986)
22. S.R. Mcjia, R.D. McLeod, W. Pries, P. Shuffelebotham, D.J. Thomas, J. White, J. Shellenberg, K.C. Kao and H.C. Card, Fabrication of a-Si:H films by microwave plasmas under electron cyclotron resonance conditions. J. Non-Cryst. Solids 77&78: 765 (1985)
23. J. Asmussen, Chapter 11, this volume.
24. M.J. Helix, K.V. Vaidyanathan, B.G. Streetman, H.B. Dietrich and P.K. Chatterjee, RF plasma deposition of silicon nitride layers. Thin Solid Films 55: 143 (1978).
25. R.P.H. Chang, S. Darack, E. Lane, C.C. Chang, D. Allara and E. Ong, Plasma enhanced beam deposition of thin films at low temperatures. J. Vac. Sci. Technol. B1: 935 (1983).
26. P.D. Richard, R.J. Markunas, G. Lucovsky, G.G. Fountain, A.N. Mansour and D.V. Tsu, Remote plasma enhanced CVD deposition of silicon nitride and oxide for gate insulators in (In,Ga)As FET devices. J. Vac. Sci. Technol. A3: 867 (1985).
27. R.A. Rudder, G.G. Fountain and R.J. Markunas, Remote plasma- enhanced chemical-vapor deposition of epitaxial Ge films. J. Appl. Phys. 60: 3519 (1986).
28. G. Lucovsky and D.V. Tsu, Deposition of silicon based dielectrics by remote plasma enhanced chemical vapor deposition. J. Cryst. Growth 86: 804 (1988).
29. R. Deloche, P. Monchicourt, M. Eheret and F. Lambert, High-pressure helium afterglow at room temperature. Phys. Rev. A13: 1140 (1976)
30. A. Garscadden, G.L. Duke and W.F. Bailey, Electron kinetics of silane discharges, Appl. Phys. Lett. 43: 1012 (1983)
31. D.V. Tsu and G. Lucovsky, Silicon nitride and silicon diimide grown by remote plasma enhanced chemical vapor deposition. J. Vac. Sci. Technol. A4: 480 (1986).
32. D.V. Tsu, G. Lucovsky, M. Mantini and S.S. Chao, Deposition of silicon oxynitride thin films by remote plasma enhanced chemical vapor deposition. J. Vac. Sci. Technol. A5: 1998 (1987).
33. S.S. Kim, D.V. Tsu, G.N. Parsons, and G. Lucovsky, unpublished data.
34. S.V. Hattangady, G.G. Fountain, R.A. Rudder and R.J. Markunas, High density, low hydrogen content silicon nitride deposited at low temperature by novel remote plasma technique. J. Vac. Sci. Tech. A7: (1989), in press.
35. S.S. Kim, G.N. Parsons, D.V. Tsu and G. Lucovsky, Deposition of silicon oxide and nitride thin films by remote plasma enhanced chemical vapor deposition. IEEE Trans. Electron Devices (1989) in press.
36. D.V. Tsu and G. Lucovsky, Properties of the Si-H bond-stretching absorption band in a-Si:H grown by remote plasma enhanced CVD (RPECVD). J. Non-Cryst. Solids 97&98: 839 (1987).
37. G.N. Parsons, D.V. Tsu and G. Lucovsky, Optical and electrical properties of a-Si:H films grown by remote plasma enhanced chemical vapor deposition (RPECVD). J. Non-Cryst. Solids 97&98: 1375 (1987).

38. G. Lucovsky and D.V. Tsu, Differences between direct and remote plasma enhanced CVD. J. Non-Cryst. Solids 97&98: 265 (1987).
39. G.N. Parsons, D.V. Tsu and G. Lucovsky, Properties of intrinsic and doped a-Si:H deposited by remote plasma enhanced chemical vapor deposition. J. Vac. Sci. Technol. A6: 1912 (1988).
40. D.J. Vitkavage, R.A. Rudder, G.G. Fountain and R.J. Markunas, Plasma enhanced chemical vapor deposition of polycrystalline diamond and diamondlike films. J. Vac. Sci. Technol. A6: 1812 (1988).
41. S.S. Kim, D.V. Tsu and G. Lucovsky, Deposition of device quality silicon dioxide thin films by remote plasma enhanced chemical vapor deposition. J. Vac. Sci. Technol. A6: 1740 (1988).
42. D.V. Tsu and G. Lucovsky, The growth of silicon oxide thin films by remote plasma enhanced CVD. Mat. Res. Soc. Symp. 77: 595 (1987)
43. B. Chapman, Glow Discharge Processes (John Wiley and Sons, New York, 1980)
44. D.V. Tsu, G.N. Parsons and G. Lucovsky, Spectroscopic emission studies of O<sub>2</sub>/He and N<sub>2</sub>/He plasmas in remote plasma enhanced chemical vapor deposition. J. Vac. Sci. Technol. A6: 1849 (1988).
45. G.N. Parsons, D.V. Tsu and G. Lucovsky, Deposition mechanisms for remote plasma enhanced deposition (RPECVD) of amorphous silicon hydrogen alloys. J. Vac. Sci. Technol. A7: (1989) in press.
46. B.A. Scott, R.M. Plecenik and E.E. Simonyi, Kinetics and mechanism of amorphous hydrogenated silicon growth by homogeneous chemical vapor deposition. Appl. Phys. Lett. 39: 73 (1981).
47. B.A. Scott, J.A. Reimer, R.M. Plecenik, E.E. Simonyi and W.Reuter, Low defect density amorphous hydrogenated silicon prepared by homogeneous chemical vapor deposition. Appl. Phys. Lett. 40: 973 (1982).
48. G.N. Parsons, D.V. Tsu and G. Lucovsky, Chemical reaction pathways in the formation of amorphous silicon thin films by remote plasma enhanced chemical vapor deposition (RPECVD). Presented at MRS Conf, Boston (1988).
49. K. Tanaka and A. Matsuda, Glow-discharge amorphous silicon: Growth process and structure. Mat. Sci. Reports 2: 139 (1987).
50. G. Lucovsky, R.J. Nemanich and J.C. Knights, Structural interpretation of the vibrational spectra of a-Si:H alloys. Phys. Rev. B19: 2064 (1979).
51. R.A. Rudder, J.W. Cook, Jr., J.F. Schetzina and G. Lucovsky, Planar magnetron sputtering of a-Si:H and a-Ge:H thin films. J. Vac. Sci. Technol. A2: 326 (1984).
52. P.A. Longeway, R.D. Estes and H.A. Weakliem, Decomposition kinetics of a static direct current silane glow discharge. J. Phys. Chem. 88: 73 (1984).
53. D.V. Tsu, G.N. Parsons and G. Lucovsky, Studies of the reaction process in the remote plasma enhanced CVD of SiO<sub>2</sub>. J. Vac. Sci. Technol. A7: (1989) in press.
54. J.H. Kolts and D.W. Setser, Electronically excited long-lived states of atomic and diatomic molecules in flow systems. in Reactive Intermediates in the Gas Phase, ed. by D.W. Setser (Academic Press, New York, 1979), p.195.
55. S.S. Kim, D.V. Tsu and G. Lucovsky, unpublished.



56. D.V. Tsu, S.S. Kim and G. Lucovsky, Deposition of SiO<sub>2</sub> thin films by remote plasma enhanced chemical vapor deposition (Remote RECVD). Proceedings of Electrochemical Society Meeting, Spring 1988, Atlanta, GA (in press).
57. D.V. Tsu, G. Lucovsky and M. Mantini, "Local atomic structure in thin films of silicon nitride and silicon diimide produced by remote plasma enhanced chemical vapor deposition", *Phys. Rev. B* 33, 7069 (1986).
58. G. Lucovsky, J.T. Fitch, E. Kobdea and E.A. Irene, Local atomic structure of thermally grown SiO<sub>2</sub> films. Proceedings of Electrochemical Society Meeting, Spring 1988, Atlanta, GA (in press).
59. G.G. Fountain, R.A. Rudder, S.V. Hattangady, R.J. Markunas and P.S. Lindorme, Low interface state density SiO<sub>2</sub> deposited at 300°C by remote plasma-enhanced chemical-vapor deposition on reconstructed Si surfaces. J. Appl. Phys. 63: 4744 (1988).
60. R.A. Rudder, unpublished.
61. G.G. Fountain, S.V. Hattangady, R.A. Rudder, R.J. Markunas, S.S. Kim, D.V. Tsu and G. Lucovsky. Evidence for the occurrence of subcutaneous oxidation during low temperature remote plasma enhanced deposition of silicon dioxide films. J. Vac. Sci. Technol. A7: (1989) in press.

---

## Selective Bias Sputter Deposition

---

**Soren Berg and Claes Nender**

### 17.1 INTRODUCTION

It is quite common, during sputter deposition, to introduce some bias to the substrate. This normally improves the quality of the deposited film, due partly to a low energy ion bombardment of the growing film that may preferentially remove loosely bonded atoms or molecules from the surface. The energy released by low energy ions to the surface may also increase the surface mobility of the incoming atoms. Thus more of these atoms will find stable sites before nucleation. The normal energy of the substrate bombarding ions in bias sputtering is in the range of 50-150 eV. In this energy interval the sputtering yield values for most materials are very low. However, the situation may drastically change if the bias is increased to a somewhat higher level. In this case a competition will take place between deposition of material from the target to the substrate and sputter removal of this material from the substrate by the high energy ions. In Fig.1 a schematic drawing of a typical bias sputtering system is shown. In this system the substrates are resting on the substrate table. The target and the substrate table may be excited individually. In such a system the sputtering of material from the target may be kept almost constant by keeping the target voltage fixed at a certain value,  $V_T$ . The voltage applied to the substrate table,  $V_S$ , may then be varied independently. By increasing the substrate bias  $V_S$  and keeping  $V_T$  constant one can expect the net deposition rate to decrease. This is due to an increasing fraction of the deposited material that will be removed by physical sputtering. At a certain bias value,  $V_S$ , one will find that the sputter removal rate equals the material deposition rate. The net deposition rate at the substrate will then be zero. If the substrate bias is further increased a net substrate etching will occur. The above described effect has been observed and is well known since the time of the introduction of the bias sputtering technique.

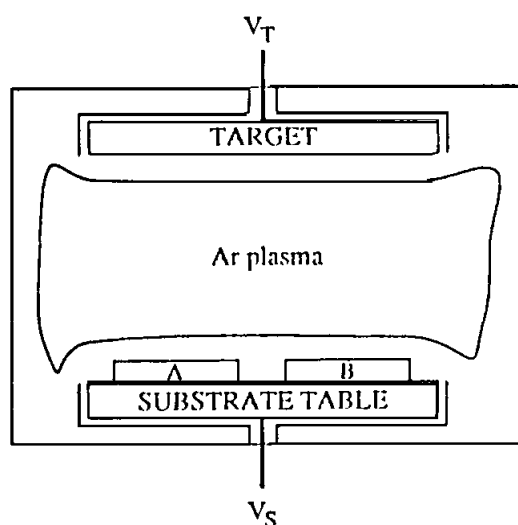


**Figure 1:** Schematic drawing of a bias sputtering system used for selective bias sputter deposition.  $V_T$  and  $V_S$  represent the voltages exciting the target and the substrate respectively.

## 17.2 SUBSTRATE DEPENDENT BIAS SPUTTER DEPOSITION

The region, close to zero net deposition rate in bias sputtering, has not been studied earlier in any greater detail. It has recently been observed that this processing region exhibits substrate dependent properties (1-4). It is thus possible to obtain different effects on different substrate materials during identical processing conditions. Fig. 2 illustrates schematically what can be observed during bias sputter deposition of target material onto two different substrates during identical processing. The result is usually that the bias values for zero net deposition rates  $V_{SA}$  and  $V_{SB}$ , as described in the figure, are not identical for different substrate materials. In the substrate bias region, where  $V_{SA} < V_S < V_{SB}$ , a net target film deposition will occur on substrate material B while no material will be deposited onto substrate material A. In fact the substrate surface of material A will be slightly sputter etched (negative "deposition" rate). In the processing region  $V_{SA} < V_S < V_{SB}$  a selective bias sputter deposition region is found. A patterned substrate wafer may thus be selectively coated with one of the materials in this processing region. A schematic drawing of such a substrate structure before and after selective bias sputter deposition is shown in Fig 3. As indicated in this figure, it is possible to fill a hole selectively on a patterned substrate structure without using any masking technique.

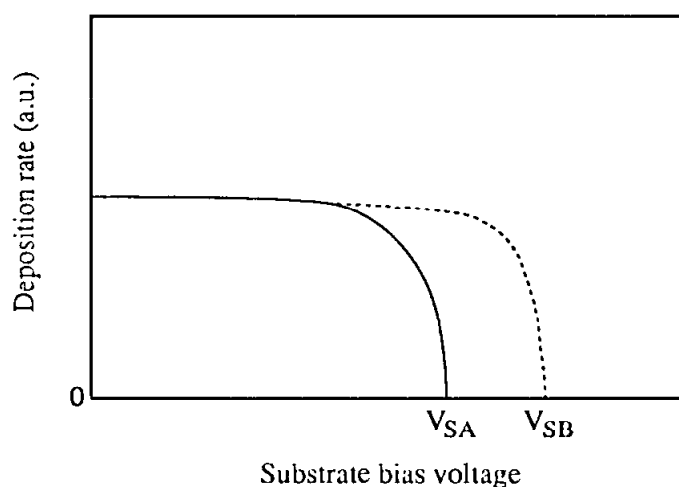


**Figure 2:** Schematic drawing of the deposition rate as a function of bias voltage  $V_S$  for the system shown in Fig. 1.  $V_T$  is assumed to be kept constant. The two curves represent deposition on two different substrates (A and B).

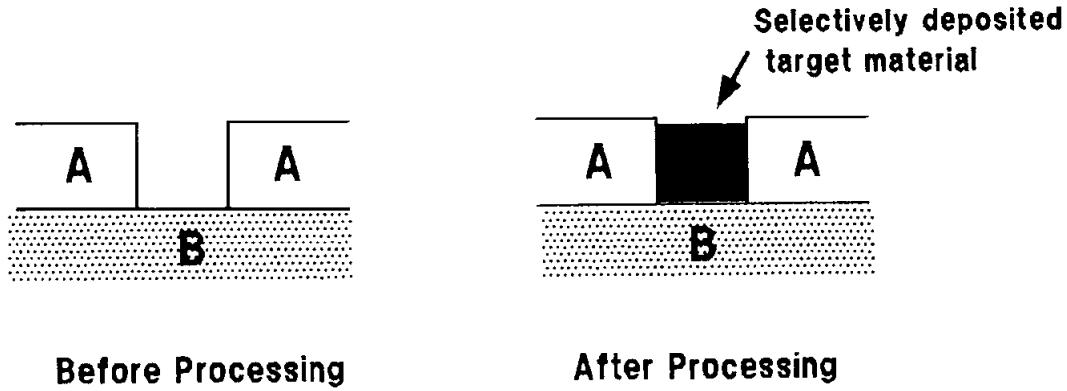


**Figure 3:** Schematic drawing of a patterned substrate consisting of the two materials A and B exposed to the bias sputtering process operating in the region  $V_{SA} < V_S < V_{SB}$  as defined in Fig. 2.

### 17.3 DEPOSITION-ETCHING BALANCE IN BIAS SPUTTERING

The fact that the deposited target material is more easily removed from substrate A than from substrate B in Fig.2 is due to differences in the surface phenomena at the interface between the substrate and the ion-assisted growing film. This interface formation may at a first approximation be described as a balance between deposition of target material and sputter removal of this material from the substrate surface. The situation, at the substrate surface, is shown in Fig. 4. The substrate surface is, at a certain time  $t$ , partially covered by the deposited target material. The fraction of the surface covered by a film is denoted  $\Theta$ . The arrow  $F_T$  represents the flux of sputtered target atoms arriving at the substrate. Those atoms that arrive at the fraction  $(1 - \Theta)$  of the substrate will have a certain sticking probability  $\alpha_S$  to the original substrate material. Atoms from the target arriving at the  $\Theta$  fraction of the substrate surface will face a film consisting of target material. The sticking probability for atoms arriving on this area may be different from others and will be denoted  $\alpha_T$ . The number  $N_r$  of sputter deposited target atoms on the substrate will be

$$N_r = F_T[(1 - \Theta)\alpha_S + \Theta\alpha_T] \quad (1)$$

Due to the biasing conditions, the substrate is bombarded by an argon ion flux  $J$  that causes sputter removal of some of the deposited film. The sputtering yield of the deposited film is denoted  $S$ . The bias sputtering will erode some of this deposited material. The number  $N_s$  of target atoms sputtered away from the deposited substrate surface will be

$$N_s = J \Theta S \quad (2)$$

By definition there is no film of target material on the  $(1 - \Theta)$  fraction of the substrate surface. When  $\Theta$  approaches 1, the original substrate is completely covered by a film of the target material. Therefore the conditions during further deposition will not depend on the original substrate material. To understand the selective deposition shown in Fig. 2, we have to investigate in some detail the deposition/etching balance on the surface in the region  $0 < \Theta < 1$ . This can easily be done by plotting the  $N_r$  and  $N_s$  from Eqs. (1) and (2) in the nomogram, shown in Fig. 5. The two solid lines represent the deposition fluxes onto two different substrate materials, Eqs. (1). The two dotted lines represent two different sputter removal fluxes from these substrates due to the bias applied to the substrate table, Eqs. (2).

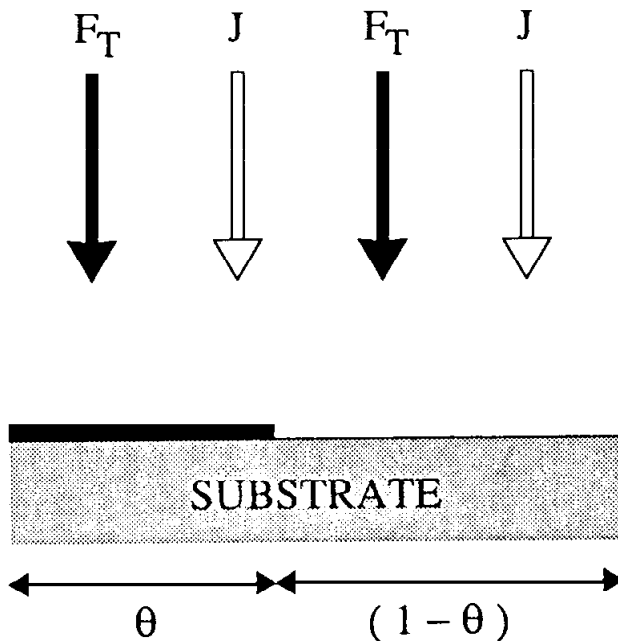


**Figure 4:** Schematic of particle fluxes on a substrate surface during the bias sputter deposition process.  $\Theta$  represents the fraction of the substrate surface covered by target atoms.  $F_T$  represents the incoming flux of sputtered target atoms and  $J$  is the Ar ion flux that causes sputter erosion from the substrate surface.

When the surface is completely covered by a thin film of the target material ( $\Theta = 1$ ), the sticking coefficient is  $\alpha_T$  in both cases. That is why the two solid lines coincide at this point for  $\Theta = 1$ . However, at the initial stage of the deposition process ( $\Theta = 0$ ), the incoming flux of sputtered target atoms will face an uncoated original substrate surface. The two substrate surfaces may differ in the sticking probabilities  $\alpha_A$  and  $\alpha_B$  to the incoming flux of sputtered target atoms. This is the reason why the deposition fluxes start at different values at  $\Theta = 0$ . Two levels of sputter erosion,  $J_1$  and  $J_2$ , are shown in the nomogram.  $J_1$  is selected so that  $J_1 S > F_T \alpha_T$ . The dotted line that represents this sputter erosion level in Fig. 5 crosses both solid lines. Before these crosspoints the deposition rate is larger than the sputter removal rate and a net deposition of target material occurs at the substrate surface. However, at the crosspoints the net deposition will be zero. At these points the deposition saturates and no further net deposition will take place. The substrates will thus only partly become covered by the target material. This fractional coverage  $\Theta$  will be slightly different for the two substrates.  $J_2$  may be selected in a way so that  $J_2 S < F_T \alpha_T$ . In this case the deposition rate always exceeded the sputter erosion rate. A net deposition will therefore, in this case, always occur onto both substrates. The net deposition rate will be different for the two substrate materials as long as  $\Theta < 1$ . However, as  $\Theta > 1$  the deposition rates will be equal and constant onto both substrates. The flux  $N_a$  of deposited atoms will simply be

$$N_a = F_T \alpha_T - J_2 S \quad (3)$$

This simple description indicates that the deposition conditions depend on the original substrate before the substrate is completely covered by target material during bias sputtering. However, it did not enable us to explain the possibility of depositing a thick film on one substrate while obtaining an almost uncovered surface on the other substrate surface.

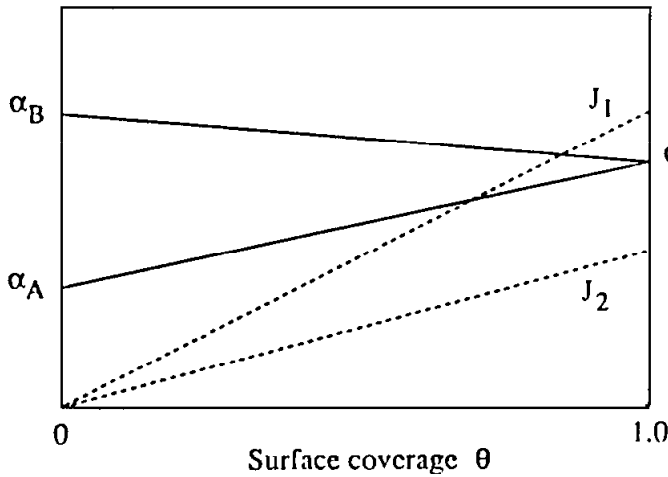


**Figure 5:** Nomogram representing, in the region  $0 < \theta < 1$ , the rate of deposition on to two different substrates, A and B (solid lines). The etching of the deposited material is represented by the dashed lines. Two different etching intensities  $J_1$  and  $J_2$  are shown. The sputtering yield value was assumed to be constant during processing according to expression (2) in the text.

#### 17.4 SPUTTERING YIELD VALUES AT THE FILM-SUBSTRATE INTERFACE

Expression (2) above neglects that the deposited atoms that arrive from the target to the substrate surface, at the initial stage, will bind to the partly covered substrate surface with a binding energy that depends on the composition of this surface. According to the sputtering theory (5) the sputtering yield value  $S$  is determined by

$$S = \frac{3\sigma M_{Ar} M_T E}{4\pi^2 (M_{Ar} + M_T)^2 E_{Bi}} \quad (4)$$

where  $E$  is the energy of the incoming argon ion,  $M_{Ar}$  is the mass of the argon ion,  $M_T$  is the mass of the target (film) atom,  $E_{Bi}$  is the binding energy of the atom to be sputter removed and  $\sigma$  is a constant. At the initial stage of deposition ( $\theta = 0$ ), the incoming target atoms will stick to a surface purely consisting of original substrate atoms. The binding energy of a target atom on this surface may be denoted  $E_{TS}$ . When this atom is removed by sputtering it will have a sputtering yield value  $S(E_{TS})$  given by Eq.(4) using  $E_{Bi} = E_{TS}$ . When the substrate is completely covered by a film of target material ( $\theta > 1$ ) further incoming target atoms will bind to the deposited film with a binding energy

$E_{TT}$ . The corresponding sputtering yield value will be  $S(E_{TT})$  where  $E_{Bi} = E_{TT}$  in Eq.(4). The binding energy  $E_{Bi}$  will gradually change from  $E_{TS}$  to  $E_{TT}$  as  $\Theta$  increases from 0 to 1. One may therefore conclude from Eq.(4) that the sputtering yield of the deposited target material gradually changes from  $S_{TS}$  to  $S_{TT}$  in the fractional surface coverage interval  $0 < \Theta < 1$ . To describe the bias sputter deposition process more correctly the sputtering yield value in Eq. (2) has to be replaced by a yield value that depends on the surface fractional coverage  $\Theta$ . At a first approximation the sputtering yield may be written as a linear function

$$S(\Theta) = S_{TT}[1 - \mu(1 - \Theta)] \quad (5)$$

where  $\mu$  is a constant that may be positive or negative depending on which of  $S_{TT}$  or  $S_{TS}$  has the largest value. Inserting Eq.(5) into the Eq. (2) will give a new expression for the flux  $N_s$  of material sputtered away from the surface

$$N_s = J \Theta S_{TT}[1 - \mu(1 - \Theta)] \quad (6)$$

This expression is no longer linearly dependent on  $\Theta$ .

### 17.5 SELECTIVE BIAS SPUTTER DEPOSITION

Figure 5 may be replaced by a new nomogram using Eq. (6) as a measure of the sputter removal effect. This is shown in Fig. 6. In this figure the solid lines represent the deposition process identical to those in Fig. 5. The dotted curves represent the sputter removal effect according to Eq. (6). If  $J = J_1$  is made high the sputtering curve will cross the deposition lines for both substrate surfaces somewhere in the interval of  $0 < \Theta < 1$ .

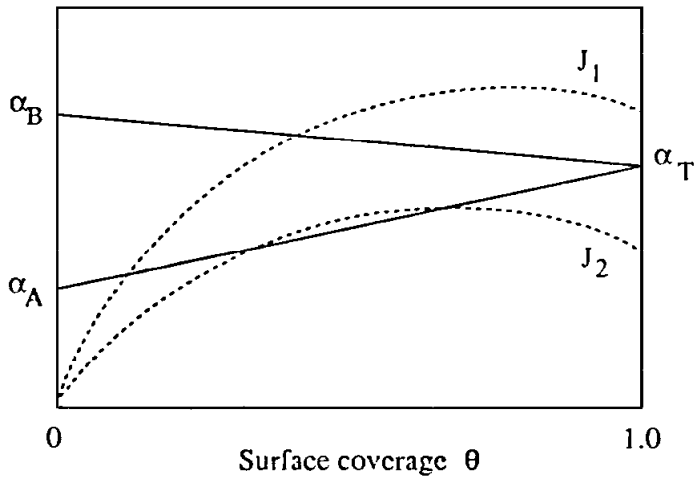


**Figure 6:** Nomogram identical to Fig. 5, but using a sputtering yield value that depends on the fractional coverage  $\Theta$  as in Eq. (6).

The net deposition rate at these points then will be zero and the surface coverage saturates at a value of  $\Theta < 1$ . This processing condition does not give rise to any selective

bias sputter deposition. However, if the sputter intensity is somewhat reduced to  $J = J_2$  a very interesting situation may occur. The sputtering curve will now cross only one of the substrate deposition lines. This indicates that we have a situation where we will obtain film deposition on the substrate surface B but not on substrate A. The film thickness on substrate material A will saturate at a fraction of a monolayer. The film thickness on substrate B may be grown to any desired thickness. A selective bias sputter deposition processing region may thus be theoretically predicted from this nomogram.

In Fig. 7 the general shapes of the time dependent growth in film thickness on the above described substrates are shown. At  $\Theta = 1$  the substrate is completely covered by a film of target material. The film thickness on substrate A will never reach this level. This substrate will thus never be completely covered by a film irrespective of the processing time. The deposition thickness on substrate B will exceed  $\Theta = 1$  and continue to grow as long as the process continues.

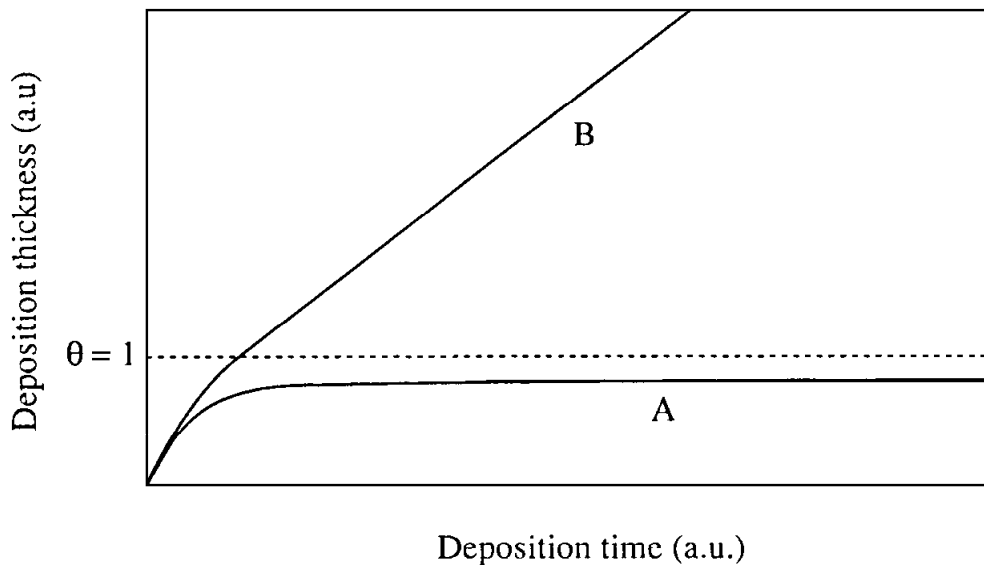


**Figure 7:** Time dependent growth in film thickness on the two substrates described in Fig. 6 for the conditions that  $J = J_2$ . On substrate B the deposition rate always exceeds the etching rate. Film growth will proceed during the whole processing time. On substrate A deposition rate will be identical to the etching rate at a certain value of  $\Theta$ ,  $0 < \Theta < 1$ . The film thickness will saturate at this coverage value.

Selective bias sputter deposition has been observed experimentally (2). In Fig. 8 the results from rf bias sputter deposition of Ti in argon onto substrates of Si, Au and Pt are shown. During this experiment the bias voltage  $V_S$  was kept constant. These results clearly demonstrate that selective bias sputter deposition can be obtained. At  $V_T = 1.75\text{kV}$ , Ti will be deposited onto Si and Au substrates but not on the Pt substrate (The substrates were made up by thin films of Si, Au and Pt deposited onto silicon wafers).



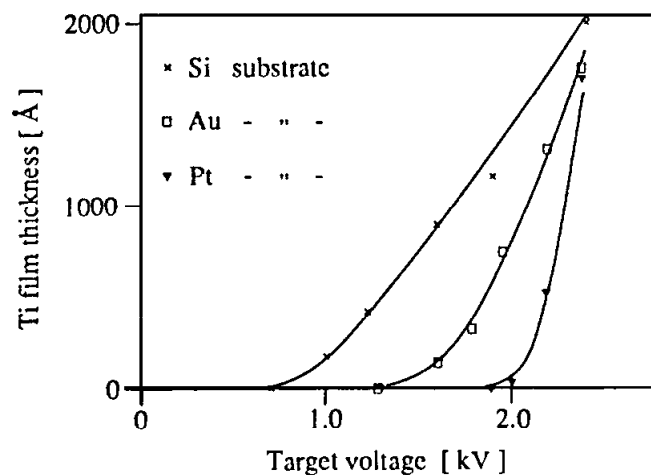


**Figure 8:** Experimentally observed Ti film thicknesses on three different substrates after selective bias sputter deposition in 15 minutes. The substrate bias was kept constant 0.8 kV. From ref. (2).

## 17.6 SELECTIVE BIAS SPUTTER ETCHING

A fundamental feature should be pointed out of the selective bias sputtering process. No substrate can be deposited on by this technique without undergoing a certain amount of sputter erosion of the original substrate surface (4). Before the surface is completely covered by a thin film ( $\Theta < 1$ ), the fraction  $(1 - \Theta)$  of the original substrate surface is exposed to argon sputter erosion. This sputter erosion will decrease as the value of  $\Theta$  increases. Finally, when  $\Theta$  approaches unity,  $(1 - \Theta) = 0$ , and further erosion is now prevented by the film that has been formed on top of the substrate surface. A schematic drawing of this substrate etching effect during bias sputtering is shown in Fig 9. In this figure the substrate is shown before and after bias sputter deposition of a thin film. It is important to realize that some part of the upper layers of the original substrate has been etched away during the period when  $\Theta < 1$ . Therefore the value of the film thickness  $d_0$  is different from the value of the step height  $d$ .

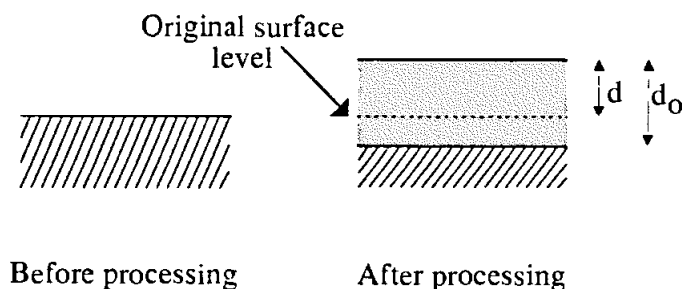


**Figure 9:** Schematic of unavoidable substrate etching during high bias sputter deposition. The original substrate is etched ( $d_0 - d$ ) before the substrate surface is completely covered by a film of target atoms.

In normal bias sputtering ( $V_s < 100\text{Volts}$ ) the difference ( $d_o - d$ ) is negligible. However, at high bias sputter deposition this difference may be as large as several thousand Ångströms. A mechanical stylus or multiple interference microscope thickness measurement will not produce a proper measurement under these biasing conditions. These techniques normally measure the stepheight  $d$  instead of the actual film thickness  $d_o$ .

The selective bias sputtering deposition technique may also be used as a mask-less selective etching process. In Fig. 2 it was pointed out that in the region  $V_{SA} < V_s < V_{SB}$  deposition took place onto substrate B while etching occurred at substrate A. Selective etching of material A takes place in this processing region. By using e.g. carbon as the target material, substrate areas of material B will be covered by a carbon film while substrate areas of material A will be etched to the desired depth. After processing, this carbon layer can easily be removed by stripping in an oxygen plasma. A simplified drawing of the three steps involved are shown in Fig. 10.

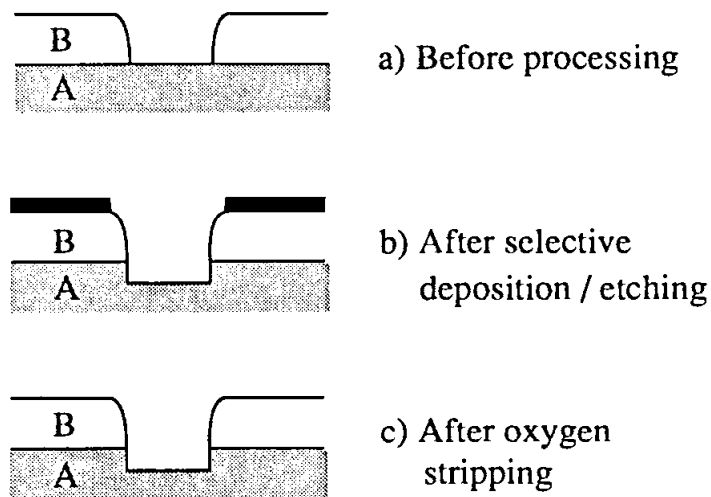


**Figure 10:** Principle of mask-less selective bias sputter etching. (a) Patterned structure before processing. (b) Target material (e.g. carbon) is selectively bias sputter deposited onto substrate areas of material B. Substrate areas of material A will be exposed to a net etching effect assuming that A and B behave like in Fig. 7. (c) The deposited carbon can easily be removed by conventional oxygen plasma stripping, leaving a selectively etched patterned substrate.

## 17.7 THE SELF LIMITING ETCH DEPTH TECHNIQUE

A further unique property of this bias sputter deposition process is that it enables etching to a predetermined depth without using the etching time as a parameter to determine the etch-depth. In Fig. 9 is shown that it is unavoidable to etch away some substrate material before the substrate is completely covered by a film of the target material. This etch depth is determined by the processing parameters and the properties of the substrate material. However, once the substrate has been covered by some monolayers of the target atoms no further etching of the original substrate surface will take place. This effect is called the Self Limiting Etch Depth effect (1). Without going into the mathematical details, Fig. 11 shows a schematic drawing of the etch-depth penetrations into two different substrates (called X & Y) as a function of bias sputter etching/deposition time. The processing conditions have been assumed to satisfy the requirements that the substrates

will be completely covered by a film of target atoms. From Fig. 11 it is seen that the etch depths saturate ( $d_X$  and  $d_Y$ ) after certain times ( $t_X$  and  $t_Y$ ). These length of times are the times needed to deposit some monolayers of film onto the substrate surface. This film will then prevent further etching of the underlying original substrate surface. If the processing continues further, the film deposition will continue also, but no more etching of the underlying substrate will be possible. Thus, as long as the processing time  $t_P$  is made long enough ( $t_P > t_X, t_Y$ ) the etch depth into the original substrate will depend only on the plasma/substrate conditions and not by the processing time. Neither conventional argon sputter etching, nor plasma etching have this property of etch depth saturation.

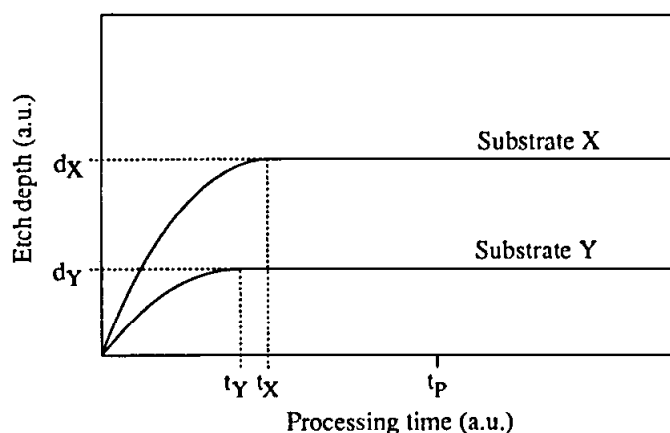


**Figure 11:** Principle of etch depth penetration into original substrate surface during selective bias sputter deposition onto two materials X and Y. The substrates are covered by a film of target atoms after the times  $t_X$  and  $t_Y$  respectively. Etch depths saturate at  $d_X$  and  $d_Y$  in the two substrates.

## 17.8 CONCLUSIONS

High bias sputter deposition may introduce substrate dependent film thickness formation. The reason for this effect is that sputter etching of the substrate takes place simultaneously with film deposition. This causes the substrate/film interface to be exposed to ion bombardment for a prolonged time. During this ion bombardment of the interface, the sputter erosion rate is substrate dependent. As soon as the interface is completely covered by the deposited film, the substrate dependence of the film growth-rate disappears. Utilizing this property of the plasma exposed interface, makes it possible to design bias sputter processing conditions that enables selective deposition or selective etching of patterned substrates. Thus it is possible to obtain maskless deposition or etching of patterned substrates with this technique.

## 17.9 REFERENCES

1. S.Berg, B.Gelin, M. Östling and S.M.Babulanam, *J. Vac. Sci. Technol.* A2(2): 470 (1984).
2. S.Berg, C. Nender, B. Gelin and M. Östling, *J. Vac. Sci. Technol.* A4: 448 (1986).
3. C.Nender, S.Berg, B.Gelin and B.Stridh, *J. Vac. Sci. Technol.* A5(4): 1703 (1987).
4. L.P.Andersson and S.Berg, *Vacuum*, 28: 449 (1978).
5. P. Sigmund, *Phys. Rev.* 184: 383 (1969).

---

## Vacuum Arc-Based Processing

---

**David Sanders**

### 18.1 INTRODUCTION

Vacuum arcs have been employed for current interruption in commercial power systems since the early 1960's. While they were first suggested as a source for making vacuum coatings by Wroe (1) in 1958 and Gilmour (2) in 1972, it was only with the appearance of American and Russian patents by Snaper (3-4) in 1971 and Sablev (5-6) in 1974, respectively, that the use of arcs for the production of coatings achieved any commercial significance, and then only in the USSR in the late 1970's. In the United States, vacuum arcs have been employed since the mid-1980's for the application of titanium nitride to prolong the lifetime of cutting tools used to machine metals. The technology involved has been based either on the Snaper patent coupled with more recent patents by Mularie (7-8) or on that originating with Sablev. The chief advantages touted in using arc technology for this application are its intrinsic high coating rate and the ability to produce adherent stoichiometric nitrides having relative insensitivity to nitrogen partial pressure.

In the last five years, there has been an increasing body of experimental (9-10) and theoretical (11-12) evidence that energetic physical vapor deposition techniques can enable the production of coatings having improved physical and chemical properties (e.g., improved density, enhanced adhesion, improved stoichiometry, and a more bulk-like index of refraction). Since the highly ionized coating atoms produced by arc technology can be used to supply such energy at exactly the location where it can do the most good, (i.e., the interface where the coating is being formed) it would seem beneficial to explore arc coating technology for additional application opportunities.

In Russian literature there are many examples where the high degree of ionization of arc-produced vapor makes it possible to achieve combinations of coating properties and structure with processing conditions which cannot be achieved using competitive techniques such as electron beam evaporation or magnetron sputtering. This is due to the opportunity to control the ionized coating atoms using the combination of magnetic and electric fields. One example of such a combination is the ability to produce dense coatings

at high rates and low substrate temperatures. Another is the possibility of achieving good adhesion with a wider variety of coating - substrate combinations. In addition, the ionized plasmas available from the cathodic arc show an enhanced reactivity during reactive coating. This leads to excellent composition control during the fabrication of compound coatings such as oxides and nitrides. Finally, the increased energy available makes possible unusual coating structures such as carbon coatings having hardnesses reported to exceed that of natural diamond.

The purpose of the present chapter is to review some of these opportunities as well as to identify deficiencies in current understanding in order to stimulate further investigation. To achieve this purpose, vacuum arc technology will be discussed in general terms to show how it is related to other vacuum processing, particularly with respect to the production of coatings. Emphasis will be devoted to source design considerations because, as will be stated, the design of suitable sources is a critical aspect in the further development of arc technology for exciting new applications. Representative examples of superior physical properties of coatings produced by vacuum arcs will be presented, followed by a description of some of the applications which could be addressed using those coatings. Finally, some of the areas requiring further investigation will be identified.

## 18.2 CATEGORIES OF VACUUM ARCS

Karl T. Compton of Princeton University defines an arc as "a discharge in a gas or vapor, that has a voltage drop at the cathode of the order of the minimum ionizing or minimum exciting potential of the gas or vapor". J.M. Lafferty adds that "the arc is a self-sustained discharge capable of supporting large currents by providing its own mechanism of electron emission from the negative electrode" (13). The "arcs" discussed in this chapter will be those which are sustained at least in part on the plasma produced by the erosion of one or both electrodes. These are the arcs which can provide high current densities ( $>10 \text{ As/cm}^2$ ) of metal plasma for subsequent vacuum processing.

Figure 1, based on Refs. 13 and 14, illustrates the relationship between the vacuum arcs and other discharges. At high voltages and low currents, one sees a "normal glow" discharge when there is an appropriate pressure of gas in the vacuum chamber to sustain it. In this region, increases in current do not increase voltage appreciably and there is insignificant erosion of the electrodes. As the current is increased further, the voltage also increases, indicating the transition into the "abnormal glow" region. It is in this regime where removal of material from the negatively charged electrode (cathode) occurs by sputtering (15). The behavior of the discharge within the abnormal glow region depends on the extent of electron emission of the cathode. With a cold cathode having a low value of electron emission, an abrupt change in the voltage/current behavior will sometimes occur where the voltage drops by more than an order of magnitude and then increases only slightly as the current is further increased. This occurs only in the discrete cathode spot case. With a sufficiently hot cathode yielding increased electron emission, there is a more gradual transition to a different arc mode where the current density of the electron emission site is many orders of magnitude lower than in the discrete spot case. This is the distributed discharge vacuum arc. With appropriate power supplies and electrode configurations it is possible to limit the current so that the arcing occurs at a higher voltage to produce still another type of vacuum arc, designated the "high voltage arc" in this chapter. Examples will be presented where each of these modes of arc behavior is employed.

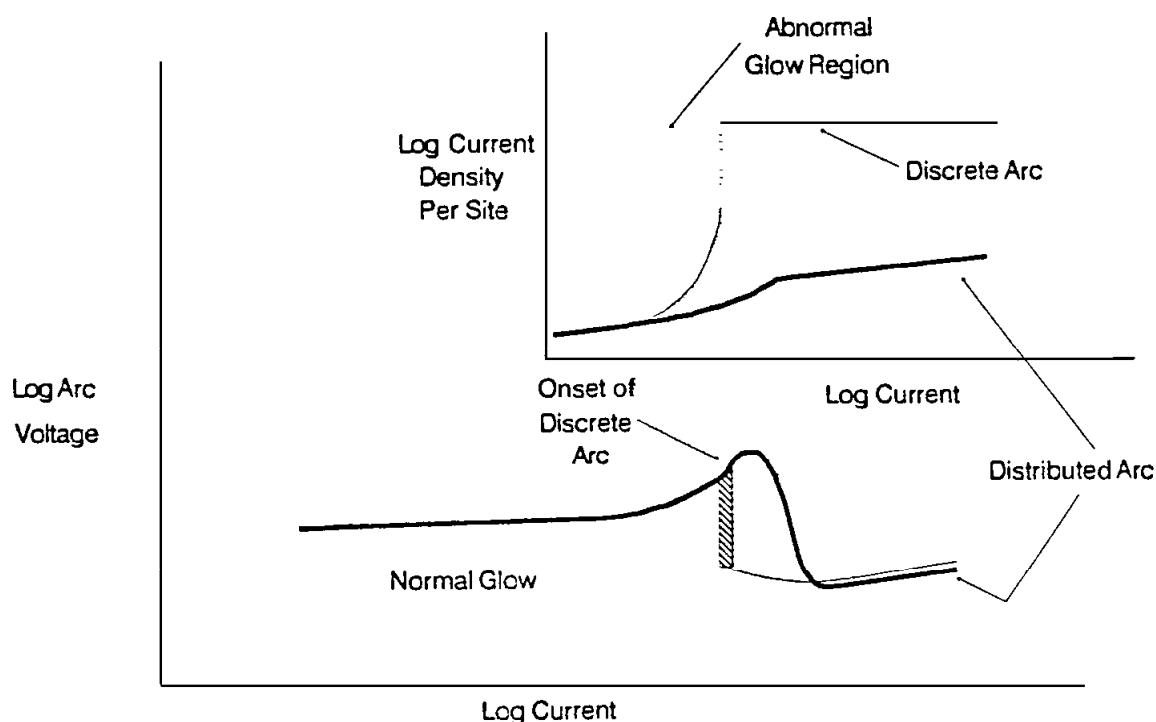


**Figure 1:** Voltage/current behavior of various types of vacuum discharges.

### 18.2.1 The Discrete Cathodic Arc

Figure 2 illustrates the emission site from a localized cathodic arc. This site or arc spot can sustain between 10 and 150 A depending on the cathode material. The uncertainty in the current density passing through these arc spots results from the uncertainty in the size of the spots themselves. This current density, as reported by various investigators, ranges widely from  $10^4$  to  $10^8 \text{ A/cm}^2$  (16-21). The arc spot is active for a short period of time, extinguishes and then re-forms in a new location adjacent to the previous arc crater. This gives rise to the appearance of motion of the arc. The apparent rate of motion is a function of the cathode material, the temperature, the magnetic fields, and the presence of gas molecules as will be discussed shortly.

As illustrated in Fig. 2, electrons, ions, macroparticles and neutral vapor species are emitted from the cathode spot. Electrons flow through the arc spot to surfaces in the chamber having a positive potential with respect to the cathode. For a wide variety of materials, the positive ion current is of the order of 10% of the arc current (22).

Table 1 gives the characteristics of ions emitted by the discrete cathode arc for a number of compositions. As can be seen, the energy of the ions exceeds the arc potential in all cases. This is thought to be due to positive space charge which is built up in front of the cathode caused by the plasma jet formed in front of the arc spot (17,20). The charge state of ions from the arc spot also varies according to composition (22). Metals that are more refractory tend to have a greater proportion of higher charge states.

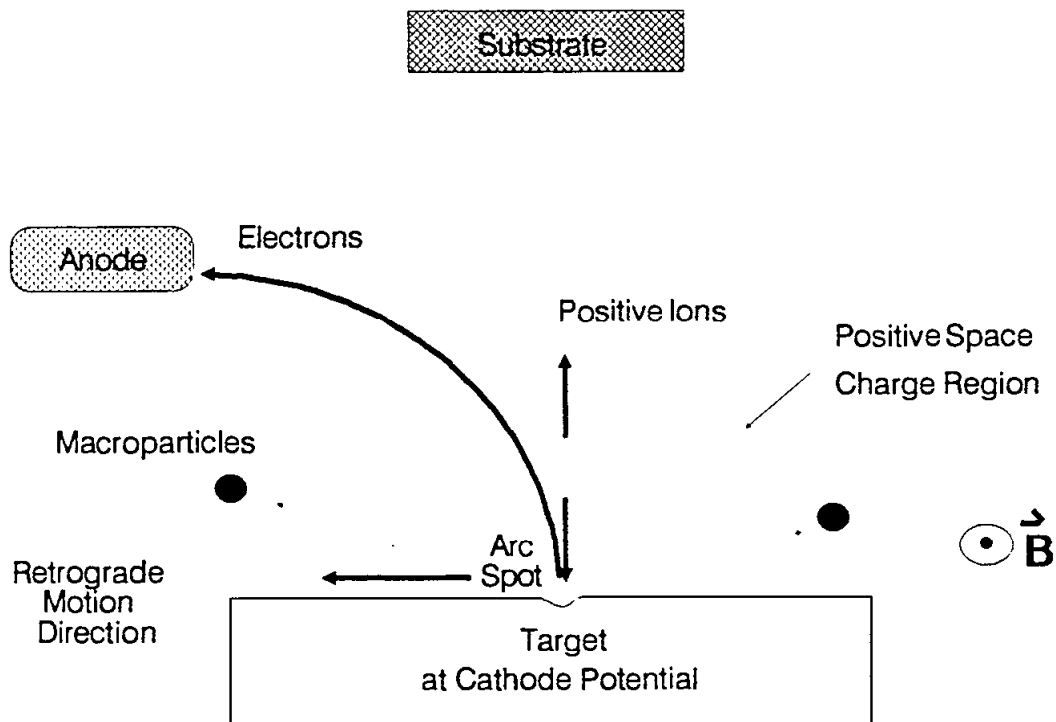


**Figure 2:** Schematic of the discrete cathodic arc spot. Note the retrograde direction defined by the magnetic field and the plasma flux.

The greatest drawback of the localized cathodic arc process involves the emission of macroparticles. These chunks of material vary in size depending on the cathode composition and temperature. They are thought to result from spattering of molten material from the edges of the arc crater. As illustrated in Fig. 2, the vast majority of these macroparticles is emitted at an angle of roughly 10-20 degrees from the cathode plane (23). The reduction of macroparticle formation and/or the subsequent filtering to remove macroparticles has been an active area of investigation since arcs were first considered for coating sources.

The neutral species emitted from the cathode arc spot are thought to be due the vaporization of small macroparticles by the interaction with the plasma (24). The fraction of ions to neutrals depends on the cathode material, this ratio being greatest for refractory metals such as molybdenum and tungsten.

As stated earlier, there are three major external influences on the cathode arc spot behavior. One is the presence of a magnetic field. Magnetic fields affect the arcing voltage as well as the rate and direction of motion of the arc spot (25-28). Fig. 2 illustrates the so-called retrograde motion which is observed as a result of magnetic fields which are parallel to the cathode surface. The retrograde velocity increases with magnetic field strength to a saturation point. The motion of the arc in an inhomogeneous magnetic field oriented at an angle with the cathode surface is described in the section on arc control using magnetic fields.

**Table 1:** Comparison of characteristics of some vacuum deposition processes.

Process	Macros?	Source of Discharge Material	Emission Type	Overall Source Temp.	Current Density A/Cm <sup>2</sup>	% Ionization of Vapor	Energy of Particles (ev)	Ref. #
Discrete Cathodic Arc	Yes	Cathode	Thermionic Field Emission	Low	$10^{-4} - 10^{-8}$	10 - 90	10 - 100	14
Distributed Discharge Cathodic	No	Cathode	Anomalous Emission	High	5 - 100	100	1 - 2	14
Anodic Arc	No	Anode	Anomalous Emission	High	1 - 10	5 - 100	0.1 - 1	14
High Voltage Arc	Possible	Both Electrodes	Thermionic Emission	High	5 - 100	?	?	39
Magnetron Sputtering	No	Process Gas	Ion Induced Secondary Emission	Generally Low	0.03 - 0.3	< 1%	~ 10	81
E-Beam Evaporation	No	n/a	Thermionic Emission	High	n/a	0.1 - 0.3	~ 1	81



Gas molecules also have an effect on arc behavior (29). There is a profound difference, for instance, between the arcing behavior of a pristine surface and one which has adsorbed gas molecules. Arcs occurring in the presence of reactive gas tend to move faster and produce smaller macroparticles which are fewer in number (30,31). At still higher pressures the discharge changes in character and the electrodes are no longer eroded by the arc (13).

The final influence on arc behavior is the cathode temperature. At low temperatures, the arc tends to move more rapidly, producing smaller macroparticles. At higher temperatures, the arc spots move in concert at slower rates (32-33). This change in behavior coincides with an increase in size and quantity of emitted macroparticles. As described earlier, at still higher temperatures the nature of the discharge changes completely so that the discharge no longer occurs through discrete arc spots, but rather is distributed over the cathode. More will be said about this shortly.

Table 2 shows the influence of cathode composition on current carried by an arc spot as well as the voltage required to sustain that arc spot. As the arcing current increases, the current passing through a particular spot is able to remain constant because the increased current is carried by the formation of additional spots which exist simultaneously on the cathode surface. This simultaneous existence of multiple cathode spots gives rise to one of the names assigned to this particular type of discharge, i.e., "the multiple cathodic arc".

The localized cathodic arc is characterized by high frequency fluctuations in both voltage and current. These variations are due to the extinguishing of old arc spots and the formation of new ones (33).

**Table 2:** Characteristics of the discrete cathodic arcs of some selected elements.

Element		Mo	Ta	Zr	Ti	Cu	Ni	Ag	Ref #
Arc Voltage		26.5	24.0	21.5		20.0	18.0	17.5	22
Ion K.E. (ev)		153	177	98		87.5	54	60	22
% in Charge State	1	3	13	14	65	38	48	16.5	80
	2	33	35	60	39	55	48	65	
	3	42	28	21	34	7	3	34	
	4	19	13	5		15		1	
	5	3	10						

### 18.2.2 The Diffuse Arcs:

At high temperatures where there is substantial electrode emission, so-called distributed or diffuse arcs are formed. These diffuse arcs have the potential for producing extremely high ion currents without the presence of macroparticles (14)(34). Anodic arcs are formed when the anode presented to the cathodic arc plasma is permitted to heat up and emit ions (35-37). Once erosion of the anode starts to occur, plasma from the anode forms the basis for the discharge and the erosion of the cathode stops. The distributed discharge cathodic arc is formed when the cathode is allowed to increase in temperature to the point where the cathode material has sufficient vapor pressure to lead to this type of arc. Little is understood concerning the exact nature of either of the diffuse discharge arcs, particularly with respect to the mechanisms of electron emission (37). Nevertheless, as is illustrated in the section on source design, both show promise as sources for new ion beams where the presence of macroparticles is of concern.

The least understood of the discharges, from a coating-source point of view, are the high voltage arcs described in Refs. 38-41. These arcs are apparently operated near the maximum in the voltage/current curve in Fig. 1. As one might expect, the current must be limited by some means to prevent the natural tendency of the system to go to higher currents and lower voltages characteristic of the arcs just discussed. The current limiting is accomplished with the power supply and/or by disruption of the discharge. The characterization of the plasmas produced by these discharges is not discussed in the references cited as these investigations were restricted to the analysis of the coatings produced. The encouraging results which were discussed suggest that measurements of the plasma characteristics are justified to fully make use of this type of arc for the production of coatings.

### 18.2.3 Summary of Arc Types

Table 1 summarizes the categories of arcs which have been described in this section emphasizing their characteristics for coating sources. Some other types of coating sources are also listed for comparison. The cathodic arc offers the highest energy vapors because it produces multi-charged ions with potentials which are greater than the arcing voltage. The cathode is cooled, making it possible to operate it in any orientation. The disadvantage of the cathodic arc is the production of macroparticles. While the negative effects of these macroparticles can be minimized or eliminated using concepts to be discussed shortly, such efforts complicate source design. The distributed discharge cathodic arc and the anodic arc both operate with hot eroding electrodes. They provide a means of producing ionized vapor without macroparticles. The energy of the ions is not as high as in the cathodic arc case and the ions are singly charged. Nevertheless, the fraction of vapor which is ionized can approach 100% and these ions can be accelerated using electric fields to achieve enhanced coating properties. The most poorly characterized plasmas are those from high voltage arcs. While interesting coating properties are reported (e.g., epitaxy at lower substrate temperatures), at this point the degree of ionization of the vapor flux is an unknown. Certainly, further investigation in this area will be required if high voltage arcs are to be exploited for making coatings.

## 18.3 SOURCE DESIGN CONSIDERATIONS

The purpose of this section is to provide a picture of the wide diversity that is possible in vacuum arc and coating technology. To accomplish this, the section will be divided into

two parts. One section will discuss general considerations related to vacuum arc source design, while the other will provide specific examples to illustrate the results of those considerations.

### **18.3.1 General Considerations**

In general, some means must be provided to initiate the arc. Once initiated, the arc must be controlled with respect to its position on the cathode surface. Then, to take advantage of the benefits provided by the high degree of ionization of the arc-produced vapor, the plasma must be controlled in some manner. Therefore, arc initiation, arc control, and plasma control comprise the three general considerations which need to be taken into account in designing cathodic arc coating sources.

#### **18.3.1.1 Arc Initiation**

There are at least four techniques successfully employed to initiate vacuum arcs. One of the simplest and earliest, depicted in Fig. 3, was the mechanical touching and removal of an electrode from the cathode, drawing an arc. This technique is still used in some commercial arc services for the production of titanium nitride coatings on cutting tools. Its main advantage is its simplicity. One disadvantage is the possibility of the electrode becoming welded to the cathode surface. This can be minimized by the insertion of a resistor between the electrode and the ground. The resistor limits the amount of current which can flow during the arc initiation process. A further drawback is the inability of this approach to achieve high repetition rates which are required for operation of arc sources in a pulsed mode.

An arc initiation technique which does allow for high repetition rates employs the sudden vaporization and subsequent ionization of a thin film metal coating connecting the cathode surface and an auxiliary electrode (42-43). This is accomplished through the discharge of a capacitor. The technique is simple and can be extremely reliable, if geometries are chosen correctly. Once started, the arc continually replenishes the thin film required for its next initiation. A means, however, must be provided for starting the arc for the first time with a fresh target.

The third method involves the discharge of a capacitor which has been charged to several thousand volts by passing an impulse of gas through a tube which is connected to that capacitor. The gas pulse is ionized to form a plasma which carries the current from the capacitor to the cathode until sufficient plasma density has been achieved to initiate the arc. While this is a reliable means for arc initiation without the necessity of touching the cathode, it does introduce a small amount of inert gas into the system and thus would not be appropriate for highly repetitive arc initiation requirements.

The final means of starting an arc involves the use of a laser pulse (44). Such a pulse produces a plasma on the cathode surface. The plasma serves to form the basis of the first cathode spot. If the laser pulse is directed at the cathode surface and local melting occurs, smoothing of the surface may inhibit further initiation. One way to overcome this is to start the arc on an auxiliary electrode made of a material such as carbon which remains unreflective. In using the laser technique, care must be taken to avoid coating the window through which the laser beam is introduced.

### 18.3.1.2 Arc Control

In order to be useful, the cathodic arc must be controlled. This is critical because the loss of such control can result in the rapid destruction of the arc coating equipment. Arc control can also serve to reduce the presence of macroparticles.

Both electrostatic and magnetic means have been employed to control the location of the cathodic arc. Electrostatic constraints make use of the requirement for the cathodic arc to have access to an anode to complete its electrical circuit. While this anode may be a discrete component in the vacuum chamber, it may also be a combination of components including the vacuum chamber walls. These concepts are illustrated in Fig. 3 where two forms of passive cathodic arc control are shown. On the left side, a screen is employed which is floating electrically and prevents electrons from flowing from the cathode to the chamber, which in this case is the anode (5). On the right hand side, ceramic material with low electron emissivity such as boron nitride is employed (7,8,45,46). In the case of the screen, the arc extinguishes when it reaches the edge of the water cooled target. If additional arcs simultaneously exist on the target surface, or if there is sufficient inductance in the circuit to provide the necessary restarting voltage, then the arc will reform and the process will continue. If not, the arc will remain extinguished and will need to be re-ignited. In the case of the boron nitride restraint, arcs reaching the target-restraint interface are thrown back onto the target, making re-ignition unnecessary.

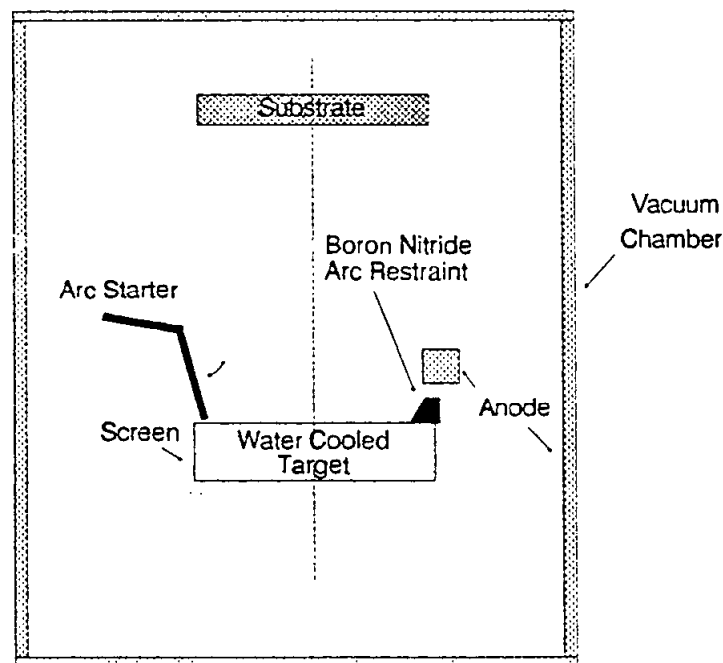


**Figure 3:** A typical passive cathodic arc configuration. (The shaded pattern codes are used consistently throughout the figures in this chapter for components having similar function).

The advantages of electrostatic arc confinement are its simplicity and good target utilization. One disadvantage, already cited, is the possibility of the arc remaining extinguished and requiring re-ignition. The second disadvantage, involving the boron nitride

approach, relates to a tendency for the arc to burn selectively at the insulator metal interface. If this process continues for any length of time, the insulator is destroyed and must be replaced.

The other approach for arc control involves the use of magnetic fields. As already discussed, the arc normally undergoes the so called retrograde motion occurring in response to the component of the magnetic field which is parallel to the cathode surface. The direction of this motion is shown in Fig. 2. The rate of retrograde motion increases with magnetic field (28). One might expect a reduction in macroparticle formation to accompany the more rapid arc motion. While such a reduction appears during reactive arcing of refractory metals (31), it was not observed in the case of titanium metal (10).

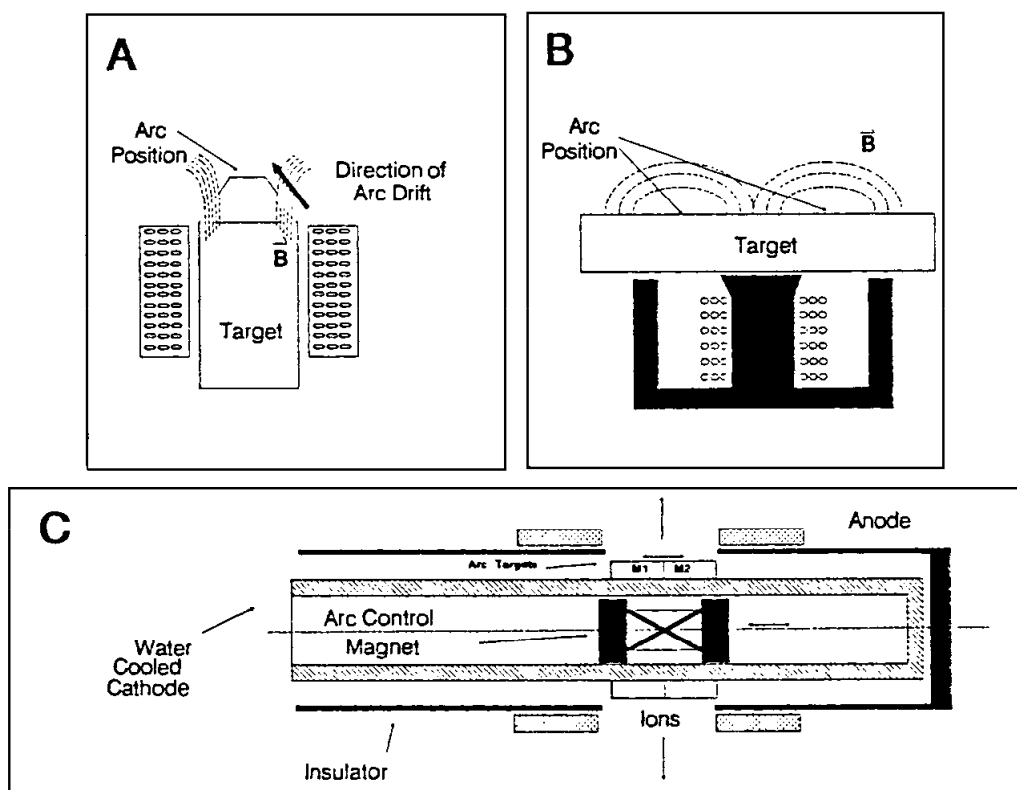
The effect of the perpendicular component of magnetic field and arc motion is illustrated in two cases of Fig. 4. In Fig. 4(a) the magnetic field produced by the solenoid is imposed such that the field lines intersect the target at an angle other than 90 degrees. Under these conditions the arc circulates around the perimeter of the cylindrical target, but drifts in the direction of the acute angle between the magnetic field and the target surface. This behavior was first observed by Wroe (1,48) in early work and utilized over the years by a number of investigators (18,27,42,49). Wroe worked with magnetic fields in excess of 500 gauss and provided an anode in close proximity to the cathode; the other investigators used smaller fields ( $\approx 40 - 50$  gauss) with remote anodes.

Figure 4(b) illustrates the second principle, first discussed by Kesaev (50) in his extensive studies in the motion of arcs on mercury surfaces in the presence of an "arched" magnetic field. Under these circumstances, the arc moves in a circular pattern in a position where the normal component of the magnetic field is minimal as indicated in the figure. The rate of circulation is determined by the parallel component of the magnetic field with the target surface (28).

### 18.3.1.3 Plasma Control

One advantage of using the magnetic fields to control the arc position is that they are well suited for integration into sources where plasma from the arc source must also be controlled. For example, a plasma emitted from the source pictured in Fig. 4(a) is naturally accelerated towards the substrate due to the Hall effect (18). Hall acceleration of the cathodic arc plasma has been found to increase the energy of the ions to values as high as 300 electron volts (10,18). This effect may account for observed improvements in coating properties such as the hundred-fold improvement in the adhesion of copper to glass reported in Ref. 51.

Besides the benefits of Hall acceleration, a substantial reduction in the number of macroparticles can be achieved by passing the plasma emanating from a cathodic arc through the proper magnetic field (10,51,52). In addition, concentration of the arc plasma can lead to a five-fold improvement in condensation rate with an associated reduction in wasted coating material. The introduction of arc plasma into the magnetic field of the solenoid has also been observed to enhance the already high degree of ionization of this plasma (52).



**Figure 4:** Cathodic arc devices featuring active magnetic control of the arc. (a) Arc source described in Ref. 42. The arc position rotates rapidly around the target in the retrograde direction and drifts in the direction of the reduced normal component of the magnetic field (in this case the acute angle). The coils represent an electromagnet. (b) Another example of magnetic control of the cathodic arc. Again the direction of circulation is defined by the parallel component of the magnetic field and the resulting arc circle resides at the position where the normal component of the magnetic field is minimal. (c) This schematic shows a cylindrical arc geometry. The arc targets are thick walled tubes. This geometry can be used directly where macroparticles can be tolerated in small quantities for coating the inside of tubes. This schematic illustrates how the arc ring can be oscillated over two different target compositions to produce either multilayered coatings or alloy coatings - depending on the rate of oscillation. The "X" represents a permanent magnet.

The final use of plasma control is illustrated in Fig. 5(a). In this case, an electromagnetic filter is employed to separate the macroparticles, produced at the target, from the plasma. This separation is accomplished by causing the plasma to flow through the curved passage indicated toward the substrate surface. Any macroparticles emanating from the target have essentially straight trajectories causing them to be collected on the walls of the plasma filter (53).

The physical basis for the control of the cathodic arc plasma has been understood for some time (53-55). Since the Larmor radius for heavy metal ions is large with respect to

the dimensions of the components being discussed here, the magnetic field has little direct effect on the motion of these ions (15). On the other hand, much lighter electrons are easily constrained to rotate around the magnetic field lines and can drift along these lines quite freely as long as these lines do not converge too rapidly. There is a natural resistance of electrons to pass across magnetic field lines, thereby, allowing the building of electrical fields perpendicular to the magnetic field surfaces. These electric fields have a profound influence on the motion of the ions from the cathodic arc and can be used to an advantage in controlling the path of those ions. One of the benefits of using this strategy for plasma control is the possibility for positive ions having different charges and masses to follow similar paths.

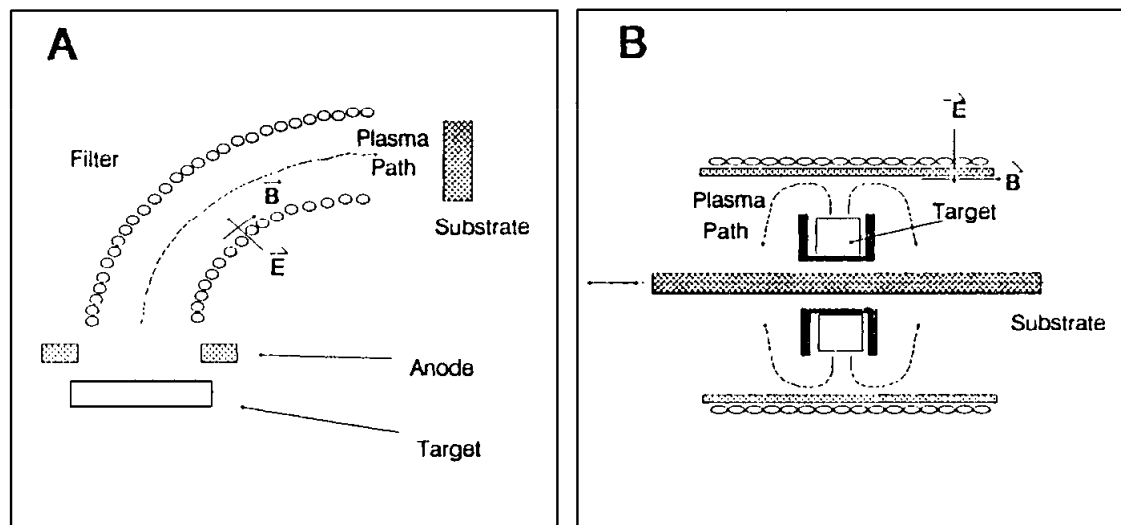


**Figure 5:** Two schemes for removal of macroparticles. In both cases, the electric field is thought to repel the positive ions and direct them toward the target surface. The macroparticles have no line-of-sight between the target surface and the substrate to be coated.

Quasineutral plasma behavior (such as that from cathodic arcs) in magnetic and electric fields has recently been modeled quantitatively by several investigators (54,56,57). One reason for this interest lies in the potential for developing arc-based ion beams for making coatings. Additional uses for quasineutral beams are for drivers in inertially confined fusion and as supplementary heating for magnetically confined plasmas. In the current context, it is hoped that the development of suitable computer models will make it possible to design sources which make the most effective use of the plasma produced by the vacuum arc.

### 18.3.2 Specific Examples:

One of the most difficult aspects of discussing specific examples of cathodic arc-based devices is the selection which must be made from such a diverse variety of possible choices. Arc sources can be continuous in operation or pulsed. They can be based on a random arc or one which is tightly controlled. They can employ some method of macro-

particle filtration, or can be based on a type of discharge which requires no such filtration, such as the distributed cathodic or anodic arcs. All of these arc sources can form the basis for extremely high current density ion beams. These ion beams can be used by themselves or serve as the starting point for a more complex process or piece of equipment such as an ion implanter. This section will discuss these major categories in general terms only, referring the reader to the references cited for more specific details.

From earliest times, cathodic arc devices for producing coatings could be divided into pulsed and continuous types. The pulsed devices will be described first. In the pulsed mode, the arc is repeatedly ignited and extinguished using a capacitor bank to supply the arc power (2,43,58). Pulsed arcs have the advantage of allowing the target material to cool between arc events. This makes it possible to arc an extremely wide variety of materials with less concern for the overheating of the target. Pulsed arcs, on the other hand, have a dead time in between arc events which limits the steady state coating rate. Since the arc initiates from the same point each time, it is possible to design the length of the discharge such that the arc does not have sufficient time to leave the preferred arcing position before the capacitor is discharged. In other words, the arc constraint requirement in pulsed arc devices tends to be less stringent than for the continuous variety. Pulsed arcs have been employed in conjunction with subsequent macroparticle filtration (59), and have formed the basis for ion beams for ion implanters (43).

The continuous cathodic arc can either be random in nature or controlled. Fig. 3 shows several examples of a random arc source where the arc is constrained at the edge of the target, but allowed random motion within that constraint. Random arc sources have the advantage of simplicity and excellent target utilization because the entire target (except near the very edge) is utilized in the arc process. These sources can be scaled in a straightforward manner to provide for uniform coating of very large parts. The main disadvantage of random arcing is the formation of macroparticles which may cause the resulting coating to be unsuitable in some applications. As pointed out in the discussion of Fig. 2, the macroparticles are ejected at small angles with respect to the target surface, and can therefore be minimized using appropriate shielding. Such a strategy has made possible arc-produced decorative coatings where surface finish and optical specularity are of concern (31).

As discussed earlier, magnetic fields can be used to control the trajectories of the arcs. These fields can be used to discourage the arc from leaving the desired portion of the target surface (as illustrated in Fig. 4) or can actually be used to define a well controlled path for the arc to follow in the so called "steered arc" devices (50,61,62). While the mechanism is still the subject of some debate, it is clear, at least in the case of ceramic coatings based on refractory metals, that steered arcs can produce coatings having extremely low or no measurable macroparticle component (61).

One of the difficulties of tightly controlling the path of the arc, is the tendency to cut a narrow slot into the target surface resulting in extremely poor target utilization. This has been overcome by the strategy of moving the arc controlled magnets with respect to the target so as to make full use of the target surface (60,61). A second advantage of this control of the arc position is the potential for production of coatings having variable composition through suitable programming of the arc motion over segmented targets of multiple composition (62). The target configuration pictured in Fig. 4(c) illustrates one technique for achieving such composition control; the figures in Ref. 61 illustrate another.



Where macroparticles present a problem in the final application, they can be removed through the use of a suitable filter. Figure 5 shows two examples of such filters, both of which are based on the same principle discussed earlier. In Fig. 5(a), a quarter segment of a torus is used to cause the plasma to follow a curved path leaving the macroparticles to collide on the inside of the filter (53). For effective removal of the macroparticles, it is necessary for the filters to be designed to require multiple bounces. In the case shown in Fig. 5(b), a ring target is employed (62), with the arc surface on the outside circumference. In this case, the arc plasma is reflected by the electric field set up due to the insulating property of the magnetic lines running parallel to the surface of the coil (as illustrated). The part being coated is moved, as indicated, to achieve coating uniformity. This particular scheme is most effective in cases where it is desired to obtain a radially symmetric coating.

As described in the section on general considerations, one strategy for dealing with the problem of macroparticles is to employ an arc which does not produce them. Figure 6 shows two categories of diffused arc which do not produce macroparticles. The first is called the cathodic arc distributed discharge. In this case, the cathode is designed in the form of a crucible to contain the target material (34). This crucible is allowed to heat up until the target material reaches a temperature where it has a substantial vapor pressure. At this point the arc voltage decreases. In the case of chrome, for instance, the random arc voltage of 18-20 volts decreases to a voltage of 12-14 volts. As shown in Fig. 1, the current density decreases drastically and, in addition, the plasma becomes brighter due to increased electron emission from the target surface. Macroparticles are no longer formed, and the ions now become singly charged rather than having the multiple charges of the random cathodic arc. The degree of ionization in this process can achieve 100% and the conversion efficiency of arc power to these ions can be extremely high since little energy in the form of heat is conducted to the electrode. A shutter is absolutely necessary with this type of source because, during the heating process, the target actually emits more macroparticles as the target heats to the point where it converts over to the distributed discharge mode. The design of a distributed discharge cathodic arc for practical coating systems becomes quite a challenge due to the necessity of bringing the surface of the target to the appropriate temperature without having spattering from the arc process.

A more straightforward approach for obtaining ionized evaporation material involves the so called anodic arc (36). One version is pictured in Fig. 6(b). In this process, the cathode initially supplies both electrons and ions until the anode target material heats up. Once sufficient electron emission occurs, a diffuse arc forms on the hot anode target material which supplies the ions necessary to sustain the discharge. At this point the cathode material is not expended, but rather becomes coated with some of the vapor emanating from the anode. This process produces no macroparticles and achieves some degree of ionization of the plasma. High rates of condensation have been demonstrated with the process. For instance, adherent and pinhole-free aluminum was deposited at a rate of 10 nm/sec at 30 cm distance from the target. This technique has been used for a wide variety of materials including Al, Ti, V, Cr, Mn, Fe, Ni, Cu, Pd, Ag, Au, Pt, and Pb (35). The process leaves the substrate relatively cool, making it possible to produce adherent coatings on plastics at temperatures less than 70°C.

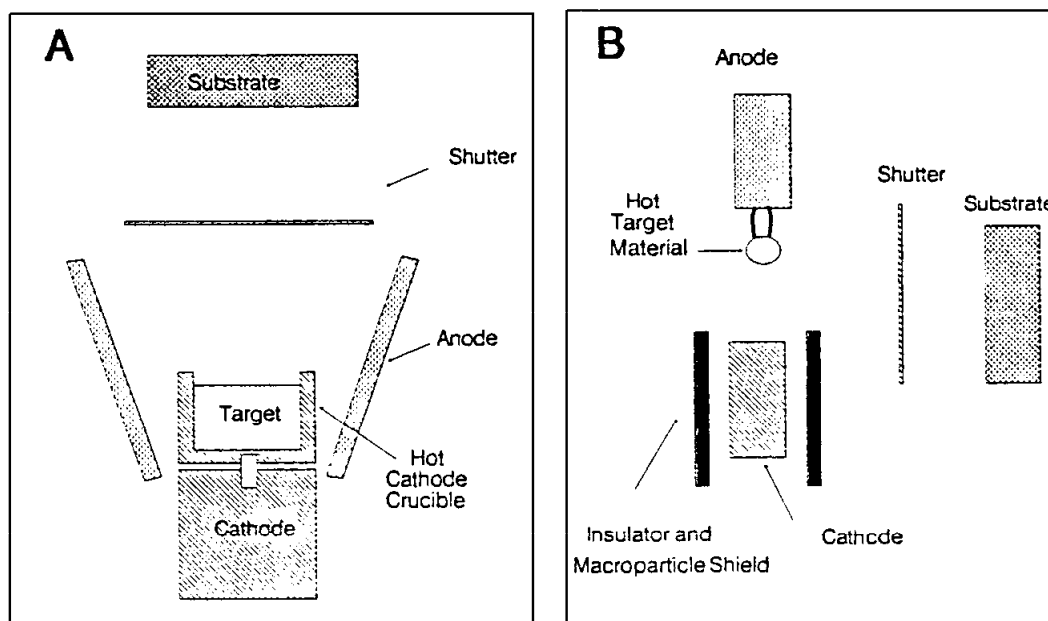


**Figure 6:** Two configurations for diffuse arcs which do not produce macroparticles. (a) With the polarity shown, this is a schematic of the diffuse cathodic arc. With the polarity reversed, it would be a type of anodic arc. (b) One form of anodic arc.

Alternative configurations exist for the anodic arc. One can be pictured by reversing the electrode polarity of the elements in Fig. 6(a) (36). Another, described in Ref. 63, involves a separate low voltage/high current electron beam originating from a filament source. The hot hollow cathode deposition process (described in another chapter in this book) can also be viewed as a type of anodic arc. It is not clear to this author that each of these configurations produces the same degree of ionization. In fact, it is likely that the basic electron emission mechanisms are different. Some require the addition of a process gas, while others exist solely on the plasma produced from evaporating electrode material. A systematic comparison would seem to be in order, particularly with respect to the degree of ionization of the plasmas produced.

One disadvantage of the process pictured in Fig. 6(a) is the necessity of containing the hot evaporating material. This containment of hot material may lead to contamination if a totally inert crucible material is unavailable. A disadvantage involving the process illustrated in Fig. 6(b), is that the anode surface must be relatively small in order to obtain the proper anodic discharge. Such a small area for the evaporating metal requires some means such as a wire feed device for frequent replenishment of the evaporation material. As discussed earlier, the extent of ionization as well as the energy of those ions, may be lower than the competing cathodic arc process. This last point is still subject to debate

due to conflicting claims concerning the degree of ionization from a particular anodic arc source configuration.

Using the same strategy which is employed for controlling the plasma to remove macroparticles, it is possible to generate intense ion beams from an arc source. Figure 7(a) contains an example of one such ion beam described in more detail in Ref. 64. These beams do not suffer the same constraints and current density limitations that are found with multi-aperture sources. In addition, they can operate using any ion for which a suitable cathode can be obtained. As the design of such arc-based ion beams becomes more common, more applications are likely. One recent application was the use of such an ion beam to study a new process called arc ion beam self-sputtering for the development of a sputtering source not requiring process gas for possible operation in UHV conditions (64).

Figure 7(a) illustrates the arc ion beam self-sputtering process also described in Ref. 64 in more detail. The ion beam provides the source of positive ions which are accelerated to the negatively biased sputtering target. If the voltage of the target is appropriate, it will become coated with ions from the arc source. As the target voltage is raised and the sputtering rate increases, the ions from the arc source are converted to neutrals of the same composition. This entire process can be carried out without the presence of a process gas. In addition, one can design a sputtering angle to optimize the efficiency of the sputtering process since the sputtering efficiency tends to be angularly dependent. Also, having the ions of the same composition as the atoms to be sputtered leads to very effective interaction for an efficient process.

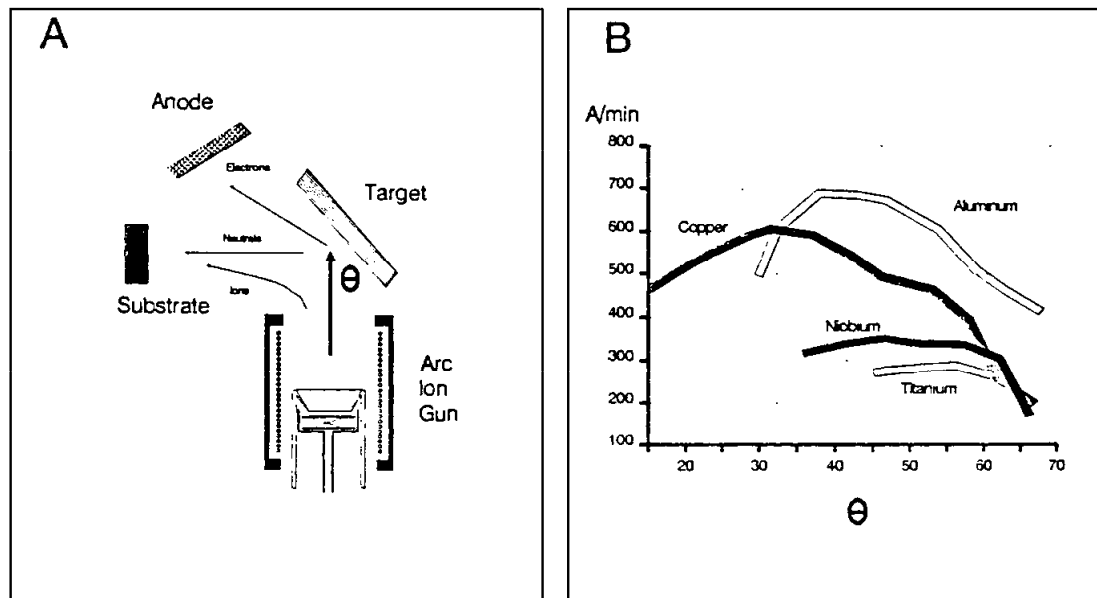


**Figure 7:** Schematic of arc ion-beam sputtering process. (a) Drawing showing an arc-ion-gun and a setup to determine optimal target angle for an arc sputtering process. (b) Rate dependence on target angle for four elements.

Figure 7(b) shows the effect of the target angle as defined in the schematic on the rate of condensation at the target. In the case of copper, the rate varies with target angle by a factor of two over the range shown. In the case of titanium, there was surprisingly little effect of target angle on rate. Further studies will be required to fully understand the observed effects.

Figure 8 shows a possible source based on the principles of arc based self-sputtering. In this case, the arc target has a cylindrical geometry. The sputtering target is cone shaped. The surface of the cone has a shallow angle with respect to the incoming ions. This angle can be optimized for a particular material, if desired, but this may not be necessary for materials whose self-sputtering rate is insensitive to angle. In addition to allowing sputtering without the need for process gas (true UHV sputtering), this process can present an extremely large effective deposition target area for coating large parts uniformly without the associated requirement for a large arc target. This is desirable because there are many examples of materials (such as the refractory metals) where dense and pure targets are not available in large sizes.

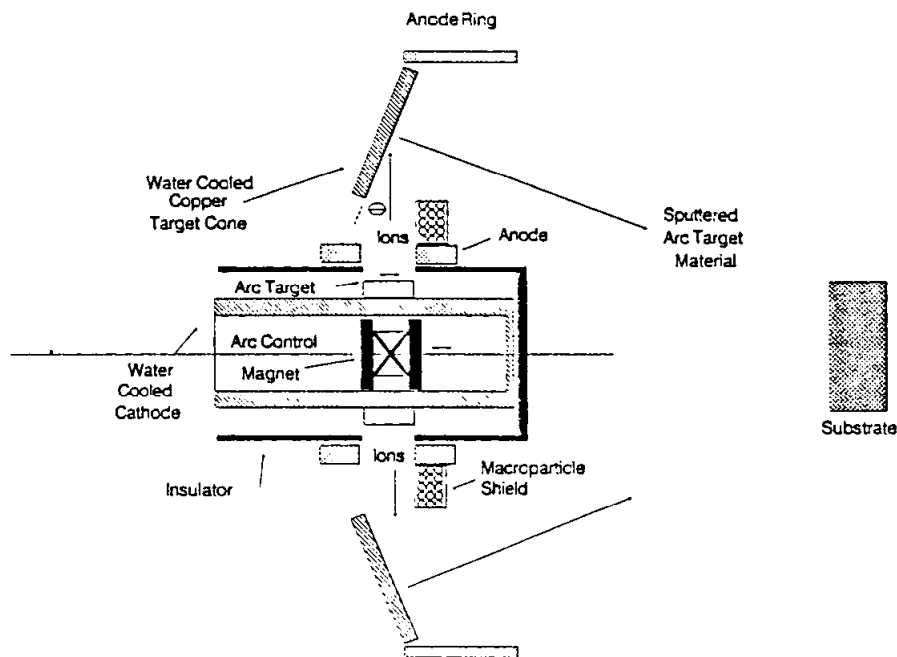


**Figure 8:** Design of a possible UHV sputtering source based on a vacuum arc. The arc target material condenses on the conical sputtering target and self-sputters toward the substrate. The macroparticles produced by the arc are collected at the anode.

While most of the arcs discussed thus far operate in the low voltage regime shown in Fig. 1, there are examples of studies making use of arcs operating near the maximum voltage of the anomalous glow region (38-41,65). As discussed earlier, these arcs appear to provide some improvements in coating properties, but insufficient understanding exists to define the cause for such improvements. As in the other cases requiring small electrode surface areas to obtain sufficient electron emission, these arc sources are likely to have very specialized applications.

In addition to the arc-based plasma sources described so far, the attention of the reader is directed to Refs. 66 and 67 for reviews of thermionic discharge and hollow

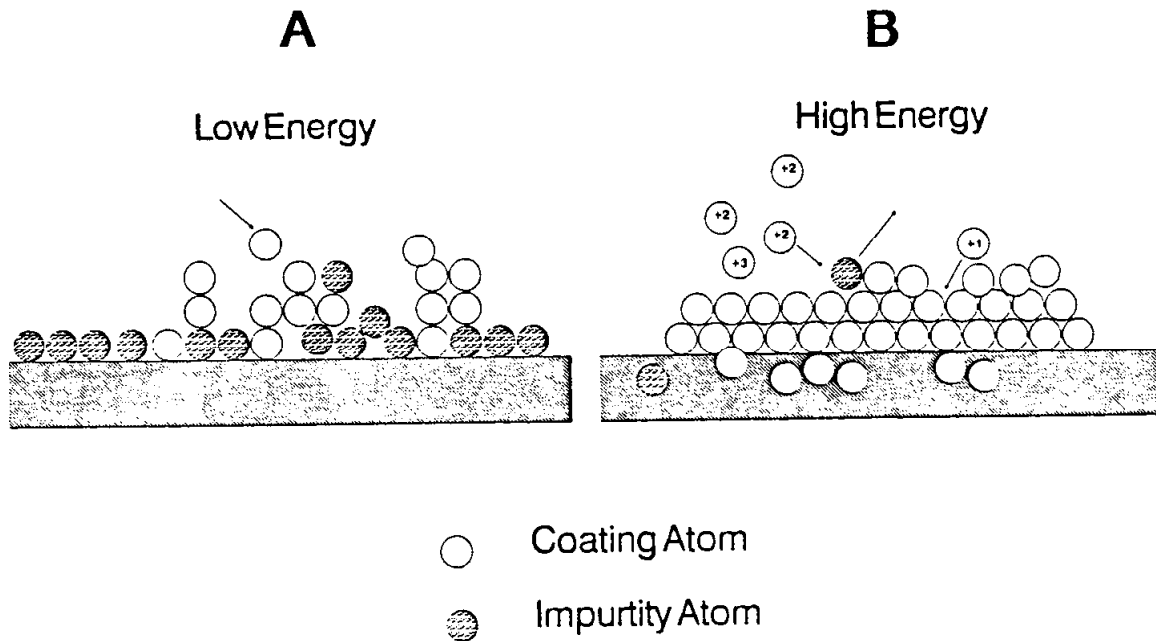
cathode discharge sources. The hollow cathode is also treated in another chapter of this book.

#### **18.4 COATINGS FROM ARCS (STRUCTURES AND PROPERTIES)**

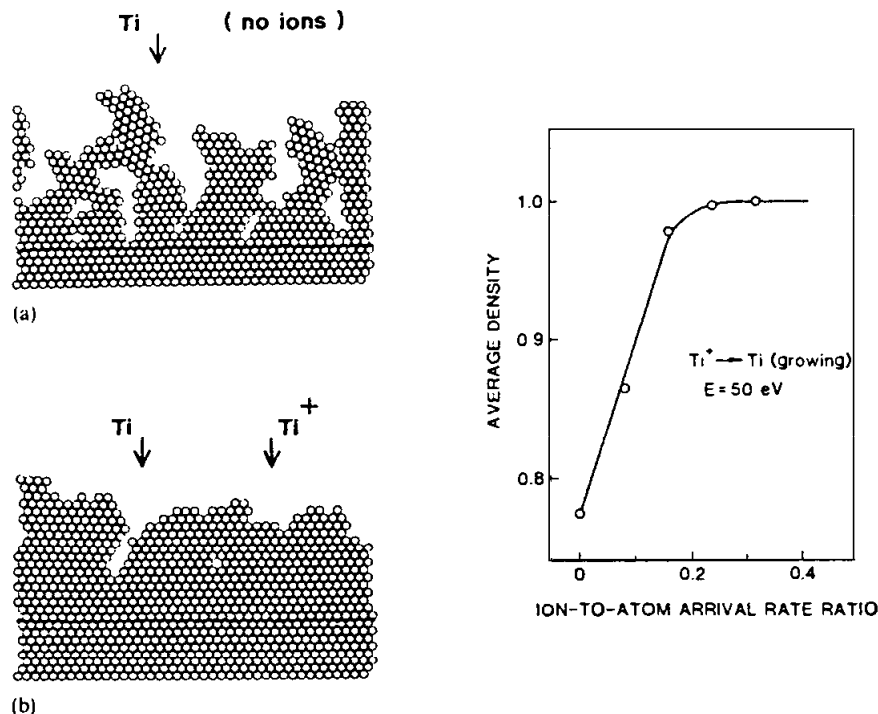
As mentioned earlier, arc technology shows promise for producing coatings with superior properties because it allows control over the depositing coating atoms by virtue of their charge. This improvement is predicted by theoretical molecular dynamic calculations (10-12). In addition, it has been substantiated by experiments. Such improvements include finer coating morphologies, improved coating density, and reduced intrinsic coating stress (68). All these property improvements occur at lower substrate temperatures than would occur with less energetic techniques. Other considerations suggest an improved adhesion. In the production of ceramic coatings by reactive deposition, the ionized nature of the coating atoms enhances reactivity and leads to coatings with excellent stoichiometry (69). Arc technology can also be employed to produce coatings having tailored compositions, particularly with respect to the interface region (61). Finally, the energetic nature of the arc plasma gives rise, in some cases, to unusual bonding such as the diamond-like bonds found in carbon coatings produced by the arc process (70). This section will present some examples of each of these to provide a motivation for further investigation into the production of coatings using arc technology.

Figure 9 illustrates, on a molecular scale, the case for energetic arc technology. In the case of low energy deposition such as electron beam evaporation, neutral atoms of the coating material arrive at the substrate surface and deposit on top of that surface. Since there is little energy available for coating mobility, particularly during room temperature deposition, the atoms stick at the point where they arrive. If the surface has adsorbed contamination atoms between the substrate and coating, the resulting coating may have poor adhesion. The result of the lack of atomic mobility is predicted to be a coating of poor density, filled with voids and impurity atoms as pictured.

In contrast, as shown in Fig. 9(b), positive ions arrive at the surface with increased kinetic energy due to the acceleration they undergo as they are attracted to the negatively charged substrate. (Alternatively, they may have benefitted from the Hall acceleration discussed earlier.) In either case, they have sufficient energy to clean off the surface atoms prior to forming the coating. In addition they have sufficient mobility to diffuse to low free energy sites, a factor which results in denser coatings. When the substrate has adequate negative bias to accelerate the coating ions sufficiently, implanting these ions into the interfacial region can further strengthen the adhesive bond. To be thorough, it is necessary to point out that such implantation may also lead the introduction of impurity atoms into the substrate (as illustrated in Fig. 9(b)) unless care is taken. Fig. 10 shows the results of an actual molecular dynamic calculation predicting the densification of a model coating structure due to the energetic deposition based on a cathodic arc process (10).



**Figure 9:** Conceptual diagram showing the case for the energetic cathodic arc process. (a) Sputtering and electron beam evaporation coating atoms are neutral and have limited energy to contribute to atomic mobility after condensation. (b) The arc processes produce positive ions which can be accelerated into the part to be coated. Increased atomic mobility can result in improved properties as discussed in the text.



**Figure 10:** Results of a molecular dynamic modeling calculation carried out by P.J. Martin, et.al., in Ref. 10. Used with permission.

In addition to improvements in coating density, several investigators (38)-(41) have found that high voltage arcs produce epitaxial coatings of refractory metals at lower temperatures than would be expected by other techniques. Since the plasmas produced by such arcs have not been well characterized, the exact mechanism for the creation of such structures is not yet understood. One speculation has been that such arcs produce clusters which may enhance such epitaxy. In contrast to the behavior of low voltage arcs where the morphology is strongly dependent on the substrate bias, coatings produced by high voltage arcs show no such dependence. This observation tends to suggest that the evaporation product from the high voltage arc may not be strongly ionized, as in the low voltage case.

Examples of improved adhesion due to the proper use of arc technology abound. As will be described in the application section, the most important commercial application for the use of arc technology in coatings has been the production of hard coatings of titanium nitride for cutting tools. In this application, it is clear that the coating must be extremely adherent during the violent mechanical abuse to which the cutting tool is subjected for such a coating to have any beneficial effect. As found by a number of investigators (51,52), coating adhesion can be further enhanced by the use of magnetic fields to accelerate the ions of the arc plasma to higher energies. A hundred- fold improvement of the adhesion of copper to glass for instance, has been achieved with such a strategy (51).

Surprisingly little experimental information exists on the stresses produced in the coatings produced by arc technology. Such stresses can be highly compressive in some instances or extremely low in others depending on the details of the process during which the coating is being produced. This area will require much additional investigation if molecular dynamic modeling predictions concerning reductions in stress are to be realized.

Another area which will require substantial further investigation concerns the extent of heating of the substrates by the various arc technology techniques. While it is possible to supply sufficient energy to large substrates to cause them to rise in temperature to values in excess of 500°C, it is also possible to produce dense adherent coatings on plastics at room temperature (35). Part of this difference in behavior involves the separation of the electrons from the ions to minimize heating effects when cold substrate temperatures are necessary. Pulsed arcs offer another approach for maintaining a low substrate temperature; the dead time between pulses can be adjusted to allow for cooling.

Examples of the enhanced chemical reactivity of the plasmas produced by the arc process are also available (10,44,55,71,72). These are particularly evident in the case of the discrete cathodic arc which produces multi-ionized coating material. Such multi-charged ions undergo charge exchange reactions with the reactive gas leading to ionization of the latter. The coatings which are produced tend to be stoichiometric in composition over a broader range of reactive gas partial pressure than is the case with competing magnetron technology (69).

While carbon coatings with the diamond structure are receiving considerable attention currently, it is interesting to note that one of the earliest methods for producing such coatings made use of the vacuum arc (73). Once again, Russian investigators are well represented in early work in this area (74-76). More recent structural studies by other workers (70) have verified that arc technology is capable of producing diamond-type sp<sup>3</sup>

bonds without appreciable  $sp^2$  graphitic bonds and without the need for hydrogen to be present as is the case in competing glow discharge techniques.

### 18.5. APPLICATIONS AND OPPORTUNITIES

The most widely implemented application of arc deposited coatings has been for improving the lifetime and operational characteristics of cutting tools used in machining of metals. Cutting tools such as drills, endmills, taps, hobs and broaches coated with TiN not only show improvements in service lifetimes due to reduced wear, but operate more efficiently. Due to their improved lubricity and reduced chemical reactivity, it is possible to operate coated tools at higher rates and the parts produced have improved surface finishes (77).

While the variety of current applications is small, this is likely to increase quite quickly as practical sources are developed which reduce or eliminate the macroparticles which are produced by the conventional cathodic arc process. One market which is likely to be impacted is the one for gold-colored decorative coatings. Many consumer products such as watch cases, pens, and the like make use of titanium nitride produced by reactive deposition of the metal. Titanium nitride produced using low macroparticle sources is likely to gain market share in this arena in the near term due to characteristics of the process such as high adhesion, high rates, and ability to achieve excellent stoichiometry in compound coatings over a broad range of processing conditions (31).

Another group of manufacturers which will likely be impacted is the printed circuit board producers. In this case, there is pressure to improve performance and quality due to demands for reducing the size of electronic equipment. The cathodic arc process offers the possibility of producing adherent conductive coatings at high rates. In addition, the process has excellent "throwing power" which allows for coating through holes (31).

The longer term applications are harder to predict because they rely on improved coating properties which are only now being realized. Because the cathodic arc process is well suited for depositing adherent refractory metals on virtually any substrate at high rates, one can speculate on the possibility of coating copper structures with materials such as tungsten and molybdenum for fusion devices, for instance.

Macroparticle-free magnetic coatings would quickly find application in the recording industry for the optical and magnetic storage of data. In this case the ability to produce dense adherent magnetic coatings at high rates is of great interest. In addition to these excellent physical properties, the arc process offers a straightforward means to tailor alloys and to vary the composition during the coating process (as discussed earlier).

With the recently developed capability to produce ceramic coatings which have extremely low or no macroparticle content (61), broad new opportunities are opened up in a variety of industries. While macroparticle-laden arc-produced ceramic coatings have been available for some time for corrosion protection and wear resistance, the reduction in size and numbers of macroparticles makes it possible to use such coatings at high temperature with less concern for macroparticle-induced failure. One mechanism for such failure in coatings containing macroparticles is the localized reduction of the oxide or nitride to sub-stoichiometric levels during heating. Such metal-rich regions might be more reactive to the hostile environments. Even at low temperatures these metallic macropar-



ticles are of concern because of their inferior chemical and tribological behavior. Potential uses for low macroparticle content ceramic coatings as barrier coatings include corrosion protection for turbine blades and chemical reaction vessels.

If the presence of macroparticles can be completely eliminated, it may become possible to employ arc technology for the production of coatings for integrated circuits. Once again the advantages of being able to produce stoichiometric ceramic coatings having excellent adhesion and density at low process substrate temperature make such an approach highly desirable for insulating structures. Dense and adherent refractory metal coatings for conductive elements in integrated circuits are another potential application.

Coatings that are denser than currently produced for optical components would have increased stability in the value of the refractive index of each layer. (Refractive index instabilities result from adsorption of moisture into open coating structures). The improvements in adhesion and stoichiometry might improve the resistance of coatings to laser damage in applications as diverse as laser diodes for telecommunications and large inertial confinement laser systems envisioned for the production of power in the next centuries.

Another far reaching potential application is the possible production of high  $T_c$  superconducting thin films which do not require subsequent heat treatment to produce superconducting structures; the energy supplied by the ions might be sufficient. Such coatings might be produced on low temperature substrates which would increase the possibilities for unusual applications.

A final class of applications makes use of the possibility of producing non-equilibrium structures due to the energetic nature of the ions produced by the arc process. Diamond coatings produced using plasma from a cathodic arc might be used for protecting recording disks, optical lenses and fiber optic transmission lines from reactions and mechanical abrasion. If defect-free single crystal diamond coatings could be produced using this approach, they could be employed as active semiconductors for high frequency applications.

#### **18.5.1 Non-Coating Applications**

In addition to applications discussed thus far, several suggestions have been made concerning uses for the ions potentially available using arc technology. Arcs can be used as the basis for a sublimation-ion vacuum pump (78). Since the vacuum arc can be operated without the presence of process gas, it is possible to consider a "poor man's" ion implanter in which the part to be implanted is pulsed to a high negative potential for a very short time, having the effect of accelerating the positive ions into the surface of the part. Rather large parts might be treated in this manner without the necessity for expensive and complicated ion-optical systems. Where such ion implantation systems are indicated, the vacuum arc can serve as the source of ions (43). Still another application of arc-generated ion beams is the smoothing of surfaces through the combination of deposition and sputtering (79). In this case, the energy of the cathodic arc plasma-based accelerator is claimed to be ideal for the process. All of these ideas, while exciting in principle, need to be verified experimentally.

## 18.6 GAPS IN UNDERSTANDING

These suggestions for possible applications are not intended to be an exhaustive list, but rather to serve to suggest the diverse and potentially significant opportunities which may exist with the proper utilization of arc technology. The reason that these opportunities have not been realized is that there still exist serious gaps in the understanding of the technology.

The most obvious is the lack of commercially available macroparticle-free arc sources. While several approaches have been suggested in this chapter which may lead to this objective, the goal has not yet been achieved outside the laboratory. (In fact many of the ideas and claims made by various workers need to be substantiated by independent investigators). Such investigations will naturally lead to improvements in understanding of techniques for control of the arc and its plasma.

In addition, improvements in the quantitative understanding of the condensation behavior of energetic particles will allow for the determination of the limits which may be possible in terms of producing dense coatings at high rates, for instance. As mentioned before, there is surprisingly little information concerning the intrinsic stress in arc coatings and the mechanism for its origin. While workers in the area are aware of the possibility for large compressive stresses, it is not clear which process conditions result in such stresses. On some occasions, coatings having very low stress are observed. Once again computer modeling may offer the necessary understanding.

While other types of ion bombardment, (such as argon bombardment from a multi-aperture ion source), for instance, do not involve the coating atoms themselves directly, the plasma produced by the arc process can be composed of only coating ions. This may lead to some opportunities which may be exploited if there is a quantitative understanding of the events which occur during the condensation of these ions. Currently, for instance, there is virtually no quantitative understanding concerning the details of the chemical interactions of these ions with surfaces.

Finally a detailed understanding of the chemical reactions which occur as a result of coating ions interacting with reactive gas ions and electrons in a magnetic and electric field may lead to the invention of new compound coating structures such as the high  $T_c$  superconductors mentioned earlier.

## 18.7 CONCLUSION

While vacuum arc technology has come a long way since its inception, it still has a long way to go to fully utilize what appear to be some exciting opportunities. This advancement will occur if systematic efforts are made to understand the coating properties which are possible with such technology and if simultaneous efforts are made to understand quantitatively the arc, the plasma from the arc, and the condensation behavior of that plasma to form coatings or to interact with surfaces in the presence of electric and magnetic fields.

**18.8 REFERENCES**

1. Wroe, H. The Magnetic Stabilization of Low Pressure D.C. Arcs. Br. J. Appl. Phys. 9: 488-491 (1958).
2. Gilmour, A.S., Jr., Lockwood, D. L., Pulsed Metallic Plasma Generators Proc. IEEE 60: No. 8, 977-991 (1972).
3. Snaper, A.A. Arc Deposition and Apparatus, U.S. Patent No. 3,625,848 (1971).
4. Snaper, A.A. Arc Deposition and Apparatus, U.S. Patent No. 3,836,451 (1974).
5. Sablev, L.P. Apparatus for Vacuum Evaporation of Metals under the Action of an Electric Arc, U.S. Patent No. 3,783,231 (1974).
6. Sablev, L.P. Apparatus for Metal Evaporation Coating, U.S. Patent No. 3,793,179 (1974).
7. Mularie, W.M. Evaporation Arc Stabilization, U.S. Patent No. 4,430,184 (1984).
8. Mularie, W.M. Apparatus for Evaporation Arc Stabilization During the Initial Clean-up of an Arc Target, U.S. Patent No. 4,559,121 (1984).
9. Martin, P.J., Netterfield, R.P., et al., Ion-Assisted Deposition of Bulk-Like  $ZrO_2$  Films. Appl. Phys. Lett. 43: 711-713 (1983).
10. Martin, P.J., McKenzie, D.R., et al., Characteristics of Titanium Arc Evaporation Processes Thin Solid Films 153: 91-102 (1987).
11. Müller, K.H., Model for Ion-Assisted Thin Film Densification. J. Appl. Phys. 59: 2803-2807 (1986).
12. Müller, K.H., Modeling Ion-Assisted Deposition of  $CeO_2$  Films. Appl. Phys. A 40: 209-213 (1986).
13. Cobine, J.D., Introduction to Vacuum Arcs. in Vacuum Arcs: Theory and Application ed. by J.M. Lafferty John Wiley, New York 1-18 (1980).
14. Dorodnov, A.M. and Petrosov, B.A., Physical Principles and Types of Technological Vacuum Plasma Devices. Sov. Phys. Tech. Phys. (Engl. Transl. of Zh. Tekh. Fiz.) 26: 304-315 (1981).
15. Thornton, J.A. Plasma-Assisted Deposition Processes: Theory, Mechanisms, and Applications. Thin Solid Films 107: 3-19 (1983).
16. Daalder, J.E. Erosion Structures on Cathodes Arced in Vacuum J. Phys. D: Appl. Phys. 16: 17-27 (1983).
17. Davis, W. D., Miller, H. C., Analysis of the Electrode Products Emitted by DC Arcs in Vacuum Ambient. J. Appl. Phys. 40: 2212-2221 (1969).
18. Dorodnov, A.M., Muboyadzhyan, S.A., et al., A Cold Cathode Hall Plasma Accelerator. J. Appl. Mech. and Tech. Phys. (Engl. Transl. of PMTE) 22: 28-32 (1981).
19. Kimbin, C.W. Erosion and Ionization in the Cathode Spot Regions of Vacuum Arcs. J. Appl. Phys. 44: 3074-3081 (1973).
20. Plyutto, A.A., Ryzhkov, V.N., et al., High Speed Plasma Streams in Vacuum Arcs. Sov. Phys. JETP (Engl. Transl. of Zh. Eksp. Teor. Fiz.) 20: 328 (1965).
21. Rakhovsky, V.I. Current Density Per Cathode Spot In Vacuum Arcs. IEEE Trans. Plasma Sci. PS12: 199-203 (1984).

22. Daalder, J. E. Cathode Erosion of Metal Vapor Arcs in Vacuum, Ph.D Thesis (Eindhoven, Netherlands) (1978).
23. Arkscenov, I.I., Konovalov, I.I., et al., Droplet Phase of Cathode Erosion in a Steady Vacuum Arc. Sov. Phys. Tech. Phys. (Engl. Transl. of Zh. Tekh. Fiz. ) 29: 893-894 (1984).
24. Boxman, R.L., Goldsmith, S., The Interaction Between Plasma and Macroparticles in Multi-Cathode Spot Vacuum Arc. J. Appl. Phys. 52: 252-161 (1981).
25. Argarwal, M.S., Holmes, R., Arcing Voltage of the Metal Vapor Vacuum Arc. J. Appl. Phys. 16: 757-767 (1984).
26. Agarwal, M.S., Holmes, R., Cathode Spot Motion in High-Current Vacuum Arcs under Self-Generated Azimuthal and Applied Axial Magnetic Fields. J. Phys. D: Appl. Phys. 17: 743-756 (1984).
27. Aksenov, I.I., Andreev, A.A., Motion of the Cathode Spot in a Vacuum Arc in an Inhomogeneous Magnetic Field. Sov. Tech. Phys. Lett. (Engl. Trans. of Pis'ma Zh. Tekh. Fiz. ) 3: 525-526 (1977).
28. Fang, D.Y., Cathode Spot Velocity of Vacuum Arcs. J. Appl. Phys. 15: 833-844 (1982).
29. Moizhes, B.Y., Nemchinski, V.A., Influence of External Gas Pressure on Cathode Spot Motion in a Magnetic Field. Sov. Phys. Tech. Phys. (Engl. Transl. of Zh. Tekh. Fiz. ) 30: 136 (1985).
30. Guile, A.E., Juttner, B., Basic Erosion Processes of Oxidized and Clean Metal Cathodes by Electric Arcs. IEEE Trans. Plasma Sci. PS8: 259-269 (1980).
31. Randawa, H., Johnson, P. C., Technical Note: A Review of Cathodic Arc Plasma Deposition Processes and Their Applications. Surf. Coat. Technol. 31: 308-318 (1987).
32. Aksenov, I.I., Konovalov, I.I. et al., Plasma in a Stationary Vacuum-Arc Discharge. High Temp. (Engl. Transl. of Teplofiz. Vys. Temp.) 21: 484-488 (1983).
33. Harris, L. P., Arc Cathode Phenomena. in Vacuum Arcs: Theory and Application ed. by J.M. Lafferty, John Wiley, New York 120-168 (1980).
34. Vasin, A.I., Dorodnov, A.M. et al., Vacuum Arc with a Distributed Discharge on an Expendable Cathode. Sov. Tech. Phys. Lett. (Engl. Trans. of Pis'ma Zh. Tekh. Fiz. ) 5: No. 23-24, (1979).
35. Ehrich, H., Hasse, B. et al., The Anodic Vacuum Arc. Proc. 8th Intl. Conf. Gas Discharge Appl. (Essen Univ.) 591-592, 596 (1985).
36. Dorodnov, A.M., Kunetsov, A.N. et al., New Anode-Vapor Vacuum Arc with Permanent Hollow Cathode. Sov. Tech. Phys. Lett. (Engl. Trans. of Pis'ma Zh. Tekh. Fiz. ) 5: 418-419 (1979).
37. Ehrich, H., The Anodic Vacuum Arc I, Basic Construction and Phenomenology. J. Vac. Sci. Technol. A6: 134-138 (1988).
38. Igarashi, Y., Kanayama, M, High-Quality Single-Crystal Niobium and Tantalum Films Formed by an Ultra-High Vacuum Arc Method. J. Appl. Phys. 57: 849-854 (1985).
39. Igarashi, Y., Kanayama, M, Growth of Tungsten Single-Crystal Films Deposited on MgO (100) Substrate. J. Appl. Phys. 52: 7208-7211 (1981).

40. Igarashi, Y., Kanayama, M., New Evaporation Method of High Melting Temperature Materials, Utilizing A Vacuum Discharge. Appl. Phys. Lett. 28: 481-482 (1976).
41. Krohn, M., Meyer, K.P. et al., Epitaxy by Vacuum Arc Evaporation. J. Cryst. Growth 64: 326-332 (1983).
42. Aksenov, I.I., Belous, V.A., Ignition of a Vacuum Arc in Stationary Sources of a Metal Plasma from an Autonomous Plasma Injector. Instrum. and Exp. Tech. (Engl. Transl. of Prib. Tekh. Eksp. ) No. 3, Pt. 2, 785-786 (1979).
43. Brown, I., Washburn, J., MEVVA Ion Source for High Current Metal Ion Implantation, Intl. Conf. on Ion Implantation Technol. (Berkeley CA) NTIS DE87000069: (1986).
44. Shinno, H., Fukutomi, M. et al., In Situ Coating of Low-Z Materials by Reactive Vacuum Arc Deposition with a Stabilized Arc Cathode. J. Nucl. Mater. 133-134: 749-753 (1985).
45. Morrison Jr., C. F. Method and Apparatus for Arc Evaporating Large Area Targets, U.S. Patent No. 4,724,058 (1984).
46. Morrison Jr., C. F. Method and Apparatus for Evaporation Arc Stabilization Including Initial Target Cleaning, U.S. Patent No. 4,448,659 (1984).
47. Mularie, W.M. Method and Apparatus for Evaporation Arc Stabilization for Permeable Targets, U.S. Patent No. 4,559,121 (1983).
48. Wroe, H. Stabilization of Low Pressure D.C. Arc Discharges, U.S. Patent: 2,972,695 (1961).
49. Sablev, L.P., Dolotov, Y.I. et al., Electrical-Arc Vaporizer of Metals with Magnetic Confinement of Cathode Spot. Instrum. and Exp. Tech. (Engl. Transl. of Prib. Tekh. Eksp. ) 19: 1211-1213 (1976).
50. Kasaev, I.G., Pashkova, V.V., The Electromagnetic Anchoring of the Cathode Spot. Sov. Phys. Tech. Phys. (Engl. Transl. of Zh. Tekh. Fiz. ) 4: No. 254-264, (1959).
51. Sanders, D.M., Pyle, E.A., Magnetic Enhancement of Cathodic Arc Deposition. J. Vac. Sci. Technol. A5: 2728-2731 (1987).
52. Aksenov, I.E., Bren', V.G. et al., Mechanism Shaping the Ion Energy Distribution in the Plasma of a Vacuum Arc. Sov. Phys. Tech. Phys. (Engl. Transl. of Zh. Tekh. Fiz. ) 7: No. 10, 497-489 (1981).
53. Aksenov, I.I., Belous, V.A. et al., Apparatus to rid the Plasma of a Vacuum Arc of Macroparticles. Instrum. and Exp. Tech. (Engl. Transl. of Prib. Tekh. Eksp. ) 21: No. 5, Pt. 2, 1416-1418 (1978).
54. Aksenov, I.I., Belokhvostikov, A.N. et al., Plasma Flux Motion in a Toroidal Plasma Guide. Plasma Phys. Contr. Fusion (GB) 28: No. 5, 761-770 (1986).
55. Aksenov, I.I., Bren', V.G. et al., Chemical Reactions in the Condensation of Metal-Plasma Streams. Sov. Phys. Tech. Phys. (Engl. Transl. of Zh. Tekh. Fiz. ) 23: No. 6, 651-653 (1978).
56. Hitchon, W.N.G., A Plasma-Optical System Modeled Using Particles, J. Plasma Phys. (UK) 38: Pt. 1, 87-94 (1987).
57. Robertson, S., Magnetic Guiding, Focusing and Compression of an Intense Charge-Neutral Ion Beam. Phys. Fluids. 26: No. 4, 1129 (1983).

58. Boxman, R.L., Goldsmith, S., et al., Fast Deposition of Metallurgical Coatings and Production of Surface Alloys Using a Pulsed High Current Vacuum Arc" Thin Solid Films 139: No. 1, 41-52 (1986).
59. Chernyaev, V.N., Korze, V.F. et al., The Manufacture of Strip-Line Microwave Devices Using Pulsed Plasma Accelerators. Radioelectron. and Commun. Syst. (Engl. Transl. of Izv. Vyssh. Uchevn. Zaved. Radioelektron. ) 25: No. 12, 68-71 (1982).
60. Drodnov, A.M., Miroshkin, S.I. Vacuum Erosion-Type Generators and Plasma Accelerators Working on Alternating High Temp. (Engl. Transl. of Teplofiz. Vys. Temp. ) 18: No. 5, 821-830 (1980).
61. Ramalingam, S. Controlled Vacuum Arc Material Deposition, Method and Apparatus, World Patent #85/03954 (1985).
62. Kljuchko, G.V., Padalka, V.G. et al., Plasma Arc Apparatus for Applying Coatings by Means of a Consumable Cathode, U.S. Patent No. 4,492,845 (1982).
63. Buhl, R., Moll, E. et al., Method and Apparatus for Evaporating Material Under Vacuum using both an Arc Discharge and Electron Beam, U.S. Patent No. 4,448,802 (1981).
64. Sanders, D.M. Ion Beam Self-Sputtering Using a Cathodic Arc Ion Source. J. Vac. Sci. Technol. A6: No. 3, 1929-1933 (1988).
65. Kanayama, M., Igarashi, Y. Ultrahigh Vacuum Arc Method to Form Thin Refractory Metal Films. Rev. Sci. Instrum. 54: No. 2, 220-225 (1983).
66. Saenko, V.A., Vladimirov, A.I. et al., Thermionic Deposition Devices" Instrum. and Exp. Tech. (Engl. Transl. of Prib. Tekh. Eksp. ) No. 3, 9-21 (1985).
67. Saenko, V.A., Vladimirov, A.I. et al., Hollow Cathode Evaporators. Instrum. and Exp. Tech. (Engl. Transl. of Prib. Tekh. Eksp. ) 28: No. 1 Pt. 2, 131-264 (1985).
68. Muller, K. H. Stress and Microstructure of Sputter-Deposited Thin Films: Molecular Dynamics Investigations. J. Appl. Phys. 62: No. 5, 1796-1799 (1987).
69. Poppov, D.N., Uzunov, T.D. et al., Influence of the Nitrogen Partial Pressure on the Composition and Color of Titanium Nitride Coatings, Obtained by Reactive Magnetron Sputtering and Reactive Arc Deposition. Bulg. J. Phys. 13: No. 5, 470-476 (1986).
70. Martin, P.J., Filipczuk, S.W. et al., Structure and Hardness of Diamond-Like Carbon Films Prepared by Arc Evaporation. To be published in J. Mater. Sci. Lett.
71. Freller, H., Haessler, H.  $Ti_xAl_{1-x}N$  Films Deposited by Ion Plating with an Arc Evaporator. Proc. Intl. Conf. on Metal. Coatings (1987).
72. Randhawa, H. Cathodic Arc Plasma Deposition of TiC and  $TiC_xN_{1-x}$  Films Thin Solid Films 153: 209-218 (1987).
73. Aisenberg, S., Chabot, R. Technol. 8: No. 1, (1971).
74. Aksenov, I.I., Vakula, S.I. et al., High-Efficiency Source of Pure Carbon Plasma. Sov. Phys. Tech. Phys. (Engl. Transl. of Zh. Tekh. Fiz. ) 25: No. 9, 1164-1166 (1980).
75. Stel'nitskii, V.E., Padalka, V.G. et al., Properties of Diamond-Like Carbon Film Produced by the Condensation of Plasma Stream with a RF Potential. Sov. Phys. Tech. Phys. (Engl. Transl. of Zh. Tekh. Fiz. ) 23: No. 2, 222-224 (1978).

76. Strel'nitskii, V.E., Arksenov, I.I. et al., Properties of Diamond-Like Carbon Coatings Produced by Plasma Condensation. Sov. Phys. Tech. Phys. (Engl. Transl. of Zh. Tekh. Fiz. ) 4: No. 11, 546-547 (1978).
77. Randhawa, H. TiN - Coated High-Speed Steel Cutting Tools. J. Vac. Sci. Technol. A4: 2755-2758 (1986).
78. Dorodnov, A. M., Minaichev, V. E. et al., High-Vacuum Plasma Pump. Instrum. and Exp. Tech. (Engl. Transl. of Prib. Tekh. Eksp. ) 23: No. 6, 1449-1452 (1980).
79. Dorodnov, A. M., Miroshkin, S. I. et al., Surface Machining by Ion Sputtering. Sov. Tech. Phys. Lett. (Engl. Trans. of Pis'ma Zh. Tekh. Fiz. ) 5: No. 4, 172-173 (1979). 80. Lunev, V. M., Ovcharenko, V. D. et al., Plasma Properties of a Metal Vacuum Arc. Sov. Phys. Tech. Phys. (Engl. Transl. of Zh. Tekh. Fiz. ) 22: No. 7, 856-861 (1977).

---

## **Ion-Surface Interactions: General Understandings**

---

**Russell Messier, Joseph E. Yehoda and Lawrence J. Pilione**

### **19.1 INTRODUCTION**

Ion-surface interactions are present and play a significant role in many plasma-based thin film deposition techniques (1). The term ion has often referred to both ionized and neutral energetic particles in the literature. It has been shown in previous chapters that plasmas are sources of both non-equilibrium gas phase/surface chemistry and particle bombardment. The net effect is that very often specific materials can be obtained at lower deposition temperatures, and as a result a wide and controllable range of film properties can be attained, in addition to new metastable structures or compositions. In this chapter we will restrict our discussions to the physical effects of ion-surface interactions on relatively low temperature surfaces, and thus, mainly inert gas ion bombardment will be considered. Furthermore, we will focus attention on the atomistic aspects of ion-surface interactions especially at low ion energies and ion-to-atom arrival rate ratios.

Thin films are generally not the same as bulk materials since, in most cases, they contain impurities, internal and external surfaces/interfaces, density variations with thickness, short range density fluctuations, etc., which are highly dependent upon the particular deposition technique parameters and fundamental processes such as energetic particle bombardment. The result is a virtual infinity of thin film materials covering a broad continuum of free energy states and macroscopic and microscopic structures. It is this variability which leads to the wide range of possible characteristics and resulting properties that make thin films such extensively used materials both scientifically and technologically. At the same time, quantitative preparation-characterization-property relations remain an elusive goal, in large part due to the seeming simplicity - and yet actual complexity - of vapor-deposited films (2,3).

### **19.2 PREPARATION-ION BOMBARDMENT RELATIONS**

It has only been since the mid-1960's that a number of new deposition processes based upon plasma generation and activation of species have been developed. Although dc-sputtering was invented over a hundred years before, it was not until the advent of commercial rf-diode sputtering systems that plasma-based processes became extensively used. Since then such deposition techniques as triode sputtering, rf- and dc-magnetron sputtering, ion plating, activated reactive evaporation (ARE), dc-, rf-, and microwave-



plasma assisted chemical vapor deposition (PACVD), remote PACVD, ion-beam assisted evaporation, ion beam sputtering, dual ion beam sputtering, and direct ion beam deposition have become commonly used both scientifically and technologically (1). In addition, many variations on these techniques have been developed. Except for the ion beam-assisted processes, where ion energy and flux can be independently and precisely controlled, the ion energy and flux of species bombarding the growing film can be highly dependent upon the various deposition parameters. For instance, both the plasma current density and the floating self-bias potential ( $V_{sb}$ ) of surfaces in contact with a diode sputtering plasma increase, with different functional relationships, with an increase in the plasma power density. Besides floating potential induced bombardment processes, sputtering gas ions can also be reflected, and neutralized, at the target. In both cases the energy, energy distribution, and energetic particle flux are not easy to measure or predict.

The bombarding flux of particles (energy and angle) from a sputtering target due to sputtered atoms ( $E_0 \approx 5$  to  $10\text{eV}$ ) and reflected neutrals ( $E_0 > 100\text{eV}$ ) can be modified as a function of: total gas pressure, target-substrate distance, target voltage and power, substrate self-bias, plasma temperature, collision and charge exchange cross-sections, collision mean free path, scattering angle, and the masses of the target and gas atoms. The interdependence of some of these parameters makes it extremely difficult, if not impossible, to control any one of them independent of the others. Such is the case in magnetron (dc and rf), triode, and diode sputtering where the operating pressures and/or lack of plasma confinement near the target surface dictates an "averaging approach" to selecting deposition parameters. That is, one selects the deposition conditions to produce final film properties that are the result of a number of intertwined sputtering parameters.

A number of studies (4-13) have been reported that investigate the interaction of atoms/ions with the plasma and the subsequent effects at the target (sputtering process) and the substrate (film evolution). Important parameters in these analyses are the collision and charge exchange cross-sections, both of which are energy dependent (7). The careful use of these cross-sections allows one to predict the energy exchange and post-collision scattering angle between colliding atoms. This information, coupled with the make-up of the plasma (mass of sputtering gas, total gas pressure and target-to-substrate distance), can be used to calculate the effects of multiple collisions. The averaged energy loss per collision is normally used to calculate the mean free path and the final angular and energy distributions of the particles (4,5,10,12). However, recently Monte Carlo calculation methods have been introduced by Motohiro and Taga (8) and Somekh (7) to study what occurs along the trajectory of an atom/ion, and give insights into the particle transport process. These studies show in more detail than in previous ones (4,5,12) that the reduction in initial energy of sputtered atoms and reflected neutrals is a function of the product of gas pressure and target-substrate distance (7), i.e., pressure-distance product. Figure 1 illustrates the trajectories of sputtered Ag particles as a function of gas pressure and target-substrate distance. It is evident from this modeling that significant modification of the initial angular and energy distributions of sputtered and reflected neutrals occurs in the plasma as the deposition parameters are changed. Major changes can also occur in final particle distributions by varying the type of gas used in the plasma, the target-substrate distance, and the target material. In addition to these effects, it has been found that the return rate to the target of the sputtered particles depends on gas pressure and target-substrate distance. Also, the ratio of the atomic numbers between the target and sputtered gas atoms can control the arrival rate at the substrate and the return rate to the target of the sputtered atoms (8). Such dependencies can affect the composition and/or

structure of the final film as can different atomic masses having different angular distributions at the substrate. Rarefaction of the gas density in front of a magnetron target as a function of the magnetron current has also been reported (13). This reduction in gas density is due to collisional heating of the gas by sputtered atoms, and results in changes in film bombardment. These changes, in turn, can produce variations in composition as well as film stress and grain size.

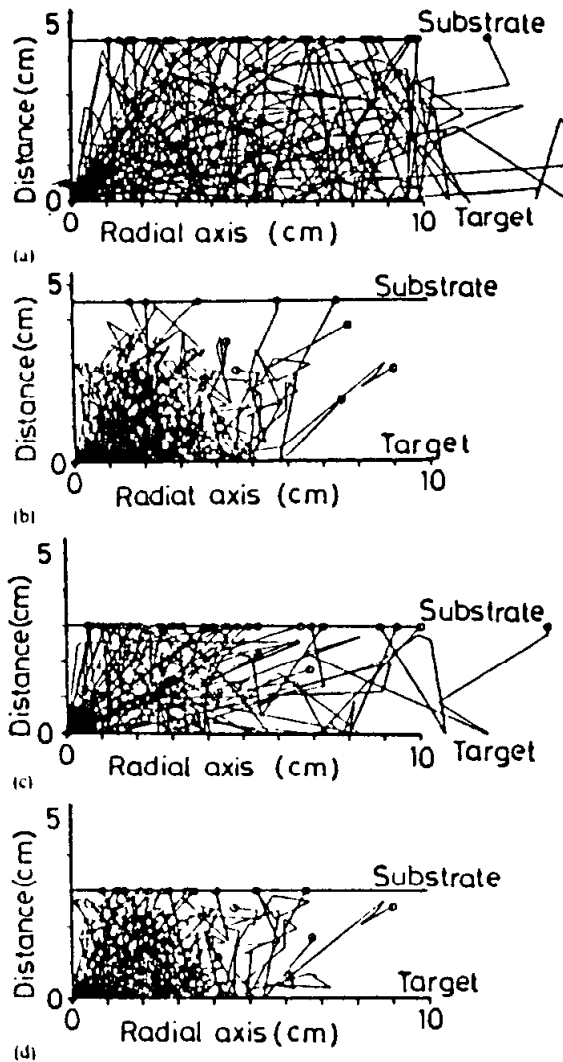


**Figure 1:** Computer generated trajectories of 50 silver atoms ejected into an argon gas at a pressure,  $P$ , and target-substrate distance,  $D$ . (a)  $P = 5\text{mTorr}$ ,  $D = 45\text{mm}$ ; (b)  $P = 15\text{mTorr}$ ,  $D = 45\text{mm}$ ; (c)  $P = 5\text{mTorr}$ ,  $D = 30\text{mm}$ ; (d)  $P = 15\text{mTorr}$ ,  $D = 30\text{mm}$ . (data from ref. 8).

Ion beam sources have become essential tools in fundamental studies of ion-surface interactions because they allow for the independent control of energetic particle bombardment processes. With the development of efficient Kaufman type broad beam ion sources capable of both low energy and high ion flux (14), it is possible to controllably bombard a growing film with an energy input ranging from 1 to 1000eV per depositing atom. These sources typically operate at low gas pressures ( $< 10^{-4}$  Torr) and as such do not have the added complication of gas scattering events. Generally the ion energy ( $E_i$ ) can be varied from 10 to more than 1000eV with the ion flux ranging from 0.02 to 2 mA/cm<sup>2</sup>, with independent control over both bombardment parameters. Together with the mass of the bombarding ions and the depositing atoms, the ion-surface interaction is defined in a quantitative and reproducible manner. For typical deposition rates (1 to 30 Å/sec) this allows for either low ion energy or low ion flux while still maintaining the range of energy per depositing atom indicated above. This can be important when the

particular property being controlled requires a limited range of acceptable parameters: for example, low ion energy to minimize bombardment induced short range disorder.

### 19.3 ION BOMBARDMENT-PROPERTY RELATIONS

The modification of thin film properties by simultaneous ion bombardment during deposition has been the topic of a number of papers over the years. Harper et al. (15) have summarized 16 examples where sufficient data was obtainable (Table 1) to compare structure related property modification using a "universal plot" which is shown in Fig. 2. As seen in this figure and table, most of the data are for ion energies greater than 100eV. This is representative of the available literature. Only within the last several years have an increasing number of such studies explored the lower energy regime ( $<100\text{eV}$ ). Since most of these property changes have only been phenomenologically related to the ion bombardment conditions, no fundamental understandings have been developed in large part. Several recent studies have gone beyond the simple empirical preparation-property relations and are providing insights into the atomic level connections between controlled ion-surface interactions and resulting lattice distortion and, in turn, the compressive stress in polycrystalline thin films.

**Table 1:** Examples plotted in Fig. 2 of thin film property modification by ion bombardment during deposition (from Ref. 15)

Num.	Film material	Ion species	Property modified	Ion energy (eV)	Ion/atom arrival rate ratio
1	Ge	Ar <sup>+</sup>	stress, adhn.	65-3000	$2 \times 10^{-4}$ to $10^{-1}$
2	Nb	Ar <sup>+</sup>	stress	100-400	$3 \times 10^{-2}$
3	Cr	Ar <sup>+</sup> , Xe <sup>+</sup>	stress	3400-11500	$8 \times 10^{-3}$ to $4 \times 10^{-2}$
4	Cr	Ar <sup>+</sup>	stress	200-800	$\approx 7 \times 10^{-3}$ to $2 \times 10^{-2}$
5	SiO <sub>2</sub>	Ar <sup>+</sup>	step coverage	500	0.3
6	SiO <sub>2</sub>	Ar <sup>+</sup>	step coverage	$\approx 1 - 80$	$\approx 4$
7	AlN	N <sub>2</sub> <sup>+</sup>	preferred orientation	300-500	0.96 to 1.5
8	Au	Ar <sup>+</sup>	coverage at 50 Å thickness	400	0.1
9	GdCoMo	Ar <sup>+</sup>	magnetic anisotropy	$\approx 1 - 150$	$\approx 0.1$
10	Cu	Cu <sup>+</sup>	improved epitaxy	$50 \approx 400$	$10^{-2}$
11	BN	(B-N-H) <sup>+</sup>	cubic structure	200-1000	$\approx 1$
12	ZrO <sub>2</sub> , TiO <sub>2</sub>	Ar <sup>+</sup> , O <sub>2</sub> <sup>+</sup>	refractive index amorph. → crys.	600	$2.5 \times 10^{-2}$ to 0.1
13	SiO <sub>2</sub> , TiO <sub>2</sub>	O <sub>2</sub> <sup>+</sup>	refractive index	300	0.12
14	SiO <sub>2</sub> , TiO <sub>2</sub>	O <sub>2</sub> <sup>+</sup>	optical transmission	30-500	0.05 to 0.25
15	Cu	N <sup>+</sup> , Ar <sup>+</sup>	adhesion	50000	$10^{-2}$
16	Ni on Fe	Ar <sup>+</sup>	hardness	10000-20000	$\approx 0.25$

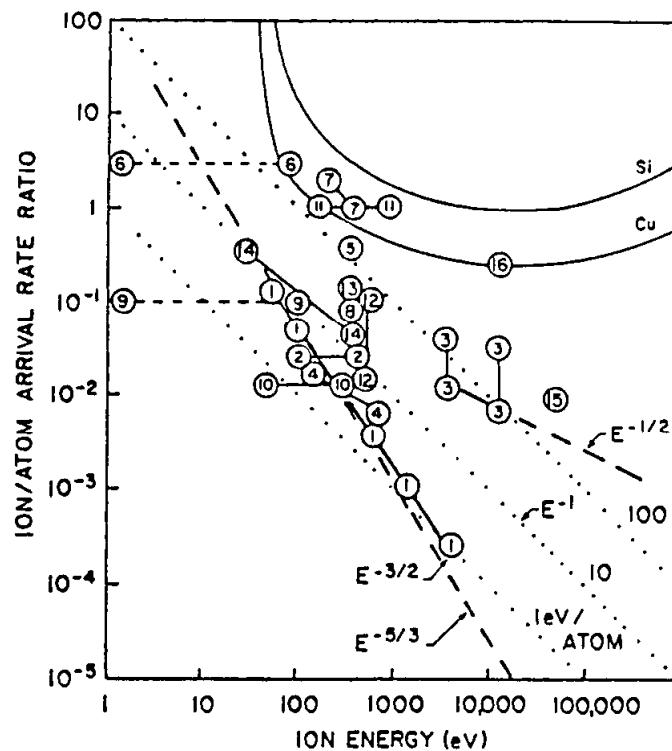


**Figure 2:** Ion bombardment modification of several different thin film properties as a function of the ion energy and ion to atom arrival rate ratio needed to cause modification. (from Ref 15.)

Windischmann (16) has developed a model based upon the elastic modulus and the molar volume of the film material and the lattice distortion resulting from energetic particle bombardment. An assumption in this model is that the thin film material-specific properties are the same as the bulk properties, which is reasonable in light of the preponderance of evidence reporting dense (low void volume) films for ion bombarded films with associated high compressive stress state when deposited with concurrent ion bombardment. Based upon Sigmund's theory of forward sputtering (17) in a film under energetic particle bombardment, Windischmann derived an expression for stress ( $S$ ),

$$S = 1.91K \Phi_i E_i^{1/2} Q / N_o \quad (1)$$

in which  $K$  is a proportionality factor relating relative volumetric strain to the fractional number of atoms displaced from equilibrium sites under the energetic bombardment,  $\Phi_i$  is the ion flux,  $E_i$  is the energetic particle's energy,  $N_o$  Avogadro's number, and  $Q$  represents the elastic energy per mole [ $Q = EM / (1 - \nu)D$ ] where  $E$  is Young's modulus,  $M$  is the atomic mass, and  $\nu$  is Poisson's ratio. Thus the bombardment induced stress is related to the physical properties of the material, the relative atomic number and mass of the bombarding particle and film material, and to the bombarding particle energy and flux.

The ideas of ion-surface interactions leading to both elastic (18,19) and elastic plus plastic (20) lattice distortions are clearly reflected in lattice spacing dilation measurements. These and similar studies are consistent with Windischmann's work. An important further conclusion from his model is that stress is related to the momentum rather than the energy of the incident particle, as indicated by the square-root dependence of  $E_i$ . This is supported by previous experimental studies of Hoffman and Gaertner (21), and Ziemann and Kay (22) for polycrystalline metal films and Nir (23) for amorphous diamond-like films.

Windischmann measured the stress vs.  $Q$  relation for 30 samples from both his study (by ion beam sputtering) and others (mainly magnetron sputtering) and found a linear curve fit the data. This is shown in Fig. 3, and Table 2. The samples were all about the same thickness and subjected to sufficient energetic particle bombardment to insure nearly fully-dense films. It is interesting to note that for thermal evaporation without concurrent ion bombardment the stress is tensile and shows no correlation with the  $S$  vs.  $Q$  linear relation. One possible explanation suggested was that films prepared under low mobility conditions are known to contain a significant percentage of void volume which may invalidate the use of bulk properties in calculating  $Q$ .

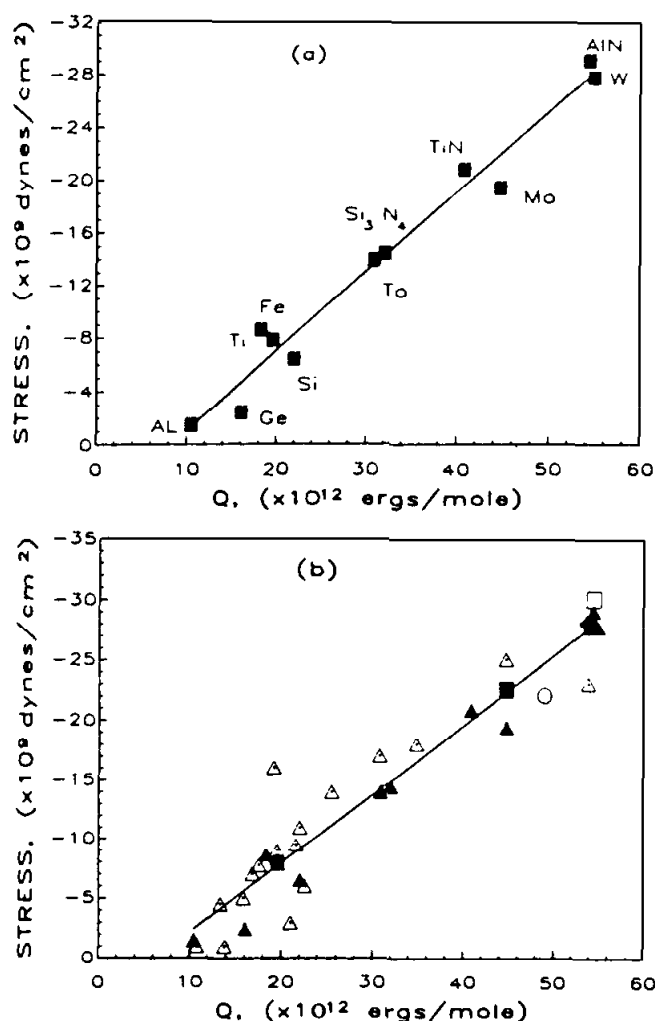


**Figure 3:** Variation of intrinsic stress with  $Q$ , the elastic energy/mole, for films prepared by (a) ion beam sputtering and (b) the present data superimposed on data taken from the literature for other deposition techniques, as shown in Table 2. (data from Ref 16.)

**Table 2:** Compressive stress data from the literature and calculated Q values for films deposited by various sputtering techniques (from Ref. 16).

Material	Stress ( $\times 10^9$ dyne/cm <sup>2</sup> )	Q ( $\times 10^{12}$ erg/mole)	Deposition technique
Al	1	10.4	MS
Ni	3	21.1	MS
Ti	16	18.3	MS
V	7	16.8	MS
Gd	5	15.8	MS
Cr	12-14	25.5	MS
Rh	18	34.8	MS
Zr	9	21.6	MS
Pt	6	22.5	MS
Si	11	22.0	MS
Nb	9	19.5	MS
Nb	9.5	19.5	MS
Mo	20-25	44.7	IBS
Mo	25-30	44.7	MS
Ta	18-20	30.8	MS
W	23	54.0	MS
W	29	54.0	RFS/triode
ZrO <sub>2</sub>	22	49.0	RFS/diode
AlN	30	54.5	MS

MS = magnetron sputtering. RFS = rf sputtering. IBS = ion beam sputtering.

A more direct method for examining the bombardment induced lattice distortion during ion-assisted evaporation is to perform a molecular dynamics (MD) calculation of the deposition and concurrent energetic bombardment processes. Müller (24) has carried out 2-dimensional MD calculations using a Lennard-Jones potential for film-atom inter-atomic potentials, descriptive of close packed metal atomic structures, while the Ar bombarding particle-film atom interaction is described by a Moliere potential. Further assumptions include normal incidence of both the depositing vapor and bombarding particles, an absolute zero temperature substrate, a limited number of atoms considered ( $\approx 500$ ) and related small simulation cell with periodic boundary conditions, and a purely repulsive Ar-film atom interaction which excludes the possibility of Ar entrapment.

Despite these limitations, imposed in part by the cost and speed of present-day computers, it has been shown that simple stress calculations of the final simulation cell atomic positions for Ar<sup>+</sup> bombardment of a Ni growing film lead to a stress vs. bombarding energy curve in qualitative agreement with experimental data such as that described by Windischmann (16) and references therein. Under zero and low bombardment energy the

stress is tensile and increases, instead of decreasing, to a maximum value at 3.2eV per deposited film atom before decreasing as Windischmann has shown. At these conditions the voids are still present, though becoming smaller and less connected, and related to the tensile stress. Only at higher Ar bombardment energies (at a fixed ion-to-atom rate ratio ( $\Phi_i/\Phi_a$ ) of 0.16) does the tensile stress decrease and at the same time the voids are even smaller and fewer in number. Unfortunately his simulations were not carried out to high enough energies or arrival rate ratios to reach a dense morphology (minimal void content) with a maximum value of compressive stress. Thus, his simulations cannot be directly compared to the Windischmann model (16) calculations.

#### 19.4 ION BOMBARDMENT-STRUCTURE RELATIONS

The present status of models describing thin film morphology is the qualitative representations provided by the structure zone models (SZM's) of Movchan and Demchishin (25), Thornton (26), and Messier et al. (2,27). The salient features of each representation are the effects of: temperature on evaporated films (25); temperature and bombardment from both normal and oblique deposition components and variations with sputtering gas pressure (26) and thickness evolution and the bombardment controlled by the  $V_{sb}$  dependence on the sputtering gas pressure (27). These classification schemes are discussed in more detail in another chapter.

The density deficit regions (normally referred to as voids) which are seen in Fig. 4, and have been noted in the SZM's described above, are not uniformly dispersed throughout a thin film but form in a self-organized array, commonly referred to as a void network throughout the film. These are most easily imaged using a defocused phase-contrast technique in a transmission electron microscope (28) and are directly related to the cauliflower-like structures seen in SEM micrographs of thicker films typically used to define the SZM's. These void regions delineate the columns found in thin films, especially those grown under low adatom mobility conditions. It is the competition between these columnar units which is directly affected by ion-surface interactions. In turn, the optical density and properties which are affected by density change, can be influenced to a large extent. It is apparent that understanding the clustering of adatoms and the competition between the resulting columnar structures is imperative if a quantitative connection between these microscopic processes and measured macroscopic properties are to be achieved. Unfortunately, these structural units contain many atoms, and solutions will have to await more powerful computers and computation schemes.

The importance of molecular dynamics calculations in linking our understanding between ion-surface interactions, resulting short- and intermediate-range structure, and film properties are seen in the above example. At the same time it points out the practical difficulties in this approach. If computers were available to carry out the simulations that are clearly needed, then significant progress in our fundamental understanding of ion-surface interactions could be made rapidly. However, that not being the case, limited MD calculations which address only portions of the larger problems, will have to be used. Furthermore, the coordination of such simulation studies with highly defined experimental studies should lead to progress in the ion-surface interaction field.

Early attempts at simulating thin film growth involved simple hard sphere (billiard ball) approach (29), to more sophisticated Monte Carlo (30-32) and molecular dynamics (24,29,33,34) methods. Recent studies, though, have provided the most detailed and re-

alistic modeling efforts to date. For instance, in an extension of the MD simulations described above, Müller (24) has determined the density of his computer generated Ni "films" as a function of both  $E_i$  (0 to 100 eV  $\text{Ar}^+$ ) and  $\Phi_i/\Phi_a$  (0 to 0.16) and shown that the trends in his simulated experiments are consistent with real deposition experiments.

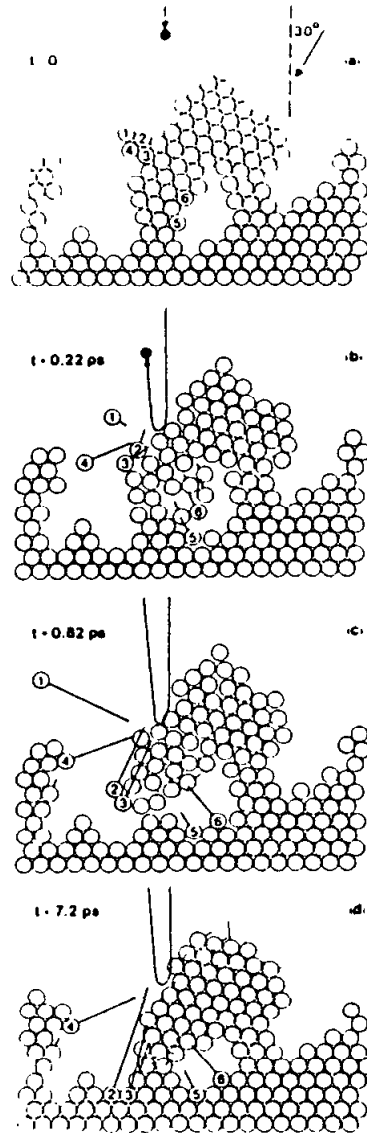


**Figure 4:** Molecular dynamics simulation of a low energy ion-surface interaction. (from Ref 35.)

Film density is a fundamental factor in any preparation-property relation. Furthermore, it is not expected that the average density will be nearly as crucial as the atomistic details - lattice distortions, interstitials, vacancies, vacancy clusters, and voids, and atomic-level fluctuations in these structural defects which lead to void networks and density fluctuations. The latter structural details are not singular entities but will need to be described by distribution functions if a detailed and realistic understanding of thin film structure (or what is often called microstructure or morphology) is to be developed. At this stage of understanding it is known that such nanometer-level defects are present, but there is no quantitative description of them, and it is not known if such detailed information can be combined into an average quantity, such as average film density, without losing the fundamental aspect of the structure-property relation. Thus, it is suggested that the statistical nature of film microstructure must be addressed if any significant fundamental progress in ion-surface interaction effects is to be made.



In order to demonstrate the complexity of the various processes occurring during ion-surface interactions and their effects on atomic-level structure, a time sequence during an ion-surface collision process is considered. In Fig. 4, Müller (35) simulates an ion-surface interaction event in which a low energy  $\text{Ar}^+$  ion (100 eV) collides with a porous columnar Ni film at its early stages of formation on a perfect 2-dimensional Ni lattice. The Ni vapor, with energy representative of thermally evaporated atoms (0.1 eV), impinges at  $30^\circ$  from the surface normal while the  $\text{Ar}^+$  bombardment is at normal incidence. These deposition conditions and configurations are typical of the ion-assisted deposition process. Upon impact the Ar ion transfers a part of its kinetic energy to the surface atoms which, in turn, transfer their kinetic energy to other surface and sub-surface atoms. A large number of atoms are displaced (Fig. 4) and are indicated by the straight lines (not trajectories) which indicate only their initial and final (or intermediate) positions. Six atoms which suffered large displacements are numbered and are indicative of the range of different mechanisms of bombardment induced structural rearrangement. Atom 1 is completely sputtered from the film while the other five atoms are driven deeper into the film structure. Atoms 2 and 3 migrate along the surface of the central cluster and end finally at the bottom of the cluster at the original substrate interface. Atom 4 is sputtered from the surface and redeposits on an adjoining column while atoms 5 and 6 are also sputtered/redeposited but within a closed void. In addition to these large displacements, a large number of smaller displacements occur collectively at the latter stages of the lattice relaxation process. It is noted that the loosely bound overhanging atoms (1-4) have been eliminated and many atoms have been driven to lower-lying states as a result of just a single ion-surface interaction event.

### 19.5 THE INTERACTION OF IONS WITH THE GROWING FILM

The processes occurring when a growing film is bombarded by energetic ions or neutral species must be considered (36). For "non-reactive" bombarding species (not chemically reactive with the depositing species), the situation is simplified somewhat. The main processes which can occur are: (1) momentum transfer (knock-on) displacement; and (2) direct temperature effects (thermal annealing due to temperature rise caused by thermal spikes). These processes can in turn cause various effects as the thin film grows, including enhanced surface mobility, enhanced accretion of nuclei, desorption of surface impurities, redistribution of atoms in the film, and also the implantation of bombarding species into the growing film (37).

The idea of thermal spike generation is not new and has been considered by others as a mechanism for sputter ejection of atoms (38). Weissmantel et al. (39) have used the idea of thermal spike generation and the production of a shock zone front to explain the formation of metastable phases of cubic BN and diamond-like carbon films. Because of the rapid rise and fall of the temperature spike and the higher pressures caused by the shock wave generated by an impacting ion it has been suggested that a high pressure metastable structure can be formed and then frozen in. Hirsch and Varga (40) have also suggested that an annealing affect is present in thin films undergoing simultaneous ion bombardment during growth due to thermal spike generation, and that this has a threshold which is dependent on the "intensity" of ion bombardment. Martin et al. (41) have also suggested that ion impact crystallization, via thermal spikes, may be the mechanism responsible for the appearance of the cubic phase of  $\text{ZrO}_2$  undergoing energetic ion bombardment.

Müller (30) has used 2-dimensional Monte Carlo calculations to simulate the effects of thermal spike generation on the structure of vapor deposited films. He has shown that the elongated voids found in thin films due to low adatom mobility are bridged, forming a structure with isolated pockets, but still appearing to have a large fraction of voids left in the films. He also finds a dependence on the energy of the incoming ions and the ion to atom arrival rate ratio; namely for  $E_i = 150 \text{ eV Ar}^+$ , as  $\Phi_i/\Phi_a$  is increased, the elongated voids are bridged to a greater extent. If, however,  $E_i$  is increased, the arrival rate ratio needed to cause the same degree of bridging is now less. In both cases, however, there still exists a large fraction of voids. From this it can be concluded that, although thermal spike generation can affect the thin film structure, it appears not to be a dominant process. Thus the generation of thermal spikes appears to be a mechanism of inducing a phase change (39,41), but not a dominant mechanism in densification of films due to the filling in of voids.

The momentum transfer process takes into account the displacement of deposited atoms due to bombarding species. This displacement can take on several forms; resputtering of deposited atoms which results in a net loss of film atoms, forward sputtering which leads to a densification and filling in of voids, lattice relaxation, and, of course, the impacting ion may also implant in the growing thin film, acting as an impurity. Several of these effects are shown in Fig. 4. Because of the variation in sputtering yields as a function of incident ion energy, the use of lower energy ions ( $\approx 100 \text{ eV}$ ) will result in more forward sputtering and redistribution than the complete resputtering of deposited species. In addition, since the incorporation of bombarding species has been shown to be dependent on incident ion energy, the use of lower energy ions has an advantage of minimizing these incorporated atoms.

It has been shown previously (16) that momentum characterizes the behavior of stress in a series of materials covering the range from metals to semiconductors to insulators, thus showing wide applicability. Targrove et al. (42) have also addressed the question of momentum transfer, and found it to be the dominant mechanism in the densification of  $\text{LaF}_3$  thin films, using ion-assisted evaporation. By observing the changes in the index of refraction as a function of the momentum imparted to the film, a good correlation with momentum was observed.

In recent studies (43,44), the role of lower energy ion bombardment on the changes in density (void fraction) and other properties (optical band gap and inert gas incorporation) using ion-assisted evaporation has also pointed to momentum transfer being an important aspect in modifying the density, a fundamental characteristic of a material upon which many properties depend. Amorphous Ge was used as a model system for these studies, and in view of the general applicability of such representations as the structure zone models (2,25-27), the results are believed to be of general applicability to other material systems.

Using spectroscopic ellipsometry for the determination of the density (void fraction), it has been shown that the density exhibits a common behavior when plotted in terms of the energy deposited per arriving atom ( $E_n$ ) for the energy range of 15 to 600 eV (Fig. 5). Several unique features are observed, with three distinct regions present. At low levels of bombardment, there is a sharp rise in density followed by a leveling off. This can be explained as due to bombardment induced densification and "annealing" of the film as it grows. However, as the energy of the incoming ion increases, another competing effect

must be addressed: bombardment-induced damage. This is believed to be the cause of the sudden drop in density seen in Fig. 5. Whether this damage is due to network induced disorder or to an increase in the implantation of Ar is not known. It is apparent, though, that the combined effects of energy and flux are important for the film densification process.

To better understand the nature of this possible effect, the previous literature on bombardment-induced damage is considered. From the literature on sputtering yield measurements and radiation damage (45), the critical energy which is necessary to cause displacements can be taken to first order as 4 times the heat of sublimation, i.e.  $4\Delta H_{\text{subl}}$ . For Ge,  $\Delta H_{\text{subl}} = 4.08 \text{ eV}$  (46). Using this value, a critical  $\Phi_i/\Phi_a$  for each incident ion energy can be calculated. If an elastic energy transfer is assumed and correction is made for the angle-of-incidence of the ions with respect to the substrate normal, then a  $(\Phi_i/\Phi_a)_{\text{critical}}$  can be given as follows:

$$(\Phi_i/\Phi_a)_{\text{critical}} = \frac{\Delta H_{\text{subl}}(m_i + m_a)^2}{m_i m_a E_i \cos \Theta_i} \quad (2)$$

where  $m_i$  and  $m_a$  are the ion and atom masses, respectively. In Table 3 are the calculated  $(\Phi_i/\Phi_a)_{\text{critical}}$  values along with the  $(E_n)_{\text{critical}}$  values obtained by multiplying  $(\Phi_i/\Phi_a)_{\text{critical}}$  by  $E_i \cos \Theta_i$ . This represents the critical threshold energy per deposited atom necessary to cause displacement type damage. This value of  $E_n = 17.8 \text{ eV/Ge}$  is in good agreement with Fig. 5 ( $E_n \approx 18 \text{ eV/Ge}$  with an uncertainty of a few eV/Ge), thereby lending support for this mechanism.

**Table 3:** Calculation of the critical  $\Phi_i/\Phi_a$  and  $E_n$  for  $\text{Ar}^+$  bombardment of a-Ge using Eqn. 2, which assumes elastic energy transfer and corrects for the angle-of-incidence of the ion with respect to the substrate normal ( $\Delta H_{\text{subl}} = 4.08 \text{ eV}$  and  $\Theta_i = 30^\circ$ ) (from Ref. 43).

$E_i$ (eV)	$(\frac{\Phi_i}{\Phi_a})_{\text{critical}}$	$(E_n)_{\text{critical}}$ (eV/Ge)
600	0.034	17.8
400	0.051	"
200	0.103	"
90	0.229	"
70	0.294	"
50	0.412	"
30	0.686	"
15	1.372	"

As mentioned previously, Müller (24) has modeled the effects of momentum transfer using a 2-dimensional MD simulation for evaporated Ni with  $\text{Ar}^+$  assist;  $E_i$  varied from 0 to 100 eV and  $\Phi_i/\Phi_a$  from 0 to 0.16. He found that low energies and small  $\Phi_i/\Phi_a$  are

enough to cause substantial modification of the void structure with the packing density increasing from 0.74 (as-deposited Ni with no bombardment) to 0.84 (10 eV Ar) and 0.95 (50 eV Ar), both at  $\Phi_i/\Phi_a = 0.16$ . This range of energies and arrival rate ratios is similar to that used by Yehoda et al. (43) and Yehoda (44). However, care must be taken when making exact comparisons due to the 2-dimensional nature of the simulations, but general trends should be similar. Although Müller (35) does not show a saturation in the packing density at the higher levels of bombardment, he does indicate that this saturation was observed but was not studied extensively due to the high cost of computation time. If the simple model of Eqn. 2 is applied to his work, it is found that  $(\Phi_i/\Phi_a)_{\text{critical}} = 0.64$  for 50 eV Ar bombardment, corresponding to  $(E_n)_{\text{critical}} = 24\text{eV/Ni}$  ( $\Delta H_{\text{subl}} = 6.72\text{eV}$  for Ni). Since his simulations do not consider flux ratios larger than 0.16, the correspondence with Eqn. 2 could not be checked.

Using a 3-dimensional Monte Carlo collision cascade simulation, Müller (31) has developed a model which attempts to explain the densification which takes place during ion bombardment due to surface sputtering and recoil implantation, followed by constant re-filling from the vapor atoms. He was able to generate density profiles of  $\text{ZrO}_2$  films bombarded by  $\text{O}^+$ , in addition to film density changes versus  $\Phi_i/\Phi_a$  for 600 eV  $\text{O}^+$ . His results are in agreement with similar experimental evidence by Martin et al. (41) for ion assisted  $\text{ZrO}_2$  evaporated films. The theory starts to breakdown at higher  $\Phi_i/\Phi_a$  where experiments find that densification saturates while the theory predicts a continual increase. This discrepancy can easily be accounted for, though, since repulsive effects between the film atoms were not taken into account. It would be interesting to perform depth profiling on films of this type to compare an experimental depth distribution of the atoms with those generated by Müller.

Similarly, using experimental results on  $\text{CeO}_2$  evaporated with  $\text{O}_2^+$  ion assist (47) Müller (32) has formulated a simulation which describes the bulk density changes in an ion assisted film in terms of the sputtering yields of atoms on the surface, their recoil implantation, and the incorporation of ions. What he finds is that there exists a density increase with increasing  $\Phi_i/\Phi_a$  at fixed  $E_i$ . Additionally, if  $\Phi_i/\Phi_a$  is held constant with  $E_i$  varying, an optimum film density occurring at  $E_n \approx 167\text{eV/CeO}_2$  was found, with the density decreasing at higher  $E_i$ . Experimentally this is also observed, but the fall off is at a much slower rate. This behavior was similarly observed for the a-Ge when plotted in terms of  $E_n$  (Fig. 5). If Eqn. 2 is applied to  $\text{O}^+$  bombarding  $\text{CeO}_2$  ( $\Theta_v = 30^\circ$ ), then  $(E_n)_{\text{critical}} \approx 78\text{ eV/CeO}_2$ , since  $\Delta H_{\text{subl}} = 7\text{ eV}$  (32). It is apparent that this value of  $(E_n)_{\text{critical}}$  is approximately half that found by Müller. Four possible explanations for these differences are: (1) Eqn. 2 is only a very simplified representation taking into account damage due to impinging ions, and does not address other important factors such as recoil implantation and ion incorporation, which Müller includes; (2) the value  $4\Delta H_{\text{subl}}$  used in obtaining Eqn. 2 is only an approximation to the damage threshold in a material, where significant damage may not occur until several times this value is transferred to the structure; (3) since the material is being bombarded with a chemically active ion, its effects on adatom mobility may be such that more energy is necessary to cause rearrangement; (4) the choice of target mass in Eqn. 2 is not all that straightforward for a compound, whereas for a single component film the choice is obvious. At this stage more work is needed to understand the relative importance of these factors.

For films of  $\text{SiO}_2$  and  $\text{TiO}_2$  deposited by ion-assisted evaporation, with energies of 30 and 500 eV, McNeil et al. (48) observed a change in the optical transmission

( $T_{\text{substrate}} - T_{\text{film/substrate}}$ ) of the films with respect to the bare silica substrate at  $\lambda = 2500\text{\AA}$ . For  $\text{SiO}_2$  films, the transmission changed little under 30 eV  $\text{O}_2^+$  bombardment while under 500 eV bombardment it decreased by up to 12%. In  $\text{TiO}_2$  the changes at 30 eV were again small, while 500 eV bombardment caused an even greater decrease under low to moderate fluxes. Their explanation for this behavior is the preferential resputtering of oxygen which causes an enrichment in Si or Ti, resulting in increased absorption. Thus, selecting the degree of bombardment is seen to be important in achieving a desired result.

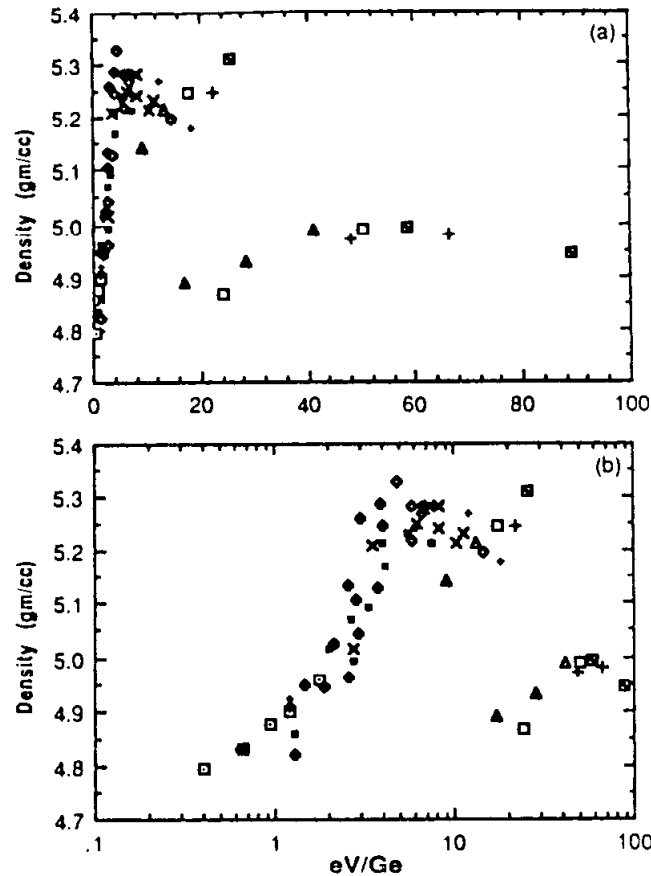


**Figure 5:** Density versus energy deposited per arriving Ge atom ( $E_n$ ) for different ion energies. 15 eV ( $\square$ ); 30 eV ( $\blacklozenge$ ); 50 eV ( $\blacksquare$ ); (b) 70 eV ( $\diamond$ ); 90 eV (X); 110 eV (+); 200 eV ( $\blacktriangle$ ); 300 eV ( $\triangle$ ); 400 eV ( $\square$ ); 500 eV (+); and 600 eV ( $\square$ ) Ar. (from ref. 43.)

Hultman et al.(49) have observed a critical substrate bias voltage where the dislocation loop density is a minimum in epitaxial TiN films grown by reactive magnetron sputtering. Above this critical voltage the dislocation loop density is found to increase, a result of lattice damage from excessive ion bombardment. At the low bias voltages, they attribute the increased defect density to the low adatom mobility of the films which results in point defects aggregating to form dislocation loops. Since no values for ion densities bombarding the film are given, Eqn. 2 cannot be used for a comparison.

Whereas most of the previous examples have dealt with compound systems, Huang et al. (18) and Parmigiani et al. (50) looked at the effects of Ar bombardment on Ag films grown by dual ion beam sputtering as a function of the normalized energy  $E_n$  (eV/Ag atom). Their results for the dislocation density did not show a minimum as did Hultman

et al. (49). This may be a consequence of the minimum energy deposited into the film already being surpassed. If Eqn. 2 is used to calculate the  $(E_n)_{\text{critical}}$  for Ar on Ag, it gives  $E_n = 21.8 \text{ eV/Ag}$ , the value at which we would expect damage to start to occur. In their study, the minimum  $E_n$  was approximately 20 eV/Ag, very close to the calculated critical value. Void fractions in these films show a continual decrease with increasing  $E_n$ . This may not show the initial increase followed by a plateau and then a decrease as seen in Fig. 5, because of the higher initial starting value of  $E_n$ .

These are just a few representative examples which show the importance of ion-surface interactions and how controlling ion flux and energy can have important consequences on thin film characteristics and related properties.

## 19.6 CONCLUSIONS

The state of knowledge concerning ion-surface interactions with regard to thin film growth and evolution has only recently been addressed in a systematic and quantitative manner. The low energy regime of bombardment ( $< 100 \text{ eV}$ ) is found to be necessary and desirable in view of the results concerning densification and inert gas incorporation, and is an area where attention has only recently been given. In addition, the importance of momentum transfer in modifying the thin film structure is apparent. Although not specifically addressed in this chapter, molecular dynamics simulations of epitaxial growth have shown that optimum energies of the depositing atoms are on the order of 5 to 10 eV (51,52), again pointing toward low energy processes. Extension of the molecular dynamics modeling to thicker films and especially to 3-dimensions is necessary to gain a more complete understanding between theory and experiment. Each of these approaches will help lead to a quantitative description of thin film growth and the role that ion-surface interactions play.

## 19.7 REFERENCES

1. For instance: Vossen, J.L. and Kern, W. (eds), *Thin Film Processes*, (New York: Academic Press, Inc., 1978) (1978); Bunshah, R.F., et al. (eds), *Deposition Technologies for Films and Coatings: Developments and Applications*, (Noyes Publications, New Jersey 1982); Chapman, B., *Glow Discharge Processes: Sputtering and Plasma Etching*, (John Wiley & Sons, New York, 1980).
2. Messier, R., Toward quantification of thin film morphology. *J. Vac. Sci. Technol.* A4: 490-95 (1986).
3. Yehoda, J.E. and Messier, R., Quantitative analysis of thin film morphology evolution. *Proc. SPIE* 678: 32-40 (1986).
4. Wu, C.T., Kampwirth, R.T., and Hafstrom, J., High-rate magnetron sputtering of high  $T_c$   $\text{Nb}_3\text{Sn}$  films. *J. Vac. Sci. Technol.* 14: 134-37 (1977).
5. Cadieu, F.J. and Chencincki, N., Selective thermalization in sputtering to produce high  $T_c$  films. *IEEE Trans. Mag.* 11: 227-30 (1975).
6. Robinson, R.S., Energetic binary collisions in rare gas plasmas. *J. Vac. Sci. Technol.* 16: 185-88 (1979).
7. Somekh, R.E., Calculations of thermalization during the sputter deposition process. *Vacuum* 34: 987-90 (1984).

8. Motohiro, T. and Taga, Y., Monte Carlo simulation of the particle transport process in sputter deposition. Thin Solid Films 112: 161-67 (1984).
9. Schuller, I.K., New class of layered materials. Phys. Rev. Lett. 1597-600 (1980)
10. Meyer, K., Schuller, I.K., and Falco, C.M., Thermalization of sputtered atoms. J. Appl. Phys. 52: 5803-08 (1981).
11. Hoffman, D.W. and Thornton, J.A., Internal stresses in sputtered chromium. Thin Solid Films 40: 355-63 (1977).
12. Westwood, W.D., Calculation of deposition rates in diode sputtering systems. J. Vac. Sci. Technol. 15: 1-9 (1978).
13. Rossnagel, S.M., Gas density effects in magnetrons. J. Vac. Sci. Technol. A6: 19-24 (1988).
14. Kaufman, H.R., Cuomo, J.J., and Harper J.M.E., Technology and applications of broad-beam ion sources used in sputtering. Part I. Ion source technology. J. Vac. Sci. Technol. 21: 725-36 (1982); and Harper, J.M.E., Cuomo, J.J., and Kaufman, H.R., Technology and applications of broad-beam ion sources used in sputtering. Part II. Applications. J. Vac. Sci. Technol. 21: 737-56 (1982).
15. Harper, J.M.E., Cuomo, J.J., Gambino, R.J., and Kaufman, H.R., Modification of thin film properties by ion bombardment during deposition. Nucl. Instrum. & Methods Phys. Res. B7/8: 886-92 (1985).
16. Windischmann, H., An intrinsic stress scaling law for polycrystalline thin films prepared by ion beam sputtering. J. Appl. Phys. 62: 1800-1807 (1987).
17. Sigmund, P., in: Sputtering by Particle Bombardment I, ed. by R. Behrisch, Chapter 2 (Springer-Verlag, New York 1981).
18. Huang, T.C., Lim, G., Parmigiani, F., and Kay, E., Effects of ion bombardment during deposition on the x-ray microstructure of thin silver films. J. Vac. Sci. Technol. A3: 2161-66 (1985).
19. Kay, E., Parmigiani, F., and Parrish, W., Effects of energetic neutralized noble gas ions on the structure of ion beam sputtered thin metal films. J. Vac. Sci. Technol. A5: 44-51 (1987).
20. Window, B. Sharples, F., and Savvides, N., Plastic flow in ion-assisted deposition of refractory metals. J. Vac. Sci. Technol. A6: 2333-40 (1988).
21. Hoffman, D.W. and Gaerttner, M.R., Modification of evaporated chromium by concurrent ion bombardment. J. Vac. Sci. Technol. 17: 425-28 (1980).
22. Ziemann, P. and Kay, E., Correlation between the ion bombardment during film growth of Pd films and their structural and electrical properties. J. Vac. Sci. Technol. A1: 512-16 (1983).
23. Nir, D., Energy dependence of the stress in diamond-like carbon films. J. Vac. Sci. Technol. A4: 2954-55 (1986).
24. Müller, K.-H., Ion-beam epitaxial vapor-phase growth: A molecular-dynamics study. Phys. Rev. B35: 7906-13 (1987).
25. Movchan, B.A. and Demchishin, A.V., Study of the structure and properties of thick vacuum condensates of nickel, titanium, tungsten, aluminium oxide and zirconium dioxide. Physics of Metals and Metallography 28: 83-90 (1969).

26. Thornton, J.A., High rate thick film growth. Ann. Rev. Mater. Sci. 7: 239-60 (1977).
27. Messier, R., Giri, A.P., and Roy, R.A., Revised structure zone model for thin film physical structure. J. Vac. Sci. Technol. A2: 500-03 (1984).
28. Staudinger, A. and Nakahara, S., The structure of the crack network in amorphous films. Thin Solid Films 45: 125-33 (1977).
29. Leamy, H.J., Gilmer, G.H., and Dirks, A.G., The microstructure of vapor deposited thin films. Current Topics in Materials Science Vol. 6, ed. E. Kaldis (North Holland, New York, 1980) 310-344.
30. Müller, K.-H., Monte Carlo calculation for structural modifications in ion-assisted thin film deposition due to thermal spikes. J. Vac. Sci. Technol. A4: 184-88 (1986).
31. Müller, K.-H., Model for ion-assisted thin-film densification. J. Appl. Phys. 59: 2803-07 (1986).
32. Müller, K.-H., Modelling ion-assisted deposition of CeO<sub>2</sub> films. Appl. Phys. A40: 209-13 (1986).
33. Müller, K.-H., Stress and microstructure of sputter-deposited thin films: Molecular dynamics investigations. J. Appl. Phys. 62: 1796-99 (1987).
34. Müller, K.-H., Molecular dynamics and collision cascade studies of ion-assisted thin film deposition. J. Vac. Sci. Technol. A5: 2161-62 (1987).
35. Müller, K.-H., unpublished
36. Kelly, R. and Auciello, O. (eds), Ion bombardment modification of surfaces: Fundamentals and applications, (Elsevier, New York, 1984).
37. Takagi, T., Role of ions in ion-based film formation. Thin Solid Films 92: 1-17 (1982).
38. Webb, R.P. and Harrison, D.E., Evidence for ion-induced hypersonic shock waves for computer simulations of argon ion bombardment of copper. Appl. Phys. Lett. 39: 311-12 (1981).
39. Weissmantel, C., Bewilogua, K., Dietrich, D., Erler, H.-J., Hinneberg, H.-J., Klose, S., Nowick, W., and Risse, G., Structure and properties of quasi-amorphous films prepared by ion beam techniques. Thin Solid Films 72: 19-31 (1980).
40. Hirsch, E.H. and Varga, I.K., Thin film annealing by ion bombardment. Thin Solid Films 69: 99-105 (1980).
41. Martin, P.J., Netterfield R.P., and Sainty, W.G., Modification of the optical and structural properties of dielectric ZrO<sub>2</sub> films by ion-assisted deposition. J. Appl. Phys. 55: 235-41 (1984).
42. Targove, J.D., Lingg, L.J., and Macleod, H.A., Verification of momentum transfer as the dominant densifying mechanism in ion-assisted deposition. Optical Interference Coatings 1988 Technical Digest Series (Optical Society of America) 6: 268-71 (1988).
43. Yehoda, J.E., Yang, B., Vedam, K., and Messier, R., Investigation of the void structure in amorphous germanium thin films as a function of low-energy ion bombardment. J. Vac. Sci. Technol. A6: 1631-35 (1988).
44. Yehoda, J.E., Influence of bombardment on the nanostructure and microstructure in amorphous germanium. Ph.D. Thesis, The Pennsylvania State University, (1988).



45. Stuart, R.V. and Wehner, G.K., Sputtering yields at very low bombarding energies. J. Appl. Phys. 33: 2345-52 (1962).
46. Smithells, C.J., Metals Reference Book, Fifth Ed., (Butterworths, London 1976).
47. Netterfield, R.P., Sainty, W.G., Martin, P.J., and Sie, S.H., Properties of CeO<sub>2</sub> thin films prepared by oxygen-ion-assisted deposition. Applied Optics 24: 2267-72 (1985).
48. McNeil, J.R., Barron, A.C., Wilson, W.C., and Herrmann, W.C., Ion-assisted deposition of optical thin films: Low energy vs high energy bombardment. Applied Optics 23: 552-59 (1984).
49. Hultman, L., Helmersson, U., Barnett, S.A., Sundgren, J.-E., and Green, J.E., The role of low-energy ion bombardment during the growth of epitaxial TiN (100) films by reactive magnetron sputtering: Defect formation and annihilation. J. Vac. Sci. Technol. A5: 2162-64 (1987).
50. Parmigiani, F., Kay, E., Huang, T.C., Perrin, J., Jurich, M., and Swalen J.D., Optical and electrical properties of thin silver films grown under ion bombardment. Phys. Rev. B33: 879-88 (1986).
51. Dodson, B.W. and Taylor, P.A., Interaction of a 10 eV silicon beam with the Si (111) surface: A molecular dynamics study. J. Mater. Res. 2: 805-08 (1987).
52. Garrison, B.J., Miller, M.T., and Brenner, D.W., Kinetic energy enhanced molecular beam epitaxial growth of Si {100}. Chem. Phys. Lett. (in press).

---

## **Ion Assisted Deposition**

---

**James J. McNally**

### **20.1 INTRODUCTION**

The optical, electrical, mechanical and chemical properties of materials in thin-film form can vary significantly from their bulk properties. These differences in properties are directly related to film microstructure which, for vacuum deposited films, is predominantly columnar, containing voids and material inhomogeneities. Modifications to film properties can occur when the film is subject to ion bombardment during growth. In fact, significant improvements have been realized with controlled ion bombardment of growing films. A detailed review of ion-surface interactions is not the intent of this chapter; nor, is a discussion of the various technique used to achieve film bombardment. Excellent treatment of those topics can be found in Reference 1 and the earlier chapters of this book.

The discussion in this chapter is focused on ion-assisted deposition (IAD). Ion assisted deposition is a plasma-based deposition technique that employs a separate ion source to direct a beam of ions at a growing film during deposition. A key distinction between conventional ion bombardment configurations and IAD is the isolation of the substrates from the ion production and acceleration process. This, in turn, permits separate control of the ion bombardment parameters independent of the material deposition process.

The following material is oriented toward a general overview with an emphasis on the fundamentals of the IAD process. References are given for in-depth treatments of several topics. In this chapter a brief background of the IAD process is given, followed by details on experimental arrangements and procedures. A results section follows that discusses specific effects that IAD has on film properties. The chapter concludes with a discussion of the limitations in applying IAD and some advantages over other energetic deposition techniques.

### **20.2 BACKGROUND**

The fundamental properties of vacuum deposited films vary significantly from their bulk values due to poor film microstructure. Microstructure-related effects on film prop-

erties can be observed in low optical refractive index, high optical scatter, low dielectric constant, varying grain size, low density and poor environmental durability and optical stability. A number of novel deposition techniques have been developed to overcome the weaknesses of films relative to bulk materials. In these techniques, energetic processes are employed to supply sufficient activation energies to increase adatom mobility and eliminate the formation of columnar microstructure (see detailed discussions in other chapters of this book). A shortcoming of some of these techniques is the lack of versatility in controlling the energetic/reactive process parameters independent of the film deposition parameters. Ion-assisted deposition uses a separate, well-controlled ion source to direct a beam of ions at the film surface during deposition. A separate ion source allows control of the ion energy, current density, arrival direction and species independent of the material deposition process (e.g. evaporation or sputtering). Note: the discussion in this chapter is restricted to using the Kaufman ion source for bombardment. See Ref. 2 for discussion of other ion sources.

The flexibility provided by a separate ion source allows the tailoring of the optical, electrical, structural and chemical properties through proper selection of ion parameters. It allows an examination of thin film growth processes and the fabrication of unique film properties. Examples of this are found in the low temperature deposition onto sensitive substrates of materials normally requiring elevated substrate temperatures (3). Examples are found in coatings where the film stoichiometry can be varied as a function of thickness (4,5). Other examples are found in the modification of stress in Nb films (6), and in the control of the microstructure of Cu films (7).

To fully understand and model the effects of ion bombardment, one must examine the ion-surface interactions. The energetic ions and ad-molecules arrive at the surface and dissociate resulting in enhanced adatom migration. The high surface diffusion energies, equivalent to elevated substrate temperatures, result in diminished film columnar microstructure. A detailed discussion of ion-surface interactions are given in Chaps. 19 and 21. and results from an experiment to investigate ion-surface reactions are given in Ref. 8. Also, a very good discussion on modeling the IAD film growth process is given by Müller (9).

## **20.3 EXPERIMENTAL APPARATUS**

Two general arrangements are most popular for application of the ion source to thin film coating. Ions from the source are directed to the substrate which is being coated with material generated by thermal or e-beam evaporation. This is termed ion assisted deposition (IAD). Second, ions from one source are directed at a target which is sputtered, and the sputtered material is deposited on a substrate while a second ion source bombards the growing film. This is termed dual ion beam sputter deposition (DIBS).

### **20.3.1 Ion Source**

Broad-beam ion source technology is discussed in detail in an earlier chapter. A brief description is given here only to cite some specific examples of operational characteristics that impact the system design of IAD tasks. Ion sources are like most apparatus, in that when they are optimized for a specific process, they tend to sacrifice performance in other areas. This tendency leads to groupings of types of sources that conform to the process parameters of interest.

Briefly, the ion source operates as follows. Gas is introduced into the discharge chamber; electrons emitted from the cathode impact ionize the gas molecules. The discharge-chamber contains a conducting plasma composed of approximately equal numbers of ions and electrons. The plasma potential is essentially equal to the anode potential, therefore the ions originate at approximately the anode potential ("beam voltage"). The screen grid aligns the ions that are accelerated from the source by the electric field established in the region between the screen and accelerator grids. The ions travel from the source to the substrates which are held at ground potential.

Two collisional processes that could occur for the ions traveling to the substrates are resonant charge exchange and elastic collisions. The mean-free paths, at a standard operating pressure used ( $10^{-4}$ Torr), are greater than 100 cm for resonant charge exchange collisions. Therefore, the ion source-to-substrate or to-target distance should be less than 100 cm. The mean free paths for elastic collisions are about ten times larger than for resonant charge exchange collisions. Therefore, the ions reach the substrate or target with negligible scattering.

An attractive feature of a Kaufman ion source is the monoenergetic ion beam it produces. The energy distribution can be characterized using a retarding grid arrangement in front of a Faraday probe. The energy spread is approximately 10 eV over a range of beam energies from 300-2000 eV for the dual grid extraction arrangement (10). The energy spread from a source with a single grid arrangement is somewhat larger (10).

For the discussion in this chapter one can classify an ion source as a sputtering source or an enhancement source. Sputtering sources are those used to remove the maximum amount of deposition material from a target in the minimum time. In general, beam uniformity is not of great importance; the source operates at 1 to 2 kV (11) and it is desirable to deliver as much ion current to the sputter target as possible. More details on the specific parameters for sputtering sources are given in the section on dual ion beam sputtering. Enhancement sources provide ion bombardment to growing film material produced by another means. Beam uniformity is important; the source typically operates at low beam energies and current densities; and it is frequently required to operate with reactive gases which severely impact filament lifetimes.

The point of this discussion is to make the reader aware of the variety of potential tasks (others, such as ion beam etching, are discussed in an earlier chapter) that can be accomplished using broad-beam ion sources, and that the devices can be optimized for various tasks. Frequently, the optimization from one specialized task to another can be accomplished by something as simple as a grid change. Other optimization can require extensive hardware changes (such as the incorporation of a hollow-cathode emitter in the main chamber and as the neutralizer emitter), and include significant variations in control systems and operating procedures.

### **20.3.2 Operational Considerations**

All ion sources that produce beams using electrostatic acceleration present certain potential problems. The beam is extracted and accelerated by significant dc potentials (200-2000 eV typically). The workchamber contains a moderate current ( $> 1$ A) beam and is filled with a dilute, conducting plasma. Care must be taken to electrostatically shield the high potential leads to the source. Electrical breakdown is possible between

closely spaced leads, and this is enhanced by the dilute plasma. Some ion sources are designed in which gas flow lines are isolated from ground potential near the ion source; other sources have a conducting gas line at high voltage that passes through an insulator in the vacuum system wall and is electrically isolated outside the chamber. This line is often overlooked as a high voltage electrode source and can also be a significant safety factor.

The pressure inside the gas line goes from a few psi above atmosphere at the gas cylinder to approximately  $10^{-3}$  Torr in the ion source plasma region. Screens of metal wool pads are frequently used to provide large area surfaces on which ions can recombine and this prevents electrical breakdown in the gas feed tubes.

Oxidation can occur if a hot ion source is vented at atmosphere too soon after operation. The oxide films on the various electrodes can become sufficiently insulating to prevent source operation on a subsequent pump down. Similarly, sputtering of materials in a reactive atmosphere can produce insulating coatings. To avoid problems in this situation, regular cleaning of the ion source is important. This can be accomplished mechanically, for example, using bead blasting, or chemically, using acids to remove non-conductive thin film material.

The applications of ion beams to thin film deposition require knowledge of the ion flux at the substrate or target. For ion assisted deposition this measurement is very important; knowing just the total beam current is not sufficient.

When a standard Faraday probe arrangement is used while depositing conducting film materials, no special precautions are necessary. The probe element should remain insulated from the rest of the probe body, and the electrical characteristics of the probe element should remain constant. The probe might be moved into the ion beam just prior to the deposition process in order to check the beam condition. The probe would then be moved out of the beam.

When insulating materials are being deposited, care should be exercised to prevent the probe element from becoming coated. This would change the probe characteristics to provide incorrect indications of ion beam current density. During deposition the probe might be moved to an area where it is shielded from the film material, or the probe might have a shield attached. If the beam is to be monitored during deposition, some accumulation on the probe element is inevitable, and the probe should be later cleaned.

### **20.3.3 Ion Preclean of Substrates**

Substrate condition prior to coating is extremely important for proper film adhesion; in addition, it has an influence on subsequent film growth characteristics. In this section the application of ion beams as the final step of cleaning a surface immediately before film deposition is discussed. Results of ion beam cleaning and the improved adhesion of films which this can provide, such as Au on BK-7 glass, are discussed in Ref. 12. Ion beam cleaning obviously represents no added equipment to the deposition system when IAD is employed.

The processes which occur on the substrate due to ion bombardment include a number of things. This includes desorption of adsorbed water vapor, hydrocarbons and other gas atoms. Chemisorbed species and occluded gases are sputtered. If the bombarding

ion is an oxygen species, chemical reactions with organic species on the surface can result in compounds which are more volatile and hence more easily removed. For the levels of ion flux ( $20\text{--}100\ \mu\text{A}/\text{cm}^2$ ) and energy employed, and for the small time required for cleaning, the substrate temperature rise is usually negligible, and this has little effect on substrate outgassing. Relatively low energy (300 eV) ions are preferable to higher energy ions to minimize substrate sputtering, while still being sufficiently energetic to produce the effects mentioned above. Ion bombardment causes substrate defect production which in general is beneficial for subsequent film nucleation and adhesion.

If there is only single-axis rotation of the substrates, the ion source might be placed directly below the center of the substrates; if it is not directly below the substrates, then the beam pattern is simply spread over a larger area. If the fixturing involves planetary rotation, then the beam should be directed to a region that will ultimately provide bombardment of all substrates. In this case, the ion beam is obviously not on a particular substrate continuously; it is "time-shared" between all substrates. This, however, does not present the potential problems that are discussed in connection with IAD of substrates in planetary arrangements.

To estimate the time required for cleaning substrates, one should consider the amount of material which is sputtered. This is determined in part by the sputter yield of the substrate material and that of the unknown species on the substrate. Sputter yields for many materials are well characterized for various incident ions and ion energies; typical values range from 0.1 to 3 atoms/ion for inert gas ions of 0.5 to 2 keV energy (11). If a sputter yield ( $S$ ) of 0.1 atoms/ion is assumed, the thickness ( $L$ ) of the layer of material removed in 5 minutes ( $t$ ) due to a beam of  $50\ \mu\text{A}/\text{cm}^2$  current density ( $J$ ) is given by

$$L = S J V t / q \quad (1)$$

Or equivalently,  $L = 25\text{\AA}$ . Here  $V$  is an assumed volume of the sputtered atoms, taken to be  $27\text{\AA}^3$ , and  $q$  is the charge of the ion in Coulombs. This simple calculation illustrates how several atomic layers of material can be quickly removed from the substrate even at relatively low current densities to leave it atomically clean. However, it leaves open to question what the effective sputter yield of the contaminant layer is. If the beam is time-shared as described above in connection with planetary fixturing, then one must estimate the fraction of time  $F$  the substrates are in the ion beam; in the expression above,  $t$  would become  $t/F$ .

There are four considerations one should be aware of in applying ion bombardment to clean substrates. The first is the influence of ion bombardment on the substrate microroughness. If the substrate is polycrystalline and composed of relatively large crystallites, the microroughness of the substrate increases significantly if the substrate is ion bombarded for a long time. For example, Cu substrates have demonstrated an increase in rms roughness from approximately  $25\text{\AA}$  to nearly  $50\text{\AA}$  when  $1200\text{\AA}$  of the substrate was removed using ion beam sputtering (12). (This amount of material removal is somewhat severe in terms of substrate cleaning, but it illustrates the point.) On the other hand, amorphous or very small-grained polycrystalline substrates as well as single crystalline materials are less likely to develop a significant surface topography with this level of sputtering.

The second consideration when applying ion precleaning is that the stoichiometry of the top few atomic layers of substrates composed of compound species can be altered. This is due to the ions preferentially sputtering one atomic species, leaving the surface rich in the other atomic species. The extent of this altered layer production is naturally minimum with minimum ion energy (for energies less than approximately 2 keV) and flux.

A third consideration when applying ion beam precleaning involves the potential damage to a crystalline substrate surface, such as semiconductor materials. It is very difficult to obtain a clean semiconductor surface and maintain the bulk properties at the surface; atoms in the crystal lattice structure are displaced due to the ion bombardment. A general guideline is to reduce the ion energy to the lowest level possible if substrate damage is a concern.

A fourth consideration in applying ion precleaning involves contaminating the surface of the substrate being cleaned with the material from the fixturing holding the substrate. Slight contamination, especially around the periphery of the substrate is usually unavoidable. When possible, the fixturing material should be constructed of material which is similar to the film material.

#### **20.3.4 Ion Assisted Deposition**

Ion assisted deposition (IAD) employs an ion source to direct a beam of ions at the substrate during deposition where the vapor source is either thermal or electron-beam evaporation. (Dual ion beam sputter deposition is discussed in the next section.) An obvious advantage to utilizing IAD is that the process can easily be incorporated into an existing vacuum deposition system. In this section we describe the equipment to deposit thin films using IAD.

A schematic of a vacuum deposition system configured for IAD is shown in Fig. 1. The operation of the source to provide the thin film material is totally independent from the ion source, and the configuration provides the ability to accurately measure all critical deposition parameters. The ion source provides a neutralized ion beam directed at the substrates.

As illustrated in the schematic, the gas is introduced through the ion source into the chamber. IAD is inherently a low pressure process ( $10^{-5}$  to  $10^{-4}$  Torr) that permits a great deal of flexibility in deposition configurations. Any number of gas species may be introduced through the ion source depending upon the complexity of the gas manifold. Neutral background gas may also be introduced into the vacuum chamber through another inlet if desired. An attractive feature with IAD is that substrate cleaning (Section 20.3.3) may be readily accomplished before deposition by controlling the appropriate gas species through the ion sources. Immediately upon completion of the cleaning process, deposition can commence. The minimal time lag between the two processes is due to the delay, if any, associated with changing the gas species flowing through the ion source.

As described in Sect. 20.3.2, it is essential that ion beam probing be undertaken carefully. For certain materials, film properties are sensitive to bombarding ion flux levels (examples are given later in this chapter). As illustrated in Figure 1, an ion current probe is located just below the substrates. The probe platform is mounted on a rotary feedthrough such that it can be moved through the ion beam immediately below the

substrates. After the ion flux value is measured, the probe is rotated away from the substrate area to minimize the coating of the probe. Not shown in the figure is a shield attached to the probe platform which protects the probe from film material during deposition.

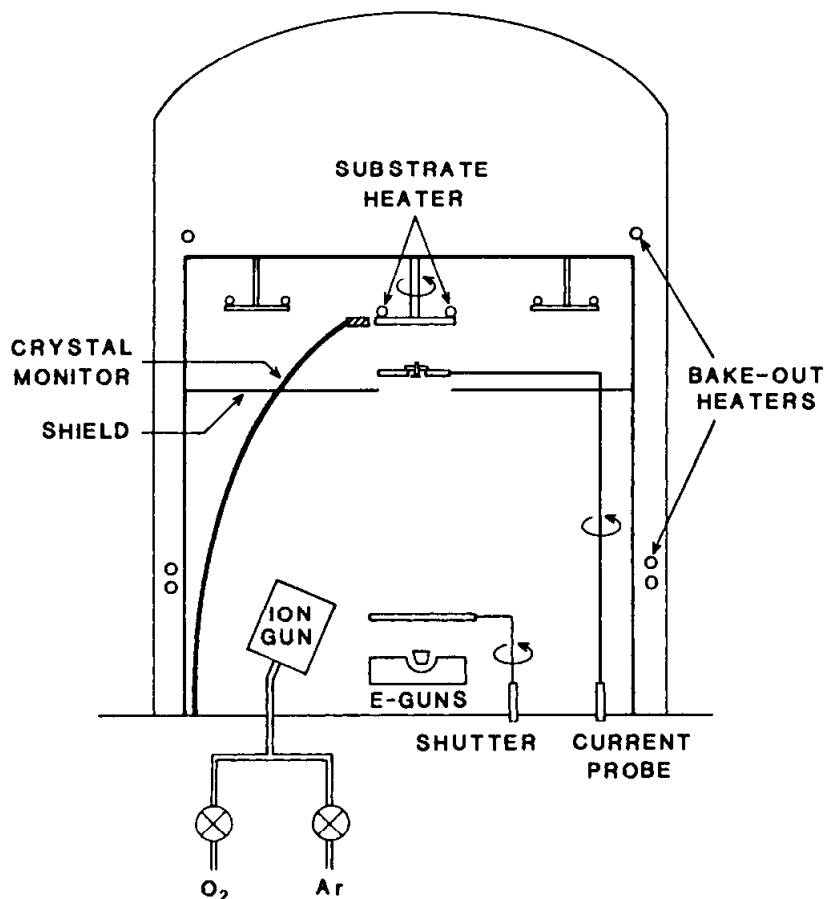


**Figure 1:** Schematic of Ion Assisted Deposition (IAD) system.

An important parameter in depositing thin films using IAD is the ratio of the ion-to-depositing atom arrival rates. Proper beam probing allows accurate determination of the ion flux. One method to determine the flux of arriving, condensing film atoms is measurement of the film deposition rate using a crystal monitor. As illustrated in Fig. 1, the monitor may be located very close to the substrates. However, it should be shielded from the direct ion beam to minimize sputtering of the monitor material. The monitor must be calibrated to determine an accurate tooling factor for different film materials and for various ion source conditions (i.e. accurately account for sputtering). If the substrate fixturing involves planetary rotation, then the monitor cannot be located immediately adjacent to the substrates. In this arrangement, determination of the flux of depositing atoms is more difficult. Usually the substrates are exposed to the ion beam for only a fraction of time ( $F$ ). This complicates the procedure to account for sputtering when determining the flux of film atoms. For the fixed geometry illustrated in Fig. 1, the substrates are exposed to the ion beam continuously. Modification to the thin film properties can occur on a continuous basis. When using IAD with a planetary rotation geometry, care must be employed in selecting the ion beam parameters which result in the desired thin film properties.



Another important consideration when applying IAD is the respective arrival directions of the bombarding ions and the film molecules. As illustrated in Fig. 1, when employing a fixed-position substrate geometry with an off-axis ion source, it is important that substrate rotation be employed. The rotation of the substrates is necessary to minimize anisotropic properties in the films due to the different arrival directions of the ions and the molecular species.

For the ion source proper selection of the discharge voltage is important. The value should be high enough to sustain an appropriate discharge in the source (typically 40 V). However, too high a value (70-90 V) will cause increased production of doubly ionized atomic (molecular) ions. The doubly ionized species will be accelerated to twice the beam energy (the energy of the singly ionized ions). This results in increased sputtering of the sample, which may be desirable, but can also lead to increased damage of sensitive samples. Also, high values of discharge voltage can decrease the lifetime of the cathode filament in the source and cause additional sputtering inside the source, leading to contamination of the beam. For a 10 cm source, cathode filament lifetime for average IAD conditions (500 eV,  $30\mu\text{a}/\text{cm}^2$ ) operating in oxygen is approximately 4-hours for 0.4 mm (0.015 in.) diameter tungsten wire. The lifetime for 0.5 mm diameter (0.020 in.) tantalum wire is only 1-1.5 hours under similar conditions. For this reason, one might consider using thoreated filaments to increase lifetime.

As mentioned earlier, it is necessary to provide a compensating density of electrons to the ion beam, especially when bombarding an insulating target. This is often accomplished using a thermionic neutralizer filament which emits the appropriate electron current into the beam. The value of this neutralizer current is matched to the beam current. Note that the ions are not neutralized in-flight but rather the total beam current is zero due to the intermixing of the electrons into the ion beam. When using this simple arrangement for beam neutralization, consideration must be given to contamination arising due to neutralizer filament sputtering. Another technique for beam neutralization is the use of a plasma bridge neutralizer arrangement.

**20.3.4.1 Procedures.** It is critical that the ion flux is stable and accurately measured before deposition begins. The film material should be pre-heated and a shutter employed to prevent deposition before the ion source is stable. The gas discharge of the ion source should be established and the desired beam parameters (ion energy, flux and neutralizer current) set at the ion source controller. When the ion flux is measured by the probe, an accurate record of its value and all ion source parameters should be made. When the probe is rotated out of position, deposition may commence. During deposition the beam energy and current must be monitored to ensure stable ion source operation. At the completion of deposition, the ion flux should be checked by rotating the probe back to the original measurement position.

### 20.3.5 Dual Ion Beam Sputtering (DIBS)

When energetic ions or neutral atoms strike a surface, many processes can occur. One of these is the ejection of atoms of the surface (target) materials, and this is known as sputtering. Of primary concern in sputtering is the sputter yield ( $S$ ), in atoms/ion, and the relation of  $S$  to parameters involved such as ion and target species, ion energy, ion incident angle and target condition. In addition, it is very important to have an idea of the average ejection energy of sputtered atoms, as this has a significant influence on resulting

thin film properties. Similarly, the angular distribution of the sputtered atoms is of importance in determining film deposition rate, uniformity, etc. Detailed treatments of sputtering are given in an earlier chapter as well as in Reference 2. In this section experimental aspects of dual IBS will be described.

Figure 2 illustrates the apparatus used in ion beam sputtering. In this case, two ion sources are shown, one for sputtering and one for bombarding the substrate prior to coating or during deposition. Also shown is a probe to characterize the beam in the vicinity of the target, as well as the other shutters typically found in a deposition system.

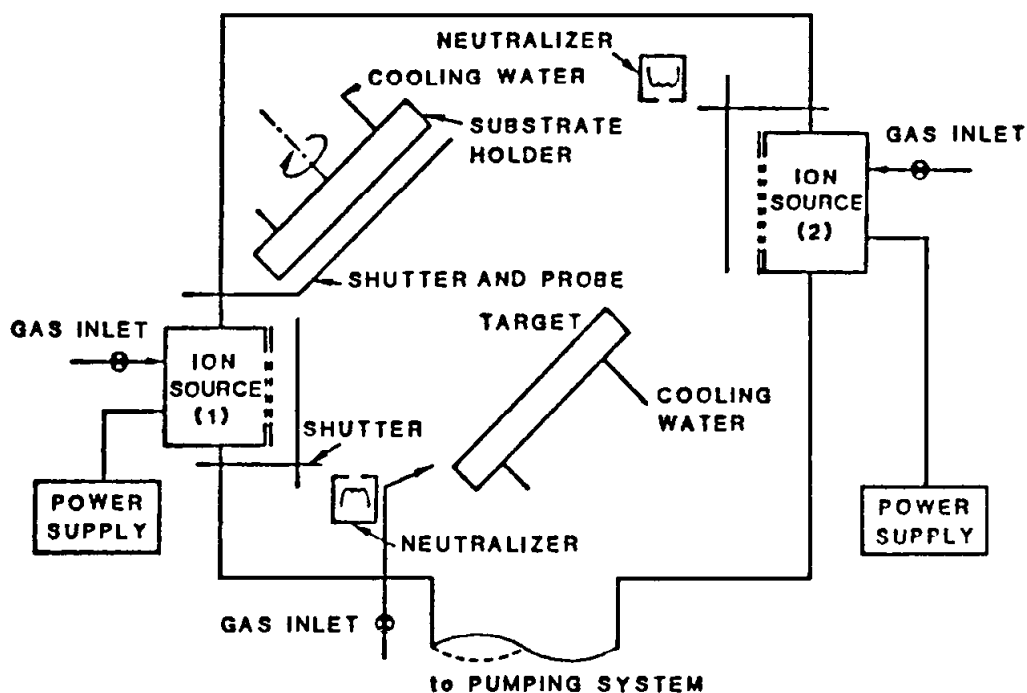


**Figure 2:** Schematic of Dual Ion Beam Deposition (DIBS) system.

Chamber size requirements are influenced little by addition of a small ion source; more elaborate arrangements such as illustrated in Fig. 2 require a specially designed system. Typical size of the arrangement shown in the figure is roughly 50 cm in diameter. Similarly, vacuum pumping requirements are not influenced greatly with the addition of a small ion source; typical added gas load is 2-4 SCCM ( $\text{cm}^3/\text{min}$ ) for a 2.5 cm diameter ion beam source. A 6-inch diffusion-pumped or cryogenically-pumped system will typically operate in the  $10^{-5}$  to low  $10^{-4}$  Torr region with this gas load. Incorporating large ion sources into a system may require additional pump capability.

The arrangement of the sputter target and the substrates is often as illustrated in Fig. 2. A typical separation between the ion source and the target is 30 cm. The target is arranged at an angle of approximately 45 degrees to the ion beam to increase the sputter

yield (2). The energetic neutralized ions which are reflected from the target can, in some situations, be detrimental to the film if they are allowed to bombard the substrate. This is the case, for example, when high quality oxide films are being deposited using Ar ions to sputter a target and an O<sub>2</sub> partial background pressure (13). To minimize this effect, the substrates are arranged as shown in Fig. 2. Although the neutralized ions do not all reflect in a specular sense, it is believed they are predominantly directed in this "direction.

For ion beam sputtering it is usually desirable to deliver as much ion current to the sputter target as possible, and this dictates the use of large ion sources (e.g. 10-15 cm diameter). Wire filament cathodes and neutralizers can be used which are made of W or Ta typically 0.010 to 0.015 inches in diameter. Both have lifetime limits of several (one to over ten) hours. Lifetime of the neutralizer is increased if it is placed near the edge of the ion beam and not through the center. This can be tedious to achieve, as the beam profile and therefore the position of the neutralizer are somewhat dependent on operating conditions (pressure, beam energy, etc.). Both the cathode and neutralizer lifetime are greatly reduced if a reactive gas is passed through the ion source. In addition, the W or Ta material can contaminate the target and be deposited in the film at a low level. In place of the wire cathode, a hollow cathode discharge device can be used to supply electrons to the main discharge of the ion source. Although this operates very well with inert gas, operation with O<sub>2</sub> has not been satisfactory. Similarly, the wire neutralizer can be replaced with an auxiliary discharge device, a plasma bridge neutralizer, to supply neutralizing electrons to the beam. This must remain outside of the beam to avoid being sputtered and contaminating the target material. Another approach is to construct the housing of the plasma bridge neutralizer of a material which is compatible with the target and film.

When larger loads of substrates need to be coated, larger diameter sources are used and the source - target - substrate distances are increased. This geometric scaling results in inverse square losses, with corresponding reduction in deposition rates.

In general, the angular distribution of sputtered particles is peaked in a forward direction, at an angle roughly comparable to that of the incident ions. A cosine distribution has been used to describe this, although several factors have an influence. In particular, the target condition is very important. The distribution pattern will vary depending on target crystallinity, target age, a target of solid material will provide a distribution pattern different from that of one made of pressed powder and the ion-target incidence angle.

From what has been described, it is apparent that the best approach to characterize the distribution pattern in applications in which it is critical is to simply use trial and error. For example, sample substrates might be coated. Film deposition rate and uniformity could be determined from subsequent examination using a spectrophotometer or other types of interferometry.

Target size should be sufficient to insure that none of the beam passes the target and sputters other material. In optical coating arrangements in which large ion sources are used, target size is typically 20 cm wide and 30 cm long. Placement of the target and the influence of this on the distribution of sputtered atoms has been discussed.

In the case of optical coatings, elemental targets of Si, Ti, Ta, etc., are often preferred because of the higher sputter yields and therefore large deposition rates provided, compared to targets composed of the oxide materials. In this particular situation, Ar ions are

often used to sputter the target; the second ion source, possibly with a single-grid arrangement to provide very low-energy ion extraction, is often used with  $O_2$  to improve film stoichiometry. Deposition rates of 1-2 Å/sec can be achieved (13). Similar techniques have been used in the case of nitride film deposition (8).

In general, there is no restriction placed on a target used in ion beam sputtering; the target can be an insulator since the ion beam can be neutralized. Sputter targets are often water-cooled due to the incident power (e.g., 0.25 A at 1500 V in vacuum).

A technique which has been used to ion beam sputter compounds of materials involves placing pieces of one target material on a second target material (2,14). The film composition depends on the relative sputter yields, the relative areas of the targets which are sputtered and the relative sticking coefficients of the atoms at the substrate.

## 20.4 PROPERTIES OF IAD FILMS

Early studies utilizing an ion beam to modify the properties of evaporated films were reported by Heitman (15). Another study utilizing a separate ion source to bombard evaporated  $SiO$  with 5 keV oxygen ions during deposition was done by Dudonis and Pranevicius (16). They investigated the effects of ion flux on film stoichiometry and found that for increasing flux values, the O/Si ratio approached two. Cuomo, et al. (6) obtained superconducting NbN films by bombarding evaporated Nb with  $N_2^+$  during deposition. Netterfield and Martin have studied the effects on the properties of  $ZrO_2$  and  $CeO_2$  films bombarded with  $O_2^+$  and  $Ar^+$  during deposition (17-19). They reported increased packing densities, reduced permeability to water and changes in film crystal structure. Argon ion bombardment produced changes in film stoichiometry. McNeil et al. (20,21) have examined the effects of 30-500 eV oxygen ion bombardment on the properties of  $TiO_2$  and  $SiO_2$  films deposited using  $TiO$  and  $SiO$  starting materials. They reported that improvements in optical properties were obtained at 30 eV; in particular, better film stoichiometry. McNally, et al. (22,23) reported the effects of oxygen ion bombardment on the properties of  $Ta_2O_5$ ,  $Al_2O_3$ ,  $TiO_2$ , and  $SiO_2$  films. Increases in the values of refractive index were reported for 200, 300, 500 and 1000 eV bombardment.

The values of  $n$  (at  $\lambda = 400\text{nm}$ ) for  $Ta_2O_5$  coatings bombarded with 200, 300 and 500 eV oxygen ions are plotted in Fig. 3 as a function of  $O_2^+$  current density. The error bars indicate the uncertainty in the index measurements. The values increase from 2.16 for coating deposited without bombardment to maximum values of 2.25, 2.28 and 2.19 for films bombarded with 500, 300 and 200 eV  $O_2^+$ , respectively.

The current density value (for a fixed ion energy) at which the maximum  $n$  occurs is termed the critical value. The results in Fig. 3 illustrate that film index values decrease for ion current densities greater than the critical values. The decrease in index may be explained as a result of degradation in film stoichiometry, creation of closed isolated voids or oxygen incorporation into the films. Similar results for which the values of refractive index decrease for current densities greater than the critical values have been reported for ion assisted  $ZrO_2$  films (18) and  $CeO_2$  films (19).

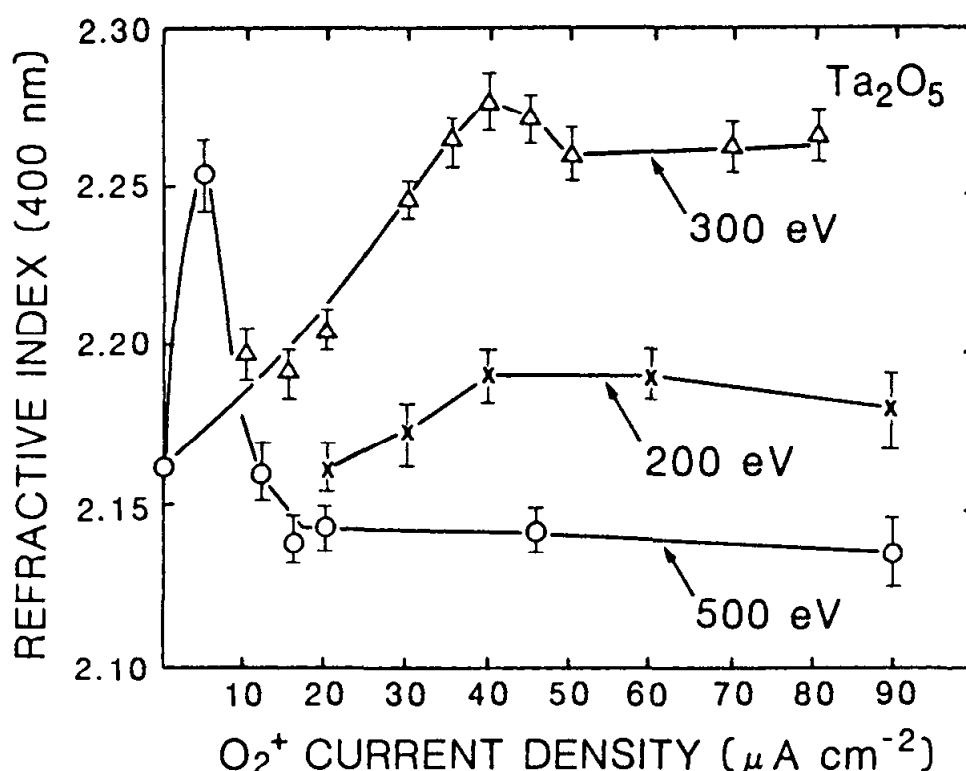


**Figure 3:** Refractive index as a function of oxygen ion beam current density for Ta<sub>2</sub>O<sub>5</sub> films as a function of ion energy during deposition.

The coatings bombarded during deposition at oxygen ion current densities up to approximately the critical values exhibit good optical characteristics. For higher levels of bombardment, the optical absorption of the coatings increase. In Fig. 4, values of extinction coefficient ( $k$ ) for Ta<sub>2</sub>O<sub>5</sub> coatings (300 nm thick) bombarded with 500, 300 and 200 eV oxygen ions are plotted as a function of O<sub>2</sub><sup>+</sup> current density. The values of  $k$  were calculated at  $\lambda = 400$  nm. The error bars indicate the uncertainty in the measurements. The dashed line across the bottom at  $k = 2.0 \times 10^{-4}$  indicates the level below which the values of  $k$  were too small to be regarded as reliable because of the minimum sensitivity of the measurement technique.

As illustrated in Fig. 4, film optical absorption increased with higher levels of oxygen bombardment. The most probable mechanism for this is the preferential sputtering of oxygen in the Ta<sub>2</sub>O<sub>5</sub> molecule. This damage mechanism has been observed in other IAD films (18). This highlights the requirement for proper beam probing to avoid compositional change by preferential sputtering.

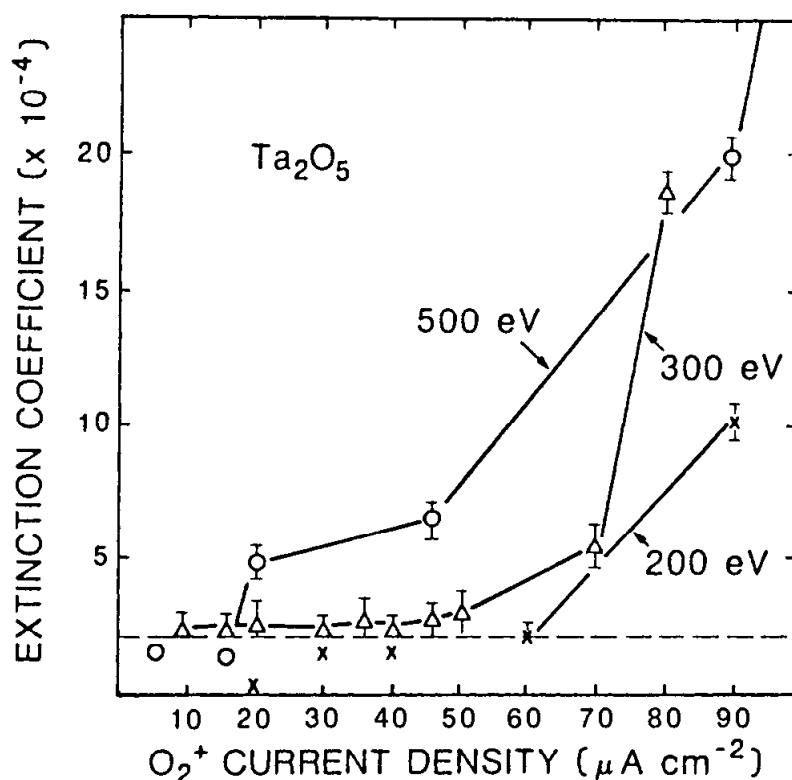


**Figure 4:** Extinction coefficient as a function of oxygen ion current density and ion energy for Ta<sub>2</sub>O<sub>5</sub> films.

The environmental stability of optical coatings is in large part limited by the porosity of the film microstructure. Results have been reported for IAD ZrO<sub>2</sub> and Ta<sub>2</sub>O<sub>5</sub> coatings (22) where the refractive index value remained stable to less than 0.3% after exposure to high humidity. IAD can affect intrinsic stress in films. Changes in stress for Ta<sub>2</sub>O<sub>5</sub> coatings have been reported (22). Cuomo, et al.(6) reported a change in stress from tensile to compressive for evaporated Nb films bombarded with 100-800 eV Ar<sup>+</sup> during deposition. They attributed the changes in stress to modifications in film microstructure and incorporation of argon. Hirsh and Varga (24) measured stress relief in evaporated Ge films bombarded with 100-300 eV Ar<sup>+</sup> during deposition. The stress changed toward compressive values.

Another example of recent IAD work is the deposition of protective coatings on sensitive substrates at low temperatures (3). MgF<sub>2</sub> films were successfully deposited on heavy metal fluoride glass substrates at 100°C. The films were bombarded with 300 eV Ar<sup>+</sup> during deposition. Conventional evaporated MgF<sub>2</sub> films are soft when deposited at substrate temperatures less than 250°C(25). The IAD MgF<sub>2</sub> films were hard and robust. ThF<sub>4</sub> films have also been successfully deposited at ambient temperatures using IAD (26). Film stability to humidity was significantly improved for the IAD films.

IAD has been used to affect the microstructure and properties of metal films (27). An excellent recent report (6) examines the effects of IAD on resistivity, stress, hardness, crystallinity and the surface morphology of evaporated Cu films. Films were bombarded

with 600, 125 and 62 eV Ar ions at various ion flux levels. The results illustrated that using a general energy parameter (i.e. eV/atom) to predict film property modifications is incorrect. Thus, the effect of ten 600 eV ions is different than the effect of one hundred 60 eV ions. This work demonstrates the independence of ion energy -and ion flux as they affect film properties.

Control of stoichiometry is important in tailoring the optical and electrical properties of films. The results of  $N_2^+$  and  $O_2^+$  bombardment during the evaporation of Si and Al can be found (4,5,28). Netterfield (28) examined the effects of 60 and 100 eV  $N_2^+$  bombardment on the optical constants of  $Si_3N_4$  films. With 60 eV ion bombardment the films were lossless. At 100 eV bombardment the refractive index value increased but the films became lossy. Donovan (5) investigated the feasibility of designing rugate filters by varying the flux of 500 eV  $N_2^+$  bombarding the substrate during deposition. Al-Jumaily, et al. (4) varied the stoichiometry of silicon and aluminum oxynitrides by varying the gas mixture in the ion beam. They studied the optical properties and the humidity stability of the resulting films.

## 20.5 PROPERTIES OF DUAL IBS FILMS

A number of references (2,29) are available that describe the properties of thin films deposited by dual IBS. Improvements in the properties of carbon films are presented in Ref. 30. A graphite target is sputtered by argon gas or a mixture of argon/methane gas. The second ion source also uses either argon or argon/methane mixture as its working gas. The films sputter-deposited with no ion assist were amorphous, a dark brown color and soft. The films deposited with low energy ion bombardment of the substrates were insulating, transparent and hard. However, if the ion energy or flux levels were increased too much the films became brittle. In another study, (29) dual IBS was applied to deposit Al-N films. A 1500 eV  $Ar^+$  sputters the Al target while a 100- 500 eV  $N_2^+$  beam bombards the substrate. The properties of the thin films were examined as a function of varying ion flux levels. The films' visual appearance changed as the amount of nitrogen in the films varied: from a shiny metallic appearance for N-Al ratios less than 0.54, to a shiny gray for  $0.82 < N/Al < 1.0$ , to transparent for stoichiometric AlN. The electrical properties also varied as a function of N-Al ratio.

The optical properties of Cu films deposited under different ion flux levels were found to vary (31). Films deposited with a factor of three variation in the bombarding ion current density were found to have differences in microstructure (voids and grain size) which caused differences in the films optical constants. Recently, dual IBS oxides were found to exhibit optical properties which equal or surpass conventionally deposited films (13,32). In one example, low-scatter optics are critical to the proper operation of ring laser gyroscopes and low-gain laser systems. (Scattering in laser gyroscopes is detrimental because it causes an effect called lock-in which severely decreases output precision.) Demiryont, et al. (32) used dual IBS to study the effects of various  $Ar/O_2$  gas mixtures on  $TiO_2$  and  $Ta_2O_5$  film properties. Holmes (13) has deposited films with total optical losses less than 100 parts per million as measured in a ringdown laser arrangement. These films were highly stable with temperature cycling to 300°C in atmosphere for several hours.

## 20.6 ADVANTAGES and LIMITATIONS

The two configurations for using ion beams for thin film deposition (Figs. 1 and 2) each contain their distinct advantages. Direct comparison of the two configurations to determine which provides the "best" coatings is difficult. The decision as to which configuration to employ must be made with consideration of the end application, the existing deposition system (if any), total costs and the issues discussed in previous sections. In this section, a discussion summarizing the advantages and disadvantages of dual IBS and IAD is given with the emphasis on listing information to aid the users in deciding which configuration would better serve their needs.

The improvements in the properties of thin films produced using dual IBS and IAD are given in a previous section. It appears that each technique results in thin films of similar quality. Thus, a decision based on film quality would need to be made on a case-by-case basis. However, it is clear that films produced using dual IBS or IAD possess properties superior to films deposited by evaporation alone.

A direct advantage of IAD is that the technique is readily implemented with the addition of an ion source apparatus to an existing vacuum deposition system. This offers significant savings in both time and money. On the other hand, dual IBS may require more modifications to an existing deposition system, or the purchase of a totally dedicated one. Either choice requires a major investment. Another advantage of IAD is the ease in which the technique can be scaled to large geometries. Scaling the dual IBS process is more limited than the IAD process by the size of ion sources available. A number of trade-offs among the deposition parameters (deposition rate, uniformity, etc.) exist, and they must be considered before choosing which technique would best achieve the desired results.

In sputter applications, ion beams provide control of ion energy, flux, species and angle of incidence. These parameters are not only controllable over a wide range, they can be controlled nearly independently of each other. This represents significant advantages compared to other forms of sputtering. In addition, the gas discharge of the ion source is contained and separate from the rest of the deposition system. For example, in the case of magnetron sputtering the ion energy cannot be controlled over a wide range, and it is closely coupled to the magnetron discharge current. Being able to arrange the sputter target at an angle to the incident ion beam is advantageous both in terms of sputter yield and sputtered atom energy, as well as allowing flexibility in the experimental arrangement. In the case of magnetron sputtering or other processes in which the sputter target is in contact with the discharge, there is no control of the incident angle. Ion beam sputtering allows greater flexibility in target material and composition than in other forms of sputtering. As another example, the species in the ion beam can be easily and accurately controlled by adjusting the flow of one or more types of gas through the source; reactive ( $O_2$ ,  $N_2$ , etc.) or inert ion species can be present in practically any ratio desired. The low background pressure present during ion beam sputtering might lead to less gas inclusion compared to other processes. However, substrates will be bombarded with energetic neutralized ions which are reflected from the target unless special precautions are taken. In this case the incorporation could increase significantly due to a larger sticking coefficient of the energetic atom.

An obvious disadvantage of application of ion beams in general is the added expense and complexity of the coating process. However, neither of these is severe. It is more



difficult to scale the ion beam sputter process compared to magnetron or some other sputter process. Geometries of the ion beam sputter arrangement sometimes must be small in order to avoid prohibitively slow deposition rates, and this might be a problem.

## 20.7 CONCLUSION

In this chapter, I presented a general overview of two specific ion deposition techniques. The advantages offered by dual IBS and IAD are the degree of flexibility and independence provided, compared to other gas discharge techniques. The capability to tailor and study film properties for varying controlled bombardment conditions is unique. As improvements in ion beam technology continue, a wide variety of "novel" deposition arrangements will appear. Further improvements in film properties and expanded applications to production (electronics, optics, protective) coatings will allow the advantages of dual IBS and IAD to outweigh the disadvantages.

## ACKNOWLEDGMENTS

The author thanks J. R. McNeil for many helpful discussions and G. A. Al-Jumaily for making manuscripts available prior to publication.

## 20.8 REFERENCES

1. J.M.E. Harper, J.J. Cuomo, R.I. Gambino and H.R. Kaufman, Ion Bombardment of Surfaces: Fundamentals and Applications O. Auciello and R.Kelly, eds., pp 127-162, (Elsevier, Amsterdam 1984).
2. J.M.E. Harper, Thin Film Processes, ed. by J.L. Vossen and W.Kerns pp 175-206 (Academic Press, New York (1978).
3. J.J. McNally, G.A. Al-Jumaily, J.R. McNeil and B.Bendow, Appl. Opt. 25: 1973 (1986).
4. G.A. Al-Jumaily, T.A. Mooney, W.A. Spurgeon and H.M. Dauplaise, J. Vac. Sci. Technol. A7: to be published (1989).
5. E.P. Donovan, D. Van Vechten, A. Khan, C.A. Carosella, and G.K. Hubler Optical Interference Coatings, 1988 Technical Digest Series 6: 122 (1988).
6. J.J. Cuomo, J.M.E. Harper, C.R. Guarnieri, D .S. Yee, C.J. Attanasio, J. Angilello, C.T. Wu and R. H. Hammond, J. Vac. Sci. Technol. 20: 349 (1982).
7. R.A. Roy, J.J. Cuomo and D.S. Yee, J. Vac. Sci. Techol. A6: 1621 (1988).
8. C. Weissmantel, Thin Solid Films 32: 11 (1976).
9. K.H. Müller, J. Vac. Sci. Technol. A6: 1690 (1988); Also, J. Appl. Phys., 61: 2516 (1987).
10. H.R. Kaufman and H.R. Robinson, AIAA Journal 20: 745 (1982).
11. J.L. Vossen and J.J. Cuomo, Thin Film Processes ed. by J.L. Vossen and W. Kern, pp 11-73 (Academic Press, New York, 1978)
12. W.C. Herrmann, Jr. and J.R. McNeil, Proc. SPIE 325: 101 (1982).
13. S. Holmes, private communication.
14. S. Masaki and H. Morisaki, Proc. 10th Symp. on ISLAT 86, 427, Tokyo (1986).

15. W. Heitman Appl. Opt. 10: 2414 (1971).
16. J. Dudonis and L. Prannevicius, Thin Solid Films, 36: 117 (1976).
17. P.J. Martin, H.A. Macleod, R.P. Netterfield, C.G. Pacey and W.G. Sainty. Appl. Opt. 22: 178 (1983).
18. P.J.Martin, R.P. Netterfield and W.G. Sainty, J. Appl. Phys. 55: 235 (1984).
19. R.P. Netterfield, W.G. Sainty, P.J. Martin and S.H. Sie, Appl. Opt. 24: 2267 (1985).
20. J.R. McNeil, G.A. Al-Jumaily, K.C. Jungling and A.C. Barron, Appl. Opt. 24: 486 (1985).
21. J.R. McNeil, A.C. Barron, S.R. Wilson and W.C. Herrmann, Jr., Appl. Opt. 23: 552 (1984).
22. J.J. McNally, G.A. Al-Jumaily and J.R. McNeil, J. Vac. Sci Technol., A4: 437 (1986).
23. J.J. McNally, F.L. Williams, K.C. Jungling and J.R. McNeil, J. Vac. Sci. Technol., A5: 2145 (1987).
24. E.H. Hirsh and I.K. Varga, Thin Solid Films, 69: 99 (1980).
25. P.J. Martin and R.P. Netterfield, Appl. Opt. 24: 1731 1985.
26. G.A. Al-Jumaily, L.A. Yazlovitsky, T.A. Mooney and A. Smajkiewicz, Appl. Opt. 26: 3752 (1987).
27. G.A. Al-Jumaily, L.A. Yazlovitsky, T.A. Mooney and A. Smajkly, K.C. Jungling and J.R. McNeil, J. Vac. Sci. Technol. A4: 439 (1986); also, G.A. Al-Jumaily, S.R. Wilson, J.J. McNally, J.R. McNeil, J.M. Bennett and H.H Hunt, Appl. Opt. 25: 3631 (1986).
28. R.P. Netterfield, P.J. Martin and W.G. Sainty, Appl. Opt. 25: 3808 (1986).
29. J.M.E. Harper, J.J. Cuomo and H.T.G. Hentzel, Appl. Phys. Lett. 43: 547 (1983).
30. C. Weissmantel, E. Achemann, K. Bewilogua, G. Hecht, H. Kupfer and B. Rau, J. Vac. Sci. Technol. A4: 2892 (1986).
31. F. Parmigiani, E. Kay, T.C. Huang and J.D. Sawlen, Appl. Opt. 24: 35 (1985).
32. H. Demiryont, J.R. Sites and K. Geib, Appl. Opt. 24: 490 (1985).

---

## Microstructural Control of Plasma-Sputtered Refractory Coatings

---

**David W. Hoffman and Robert C. McCune**

### 21.1 INTRODUCTION

One of the foremost attractions of sputtering versus thermal evaporation for the vacuum deposition of materials is the relative ease with which refractory elements and compounds can be vaporized. It is well known that the sputtering yields of materials vary less widely than their vapor pressures. Thus, although refractory materials are characterized by high melting temperatures and very low vapor pressures, they sputter almost as readily as other substances. Even when sputtered, however, the sedentary nature of refractories asserts itself at the point of deposition, where their low mobility restricts diffusion from the random points of impingement onto energetically favorable sites. Consequently the very materials for which sputtering is most advantageous at vaporization tend to yield the greatest disorder and anomalous properties in their deposits. This chapter considers the manipulation of the plasma sputtering environment to influence the microstructure and properties of coatings deposited under conditions where the materials in question have low adatom mobilities. Examination of primitive growth structures obtained without modification will be followed by discussions of stimulated bombardment by bias sputtering, and coincidental control by sputtering at low gas pressures. The chapter will conclude with a discussion of selected mechanisms and models relevant to the influence of the plasma environment on resulting film microstructures and properties.

#### 21.1.1 Primitive Microstructures

The tapered grain microstructure consisting of a multitude of competitively growing, domed "grains", which may be touching but not strongly interbonded, is a common feature of materials deposited at low temperatures that has long been associated with degraded appearance and physical properties. The deposition of thermally evaporated metals in the form of tapered grains was determined by Movchan and Demchishin (1) to occur at temperatures below about one third of the respective melting temperatures, as

their classic diagram indicates in Fig. 1(a). When deposited above this temperature, evaporated materials exhibit different features such as faceted surfaces and strongly interbonded, columnar microstructures. The temperature regimes below and above the transition have become known as Zone 1 and Zone 2 respectively. Although the transition may be somewhat gradual, the interzone boundary is sufficiently well defined to reveal a secondary dependence on the class of material, e.g., pure metals versus ceramic compounds. The suggestion of Movchan and Demchishin that the location of the transition is determined by a competition between geometric impingement effects, e.g., self-shadowing, that promote the growth of isolated grains and the onset of surface diffusion has been theoretically quantified by Srolovitz, Mazor, and Bukiet (2).

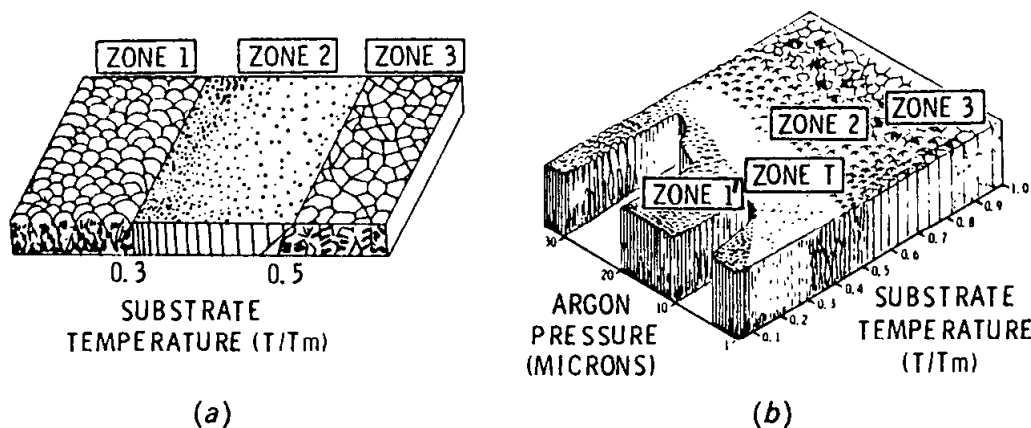


**Figure 1:** Structural zone models for coating growth. (a) Model proposed by Movchan & Demchishin (1). (b) Model proposed by Thornton for sputtered metal coatings (3). The zone notation "1'" is inserted into Thornton's model to distinguish the sputtered microstructure from the Zone 1 microstructure produced by evaporation.

From observations on metal coatings deposited by plasma sputtering Thornton (3) adapted the zone diagram of Movchan and Demchishin by adding a second axis for sputtering gas pressure, as shown in Fig. 1(b). Bearing in mind the qualitative nature of such diagrams, it seems nevertheless evident that the lower limit of Zone 2 microstructures is retracted to higher temperatures for deposition by plasma sputtering, extending no lower than one-half the melting temperature as opposed to one-third  $T_m$  by thermal evaporation. In other words, plasma sputtering appears to expand the range below Zone 2 of refractory deposition, implying that self-shadowing effects become relatively more potent in the competition with surface diffusion. Thornton (4) proposed that enhancement of tapered grain deposition (sometimes also confusingly called columnar) results from gas scattering of the sputtered vapor, thereby randomizing the directions of incidence of the coating flux upon the substrate, as sketched by him in Fig. 2. The indicated geometric shadowing favors preferential accumulation toward the tips of the surface protrusions thereby increasing the amount of counteracting diffusion transport required to achieve a Zone 2 microstructure. Since Thornton's original determination it has become clear that

the randomized coating flux also alters the internal structure of tapered grains to such an extent that a special nomenclature, Zone 1', may be useful to distinguish the sputtered coatings. Thornton (3) postulated the interpolation of a transitional Zone T between Zones 1' and 2, when sputter deposition was performed at reduced gas pressures.

The empirical zone models derive from observations at the magnifications available in light and scanning electron microscopy having resolutions no finer than 0.1 micrometer, thereby inviting speculation about the internal structures of the grains and columns. Although debate flourished about crystalline defect densities and atomic configurations within tapered grains, evidence for substructure of a different sort was inferred by Westwood (5) from decreasing physical densities measured on platinum films sputter deposited at increasing gas pressures. Since platinum was selected to minimize the possibility of reactive gas pickup, these results suggest the existence of an array of fine internal voids variable over a substantial range of macroscopic densities. Subsequently Nakahara et al. (6) observed copious atomic scale voids in evaporated refractory coatings of a nickel-iron alloy by transmission electron microscopy, where self-shadowing was accentuated by depositing at oblique incidence. Startling images of highly convoluted morphologies that refractory microstructures may incorporate were also generated by computer modelling studies of ballistic aggregation beginning with Henderson et al. (7,8), motivated by the observation of anisotropy in amorphous Gd-Co magnetic bubble films. When deposited at oblique incidence to the substrate, the simulated growth structures incorporated a host of elongated, atomic-scale voids tilted to a degree studied by Meakin et al. (9) toward the direction of the incoming condensate. Notably both the TEM observations and simulated microstructures represent thermally evaporated (not plasma sputtered) coatings with self-aligned vapor streams, and both indicate that oblique incidence accentuates the generation of numerous voids. In fact physical property observations suggest that thermally evaporated metallic coatings grown under Zone 1 conditions, while incorporating tapered grains, may not necessarily develop a voided intragrain substructure when deposited at normal incidence.

Void incorporation in plasma sputtered coatings, however, is exacerbated by the gas scattering mechanism of Fig. 2 when extrapolated to the atomic scale. By transmission electron microscopy of sputtered stainless steel Fabis (10) observed microporosity that may, however, not represent a totally primitive structure, owing to the use of a relatively low argon pressure. An instructive ballistic simulation was carried out by Dirks and Leamy (11,12), using oblique incidence from two opposing angles (an approximation to randomized incidence) as shown in Fig. 3. Near the center of the finite simulated structure appear elongated microvoids oriented normal to the plane of the substrate. Microvoid formation was also promoted by the use of two atom sizes simulating a binary alloy. While the atomic scale substructure of Zone 1' plasma sputtered coatings remains the subject of active investigation, their physical and mechanical properties indicate that it is substantially different from Zone 1 of evaporated coatings, representing a more extreme state of dis-equilibrium. The intragrain microstructure of coatings plasma sputtered in Zone 1' may approach a steady state, as deduced by Ball and Witten (13) and Meakin (14), having an interconnected void network and highly non-bulklike physical properties. Such a sponge-like microstructure would also be consistent with low physical density and the state of near-zero residual stress observed in Zone 1' plasma-sputtered materials (15,16).

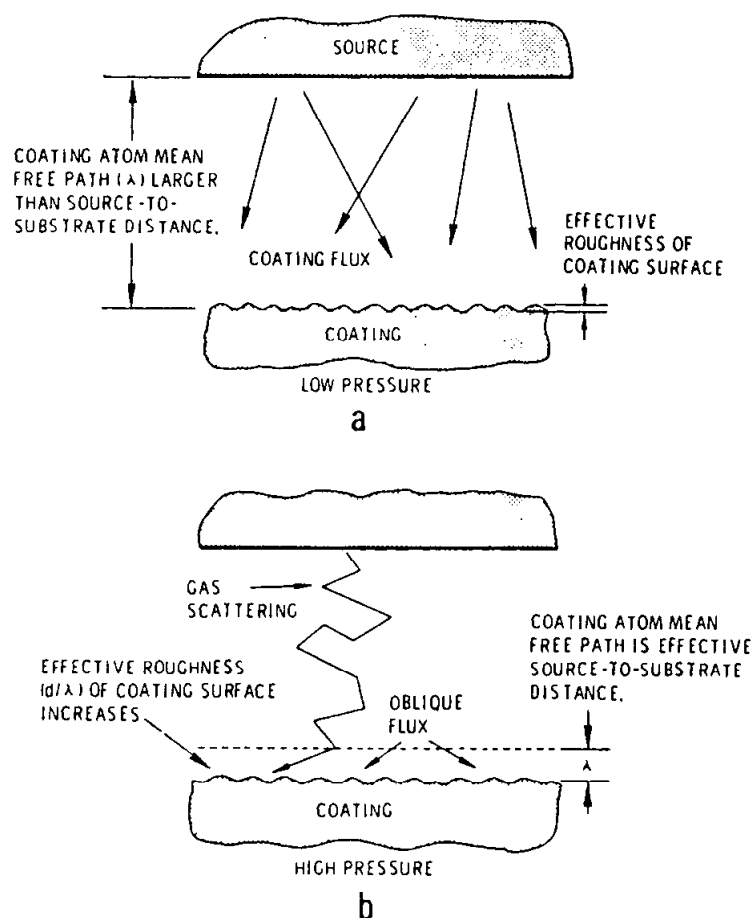


**Figure 2:** Schematic representation of influence of sputtering gas pressure in producing oblique component in coating flux (4).

Messier et al. (17) have elaborated the evolutionary nature of thin film microstructures noted by Movchan and Demchishin (1) in their reference to tapered grains. Yehoda and Messier (18,19) propose a self-similar fractal model of void coarsening during film growth. Film microstructures were observed to pass through successive stages of increasing scale as a function of thickness. In this context Zone T is regarded as the retention of less-coarsened Zone 1 (or 1') structures to greater thicknesses owing to the counteracting stimulation of adatom mobility by temperature and/or bombardment. However, this interpretation does not account for the unique properties of Zone T films, in particular the development of compressive residual stress. The accumulated evidence provides a concept of the unmodified or primitive microstructure of materials plasma sputtered and deposited under refractory conditions. The picture is one of competitively growing tapered grains containing a finer structure of atomic-scale elongated voids (20), which impart directional properties to even amorphous materials. Surface roughness may evolve in proportion to a power of film thickness, while incorporated microvoids develop a semi-independent internal distribution. Succeeding sections will examine how this primitive microstructure can be modified and densified during discharge sputter deposition by stimulated bombardment or coincidental control.

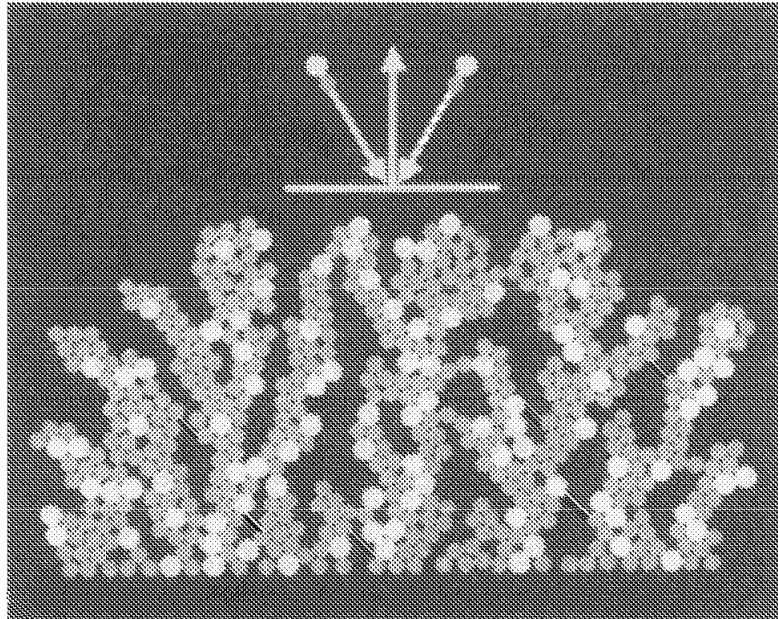


**Figure 3:** Structure formed by oblique-incidence deposition of hard disks from two directions at  $\pm 30^\circ$  relative to the substrate normal. Disks were allowed to relax to the nearest point of contact with two other disks (12).

### 21.1.2 Comparative Modification Strategies

Before discussing bias sputtering and coincidental control individually, it is instructive to compare these and other microstructural control schemes from a mechanistic perspective. The gas pressure axis on Thornton's zone diagram for sputtering in Fig. 1 (b) involves the two overlapping mechanisms of directional scattering of the coating flux at higher pressures and coincidental bombardment by backscattered neutrals and sputtered atoms at reduced pressures. To separate these effects it is useful to construct a new vertical axis from the temperature-pressure plane of Fig. 1(b) to represent bombardment of the coating by energetic atomic or ionic particles. Moreover, the old pressure axis can now represent merely the geometrical component of gas scattering in terms of the reciprocal mean-free-path. Fig. 4 illustrates schematically an isothermal section through such a plot at a temperature below Zone 2, where the mean-free-path has been divided into the source-to-substrate distance to generalize the scale.

The general configuration of this specialized zone diagram derives as follows. Along the horizontal scattering axis at zero bombardment is found classical Zone 1 deposition, when the mean-free-path is greater than the distance to the substrate, i.e.,  $L/\lambda < 1$ , so there is little or no scattering of the coating material in transit. Further out the scattering axis, where the mean-free-path is less than about one-half  $L$ , the coating flux is well randomized before reaching the substrate leading to Zone 1' microstructures with the incorporation of copious microvoids. Between these limiting cases lies a transition, shaded on the plot, from Zone 1 to Zone 1' microstructures as a function of increasing scattering. The vertical dimensions of the Zone 1, Zone 1', and transition regions schematically indicate the relative amounts of bombardment required to convert the respective deposition

to the Zone T microstructure. The postulation of greater densifying bombardment for Zone 1' than for Zone 1 derives from the substantial difference between these primitive microstructures. Supporting evidence is given by Leamy et al. (21) who showed by molecular dynamics simulation that particle energies sufficient to densify normal-incidence deposits were insufficient to densify oblique deposits accumulated under otherwise identical conditions.

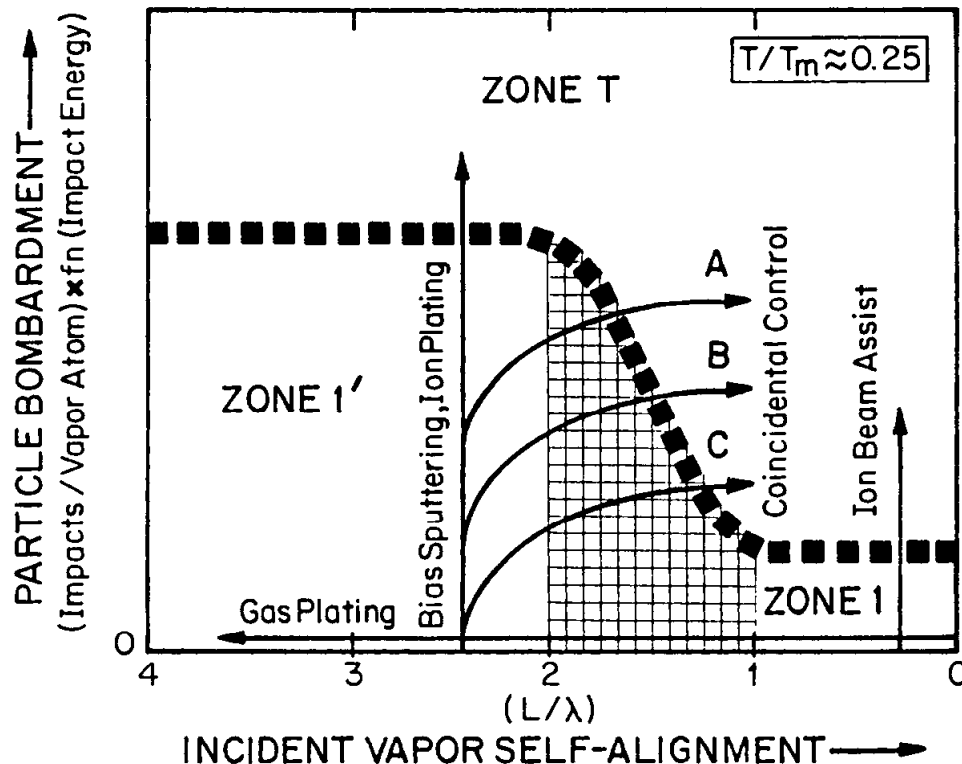


**Figure 4:** Low temperature zone diagram produced by resolving the gas pressure axis of Thornton's model for sputtered film structures into the mechanistic components of incident vapor self-alignment (opposite to directional scattering) and energetic particle bombardment during growth.

Locus lines superimposed on Fig. 4 indicate the comparative regimes of various treatments such as bias sputtering, coincidental control, pressure plating, ion plating, and ion beam assistance. The vertical locus line near the right edge of the figure indicates ion beam bombardment or "assistance" of metal coatings deposited by thermal evaporation at low background pressures. Only moderate bombardment is required to convert such pure metal coatings to the Zone T microstructure. Biased deposition of arc evaporated coatings and simple ion beam deposition could also fall along this locus. A locus line along the base of the figure indicates the regime of pressure plating, which employs gas scattering to increase the throwing power of evaporated coatings beyond line-of-sight incidence, but which also incurs a microstructural transition from Zone 1 to Zone 1'. In the Zone 1' regime lies a vertical locus line representing the regime of bias sputtering and ion plating. A heavier dose of ion bombardment is required to suppress the Zone 1' microstructure incurred by deposition at the elevated pressures characteristic of these processes. Curved loci illustrate the course of treatment by coincidental control wherein both the scattering and the bombardment change with reduction of the sputtering gas pressure.



As indicated, the reduction of directional scattering allows the Zone T microstructure to be achieved with less coincidental bombardment and consequent damage.

Figure 4 highlights the difference between the techniques of bias sputtering and coincidental control for improving the microstructures and properties of refractory materials deposited by plasma sputtering. While bias sputtering employs sufficient bombardment to suppress the unmitigated effects of directional scattering, coincidental control felicitously reduces the detrimental gas scattering simultaneous with the administration of mild bombardment to achieve a similar effect. This perspective sets the stage for further discussions of these two control strategies.

## 21.2 BIAS SPUTTERING

In this, and the following section of the chapter, consideration is given to generic means for harnessing the available energy in rf and dc discharge sputtering processes for control of film structure and consequent physical properties. This section considers bias sputtering while the following section reviews phenomena occurring coincidentally as the sputter gas pressure is reduced through use of magnetron arrangements or supported plasma discharges. The use of impressed substrate biases in dc and rf diode sputter depositions is historically one of the first attempts to control film properties through particle bombardment of the growing film. Reviews of bias sputtering have been previously prepared (22-25) and specific details of its various means of implementation will therefore be minimal. The focus of this section will be instead on the utility of bias sputtering as a means of film property control for a wide variety of materials.

The understanding of structure/property-tailoring by particle bombardment of growing films has perhaps reached its greatest extent in the case of ion beam-assisted depositions. In these processes, it is often possible to reduce the number of variables that exist in plasma-diode type configurations. Thus, models which prescribe a roadmap for property modification in terms of bombarding ion energy and ion/atom arrival rate ratios have been developed for ion assisted depositions (26-29). It is generally recognized that the decoupling of various modes of momentum transfer into growing films (e.g. reflected neutrals, charge-exchange collisions, and negative ion emission) by use of ion beam techniques has allowed this level of sophistication.

Certain specific versions of plasma-based sputtering have also permitted modelling in terms of the bombardment flux/deposition rate domain. In particular, Ziemann and Kay (30,31), using variations of a model for triode bias sputtering developed earlier by Kay and Heim (32), measured film property changes in Pd as a function of the energy deposited per arriving film atom. The triode arrangement lends itself to such an analysis by virtue of its relatively low operating pressure (ca. 1 mTorr), which minimizes the need for consideration of charge exchange collisions and attendant changes in the energies of ions taking part in primary and bias-induced sputtering.

Recognizing the complexity of the plasma/film interaction and its characterization, Thornton (33) proposed using the resputter fraction as a fundamental measure of the deposited energy required to control film morphology and properties. This theme can also be found in a number of studies where control of film features has been promoted through manipulation of variables which affect bias and coincidental bombardment. The use of resputter fraction for growing films as an indicator of the extent of film

bombardment during growth provides a parameter which is decoupled from the particulars of the deposition process; requiring neither a measure of the incident particle type, flux or energy distribution. This viewpoint will be revisited in the discussion of the role of bias sputtering in control of film structure and morphology.

### 21.2.1 Fundamental Aspects of Bias Sputtering

A common feature among various embodiments of bias deposition is the introduction of ion bombardment at the surface of a growing film by imposition of a negative potential at the surface of the growing film relative to the plasma. In this case, positive ions from the plasma are accelerated across the sheath created by the substrate bias and impart sufficient energy to the growing film that atomic rearrangements, including enhanced re-sputtering and recoil bombardment, are promoted. Such modification of a growing film can substantially alter the Zone 1 or Zone 1' type primitive structures, which would otherwise occur at low deposition temperatures, and promote transformation to Zone T morphologies.

In general, the establishment of a substrate bias condition acts in concert with other features of the plasma and deposition geometry, such that the total collisional energy brought to the surface of the growing film arises from a number of contributions. In a simplified diode sputtering arrangement with biased substrate, these factors include: energetic atoms from the target material, reflected neutrals, negative ions from the target, electrons, and ions from the plasma accelerated across the sheath. This latter group includes charge-exchange ions produced in the vicinity of the substrate sheath, since positive ions produced near the cathode cannot overcome the applied potential. The energy with which particles emanating from the cathode strike the substrate is mitigated by the system pressure. The measured or applied bias voltages represent only upper limits to the energies of bombarding ions from plasma, since the ion energy distribution will be determined by the mean free path for charge exchange collisions and the potential across the sheath developed between the substrate and the plasma (34-37).

Several limiting cases for plasma-based processes exist, where the bombardments of the growing film are largely from a single species. One such limiting case is "ion plating" (38), where the principal introduction of collisional energy deposition into a growing film is from bias-induced ion impact. In this process, the film deposition is often from an evaporative source, which of itself would normally lead to Zone 1 structures in the deposited film at low temperatures and low pressure. By utilizing the substrate as a primary cathode, and with introduction of sufficient gas to sustain a glow discharge, the growing film is bombarded with ions from the plasma so created. With regard to Figure 4, the effect of increasing the system pressure is to promote movement to the left along the "gas plating" locus, promoting a Zone 1' ultrastructure. The bias-induced bombardment now refines this structure, although a greater energy/particle flux is needed to effect the transition to Zone T than would be required for the case of evaporation at low pressures, since the effect of increasing the system gas pressure is to promote the Zone 1' structure.

In ion plating, it has been estimated that only about 1% of the collisional energy deposition is from impact of ionized atoms of the film material itself (37), the remainder being due to the effects of gas ions created by the discharge. While various arrangements of the ion plating process have been developed, nominally high gas pressures and cathode voltages are required to initiate and sustain the plasma discharge. Since the substrate

becomes a sputter cathode, overall film deposition rates may be lower than expected in the absence of the plasma-assisted process.

The cathodic arc process (39) is another limiting case wherein the ionized target atom flux is now the dominant contributor to the energy deposition in the growing film. Since the arc plasma is sustained chiefly by vaporized atoms of the target material, the necessity for a gas to sustain the discharge is primarily limited to those embodiments of the process where reactive species are introduced for the formation of compound films. Furthermore, multiple charge states of target ions usually exist, thus greatly increasing the energy input from these ions under bias conditions at the growing film.

In a particularly interesting implementation of "unbalanced magnetron" sputtering, Window and Savvides (40,41) have developed a plasma-based deposition process in which a degree of control exists over both bias voltage and plasma density. This control is made possible by spatially tuning the plasma plume associated with a planar magnetron by adjusting the degree of electron confinement with an electromagnet. In this manner, the flux of impinging ions, acting under the influence of an imposed substrate bias, can be adjusted over several orders of magnitude. Since dc biasing in balanced magnetrons is ineffectual due to the plasma confinement near the cathode, this arrangement allows a compromise in terms of enhanced sputter flux from the cathode and reduced operating pressures, in tandem with an ability to impose a dc sheath at the substrate position.

As had been suggested by Thornton (33), the refinement of Zone 1' primitive microstructures through bias sputtering may be viewed in terms of resputtering. Historically, the concept of introducing a second level of sputtering at the growing film for adjustment of film properties has been attributed to Frerichs (42) who developed an asymmetric ac deposition system for diode sputtering. Maissel and Schaible (43) described a dc bias system for deposition of tantalum films, wherein a substrate bias of approximately -200V resulted in films of minimum resistivity. For conductive targets and substrates dc biasing represents a straightforward approach, in which the substrate becomes a secondary cathode with respect to the system ground or alternate anode. The limiting energy of impinging ions across the substrate sheath will be the difference between the applied potential and that of the plasma. Depending on the extent of inelastic collisions (which will be a function of gas pressure and sheath dimension), the ions impacting the surface will have a distribution of energies with usually only a small fraction of the total flux having the full potential of the sheath (34-37). Sputter deposition configurations which operate at lower pressure regimes (e.g. triodes (33) or magnetrons (44)), will, in general, permit a distribution of ion energies with a greater proportion having the full energy of the sheath. Both triode and magnetron arrangements, however, also permit more non-randomized bombardment by reflected neutral atoms of the sputter gas produced at the cathode surface. Of themselves, these arrangements promote Zone 1/Zone T transitions by coincidental bombardments, and minimization of Zone 1' primitive microstructures. With regard to Fig. 4, these methodologies tend to be on the right-hand side of the diagram. Substrate biases induced by rf means (owing to the plasma localization near the cathode and typically low operating pressures), do not therefore need to produce the high degrees of particle impact energy or flux to produce a transformation to Zone T microstructures.

The ability to deposit both insulating materials as well as metals on insulating substrates has arisen from the practical development of rf sputter deposition and biasing

techniques. These methods, and various means of introducing substrate bias under rf conditions have been reviewed by Vossen (24). The upper limit to the energy of an impinging ion in an rf deposition may be as much as twice the sheath potential developed between the substrate and the plasma (45). As surmised from Figure 4, operation in a low pressure regime reduces the flux-energy product requirements permitting more modest bias potentials than those needed in ion plating for achieving the transition to Zone T.

## 21.2.2 Applications

**21.2.2.1 Impurity Atom Resputtering and Ion Implantation Effects:** One of the earliest applications of bias sputtering arose from a desire to minimize the gaseous impurity content of thin resistive and superconductor films, whose properties were greatly influenced by the uptake of, and bombardment by, reactive gases (42,43). The mechanism for the beneficial removal of contaminants from the film surface through use of substrate bias has been attributed to the preferential resputtering of the atomically lighter impurity species (e.g. oxygen, nitrogen) from the growing film surface (46). The process may become self-defeating, if the bombarding ions used to "clean" the growing films become implanted under the influence of sufficiently high applied bias. Secondly, reactive ions present in contaminated plasmas may also be implanted, rather than removed from the surface, thus tending to stabilize defects within the coating. Energetic, reflected neutrals may also be implanted in the growing film at sufficiently high cathode voltages and low operating pressures. Ion implantation accompanying bias sputtering has been addressed by various investigators (47-50). Generally, a combination of high bias voltages, low atomic number sputter gases and low atomic number matrices will promote ion implantation in biased deposition.

**21.2.2.2 Control of Film Stress and Microstructure:** Since Zone 1 or Zone 1' microstructures represent highly defective films in terms of both tapered, unbonded grains as well as atomic scale voids in the Zone 1' case, it may be expected that such structures will be stabilized against post-deposition thermal annealing by the introduction of surface active contaminants either during or after deposition. The typically tensile intrinsic stresses observed in these primitive structures (51) may promote degradation by cracking and an enhanced propensity for chemical reactions relative to the large extent of available surface area. Minimization of film impurity content through bias sputtering is one means of influencing the evolution of film microstructure through elimination of species which retard both bulk and interfacial diffusion as a consequence of their chemical affinities for the host material or segregation tendencies which tend to stabilize interfaces.

While removal of stabilizing impurities is one consequence of bias sputtering which may allow favorable microstructural evolution, there are intrinsic restructuring aspects of the bombardment which promote refinement of the primitive microstructures. These intrinsic atomic rearrangements associated with the bias sputtering process account for its utility in disrupting the Zone 1' primitive microstructures for a wide variety of film materials. Thornton discussed the morphological changes accompanying bias deposition of copper films in a hollow cathode system at various pressures (33). Resputtering in principally forward directions was believed to be primarily responsible for disruption of the primitive growth structure. Increasing the sputter gas pressure in this particular configuration was felt to promote forward resputtering in directions which were effective in suppressing large topographical features associated with a roughened substrate. Increased pressures in this geometry did not, however, reduce the effects of bias in disrupting the

Zone 1 microstructures. Thornton has reviewed a number of developments in the understanding of the evolution of thin-film microstructures which support the resputtering viewpoint (20). Results of molecular dynamics computer simulations by Müller (52) also suggest that forward resputtering of a growing film promotes elimination of Zone 1' type ultrastructures. One of the earliest indications that resputtering associated with biased deposition of film material promoted densification of films was observed for rf-sputtered  $\text{SiO}_2$  by Jones, et al. (53) as a noted difference in etch rates for the primary (biased) deposit, and the secondary deposit formed by resputtered material. Further studies of the resputtering phenomena with  $\text{SiO}_2$  (54) showed that optimum film quality (e.g. etching behavior, and dielectric strength) was achieved at a resputter fraction of approximately 60%. This degree of resputtering falls within the window of 30-70% suggested by Thornton (33) as being desirable to obtain optimum film properties.

Vossen and O'Neill (55) studied the rf bias deposition of various metals and observed that optimum densification of gold (determined microscopically) coincided with a minimum resistivity approaching the bulk value. Later tabulations by Vossen (24) suggested optimum bias voltages for various materials. In a qualitative sense, more noble fcc metals (e.g. Au, Ag, Cu) required lower degrees of bias than did more refractory metals such as tungsten and tantalum which required the highest levels of bias to obtain optimum physical properties. Vossen and O'Neill (55) also suggested the significance of the bulk recrystallization temperatures of these metals as a guideline in assessing the energy deposition required to effect an approach to bulk-like physical properties by bias deposition.

Blachman (56) also suggested classification of various metals by their refractory nature and nobility with regard to control of stress and the role of bias in impurity resputtering. In light of both high reactivities of the refractory metals for such contaminants as oxygen and nitrogen, as well as generally high activation energies for surface and bulk diffusion, relative to the more noble metals such as gold, the mechanisms which lead to structural refinement during bias sputtering may be difficult to separate when film contamination by reactive species is possible. The elimination of reactive contaminants during bias bombardment should promote both adatom diffusional processes and recoil implantation of adatoms into void regions. In the absence of reactive contaminants, the ease with which atoms of the growing film are forward scattered into void regions would appear to be governed by the extent of momentum transfer from the impinging particle flux and the imparted energy relative to the binding energy of the recoiling atom in its surface or bulk site.

In the development of a model to predict critical ion/atom arrival rate ratios as a function of energy for covalently bonded materials such as germanium, Brighton and Hubler (29) concluded that atomic rearrangements in the bulk were primarily responsible for ion-assisted stress annealing, as had previously been described by Hirsch and Varga (57). They discounted effects of enhanced surface diffusion or thermal spikes associated with the bombardment process.

Direct evidence for microstructural changes occurring with bias sputtering was obtained by Mattox and coworkers (58,59). Since that time, there have been numerous reports in the literature of both film stress and microstructural modification through use of bias deposition techniques. The ability to disrupt the Zone 1 or Zone 1' type morphologies for a variety of material types (including metals, alloys, compounds and amorphous materials) suggests the importance of models involving material redistribution. Table 1

summarizes a number of reported film modification results from the literature, where bias sputtering had been employed to change film properties and structure.

**Table 1:** Summary of selected applications of bias sputtering for thin film property modification

Material	Bias/configuration	Property change observed	Ref.
Elements	Al rf-diode	Structure, Resistivity	55
	rf-diode	Planarization	64
	rf-mag.	Morphology, Step coverage	65,66
	dc-mag.	Step Coverage	67-69
	rf-dc-mag.	Resistivity, Resputtering	70
	dc-diode	Resis., Stress, Ar implantation	71
Ag	rf-diode	Physical prop.	24
Au	rf-diode	Structure, Resistivity	55
	dc-diode	Stress, Resistivity	56
Be	rf-dc-mag.	Morphology	72
C	dc-unbal.mag	C-C bonding	41
Cr	dc-triode	Microstructure, hardness	73
	rf-dc-diode	Stress, Density	59
Cu	dc-hol.cath	Microstructure	33
	dc-triode	Recrystallization behavior	74
	rf-diode	Resistivity	55
Fe	dc-unbal-mag	Stress, Resistivity	75
Ge		Physical properties	24
	dc-diode	Crystallinity	61
Mo	dc-diode	Stress, Resistivity	56,76,77
	rf-dc-diode	Purity, Structure	78
	dc-unbal-mag	Resistivity, Stress	75
Nb	ac-diode	Purity	42
	rf-dc-diode	Resistivity, Resputtering	70
	dc-triode	Purity, Lattice dilation	32
	dc-unbal. mag.	Resistivity, Stress	75
	dc mag.	Stress, Microstructure	79
Ni	dc-diode	Ar implantation	47
	rf-triode	Density, Resistivity	55
Pd	dc-triode	Stress, Resistivity	31
Pt	rf-diode	Adhesion	24,55
	dc-unbal-mag	Resistivity, Stress	75
Ta	ac-diode	Purity	42
	dc-diode	Resistivity, Structure	43,59
	rf-diode	Resistivity	55
	dc-unbal-mag	Resistivity, Stress	75
W	rf-diode	Microstructure	59
	dc-unbal-mag	Resistivity, Stress	75

**Table 1:** continued.

Alloys			
Al-Cu	rf-mag.	Microstructure	80
Co-Cr	rf-diode	Epitaxy, Magnetic anisotropy	81,82
Cu-Cr	rf-dc-diode	Crystallinity	83
Gd-Co	rf-diode	Magnetic anisotropy	84-86
Gd-Co-Fe	dc-diode	Comp., Magnetic anisotropy	87
Ni-Cr	dc-diode	Preferred Orientation	88
Ni-La, Y	dc-triode	Microstructure	89
Ti-W	rf-mag.	Composition, Resistivity	90
WC-Co	rf-dc-diode	Composition, Microstructure	91
304 Stainless	dc-triode	Composition	92
Compounds			
Al <sub>2</sub> O <sub>3</sub>	rf-diode	Step coverage, Resputtering	62
NbN	dc-diode	Composition, Superconduct.	93
SiC	rf-diode	Morphology	17
Si <sub>3</sub> N <sub>4</sub>	rf-diode	Step coverage, Resputtering	62
SiO <sub>2</sub>	rf-diode	Structure, Step coverage	54,62,63
TiC	rf-dc-diode	Adhesion, Tribology	94
	rf-react.	Composition, Lattice param.	95
TiN	rf-react.	Resistivity, Structure	96
	dc-react.	Purity	97
Ti(OC)	rf-diode	Microstructure	98
Doped ZrO <sub>2</sub>	rf-diode	Microstructure	99,100
7120 Glass	rf-diode	Thermal Expansion coef.	101

The acme of ion-assisted modification is no doubt seen in methods of arriving at high states of crystalline perfection for such materials as compound semiconductors. Greene and Barnett have reviewed the role of ion-assisted depositions in such endeavors (60). It is interesting to note that Wehner in a 1962 patent (61) claimed an ability for utilizing the energy available in a glow discharge plasma to arrive at epitaxially grown crystalline deposits, and that the optimum degree of resputtering had been specified at 12.5% for the case of germanium.

**21.2.2.3 Control of Film Topography:** Two other key applications of bias sputtering have emerged largely from requirements for topographic control of depositions in microelectronics. In the first, resputtering is accentuated through bias deposition for promoting step coverage as would occur where metallizations or other films are required to follow contours over features in integrated circuits. Seeman (22) originally showed the ability of biased deposition to promote coverage of trench sidewalls through the resputtering of material from the floor of the trench. Vossen (24) and later Kennedy (62) have shown

the utility of bias sputtering in obtaining suitable topographical coverages in microelectronics. In these cases, redistribution of material during resputtering also tends to "fill in" regions which may normally have been shadowed from the deposition leading to circuit "opens" or points of mechanical weakness due to lack of material.

A somewhat inverse situation exists where it is desirable to apply a film wherein underlying protuberances are minimized at the final surface so that lithography and further metallizations are occurring on a planarized surface. Bland, et al (59) suggested how forward resputtering of geometric features on surfaces could be used to refine surface morphology. In the case of "planarization", where it is both desired to produce a deposit and also minimize existing surface topography, the resputtering in largely a forward direction is exploited. The role of bias-induced resputtering on planarization has been discussed by various authors (20,59,63)

### **21.3 COINCIDENTAL CONTROL OF COATINGS DEPOSITED BY PLASMA SPUTTERING**

Coincidental control harnesses the forces already at play in plasma sputtering to improve the resultant coatings. These forces consist on the one hand of the energetic particles naturally issuing from the target, including both the atoms of coating material having average energies in the range of 10 eV and the neutralized sputtering ions rebounding from the surface with energies frequently in the range of 100 eV or greater. On the other hand are the forces tending to diffuse the alignment of the incident coating flux at the surface being coated. As was discussed with reference to Fig. 4, reduction of the sputtering gas pressure changes both of these effects simultaneously. Although recent attention has tended to focus on the passage of bombarding particles to the substrate, self-alignment of the incident coating material may be of equal importance by minimizing the required concurrent bombardment.

While the emission of energetic neutrals was recognized and studied prior to the development of magnetron plasmas operable at low pressures (see for instance Winters and Kay (47)) coincidental control was not purposely employed for microstructural modification of sputtered coatings. Several instances are seen in retrospect where the effects of coincidental bombardment are evident, when sputter deposition was infrequently carried out by techniques such as ion beam sputtering (Chopra (102)), triode sputtering (Stuart (103)), and others (104) at especially low gas pressures (105) or with massive target elements such as tantalum (106,107), tungsten (108-110), and platinum (111). The development of magnetron sputtering and the consequent ready access to low pressure sputtering capability set the stage for the identification and investigation of coincidental control as a deposition technique (15,16,112,113). Indeed, for low pressure magnetron sputtering with the usual well-confined plasmas (excepting the recent "unbalanced magnetron" (40)), where the absence of ionized species near the substrates precludes bias sputtering, coincidental control becomes, without the introduction of ion beams, the only plasma-based option. All that is required is to reduce the gas pressure sufficiently to decrease the randomization of the sputtered flux and simultaneously allow some of the existing energetic neutrals to penetrate through to the substrates. Motohiro and Taga (114), Graz-Marti and Valles-Abarca (115), and Somekh (116) have theoretically studied the gas scattering of particles issuing from a sputtering target with valuable insights, but the practical application of coincidental control remains empirical.



### 21.3.1 Internal Stresses and Physical Properties

While the physical properties of sputtered refractory coatings may often be of primary importance in application, the intrinsic (i.e. nonthermal) film stress is a highly structure-dependent property that can serve as a sensitive barometer of deposition conditions and resultant physical properties. For the case of molybdenum sputtered in argon from a cylindrical magnetron Fig. 5 illustrates the wide variations of intrinsic stress typically found in metal films deposited at various gas pressures down to 1 mTorr (0.13 Pa) (117). At high pressures the stress approaches zero. This differs from the fixed tensile stress normally observed in thermally evaporated metals, as indicated for molybdenum on Fig. 5 (118). Consistent with the deduced microporosity of such sputtered films the trend toward zero stress coincides with the diminishing lateral connectivity of the structure and the consequent inability to support appreciable stress. By comparison the evaporated materials are sufficiently strong in the lateral direction to support high tensile stresses. Klokholm and Berry (51) report intrinsic tensile stresses of 1.1 GPa in evaporated molybdenum, which exceeds the 0.6 GPa tensile strength of the bulk pure metal (119), owing to the refined grain size of evaporated films. Clearly there is not much weakness from voids or weak grain boundaries in evaporated molybdenum. These differences are consistent with the hypothesis of Figs. 1(b) and 4 that the Zone 1' structure in sputtered materials is distinct from and less bulklike than the Zone 1 structure of evaporated metal coatings. Physical property measurements supporting this observation are seen in Table II, where more anomalous values of resistivity and reflectivity are reported for Zone 1' sputtered molybdenum.

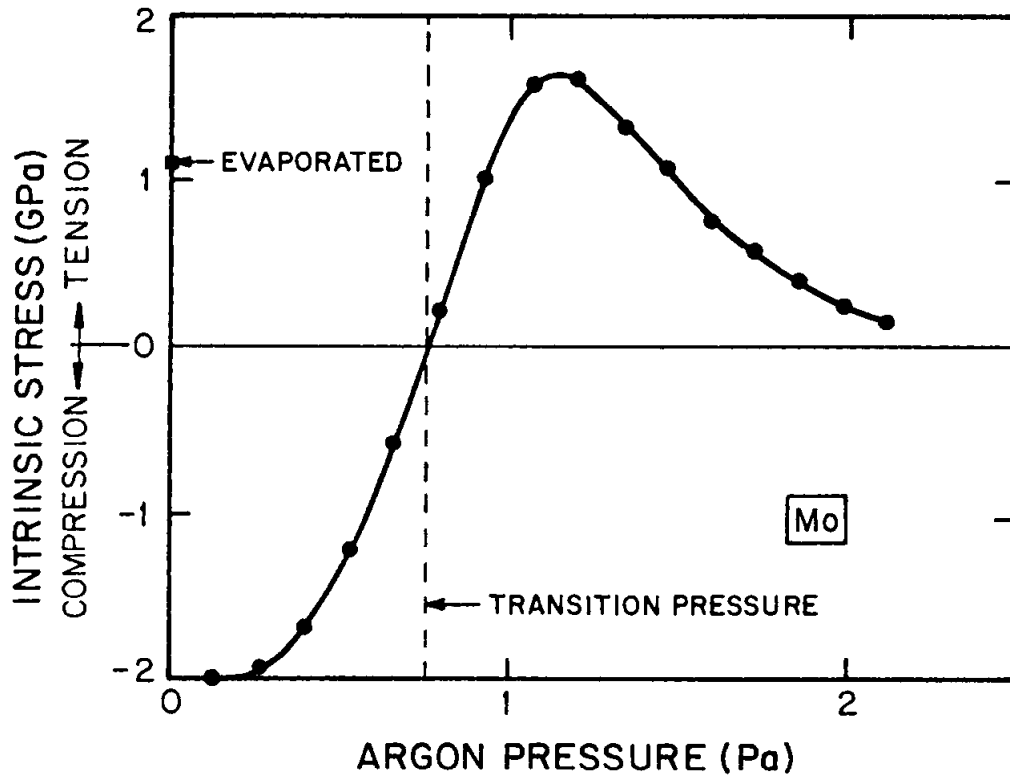
**Table 2:** Properties of Bulk, Sputtered and Evaporated Molybdenum

Material	Microstructure	Intrinsic	Resistivity	Reflectivity	Ref.
Mo	Zone	stress (GPa)	( $\Omega - \text{cm} \times 10^6$ )	(% at 560nm)	
bulk	3	0	5.6	58	119
evaporated	1	1.1 (tens.)	30	50	120
sputtered*	1'	$\approx 0$	100	35	121

\*Even higher resistivity and lower reflectivity are observed when film preparation conditions allow the possible incorporation of oxygen from background gas.

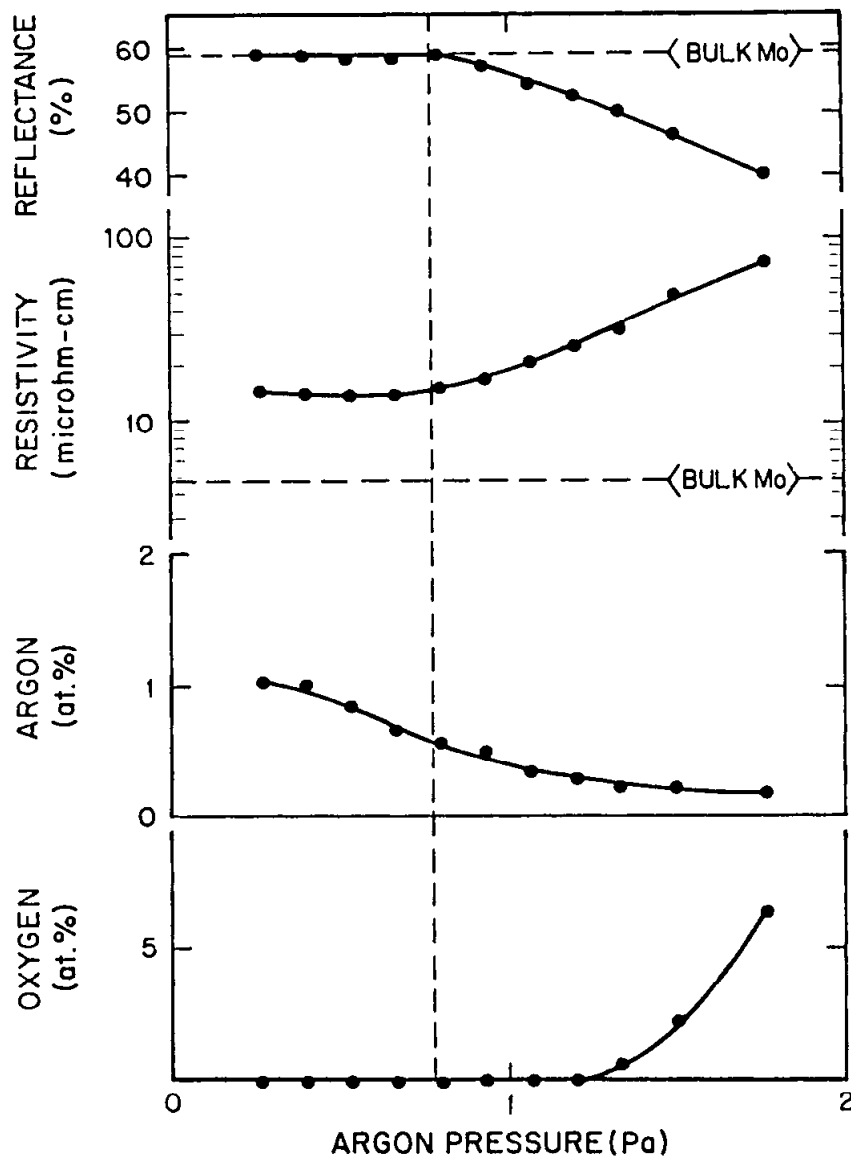
From the high pressure extreme of the Zone 1' microporous microstructure Fig. 5 shows that films deposited at successively lower gas pressures support tensile intrinsic stresses increasing to a peak value of substantial magnitude. The evident gain in film integrity indicates that microporosity must be largely suppressed at pressures approaching the tensile maximum. With continued reductions of the pressure the trend in intrinsic stress reverses moving sharply through zero to large compressive stresses. While the tensile stress excursion may result in part from reduced scattering and increased alignment of the coating flux, the reversal of stress toward compression clearly indicates the increasing effects of particle bombardment, sometimes likened to atomic shot peening (122). Moreover, the incorporation of high compressive stresses suggests the accumulation of impact damage and resultant overcrowding of coating atoms in disordered re-

gions such as grain boundaries. The zero intercept at the point of stress reversal has been termed the transition pressure for the sake of reference and may also represent an adjustment by coincidental control that yields coatings with the least structural disorder (81).



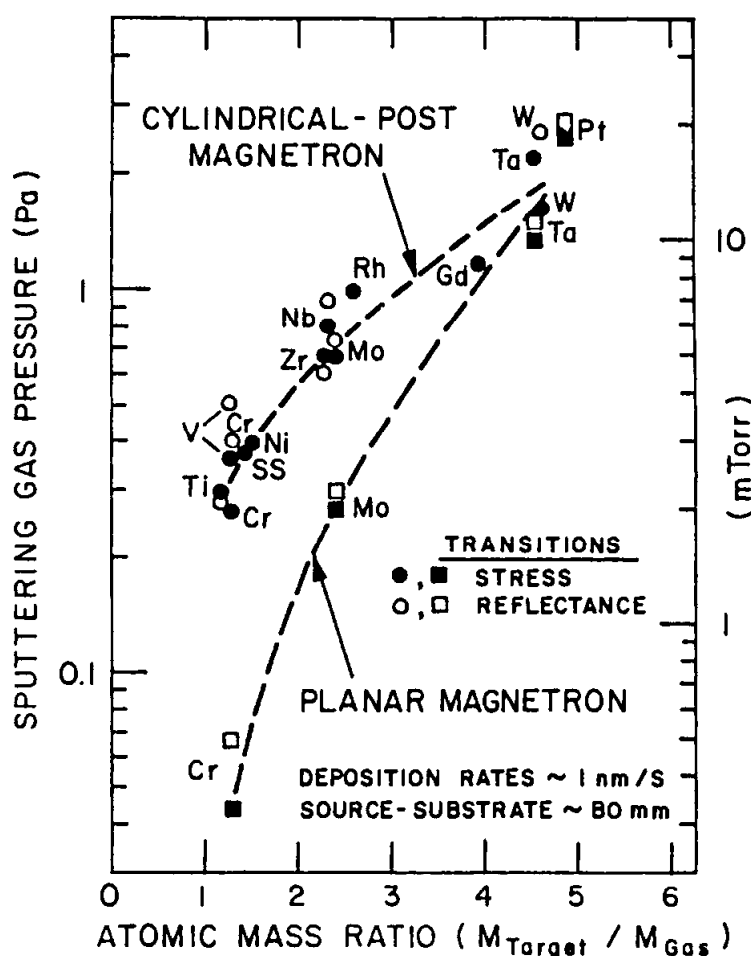
**Figure 5:** Argon pressure dependence of intrinsic film stress in molybdenum metal films sputtered from a cylindrical magnetron and deposited at 1 nm/s onto molybdenum coated substrates at a distance of 0.1 m (121).

Figure 6 shows corresponding changes in physical properties and gas incorporation in coatings deposited at various argon pressures. The reflectance reaches bulklike values at the transition pressure. The resistivity decreases markedly with decreasing pressure and passes through a shallow minimum below the transition pressure. The slight increase at lower pressures correlates with the increasing content of argon embedded in the metal, which again evidences substantial bombardment. The presence of oxygen, which is detected only in films deposited at the higher pressures, is believed to result from oxygen uptake and absorption in the corresponding microporous structure after deposition. Judging from the argon incorporation in the sputtered molybdenum coatings, as well as the relative atomic masses which indicate that argon will backscatter from molybdenum with 41 percent or more of its primary energy, the locus of coincidental control for the depositions of Figs. 5 and 6 is expected to lie on the zone diagram of Fig. 4 along a curve such as that labeled "A". This is an example of the locus to be expected when the coincidental bombardment is relatively vigorous. Consequently the events and the resulting films should resemble those obtained by bias sputtering.



**Figure 6:** Argon pressure dependence of reflectance (at 560 nm), resistivity, and argon and oxygen concentrations detected by electron microprobe in molybdenum films sputtered from a cylindrical magnetron at 1 nm/s onto molybdenum coated substrates at a distance of 0.1 m.

Observations on a variety of sputter deposited coatings have established that the effects induced in molybdenum by coincidental control are representative of other materials (15,16,112,113). For any given material, however, the salient pressure regime characterized by the transition pressure is strongly dependent on the relative atomic masses of the sputtering target and gas. Figure 7 shows a systematic shift of the transition pressure with target atomic mass for elemental metals sputtered with argon. The two separate data lines for cylindrical and planar magnetrons indicate a further dependence on target geometry. Although the trends are universal, the specific location of the curves will vary with differing apparatus geometries.



**Figure 7:** Sputter-deposition map on coordinates of sputtering gas pressure and target-to-gas atomic mass ratio showing the stress/reflectance transition boundaries for metals dc sputtered from cylindrical and planar magnetrons and deposited at 1 nm/s at distances of 0.1 to 0.2 m. Sputtering conditions below and to the right of the transition pressure line yield coatings with compressive stresses, maximum reflectance, and otherwise optimized physical properties (16).

A similar shift occurs when a given target is sputtered with the other inert gases. Figure 8 shows the results of stress measurements bracketing the transition pressure for molybdenum films deposited with neon, argon, krypton, and xenon (123). A systematic shift with atomic mass is again evident. Of special significance, however, is the presence at sufficiently low pressures of compressive residual stresses even when Mo is sputtered with Xe. Since the atomic mass of xenon exceeds molybdenum, the energy of gas particles rebounding from the target should be quite low, similar to the energies of the sputtered particles themselves. Consequently the potential for bombardment in this case is limited and coincidental control relies more heavily on the directional self-alignment mechanism. The relevant locus on Fig. 4 is indicated by the curve labeled "C". When embedded gas contents of the same four gases were measured on the compressive molybdenum coatings, the levels varied systematically from 5 percent of neon to undetectable amounts of xenon, i.e., less than 0.01 percent. Again this suggests minimal bombardment in the latter instance.

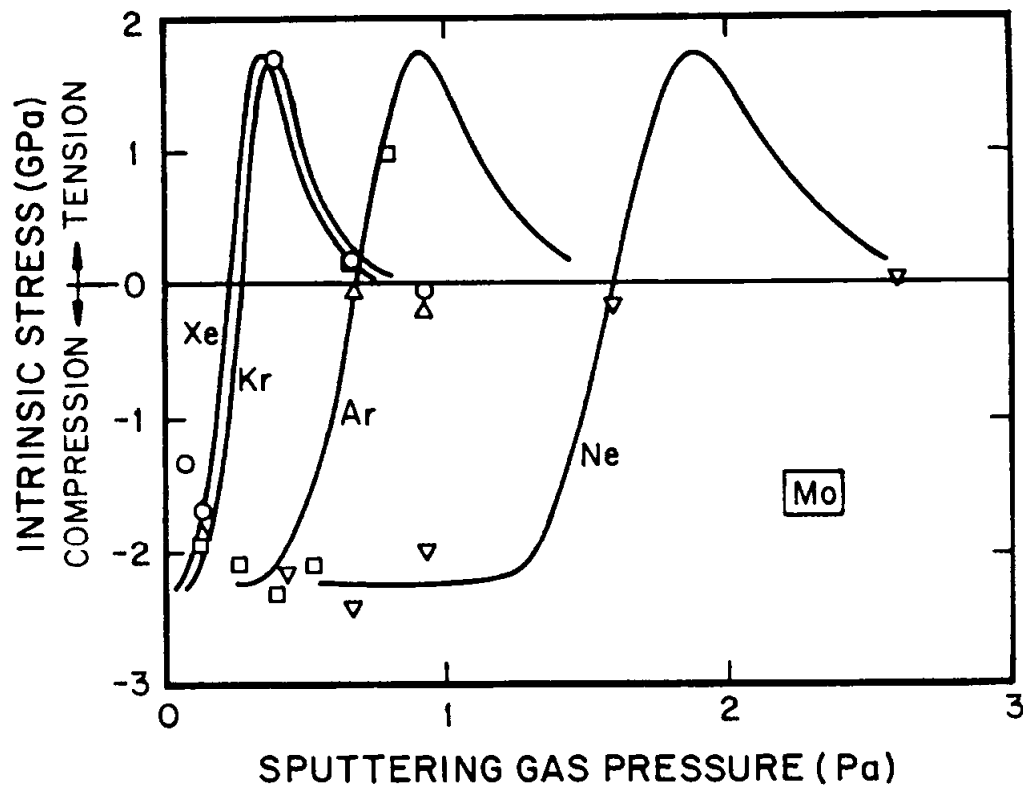


**Figure 8:** Gas pressure dependence of intrinsic film stress in molybdenum metal films sputtered from a cylindrical magnetron with Ne, Ar, Kr, and Xe noble gases and deposited at 1 nm/s at a distance of 0.1 m (123).

The preceding discussion indicates that the choice of sputtering target material and sputtering gas with respect to their relative atomic masses is an important if not crucial consideration for the application of coincidental control. In cases where the optimization of physical properties is desired coincidental control enables the Zone T microstructure to be achieved without excessive bombardment through the self-alignment of the coating flux that accompanies reduction of the gas pressure. This can be accomplished either by the selection of lighter target materials where there is a choice, or alternatively by use of the heavier inert gases. A further instance of this approach has been reported for silicon sputtered with argon (124). The added cost of the heavier inert gases, Kr or Xe when called for, can be moderated by the practice of static chamber sputtering (125), a viable technique when practiced in conjunction with a load lock to minimize the introduction of contaminating gases (51).

In addition to the gas pressure and the choice of gas and target material, practically every other plasma sputtering process parameter exerts at least a secondary influence on coincidental control which can sometimes be used to advantage. These include the dynamic gas flow (117), the sputtering rate (121,126), the cathode voltage (127), the target shape (113,128) and the substrate proximity (117), orientation (129), and motion (129). Early recognition of the fundamental role of gas scattering in coincidental control immediately suggested a coupled effect of substrate-target proximity, however preliminary measurements were inconclusive. Then Wu (79), sputtering niobium with argon, dem-

onstrated that close proximity to the target increased the transition pressure in a manner consistent with such coupling. Somekh (116) suggested that the product of pressure and distance could be usefully plotted rather than pressure alone to rationalize results from coatings prepared at various distances from the target. An experimental test, however, did not bear out the quantitative applicability of this approach (117), owing most probably to the additional effect of the self-alignment of coating flux on coating microstructure and properties, beyond the simple bombardment concept. While the cathode voltage is not ordinarily an independent control parameter in magnetron sputtering, Thornton et al. (127) varied the confining magnetic field to enable independent excursions of the voltage, thereby demonstrating a marked dependence.

Perhaps more unexpectedly, increasing the rate of sputtering as determined by the cathode current also moves the deposited microstructure and properties along the locus of coincidental control toward Zone T (121). Since the cathode current is, in addition to pressure, the principal control parameter in magnetron sputtering, this provides another practical stratagem for coincidental control. As demonstrated by Rossnagel (130) and detailed elsewhere in this volume, the rate effect arises from heat dissipation in the sputtering gas with consequent thinning of its density in the vicinity of the target, thereby reducing the associated gas scattering.

An attribute of magnetron sputtering is the relative freedom afforded in the placement and manipulation of a substrate, owing to its de-coupling from the electrodes. Substrates are frequently rotated or moved past the source in order to distribute the coating more uniformly. A consequence, however, is to present the surface being coated at a variety of angles to the arriving flux, thereby simulating the dis-alignment of the flux by gas scattering. It is not surprising, therefore, that substrate inclination and rotation have been reported to move a coincidental control point along its locus away from Zone T toward Zone 1' with more porous, tapered grain microstructures, tensile stress, and anomalous physical properties resulting (129).

### **21.3.2 Special Investigations and Applications**

While the possibility of coincidental control has been established for some time, published reports of its application remain infrequent. This may derive in part from a failure to identify its advantage over bias sputtering in utilizing less bombardment to effect Zone T deposition. Nevertheless some notable examples of coincidental control have appeared. Entenberg et al. (131) studied the residual stress, physical properties, and microstructure of copper sputtered onto polyimide webbing. Although copper is a relatively soft and noble metal in terms of Blachman's classification (56), their results offer a striking demonstration of coincidental control of copper films on flexible substrates of low thermal capacity, confirming in detail the phenomena seen with more refractory materials. Amorphous coatings of a Mo-Ru-B refractory alloy were sputtered by Bieg (132) onto inertial confinement microspheres with stress minimization by coincidental control in order to build up heavier deposits, thereby demonstrating its application to noncrystalline materials. Thakoor et al. (133) also included W-Ru-B alloys in their study of metallic glasses for corrosion and wear applications, minimizing internal stresses by coincidental control to obtain thick, dense, protective coatings. They point out that the observation of coincidental control and associated phenomenology in glassy metals constrains models of intrinsic tensile and compressive stresses not to rely on crystalline mechanisms.

It has been noted that the sharpness of the transition from tensile to compressive stress as a function of sputtering gas pressure poses a difficulty when coincidental control at the zero stress crossover is desired. Bensaoula et al. (126) reported that the stress transition for Mo and W becomes more gradual at higher sputtering rates, thereby easing the margin of error in process control. In addition they employed rf substrate bias to broaden the parameter space for control at zero stress. This can be understood with reference to Fig. 4 where it is apparent that an excursion by biasing from a coincidental control pathway into the direction of pure bombardment will cross into Zone T more gradually, albeit at the possible cost of greater resputtering, impact damage, gas entrapment and heating. A hybrid approach, however, may offer a way to minimize this penalty while improving control stability. An alternative control scheme has been investigated and practiced by Cuthrell et al. (134) in a unique application requiring a coating with high uniformity, low resistivity, and tensile or zero stress having minimal stress anisotropy in the plane of the film. By toggling the argon pressure alternately between settings above and below the stress transition they achieved reproducible control yielding nearly isotropic tensile, compressive, or zero stress as desired, while retaining a suitably low resistivity.

While the study of coincidental control has adhered almost exclusively to metals and alloys, Este and Westwood (135) applied it to the reactive deposition of Al and Ti nitrides, materials often obtained with undesirably high compressive stresses under reactive sputtering conditions. Raising the nitrogen pressure or adding a partial pressure of argon caused a moderation of the compressive stress and a transition into tension, however the correlation of the stress transition with optimum physical properties seems to be different from metals. Full density and bulklike physical properties in the nitrides may be achieved only at elevated values of compressive stress, owing most probably to directional nonmetallic bonding and a resulting propensity to incorporate microporosity even without dis-alignment of the coating flux by gas scattering. In other words, the regime of Zone 1' in Fig. 4 may extend further to the right for this class of materials so that Zone T cannot be entered as readily by a reduction of directional scattering, but requires in addition a greater dose of bombardment.

In metals the correlation of optimum physical properties with the stress transition suggests that the corresponding microstructure may incorporate a minimum of defects, balanced as it were between the onset of microporosity on the one hand and the overcrowding of atoms at the other. In this light, the report of Leu et al. (81) offers the intriguing possibility of epitaxial growth of sputtered Co-Cr magnetic films on MgO single crystals by coincidental control. The best results were obtained at the low argon pressures of 1 to 2 mTorr (0.13-0.27 Pa) on unheated substrates with chromium contents of 21 to 23 percent. By comparison sputter deposition at 5 mTorr (0.68 Pa) or with negative substrate bias of 25 and 50 volts produced polycrystalline films. The atomic masses of cobalt and chromium are sufficiently close to argon that the energies of argon neutrals rebounding from the target will be mild. The locus of coincidental control for this combination should resemble curve "C" on Fig. 4. Apparently the directional alignment plus mild bombardment incurred by coincidental control promotes full density epitaxial growth without the incorporation of excessive defects or impurities leading to renucleation.

Other studies of coincidental control include the combined effects of argon pressure and substrate-to-source proximity on the microstructure of sputter deposited Cu-Ni alloys by Barber and Somekh (136), as detected by changes in thermopower. Hoshi et al. (137)

investigated the effects of pressure on the magnetic properties, surface smoothness, elastic modulus, and corrosion resistance of sputter deposited Co-Pt magnetic recording films, finding the best magnetic response at high pressures where the other properties were degraded. Significantly, microporosity caused by sputtering at 30 mTorr (4 Pa) reduced Young's modulus of the films to a quarter of the bulk value. Nakahara et al. (138) followed the microstructural transition as a function of sputtering pressure in Fe and amorphous Fe-Tb magneto-optic films by transmission electron microscopy. Jankowski et al. (139) utilized coincidental control to fabricate stress-free Al/Ta multilayers with more than a thousand laminations for transmissive X-ray optics. The argon pressure was cycled between 5 and 50 mTorr under computer control in deposition of the aluminum and tantalum layers respectively in order to maintain strict planarity of the laminate.

A final example involves the deposition of highly refractory molybdenum metal coatings onto exceedingly soft plastic substrates. In this case coincidental control was practiced by varying the cathode current and consequent sputtering rate while holding the argon pressure constant. Stresses in coatings deposited at various rates were determined from the associated substrate bending. Elastic strains in the same coatings were deduced from X-ray peak shifts and lattice spacings normal to the plane of the films. Together these results yield the stress-strain plot of Fig. 9, where the central near-linear portion of the curve corresponds to the tensile-to-compressive stress transition and has a slope in good agreement with the appropriate combination of handbook elastic constants (140).

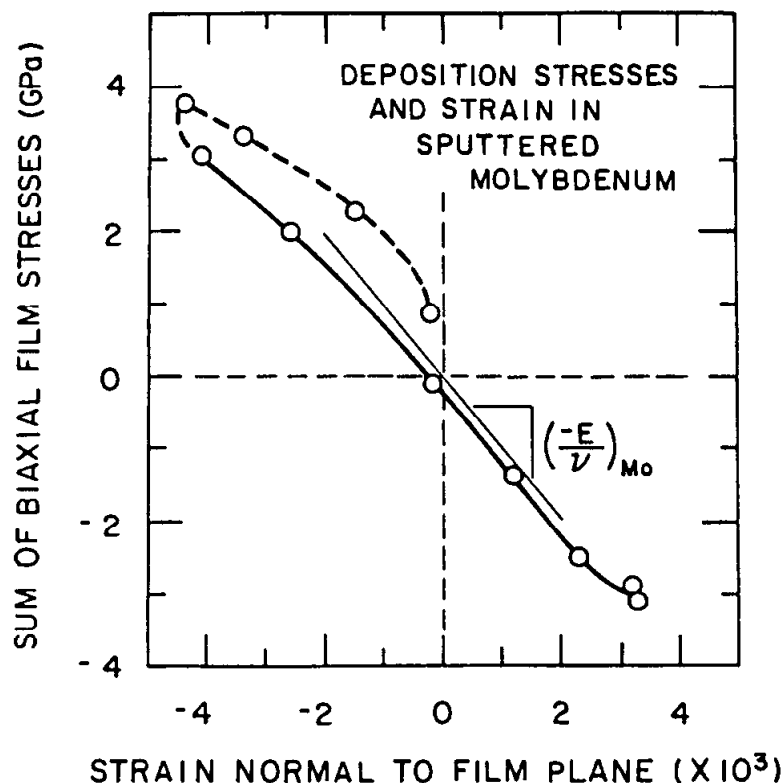


**Figure 9:** Sum of biaxial film stresses vs X-ray lattice strain in Mo films sputtered at various rates from a cylindrical magnetron with argon at 0.74 Pa pressure and deposited at a distance of 0.1 m (140).



The loop at the top of the curve corresponds to films in Zone 1' where the increasing microporosity gives rise to non-linear behavior. Again by varying only the sputtering rate, molybdenum films with tensile, zero, and compressive stress were deposited onto lacquered ABS plastic substrates of the type frequently used for decorative metallization. The low magnification photographs of Fig. 10 show the resultant cracked, specular, and buckled coatings. For such an application, where the substrate is non-conductive, heat-sensitive, and easily deformed, the technique of coincidental control is eminently suited by not requiring electrical coupling to the substrate and by the use of only a moderate amount of bombardment and consequent heating to achieve a stress-free, bulklike metallization.

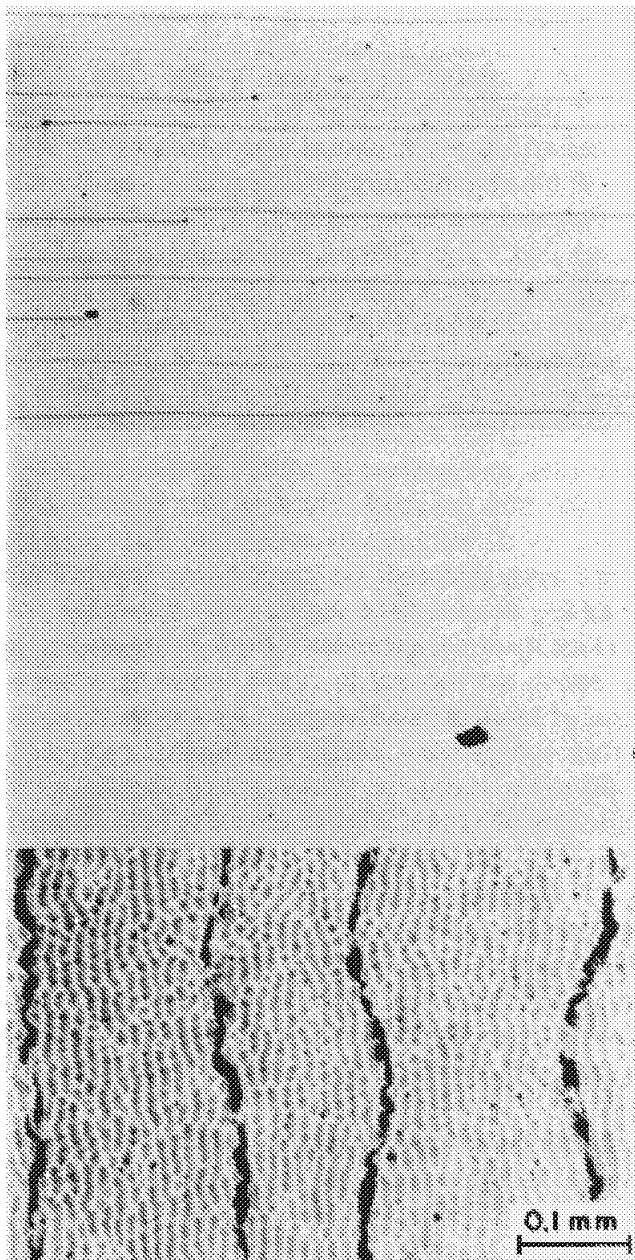


**Figure 10:** Coating failure modes on ABS plastic substrates observed by optical microscopy on molybdenum films sputter-deposited at rates of a) 0.23 nm/s, b) 1.5 nm/s, and c) 3.5 nm/s at a distance of 0.1 m from a cylindrical magnetron cathode operated in argon at 0.74 Pa pressure (140).

## 21.4 MODELLING OF MATTER-ENERGY CO-DEPOSITION IN REFRACTORY COATINGS

The differing positions of the Zone 1-T and Zone 1'priem -T boundaries in Fig. 4 are each determined by a balance of competing mechanisms, where the deposition of directionally diffuse coating flux favoring Zone 1' is clearly the more difficult for counteracting bombardment to overcome. The understanding and modelling of these two cases will necessarily also be distinct. A number of modelling approaches have been attempted for various sets of assumptions that throw light on portions of the processes at hand. These include ballistic computer simulations of various sophistication and scope, and parametric analysis based on continuum approximation. Ultimately it should be possible to formulate an analysis that will predict the dissimilar locations of the limiting boundaries and the interconnecting transition.

Brighton and Hubler (29) predict a critical ion-to-atom arrival ratio for relief of tensile intrinsic stress in the Zone 1-T structural transition by positing that the region affected by a collision cascade becomes effectively annealed and consequently stress free. Invoking the criterion that the input of binary collision cascades must be sufficiently dense to affect all deposited atoms, they obtained results agreeing in magnitude and energy dependence with observations on Hirsch and Varga (28) on bombarded germanium. While the mechanism of overlapping collision cascades is appealing, it lacks in this manifestation the capacity to simulate the continuous transition from tensile to compressive stress observed experimentally in a majority of cases.

The computer models of Müller (141,142) simulate the effects of energetic particle bombardment on the structures, densities, and stresses of vapor deposits incident without directional scattering, providing insights into the mechanisms at play in bombardment of both Zone 1 and Zone 1' microstructures. It has been demonstrated that energetic particle bombardment during growth can densify microporous structures by forward sputtering of condensed atoms from the advancing near-surface region into underlying pores in a steady state manner. Density increases have been simulated both by increasing the incident energy of metal vapor atoms above the thermal level (143) and by simultaneously bombarding with a secondary beam of inert or reactive gas. As expected, fewer bombarding gas atoms are required as their energy rises. Müller has found, however that pore bridging is promoted by transient diffusion during the dissipation of thermal spikes associated with energetic particle bombardment (144). Also observed is behavior suggesting the possibility of near-perfect epitaxy as the intensity of bombardment becomes great enough to eliminate microporosity. Müller has computed intrinsic stresses in the simulated films and found tensile stresses that pass through a maximum with increasing bombardment by inert gas or fast vapor atoms in a manner reminiscent of experimental observations (145). However, the experimentally observed continuous transition to compressive stress does not reasonably occur in the model, again raising a cautionary flag concerning the presently remaining deficiencies of the computer as an ultra-microscope.

The interchangeability of bombarding particle energy and flux can be quantitatively examined from Müller's results on Ni growing under Ar and self-bombardment (142,143). In Fig. 11 the reported packing densities have been replotted against the product of relative ion flux and the particle energy scaled to the sputtering threshold energy (21 eV) and raised to the powers of one (Fig. 11 (a)) and one-half (Fig. 11(b)). Four sets of results are included for nickel bombarded with varying fluxes of argon at 10

and 50 eV, at varying voltages with a fixed flux ratio, and with the nickel vapor accelerated in the absence of argon. Straight lines indicate the effect of varying the ion flux from 0 to 0.16 at the constant accelerating voltages of 10, 25, 50, 75, and 100 eV. Intermediate flux points reported by Müller at 10 and 50 eV are also indicated. Figure 11 reveals that the square-root scaling of energy affords a consolidation of results along a linear trendline.

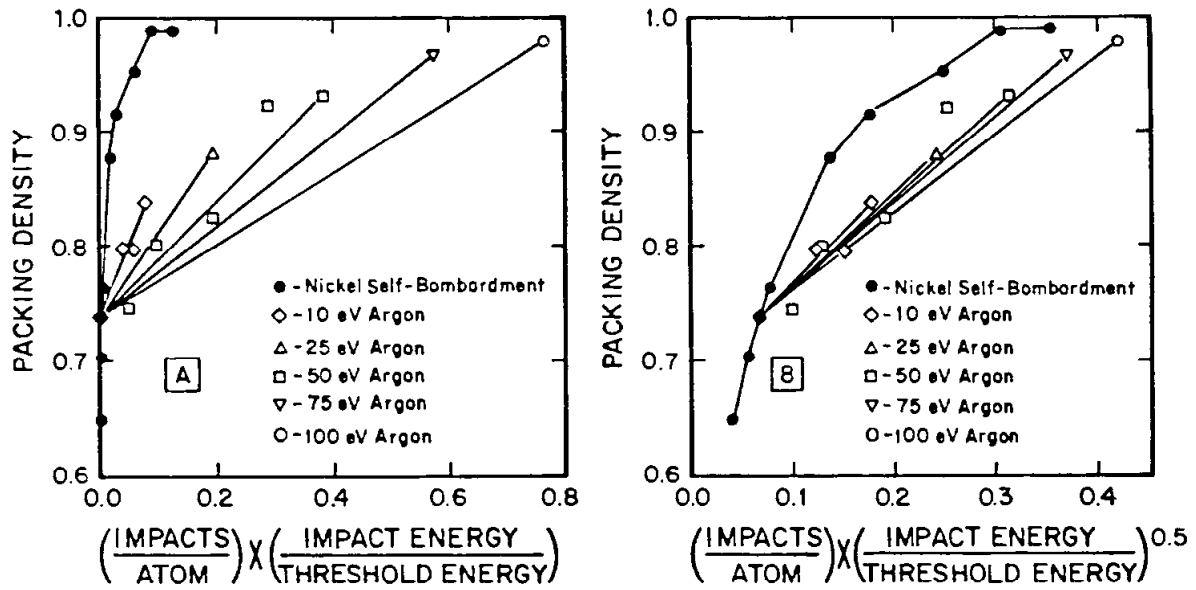


**Figure 11:** Simulated packing densities of nickel vapor deposits determined by molecular dynamics computer modelling showing the densifying effects of Ni self-bombardment and supplementary argon bombardment (142,143). Scaling the bombarding particle energy to a) the first power and b) the one-half power reveals a linearization of results versus the square root.

On the other hand, Yehoda et al. (146) find their experimental observations of void fraction in ion bombarded germanium to scale as the first power of energy, in agreement with the findings of Ziemann and Kay (30) for bias sputtering. Thus, in general it appears that changes in density and derivative properties caused by irradiation with particles having energies in range of 10-100 eV or greater can be represented by functionality of the form

$$X - X_0 = \beta \cdot (J_i/J_v) \cdot (E_i/E_0)^p \quad (1)$$

where  $X$  is a property of interest for which  $X_0$  is a reference value,  $J_i/J_v$  is the ion-to-vapor ratio, and  $E_i/E_0$  is the ratio of ion energy to a reference energy such as the sput-

tering threshold energy. The slope  $\beta$  is independent of the ion flux and particle energies but will depend on the relative ion and vapor atomic masses. The findings of 0.5 and 1.0 for the exponent  $p$  respectively for Ni and Ge may relate to the different natures of interatomic bonding in these materials (or to the two-dimensional nature of the simulation). Processing to a constant or completion value of  $X = X_c$ , say 95 percent density, enables a determination of  $p$  from the negative slope of  $\log(J_i)$  vs  $\log(E_i)$  as originated by Hoffman and Gaertner (26) and developed by Harper et al (27).

Of special significance for plasma sputtered coatings are the results for self-bombardment ( $J_i/J_v = 1$ ) shown in Fig. 11, where the individual particle energies varied from 0 to 2.6 eV. In contrast to gas bombardment it is clear that self-bombardment at low particle energies does not scale linearly with the square-root of energy, and is, moreover, more effective in increasing the packing density than bombardment with fewer but higher energy gas ions. These various observations imply, on the one hand, that a category of displacement mechanism dominates for bombardment with 10-100 eV particles, where the number of impacts and the particle energy are interchangeable in their effect and may be substituted one for the other using an energy scaling exponent that varies among classes of materials with different bonding types. On the other hand, the rather different behavior under low energy self-bombardment implies a fundamental change in the nature of the displacement cascades that more effectively suppresses microporosity. As pointed out by Müller (144), the self-energies required to simulate full density nickel fall well within the range of sputtered particle energies.

It seems evident that an advantageous route to achieving Zone T microstructures and properties in plasma sputtered refractory coatings with the least application of force is to take the greatest possible advantage of the self energies of the sputtered vapor particles. This is the situation represented along locus C in Fig. 4, achieved by sputtering at low pressures with ions heavier than the target atoms, so that vapor particles are the principal energetic species exiting the source. Additional atomic peening by higher energy gas neutrals reflected from the sputtering target should be largely unnecessary, although in many practical cases unavoidable. Where practical or desirable it should be possible to obtain Zone T microstructures with the most bulklike physical properties by judicious choice of gas and/or target material to minimize the energy of backscattered neutrals, thereby minimizing gas entrapment and gratuitous damage to the coating or substrate. Indeed under careful process tuning the possibility of epitaxial growth by coincidental control with a minimum of substrate heating is indicated. Where necessary, Zone T deposition can be attained under increased peening by backscattered neutrals or bias sputtering. Although the point of view adopted herein has been to apply just sufficient bombardment to overcome microporosity as promoted by directional scattering of the vapor flux, situations may arise in practice, say when sputtering heavy metals with argon, where gas scattering of the vapor is purposely increased to balance off excess atomic peening by backscattered neutrals.

In some cases, the excess bombardment and consequent compressive residual stress may be desired. It is commonly observed that the compressive residual stresses appear to reach a saturation level in coatings sputtered with sufficient bias or coincidental bombardment. From a consideration of the linear cascade theory of forward sputtering Windischmann (147) has shown that these saturation stresses correlate remarkably well with the product of elastic Young's modulus and molar volume over a wide selection of elements and nitrides sputtered from both plasma and ion beam sources. Of particular

interest are his observations of Zone T properties in ion beam sputtered coatings of aluminum, aluminum nitride, and silicon. The fact that these elements are less massive than the argon sputtering ion implies that backscattered neutrals carried little energy to the coatings and that coincidental self-bombardment by the sputtered vapor was indeed sufficient to densify the structure into the Zone T configuration.

In summary, experimental and simulation studies have provided a fundamental understanding of the porous and evolutionary nature of the primitive Zone 1 growth structures of vapor deposited refractory materials, however the effect of directional diffusion of the vapor by gas scattering in plasma processes adds an additional factor that leads to marked further structural disorder and degradation of properties in Zone 1'. Application of energetic particle bombardment works to counteract these effects leading to densification and Zone T microstructure with bulklike properties and compressive residual stresses, when sufficient doses are administered to counteract low adatom mobility and the preferential accumulation on growth tips caused by oblique components of scattered vapor. The latter effect requires greater offsetting doses by conventional bias sputtering with consequent undesirable side effects such as gas entrapment and substrate damage. An alternative plasma deposition treatment is coincidental control, which effects a reduction of vapor scattering in concert with greater or lesser bombardment, depending on the choice of target and gas constituents, to enter Zone T. It appears that the critical bombardment for densification may follow a power scaling law, when administered by gas ions, but may be most effective requiring the least treatment, when administered by low energy vapor self-bombardment.

## 21.5 REFERENCES

1. B.A. Movchan and A.V. Demchishin, Study of the structure and properties of thick vacuum condensates of nickel, titanium, tungsten, aluminum oxide and zirconium oxide. Fiz. Metal. Metalloved. 28: 653 (1969).
2. D.J. Srolovitz, A. Mazar, and B.G. Bukiet, Analytical and numerical modeling of columnar evolution in thin films. J. Vac. Sci. Technol. A6: 2371 (1988).
3. J.A. Thornton, Influence of apparatus geometry and deposition conditions on the structure and topography of thick sputtered coatings. J. Vac. Sci. Technol. 11: 666 (1974).
4. J.A. Thornton and D.W. Hoffman, Stress-related effects in thin films, Thin Solid Films, in press.
5. W.D. Westwood, Porosity in sputtered platinum films, J. Vac. Sci. Technol. 11: 466 (1974).
6. S. Nakahara, K. Kuwahara, and A. Nishimura, Microstructure of permalloy and copper films obtained by vapor deposition at various incidence angles. Thin Solid Films 72: 297 (1980).
7. D. Henderson, M.H. Brodsky, and P. Chaudhari, Simulation of structural anisotropy and void formation in amorphous thin films. Appl. Phys. Lett. 25: 641 (1974).
8. S. Kim, D. Henderson, and P. Chaudhari, Computer simulation of amorphous thin films of hard spheres. Thin Solid Films 47: 155 (1977).

9. P. Meakin, R. Ramanlal, L.M. Sander, and R.C. Ball, Ballistic deposition on surfaces. Phys. Rev. A 34: 5091 (1986).
10. P.M. Fabis, Microporosity in 304 stainless steel films prepared by vapor quenching. Thin Solid Films 128: 57 (1985).
11. A.G. Dirks and H.J. Leamy, Columnar microstructure in vapor deposited thin films. Thin Solid Films 47: 219 (1977).
12. H.J. Leamy and A.G. Dirks, Microstructure and magnetism in amorphous rare-earth transition-metal thin films. I. Microstructure. J. Appl. Phys. 49: 3430 (1978).
13. R.C. Ball and T.A. Witten, Causality bound on the density of aggregates. Phys. Rev. A 29: 2966 (1984).
14. P. Meakin, Effects of particle drift on diffusion-limited aggregation. Phys. Rev. B 28: 5221 (1983).
15. D.W. Hoffman and J.A. Thornton, Internal stresses in sputtered chromium. Thin Solid Films 40: 355 (1977).
16. D.W. Hoffman and J.A. Thornton, Internal stresses in Cr, Mo, Ta, and Pt films deposited by sputtering from a planar magnetron source. J. Vac. Sci. Technol. 20: 355 (1982).
17. R. Messier, A.P. Giri, and R.A. Roy, Revised structure zone model for thin film physical structure. J. Vac. Sci. Technol. A2: 500 (1984).
18. J.E. Yehoda and R. Messier, Are thin films physical structures fractals? Appl. Surf. Sci. 22/23: 590 (1985).
19. R. Messier, Toward a quantification of thin film morphology. J. Vac. Sci. Technol. A4: 490 (1986).
20. J.A. Thornton, The microstructure of sputter-deposited coatings. J. Vac. Sci. Technol. A4: 3059 (1986).
21. H.J. Leamy, G.H. Gilmer and A.G. Dirks, The microstructure of vapor deposited thin films. Current Topics in Materials Science 6: 309 (1980).
22. J. M. Seeman, Bias sputtering: its techniques and applications. Vacuum 17: 129 (1967).
23. O. Christensen, Characteristics and applications of bias sputtering. Solid State Technol. 13: 39 (1970).
24. J. L. Vossen, Control of film properties by rf-sputtering techniques. J. Vac. Sci. Technol. 8: 12 (1971).
25. W. D. Westwood, Glow discharge sputtering. Progr. in Surf. Sci. 7: 71 (1976).
26. D. W. Hoffman and M. R. Gaertner, Modification of evaporated chromium by concurrent ion bombardment. J. Vac. Sci. Technol. 17:425 (1980).
27. J.M.E. Harper, J.J. Cuomo, R.J. Gambino and H.R. Kaufman, Modification of thin film properties by ion bombardment during deposition. p. 127 in Ion Bombardment Modification of Surfaces, ed. by O. Auciello and R. Kelly (Elsevier, Amsterdam 1984).
28. E. H. Hirsch and I.K. Varga, Thin film annealing by ion bombardment. Thin Solid Films 69: 99 (1980).

29. D. R. Brighton and G. K. Hubler, Binary collision cascade prediction of critical ion-to-atom arrival ratio in the production of thin films with reduced intrinsic stress. Nucl. Instr. and Meth. B28: 527 (1987).
30. P. Ziemann and E. Kay, Model of bias sputtering in a dc-triode configuration applied to the production of Pd films. J. Vac. Sci. Technol. 21: 828 (1982).
31. P. Ziemann and E. Kay, Correlation between the ion bombardment during film growth of Pd films and their structural and electrical properties. J. Vac. Sci. Technol. A1: 512 (1983).
32. E. Kay and G. Heim, Model of bias sputtering applied to the control of Nb film properties. J. Appl. Phys. 49: 4862 (1978).
33. J. A. Thornton, The influence of bias sputter parameters on thick copper coatings deposited using a hollow cathode. Thin Solid Films 40: 335 (1977).
34. W.D. Davis and T. A. Vanderslice, Ion energies at the cathode of a glow discharge. Phys. Rev. 131: 219 (1963).
35. R. T. C. Tsui, Calculation of ion bombarding energy and its distribution in rf sputtering. Phys. Rev. 168: 107 (1968).
36. J.W. Coburn and E. Kay, Positive-ion bombardment of substrates in rf glow discharge sputtering. J. Appl. Phys. 43: 4965 (1972).
37. D.G. Teer, Adhesion of ion plated films and energies of deposition. J. Adhes. 8: 289 (1977).
38. D. M. Mattox, Film deposition using accelerated ions, Electrochem. Tech. 2: 295 (1964).
39. R.L. Boxman and S. Goldsmith, Cathode-spot arc coatings: physics, deposition and heating rates and some examples. Surf. and Coat. Technol. 33: 153 (1987).
40. B. Window and N. Savvides, Charged particle fluxes from planar magnetron sources. J. Vac. Sci. Technol. A4: 196 (1986).
41. N. Savvides and B. Window, Unbalanced magnetron ion-assisted deposition and property modification of thin films. J. Vac. Sci. Technol. A4: 504 (1986).
42. R. Frerichs, Superconductive films made by protected sputtering of tantalum or niobium. J. Appl. Phys. 33: 1898 (1962).
43. L.I. Maissel and P. M. Schaible, Thin films deposited by bias sputtering. J. Appl. Phys. 36: 237 (1965).
44. J. A. Thornton, High rate sputtering techniques. Thin Solid Films 80: 1 (1980).
45. J. L. Vossen and J. J. Cuomo, p. 56 in Thin Film PRocesses ed. by J. L. Vossen and W. Kern (Academic Press, New York 1978).
46. J. J. Cuomo, J.M.E. Harper, C.R. Guarnieri, D.S. Yee, L.J. Attanasio, C.T. Wu and R. H. Hammond, Modification of niobium film stress by low-energy ion bombardment during deposition. J. Vac. Sci. Technol. 20: 349 (1982).
47. H. F. Winters and E. Kay, Gas incorporation into sputtered films. J. Appl. Phys. 38: 3928 (1967).
48. J. Comas and E. A. Wolicki, Argon content in (111) silicon for sputtering energies below 200 eV. J. Electrochem. Soc. 117: 1197 (1970).

49. I. V. Mitchell and R. C. Maddison, Gas incorporation in sputtered and evaporated gold films. Vacuum 21: 591 (1971).
50. G. Heim and E. Kay, Ion implantation during film growth and its effect on the superconducting properties of niobium. J. Appl. Phys. 46: 4006 (1975).
51. E. Klokholm and B.S. Berry, Intrinsic stress in evaporated metal films. J. Electrochem. Soc. 115: 823 (1968).
52. K.-H. Müller, Ion-beam induced epitaxial vapor-phase growth: A molecular-dynamics study. Phys. Rev. B 35: 7906 (1987).
53. R. E. Jones, C. L. Standley and L.I. Maissel, Re-emission coefficients of Si and SiO<sub>2</sub> films deposited through rf and dc sputtering. J. Appl. Phys. 38: 4656 (1967).
54. L. I. Maissel, R.E. Jones and C.L. Standley, Re-emission of sputtered SiO<sub>2</sub> during growth and its relation to film quality. IBM J. Res. and Dev. 14: 76 (1970).
55. J. L. Vossen and J. J. O'Neill, Jr., rf Sputtering processes. RCA Review 29: 149 (1968).
56. A. G. Blachman, Stress and resistivity control in sputtered molybdenum films and comparison with sputtered gold. Met. Trans. 2: 699 (1971).
57. E. H. Hirsch and I.K. Varga, Thin film annealing by ion bombardment. Thin Solid Films 69: 99 (1980).
58. D. M. Mattox and G. J. Kominiak, Structure modification by ion bombardment during deposition. J. Vac. Sci. Technol. 9: 528 (1971).
59. R. D. Bland, G.J. Kominiak and D. M. Mattox, Effect of ion bombardment during deposition on thick metal and ceramic deposits. J. Vac. Sci. Technol. 11: 671 (1974).
60. J. E. Greene and S. A. Barnett, Ion-surface interactions during vapor phase crystal growth by sputtering, MBE and plasma enhanced CVD: Applications to semiconductors. J. Vac. Sci. Technol. 21: 285 (1982).
61. G. K. Wehner, Growth of solid layers on substrates which are kept under ion bombardment before and during deposition, U. S. Patent 3,021,271 Feb. 1962.
62. T. N. Kennedy, Sputtered insulator film contouring over substrate topography. J. Vac. Sci. Technol. 13: 1135 (1976).
63. C. Y. Ting, V. J. Vivalda and H. G. Schaefer, Study of planarized sputter-deposited SiO<sub>2</sub>. J. Vac. Sci. Technol. 15: 1105 (1978).
64. H. P. Bader and M. A. Lardon, Planarization by rf bias sputtering of aluminum as studied experimentally and by computer simulation. J. Vac. Sci. Technol. A3: 2167 (1985).
65. N. McIntyre and S.J. Wright, Characterization of bias sputtered metallization for IC technology. Vacuum 34: 963 (1984).
66. Y. Homma and S. Tsunekawa, Planar deposition of aluminum by rf/dc sputtering with rf bias. J. Electrochem. Soc. 132: 1466 (1985).
67. D. W. Skelly and L. A. Gruenke, Significant improvement in step coverage using bias sputtered aluminum. J. Vac. Sci. Technol. A4: 457 (1986).
68. J. F. Smith, Influence of dc bias sputtering during aluminum metallization. Solid State Technology 27: 135 (1984).



69. J. F. Smith, F.T. Zold and W. Class, The influence of bias sputtering and wafer preheating on the step coverage of sputtered aluminum. Thin Solid Films 96: 291 (1982).
70. J. J. Cuomo, R. J. Gambino and R. Rosenberg, The influence of bias on the deposition of metallic films in rf and dc sputtering. J. Vac. Sci. Technol. 11: 34 (1974).
71. A. G. Blachman, dc bias-sputtered aluminum films. J. Vac. Sci. Technol. 10: 299 (1973).
72. C. W. Chen and C. S. Alford, Optimization of the sputter deposition process for preparing smooth coatings of beryllium on microspherical substrates. J. Vac. Sci. Technol. A6: 128 (1988).
73. J.W. Patten and E.D. McClanahan, Effect of substrate bias and deposition temperature on the properties of thick sputtered chromium deposits. J. Appl. Phys. 43: 4811 (1972).
74. J.W. Patten, E.D. McClanahan and J.W. Johnston, Room temperature recrystallization in thick bias-sputtered copper deposits. J. Appl. Phys. 42: 4371 (1971).
75. B. Window, F. Sharples and N. Savvides, Plastic flow in ion-assisted deposition of refractory metals. J. Vac. Sci. Technol. A6: 2333 (1988).
76. R. Glang, R. A. Holmwood and P.C. Furois, Bias sputtering of molybdenum films. Proc. 3rd. Int. Vacuum Congress, Stuttgart, v.2, pt.3, (Pergamon, 1966-67).
77. F. M. d'Heurle, Resistivity and structure of sputtered molybdenum films, Trans. AIME 236: 321 (1966).
78. R. S. Nowicki, W. D. Buckley, W. D. Mackintosh and I.V. Mitchell, Effect of deposition parameters on properties of rf sputtered molybdenum films. J. Vac. Sci. Technol. 11: 675 (1974).
79. C. T. Wu, Intrinsic stress of magnetron-sputtered niobium films. Thin Solid Films 64: 103 (1979).
80. T. Lin, K.Y. Ahn, J.M.E. Harper, P.B. Madakson and P.M. Fryer, Relationship between substrate bias and microstructure in magnetron sputtered Al-Cu films. Thin Solid Films 154: 81 (1987).
81. C. Leu, G. Chen, J. M. Sivertsen and J. H. Judy, Epitaxial growth of Co-Cr films and their characterization. J. Appl. Phys. 57: 4003 (1985).
82. M. Ohkoshi and T. Kusuda, Effect of negative substrate bias on the film structure and magnetic properties in sputter-deposited Co-Cr films. J. Vac. Sci. Technol. A5: 2859 (1987).
83. S. M. Shin, M.A. Ray, J.M. Rigsbee and J.E. Greene, Growth of metastable  $\text{Cu}_{1-x}\text{Cr}_x$  solid solutions by ion mixing. Appl. Phys. Lett. 43: 249 (1983).
84. P. Chaudhari, J.J. Cuomo and R.J. Gambino, Amorphous metallic films for bubble domain applications, IBM J. Res. Dev. 17: 66 (1973).
85. R. J. Gambino and J.J. Cuomo, Selective resputtering-induced anisotropy in amorphous films. J. Vac. Sci. Technol. 15: 296 (1978).
86. T. Kusuda, S. Honda and M. Ohkoshi, Perpendicular anisotropy of bias-sputtered GdCo film. J. Appl. Phys. 53: 2338 (1982).

87. C. T. Chen and W.L. Wilson, Jr., Magnetic properties of bias-sputtered Gd-Co-Fe amorphous films with uniaxial perpendicular anisotropy. J. Appl. Phys. 49: 1756 (1978).
88. E. Stern and T.B. Light, Preferred orientation in bias-sputtered nickel chromium films. Appl. Phys. Lett. 13: 381 (1968).
89. R. W. Knoll, E.D. McClanahan and H. E. Kjarmo, Heterogeneous growth in transition metal-rare earth films during bias sputter deposition. Thin Solid Films 118: 93 (1984).
90. L. D. Hartsough, Resistivity of bias-sputtered Ti-W films. Thin Solid Films 64: 17 (1979).
91. B. Eser, R.E. Ogilvie and K.A. Taylor, The Effect of bias on dc and rf sputtered WC-Co coatings. Thin Solid Films 67: 265 (1980).
92. S. D. Dahlgren and A. G. Graybeal, Reduced nickel concentration in a stainless steel deposit from bias sputtering. J. Appl. Phys. 41: 3181 (1970).
93. T. Goto and P. Anprung, Fabrication of NbN films by dc bias sputtering and their application to superconducting bridges. Jpn. J. Appl. Phys. (Part 1) 22: 955 (1983).
94. L.C. Wu, J.L. Zilko, J.L. Mukherjee, J.E. Greene and H.E. Cook, Tribology, chemistry and structure of bias sputtered TiC films on steel substrates, p. 364. in Wear of Materials ed. by W.A. Glaeser, K.C. Ludema and S.K. Rhee, (ASME, New York 1977).
95. J.-E. Sundgren, B.-O. Johansson and S.-E. Karlsson, Influence of substrate bias on composition and structure of reactively rf-sputtered TiC films. Thin Solid Films 80: 77 (1981).
96. Y. Igasaki and H. Mitsuhashi, The Effects of substrate bias on the structural and electrical properties of TiN films prepared by reactive rf sputtering. Thin Solid Films 70: 17 (1980).
97. J. M. Poitevin, G. Lamperiere and J. Tardy, Influence of substrate bias on the composition, structure and electrical properties of reactively dc sputtered TiN films. Thin Solid Films 97: 69 (1982).
98. W.W. Carson, Sputter gas pressure and dc substrate bias effects on thick rf diode sputtered films of Ti-Oxycarbides. J. Vac. Sci. Technol. 12: 845 (1975).
99. J.E. Greene, R.E. Klinger, L.B. Welsh and F.R. Szofran, Growth and characterization of doped ZrO<sub>2</sub> and CeO<sub>2</sub> films deposited by bias sputtering. J. Vac. Sci. Technol. 14: 177 (1977).
100. R. W. Knoll and E.R. Bradley, Correlation between the stress and microstructure in bias-sputtered ZrO<sub>2</sub> – Y<sub>2</sub>O<sub>3</sub> films. Thin Solid Films 117: 201 (1984).
101. D. M. Mattox and G.J. Kominiak, Physical properties of thick sputter-deposited glass films, J. Electrochem. Soc. 120: 1535 (1973).
102. K.L. Chopra, Thin Film Phenomena (McGraw-Hill, New York, 1969) p.311.
103. P.R. Stuart, Some measurements of stress in thin films prepared by low pressure triode sputtering. Vacuum 19: 507 (1969).
104. R. Messier, T. Takamori, and R. Roy, Structure-composition variation in rf-sputtered films of Ge caused by process parameter changes. J. Vac. Sci. Technol. 13: 1060 (1976).

105. F. Shoji and S. Nagata, Internal stress in thin metal films prepared by low pressure plasma sputtering. Oyo Butsuri 42: 115 (1973).
106. E. Krikorian and R.J. Sneed, Deposition of tantalum, tantalum oxide, and tantalum nitride with controlled electrical characteristics. J. Appl. Phys. 37: 3674 (1966).
107. S.S. Lau and R.H. Mills, Properties of rf sputtered  $\beta$  -Ta films. Phys. Stat. Sol.(a) 17: 609 (1973).
108. W.W.Y. Lee, High resistivity of dc-sputtered metal films. J. Appl. Phys. 42: 4366 (1971).
109. R.C. Sun, T.C. Tisone, and P.D. Cruzan, Internal stresses and resistivity of low-voltage sputtered tungsten films, J. Appl. Phys. 44: 1009 (1973).
110. R.S. Wagner, A.K. Sinha, T.T. Sheng, H.J. Levinstein, and F.B. Alexander, Tungsten metallization for LSI applications. J. Vac. Sci. Technol. 11: 582 (1974).
111. S.P. Murarka, R.F. diode sputtered platinum films. Thin Solid Films 23: 323 (1974).
112. J.A. Thornton and D.W. Hoffman, Internal stresses in Ti, Ni, Mo and Ta films deposited by cylindrical magnetron sputtering. J. Vac.Sci. Technol. 14: 164 (1977).
113. D.W. Hoffman and J.A. Thornton, The compressive stress transition in Al, V, Zr, Nb, and W metal films sputtered at low working pressures. Thin Solid Films 45: 387 (1977).
114. T. Motohiro and Y. Taga, Monte carlo simulation of thermalization process of sputtered particles. Surf. Sci. 134: L494 (1983).
115. A. Graz-Marti and J.A. Valles-Abarca, Slowing down and thermalization of sputtered particle fluxes: Energy distributions. J. Appl. Phys. 54: 1071 (1983).
116. R. E. Somekh, The thermalization of energetic atoms during the sputtering process. J. Vac. Sci. Technol. A2: 1285 (1984).
117. D.W. Hoffman and C.M. Kukla, Determination of film stresses during sputter deposition using an in situ probe. J. Vac. Sci. Technol. A3: 2600 (1985).
118. R.W. Hoffman, Mechanical properties of thin condensed films. in Physics of Thin Films Vol. 3: G. Hass and R.E. Thun, eds. (Academic Press, New York, 1966).
119. J.Z. Briggs and R.Q. Barr, Molybdenum. in Metals Handbook Ninth Edition, Vol. 2 (American Society for Metals, Metals Park, Ohio, 1979) p. 771.
120. J.E. Nestell,Jr. and R.W. Christy, Reflectance and structure of evaporated chromium and molybdenum films. J. Vac. Sci. Technol. 15: 366 (1978).
121. D.W. Hoffman, Stress and property control in sputtered metal films without substrate bias. Thin Solid Films 107: 353 (1983).
122. F. D'Heurle, Aluminum films deposited by rf sputtering. Metall. Trans. 1: 725 (1970).
123. D.W. Hoffman and J.A. Thornton, Compressive stress and inert gas in Mo films sputtered from a cylindrical-post magnetron with Ne, Ar, Kr, and Xe. J. Vac. Sci. Technol. 17: 380 (1980).
124. J.A. Thornton and D.W. Hoffman, Internal stresses in amorphous silicon films deposited by cylindrical magnetron sputtering using Ne, Ar, Kr, Xe, and Ar + H<sub>2</sub>. J. Vac. Sci. Technol. 18: 203 (1981).

125. W.W. Carson, Getter pumping to allow economical sputtering with xenon. Thin Solid Films 40: 385 (1977).
126. A. Bensaoula, J.C. Wolfe, A. Ignatiev, F-O. Fong, and T-S. Leung, Direct-current-magnetron deposition of molybdenum and tungsten with rf-substrate bias. J. Vac. Sci. Technol. A2: 389 (1984).
127. J.A. Thornton and D.W. Hoffman, The influence of discharge current on the intrinsic stress in Mo films deposited using cylindrical and planar magnetron sputtering sources. J. Vac. Sci. Technol. A3: 576 (1985).
128. D.W. Hoffman and P.J. Goodsmith, Decorative metallizing by magnetron sputtering - effects of geometry on film properties. Trans. SAE 88: 808 (1979).
129. D.W. Hoffman and J.A. Thornton, Effects of substrate orientation and rotation on internal stresses in sputtered metal films. J. Vac. Sci. Technol. 16: 134 (1979).
130. S.M. Rossnagel, Gas density reduction effects in magnetrons. J. Vac. Sci. Technol. A6: 19 (1988).
131. A. Entenberg, V. Lindberg, K. Fletcher, A. Gatesman, and R.S. Horwath, Stress measurement in sputtered copper films on flexible polyimide substrates. J. Vac. Sci. Technol. A5: 3373 (1987).
132. K.W. Bieg, Internal stress and mechanical properties of planar-magnetron-sputtered Mo-Ru-B alloys, Thin Solid Films 96: 161 (1982); K.W. Bieg, Characteristics of magnetron-sputtered metallic glass internal confinement fusion target materials. J. Vac. Sci. Technol. 20: 1347 (1982).
133. A.P. Thakoor, J.L. Lamb, R.M. Williams, and S.K. Khanna, Internal stresses in wear and corrosion resistant amorphous metallic coatings of  $(W_{0.6}Re_{0.4})_{76}B_{24}$  and  $(Mo_{0.6}Ru_{0.4})_{82}B_{18}$ . J. Vac. Sci. Technol. A3: 600 (1985).
134. R.E. Cuthrell, D.M. Mattox, C.R. Peebles, P.L. Dreike and K.P. Lamppa, Residual stress anisotropy, stress control and resistivity in post cathode magnetron sputter-deposited molybdenum films, J. Vac. Sci. Technol. A6: (1988).
135. G. Este and W.D. Westwood, Stress control in reactively sputtered AlN and TiN films, J. Vac. Sci. Technol. A5: 1892 (1987).
136. Z.H. Barber and R.E. Somekh, Magnetron sputtering of  $Cu_{55}Ni_{45}$ , Vacuum 34: 991 (1984).
137. Y. Hoshi, M. Matsuoka and M. Naoe, Dependence of magnetic properties of Co-Pt films on sputtering conditions. J. Appl. Phys. 57: 4022 (1985).
138. S. Nakahara, M. Hong, R.B. van Dover, E.M. Gyorgy, and D.D. Bacon, Microstructures of thin sputtered amorphous  $Tb_{0.26}Fe_{0.74}$  and polycrystalline Fe films. J. Vac. Sci. Technol. A4: 543 (1986).
139. A.F. Jankowski, R.M. Bionta, and P.C. Gabriele, Internal stress minimization in the fabrication of transmissive multilayer X-ray optics. J. Vac. Sci. Technol. A6: in press.
140. D.W. Hoffman and C. Peters, Control of stress and properties in sputtered metal films on nonconductive and heat-sensitive substrates. in Proceedings of the IXth Int. Vac. Cong. and Vth Int. Conf. on Sol. Surf. (Asociacion Espanola Del Vacio, Madrid, 1983) p. 415.

141. K.-H. Müller, Model for ion-assisted thin-film densification, J. Appl. Phys. 59: 2803 (1986).
142. K.-H. Müller, Ion-beam-induced epitaxial vapor-phase growth: A molecular-dynamics study. Phys. Rev. B 35: 7906 (1987).
143. K.-H. Müller, Role of incident kinetic energy of adatoms in thin film growth. Surf. Sci. 184: L375 (1987).
144. K.-H. Müller, Monte Carlo calculation for structural modifications in ion-assisted thin film deposition due to thermal spikes. J. Vac. Sci. Technol. A4: 184 (1986).
145. K.-H. Müller, Stress and microstructure of sputter-deposited thin films: Molecular dynamics investigations, J. Appl. Phys. 62: 1796 (1987).
146. J.E. Yehoda, B. Hand, K. Vedam, and R. Messier, Investigation of the void structure in amorphous Germanium thin films as a function of low-energy ion bombardment. J. Vac. Sci. Technol. A6: 1631 (1988).
147. H. Windischmann, An intrinsic stress scaling law for polycrystalline thin films prepared by ion beam sputtering. J. Appl. Phys. 62: 1800 (1987).

---

# INDEX

---

abnormal glow	420	bias sputtering	409,489
activation energy	267	black silicon	215
activated reactive evaporation	370	Bohm diffusion	170,189
activation energy	17	Bohm pre-sheath effects	169
adhesion	438	bombardment effects	341
adiabatic expansion	357	bombardment induced	
adiabatic invariants	27	amorphization	128
alloy evaporation	7	decomposition	96,121
alloy sputtering	7,91	mixing	95
AlCu etching	199	segregation	93,112
amorphous Si deposition	395	bombardment-structure	
angular yield	75,84	relations	455
anode	47	broad beam sources	183
anode sheath	54	bromine chemistry	200
arcing	246	bulk binding energy	102
arc coatings	436		
arc control	427		
arc current	424	cascade	70
arc filtering	429	cascade sputtering	100
arc initiation	426	catcher electrode	147
arc ionization	419	cathode	47
arc source design	425	cathode poisoning	163
arc spots	421	cathode sheath	52,56
ARE systems	378	cathodic arc	421
area effects	310	cathode design	148
area ratios	264	cavity applicator	299
Arrhenius plots	275	charge exchange	35,54
Arrhenius rate	17	chemical binding	92
aspect ratios	205	chemical sputtering	85
associative recombination	35	chemical vapor deposition	388
asymmetric discharge	63	Child-Langmuir Law	38
		Child's law	168
backstreaming	394	chlorine chemistry	200
baffles	249	circulator	295
balanced rf system	148	cleanliness	222
barrel reactor	19	closed drift ion source	189
barrel plating	349	cluster beam optics	360
batch processing	223	cluster emission	237
bias voltage	264,312	cluster energy	358
		cluster formation	356

- |                              |         |                                |         |
|------------------------------|---------|--------------------------------|---------|
| cluster ionization           | 358     | dual ion beam sputtering       | 467,474 |
| CMOS                         | 4       | dual power supply              | 145     |
| cold cathode plasma          |         |                                |         |
| electron beam                | 379     |                                |         |
| collision frequency          | 30      | E x B drift                    | 26, 160 |
| collisions                   | 30      | E x B drift current            | 166     |
| Coloumb logarithm            | 32      | ECR                            | 20, 29  |
| compositional change         | 100     | ECR etching                    | 298     |
| compound evaporation         | 373     | ECR deposition                 | 298     |
| confined hollow cathodes     | 312     | ECR plasmas                    | 285     |
| conical magnetron            | 161     | ECR regions                    | 292     |
| contact hole etching         | 324     | effective collision frequency  | 43      |
| continuous arc sources       | 431     | effective ionization potential | 49      |
| continuum model              | 55      | electrical models              | 143     |
| critical density             | 304     | electron capture               | 35      |
| crystallographic orientation | 347     | electron density               | 16      |
| cubic boron nitride          | 380     | electron-electron collisions   | 32      |
| CVD reactions                | 390     | electron heating               | 39      |
| cyclotron frequency          | 25,286  | electron mirror                | 311     |
| cylindrical magnetron        | 161     | electron mobility              | 40      |
|                              |         | electron multiplication        | 48      |
|                              |         | electron-neutral collisions    | 31      |
| dc breakdown                 | 47      | electron saturation            | 60      |
| dc glow discharge            | 51      | electron temperature           | 16,166  |
| Debye length                 | 21      | electron volt                  | 15      |
| Debye shielding              | 20      | electronic excitation          | 33      |
| Debye sphere                 | 22      | electronic properties, a-Si    | 401     |
| densification                | 460     | electrostatic arc confinement  | 427     |
| density                      | 345,507 | elastic collisions             | 31      |
| deposition probability       | 173     | end-Hall source                | 190     |
| device applications          | 402     | endpoint detection             | 225     |
| device processing            | 323     | energetic neutral detection    | 178     |
| diamond films                | 279     | energetic neutrals             | 449     |
| dielectric films             | 271     | energetic, reflected neutrals  | 176     |
| diffuse arcs                 | 425     | energy coupling                | 286     |
| diffuse arc systems          | 433     | energy distribution of         |         |
| diffusion                    | 36      | sputtered atom                 | 86      |
| diode plasmas                | 309     | energy reflection              | 76      |
| diode sputtering             | 240     | enhanced surface mobility      | 342,364 |
| directional coupler          | 295     | environmental film stability   | 478     |
| discharges                   | 14      | epitaxial silicon              | 274     |
| discharge current            | 169     | epitaxial temperature          | 364     |
| dished grids                 | 186     | equilibrium rearrangement      | 128     |
| dislocation loop density     | 461     | equilibrium segregation        | 111     |
| dissociative ionization      | 35      | equivalent circuit             | 294     |
| dissociative attachment      | 35      | etch directionality            | 200     |
| drift velocity               | 40      | etch selectivity               | 211     |
| doping effects on etching    | 202     | etch uniformity                | 322     |
| downstream plasma            | 20      | etching damage                 | 325     |
| drop-in cathode              | 149     |                                |         |

evaporation	373	ICB acceleration voltage	362
extraction voltage	185	ICB nozzles	358
		implantation	216
		impurity atom resputtering	492
Faraday dark space	52	inelastic collision	33,261
feedback control	253	inelastic energy loss	71
film adhesion	344	in-situ diagnostics	403
film density	456	interconnected void network	485
film microstructure	483	internal stress	497
film property changes	494	ionization	33,53
film stress	272,452, 492	ionization, degree	14
		ionized cluster beam	356
flow effects	235	ion assisted deposition	338,411
fluorine chemistry	200		466
fractal	73	ion assisted evaporation	460
fractal dimension	73	ion saturation	60
fractal film growth	486	ion optics	186
frequency effects	143	ion beam current	185
		ion beam enhanced deposition	338
GaAs	277	ion beam self sputtering	434
gas conductivity	165	ion beam sputtering	255
gas dispersal rings	394	ion bombardment-property relations	451
gas flow	269	ion enhanced etching	200
gas heating	165	ion implantation	492
gas incorporation	347	ion plating	338,490
gas phase nucleation	349	ion surface interactions	448
gas rarefaction	164	ion-to-atom ratio	506
gate oxide breakdown	216		
gettering effects	348	L-type matching network	151
glow discharge	261	Langevin equation	40
gradient drift	27	Langmuir probe	167
grain growth	483	laser interferometry	225
gridded ion sources	184	lattice damage	216,219
gridless ion source	187	lattice distortions	453
guard confined diode	309	loading effect	209
gyroradius	24	low pressure plasma	293
		low temperature zone model	488
Helmholtz coil	29		
high voltage arcs	425	Kaufman ion sources	184
hollow cathode	311	knock-on sputtering	75
hollow cathode arc	380		
hollow cathode discharge	308		
hollow cathode electron source	308		
hot wall PECVD	270	macroparticles	422
hydrogen addition	209	magnetic arc confinement	427
hysteresis curve	234	magnetic enhancement	153
		magnetic field	160



- |                                |         |                               |           |
|--------------------------------|---------|-------------------------------|-----------|
| magnetic field effects on arcs | 422     | optical emission spectroscopy | 174,225   |
| magnetic field gradient        | 290     | orbits                        | 23        |
| magnetic mirror ECR            | 298     | oscillations                  | 23        |
| magnetic moment                | 27      | oxide sputtering              | 91        |
| magnetically enhanced          |         | oxygen addition               | 206       |
| deposition                     | 280     |                               |           |
| magnetron                      | 162     |                               |           |
| magnetron ion etching          | 224     | Paschen curve                 | 50        |
| magnetron sputtering           | 160,241 | patterning                    | 154       |
| mass differences               | 127     | PECVD                         | 9         |
| matching network               | 150     | PECVD systems                 | 269       |
| Maxwellian distribution        | 15,46   | Penning effects               | 34        |
| mean free path                 | 30      | phase shifts                  | 45        |
| metal contamination            | 216     | planar magnetron              | 161       |
| metastable ions                | 392     | planar reactor                | 18        |
| metastable state               | 33      | planarization                 | 2         |
| microstructural control        | 487     | planarization                 | 496       |
| microwave absorption           | 290     | plasma                        | 14        |
| microwave load                 | 295     | plasma chemistry              | 206       |
| microwave multipolar films     | 279     | plasma enhanced CVD           | 260       |
| microwave plasma disk reactor  | 299     | plasma enhanced reaction      | 268       |
| microwave plasmas              | 286     | plasma etching                | 11        |
| mirror ratio                   | 28      | plasma frequency              | 23        |
| mirror fields                  | 293     | plasma heating mechanisms     | 289       |
| mobile ion contamination       | 217     | plasma jet                    | 421       |
| modeling-sputtering            | 72      | plasma potential              | 53,59,263 |
| modified magnetrons            | 240     | plasma-source reactions       | 375       |
| molecular dynamics             | 77,455  | plasma-substrate reactions    | 376       |
| monitoring systems             | 252     | plasma-volume reactions       | 375       |
| morphology                     | 345     | point defect accumulation     | 128       |
| multicusp                      | 301     | Poisson's Eqn                 | 21        |
| multimode cavity               | 297     | polycrystalline silicon       | 273       |
| multiple ICB                   | 360     | polymer deposition            | 321       |
| multipole ECR plasma           | 300     | polymerization                | 207,319   |
|                                |         | post-RIE corrosion            | 217       |
|                                |         | positive column               | 52,57     |
| near zone                      | 44      | power balance                 | 41        |
| negative deposition            | 410     | power dissipation             | 248       |
| negative glow                  | 52-56   | power measurement             | 155       |
| negative ions                  | 176     | power splitting rf drive      | 150       |
| negative ion emission          | 238     | preferential sputtering       | 91,100    |
| nitrides                       | 5       | processing steps              | 2         |
| noble gas addition             | 209     | pulsed arc sources            | 431       |
| normal glow                    | 420     |                               |           |
| normal mode                    | 23      |                               |           |
| nucleation density             | 347,363 | radiative recombination       | 34        |
| numerical modeling             | 53,228  | racetrack magnetron           | 161       |
|                                |         | reactive arc effects          | 424       |
| optical coatings               | 476     | reactive deposition           | 371       |

reactive deposition	503	self bombardment	508
reactive evaporation	372	self limiting etch	417
reactive ICB	365	sheaths	36
reactive ion beams	185	shock zones	457
reactive ion etching	196	Si deposition	329
reactive sputtering	9,153,233	Si etching	326
reactive sputtering models	237	sidewall etching	315
reaction kinetics	237	sidewall passivation	203
reaction steps	266	silicides	277
reaction steps	196	silicon dioxide deposition	398
reactor materials	221	silicon dioxide etching	318
reactors	221	silicon nitride	9,251,400
recrystallization	346	silicon oxynitride	273,401
redeposition probability	173	single mode cavity	297
redistribution	97	single wafer processing	223
reflectance	225	skin depth	44
reflected energetic neutrals	342	space charge effects	362
reflection	76	space charge limited current	38
refractory metals	277	spikes	71
remote PECVD	387	sputter etch system	147
relative arrival rates	179	sputter ion plating	339
remote PECVD parameters	393	sputter rates	155
resputter fraction	489	sputter yield	71,81,413
resputtering	9	sputtered atom emission	86
retrograde motion	422	sputtered atom energy	177,508
RIE damage	215	sputtered atom transport	173,449
RIE parameters	198	sputtering	70
rf breakdown	50,141	sputtering wind	164
rf bias	302	step coverage	9,332
rf current measurement	156	sticking coefficient	412
rf deposition system	146	stochastic rearrangement	127
rf diode	140	stray capacitance	151
rf discharge	141	stress	346
rf discharge modeling	65	structure-zone models	484
rf driven electrodes	61	subcutaneous oxidation	403
rf glows	58	substrate bias	147
rf leakage	157	substrate bias effects	152
rf matching network	146	substrate precleaning	469
rf power supply	149	surface binding energy	98,361
rf self bias	141	surface binding energy, alloys	103
rf voltage measurement	157	surface binding energy, oxides	107
		surface cleaning	154
		surface coverage	347,411
scaling	314	surface damage	363
secondary electron	53,245	surface diffusion	116
segregation ratios	118	surface reaction layer	208
selective bias sputter etching	416	surface recovery (RIE)	220
selective deposition	409	surface residues	216
selectivity	320	surface roughness	216
self bias	59		

surface scattering	479	tri-electrode hollow cathode	317
surface topology	484	TRIM	72
surfatron	297	turbulence	246
symmetric discharge	63		
target erosion	244	unbalanced magnetron	491
thermal spikes	457	uniformity	155
thermal sputtering	96		
thermodynamics of			
evaporation	374	vacuum arcs	419
thermalization	171	vaporization sources	343
thin film transistors	273	void formation	332
Thornton-zone model	484	void fraction	507
throwing power	349	void incorporation	485
topography	495	volatility	92,128
Townsend ionization	47	voltage ratios	144
tuned substrate bias	150		
trench etching	328		
tri-electrode discharge	145	waveguide applicator	297